



**UNIVERSITÀ
DEGLI STUDI
DI BRESCIA**

**DOTTORATO DI RICERCA IN
INGEGNERIA CIVILE, AMBIENTALE, DELLA COOPERAZIONE
INTERNAZIONALE E DI MATEMATICA - DICACIM**

Settore Scientifico Disciplinare: ICAR/09

Riabilitazione Strutturale di Edifici Storici e Contemporanei

XXXV CICLO

**INFLUENCE AND ON-SITE ASSESSMENT OF LONG-
TERM PRESTRESSING LOSSES ON SHEAR
STRENGTH OF BRIDGE GIRDERS**

**DOTTORANDO:
Stefano Giuseppe Mantelli**

**RELATORE:
Chiar.mo Prof. Fausto Minelli**

SYNOPSIS

The assessment of the residual load-bearing capacity of a precast prestressed reinforced concrete bridge deck (PRC) after more than 50 years of service can be challenging, especially if it exhibits degradation defects due to poor or missing maintenance or even if it is affected by any kind of cracking due to stress. Following an inspection program carried out on over 400 bridges in the Province of Brescia, it emerged that 6% of the PRC bridges, corresponding to approximately 44% of the infrastructure assets of the bridge manager, exhibit shear cracks in the webs that are unexpected for the load conditions to which the bridge is usually subjected. The nature of these cracks can have various causes, including an overestimation of the contribution to shear resistance provided by the prestressing of the element during the design phase. From a survey in the field and the literature, it was discovered that precast companies in the 1970s-1980s produced prestressed elements with low shear reinforcement, or even without reinforcement in some cases. This was also found in German regulations before the 1970s for the production of prestressed elements. This is because, being a prestressed element, part of the shear resistance was given to the contribution of prestressing, providing a significant saving in terms of transverse reinforcement.

This research aims to investigate two aspects: the evaluation of the reliability of some diagnostic techniques proposed in the literature for the assessment of in-situ prestressing and the influence of prestress losses on the crack pattern and shear strength of full-scale bridge beams. For these purposes, an experimental program was conducted on 4 PRC beams with a length of 10 m, an 80 cm high I-section, and minimum web reinforcement. Two beams were constructed pre-stresses strands, which differ from each other by 30% of the assigned level of prestress. The other two identical beams were designed with a system of post-tensioning stands that allows the variation of the level of prestress in a controlled way, covering several long-term loss scenarios during the experiments. On these elements, three semi-destructive methods for in-situ prestressing evaluation based on tension release were applied: core trepanning, saw-cut at intrados, and blunt pyramidal specimen. In addition, a new method, similar to the parallel saw cuts at intrados, but performed on the web, is proposed and assessed. On this method, which proved to be the most reliable among the tested methods, 2D and 3D finite element models were also performed and discussed. Subsequently, a 3-point loading test was performed on each beam, evaluating the evolution of the crack pattern with the Digital Image Correlation (DIC) technique and comparing the results with those obtained from the numerical simulation performed with the VecTor 2 software based on Modified Compression Field theory (MCFT). During the various loading phases, it was evaluated whether a

SYNOPSIS

non-destructive investigation such as dynamic identification could detect damage due to shear cracking and a reduction in prestress loss. Finally, since the verification formulas for shear strength proposed by the models of various codes (e.g. Eurocode 2, *fib* - Model Code, CSA, ACI) are very conservative for prestressed elements with stirrups, an analytical formulation based on the draft of the *fib* - Model Code 2020 LoA IIb is proposed. The formulation was validated against to some experimental tests in the literature, obtaining good results.

SOMMARIO

La valutazione della capacità portante residua di un impalcato da ponte in calcestruzzo armato precompresso (CAP), dopo oltre 50 anni di esercizio può risultare difficile, soprattutto se esso mostra difetti di degrado a causa della scarsa/assenza di manutenzione o addirittura esibisce un quadro fessurativo anomalo. A seguito di una campagna di ispezioni svolta su oltre 400 ponti della Provincia di Brescia, è emerso come il 6% dei ponti in CAP, che corrispondono a circa il 44% del patrimonio infrastrutturale del gestore, mostra fessure a taglio nelle anime, anomale per le condizioni di carico a cui il ponte solitamente è sottoposto. La natura di queste fessure può essere di varia origine, tra cui una sovrastima in fase progettuale del contributo a resistenza a taglio fornito dalla precompressione dell'elemento. Indagando in campo e in letteratura, si è scoperto che ditte di prefabbricazione negli anni 70-80, realizzavano elementi precompressi con scarsa armatura a taglio, se non addirittura assenza in alcuni casi. Notizia ritrovata anche nella normativa tedesca antecedente gli anni 70 per la realizzazione di elementi precompressi. Questo perché, essendo l'elemento precompresso, parte della resistenza a taglio veniva destinata al contributo della precompressione e quindi si poteva «risparmiare» in termini di armatura trasversale.

Il presente lavoro di ricerca intende approfondire due aspetti: la valutazione della bontà di alcune tecniche diagnostiche proposte in letteratura per la valutazione della precompressione in situ e l'influenza delle perdite da precompressione sul quadro fessurativo e sulla resistenza a taglio di travi da ponte in scala reale. Per questi scopi è stata condotta una campagna sperimentale indirizzata alla realizzazione di 4 travi in CAP della lunghezza di 10 m, sezione a "I" alta 80 cm e con staffatura minima. Due travi sono state realizzate con la tecnologia di trefoli pre-tesi aderenti, che differiscono tra loro per un 30% di livello di precompressione assegnata. Le altre due travi, identiche, sono state progettate con un sistema di post-tensione dei cavi (non aderenti) che permette la variazione del livello di precompressione in modo controllato, coprendo così più scenari di perdite a lungo termine. Su questi elementi sono stati applicati 3 metodi semi-distruttivi per la valutazione della precompressione in situ basati sul rilascio tensionale, ovvero: carota strumentata, tagli paralleli all'intradosso e provino tronco piramidale. In aggiunta viene proposto e validato un nuovo metodo, simile ai tagli paralleli all'intradosso, ma eseguito sull'anima. Su questo, dimostratosi il più affidabile tra i metodi testati, sono stati realizzati modelli ad elementi finiti in 2D e 3D in campo elastico. Successivamente, è stata eseguita una prova di carico in 3 punti su ciascuna trave, valutando l'evoluzione del quadro fessurativo con la tecnica del Digital Image Correlation (DIC) e confrontando i risultati con quelli ottenuti dalla simulazione numerica eseguita con

SOMMARIO

il software VecTor 2, basato sulla Modified Compression Field Theory (MCFT). Durante le varie fasi è stato valutato se un'indagine non distruttiva come l'identificazione dinamica possa cogliere danneggiamenti dovuti a lesioni a taglio e una riduzione della perdita di precompressione. Infine, essendo le formule di verifica della resistenza a taglio proposte dai modelli delle varie norme (e.g. Eurocodice 2, *fib* - Model Code, CSA, ACI) molto conservative per gli elementi precompressi con staffe, viene proposta una formulazione analitica basata sulla bozza del *fib* - Model Code 2020 LoA IIb. La formulazione è stata validata grazie all'applicazione ad alcune prove sperimentali presenti in letteratura, ottenendo buoni risultati.

CONTENTS

1	INTRODUCTION	1
1.1	Background and motivation	1
1.2	Objectives and scope of research	3
1.3	Structure of the thesis	4
2	LITERATURE SURVEY	5
2.1	Introduction	5
2.2	Methods for the assessment of residual prestress	5
2.2.1	Introduction	5
2.2.2	Destructive Methods	11
2.2.3	Non-Destructive Methods	16
2.2.4	Semi-Destructive Methods	22
2.3	Influence of prestress on shear strength	53
2.3.1	Introduction	53
2.3.2	Experimental programs	56
3	EXPERIMENTAL PROGRAM	75
3.1	Introduction	75
3.2	Specimen geometry	77
3.3	Design of the Beams	78
3.3.1	Beam A	79
3.3.2	Beam B	80
3.3.3	Beams C1 and C2	83
3.3.4	Prestressing step and casting	86
3.3.5	Prestressing Losses	88

CONTENTS

3.3.6	Instrumentation (Measurements tools)	94
3.3.7	Materials	104
3.4	Setup description	111
3.5	Loading Modalities	119
3.5.1	Beam A	120
3.5.2	Beam B	121
3.5.3	Beam C1	121
3.5.4	Beam C2	123
4	EXPERIMENTAL RESULTS AND DISCUSSION	125
4.1	Assessment of residual stresses	126
4.1.1	Introduction	126
4.1.2	Non-destructive methods applied	138
4.1.3	Core Trepanning method	145
4.1.4	Saw-Cut method - Intrados	156
4.1.5	Blunt Pyramidal specimen	164
4.1.6	Saw-Cut method - Web	172
4.1.7	Comparison and Discussion	194
4.1.8	Concluding Remarks	197
4.2	Shear Tests	204
4.2.1	Introduction	204
4.2.2	Beam A	208
4.2.3	Beam B	216
4.2.4	Beam C1	224
4.2.5	Beam C2	232
4.2.6	Comparisons and Discussion	236
4.2.7	Comparison of DIC crack pattern maps	252
4.2.8	Dynamic identification before and after shear damage	270
4.2.9	Concluding Remarks	275

5	NUMERICAL ANALYSIS	277
5.1	Assessment of residual prestress FEM Model	277
5.1.1	Saw-Cut method – Web 3D FEM Model	281
5.1.2	Saw-Cut method – Web 2D FEM Model	289
5.1.3	Concluding Remarks	291
5.2	Shear Test FEM Model	292
5.2.1	Introduction	292
5.2.2	VecTor 2	293
5.2.3	Numerical Modelling of Test Specimens	303
5.2.4	Modelling of Materials	310
5.2.5	Comparison of Numerical and Experimental Results	317
5.2.6	Concluding Remarks	345
6	NEW MODEL FOR PREDICTING THE SHEAR STRENGTH OF EXISTING PRC BEAMS WITH STIRRUPS	347
6.1	Introduction	347
6.2	State of the art of code analytical models	348
6.3	Comparison between codes to predict the shear strength	353
6.4	Analytical Model Proposed	358
6.5	Database and Validation of the Model	363
6.6	Results and Discussion	370
6.7	Concluding Remarks	382
7	CONCLUSIONS	383
7.1	Overall conclusions	384
7.2	Recommendation for future research	386
8	ACKNOWLEDGMENTS	387
9	REFERENCES	389

**INFLUENCE AND ON-SITE ASSESSMENT OF LONG-
TERM PRESTRESSING LOSSES ON SHEAR
STRENGTH OF BRIDGE GIRDERS**

**INFLUENZA E VALUTAZIONE IN SITO DELLE
PERDITE DI PRECOMPRESSIONE A LUNGO
TERMINE SULLA RESISTENZA A TAGLIO DELLE
TRAVI DA PONTE**

1 INTRODUCTION

1.1 Background and motivation

Prestressing is an innovative technology whose parenthood can be attributed to Eugène Freyssinet, an engineer of the last century engaged in the design of infrastructures and particularly of bridges. The Walnut Lane Memorial Bridge in Philadelphia, Pennsylvania, was built in 1950, marking the beginning of the usage of prestressed concrete beams in highway bridges in the United States. Today, prestressing is widely applied for a broad variety of purposes, from small components like railroad sleepers to more significant structures like bridges, long and light precast floors, and roofing components for buildings. Prestressed reinforced concrete (PRC) has countless advantages compared to the more common reinforced concrete (RC); among these the possibility of obtaining greater spans and slimmer structures, which has made it a widely exploited technology for the construction of bridges and viaducts, and better operating behaviour given that no cracking is foreseen in this phase and given that in this phase no cracking, is expected [Brecolotti and Materazzi, 2015]. The effective state of the prestress force determines the serviceability and safety of PRC constructions [Ho et al., 2016; Yang et al., 2020]. This allows on the one hand to have limited deformations and, in the case of bridges, to partially mitigate the effects of dead and live loads [Robertson, 2005]. On the other hand, it guarantees greater durability as the risk of infiltration of oxidative substances for the reinforcement is reduced. It can be difficult to adequately assess the structural capacity of prestressed concrete girders while they are in use, particularly after a long significant period. While there are many aspects, the following two are crucial ones that influence how prestressed concrete girders perform: the shear capacity close to the supports and the effective prestress force [Osborn et al., 2012]. Engineering practice should avoid shear collapse since it is catastrophic and brittle in concrete structures [Zwoyer and Siess, 1954]. Despite decades of research, it is difficult to anticipate and completely understand the shear behaviour of reinforced concrete members [Collins et al., 2008; Torsion, 1998]. When prestressing is used, this behaviour becomes more complicated and challenging to understand [Ma et al., 2000; Xie et al., 2011]. It is widely acknowledged that applying prestressing substantially modifies a concrete beam's shear behaviour. Sadly, there is little information on how prestressing affects the shear behaviour of concrete beams. Very few full-scale shear tests of PRC beams with low transverse reinforcement are available in the literature. In the discipline of structural engineering, determining the bearing capacity of existing bridges is becoming more

1-INTRODUCTION

and more crucial. The problem is serious because many construction projects, particularly transportation infrastructure, are older than 50 to 60 years in most European countries and need restoration based on objective assessments [Koteš and Vičan, 2012]. This requires adequate models, which can reflect the real load-carrying capacities of bridges. The residual bearing capacity has slowly diminished as a result of the years-long increase in traffic loads [Prisco et al., 2018]. Bridge collapses that have occurred recently in Italy and other countries, such, for instance, the Santo Stefano Bridge in Sicily in 1999, the Annone overpass in Lombardia in 2016 [Prisco et al., 2018], the Fossano Bridge in Piemonte in 2017, the Morandi Bridge in Liguria in 2018, the highway overpass in Wuxi in 2019 and the Albiano Magra bridge in Toscana in 2020, revealed that many existing bridges are reaching the end of their life. The poor condition of the bridges and overpasses might be attributed to these accidents' causes, which are not without serious or even lethal effects. Corrosion of the steel reinforcement is one of the major issues, in particular. The corrosion effect on stirrups in reinforced or prestressed concrete beams is especially risky because it may transform the expected ductile failure mechanism into a brittle one [Spinella et al., 2019]. In Italy, most of the structures were built between the 1950s and 1970s according to criteria aimed at guaranteeing a useful life of around 50 years [Pietrangeli, 2011]. Among these, 52% of the bridges managed by Anas S.p.A. in Italy are more than 40 years old [Gabanelli, 2019]; while 39% of the 614'387 bridges in the United States are 50 e years old or older [ASCE, 2017]. During the inspections of the bridges belonging to the Province of Brescia carried out by the DICATAM – Department of Civil, Environmental, Architectural Engineering and Mathematics of the University of Brescia, shear crack patterns emerged in a significant number of bridges, completely unexpected in PRC elements. Furthermore, following investigations carried out on site by ANAS S.p.A. technicians, in particular on elements produced by the SCAC - Società Cementi Armati Centrifugati company (which were widely used in the 70s, 80s and 90s of the last century), a shortage of transverse reinforcement. Although at the moment no documents capable of confirming or denying this situation have been found, a similar problem has emerged from the bibliographic research on the bridges built in Germany before 1970, as the regulations in force up to that year did not provide for minimum shear reinforcement for PRC beams. Also based on these statements, it is possible to deduce how the contribution of the prestress plays a decidedly important role in the shear-bearing capacity [Huber, Vill, et al., 2018]. All of this demonstrates how timely it is to evaluate the state of existing bridges. There are already thousands of existing bridges all over the world that require urgent repairs and rehabilitation. Future years will see an extraordinarily extensive field of operation dedicated to the rehabilitation of existing bridges. It is crucial to do timely retrofitting actions as this will help to reduce damages and improve the structure's service life. It might be challenging to evaluate the current stress status of "in-service" prestressed concrete structures since there is

frequently a lack of actual design/construction information and environmental factors. To determine the residual strength and to choose the potential repair options for failing prestressed concrete members, it is necessary to generate relevant data about the level of prestress using scientific methods and a methodical approach. Prestressed reinforced concrete structures are critical structures as regards the applicability of conventional investigation techniques, in the sense that the information obtained with the latter is insufficient to give an adequate cognitive framework on the real conditions of degradation. Hence the need to study and experiment with specific and innovative unconventional investigation technologies. Since the PRC structures can reach a critical structural state, before the collapse, without the appearance of obvious cracks or deflections, it was essential to develop investigation methods that could determine the real state of degradation of this type of structure. Furthermore, the forecast models proposed in international standards greatly underestimate the true shear strength of prestressed elements with transverse reinforcement. This inappropriate assessment sometimes leads to intervening with uneconomical and not entirely necessary structural reinforcements for the real conditions of the element studied, causing traffic problems with social and economic impact.

1.2 Objectives and scope of research

To comply with the still widespread lack of knowledge on the evaluation of the shear resistance of the elements in PRC and the influence that the prestress losses could influence on it, two aspects have been dealt with in this thesis work:

- evaluated the effectiveness of some diagnostic techniques, proposed in the literature, for the assessment of in situ prestress;
- the influence of prestressing losses on full-scale bridge beams, especially critical shear members

Having knowledge of the residual prestress of prestressed elements in operation for decades through reliable diagnostic investigations allows a more accurate assessment of the bearing capacity, especially in shear. As regards the first point, the functionality and safety of the PRC structures strongly depend on the effective residual prestress, i.e. downstream of the losses; an accurate determination of this parameter is thus essential. Therefore, various methods present in the literature for the determination of the residual prestress were analysed. Specifically, the efficiency was evaluated (also about the degree of invasiveness and ease of use for the operator) as well as the reliability of the results provided. Thanks to the comparison with experimental tests and numerical simulations, semi-destructive methods based on the stress release of concrete have been tested. For the second point, the aim was to better investigate the correlation between prestressing and resistant shear, with the

hypothesis that the unexpected crack patterns identified during the inspection program, are correlated to a prestressing loss higher than that expected in the design stage. Four PRC beams were then built, two with pre-tensioned strands and two with post-tensioned strands, all with minimum shear reinforcement and a size comparable to that of a bridge deck. By applying a vertical load in configuration to generate a shear failure of the element, the beams were tested at different levels of assigned prestress and compared their behaviour based on the crack pattern under typical service load conditions. The tests were supported with finite element numerical models. Based on these considerations, a database of shear tests performed on PRC elements with stirrups present in the literature was created, to which the models of the main international standards were applied. Confirming what is already present in the literature regarding their underestimation of the shear resistance of PRC elements with transverse reinforcement, an analytical formulation is proposed that better considers the contribution of prestressing in the overall shear resistance of the section.

1.3 Structure of the thesis

This work is divided into the following chapters:

- Chapter 1: The program is addressed and the research objectives are reviewed.
- Chapter 2: A literature search of all methods for the assessment of residual prestress in situ is presented. Furthermore, some studies on shear tests of PRC beams are investigated.
- Chapter 3: It concerns the entire description of the experimental program relating to the two main topics: from the design phase to the materials used, from the prestress losses to the data acquisition instrumentation used, then passing through the description of the test setup and finally the load methods.
- Chapter 4: The results obtained from the stress release tests and the shear tests on the beams are shown and discussed. A semi-destructive method for the evaluation of tension release is also proposed.
- Chapter 5: The numerical finite element models for the stress release tests and the shear tests on the beams are described here together with the comparison with the results obtained experimentally.
- Chapter 6: Here, international standard models are applied to a database of experimental tests. Furthermore, a new model for prestressed elements with stirrups is presented.
- Chapter 7: Summarises the work performed, provides conclusions, and discusses recommendations for future work.

2 LITERATURE SURVEY

2.1 Introduction

The purpose of the following chapter is to illustrate what is already present in the literature regarding two main topics on which the experimental program object of this work will be based: methods for the evaluation of residual prestress and the influence of prestress on the shear strength of bridge girder.

2.2 Methods for the assessment of residual prestress

2.2.1 Introduction

Much of the Italian national road network was designed between the post-war period and the early 1970s, so it has largely exceeded 50 years of service life; this implies that the infrastructures, bridges and viaducts in particular, today present a generalized state of degradation and instability, also because they were designed with little sensitivity to the concept of the durability of the materials, therefore not foreseeing suitable maintenance over the years. Furthermore, today's traffic loads are much higher and more frequent than those predicted decades ago at the design stage [Bencivenga et al., 2022] further accelerating the state of decay.

In this context, it is of great importance to evaluate the current state of conservation of viaducts and road bridges and their level of safety both during operation and in exceptional conditions (e.g. earthquakes). The Guidelines issued by the Higher Council of Public Works and approved by [MIMS - Ministero delle Infrastrutture e della Mobilità Sostenibili, 2022], provide road and motorway network managers and technicians in charge with an innovative tool for assessing the safety of existing bridges, concerning different types of risks, in such a way as to consciously plan the subsequent phases of monitoring and intervention for the reduction of vulnerability. In some cases, the state of decay is not visible or is scarcely visible on the surface, because it concerns the deterioration of the internal parts of the structural elements. This is the case with prestressing cables sheathed in PRC bridge beams.

As is well known, the prestressing system is naturally subject to losses due to the relaxation of the steel and due to the slow phenomena of the concrete, such as viscosity and shrinkage. These phenomena are generally foreseeable and taken into consideration in the design phase of the prestressing system. The effectiveness and intensity of the same are, however, heavily influenced by the possible corrosion

2-LITERATURE SURVEY

mechanisms of the prestressing cables, as they reduce the area of the material and drastically decrease the value of the prestressing resultant acting on the concrete [AICAP, 2016]. Corrosion is caused by the penetration of water and/or aggressive agents inside the ducts, reaching the strands thanks to a partial or poor injection of the ducts using grout; the main responsible for this mechanism is the infiltration of water due to a poor or inefficient system for conveying rainwater. In this regard, the previously mentioned Guidelines, in paragraph 3.6 provide for special inspections for all bonded post-tensioned cable bridges, precisely to investigate possible internal defects. The methods of investigation today are various, more or less destructive [Latte Bovio et al., 2022; Proverbio et al., 2008], such as endoscopic tests or sampling tests of the injection material. These techniques, although effective, are invasive and provide information only locally.

The functionality and safety of prestressed concrete structures strongly depend on the effective residual prestressing force. The calculation of prestressing losses is therefore a crucial aspect, especially in the design of PRC bridge beams; because underestimating prestressing losses can lead to early and excessive cracks and deformations during operation, while overestimation could lead to excessive mounting and uneconomic design.

Difficulties in accurately identifying prestressing losses in PRC bridge beams are related to factors including assumptions about prestressing systems and long-term phenomena, such as degradation processes, relaxation of prestressing reinforcement, creep and shrinkage of concrete and environmental parameters.

An accurate determination of the residual prestressing forces is therefore essential to assess the safety and functionality of PRC structures, also because in general there is little external evidence of damage or deterioration of the structure. For this evaluation it is possible to use analytical models, however, there are conflicting opinions in the literature regarding their reliability. There are obvious difficulties in determining the residual prestress for the same reasons as for identifying long-term losses.

The uncertainties in the analytical models, which differ from the experimental results, must add the fact that the empirical methods for the in-situ evaluation of the actual conditions of the prestressing systems are few and their reliability and applicability are still partly to be demonstrated.

The methods can be categorized according to the degree of invasiveness of the tests:

- destructive methods: they are highly invasive, they involve the destruction of a structural element, or part of it, the restoration of which is onerous if not even to be excluded;

- non-destructive methods: they do not alter the material and do not require the destruction or removal of samples from the structure under examination, it is not necessary to restore;
- semi-destructive methods: they do not alter the material, but require a limited invasiveness and/or partial removal of samples from the structure under examination; which, however, is easily restored.

As can be seen in Table 2-1, ten main types of tests have been repurposed and re-evaluated since the early 1990s. Based on the information collected in the literature, in this thesis seven parameters are proposed by the author, from which, once assigned a relative score of 1, 2 or 3 based on the grade, it is possible to determine which methods are most suitable for on-site application (Table 2-2). The parameters are as follows:

- reliability: the results obtained must be as consistent as possible with the real value;
- repetitiveness: the tests must be easily repeated in terms of time and feasibility;
- promptness: the installation procedure of the necessary instrumentation and data acquisition must be fast and stable;
- anti-invasiveness: as far as possible the tests must be as less destructive as possible, or how well the damaged part must be easily and quickly restored;
- safety: the entire operation must be performed so that the risk is reduced for both operators and users of the infrastructure;
- practicality: linked to the item repetitiveness means the relative ease in carrying out tests at height, with little workspace, single-operator;
- understandability: almost immediate and understandable data processing.

There are cases where there is a high reliability of the results, but they require a lot of time and particular environmental conditions (little interference), rather than cases where there is still a high reliability of the results, but they are impractical to perform on a deck from the bridge. Basically, there are methods for assessing residual prestress applicable only in controlled environments such as laboratories and methods, perhaps less reliable, but which can be executed in situ.

2-LITERATURE SURVEY

Table 2-1: Summary of the methods for assessing residual prestress presented in the literature.

#	Method	Description	References
1	Crack Opening and Crack Re-Opening ¹	The structure is loaded up to the crack, the cracks are instrumented with SG and LVDTs, and the structure is unloaded so that the cracks close and it is recharged to an almost ultimate condition. Once the static scheme is known, the moment of first cracking (M_{cr}) is determined and therefore the residual prestress.	[Azizinamini et al., 1996] [Pessiki et al., 1996] [Labia et al., 1997] [Baran et al., 2005] [Eder et al., 2005] [Osborn et al., 2012] [Garber et al., 2015] [Bagge, Nilimaa, and Elfgren, 2017]
2	Strand Cutting ²	Removing the concrete cover by insulating a strand for 25-30 cm, gluing a strain gauges on a strand wire, and cutting the wire. Measured the deformation of the wire following the cut, with its elastic modulus (Hooke's law) the prestress is obtained.	[Halsey and Miller, 1996] [Baran et al., 2005] [Huber, Vill, et al., 2018] [ANAS S.p.A., 2020]
3	Dynamic	With the evaluation of the natural frequencies of the structural element, its prestressed state is evaluated. With the evaluation of the natural frequencies of the structural element, its prestressed state is evaluated.	[Kim et al., 2003] [Baran et al., 2005] [Law et al., 2008] [Shi et al., 2014] [Breccolotti, 2018] [Bonopera et al., 2019] [Frizzarin et al., 2019]
4	Deflection evaluation	Load test (3 points) the deflection is measured at $1/4 L$ and $1/2 L$, known as the flexural stiffness of the element, the residual prestress can be	[Bonopera and Chang, 2021]

¹ This test is not recommended for structures that are still in service, because it requires them to be brought to conditions close to collapse, or in any case no longer operational. However, it can be applied in situ on elements intended for removal and subsequent planned replacement.

² This test can be performed in situ, but has limitations. In particular, only one wire can be cut for each strand, as long as the section of the precompressed reinforcement is not greater than 2% of the total section [ANAS S.p.A., 2020].

		known through the formulas proposed by the author.	
5	Exposed strand	Insulation of a strand for a minimum length of 85 cm, a transverse force is applied to the strand and its deformation is measured.	[Labia et al., 1997] [Civjan et al., 1998]
6	Hole Drilling	SGs are applied in a radial arrangement (along the directions of the main stresses and 45 °), a small diameter hole is made in the centre while the instruments record the deformation of the concrete caused by the discontinuity of the material. With Hooke's law and the elastic modulus of concrete, the prestress present in concrete is obtained.	[Owens, 1993] [Azizinamini et al., 1996] [Kesavan et al., 2005] [Chang et al., 2009] [Trautner et al., 2010] [Trautner et al., 2011] [ASTM E837-13a, 2013]
7	Core Trepanning	SGs are applied along the direction of prestress, around them a circular cut is made by coring with sufficient depth for surface insulation. With Hooke's law and the elastic modulus of concrete, the prestress present in concrete is obtained.	[Owens, 1993] [Kesavan et al., 2005] [Marks and Lange, 2009] [Parivallal et al., 2011] [Ruan and Zhang, 2015] [Lofrano et al., 2018] [ANAS S.p.A., 2020] [Martinello, 2021]
8	Saw-Cuts	SGs are applied along the direction of prestressing to the intrados of the structural element, in the direction transverse to them two parallel cuts are made (leaving the SGs internal) with a depth slightly less than the concrete cover (without damaging the longitudinal reinforcements). The distance between the cuts must be sufficient for surface insulation. With Hooke's law and the elastic modulus of concrete, the prestress present in concrete is obtained.	[Marks and Lange, 2009] [Kukay et al., 2010] [Shin et al., 2011] [Bagge, Nilimaa, and Elfgren, 2017] [Kral'ovanec et al., 2021]
9	Notch with flat jack	SGs are applied along the direction of prestressing, in the direction transverse to them a saw-cut is made	[Abdunur, 1982] [Marks and Lange, 2009]

2-LITERATURE SURVEY

		(leaving the SGs external), a flat jack is threaded into the notch until the SGs reads the initial value.	
10	Blunt Pyramid	SGs are applied along the direction of prestressing, four cuts are made in the concrete with an inclination of 45° out of plane, forming a blunt pyramid with a greater base of about 7cm x 7 cm and a blunt height of about 25 mm (slightly less than the concrete cover).	[Martinello, 2021] [Lupoi and de Benedetti, 2021a] [Romano and Mazzotti, 2022]

Table 2-2: Method classification based on 7 parameters.

#	Method	Reliability	Repetitiveness	Promptness	Anti-Invasiveness	Safety	Practicality	Understandability	Tot.
1	Crack Opening and Crack Re-Opening	3	1	1	1	1	1	2	10
2	Strand Cutting	3	1	2	1	1	3	3	14
3	Dynamic	2	3	1	3	3	2	2	16
4	Deflection evaluation	2	2	1	3	3	2	2	15
5	Exposed strand	2	1	2	2	2	2	2	13
6	Hole Drilling	2	2	3	2	3	2	2	16
7	Core Trepanning	2	2	3	2	3	2	2	16
8	Saw-cuts	2	3	3	2	3	3	2	18
9	Notch with flat jack	2	3	3	2	3	2	2	17
10	Blunt Pyramid	2	3	3	2	3	3	2	18

Legend: 1= Low; 2= Intermediate; 3= High

Scientific papers such as [Bagge, Nilimaa, and Elfgren, 2017; Bonopera et al., 2020; Kralovanec and Prokop, 2021] report a summary list of the different types of on-site prestressing evaluation most used over the years.

The following paragraphs distinguish the different methods based on their level of invasiveness.

2.2.2 Destructive Methods

2.2.2.1 Structural Response Method (Crack Initiation and Crack Re-Opening)

Among the methods of the structural response, it is possible to mention the crack opening method (Figure 2-1a). This method involves gradually loading the structure until the first crack occurs. In this way, the first cracking load is obtained which, combined with the knowledge of the static scheme, allows the calculation of the first cracking moment (M_{cr}); from the latter it is then possible to trace the residual prestress value. However, the M_{cr} is affected by the tensile strength of the concrete and the stress in the prestressing strand. Consequently, the results may not be sufficiently accurate, especially in cases where the exact tensile strength of the concrete is not available and it is, therefore, necessary to determine this property of the material experimentally. A similar method is that which involves reopening the crack (Figure 2-1b). The difference from the previous technique is that in this case a new crack is not triggered in the concrete element, but an existing crack is reopened, which is closed before the test due to the prestressing effect. Therefore, the inspected structure must be pre-cracked and therefore the method is considered destructive. In general, this approach is more accurate than the method of opening a new crack described above. [Bagge, Nilimaa, and Elfgren, 2017; Kralovanec and Prokop, 2021]

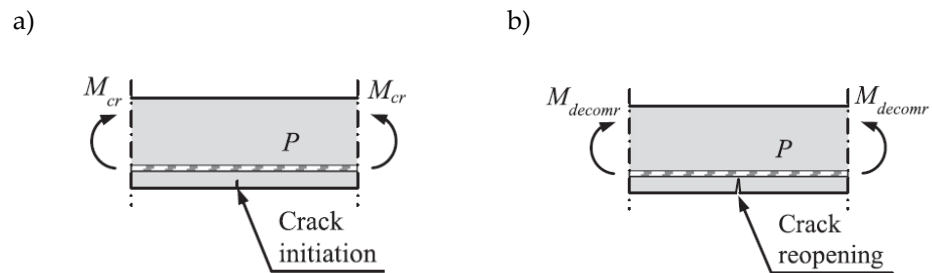


Figure 2-1: Scheme of the Structural Response Method:
a) Crack initiation Method; b) Crack Reopening Method
[Bagge, Nilimaa, and Elfgren, 2017].

During the test, simultaneously with the application of an external load, a specific crack is monitored by recording the deformations right next to it (with the use of strain gauges) or the displacements through it (with the use of LVDTs) (Figure 2-2). Initially, the deformation, or displacement, of the crack varies linearly with respect to the load, until it reaches the so-called decompression load, beyond which the crack reopens and a drastic loss of stiffness occurs.

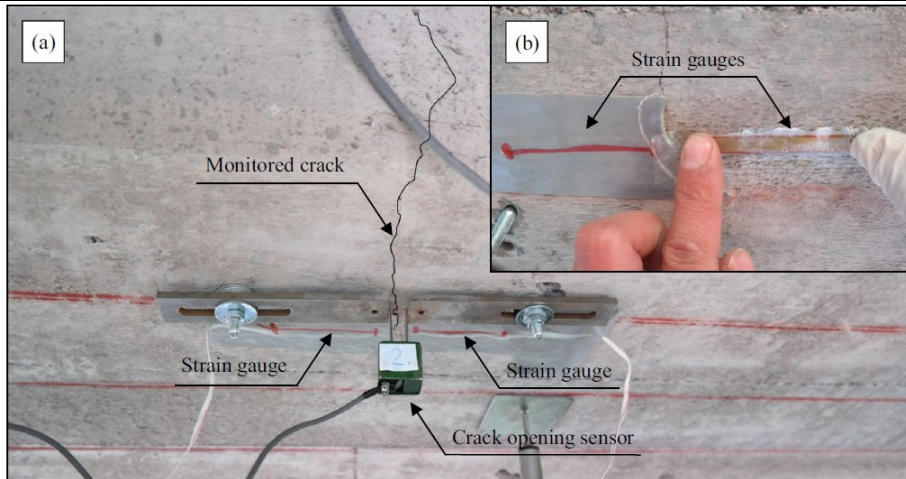


Figure 2-2: Crack Re-opening Method [Bagge, Nilimaa, and Elfgren, 2017].

Pessiki et al. (1996) conceptually divide the test into three phases:

- In the first stage of the test, a load is applied to cause and locate a series of flexural cracks, which are then marked for localization and instrumentation with strain gauges (SG) and displacement transducers (LVDT) after the load has been removed from the beams. In particular, the beams were instrumented with eight SG, i.e., four for each side of the beam as shown in Figure 2-3, with the idea of measuring in this way the distribution of the deformation along the section. Furthermore, the experimental setup proposed by the authors involved performing six loading cycles, with periodic pauses, to ensure that all flexural cracks were identified. After the completion of the sixth loading cycle, the beams were completely unloaded and then prepared for the decompression load test.
- In the second test phase, the decompression load in each beam is determined based on strain and displacement measurements of the cracks identified and instrumented in the first test phase. For example, the authors determine the decompression load during each loading cycle by three methods: (1) visual observation of the crack opening, (2) measurement of the crack opening with LVDT, (3) measurements of the crack opening using strain gauges. Using the latter for each crack, the authors positioned a pair of strain gauges, that is, an SG for each side of the beam. The decompression load was detected by examining the load-strain curves for each pair of strain gauges. These curves generally exhibited a bilinear response and the load corresponding to the transition from the first stage to the second stage was taken as the decompression load. A similar method was used starting from the measurements taken with the LVDTs: in this case, however, the load-crack opening graph is used.
- In the third phase, the beam is brought to collapse.

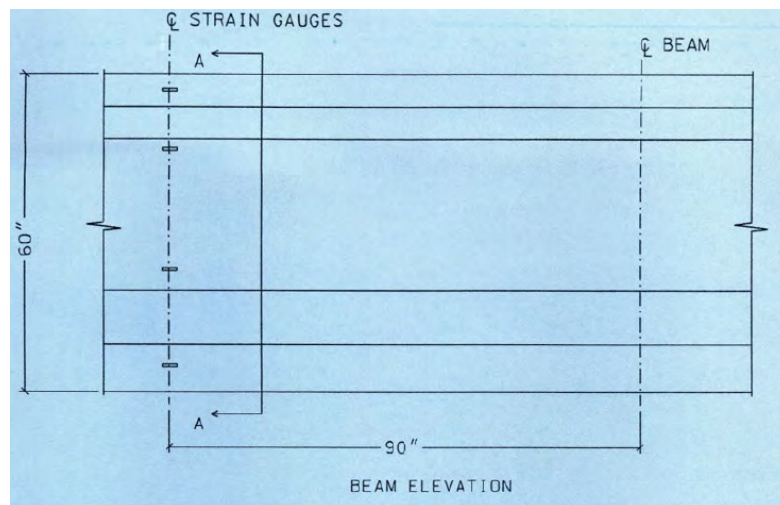


Figure 2-3: Arrangement of the Strain Gauges [Pessiki et al., 1996].

Through the Navier formula, it is possible to determine the prestressing force. In this formula, the decompression is implicitly included in the moment that takes into account the external loads (M_Q):

$$\sigma = \frac{P}{A} + \frac{P e_p y}{I} + \frac{M_R y}{I} + \frac{M_G y}{I} + \frac{M_Q y}{I} \quad (2-1)$$

where:

- σ = stress in the concrete longitudinally to the surface;
- P = prestressing force;
- A = section area;
- e_p = eccentricity of the prestressing force;
- y = distance between the neutral axis and the monitored surface;
- I = moment of inertia of the section;
- M_R = second order moment due to constraints: in the case of statically indeterminate structures it must be calculated with an iterative procedure;
- M_G = moment due to the collapse load;
- M_Q = moment due to external loads;

Analytical evaluation requires knowledge of the current position of the neutral axis and the moment of inertia. Therefore, to obtain reliable results, it is necessary to derive the neutral axis from the measurements in the analysed section and for this purpose strain gauges were applied to the steel [Bagge, Nilimaa, and Elfgren, 2017].

2.2.2.2 Strand-cutting Method

The strand-cutting method (Figure 2-4) is based on measuring the change in deformation that develops after the strand has been cut. The results of this measurement allow to evaluate the value of the prestressing force in the analysed strand, it is a direct method. The change in deformation is monitored by a strain gauge installed on the strand before doing the cut. The problems of this technique are related to the need for exposure of the wire and to the knowledge of the elastic modulus of the strand [Kralovanec and Prokop, 2021]. Importantly, this approach is only applicable to pretensioned structures.

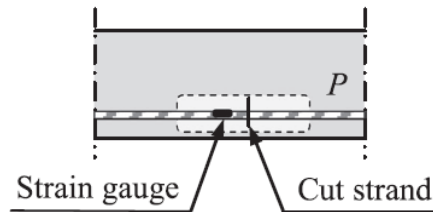


Figure 2-4: Illustration of strand-cutting method [Bagge, Nilimaa, and Elfgren, 2017].

ANAS S.p.A.³, has drawn up a manual [ANAS S.p.A., 2020] which contains the correct procedure for the application of this method based on the release of the strands.

Since in-service condition, the prestressing cable is subjected to a tension σ which induces its deformation ε , one of the wires that make up the strand is cut, or one of the wires in the case of parallel wires prestressing, which is previously instrumented with a strain gauge. The cut makes the σ acting in the wire null and causes a deformation equal to $-|\varepsilon|$ which is measured (Figure 2-5).

The purpose is to determine the tension acting in the prestressing reinforcement and this is obtained by multiplying the deformation detected (changed sign) by the elastic modulus of the steel (Hooke's law: $\sigma = E \cdot \varepsilon$).

Operationally, the test involves a local demolition of the concrete cover and the stripping of the prestressing cable for a length of at least 30 cm, the strand is then exposed for a length of at least 25 cm and the cleaning of the wire must be carried out over a length of about 2 cm. Once the strain gauge is applied to the wire of the strand and connected to the acquisition unit, the wire is cut using an electric mini-grinder at a distance of at least 3 cm from the strain gauge. The mean deformation produced

³ Italian company of the FS Italian Group that deals with road infrastructures. It manages the network of state roads and highways of national interest.

by the shear is measured 10-30 seconds after the stabilization of the $\varepsilon - t$ diagram following failure. Finally, it is necessary to provide for the protection of the exposed prestressing reinforcement with passivating paint, restoration of the removed portion of concrete, reclosing of the edges of the metal sheath (only for post-tensioned tendons) and reconstruction of the concrete cover with controlled-shrinkage fibre-reinforced mortar.

For the execution of the test, it is necessary to sacrifice a wire of a strand in the case of prestressing with strands, or a wire in the case of prestressing with parallel wires; therefore, the test must be performed on no more than one strand/wire per cable and the section of the pre-tensioned reinforcement cut must not exceed 2% of the total section.

The test, however, provides local stress, limited to the point of the tested strand; the strands of adjacent cables may have tension values and the same strand may have different stress at a point a few meters away due to the distribution of tensions produced by the injection in the cases of post-tensioned cables.



Figure 2-5: Test of cutting a wire of a strand [ANAS S.p.A., 2020] adjust.

2.2.3 Non-Destructive Methods

2.2.3.1 Dynamic Methods - evaluation of the natural frequency

Among other methods, dynamic identification has proven to be a cost-effective, time-saving, and accurate way to assess structural integrity. In 1964, [James et al., 1964] were one of the pioneers who looked at the dynamic response of a prestressed beam. They found that the modulus of elasticity of prestressed concrete beams required to be 20–30% higher than that of the companion reinforced concrete beams to obtain the same dynamic features, even though the study's main objective was to compare the flexural rigidity of reinforced and prestressed beams rather than to assess the impact of various prestressing levels applied to the same beam. One of the first approaches to the problem of evaluating residual prestress by non-destructive methods dates back to 1979, when [Cawley and Adams, 1979] proposed a method based on the measurement of the variation of the fundamental vibration frequency which, in a prestressed beam with prestress centered load, is given by:

$$\omega_n^2 = -\left(\frac{n \cdot \pi}{L}\right)^2 \cdot \frac{N}{m} + \left(\frac{n \cdot \pi}{L}\right)^4 \cdot \frac{E \cdot I}{m} \quad (2-2)$$

Dove:

- ω_n = n-th frequency;
- N = axial force applied to the beam;
- m = mass per unit of length (kg/m);
- L = length of the beam;
- $E \cdot I$ = flexural stiffness.

In particular, the first fundamental frequency is given by:

$$f = \frac{\pi}{2 \cdot L^2} \cdot \sqrt{\frac{E \cdot I}{m} \cdot \left(1 - \frac{N}{N_{Cr}}\right)} \quad (2-3)$$

where N_{Cr} is the Eulerian load. From this formula, it is clear that the fundamental frequency variation depends on the square root of the ratio between applied prestress (N) and Eulerian load (N_{Cr}) and therefore it is expected that the variation of this parameter will be perceived only for considerable variations of the prestress force [Dall'Asta and Dezi, 1996]. Therefore, additional parameters should be monitored to capture the prestress losses even for low values: these parameters must show a high sensitivity to the variation of the prestress force.

In the last few decades, several experimental programs have been conducted to solve this problem, but they have shown controversial results.

Unger et al. (2006) concentrated their studies on the identification of modal forms, without taking into account the variation of the prestressing force.

Wang et al. (2013) stated, in contrast to previous experimental results, that the bending stiffness of prestressed beams with parabolic cables decreases as the prestressing force increases, while the bending stiffness of prestressed beams with straight cables is not affected by variations of the prestressing force.

Toyota et al. (2017) again denied these considerations by carrying out a complete study aimed at also taking into account the effects of temperature.

Other studies have used "time domain" techniques to identify the prestress force without considering "frequency-based models" [Law and Lu, 2005].

Doubts, therefore, arise as to the actual applicability of this method since in some cases the effects of prestressing losses on damping are not significant enough to be perceived as the effects of temperature and humidity.

Kerr (1976) carried out several experimental tests on a steel cantilever beam with a continuously supported barycentric tendon. Based on the results and theoretical investigations, the author found that the natural frequencies were not affected by the magnitude of the prestressing force.

Hop (1991) monitored the dynamic behaviour of several PRC beams made from normal and lightweight concrete. Investigation looked at the effect of prestressing levels on the frequency and damping of concrete beams. The author found that applying an increasing prestressing force, acting unevenly on the beam, would increase the frequency of vibration. In several cases, it has been recorded that the application of further degrees of prestress increase, would result in a drop in the frequency of vibration.

Similar experimental results were obtained by Saiidi et al. (1994) who tested a PRC beam with a concentric ungrouted strand and prestressing force varying from 0 to 0.5 times the compression strength of the concrete section. Investigations demonstrated an increase in the first eigenfrequency from 11.41 Hz for the case of null prestressing force, to 15.07 Hz (+32.1%) for the maximum value of prestressing.

Miyamoto et al. (2000) tested the dynamic behaviour of prestressed beams, strengthened with external tendons. According to their findings, prestressing forces introduced to external tendons, affect the natural frequency of vibration of the girder. In particular, in the case of slightly eccentric tendon arrangement, the authors found that the natural frequency decreased for the dominance of axial force.

2-LITERATURE SURVEY

Lu and Law (2006) tested a 4.0 m long RC beam with an ungrouted seven-wire straight strand, located at the centroid of the beam cross-section. Two conditions were tested: with and without a prestressing force of 66.7 kN. The authors observed that the application of the prestressing force produced an increase in the first three eigenfrequencies in the range of 0.4–2.1%

Xiong and Zhang (2009) tested three externally prestressed, simply supported concrete beams with different paths of the external tendons. The authors observed that the natural frequency of beams increased in the first stage with the increased prestressing force. Inversely, the natural frequency decreased after the cracks produced by the prestressing forces occurred in the beams.

Kim et al. (2010) tested a laboratory-scaled PRC girder for several damage scenarios of prestress loss in the tendon. Starting from a state of no prestress loss, the external prestressing force has been gradually reduced to zero. During this unloading process, dynamic measurements allowed to identify reductions of the first four eigenfrequencies up to values of 4.0–4.4% from the initial stage to the final one.

Jang et al. (2011) tested six scaled post-tensioned concrete beams with bonded tendons. By applying a continuously increasing prestressing force from 0 to 523 kN, the authors observed a progressive increase of the first eigenfrequency from 7.6 to 8.7 Hz (+15.7%).

Maas et al. (2012) observed that in an undamaged beam subjected to compressive stress by tensioning a central reinforcement with a hydraulic jack, the increase in the first three eigenfrequencies is roughly equal to 1% for each MPa increase in the concrete compression stress. They also assumed that this stiffness increase was due to the closure of small micro-cracks in the concrete produced by compression stress.

Noh et al. (2015) carried out experimental tests on 3 PRC beams with different strand configurations. They detected that generally, the natural frequency increased as tensile force in the prestressing steel was increased. They also noted that frequencies of vibrations of internally prestressed concrete beams were affected by other parameters, such as tendon profile and boundary conditions.

In the large-scale experimental study of Bonopera et al. (2019) the results confirmed that fundamental frequency is not an appropriate parameter for prestress loss prediction in concrete bridge beams with parabolic unbonded tendons.

Frizzarin et al. (2019) conducted an experimental program on 6 beams with different prestressing levels; of which three pretensions to bonded cables and three post-tensioned. The latter differ from each other because the post-tensioned cable has been positioned at different heights and is therefore characterized by different eccentricities. Static tests up to failure were done for the pre-tensioned beams and

non-destructive tests were carried out for each load step, in particular, “dynamic free vibration test” and “ultrasonic tests”. The same tests were repeated for the three post-tensioned beams with the possibility of checking the prestress level. The authors did different load cycles for each of the 6 beams and each consisted of the:

- Loading phase;
- Stationary phase, during which cracks were detected;
- Discharge phase.

With the beam unloaded, the investigation methods mentioned above were then carried out (Dynamic free vibrations monitoring and Ultrasonic tests).

Starting from the recorded signal, the fundamental frequencies and the damping ratio were calculated: for the pre-tensioned beams, as expected, as the damage increased, an increase in the damping ratio and an increase in the fundamental frequency were recorded. In percentage terms, the damping ratio is more sensitive to the variation of the prestress forces than the fundamental frequency. From the ultrasound tests, on the other hand, a map in terms of speed is obtained which shows a reduction in speed as the damage increases. Based on the tests conducted, according to the authors, a good correspondence between the model and the experimental results was shown especially for post-tensioned beams. However, the dynamic methods for the evaluation of the natural frequency have been strongly criticized in the literature, as for low values of the prestress level (5-10% of the final compressive strength of the section) it is observed that as the prestress force increases also the natural frequencies; on the other hand, for higher prestress force values, the rate of change of the vibration frequencies is reduced. Even for even greater prestressing forces the natural frequencies tend to decrease. [Breccolotti, 2018]. To this is added the fact that during dynamic acquisitions there are generally some background noises, which are difficult to purify during the evaluation of the results. Furthermore, the dynamic methods are based on the modal characteristics of the prestressed beams, which depend on the stiffness and therefore are influenced by the prestress force. In particular, it is necessary to choose a priori the modal form to be used in the procedures and, depending on which one is chosen, there are different levels of accuracy in the estimation of the prestressing force [Bonopera et al., 2020].

2.2.3.2 **Evaluation of Deflection**

This method, devised by Bonopera and Chang (2021), involves the execution of a three-point load test and proposes an estimate of the prestressing force by measuring the vertical deflection at a quarter or in the centreline of a simple beam support. The method also requires information on the bending stiffness of the beam: in particular, Young's modulus in the elastic range must be evaluated by compression tests on cores taken at a quarter of the span after carrying out the bending test on three points. In the absence of geometric and/or material properties, flexural stiffness can be estimated as a function of free vibrations. The authors apply this method to a bridge beam simply supported post-tensioned with a parabolic cable (Figure 2-6); going to evaluate the residual prestress at different instants of time for a total of nine months, during which the beam was kept in the laboratory. The prestress was applied using hydraulic jacks, which then provide the exact residual prestress value to be used as a comparison for the evaluation of the effectiveness of the proposed method.

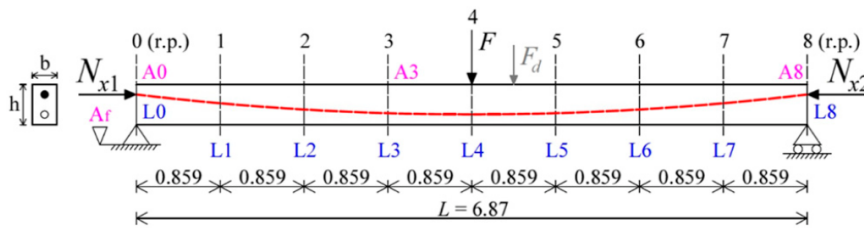


Figure 2-6: Test setup [Bonopera and Chang, 2021].

If a force F is applied in the middle, the residual prestress force can be estimated, for a simple support bridge, as:

$$N_a = \frac{\pi^2 \cdot EJ}{L^2} \left[1 - \frac{11 \cdot F \cdot L^3}{768 \cdot E \cdot J} \cdot \frac{1}{v_{tot} \cdot (L/4)} \right] \quad (2-4)$$

$$N_a = \frac{\pi^2 \cdot EJ}{L^2} \left[1 - \frac{F \cdot L^3}{48 \cdot E \cdot J} \cdot \frac{1}{v_{tot} \cdot (L/2)} \right] \quad (2-5)$$

where:

- F = vertical load applied;
- E = Young's modulus;
- J = module of inertia.

$v_{tot}(L/2)$ and $v_{tot}(L/4)$ are the displacement measured respectively in the middle or at a quarter of the span. These can be measured experimentally or some formulas allow to evaluate them analytically:

$$v_{tot}(x) = \frac{v_l(x)}{1 - N_p/N_{cr,E}} \quad (2-6)$$

where:

- N_p = applied prestressing force;
- $N_{cr,E}$ = Eulerian critical load;
- $v_l(x)$ = displacement of a prestressed bridge (PRC) in simple support in which the applied prestress force and the weight of the beam are neglected.

This can be calculated with:

$$v_l(x) = \frac{F \cdot L^3}{12 \cdot E \cdot J} \cdot \frac{x}{L} \cdot \left[\frac{3}{4} - \left(\frac{x}{L} \right)^2 \right] \quad \text{for } 0 \leq x \leq \frac{L}{2} \quad (2-7)$$

$$v_l(x) = \frac{F \cdot L^3}{12 \cdot E \cdot J} \cdot \left(1 - \frac{x}{L} \right) \cdot \left[\frac{2 \cdot x}{L} - \left(\frac{x}{L} \right)^2 - \frac{1}{4} \right] \quad \text{for } \frac{L}{2} \leq x \leq L \quad (2-8)$$

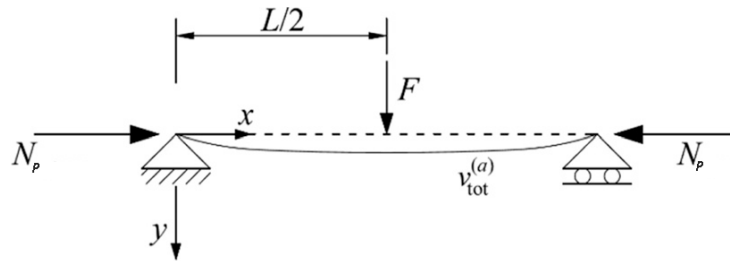


Figure 2-7: Deflection shape after the vertical load application [Bonopera and Chang, 2021].

The displacement calculated analytically has an error between -3.5% and 8% compared to the experimentally measured value: this error is influenced by Young's modulus and the moment of inertia used in the calculations. The best solution is obtained using the initial tangent elastic modulus and the moment of inertia calculated with Song's formula [Bonopera and Chang, 2021]. According to the authors, the percentage errors made in terms of estimating the prestress are less than 15%, provided that a sufficiently high vertical load F is applied (in particular in their experiments a load greater than 42 kN was required) and provided that to use Song's formula to estimate the section's moment of inertia. This method is a simple, fast and cheap procedure, which does not require a direct measurement of the tension of strand and does not require any data to be obtained through experimental tests; which takes into account the relaxation of the steel, the viscosity and the shrinkage of the concrete. However, this is a difficult method to apply, as it is difficult to define the applied load threshold F above which the result becomes reliable, as the 42 kN obtained in the tests of Bonopera and Chang (2021) is not an absolute value but strongly depend on the geometry of the beam. Furthermore, to apply this method, it is necessary to carry out a load test, which on the one hand causes inconvenience to the traffic, on the other hand, it implies that the measurement, and therefore the evaluation of the prestress, cannot be done for a single beam, in how much this will be affected by the slab effect that is generated between all the girders of the bridge.

2.2.4 Semi-Destructive Methods

2.2.4.1 Exposed strand

The idea behind the exposed strand method involves applying a transverse force F to the strand and then measuring its displacement $\delta(F)$. An important aspect of this technique is the need to have a strand exposed for a length of at least 85 cm (if using commercial instrumentation) which should then be properly restored later. [Bagge, Nilimaa, and Elfgren, 2017; Kralovanec and Prokop, 2021].

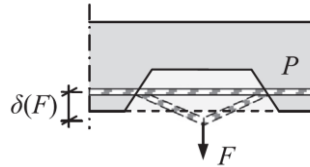


Figure 2-8: Pull of the exposed strand [Bagge, Nilimaa, and Elfgren, 2017]

This technique has been explained by Civjan et al. (1998) who apply it on a 7-wire strand with a diameter of 12.7 mm with exposed lengths ranging from 46 to 74 cm using a specially designed tool (Figure 2-9 and Figure 2-10). The authors do a series of tests per step, thus applying gradually increasing loads and measuring the transverse displacement at each step. He then compared the slope of the load-displacement diagram with a calibration graph to determine the stress in the strand. The theory behind this practical method is described below.

The impact of strand bending characteristics and the rise in tension as the strand is deflected can theoretically be predicted. Tension is influenced by the exposed strand's length, whereas bending is influenced by the strand's properties. The elastic modulus of the strand was predicted to be 193000 kN/m^2 .

Strand Tension

Figure 2-10 shows the effects of strand tension. From the geometry shown in the figure:

$$L_1 = 2 \cdot \sqrt{\left(\frac{L_0}{2}\right)^2 + y^2} \quad (2-9)$$

The change in strain:

$$\Delta\varepsilon = \left(\frac{L_1 - L_0}{2 \cdot L' + L_0}\right) \quad (2-10)$$

and the change in stress:

$$\Delta f_s = \Delta \varepsilon \cdot E \quad (2-11)$$

therefore:

$$P = 2 \cdot \left[\frac{y}{L_1/2} \cdot T \right] \quad (2-12)$$

where:

$$T = T_0 + A \cdot \Delta f_s \quad (2-13)$$

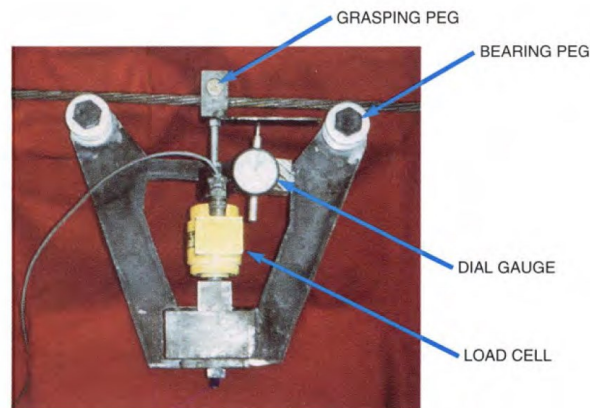


Figure 2-9: Prototype for exposed strand [Civjan et al., 1998].

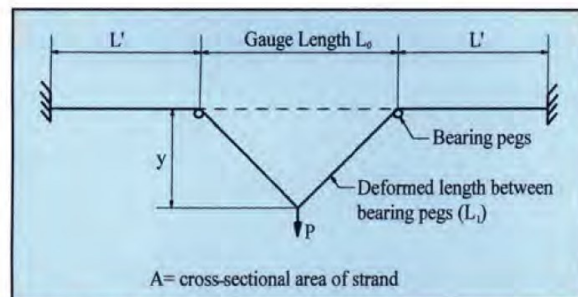


Figure 2-10: Schematic diagram for the effect of tension in strand [Civjan et al., 1998].

The effects of strand length can be compared with calibration values for the instrument. The use of $L = \text{infinity}$ is the case where changes in strand tension are negligible. As the length becomes shorter, the increase in strand tension requires more force to be applied to realize the same displacement.

Strand Bending

The other important factor is strand bending. The effects of strand bending are illustrated in Figure 2-11. For small displacements and rotations, L_1 can be taken equal to L_0 . Assuming constant tension T_0 in the strand, moments along the strand shown in Figure 2-11b can be summed. It should be noted that M_2 is taken as zero because the strand is not forced to have a zero slope at $x = 0$ and the restraint will depend on the distance from the support to the point of strand embedment in the concrete.

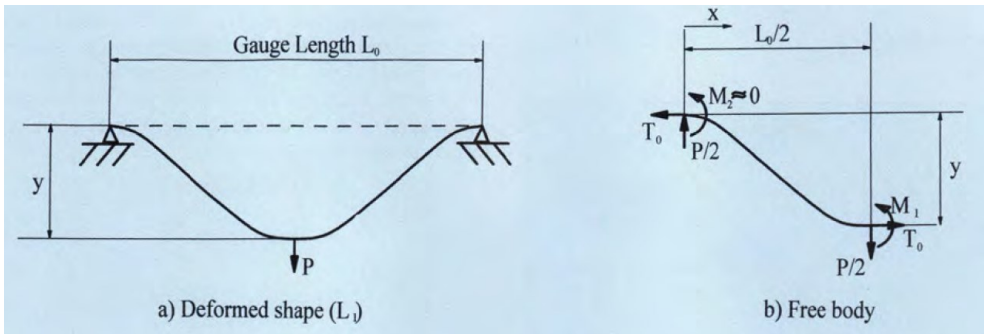


Figure 2-11: Schematic diagram for the effect of bending [Civjan et al., 1998].

$$\sum M_x = 0 \rightarrow \begin{cases} M_x + T_0 \cdot y = \frac{P}{2} \cdot x \\ M_x = -E \cdot J \cdot \frac{d^2 y}{dx^2} \end{cases} \rightarrow \frac{d^2 y}{dx^2} - \frac{T_0 \cdot y}{E \cdot J} = -\frac{P \cdot x}{2 \cdot E \cdot J} \quad (2-14)$$

Introducing the following terms:

$$k^2 = \frac{T_0}{E \cdot J} \quad (2-15)$$

$$A = k \cdot \frac{L_0}{2} \quad (2-16)$$

The differential equation becomes:

$$\frac{d^2 y}{dx^2} - k^2 \cdot y = -\frac{k^2 \cdot P \cdot x}{T_0 \cdot 2} \quad (2-17)$$

Considering the following boundary conditions:

$$x = 0, \quad y = 0 \quad (2-18)$$

$$x = \frac{L_0}{2}, \quad \frac{dy}{dx} = 0 \quad (2-19)$$

The relationship between y and P is:

$$y = \frac{P}{T_0 \cdot 2} \cdot [A - \tanh(A)] \quad (2-20)$$

The conclusion of the study says that the prestress remaining in exposed strands in a damaged prestressed concrete girder can be determined reliably, quickly, and inexpensively with this method. According to the authors, the strand tension values, and therefore indirectly the prestress level, obtained in this way show a percentage error of less than 10%.

The main problem with this procedure lies in the need to have reliable calibration data that takes into account, for example, the properties of the strand and the exposed strand length. This method is difficult to apply in practice because it is often difficult, if not impossible, to expose the strands of a functioning PRC structure. Furthermore, the need for reliable calibration data raises many doubts regarding the accuracy of the residual prestressing force obtained with this method.

2.2.4.2 Stress Release Method

Among the most widespread diagnostic techniques and preliminary to the previous ones, there is that of stress release, which consists in estimating the current state of prestress acting on specific sections of the prestressed bridge beams starting from the release of the prestress deformation acting on the concrete.

This method is based on the idea of isolating a portion of a structural element previously instrumented with strain gauges by cutting or coring from which it is possible to derive the deformations that arise in the concrete due to the cut. The volume of concrete isolated with the cuts leads in fact to a modification of the stress state. Later, it is possible to derive the stress state σ acting in the concrete through Hooke's law: $\sigma = E \cdot \varepsilon$, this is because the deformation undergone by the isolated portion following the shear is equal, and of opposite sign, to the deformation induced by the prestress and from permanent loads. The methods based on this logic, in general, have a negligible impact on the integrity of the investigated structures and cause local damage that can be easily repaired. For this reason, stress release methods are considered direct semi-destructive methods. Although this technique is widely used in professional practice, in the scientific literature there is still no robust validation of these diagnostic methods, in terms of reliability and accuracy and therefore, the stress release test of concrete is not currently standardized, at least in terms of Italy [Lupoi and de Benedetti, 2021a].

Various methods have been proposed in the literature over the decades, all similar to each other and based on the idea of tension release.

2.2.4.2.1 *Hole Drilling Method*

This approach is based on observing the stress or change in deformation in the area adjacent to a relatively small hole made in a concrete element. (Figure 2-12). Given that the variation in the deformation in concrete caused by the hole decreases as the distance from the hole increases, it is necessary to define standard conditions in which to do the test [Kesavan et al., 2005]. This method has been used several times in the literature and the various authors [Owens, 1993; Azizinamini et al., 1996; Kesavan et al., 2005; Chang et al., 2009; Trautner et al., 2011; ASTM E837-13a, 2013;] have proposed different geometric configurations both as regards the diameter and depth of the hole, and as regards the position and distance of the strain gauges with respect to the hole.

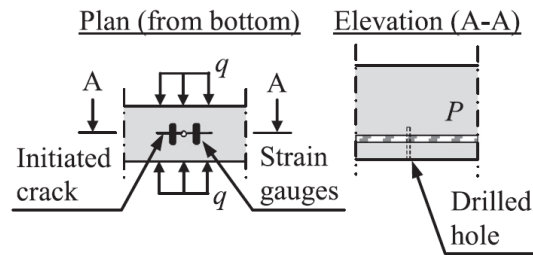


Figure 2-12: Hole Drilling method [Bagge, Nilimaa, and Elfgren, 2017].

Owens (1988) and Owens (1993) propose a method called the steel stress hole technique that involves drilling a very small circular hole (diameter of about 1.6 mm) to a depth of 1.6 mm on the surface of the rebar/ prestress steel in the concrete member to be assessed. The existing stress in the member is evaluated by measuring the released strains very close to the drilled hole in the rebar. But this method needs exposing of rebars which may not be advisable in prestressed concrete members and this method applies only to small diameter prestressing wires (Figure 2-13 and Figure 2-14). What was stated in Owens (1993) has been adopted by ASTM E837-13a (2013): "Standard Test Method for Determining Residual Stresses by the Hole-Drilling Strain-Gage Method". The procedure consists in gluing three or more strain gauge rosettes on a predominantly flat surface away from the edges and other irregularities and drilling a hole in the geometric centre of the rosettes themselves. The technique, born with reference to a generic isotropic linear elastic material, was applied only later to concrete. The most common setup, used for example by Kesavan et al. (2005), is the one shown in Figure 2-15 and foresees a hole with a diameter of 50 mm and a depth of 50 mm, with strain gauges placed in a radial position at a distance of 1.5ϕ and 50 mm long.

A more complex setup has been proposed by Owens (1993), who developed a new core drilling method using a progression of smaller holes typically $36\div 52$ mm in diameter with a radial configuration of 50 mm long strain gauges.

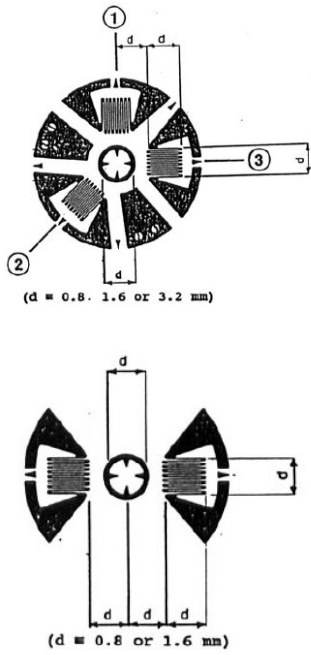


Figure 2-13: Standard Gauge geometry and two gauge layout for wires [Owens, 1993]

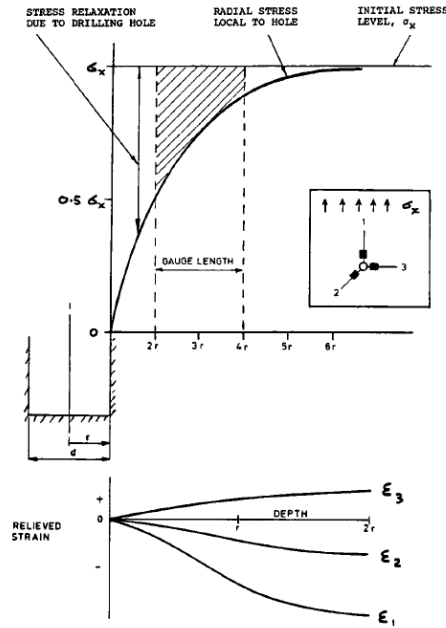


Figure 2-14: Effect of producing a hole in a uniformly stressed material [Owens, 1993]

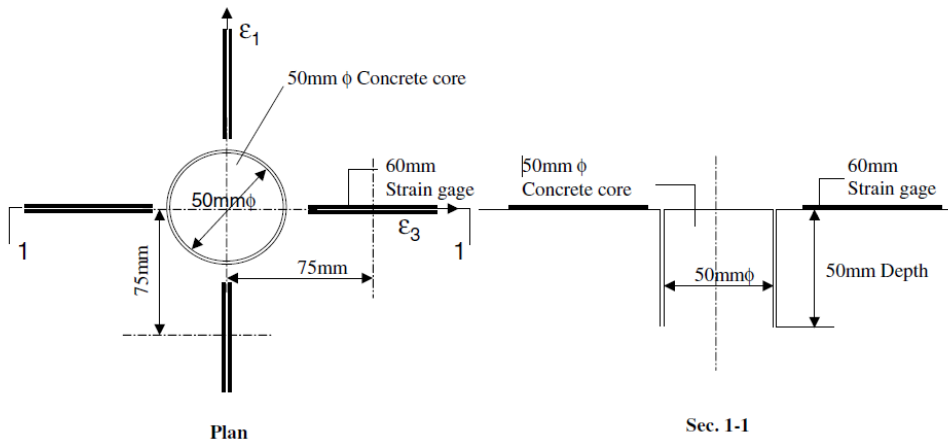


Figure 2-15: Setup Hole Drilling method [Kesavan et al., 2005].

Another completely similar test is described in the publications of Parivallal et al. (2011) and Ruan and Zhang (2015) where, however, two radial and two tangential strain gauges are positioned. In particular, Ruan and Zhang (2015), state that radial strain gauges measure strains that grow rapidly during the early stages of drilling, but without further increases beyond a certain drilling depth (20mm for their test setup).

In particular, [Ruan and Zhang, 2015], state that radial strain gauges measure strains that grow rapidly during the early stages of drilling, but without further increases beyond a certain drilling depth (20 mm for their test setup). In contrast, strains measured by tangential strain gauges have a relatively slower but stable growth.

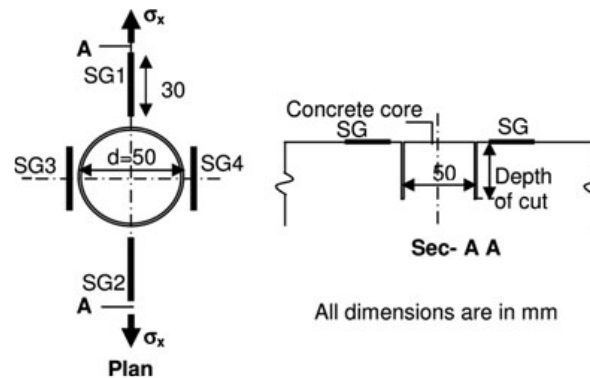


Figure 2-16: Arrangement of strain gauges used by Parivallal et al. (2011)

The prestressing force can be obtained with:

$$\sigma_{max}, \sigma_{min} = \frac{\varepsilon_1 + \varepsilon_3}{4A} \pm \frac{\varepsilon_3 - \varepsilon_1}{4B} \quad (2-21)$$

where:

- $\sigma_{max}, \sigma_{min}$ are the main maximum and minimum stress;
- $\varepsilon_1, \varepsilon_3$ are the deformations measured by the strain gauges placed in two directions orthogonal to each other;
- A and B are calibration coefficients.

To obtain the prestressing force with the drilling method, it is necessary to introduce calibration coefficients A and B because after coring there is only a partial release of deformation (about 20% of the total deformation). This is why it is also difficult to use this method when the existing stress level is low, as measurable quantities can be very small and often error-prone. The effectiveness of this method has been and is the subject of discussion in the literature [Khaled, 1999; Sánchez-Beitia and Schueremans, 2009].

2.2.4.2.2 *Photoelastic Method*

Chang et al. (2009) highlight the further limitations of the drilling method: only one point measurement is done, and it is usually necessary to drill the hole exactly in the centre of the strain gauges to avoid considerable errors. To overcome these drawbacks, Chang et al. (2009) propose to measure the stress stage around the hole with photoelastic techniques. Benefits include collecting accurate quantitative data, eliminating the need for precision drilling, measuring the stress stage in the entire region around the hole, and faster inspection process speed, mainly due to the use of a digital camera and discrete digital image processing.

The technique they presented foresees applying axial stress, thus generating the pre-existing prestress in the case of prestressed elements, and then applying a photoelastic coating on the flat surface of the test sample. A small hole 3 mm in diameter and 0.5-2.5 cm deep is then made by drilling orthogonally to the surface of the sample. To derive the pre-existing state of the residual stresses, the efforts were evaluated in four directions. The hole was made in the centre of the point that covers the photoelastic area of the coating. The amount of the residual stress is then determined by a least square's calculation using the photoelastic fringes near the hole. Finally, the calculated stresses were compared with the initial applied value.

Figure 2-17 shows that, as the drilling depth increases from 0 to 2.5 cm, the residual stresses increase, but once the drilling depth of 2 cm is reached, the distribution of the residual stresses does not change. The entire stress stage around the hole after drilling was recorded and based on the experimental observation there are four mutually orthogonal directions (0° , 90° , 180° , 270°) of residual stress distribution (Figure 2-18). It can also be seen that the released stresses are greatest near the hole and decrease as the distance from the centre of the hole increases.

Regardless of the stress concentration, the experimental stress values reasonably agree with the theoretical solution.

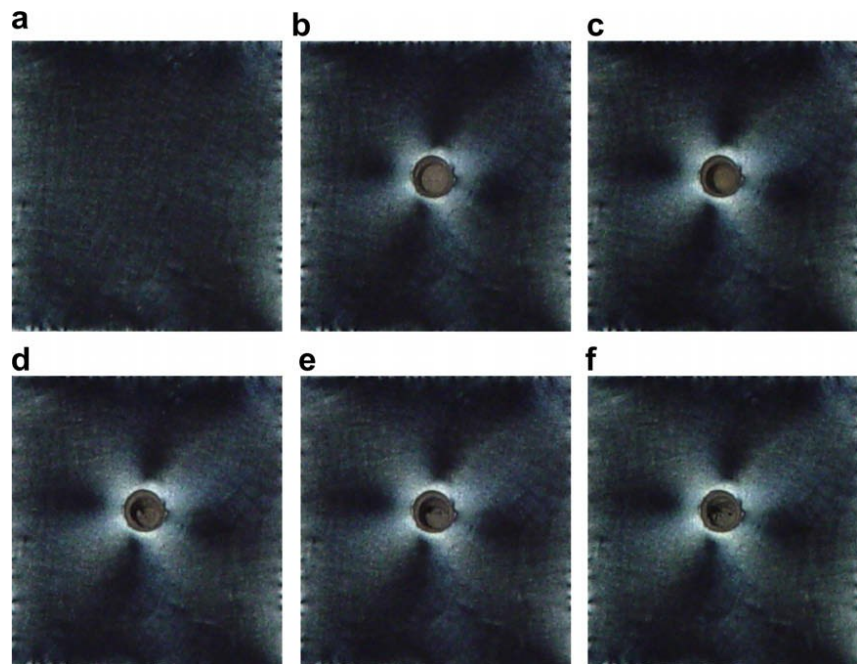


Figure 2-17: Residual stress reliefs with different drilling depths: (a) 0 cm, (b) 0.5 cm, (c) 1 cm, (d) 1.5 cm, (e) 2 cm, (f) 2.5 cm [Chang et al., 2009].

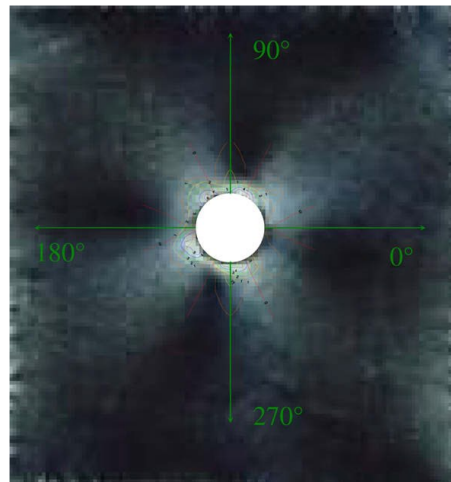


Figure 2-18: Residual stress distribution [Chang et al., 2009].

2.2.4.2.3 *Core Trepanning Method*

Due to the limitations of the Hole Drilling method, a very similar technique was developed, but in which the strain gauges are fixed to the centre of the core and no longer positioned radially outside it (Figure 2-19). In this case, the strain gauge can measure the complete stress release generated by the core drilling and therefore it is easier to analyse the data. If only one strain gauge is used, it is positioned along the main direction of stress, on the other hand when this direction is not known, for example, due to the simultaneous presence of moment and shear, it is necessary to insert three strain gauges.

Kesavan et al. (2005) operate by making a hole with a diameter of 50 mm and the drilling takes place in steps at regular intervals, each characterized by a depth of 10 mm; continuing until the desired depth is reached.

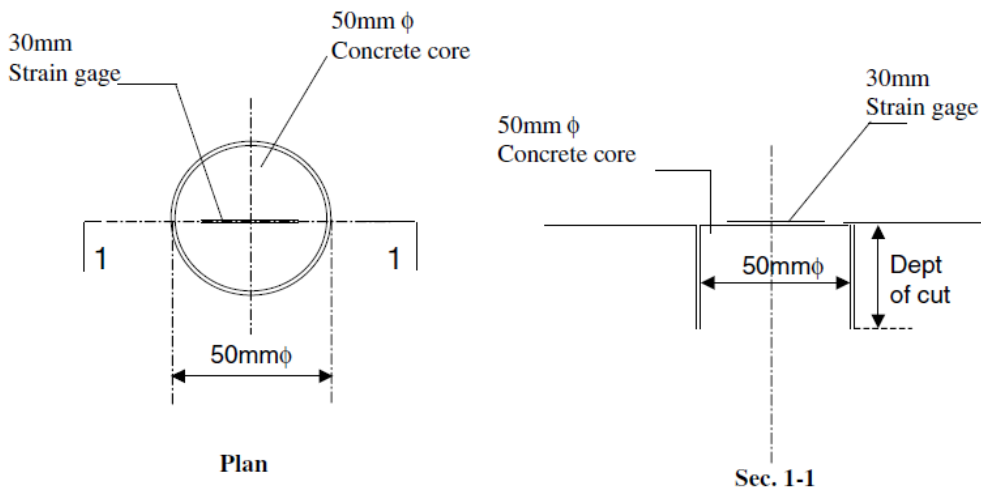


Figure 2-19: Concrete core trepanning technique [Kesavan et al., 2005].

An advantage of these methods is that the cores taken can then be tested in the laboratory to determine the elastic modulus of the concrete. A limit of these methods, on the other hand, is linked to the size of the holes: in addition to the fact that tests with different diameters are reported in the literature, it is necessary to underline that in the PRC structures there is a very dense reinforcement and therefore it can be difficult to make the hole without intercept rebars.

While remaining within the scope of measurement using strain gauges, in addition to the number and arrangement of the same, the choice of the type of sensors itself is also important, the length of which should be related to the homogeneity of the material [Guo et al., 2008; Pecht et al., 2008].

Martinello (2021) [Martinello, 2021] underlines the criticalities related to the classic Core Trepanning method and the Saw-Cut method (§2.2.4.2.4), mainly because during the cut no continuous measurements are made: the stress release is evaluated as a difference between the stress state before and after cutting, therefore the cutting history is not known.

The authors, with this consideration, have devised the instrumented core, consisting of a control unit that allows continuous acquisition during the removal of the specimens.

The instrumented cores are connected to a small instrument, called by the authors "Tensometer", which can power strain gauges, store data, run on battery, not be affected by vibrations and above all be waterproof. On the side of the fixing to the wall, it carries a gasket and on the opposite side a USB port for connection to an application that allows one to activate it, modify its reading parameters and download data. A second version, called "Tensometer online", manages data transmission in a telemetry system with ceramic mini-antennas, allowing data to be transferred in real-time while remaining inside the core drill. The cylindrical specimen has a diameter of 70 mm (Figure 2-20).

For the first phase of the study, 4 concrete specimens were prepared, with dimensions of 40 x 25 x 60 cm, with different characteristics of mechanical resistance. The specimens were instrumented with 2 strain gauges placed side by side in the vertical direction in the centre of both faces 40 x 60. On one face, that of the core drilling, the Tensometer was mounted, while on the other face, the two strain gauges were connected to a Datalogger. The specimens were placed under compression under a press, bringing the force to 2,000 kN, corresponding to a stress of 20 MPa. This force produced relative deformations between 800 and 1,000 $\mu\epsilon$.



Figure 2-20: Executive sequence of the Instrumented Core [Martinello, 2021].

The tests, being tested in the laboratory, were carried out by stopping the advancement of the core drill every 2 cm to capture the moment in which there is the complete release of the stress state. In this way, it was noticed that with the first 2 cm of depth, there is a release of about 40%, while the complete release develops at about 10 cm of depth (Figure 2-21).

Tests on specimens with different characteristics have shown that full release tends to show itself at greater depths as the strength of the material increases. Certainly, the extraction of core specimens guarantees complete tension release.

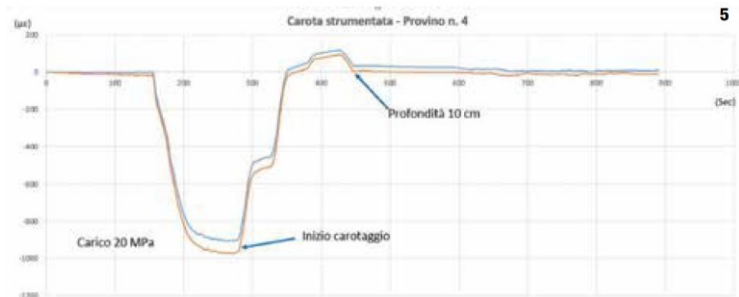


Figure 2-21: Relative deformation trend during the core drilling phase [Martinello, 2021].

However, it is not always possible to extract a core, both due to the density of the reinforcements present and not to excessively damage the structure in particularly stressed points. This condition often occurs in the case of prestressed beams in the mid-area of the intrados, where the stress deriving from accidental loads is maximum.

In the manual drawn up by ANAS S.p.A. (2020)⁴, as for the method of cutting the strand (see §2.2.2.2), the procedure for applying the Core Trepanning Method is described.

As for the release test on concrete, the aim is always to measure the tension acting in the instrumented point of the beam under the action of prestressing and permanent loads. The test consists in isolating by coring a portion of the structural element previously instrumented with strain gauges.

The deformation undergone by the isolated portion following the shear is equal and of opposite sign to the deformation induced by prestress and permanent loads, therefore, once the elastic modulus of the concrete is known, it is possible to evaluate the stress σ acting through Hooke's law: $\sigma = E \cdot \varepsilon$. In particular, the manual gives indications on where to perform the tests.

⁴ Italian company of the FS Italiane Group that deals with road infrastructures. It manages the network of state roads and highways of national interest.

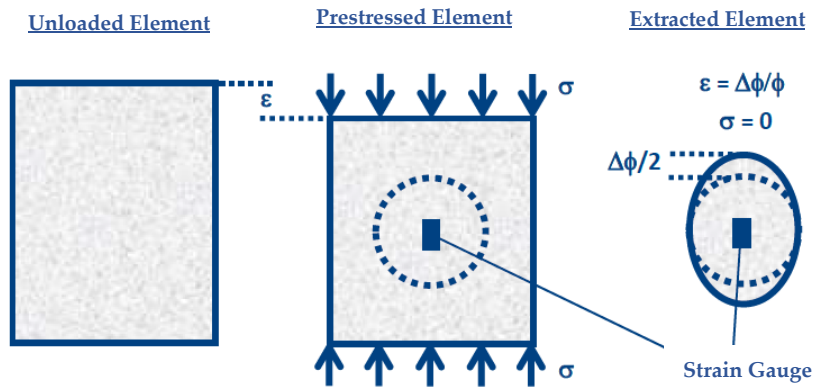


Figure 2-22: Theoretical scheme of release test on concrete [ANAS S.p.A., 2020] adjust.

On the simply supported beams, the measurement is performed at the centre section as there the bending moment due to prestressing and permanent loads is maximum while the cut is zero (Figure 2-23).

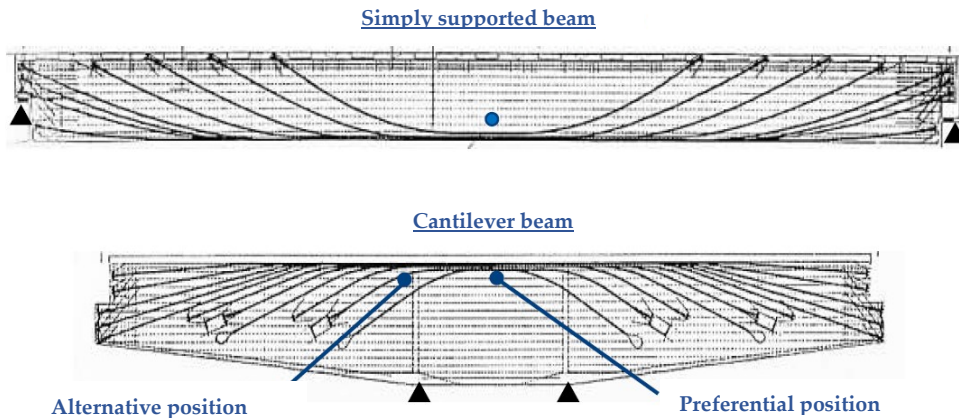


Figure 2-23: Location of the release tests on the concrete according to the static scheme [ANAS S.p.A., 2020] adjust.

The report shows the preference to perform the test on the face of the web (where the concrete is generally less damaged) and immediately above the lower bulb, it is not possible to perform it directly on the lower bulb without risking damaging the strands. (Figure 2-24).

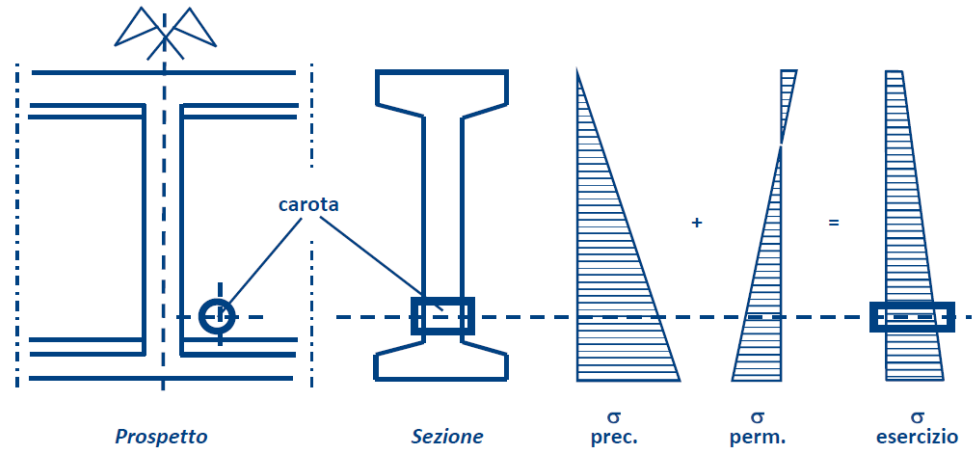


Figure 2-24: Location of the release tests on concrete for simply supported beams [ANAS S.p.A., 2020].

Since the cut is zero in the mid-section, the main stresses take on a vertical and horizontal direction and therefore the stress analysis can be performed with only two strain gauges (Figure 2-25).

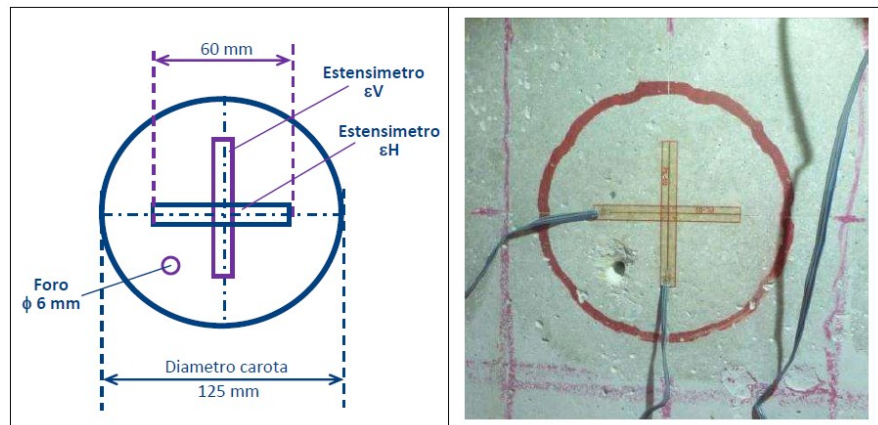


Figure 2-25: Release test on concrete: measurement scheme with 2 strain gauges [ANAS S.p.A., 2020].

In the case of "cantilever beams" the measurement is performed near the interlocking section where, however, in addition to the maximum negative bending moment value, there is also a maximum shear (Figure 2-23).

2-LITERATURE SURVEY

In this case, since the direction of the main stresses is not known due to the simultaneous presence of moment and shear, the stress analysis must be performed with three strain gauges (Figure 2-26). The measurement should preferably be performed on the face of the web and immediately below the upper wing.

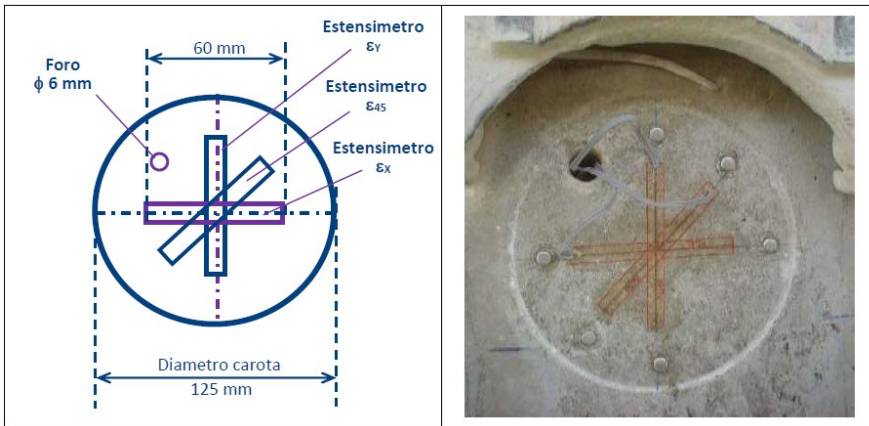


Figure 2-26: Release test on concrete: measurement scheme with 32 strain gauges [ANAS S.p.A., 2020].

Operationally, the tests provide for the identification of an area of about 50 cm x 50 cm characterized by a sufficiently smooth surface free from delamination, cracks and pores.

ANAS S.p.A. (2020) indicates that the core must have a diameter of 12.5 cm and must be carried out only after verifying the absence of rebars using a magnetic survey (covermeter). A 6 mm through hole must be made inside which the connection cables of the strain gauges are passed, recovered from the opposite side of the core and connected to the acquisition unit; in this way, it is possible to continuously acquire the release data.

The acquired deformation measurements are processed as follows:

- calculation of the mean deformations ε produced by the core trepanning, generally measured between 5 and 10 minutes after the stabilization of the diagrams $\varepsilon - t$;
- calculation of the prestressing stress acting σ_1 (in MPa), according to the relations shown in Figure 2-27 according to the measurement scheme used, where:
 - ν = Poisson's ratio of concrete; in the absence of experimental data, the value 0.15 can be assumed;

- E = Elastic modulus of the concrete, obtainable from the core extracted preferably by compression test in the laboratory or, alternatively, by ultrasonic measurements performed along the core axis.

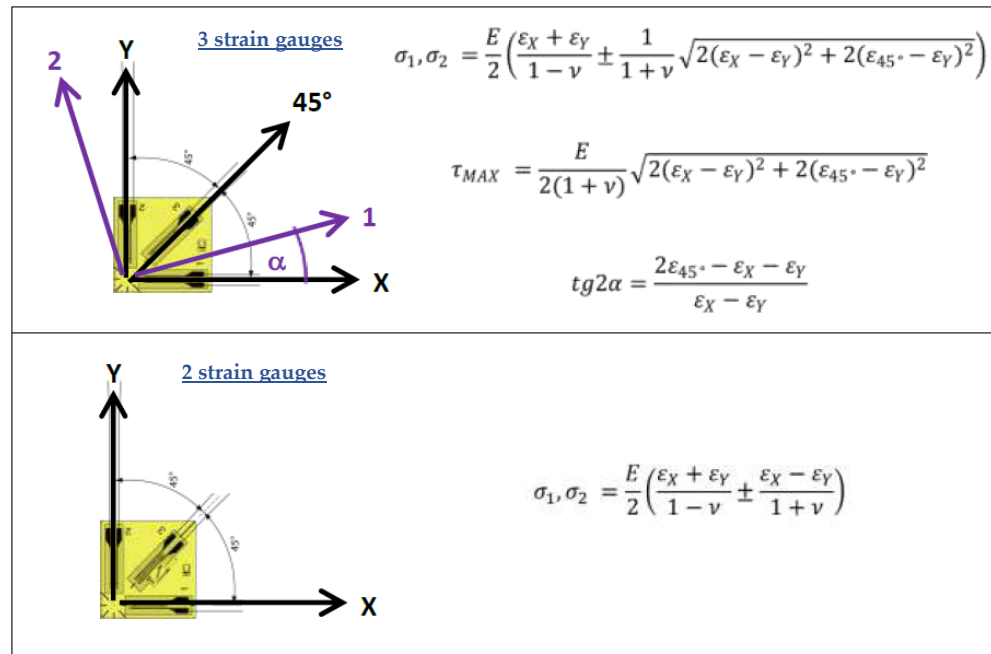


Figure 2-27: Calculation of the main stresses on the release tests [ANAS S.p.A., 2020] *adjust.*

ANAS S.p.A. (2020) declares high reliability of the release tests on the strands/wires as the installation procedures of the strain gauge are relatively simple and the deformations produced by the cut are very high.

The release tests on concrete, compared to the strand shear method (see §2.2.2.2), have a lower degree of reliability as the bonding procedure of the strain gauges is more complex and the deformations due to prestressing are of the reduced entity and the same order of magnitude as the thermal ones produced by coring.

2.2.4.2.4 *Saw-Cut Method*

The modus operandi of the Saw-Cut method is practically the same as the Hole Drilling and Core Trepanning methods. However, in this case, the stress release is caused by a series of saw-cuts made on the intrados of the prestressed element, which isolates the concrete block from the acting forces, while the variation in stress or deformation is measured in the portion between two saw-cuts performed. (Figure 2-28). [Bagge, Nilimaa, and Elfgren, 2017]

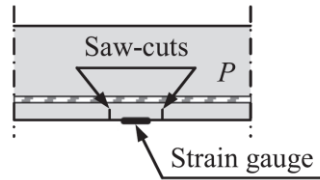


Figure 2-28: Saw-cuts method on the intrados [Bagge, Nilimaa, and Elfgren, 2017].

The insulation is considered complete when increasing the depth of the cut does not lead to further variations in the deformation on the surface. Any cutting of small-diameter reinforcements should not significantly affect the accuracy of the results obtained; while it is necessary to avoid cutting reinforcements with a larger diameter in order not to damage the integrity of the structure. Furthermore, if they were cut, the measured deformations would not be reliable because they could be affected by the cut of the reinforcement [Kralovanec and Prokop, 2021].

The prestress, as in the structural response method (see §2.2.2.1) mentioned above, can be estimated with the Navier formula:

$$\sigma = \frac{P}{A} + \frac{P \cdot e_p \cdot y}{I} + \frac{M_R \cdot y}{I} + \frac{M_G \cdot y}{I} + \frac{M_Q \cdot y}{I} \quad (2-22)$$

Kralovanec et al. (2021) apply this method in situ on an existing 60-year bridge. In particular, it makes four cuts at a distance of 120 mm from each other, performed on the intrados on the lower flange. Two cuts are 23 mm deep, while the remaining two are 31 mm deep. These depths were chosen to avoid cutting the longitudinal reinforcement of the beam. Strain gauges were then placed between the two pairs of cuts made, later called SG1 and SG2 (Figure 2-29).

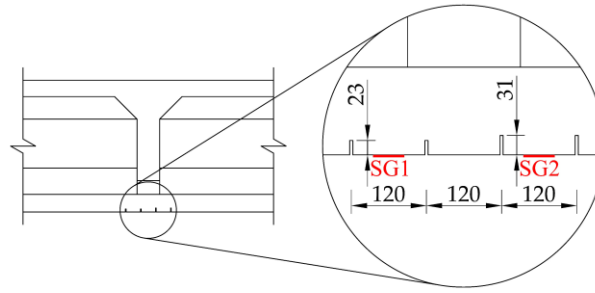


Figure 2-29: Scheme of execution of the intrados saw-cuts [Kraľovanec et al., 2021].

Based on the results obtained, the authors underline that with 23 mm deep cuts the tension release is not complete, but there is a release of about 63%. On the other hand, with 31 mm deep cuts, there is a mean release of 86%. The results obtained suggest that a relatively minimally invasive intervention in the structure could lead to a significant release from local effort; in fact, a cut with a depth of 31 mm is negligible compared to the cross-section of the beam. With this method, the integrity of the structure was preserved allowing for an almost complete insulation of the concrete block. It is obvious, however, that the possibility of obtaining a complete release depends not only on the depth of the cuts, but also on the relative distance between the two cuts: the closer the cuts are to each other, the less depth is needed to completely isolate the concrete block. This can be useful in the case of old PRC bridges that are still functioning, where the concrete cover is extremely small, and therefore the maximum depth of the saw cuts is also very limited. However, the problem remains that this semi-destructive approach, as mentioned above, can be applied and is reliable only in situations where a concrete block can be completely insulated, and are not partially. This is not always possible in evaluations of existing structures because, for example, non-prestressed reinforcement must not be damaged but is sometimes located too close to the concrete surface to make sufficiently deep saw cuts.

In such situations Bagge et al. (2017) propose to combine a finite element analysis with the experimental method just described (Figure 2-30 and Figure 2-31); that is, it models the test procedures with finite elements, then applies an iterative procedure to find the residual prestressing force corresponding to the behaviour observed in the experimental tests.

Based on the tests that they conducted on an existing bridge beam, this method was not always reliable; however, if this method could be further developed and implemented, the need to completely isolate a concrete block, with the potential structural damage associated with it, would be avoided.

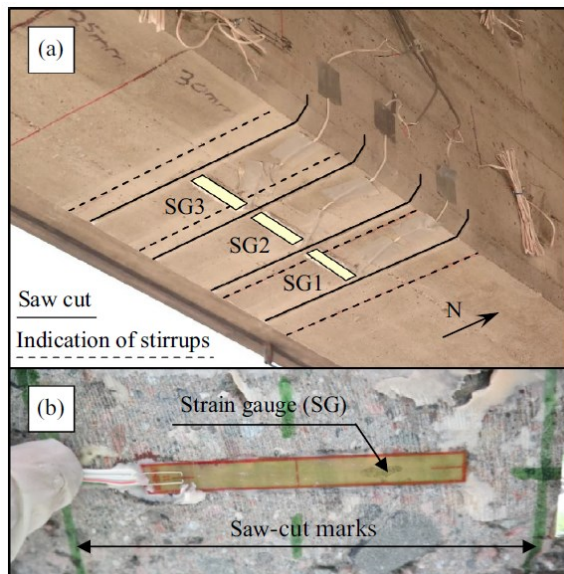


Figure 2-30: Instrumentation for non-destructive residual prestress force determination: (a) strain gauges (SG1-3) installed between alignments of saw-cuts with consideration of stirrups' locations and (b) close-up of a strain gauge glued on the concrete [Bagge, Nilimaa, and Elfgren, 2017].

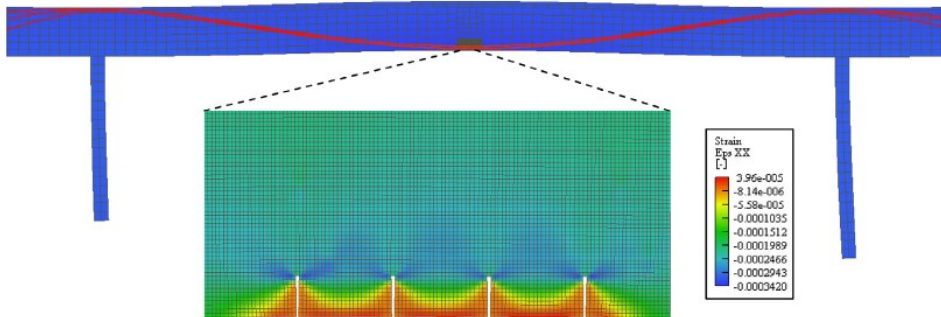


Figure 2-31: FE model for semi-destructive evaluation of the residual prestress force in midspan [Bagge, Nilimaa, and Elfgren, 2017].

2.2.4.2.5 *Notch with flat jack*

Still based on the concept of the Saw-Cut method, Abdunur (1982) proposes a technique where strain gauges are applied along the direction of prestressing, in the direction transverse to them a saw-cut is made (leaving the SGs external) and a flat jack is threaded into the notch until the SGs reads the initial value (Figure 2-32). The amount of compensating pressure is an indication of the compressive stress in the direction normal to the slot.

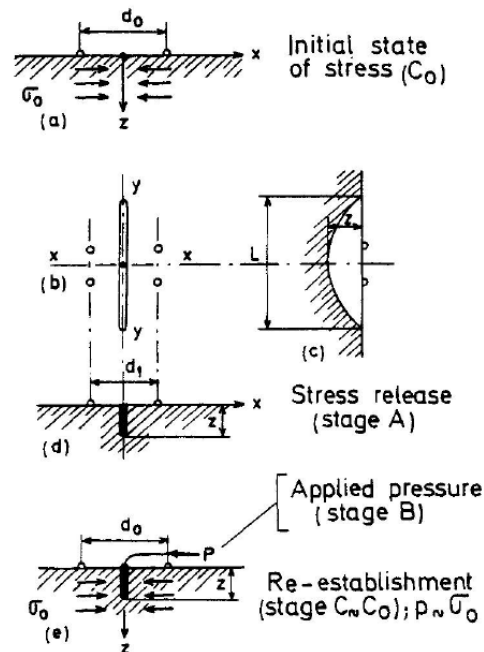


Figure 2-32: Different stages of stress measurement by partial release [Abdunur, 1982].

The author claims that the governing parameter is the depth of the cut that can be performed.

2.2.4.2.6 *Blunt Pyramidal Specimen*

One of the major critical issues related to the Hole Drilling method and the Core Trepanning method is the difficulty in carrying out the test at the points of maximum stress (such as the centreline of prestressed beams) due to reinforcement congestion. Furthermore, the poor accuracy that can guarantee a magnetic survey (covermeter) leads to the risk of intercepting the armature in depth during the core drilling phase. The Saw-Cut method proposes to remain within the thickness of the concrete cover (about 30-35mm), however, it is not always guaranteed especially in the prefabricated elements and on the intrados of the deck.

Martinello (2021), starting from these considerations, has developed an innovative method: stress release tests with blunt pyramidal specimens, which can also be performed in the points with very dense reinforcement, affecting only the thickness of the concrete cover. The author conducted several laboratory tests to identify a form of an extractable specimen that could be limited to a depth of a few millimetres. The solution identified, which provided the best response in ensuring complete release and minimum damage, was the shape of the blunt pyramidal square. After making the cuts, the blunt pyramidal specimen is in fact connected to the structure for a small section and is therefore removable with minimal effort. The thickness of the specimen is approximately 25÷30 mm, which makes it possible to carry out the test even in the presence of reinforcements provided, obviously, the concrete cover is adequate. The executive technique involves the application on the surface of the beam of a pair of strain gauges arranged in a horizontal direction (direction of prestressing) adjacent to each other. The next step consists in insulating a portion of the structural element having dimensions of 60 mm x 60 mm (or slightly higher) through four cuts made with a direction of 45 ° inwards, to create a blunt-pyramidal element with an extremely reduced head section, such as to guarantee the complete release of the incorporated deformations (Figure 2-33). Several tests were carried out in the laboratory, in the first phase operating with a manual cut and subsequently through electro-mechanical equipment, called "Discovery", which allows one to make precise cuts, always at a distance of 60 mm, perfectly orthogonal and at 45° towards the inland. The use of a machine has proved essential to obtain precise, repeatable and less operator-dependent specimens.



Figure 2-33: Test execution phases with blunt pyramidal specimen [Martinello, 2021].

The four cuts are made in succession, leaving 60 seconds between one and the other to evaluate the effect of each cut. This is made possible by a Datalogger, installed in the Discovery, to which the strain gauges are connected and which allows, through a wireless connection, to follow the trend, the effect of the stress release and therefore of the relative deformation in real-time.

The test technique as previously defined has significant advantages over the one with coring [Lupoi and de Benedetti, 2021a]:

- the reduced depth of the cuts makes it possible to carry out the test in the optimal section, i.e., at the lower bulb of the centre section, without affecting the prestressing reinforcements;
- the blunt pyramid shape allows the extraction of the specimen, thus guaranteeing complete tension release;
- allows the continuous reading of the data without having to make through holes and without having to disconnect and reattach the strain gauge connections to the control unit, an activity that generates a disturbance in the data recording, however leaving a reading "hole", and this can alter the result if one also considers the order of magnitude of the measured quantity ($\mu\epsilon$);

2-LITERATURE SURVEY

- ease and speed of execution (about 30 min.);
- the test is essentially non-destructive.

The technique proposed by Martinello (2021) was developed by the 4EMME Laboratory as part of an experimental project conceived and coordinated by Lupoi and de Benedetti (2021b) on behalf of Autostrada per l'Italia S.p.A. (Aspi) aimed at evaluating the effectiveness of various tests to be used in the context of special investigations.

Lupoi and de Benedetti (2021a) also apply the stress release method of blunt pyramidal specimens as part of an extensive experimental program that involved bridge beams with different spans, from 32 meters to 70 meters, for a total of over 50 stress release tests. This activity is part of the special inspections provided for all works of art made with post-tensioned prestressing systems by the Guidelines [MIMS, 2022]. The authors affirm that the proposed investigation and analysis methodology is characterized by simplicity of execution, reduced costs and reliability of the results.

The survey method proposed for assessing the efficiency and effectiveness of the prestressing system of reinforced concrete beams with post-tensioned cables, as for all previously described stress release methods, is based on the measurement of the stress actually acting at the point of a section of the element. Assuming the external loads are known, the only unknown factor for determining the stress state resulting in the investigated section is the prestressing stress acting, which can then be obtained by solving the well-known Navier formula:

$$\sigma = \frac{N}{A} + \frac{N \cdot e}{W} - \frac{M_G}{W} \quad \rightarrow \quad N = \frac{\left(\sigma + \frac{M_G}{W}\right)}{\left(\frac{1}{A} + \frac{e}{W}\right)} \quad (2-23)$$

where:

- s = acting stress (measured with the stress release test);
- N = prestressing agent (unknown);
- e = eccentricity of the resulting cable;
- M_G = moment due to own weight and permanent load;
- A = section area;
- W = resistance modulus.

The tension σ acting in (2-23) is obtained starting from the results of the stress release tests carried out with the cutting technique, through Hooke's law

$$\sigma = E \cdot \varepsilon \quad (2-24)$$

where:

- ε = strain measured by the stress release test;
- E = material elastic modulus.

Known N from (2-23) and the effort at the time of the initial tension N_0 from the available design documentation or, failing that, from an estimate based on experience, the effective prestress loss is determined, which compared with that estimated in the design provides a first indication of the efficiency of the prestressing system with respect to the design forecasts.

The method is based on simple concepts and theoretical notions that favour the verification of the conditions of applicability, reliability and accuracy of the results. The expressions (2-23) and (2-24) find applicability to the case of reinforced concrete beams. Since, for elements which are intact under service conditions, the response is in the linear elastic range. The accuracy of the tension obtained using (2-23) and (2-24) as a measure of the state of tension of the investigated element essentially depends on the measurement point and the reliability of the deformation data measured experimentally. The more the measuring point is in a state of uniaxial stress, the greater the accuracy of the voltage value obtained through (2-24). In the case of reinforced concrete bridge beams, the lower bulb of the central section is substantially in the ideal condition described above and is also subjected to straight deflection stress, therefore consistent with the stress state described by (2-23). Obviously, for the lower bulbs of reinforced concrete beams, there is a different scale effect compared to the samples tested in the laboratory. However, any error by default in the determination of the acting voltage is in favour of safety, that is, the prestressing agent is underestimated, so, again in relation to the objectives of the investigation, this does not constitute a limit to the validity of the proposed method. Numerical and experimental studies on the above problem are in progress. [Lupoi and de Benedetti, 2021a]

As regards the elastic modulus, considering the variability of the mechanical characteristics of the concrete, the authors recommend carrying out tests near the measuring point of the stress release test to estimate the local value of E . To this aim, pull-out tests can be performed to estimate the compressive strength of the concrete, and then derive the elastic modulus using the expression (NTC, 2018 - Chapter 11.2.10.3):

$$E_c = 22000 \cdot \left(\frac{f_{c,site}}{10} \right)^{0.3} \quad (2-25)$$

The conclusions of the experimental program of Lupoi and de Benedetti (2021a) are as follows:

- The program conducted made it possible to verify in the field the practicality and simplicity of carrying out the stress release test with blunt pyramidal specimens, which must in any case be carried out by adequately trained operators, with high-quality instrumentation and following the procedure.
- The estimates of the prestressing losses obtained from the experimental results provided reliable and overall consistent values, confirming the validity of the proposed method of investigation.
- The tests were performed both in the presence and in the absence of traffic, and it was verified that the influence on the results of the same is contained in 10%; the influence on the estimation of prestressing losses is further reduced, to the point of being substantially negligible. Furthermore, thanks to the continuous reading of the data, the possible transit of high-mass vehicles is detected and can be purified during the return phase.
- Finally, a sensitivity analysis of the estimated losses was performed for the values of the elastic modulus and permanent loads, which showed variability of the estimated data of less than 5%, therefore largely contained in the intrinsic and irreducible variability of the investigated phenomenon.
- The experimentation conducted confirmed that the stress release method with blunt pyramidal specimens provides reliable information to capture those situations in which there are anomalies of the prestressing system such as affecting the static safety of the investigated element. It can therefore be applied as part of the special inspections provided for by the Guidelines [MIMS, 2022] to assess the state of works with post-tensioned cable prestressing systems.

Romano and Mazzotti (2022) investigate the methods and procedures for carrying out stress release tests on prestressed concrete elements using strain gauges to evaluate their strengths and limits. Various extraction procedures on concrete prisms are considered and show the results of their first tests, to evaluate the importance of precise parameters on the trend of the deformation released over time and to propose an optimal geometric and shear configuration to obtain a deformation measurement reliable and easily repeatable in situ.

In the experimental study, the authors made 10 weakly reinforced concrete columns 150 cm long, with a square base of 40×40 cm² dimensions.

Each column was placed vertically inside a 6,000 kN capacity hydraulic press, which applies the desired axial compression load. Figure 2-34 shows that for each column 5 areas for extracting the specimens have been provided on two opposite faces of the column but at staggered heights, taking care to adequately distance them so that the alterations of the deformation state resulting from previous extractions did not affect

that of other areas still to be tested. In particular, three areas have been identified on one side (A) and two on the other side (B).

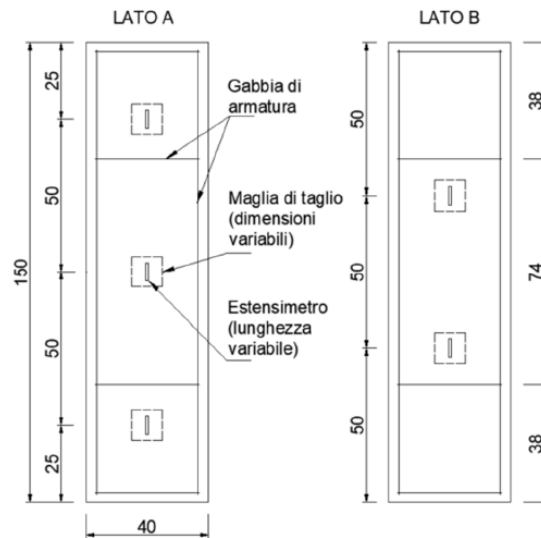


Figure 2-34: Placement of strain gauges on the RC column: (a) three strain gauges on side A; (b) two strain gauges on side B [Romano and Mazzotti, 2022].

Inside each area to be extracted, a strain gauge of variable length has been glued, placed parallel to the direction of action of the compression load, and subsequently connected to an acquisition unit together with the one present on the opposite face of the column at a height similar to the first.

Once the column was loaded at a known pressure, the volume of concrete around the strain gauge was isolated from the rest of the column by making four cuts to form a square (like the test proposed by Martinello, 2021) or rectangular around the strain gauge itself. The cuts were made using an angle grinder with a circular blade diameter of 22 cm, as shown in Figure 2-35 and Figure 2-36.



Figure 2-35: Cutting with an angle grinder on one side of the square mesh [Romano and Mazzotti, 2022].

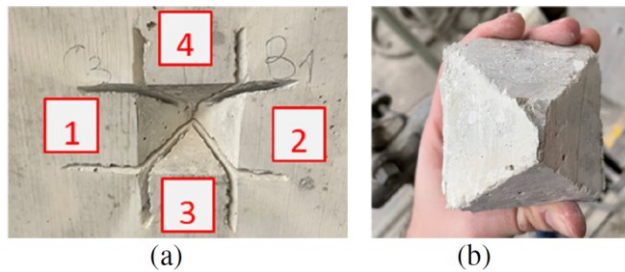


Figure 2-36: Test C3_B1: (a) the four cuts at 45 degrees on the 10×10 cm² square mesh; (b) the blunt pyramidal volume extracted [Romano and Mazzotti, 2022].

The sequence of tests, on each column, was carried out starting from the specimens present on both faces at half height and then continuing, in tests separated from the first, to those closest to the ends; this ensured to further minimize the effect of extractions on the subsequent deformation regime.

The deformation recording started before loading and then continued until the complete extraction of the concrete specimen. In this way, both the deformation consequent to the applied force and that correlated to the release phase were measured, having as a nominal target the return to a zero value (volume of concrete removed and unloaded).

The vertical positioning of the strain gauge is the only parameter that has combined the various stress release tests; the other test settings and test execution modalities have been made to vary, to observe how the extent of the release can be influenced. The test parameters are shown in Table 2-3. In particular, they are:

- the vertical compressive stress σ_v applied to the column;
- the dimensions ($B \times h$) of the extracted concrete prism;
- The length L_{sg} of the strain gauge;
- The order in which the cuts were made (V = vertical and H = horizontal);
- The angle at which the cuts were made, relative to the outer surface of the column.

The choice of using different cutting configurations is correlated to the desire to reduce the invasiveness of the test as much as possible, limiting the volume of concrete taken from the element investigated in situ. This choice is mainly constrained by the length of the strain gauge adopted; in fact, Table 2-3 shows that for the C3_A2 setup, it was possible to reduce the cutting mesh to 8×8 cm² as 30 mm strain gauges were used instead of 60 mm, as in the previous cases.

The deformation release is then compared with the variation of some of the setup or test execution parameters among those studied. In particular, among the test parameters reported in Table 2-3, the results are compared by varying:

- size of the cutting mesh;
- angle of inclination of the cuts;
- order of execution of the cuts.

Table 2-3: Setup and method of carrying out stress release tests.
[Romano and Mazzotti, 2022].

Nome prova	σ_v	$B \times h$	L_{sg}	Ordine tagli	Angolo di taglio
	MPa	cm \times cm	mm		gradi
C1_A3	10	10 \times 10	60	H + V	45° - 45°
C1_B2	10	10 \times 20	60	H + V	45° - 45°
C2_A1	10	10 \times 12	60	V + H	45° - 45°
C2_B1	10	10 \times 12	60	V + H	45° - 90°
C3_A2	10	8 \times 8	30	H + V	90° - 45°
C1_B3	10	10 \times 10	30	V + H	45° - 90°

The main results obtained by Romano and Mazzotti (2022) are:

- The execution of 45-degree inclined cuts on the side orthogonal to the tension component to be evaluated can affect the deformation release process, making it incomplete; it is recommended to adequately distance them from the edges of the strain gauges used.
- The execution of 90-degree inclined cuts on the side orthogonal to the tension component to be evaluated has proved to be very effective in completely releasing the deformations.
- The execution of 45-degree cuts on the side parallel to the stress component to be evaluated showed a modest negative influence on the deformation release only if performed first. It is therefore suggested that, to obtain a complete release of deformation and to keep the dimensions of the cutting geometry contained, it is advisable to first make the vertical cuts at 45 degrees and then the horizontal ones at 90 degrees. It should be noted that these results and conclusions are preliminary and further investigations and analyses, currently underway, are necessary to find their full confirmation.

The value of the residual prestress estimated with the release tests can be used in carrying out the checks concerning the ULS for the determination of the counter-shear [Lupoi and de Benedetti, 2021a].

2.3 Influence of prestress on shear strength

2.3.1 Introduction

In recent years, in addition to the issue of determining residual prestress on site, it has become increasingly important to evaluate the shear-bearing capacity of prestressed reinforced concrete bridge girders (PRC). As highlighted by Huber et al. (2013) in the early 1950s, the use of this technology rapidly increased, especially for the construction of large infrastructures, including bridges. Many of these structures, still in use today, have already reached (or are about to reach) their intended useful lives; furthermore, due to the increase in traffic loads, it is necessary to evaluate the residual bearing capacity. Based on the documents found in the literature, it emerged that, in Germany for example, due to the increase in loads and the evolution of regulations, more than 60% of prestressed reinforced concrete bridges are not adequate if verified following the indications of the regulations today [Gehrlein et al., 2018]. In this publication, as well as those of Huber and Kollegger (2015) and Huber et al. (2018), it is underlined that until 1966-1969 there was no minimum amount of shear reinforcement for prestressed elements, according to the German standard DIN 4227:1953. Nonetheless, about existing bridges in Germany, the publication by Gehrlein and Fischer (2019) reports that, from the inspections carried out, no signs of insufficient shear-bearing capacity emerged. Already from these statements it is possible to deduce how the contribution of the prestress plays a decidedly important role in the shear bearing capacity, this conclusion was also reached by Huber, Huber, et al. (2018) analysing the results of the experimental program they carried out. In Italy, from investigations carried out on site by technicians from ANAS S.p.A.⁵, bridge beams in prestressed reinforced concrete have been found made with a very low percentage of shear reinforcement (in some cases completely missing): in particular in elements made by S.C.A.C. – Società Cementi Armati Centrifugati, very widespread throughout the country in the 70s and 80s.

The DICATAM⁶ of the University of Brescia, in agreement with the Province of Brescia, has been carrying out a program of expeditious inspections on the infrastructures managed by the institution since 2017 to assess the state of conservation of about 500 bridges ($L > 6$ m) (Figure 2-37). To date, 401 artefacts have

⁵ Italian company of the FS Italian Group that deals with road infrastructures. It manages the network of state roads and highways of national interest.

⁶ DICATAM – Department of Civil, Environmental, Architectural Engineering and Mathematics.

2-LITERATURE SURVEY

been inspected, of which 176 in PRC, equal to 44% (Figure 2-38). These 176 artefacts were made from the 1960s up to the present day (Figure 2-39). Eleven bridges out of 176, around 6%, show an unexpected shear crack pattern (Figure 2-40). Considering the fact that the database acquired up to now for the bridges in the Province of Brescia can be considered a sufficiently representative sample, it results that 6 bridges out of 100 shows a crack pattern attributable to a brittle collapse. Therefore, it was decided to further investigate the correlation between the prestressing level and the resistant shear, with the hypothesis that these crack patterns are correlated to a prestressing loss higher than that envisaged in the design phase.

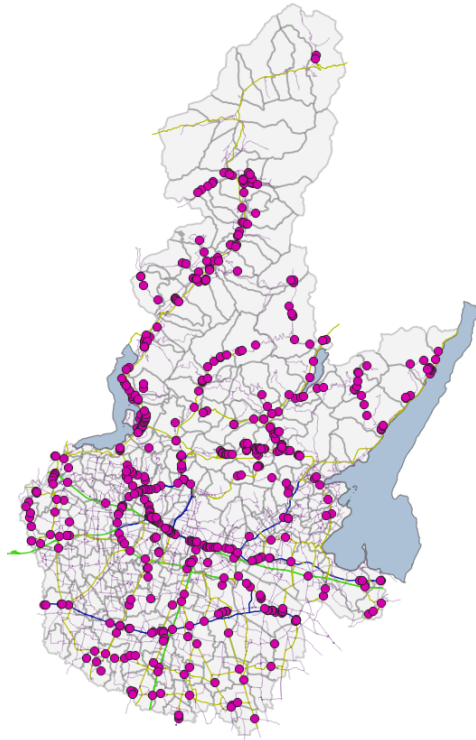


Figure 2-37: Bridges managed by the Province of Brescia

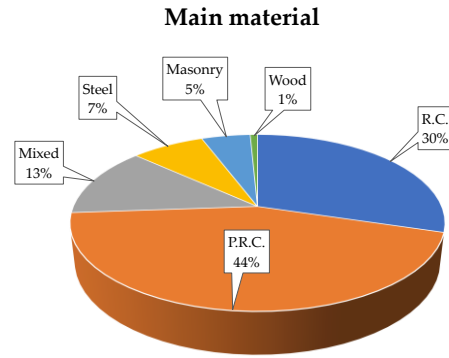


Figure 2-38: Main material used for the construction of a population of 401 inspected bridges in the Province of Brescia.

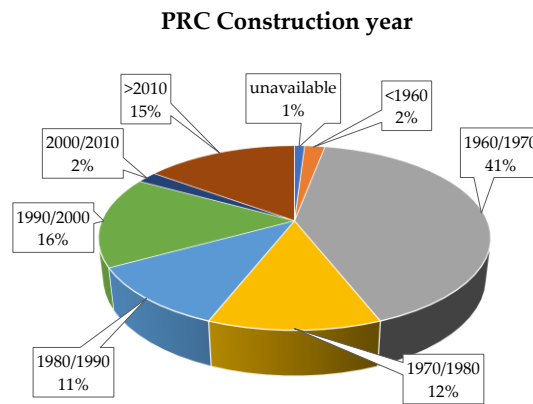


Figure 2-39: Year of construction of the 176 PRC bridges inspected in the Province of Brescia.

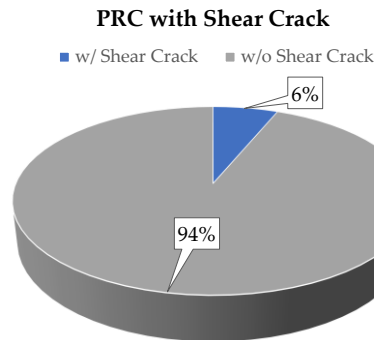


Figure 2-40: Shear crack pattern is shown in 11 out of 176 PRC bridges inspected in the Province of Brescia.

2.3.2 Experimental programs

In light of what is already present in the literature, it has emerged that some authors have carried out tests on beams made specifically for their experimental program, while others have tested elements belonging to real bridges.

Regarding this second series: both Bagge, Nilimaa, Puurula, et al. (2017) and Gehrlein and Fischer (2019) had the opportunity to carry out tests directly in situ (Figure 2-41); for example, Koppel and Vogel (1997) and Zwicky and Vogel (2000) have performed shear tests on quite rare post-tensioned bridge structures. Subsequently, Osborn et al. (2012) and Huber et al. (2013) tested real bridge beams in the laboratory, once they were taken after the dismantling of the infrastructure.

A shortcoming of this type of evidence is highlighted by Huber et al. (2013), in other words how the problem of tests on real beams is that all parameters of the beam are fixed, for this reason their influence on shear strength can hardly be investigated.

As said by Gehrlein and Fischer (2019) this kind of test is however important to validate the results of the tests carried out in the laboratory on small elements, which constitute the majority of the tests and could be affected by the scale effect. This type of test, conducted on real beams and especially those in situ, is generally carried out in such a way as to lead the beams to collapse. The common conclusion reached by the authors of the various publications is that the shear-bearing capacity of prestressed reinforced concrete bridge beams is underestimated by the formulas proposed in today's (national and European) standards. Most of the shear tests were performed on beams specially made for laboratory experiments, however, due to size and safety issues, experimental programs with shear tests on prestressed bridge beams to scale carried out in the laboratory are hardly found. As far as the experimental programs carried out using tests on beams specifically made to be tested in the laboratory are concerned: some studies are closer than others to the work presented in this document, this is the case, for example, of what is set out in the publication of Peng and Xue (2021). The previously mentioned publications in the literature allow to have a term of comparison for the results obtained in this work, as well as a reference on which instruments can be more effective in experimental programs involving shear tests on PRC elements. What has emerged from the bibliographic research carried out is the lack of shear tests on beams in which there is the possibility of varying the level of prestressing during the test, thus evaluating what happens at different load and prestressing steps.

This doctoral thesis work, therefore, has among its purposes that of bridging this gap present in the literature to date.

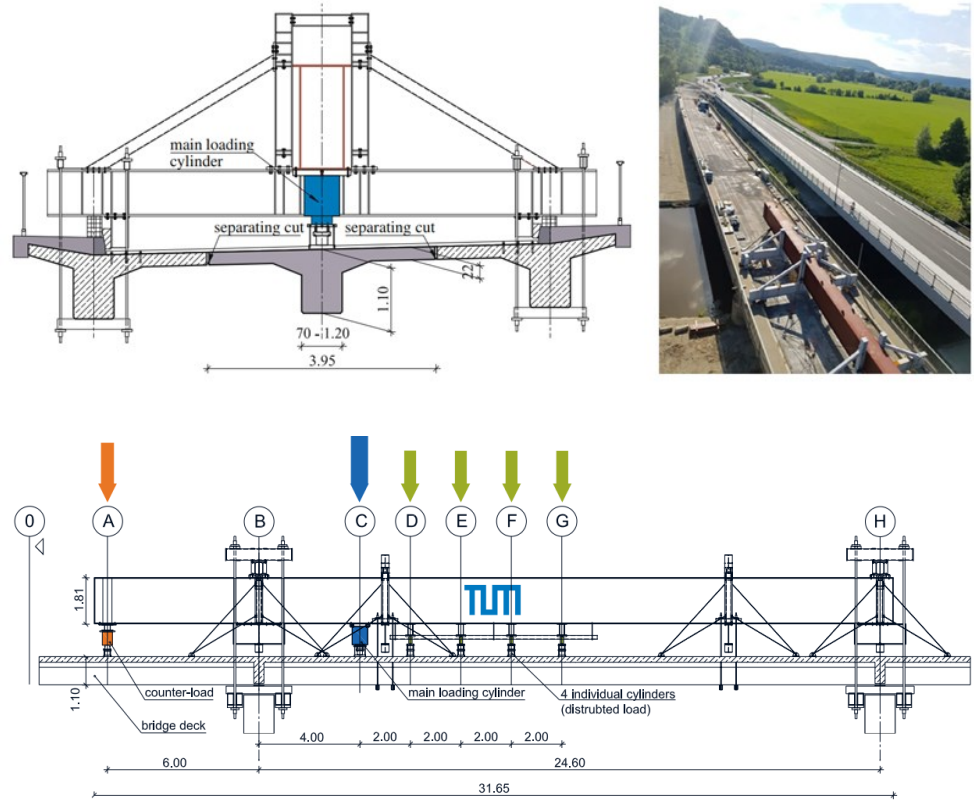


Figure 2-41: Set-up of the conducted in situ test [Gehrlein and Fischer, 2019].

2.3.2.1 Shear capacity of salvaged prestressed concrete bridge girders

[Osborn et al., 2012]

The purpose of the research illustrated by Osborn et al. (2012) approaches that of the experimental program presented in this work, the main difference being that in this publication the tested beams (AASHTO Type II) were taken from two bridges which remained in service for 42 years. The authors conducted load tests on seven prestressed beams to determine, in addition to the residual prestress level, their shear-bearing capacity. The shear tests were conducted on two of the seven available beams, to determine the shear bearing capacity when the load is applied close to the critical shear area, a total of four tests were then performed maintaining an equal a/d ratio to 1.5 (Figure 2-42). Tests were carried out on the remaining five beams to determine the residual prestress (§2.2.2.1.). Of the seven beams taken, six came from a four-span bridge dating back to 1968, the tested beams had a length of 7.2 m, the shear reinforcement was composed of 4 bars $\emptyset 13$ used as stirrups (with $f_y = 230$ MPa), placed 19.1 cm from the outer edge and arranged with a constant spacing of 58.4 cm; tests on concrete returned strength of 48.9 MPa (f'_c)

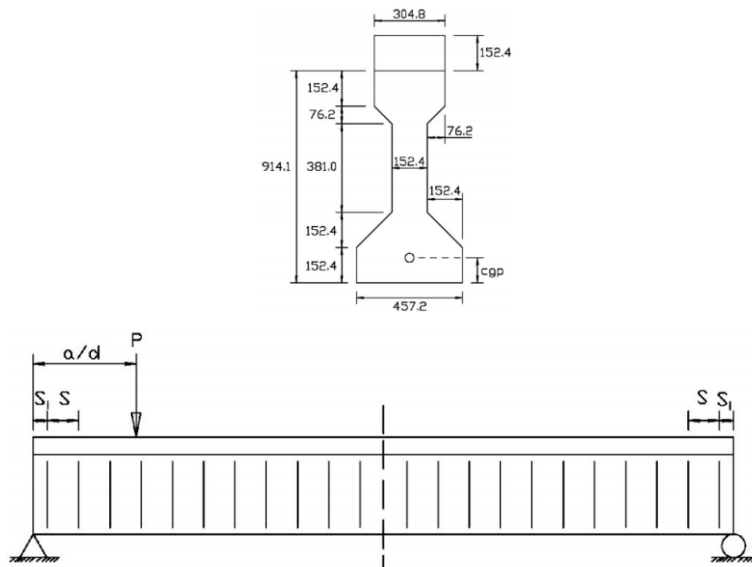


Figure 2-42: Test setup and stirrups arrangement (dimensions in mm) [Osborn et al., 2012].

As regards the prestressing reinforcement, there were 12 straight strands with a diameter of 11.1 mm (equivalent to 7/16 in.) made up of seven wires each, with an ultimate strength equal to $f_{pu} = 1780$ MPa. According to the bridge design documents, the prestressing at the jack was equal to 964 kN, while that expected as a result of the losses was equal to 783 kN. One of the two beams tested in shear belonged to this group, while the other test was conducted on a beam from a different

bridge, also in service for about 40 years, with a length of 10.5 m and whose tests on concrete yielded a compressive strength of 64.1 MPa. In this case, 14 strands with a diameter of 11.1 mm (equivalent to 7/16 in.) made up of 7 wires were used, with a total prestress of 1177 kN. In this beam the shear reinforcement started at a distance of 15.2 cm from the beam head and continued at a constant distance of 43.2 cm, the stirrups having the same properties as the other six beams. During the test strain gauges and a hydraulic jack were used to control the value of the applied load and the deformation was monitored using other strain gauges and LVDTs. The tests, conducted under load control, provided a shear strength equal to 727.7 kN for the 7.2 m long beam and 1163.2 kN for the 10.5 m long one, this result is consistent with the fact that the latter had greater strength than concrete and a smaller spacing than stirrups. The two beams exhibited a similar collapse by first developing vertical cracks, correlated to a flexural behaviour, and subsequently diagonal cracks with an inclination of about 42°. These results were compared with various formulations present in the American standards and with a strut-and-tie model: the latter proved to be the most suitable for estimating the shear bearing capacity, while the other formulations greatly underestimated the shear resistance of the tested beams. Finally, the authors also used, for the comparison, a finite element model, created using the ANSYS program, through which they were able to calibrate the parameters of the existing beams. In conclusion, the results showed that the variation of the compressive strength of the concrete has much more influence on the bearing capacity than the spacing variation of the stirrups.

2.3.2.2 Shear strength of over 50 years old post-tensioned concrete bridge girder

[Huber et al., 2013]

The following year Huber et al. (2013) conducted shear tests on bridge beams that had been in service for more than 50 years, the test results showed that there is a considerable shear strength resource in addition to that calculated using a “strut and tie” model. The test was conducted on beams 10.6 m long and 1.25 m high, which were tested with a span of 7 m and an a/d ratio of approximately 3.7. The beams were instrumented with strain gauges and LVDTs, furthermore, strain gauges were also placed on the stirrups to monitor their deformation during the load test. Since the beams in question came from the dismantling of a bridge that existed, in this experimental program the authors were only able to investigate the influence of the inclination of the strands as a parameter, since other fundamental data (such as the percentage of shear reinforcement and the dimensions of the beam) were fixed, differently from what happens when tests are carried out on beams designed and built to be tested in the laboratory.

The tested beams (Figure 2-43 and Figure 2-44) had a web 1250 mm high with a width equal to 420 mm, had a reinforcement percentage of 0.22% with Ø12 stirrups and a spacing of 250 mm, the longitudinal reinforcement was composed of only 4 Ø12 with $f_y = 435$ MPa and $f_u = 500$ MPa. There were 12 strands for post-tensioning, and each braid was composed of 16 wires each of which with an area of 30 mm², the strands present had $f_{p(1\%)} = 1440$ MPa and $f_{pu} = 1590$ MPa.

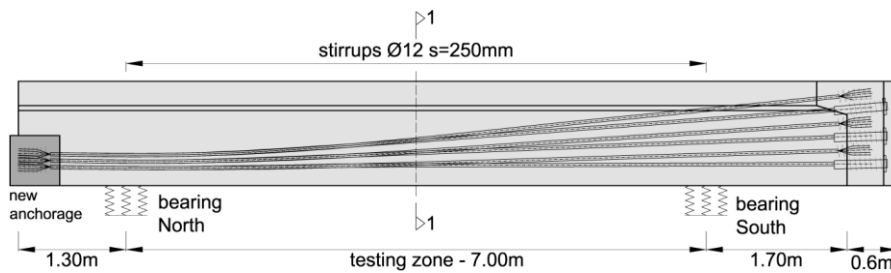


Figure 2-43: Profile of the strands in the tested beams [Huber et al., 2013].

The results of this same experimental program were also illustrated in a subsequent publication by Huber, Vill, et al. (2018), here the authors specify how the residual pretension was determined by cutting the wires that made up the strand, measuring their deformation through the use of strain gauges.

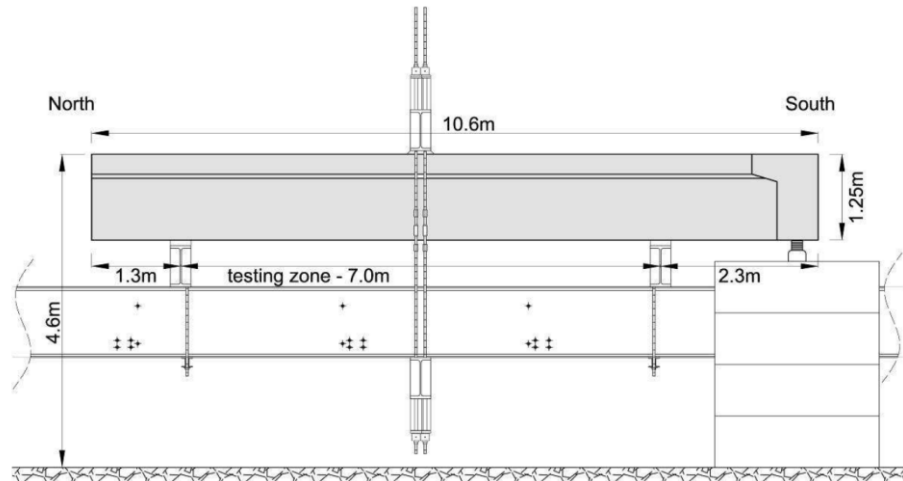


Figure 2-44: Test setup [Huber et al., 2013].

It was possible to state that the losses amounted to about 25% of the initial prestress ($\sigma_{p0} \approx 862$ MPa) and that therefore each strand had, at the moment of the test, a residual prestress force of 414 kN. Both beams tested showed the first flexural cracks at a load of 850 kN, while the first diagonal cracks required 1250 kN. The slits, with an angle of about 43° , reached a maximum opening of 1 mm. It was possible to increase the load up to 1650 kN, beyond which cracks were generated and associated with the yielding of the stirrups. Once the ultimate load of 1825 kN was reached, a brittle failure occurred with the opening of a critical shear crack and the failure of several stirrups. In this work [Huber et al., 2013] the authors have highlighted how Eurocode 2 underestimates the shear strength while the Model Code 2010, taking into account the concrete strength, provides more correct results. In particular, the experimental tests have shown that in beams with high post-tensioning, a certain force is required to induce the formation of diagonal cracks. This experimentally determined force turned out to be even higher than the shear bearing capacity calculated according to Eurocode 2, which only considers the contribution of the stirrups. In fact, the beam shear strength calculated with the Eurocode 2 approach gave a value of 841 kN, but the first diagonal cracking was only observed once a load of 1250 kN was reached, the author states that this means that up to this value, the stirrups are unloaded.

2.3.2.3 Shear strength of post-tensioned concrete girders with minimum shear reinforcement

[Huber and Kollegger, 2015]

Another interesting study, published by [Huber and Kollegger, 2015], describes a new experimental program on four post-tensioned beams with straight and inclined strands and with different percentages of transverse reinforcement. Figure 2-45 shows the dimensions of the elements, in particular: 2 beams were reinforced with 4 $\varnothing 4/200$ mm and two beams with 4 $\varnothing 4/125$ mm with reinforcement percentages of 0.056% and 0.089% respectively. The tests showed that the beams with inclined strands showed higher shear strength than those with straight strands. The results of the tests conducted confirmed what was deduced from the tests carried out on the two existing bridge beams carried out in 2013 previously illustrated, or rather how a low quantity of stirrups is sufficient to support a significant increase in load after the shear cracks have formed.

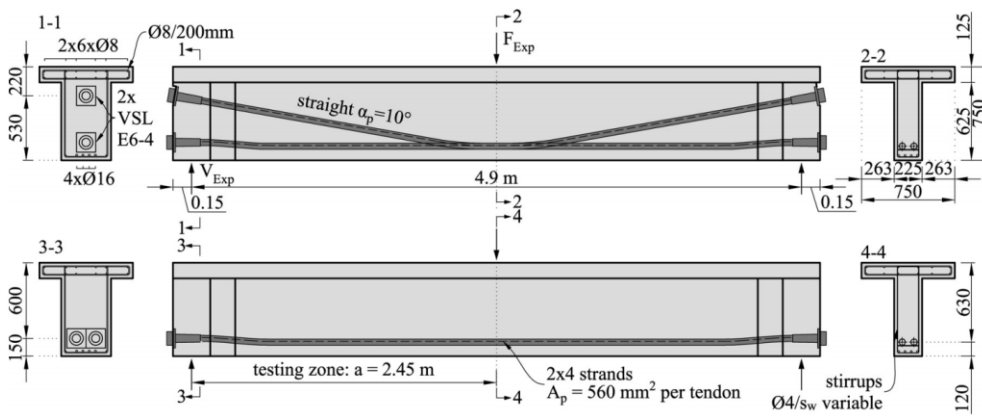


Figure 2-45: Tested Beams [Huber et al., 2013].

2.3.2.4 Assessment of the shear strength of existing post-tensioned bridges [Huber et al., 2017]

In the publication of Huber et al. (2017) the study on the same 4 beams by Huber and Kollegger (2015) was deepened. The main parameters investigated in this test are shown in Table 2-4 (Figure 2-46).

Table 2-4: Investigated parameters and shear strength of specimen [Huber et al., 2017].

Beam	Stirrups	$\alpha_{p,i}$ [°]	V_{exp} [kN]
PC056st	Ø4/200mm	0/0	453
PC089st	Ø4/125mm	0/0	475
PC056in	Ø4/200mm	0/10	549
PC089in	Ø4/125mm	0/10	537

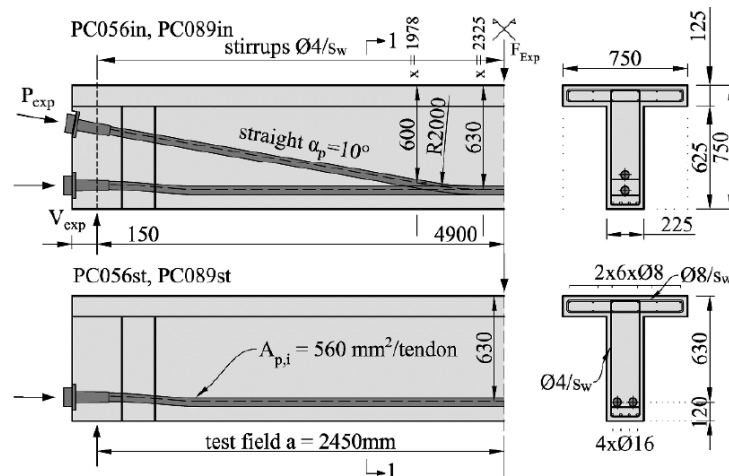


Figure 2-46: Dimensions of the test specimen, reinforcement and tendon layout [Huber et al., 2017].

The authors exploited the DIC technology to measure the evolution of critical shear cracking, through which it was possible to determine the influence of the different resistant mechanisms that were activated. Since their activation strongly depends on the shape, opening and sliding of the critical shear crack, measuring the evolution of the latter with photogrammetric analyses, combined with theory (thus taking into consideration, for example, the phenomenon of tension softening and the relations describing the aggregate interlock) it was possible to show how the "arching action" (i.e. the contribution of the non-cracked concrete in the compressed zone) is the main

2-LITERATURE SURVEY

resistant mechanism in the post-tensioned beams with a low amount of shear reinforcement (Figure 2-47).

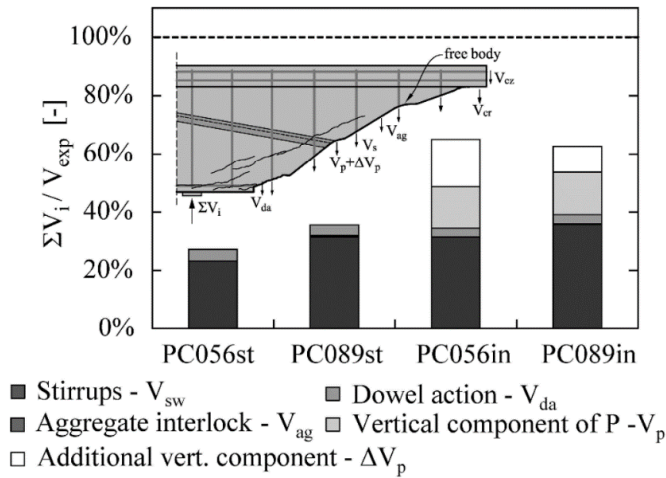


Figure 2-47: Percentage contribution of the different shear-resistant mechanisms [Huber et al., 2017]

Furthermore, the positive effect guaranteed by the inclined post-tensioned cables in increasing shear resistance is also confirmed here.

2.3.2.5 Influence of loading condition on the shear capacity of post-tensioned beams with low shear reinforcement ratio

[Huber, Huber, et al., 2018]

The following year, in the publication of Huber, Huber, et al. (2018) the results of tests carried out on eight beams are discussed, deviating from the traditional shear tests on a simply supported element with a load point, thus wanting to investigate the influence of different load conditions (Figure 2-48) on beams post-tensioned with a low percentage of shear reinforcement. Also, in this study, the authors combined the use of the DIC with theoretical formulas demonstrating, thanks to the comparison with the results of the experimental tests, how in this way it is possible to obtain satisfactory estimates of the shear bearing capacity.

Following this experimental program, it is reiterated that the contribution of the shear-resistant mechanisms offered by cracked concrete is negligible: this is because appreciable sliding along the critical shear crack in correspondence with the maximum load always occurs simultaneously with the most significant and decisive opening of the crack itself.

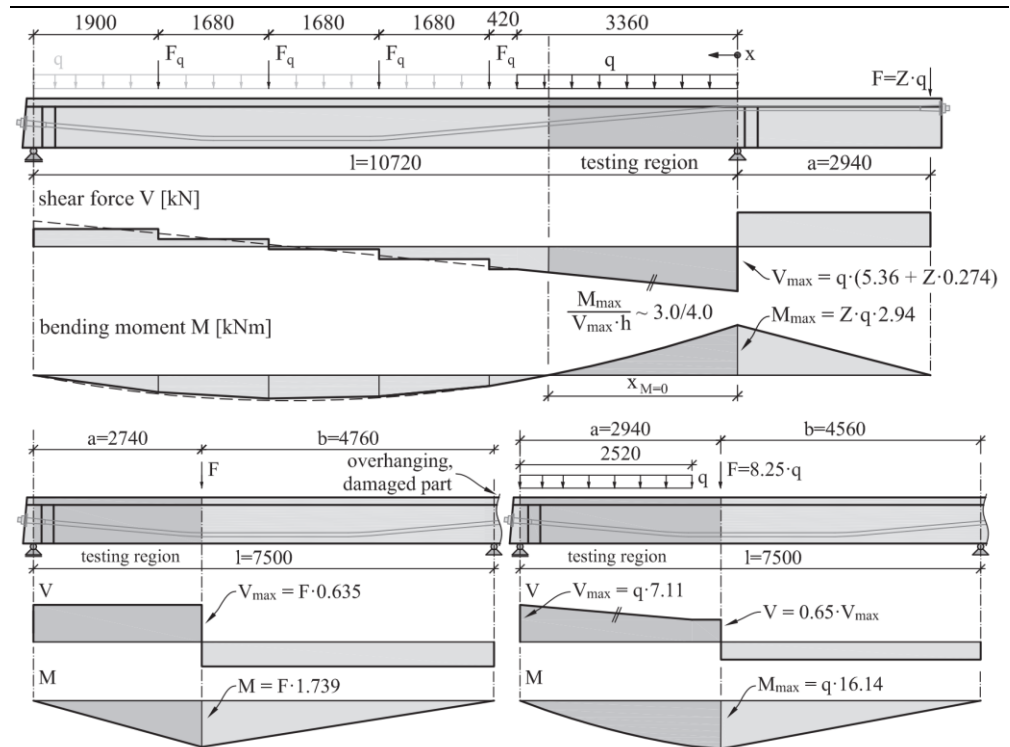


Figure 2-48: Different loading schemes used to test the beams [Huber, Huber, et al., 2018].

As far as shear reinforcement is concerned, these tests have highlighted, once again, that a reduced number of stirrups is sufficient to significantly increase the bearing capacity of the beam. Nevertheless, the test results confirmed that, after the formation of the critical shear crack, the contribution of the transverse reinforcement in the overall shear resistance of the member is relatively low. In conclusion: the use of the DIC (Figure 2-49) allowed to determine how the collapse of the tested beams occurred due to the inclined cracking in the compressed area combined with the breakage of the stirrups.

2-LITERATURE SURVEY

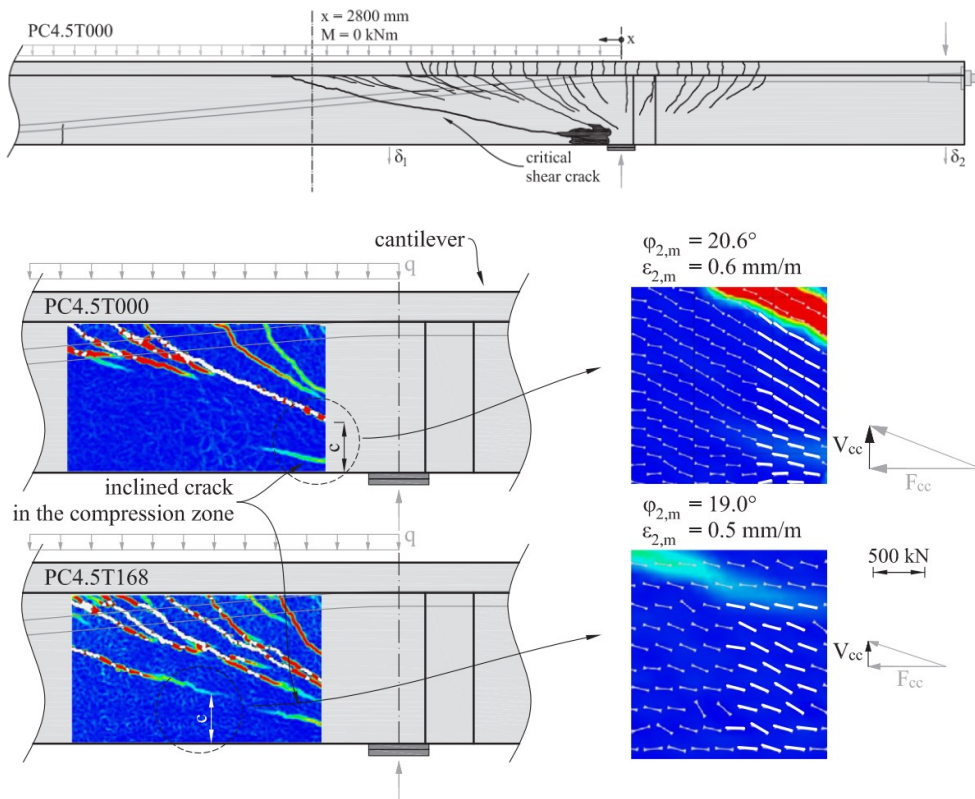


Figure 2-49: Use of DIC technology to determine the contribution of concrete in the uncracked compressed zone (V_{cc}) [Huber, Huber, et al., 2018].

2.3.2.6 Experimental and theoretical study on the shear behaviour of single and multi-span T and I-shape post-tensioned beams

[Huber et al., 2020]

In a later publication, Huber et al. (2020) describe some tests conducted to study the effect that different levels of prestress, different sections and a different percentage of transverse reinforcement have on shear strength. This work concluded what started in 2018 and illustrated by Huber, Huber, et al. (2018), adding four beams each subjected to two tests, for a total of eight new tests. Also, this experimental program has shown that it is the resistance offered by the concrete in the compressed area (identified with the term: "arching action") that gives a greater contribution to the shear-bearing capacity of the element (Figure 2-50). The activation of this mechanism mainly depends on the state of stress in the concrete in the non-cracked compressed area, consequently, it is influenced by the prestressing force, by the internal actions and by the geometry of this area.

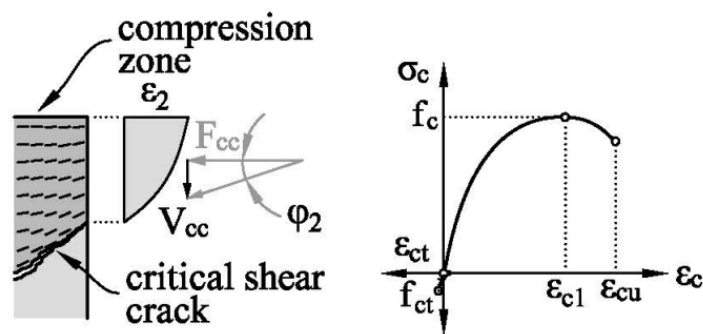


Figure 2-50: "Arching action" [Huber, Huber, et al., 2018].

As already briefly described above, in the publication of Huber et al. (2016) the authors developed a model called FSCM (Flexural-Shear Crack Model) which they claim has already been used in design practice for the determination of the shear bearing capacity of post-tensioned bridge beams. In the experimental program described by Huber et al. (2020) two test setups were adopted: in the first one each beam was simply supported with a cantilevered side to determine the shear resistance around continuity support, and a uniformly distributed load was simulated. After reaching the shear failure at the internal support, a second shear test was carried out on the undamaged part of the beam. These tests have shown how prestressing has a great impact on the shear strength of post-tensioned beams with a low percentage of shear reinforcement: a reduction in stress due to prestressing, 2 MPa instead of 4.5 MPa, leads to a drop in shear bearing capacity of 14÷19% in the case of a cantilevered beam with uniformly distributed load and of 22÷30% in the case of a beam simply supported with a load point.

2-LITERATURE SURVEY

Of all the parameters investigated, the shape of the section is the one with the least influence on the shear strength: an "I" beam increases the shear strength by 5÷7% compared to the use of a "T" beam.

This study once again confirmed the conclusions reached by the authors as a result of the experimental programs illustrated previously in this chapter, it is possible to summarize what has been demonstrated by these tests:

- Combining the constitutive laws, known from the theory, with the measurements obtained through DIC, relating to the evolution of the shear crack pattern, it is possible to trace the percentage contribution of each of the different shear-resistant mechanisms that are activated, to better understand the shear behaviour of post-tensioned reinforced concrete beams with a low percentage of transverse reinforcement.
- The transfer of actions that takes place in the area where the concrete is cracked (for example through the aggregate interlock) is negligible due to the large size of the cracks, consequently, the mechanism that plays the most important role is the contribution provided by the unbroken concrete. cracked in the compressed area (arching action).
- The resistance offered by the compressed and non-cracked portion of concrete (arching action) contributes positively to increasing the shear-bearing capacity. It should therefore be taken into consideration, as done in the FSCM model proposed by Huber et al. (2016), to obtain a good estimate of the strength of existing post-tensioned structures, to avoid reinforcement interventions when not necessary.

2.3.2.7 Shear Behaviour of Externally Prestressed Concrete Beams with Draped Tendons

[Qi et al., 2016]

Also, in the publication of Qi et al. (2016) an experimental and analytical study conducted on nine T-shaped cross-section beams is presented to investigate the effect of prestressing (in particular the bending angle of the external strands) on the shear strength of externally prestressed concrete beams. The nine beams differ from each other because the a/d ratio, the angle of inclination of the strands and the spacing of the stirrups are varied, maintaining a percentage of shear reinforcement in a range between 0.24% and 0.59 % (Table 2-5).

Table 2-5: Summary table of the properties of the tested beams [Qi et al., 2016].

Beam	Concrete strength f_c' , MPa	Shear span-depth ratio a/d	Longitudinal reinforcement ratio ρ_s , %	Transverse reinforcement ratio ρ_v , %	Space of stirrups, s , mm	Effective prestress, f_{pe} , MPa	Bend angle of tendons, α , degrees	Test parameter
S-1	58.3	2.48	2.85	0.39	120	1067.6	7.40	Benchmark beam
S-2	56.7	2.48	2.85	0.39	120	—	—	RC comparison beam
S-3	51.3	2.08	1.27	0.39	120	920.4	7.40	Effect of a/d
S-4	57.1	2.82	2.85	0.39	120	881.6	7.40	Effect of a/d
S-5	53.5	2.48	1.27	—	—	965.2	7.40	Effect of stirrups
S-6	50.5	2.48	2.85	0.59	80	883.6	7.40	Effect of stirrups
S-7	57.8	2.48	2.85	0.24	200	923.5	7.40	Effect of stirrups
S-8	51.9	2.48	2.85	0.39	120	947.9	0	Effect of tendon's bend angle
S-9	51.3	2.48	2.85	0.39	120	993.4	3.57	Effect of tendon's bend angle

All beams (Figure 2-51) have the same dimensions and geometric characteristics: squat beams (4 m long and 0.5 m high) with T-section; characterized by the presence of a full section in the middle, rib, for a length of 15 cm. The longitudinal mild reinforcement consists of 6 \emptyset 18 with f_y equal to 478 MPa. Only two beams (S-3 and S-5) have lower longitudinal reinforcement, having \emptyset 12s inside them instead of \emptyset 18s. For the stirrups instead, \emptyset 6 are used with a variable spacing from 5 to 12 cm. Except for the S-2 beam, each beam was externally prestressed with two seven-wire strands at different angles. The strands were anchored at various cross-sectional heights and thus correspond to different strand inclination angles ranging from 0 to 7 degrees. In all beams, the strands have a nominal diameter of 12.9 mm with a mean tensile strength f_{pu} of 1860 MPa and an elastic modulus E_p of 195,000 MPa. Each strand was tensioned at an initial stress of 1395 MPa and the mean effective stress value at the moment of the test was 948 MPa, thus having suffered a loss of 32%.

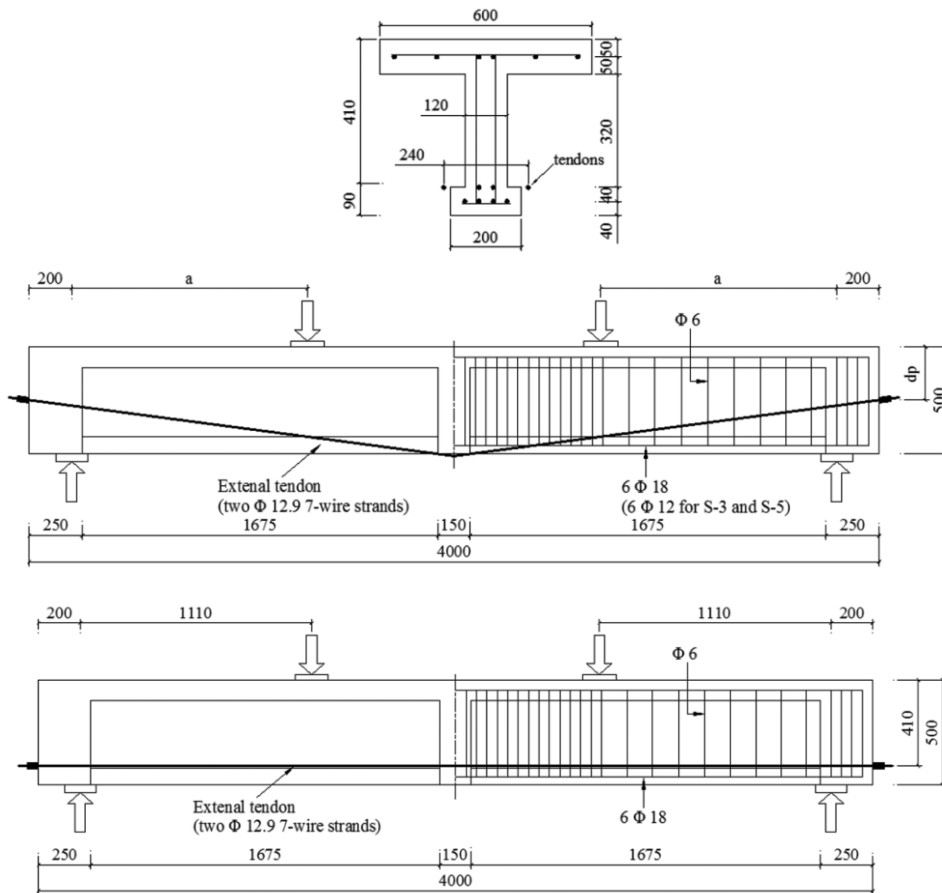


Figure 2-51: Tested beams [Qi et al., 2016].

Comparing the prestressed beams with the S-2 beam (not prestressed) it can be seen how the prestressing completely alters the shear behaviour both as regards the ultimate resistance and the cracking pattern: the prestressing delays the appearance of the first shear crack and slows down the propagation of the critical shear crack, thereby significantly increasing the first cracking shear load and shear strength, which increase by 150% and 56%, respectively.

However, the prestress does not affect the ductility: the S-4 beam, i.e., the one with the greater a/d , is the one which has shown a more ductile behaviour, perhaps because failure occurs in a section further away from the support, where the longitudinal reinforcement is greater.

Comparing the beams with different percentages of shear reinforcement it is possible to observe that the presence of stirrups allows for an increase in the applied load and causes a reduction of the tensile stress of the concrete in the web. Furthermore, beams with more stirrups deform less, with the same applied load, than those with fewer stirrups. Before the formation of shear cracks, the stirrups are substantially unloaded, however, after cracking, they undergo a rapid increase in stress against a small increase in the applied load. By keeping the other parameters constant and changing the angle of inclination of the external strands, the authors found that the stiffness of the three beams did not vary, given that the angle of inclination of the strands does not affect the second moment of inertia and that also the load of shear cracking does not change. However, the inclination of the strands modifies the crack pattern, especially in the flexural area between the two load points: with the inclined strands, a new region of fan-shaped cracks can be seen instead of flexural cracks, due to the upward force of inclined strands which causes the beam to behave as a continuous beam. This area is called by the authors "secondary fan-shaped crack region" (SFCR), highlighted in the following image by purple borders (Figure 2-52).

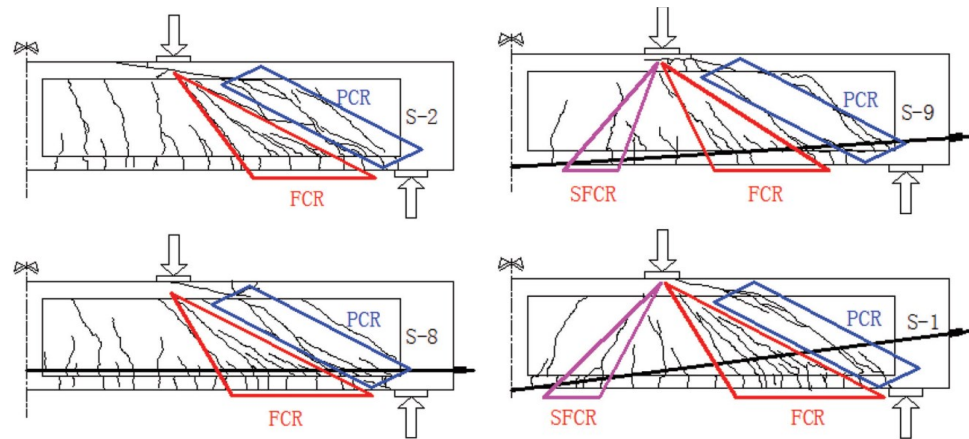


Figure 2-52: Cracking patterns as the inclination of the external strands varies [Qi et al., 2016].

In beams with straight strands an arched behaviour is observed overall; instead, the configuration of the arch mechanism is markedly altered in beams with inclined strands because the vertical, upward force induced by the external strands causes the beam to tend to behave as a continuous beam. As a result, two additional compressed struts are created which go from the load point towards the centre line (Figure 2-53).

2-LITERATURE SURVEY

The applied shear force is then partially transmitted, through these two new struts, to the strands, reducing the stress in the compressed strut directed from the load point to the support, which allows for an increase in the shear strength of the beams.

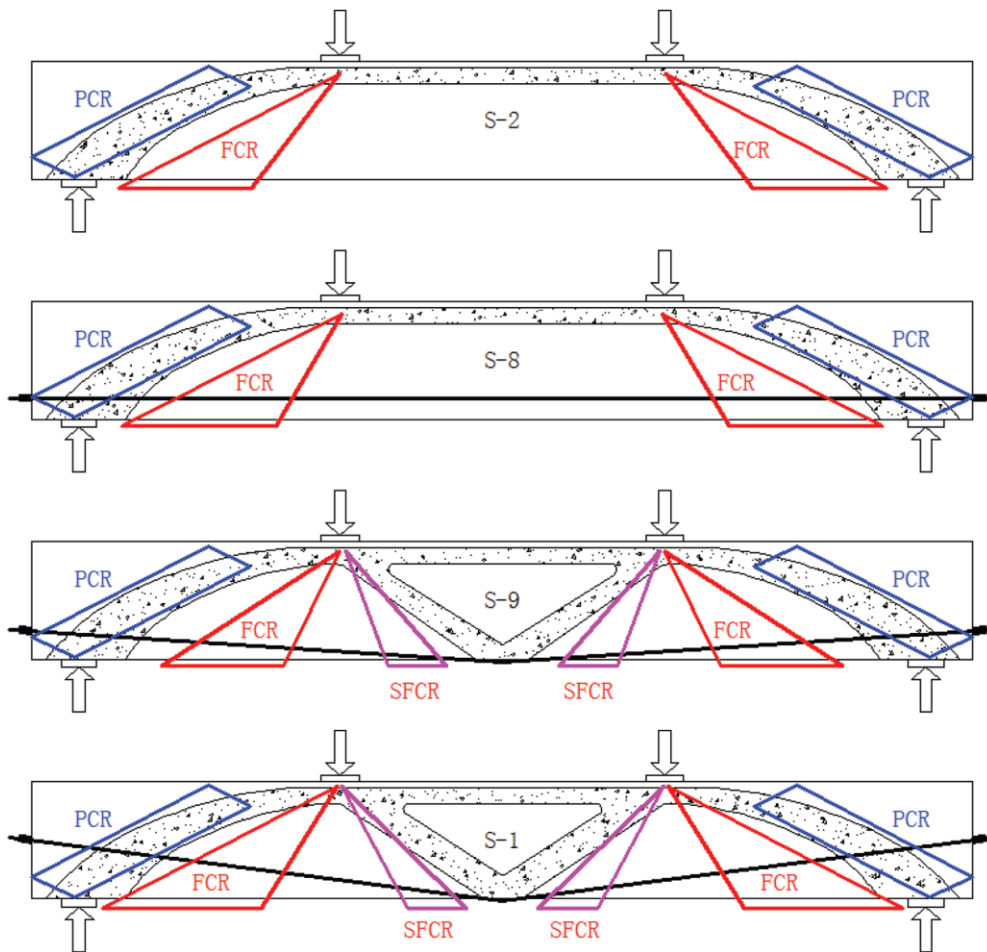


Figure 2-53: Direction of the struts as the strands vary [Qi et al., 2016].

Based on these considerations, the authors propose a new refined arch-truss model that takes into account the increase in shear strength in the case of inclined strands by adding the contribution correlated to the secondary arch.

2.3.2.8 Experimental investigation on shear behaviour of FRP post-tensioned concrete beams without stirrups

[Peng and Xue, 2021]

The publication of Peng and Xue (2021) describes an experimental program conducted on beams without stirrups and post-tensioned to investigate the behaviour of fibre-reinforced strands (CFRP), introduced as an alternative solution to traditional reinforcing bars whose corrosion is one of the main causes of deterioration of RC and PRC structures. Seven beams 5 m long and with a section of 50 cm by 25 cm were tested, supported with a clear span of 4.5 metres. To enforce shear failure the beams had an a/d ratio of about 3 and a percentage of longitudinal reinforcement was used such that the ultimate bending load was at least 1.5 times the shear load. Of the seven beams tested, two had steel strands, one with steel mild reinforcement and one in GFRP with an initial prestress of 500 kN, the strands used had a nominal diameter of 12.7 mm with $f_u = 1853$ MPa and $f_{y(1\%)} = 1725$ MPa (with ultimate strain equal to 5.2%); the concrete had $f'_c = 50$ MPa and a maximum size of the aggregates of 20 mm. The post-tensioning was obtained with an anchoring system and a hydraulic jack. The longitudinal bars and the area subject to compression were instrumented with ERSG with a length of 5 mm and 60 mm: in particular, five strain gauges were placed in correspondence with the shear light, in the load points and in the centre line. The width of the shear cracks was measured manually with a microscope and an accuracy of 0.01 mm; moreover, 5 LVDTs were installed with an accuracy of 0.001 mm on each beam to measure the deflection at the supports, load points and in the centre-line. Strains in the beam web were measured with LVDT systems installed longitudinally, transversely and at an inclination of 45° to the axis of the beam. Finally, DIC technology was exploited to detect the width and flow of critical shear cracks (Figure 2-54 and Figure 2-55).

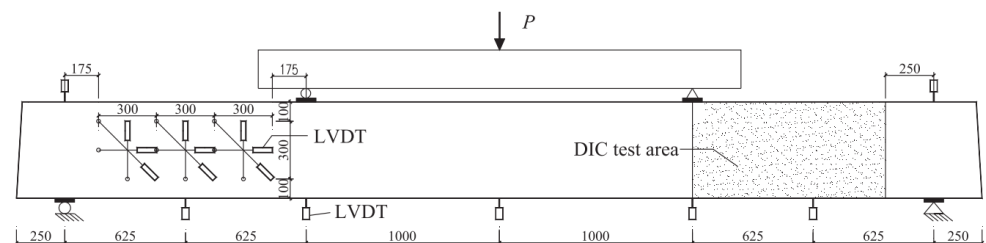


Figure 2-54: Instrumentation applied to the beam under test [Peng and Xue, 2021].

2-LITERATURE SURVEY

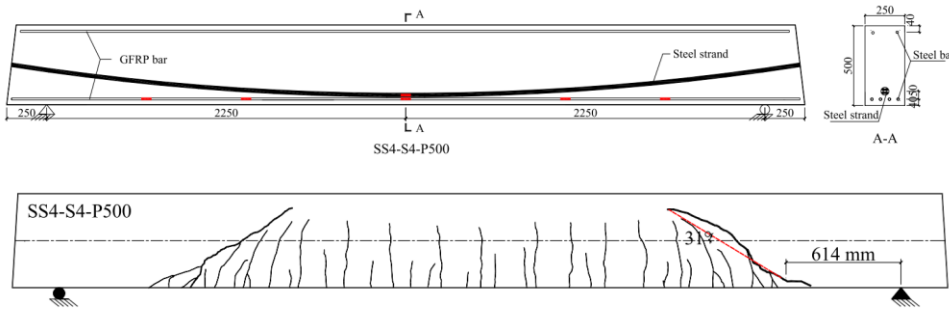


Figure 2-55: Profile of the strands and crack pattern at failure [Peng and Xue, 2021].

In their conclusions, the authors underline how shear strength increases significantly as the prestress level increases. In particular, by increasing the prestressing force from 0 to 360 kN and 440 kN, the maximum shear that the beam can withstand increases by 97.8% and 125.9% respectively. By further increasing the prestress, passing from 440 kN to 500 kN, this resistance decreases by about 5%: this phenomenon is associated with the fact that high levels of prestress could lead to premature failure in the flexural area, where normal combined compressive forces act to shear stresses. Finally, the article highlights how, in these non-reinforced shear beams with a/d equal to 3, the prestress favours the development of an arch action and how the contribution of the aggregate interlock to the shear resistance is negligible, otherwise from what happens in non-prestressed reinforced concrete beams, as also found by Huber et al. (2017).

3 EXPERIMENTAL PROGRAM

3.1 Introduction

The experimental program carried out for this thesis work was designed both to analyse the effectiveness of different diagnostic techniques for determining residual prestress, and with the aim of studying the influence of prestress losses on bearing capacity shear, referring, in particular, to bridge girders. The idea of investigating this topic arose following the inspections carried out by the University of Brescia, in collaboration with the Province of Brescia, in which crack patterns with the presence of shear cracks emerged in a significant number of elements unexpected in beams in PRC, even more, if one considers that these elements were not in a condition close to collapse. Also, based on what has emerged from the literature, where there are other studies investigating the influence of prestress losses on the shear resistance of elements in PRC (§2.3), the need to analyse this issue more deeply has emerged. Were then tested in the laboratory PRC prestressed beams lightly shear reinforced and with different levels of prestress, specially designed, and loaded with an a/d ratio such as to induce a failure due to shear. This is with the aim of observing the formation of a shear crack pattern, thus returning to the real situations detected during the inspections, and correlating the evolution of the cracks to the applied load and to the prestress present at that time in the tested beam. The beams, object of the experimental program, were therefore designed to represent a very common type of bridge beams present in the area and, moreover, they were made with real dimensions, to avoid phenomena related to the size effect. This is because, also thinking of the Kani valley, it is not easy to make small specimens and adapt them in such a way as to represent phenomena correlated to real elements [Kani, 1966, 1967]. In the preparation phase of the experimental program, a fabricator was identified who, among many, mainly produces PRC elements intended for the roofing of the warehouse. The commissioned beams have an "I" cross-section, typical of most PRC bridge decks. It was decided to build a total of 4 beams, all with the same geometry, but with different reinforcement configurations, both prestressing and mild. Two of the four beams (subsequently called Beams A and B) were made with pre-tensioning system with bonded strands at two prestressing levels fixed during the casting phase; while the remaining two beams (subsequently called Beams C1 and C2) are identical and have been designed with a hollow corrugated pipe so as to be able to subsequently allocate unbonded strands with an external post-tensioning system. The main objective on which the choice of using only 4 samples is based derives from the fact that to avoid the creation of dozens of beams with different levels of prestress,

3-EXPERIMENTAL PROGRAM

two pre-tensioned beams with fixed prestress were built (Beam B with 67% prestressing with respect to Beam A), while the post-tensioned ones have been made so that they differ as little as possible from the pre-stressed beams (in geometry, materials, mild reinforcement, test setup) to be able to evaluate the conditions of the beam at different levels of prestress. It was decided to test these beams with prestressing levels lower than the design one since the crack patterns, found following the inspections carried out by the University of Brescia, are supposed to be correlated to prestressing losses greater than those foreseen in the design phase. In this way, it was possible to investigate the correlation between prestress and shear strength. The beam tested with a tension reduced up to 70%, representing a prestress reduction of 30%, aims to reproduce the condition in which an element in CAP is found once the long-term losses have occurred. The tests carried out with a prestress equal to about 90%, 80% and 60% of the design one, were designed to analyse, with the same applied load, how other levels of losses influence the response of the structural element in question. It was decided not to go below 60%, not only for safety reasons, but also because studying the effects of a loss greater than 40% would represent an extremely burdensome and unrealistic condition. At the same time, a comparison of pre-tensioned and post-tensioned PRC beams is also performed.

3.2 Specimen geometry

The goal was to design, and subsequently test, elements that well represented the bridge beams present on the Italian territory, especially in the Province of Brescia: one of the most common types is that of I-beams with a height of 70 ÷80 cm and slim web. To optimize construction times and costs, it was decided to rely on an external prefabrication company, thus using a geometry defined by the formworks they supplied that was compatible with the needs required in the design of this experimental program. The choice of sectional dimensions was limited to the availability of the catalogues of various fabricators in the Province of Brescia. Among these, the section and configuration of the prestressing reinforcement such that there was a shear collapse was identified from a simulation on the finite element model created with VecTor 2⁷. The most suitable section for the construction of the beams of the present experimental program has an "I" section (see Figure 3-1) with a height of 80 cm and a web of 18 cm thick. These elements, each 10 m long, were made by Camuna Prefabbricati S.r.l.

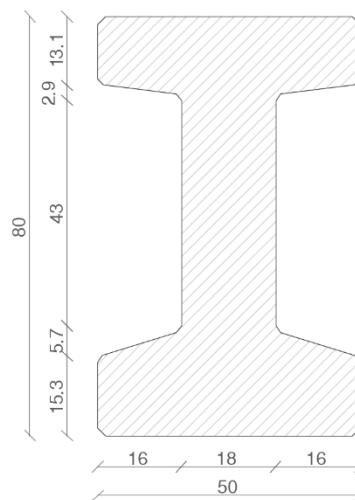


Figure 3-1: Cross section of the beams (dimensions in cm).

⁷ VecTor 2 is a nonlinear finite element analysis (NLFEA) program for the analysis of two-dimensional reinforced continuum structures subjected to quasi-static or dynamic load conditions. Developed by Professor Frank J. Vecchio at University of Toronto [Web site: <http://vectoranalysisgroup.com>]

3.3 Design of the Beams

While in the 2 beams with pre-tensioned strands, the prestressing reinforcements were calibrated so that the beams exhibited a failure due to shear, the 2 post-tensioned ones (identical to each other) were designed to have the possibility of performing tests at different levels of prestress. The choice of mild reinforcement, mainly used as a stirrup support, depended on the available configuration of the fabricator. For all beams, the stirrups have 2 legs, $\varnothing 8/300$ mm for the entire length of the beam, with $\varnothing 12$ at half spacing for the first 135 cm from the beam ends. The refinement of spacing is necessary for all that area considered D-Region (Discontinuity, Disturbed, Detail) where there is the diffusion of prestress, both pre-stressed and post-stressed. The $\varnothing 8$ stirrups were made with a single piece of reinforcement shaped like the concrete section, while the $\varnothing 12$ stirrups were only present in the web with a rectangular shape (see Figure 3-2 and Figure 3-3). The reinforcement design for each beam type is shown below.



Figure 3-2: Stirrups $\varnothing 8/300$ mm shaped like the "I" section in the central area.



Figure 3-3: Rectangular $\varnothing 12/150$ mm stirrups with $\varnothing 8/300$ mm stirrups shaped like the "I" section in the end D-regions.

3.3.1 Beam A

In Beam A, in addition to the mild reinforcement made up of 20 \varnothing 8 used as stirrup supports along the entire section, 6 bonded 6/10" 7-wire strands ($\varnothing_{nom} = 15.2$ mm $A = 139$ mm²) were used for the entire length of the beam. The strands were positioned as in Figure 3-4.

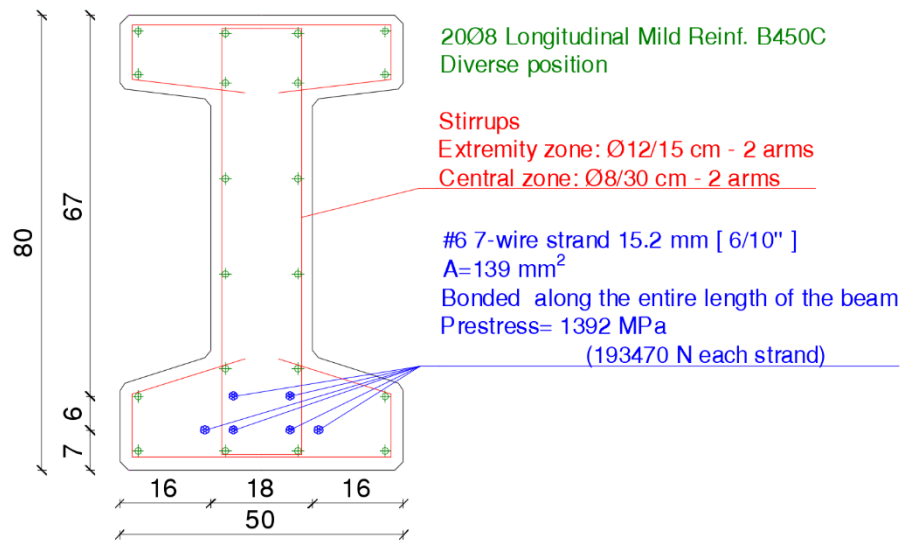


Figure 3-4: Design indications and execution of Beam A.

All strands are in perfect bond with the concrete along the entire length of the beam. Before casting phase, a pretension force was applied to each strand through a hydraulic jack equal to 193.47 kN ($\sigma_{pi} = 1392$ MPa), for a total of 1161 kN on 6 strands (§3.3.4). The prestressing losses were calculated according to EC2 both in the short and in the long term (30 days) thus obtaining an effective tension of 955 kN ($\sigma_{p\infty} = 1145$ MPa) considering 17.8% of total losses (§3.3.5). Figure 3-5 shows the reinforcement design commissioned by the fabricator.

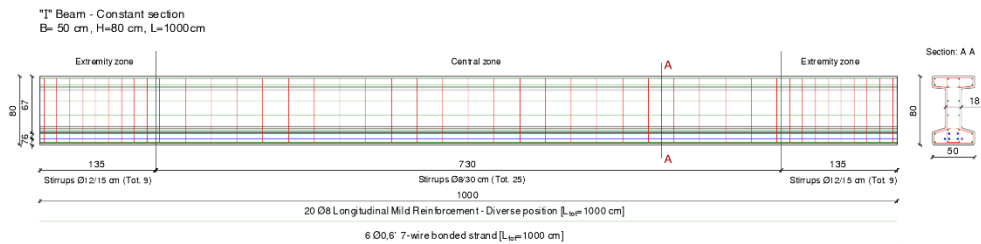


Figure 3-5: Longitudinal exploded view of Beam A.

3-EXPERIMENTAL PROGRAM

Figure 3-6 shows the reinforcement prepared in the factory before positioning the formwork and casting.

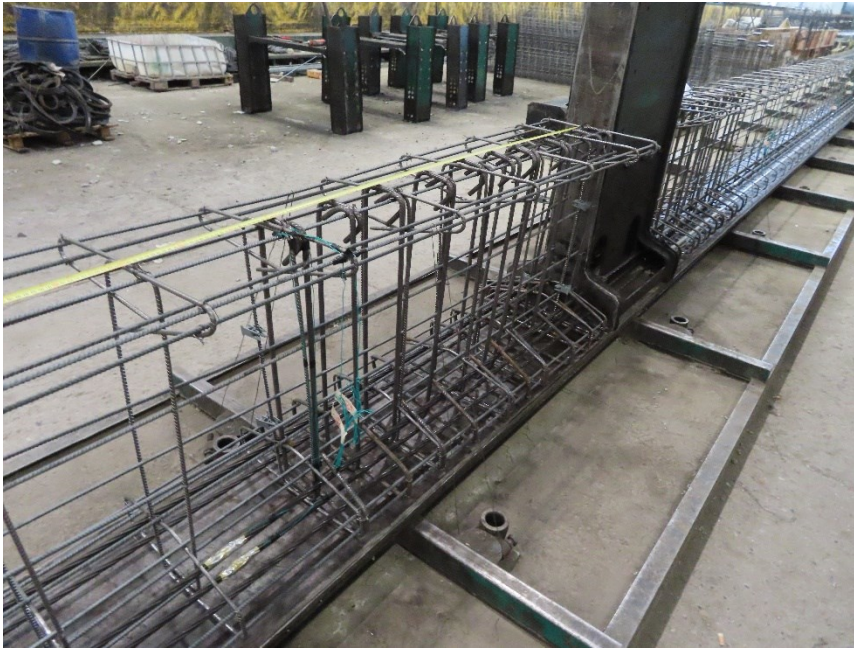


Figure 3-6: Reinforcement in the factory before casting – Beam A.

3.3.2 Beam B

In Beam B, in addition to the mild reinforcement made up of 20Ø8 used as stirrup supports along the entire section, 4 bonded 6/10" 7-wire strands ($\phi_{nom} = 15.2$ mm $A = 139$ mm²) with cables were used for the entire length of the beam (instead of 6 present in Beam A), this is to simulate a beam that had about 70% prestress for Beam A. The jack used for tensioning the individual strands can only apply 2 load steps: 50% and 100%. To speed up the casting operation and to simulate a 70% prestress, during construction for all the beams 6 strands were stretched along the track and 100% stretched, for beam B the 2 outermost strands positioned on the first layer, have been sheathed along the entire length of the beam thus inhibiting their bond. Once the casting had matured, the two sheathed strands were easily removed. To compensate for the absence of the 2 strands removed, 2Ø26 mild reinforcements were added to the same effective height to be able to more correctly simulate the behaviour of a prestressed beam subject to a 30% loss of prestress while keeping its ductility ability. This design choice certainly affects an alteration of the flexural crack pattern, resulting in closer and more numerous cracks than those of Beam A.

The strands and the integrative mild reinforcement were positioned as in Figure 3-7.

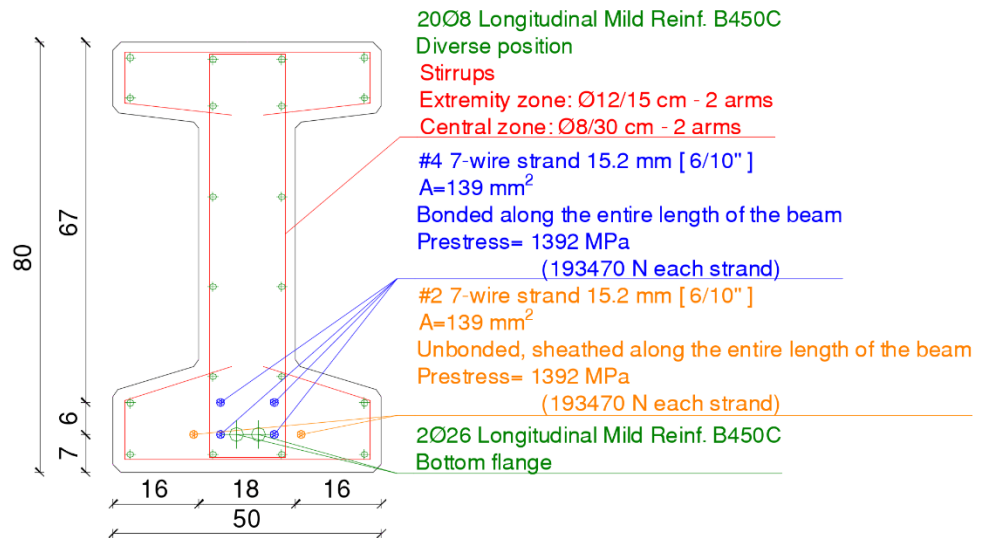


Figure 3-7: Design indications and execution of Beam B.

For Beam B, 4 strands were therefore used in perfect bound with the concrete for the entire length of the beam. As for Beam A, a pretension force was applied to each strand through a hydraulic jack equal to 193.47 kN ($\sigma_{pi} = 1392$ MPa), for a total of 774 kN on 4 strands (§3.3.4). In this way a prestress reduction of 1/3 for Beam A was simulated. Beam B, therefore, has 67% prestress of Beam A. The prestressing losses were calculated according to EC2 both in the short and in the long term (30 days) thus obtaining an effective tension of 641 kN ($\sigma_{p\infty} = 1153$ MPa) considering 17.2% of total losses (§3.3.5). Figure 3-8 shows the reinforcement design commissioned by the fabricator.

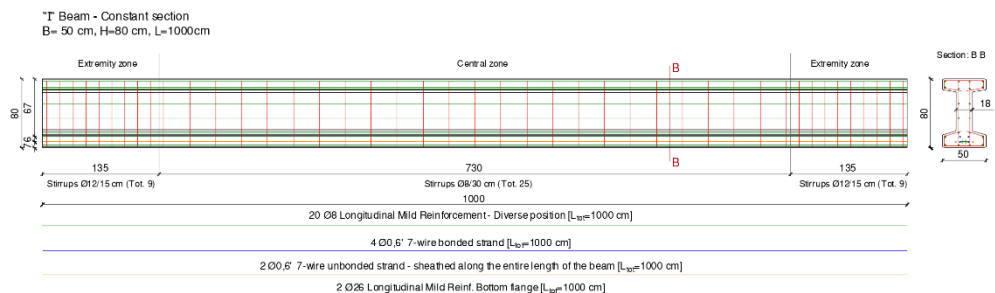


Figure 3-8: Longitudinal exploded view of Beam B.

3-EXPERIMENTAL PROGRAM

Figure 3-9 shows the reinforcement prepared in the factory before positioning the formwork and casting, while Figure 3-10 shows the detail of the reinforcement in the lower flange.



Figure 3-9: Reinforcement in the factory before casting – Beam B.



Figure 3-10: Reinforcement detail of Beam B in the factory before casting.

3.3.3 Beams C1 and C2

The two Beams C are identical to each other, in addition to the mild reinforcement made up of 16Ø8 used as stirrup supports along the entire section, 4Ø12 have been positioned in the lower flange, necessary to support its own weight during transport and handling in as in these phases there is not yet any prestress. In fact, before the casting, a corrugated sheath Ø80 was positioned so that its centre coincided with the barycentre of the pre-stressed reinforcement of Beam A. Furthermore, like Beam B, to speed up the casting operation, for all the beams, 6 strands were tensioned along the track and 100% stretched, for the two Beams C the 6 strands were sheathed for the entire length of the beam thus inhibiting their bond. In this way, after the formwork was removed and the pretension was released, the strands were easily removed from the two beams (Figure 3-11). The Ø80 sheath has the function of hosting 7 6/10" 7-wire strands ($\phi_{nom} = 15.2 \text{ mm}$ $A = 139 \text{ mm}^2$) which will slide along the entire length of the beam. At the head, the strands are constrained with clamping plates and wedges anchors. Due to the diffusion of prestressing with the sliding strands post-tensioning system, the detail of the reinforcement arranged in the heads was designed following the specifications of the PTI - Post-Tensioning Institute (Wollman and Roberts-Wollman):

- Confinement reinforcement: Ø12 spiral reinforcement for a length of 25 cm around the aluminium sheath (Figure 3-12);
- Bursting reinforcement: thickening of the Ø12 rectangular stirrups with 2 legs for 40 cm for a spacing of 5 cm (Figure 3-12);
- Spalling reinforcement: welded mesh Ø6 with a few centimetres of mesh (Figure 3-13).

Figure 3-14 shows the reinforcement design commissioned by the fabricator.

3-EXPERIMENTAL PROGRAM

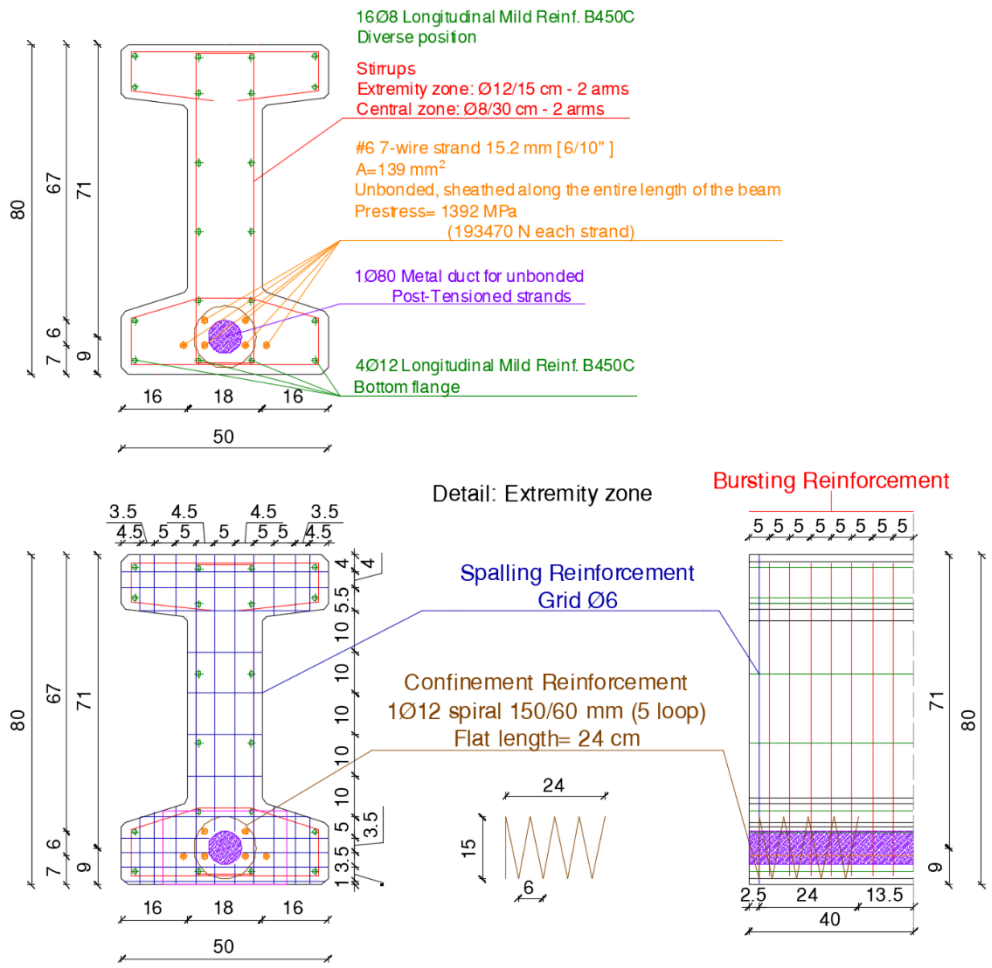


Figure 3-11: Design indications and execution of Beams C.



Figure 3-12: Confinement and Bursting reinforcement

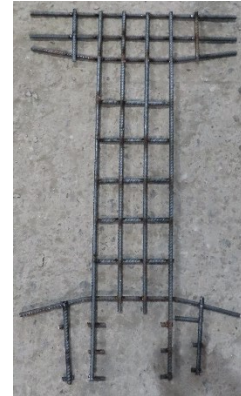


Figure 3-13: Spalling reinforcement

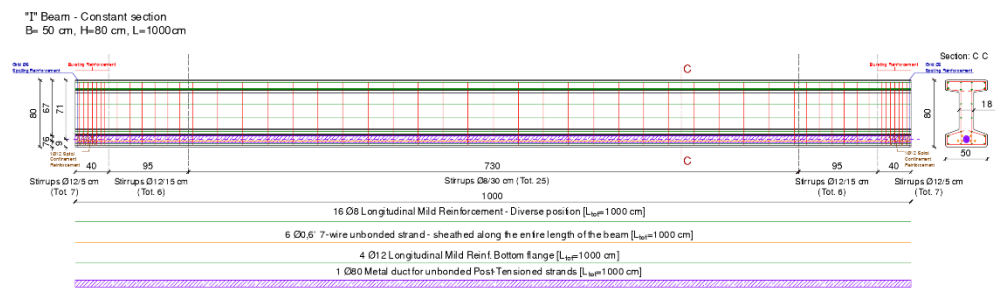


Figure 3-14: Longitudinal exploded view of Beams C.

3.3.4 Prestressing step and casting

The mild reinforcement cage of the 4 beams (*Figure 3-15*) was arranged in advance along a casting track inside the factory located in Berzo Inferiore (BS) of Camuna Prefabbricati S.r.l.. Inside the cage, in the lower flange of the beams, 6 strands were laid along the more than 40 meters of track (from *Figure 3-16* to *Figure 3-18*) and subsequently they were tensioned in 2 steps (see *Figure 3-19*) with a jack stretcher. In the first step, all the strands were pre-stressed with a force induced by the jack equal to 74.15 kN (533 MPa), in the second step the strands were individually tensioned with a force applied to the jack equal to 193.47 kN (1392 MPa). At each step, a check was made between the elongation suffered on the strand and the pressure marked by the pump.



Figure 3-15: Reinforcement cage of all beams.



Figure 3-16: Strand tensioning track head.



Figure 3-17: Intermediate beam formwork element for strand continuity.



Figure 3-18: Terminal head for strand anchoring.



Figure 3-19: Strand tensioning phases in the factory.

The work ended with the casting of the concrete in the formworks (Figure 3-20 and Figure 3-21), making one beam per day in the following order:

Data of Casting	Beam
06/07/2022	C1
07/07/2022	C2
08/07/2022	B
09/07/2022	A



Figure 3-20: I-beam formwork.



Figure 3-21: Beam casting.

3.3.5 Prestressing Losses

A calculation was carried out to estimate the losses suffered by the pre-tensioned PRC beams (Beams A and B) according to EC2. The tension with which the strands were tensioned in the factory was declared to be equal to 19'347 kg which, compared to the area of 139 mm² of the single strand, is equivalent to the stress of $\sigma_{pi} = 1392$ MPa. Below are the calculations carried out for the estimation of the prestressing losses of beams A and B, respectively with 6 and 4 strands of 7-wire 6/10" ($\phi_{nom} = 15.2$ mm $A = 139$ mm²) with bonded cables for the entire length of the beam.

As regards instantaneous losses, the following were considered:

- A loss due to wedge-cable sliding during the tensioning phase equal to 2.5%:

$\Delta\sigma_{p,st.1} = \sigma_{pi} \cdot 2.5\%$		Beam A	Beam B
$\Delta\sigma_{p,st.1}$		35 MPa	35 MPa
		2.5%	2.5%
	$\Delta P_{p,st.1}$	29.0 kN	19.3 kN

- An initial instantaneous elastic loss, in which the value of the stress drop due to the deformation of the concrete fibre at the level of the strand, is subtracted from the stress at the moment of tensioning:

$$\sigma'_p = \sigma_{pi} - n \cdot \left(\frac{P_M}{A_{id}} + \frac{P_M \cdot e \cdot e}{I_G} - \frac{M_{1,k} \cdot e}{I_G} \right) \tag{3-1}$$

$$\Delta\sigma_{p,st.2} = \sigma_{pi} - \sigma'_p \tag{3-2}$$

where:

- $n = \frac{E_p}{E_{cm}}$
- $P_M =$ Total compression tension force:
- $= n_{strands} \cdot A_{1\phi strand} \cdot \sigma_{pi}$
- $e =$ Eccentricity of the strands with respect to the centroid,
- $A_{id} = A_{Concrete} + (n - 1) \cdot (A_{Prestress Reinf.} + A_{Mild Reinf.})$
- $I_G =$ Inertia modulus
- $M_{1,k} =$ Bending moment of initial condition

	Beam A	Beam B
E_p [MPa]	200000	
E_{cm} [MPa]	36240	35070
P_M [N]	1160928	
A_{id} [cm ²]	2523.09	2563.32
e [cm]	29.88	
I_G [cm ⁴]	1811098	
$M_{1,k}$ [KNm]	76.29	
$\Delta\sigma_{p,st.2}$	50 MPa	32 MPa
	3.6%	2.3%
$\Delta P_{p,st.2}$	41.7 kN	17.7 kN

- As regards the losses due to the relaxation of the reinforcing bars, since the beams have not undergone any steam curing treatment, instantaneous losses have not been considered.

About long-term losses, reference was made to the expression 5.46 del §5.10.6 EC2:

$$\Delta\sigma_{p,c+s+r} = \frac{\varepsilon_{cs} \cdot E_p + 0.8 \cdot \Delta\sigma_{pr} + \frac{E_p}{E_{cm}} \cdot \varphi(t, t_0) \cdot \sigma_{c,q}}{1 + \frac{E_p}{E_{cm}} \cdot \frac{A_p}{A_{id}} \cdot \left(1 + \frac{A_{id}}{I_G} \cdot z_{cp}^2\right) \cdot [1 + 0.8 \cdot \varphi(t, t_0)]} \quad (3-3)$$

Considering then:

- A loss due to prestress, assuming:
 - o Relative humidity equal to 60%
 - o t_0 = time elapsed between casting and loading = 30 days

shrinkage is given by a component correlated to drying (drying shrinkage) (ε_{cd}) and one related to autogenous shrinkage (ε_{ca}):

$$\varepsilon_{cs} = \varepsilon_{cd} + \varepsilon_{ca} \quad (3-4)$$

3-EXPERIMENTAL PROGRAM

where:

- $\varepsilon_{cd}(t) = \beta_{ds}(t, t_s) \cdot \varepsilon_{cd,\infty}$
- $\beta_{ds}(t, t_s) = \frac{(t-t_s)}{\left[(t-t_s) + 0,04 \cdot \sqrt{h_0^3} \right]} = 0.46$
 - $t = 30$ days
 - $t_s = 28$ days (end of maturation)
 - $h_0 = \frac{2 \cdot A_c}{\mu_{2P}} = \frac{2 \cdot 244000 \text{ mm}^2}{3240 \text{ mm}} = 150 \text{ mm}$
- $\varepsilon_{cd,\infty} = k_h \cdot \varepsilon_{cd,0}$

These values were taken from tables 11.2 Va and 11.2 Vb present in §11.2.10.6 NTC 2018, using as input data:

- $f_{ck} = f_{cm} - 8 \text{ [MPa]}$
 - $f_{cm} = 61.2 \text{ Beam A}$
 - $f_{cm} = 62.5 \text{ Beam B}$

Tab. 11.2.Va – Valori di ε_{c0}

f_{ck}	Deformazione da ritiro per essiccamento (in ‰)					
	Umidità Relativa (in ‰)					
	20	40	60	80	90	100
20	-0,62	-0,58	-0,49	-0,30	-0,17	+0,00
40	-0,48	-0,46	-0,38	-0,24	-0,13	+0,00
60	-0,38	-0,36	-0,30	-0,19	-0,10	+0,00
80	-0,30	-0,28	-0,24	-0,15	-0,07	+0,00

Tab. 11.2.Vb – Valori di k_h

h_0 (mm)	k_h
100	1,00
200	0,85
300	0,75
≥ 500	0,70

Figure 3-22: Tables for determining the coefficients k_h and ε_{c0} (§11.2.10.6 NTC 2018).

Getting then:

- $k_h = 0.925$
- $\varepsilon_{cd,0} = -0.32$

- The average value of the deformation due to autogenous shrinkage can be calculated with expression 3.11 del §3.1.4 EC2:

$$\varepsilon_{ca}(t) = 2,5 \cdot (f_{ck} - 10) \cdot 10^{-6} \cdot (1 - e^{-0.2 \cdot \sqrt{t}}) \quad (3-5)$$

$$\blacksquare \quad t = 30 \text{ days}$$

- A loss due to relaxation of the strands, where Class 2 strands ("low relaxation") have been considered and formula 3.29 del §3.3.2 EC2 has been applied.

$$\frac{\Delta\sigma_{pr}}{\sigma_{pi}} = 0,66 \cdot \rho_{1000} e^{9,1 \cdot \mu} \left(\frac{t}{1000} \right)^{0,75 \cdot (1-\mu)} 10^{-5} \quad (3-6)$$

$$\Rightarrow \Delta\sigma_{pr} = 19,6 \text{ MPa}$$

where:

- $\rho_{1000} = 2.5\%$
- $\mu = \frac{\sigma_{pi}}{f_{pk}} = \frac{1392}{1860} = 0.75$
- $t = 30 \text{ days} = 720 \text{ h}$
- A loss due to viscosity in which the parameter $\varphi(\infty, t_0)$ was obtained from table 11.2.VI, reported in §11.2.10.7 of NTC 2018, using as input data:
 - $h_0 = \frac{2 \cdot A_c}{\mu_{2P}} = \frac{2 \cdot 244000 \text{ mm}^2}{3240 \text{ mm}} = 150 \text{ mm}$
 - $R.H. = 60\%$
 - $t_0 = 30 \text{ days}$

Tab. 11.2.VI – Valori di $\varphi(\infty, t_0)$. Atmosfera con umidità relativa di circa il 75%

t_0	$h_0 \leq 75 \text{ mm}$	$h_0 = 150 \text{ mm}$	$h_0 = 300 \text{ mm}$	$h_0 \geq 600 \text{ mm}$
3 giorni	3,5	3,2	3,0	2,8
7 giorni	2,9	2,7	2,5	2,3
15 giorni	2,6	2,4	2,2	2,1
30 giorni	2,3	2,1	1,9	1,8
≥ 60 giorni	2,0	1,8	1,7	1,6

Tab. 11.2.VII - Valori di $\varphi(\infty, t_0)$. Atmosfera con umidità relativa di circa il 55%

t_0	$h_0 \leq 75 \text{ mm}$	$h_0 = 150 \text{ mm}$	$h_0 = 300 \text{ mm}$	$h_0 \geq 600 \text{ mm}$
3 giorni	4,5	4,0	3,6	3,3
7 giorni	3,7	3,3	3,0	2,8
15 giorni	3,3	3,0	2,7	2,5
30 giorni	2,9	2,6	2,3	2,2
≥ 60 giorni	2,5	2,3	2,1	1,9

Figure 3-23: Tables for determining the coefficient $\varphi(\infty, t_0)$ (§11.2.10.7 NTC 2018)

The weighted average between 2.1 and 2.6 was done, obtaining: $\varphi(\infty, t_0) = 2.475$.

3-EXPERIMENTAL PROGRAM

Considering missing input values to be included in the formula (3-3), the total deferred losses were estimated equal to

	Beam A	Beam B
E_p [MPa]	200000	
E_{cm} [MPa]	36240	35070
f_{cm} [MPa]	61.2	62.5
$\sigma_{c,q}$ [MPa]	9.15	
A_p [cm ²]	8.34	5.56
A_{id} [cm ²]	2523.09	2563.32
$\varphi(t, t_0)$	2.48	
z_{cp} [cm]	29.88	
I_G [cm ⁴]	1811098	
$\Delta\sigma_{p,lt}$	162 MPa	173 MPa
	11.7%	12.4%
$\Delta P_{p,lt}$	135.5 kN	95.9 kN

Adding the short-term and long-term losses together gives the total:

	Beam A	Beam B
$\Delta\sigma_{p,st_1}$	35 MPa	35 MPa
	2.5%	2.5%
$\Delta\sigma_{p,st_1}$	29.0 kN	19.3 kN
$\Delta\sigma_{p,st_2}$	50 MPa	32 MPa
	3.6%	2.3%
$\Delta P_{p,st_2}$	41.7 kN	17.7 kN
$\Delta\sigma_{p,lt}$	162 MPa	173 MPa
	11.7%	12.4%
$\Delta P_{p,lt}$	135.5 kN	95.9 kN
$\Delta\sigma_p =$ $\Delta\sigma_{p,st_1} + \Delta\sigma_{p,st_2} + \Delta\sigma_{p,lt}$	247 MPa	239 MPa
	17.8%	17.2%
ΔP_p	206.3 kN	133.0 kN
$\sigma_{p\infty} = \sigma_{pi} - \Delta\sigma_p$	1145 MPa	1153 MPa
	P	954.7 kN

It is reasonable to believe that the real prestress is higher than that estimated through the calculations illustrated above. For example, an overestimation of the losses related to viscosity has been made since the coefficient $\varphi(\infty, t_0)$, refers to the viscosity exhibited in infinite time, while the tests were performed approximately one month after casting.

In the numerical model (§5.2) the prestress values supplied as input were calibrated to obtain the same tension in the strands net of all losses.

3-EXPERIMENTAL PROGRAM

3.3.6 Instrumentation (Measurements tools)

For all the acquisitions performed in the laboratory, unless otherwise specified, control units for strain gauge amplifiers QuantumX HBM - MX1615B at 16 channels were used, while for the rest of the instrumentation, four QuantumX universal amplifiers HBM - MX840B at 8 channels were used. The acquisition frequency was 1 Hz. The software for configuring and managing the output data from the instruments is HBM Catman.

3.3.6.1 Reinforcement

To monitor the behaviour of the transverse reinforcement and in particular the prestressed reinforcement, before the casting and with the prestress activated, strain gauges (SG) were installed in different positions inside all the beams. The type of strain gauges applied on the reinforcement is from SHOWA Measuring Instruments Co., Ltd, with a length of 5 mm (Figure 3-24). The products and the gluing and protection operations carried out follow a standard procedure defined by Micro-Measurements VPG Group and by ANAS S.p.A. (2020). To monitor the strands, an SG was glued to one of the 7 strand strands at different locations along the length of the strand (Figure 3-25). Before the application of the SG on the stirrups of all the beams, the two stirrups were identified (one on the fifth stirrup and one on the sixth stirrup with respect to the support which would then have been closest to the load point during the test) which would have been intercepted from a shear crack during testing, using a finite element simulation with VecTor 2 software (Figure 3-26).

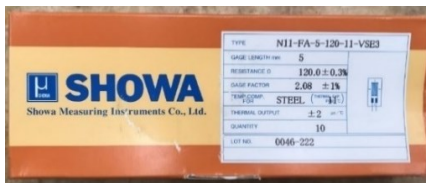


Figure 3-24: Pack of strain gauges applied to the reinforcement.



Figure 3-25: Strain Gauge on a wire of a strand.



Figure 3-26: Strain gauges with protection on the stirrups.

On Beam A a total of 11 strain gauges were installed on the strands (Figure 3-27):

- 2 at the support closest to the loading point, 1 on the lower inside row and 1 on the upper row (Figure 3-29);
- 6 below load point, 1 for each strand (Figure 3-28);
- 1 in the middle, proved to be unusable (cable damaged during transport);
- 2 at the support furthest from the loading point, 1 on the lower internal row and 1 on the upper row (Figure 3-29).

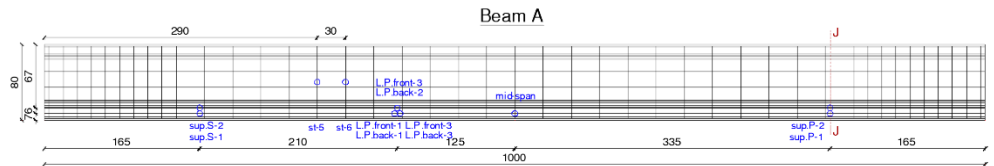


Figure 3-27: Strain gauges position Beam A.



Figure 3-28: Strain gauges below the point of load.



Figure 3-29: Strain gauges at support.

On Beam B a total of 9 strain gauges were installed on the strands (Figure 3-30):

- 2 at the support closest to the loading point, 1 on the lower inside row and 1 on the upper row (Figure 3-32);
- 4 below load point, 1 for each strand (Figure 3-31);
- 1 in the middle;
- 2 at the support furthest from the loading point, 1 on the lower internal row and 1 on the upper row (Figure 3-32).

3-EXPERIMENTAL PROGRAM

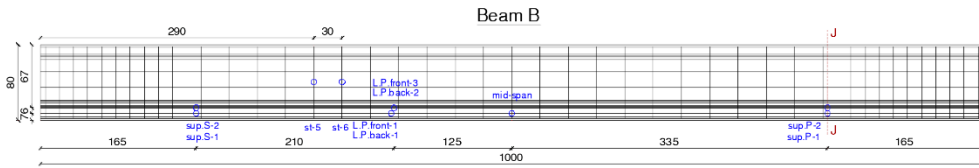


Figure 3-30: Strain gauges position Beam B.



Figure 3-31: Strain gauges below the point of load.



Figure 3-32: Strain gauges at support.

In Beams C, in this phase, strain gauges are only installed on the stirrups. The strands were instrumented in a second phase when the beams were already in the laboratory. All the connecting wires were brought to the extrados of the beam so as not to interfere with the formwork (Figure 3-33).

The strain gauges were installed on a single wire for each strand, after carrying out a treatment in which the wire is scratched with sandpaper and cleaned with special products; the strain gauge is then glued after having applied a catalyst able to guarantee the correct contact of the resistance. Through a series of tensile tests (Figure 3-34 and Figure 3-35), carried out in the laboratory on sections of strands in which all 6 external wires have been instrumented, it was possible to verify that all the instrumented strain gauges returned a similar strain value, as shown in the graph of Figure 3-36. To verify the correct method of applying strain gauges and the setup of the test, to have a term of comparison, two $\varnothing 12$ bars were tested under traction, one smooth and one with improved bound, obtaining an exhaustive answer in the comparison. In this way, it has the certainty that, even if monitoring only one wire, it is possible to trace the deformation of the strand and consequently, the state of

stress if it remains in the elastic range. It also emerged, from the scientific article by Ahmad et al. (2019), how the central wire, of the 7 that make up a strand, has a slightly larger section than the other 6 and tends to load slightly more. This leads to a stress in the external threads of about 0.5% lower than the mean value, and a stress in the central thread about 3% higher than the mean value. In the post-tensioned Beams C, the strands were instrumented (before applying the post-tension) using 10 SGs: 7 were installed at the height of the support closest to the load point, monitoring 1 wire of each strand, 3 have been installed in correspondence with the other support. The decision to place the strain gauges in correspondence with the supports is correlated to a practical difficulty in placing them near the point of maximum bending moment. However, being the post-tensioning system with unbonded cables, the tension in the strands should be constant along their entire length. To check that the actual behaviour of the strands was as described above, it was decided to instrument three strands at two symmetrically opposite points.

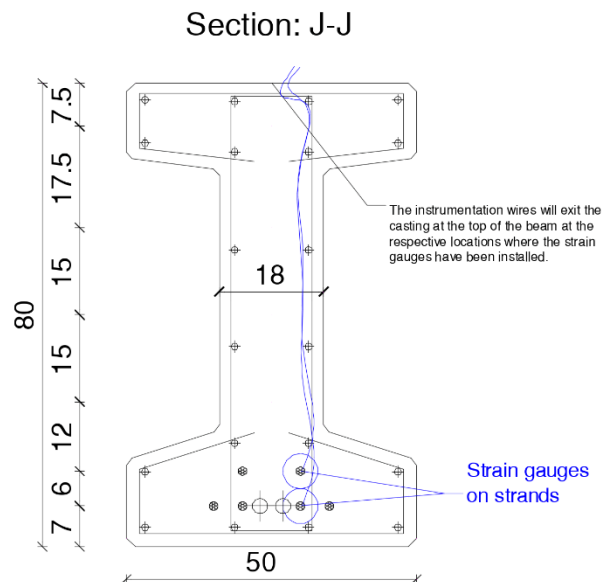


Figure 3-33: Detail in the cross-section of the strain gauges wiring.

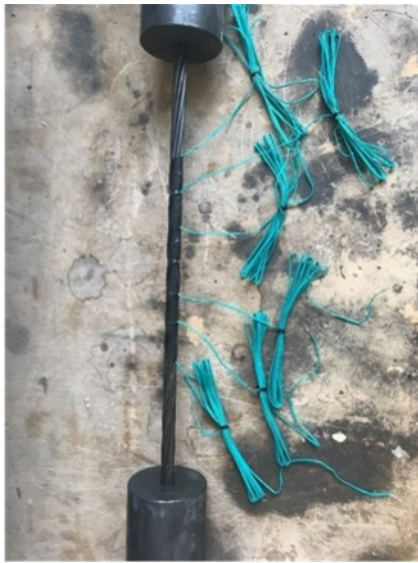


Figure 3-34: Piece of strand clamped for tensile test with 6 strain gauges applied to the external wires.



Figure 3-35: Test to verify the differences in the reading of the strain gauges.

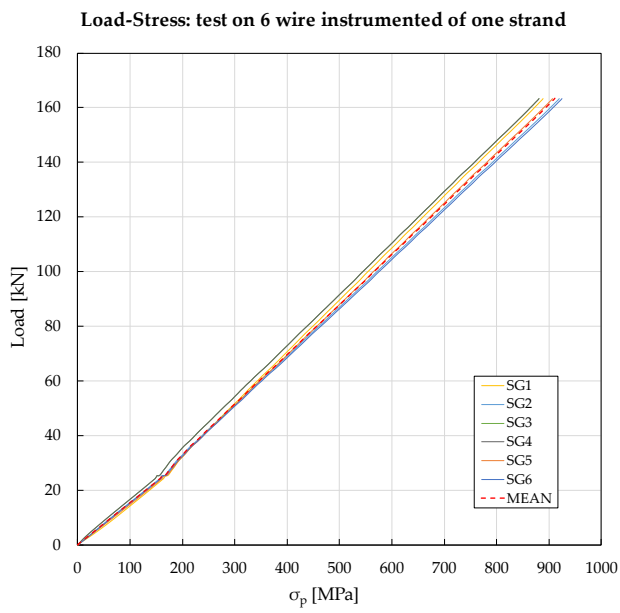
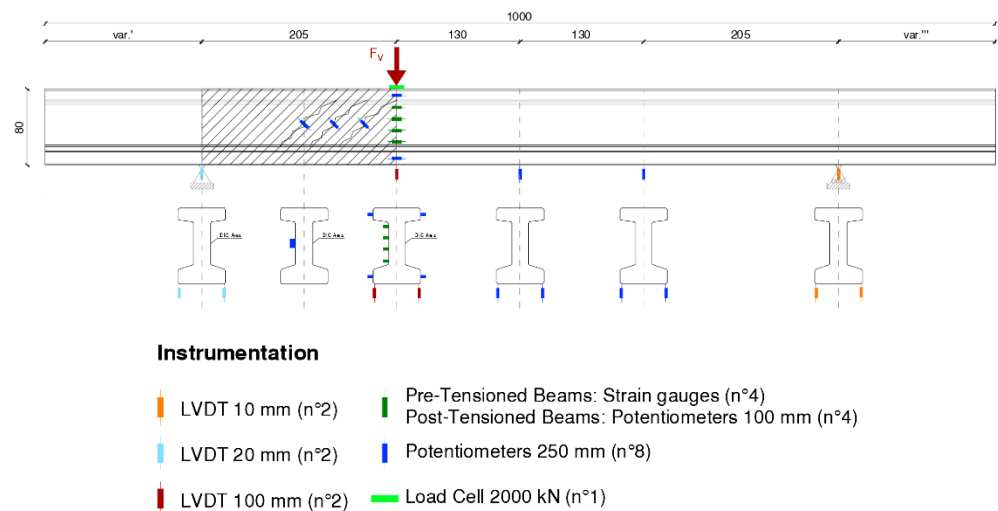


Figure 3-36: Difference between the readings of the 6 strain gauges installed on the external wires of the strand.

3.3.6.2 Concrete

As shown in Figure 3-37 and Figure 3-38, to monitor the beams during the test phases, instruments were applied in different positions. In particular, on the front side, 3 potentiometers (with a maximum excursion of 250 mm) have been installed diagonally, to detect the shear slot openings. On the upper flange, there are 2 potentiometers, one on the front and one on the back, with an overall length of 55 cm and a maximum excursion of 250 mm. Two other potentiometers of the same type have been arranged on the lower flange, one on the front and one on the back of the beam, in this case with a total length of 44 cm. In the comparison between Figure 3-39 and Figure 3-40 it can be appreciated how, in the pre-tensioned beams, strain gauges were initially used to measure the longitudinal deformations in the web. In the tests carried out on the post-tensioned beams, following an initial analysis of the results of the tests on the pre-tensioned beams, it was decided to replace them with 4 potentiometers, in this case with a maximum excursion of 100 mm. This choice is correlated to the fact that, as soon as the crack pattern intercepts a strain gauge, it is no longer able to provide reliable readings. Potentiometers, although less precise, are not affected by this problem.



3-EXPERIMENTAL PROGRAM

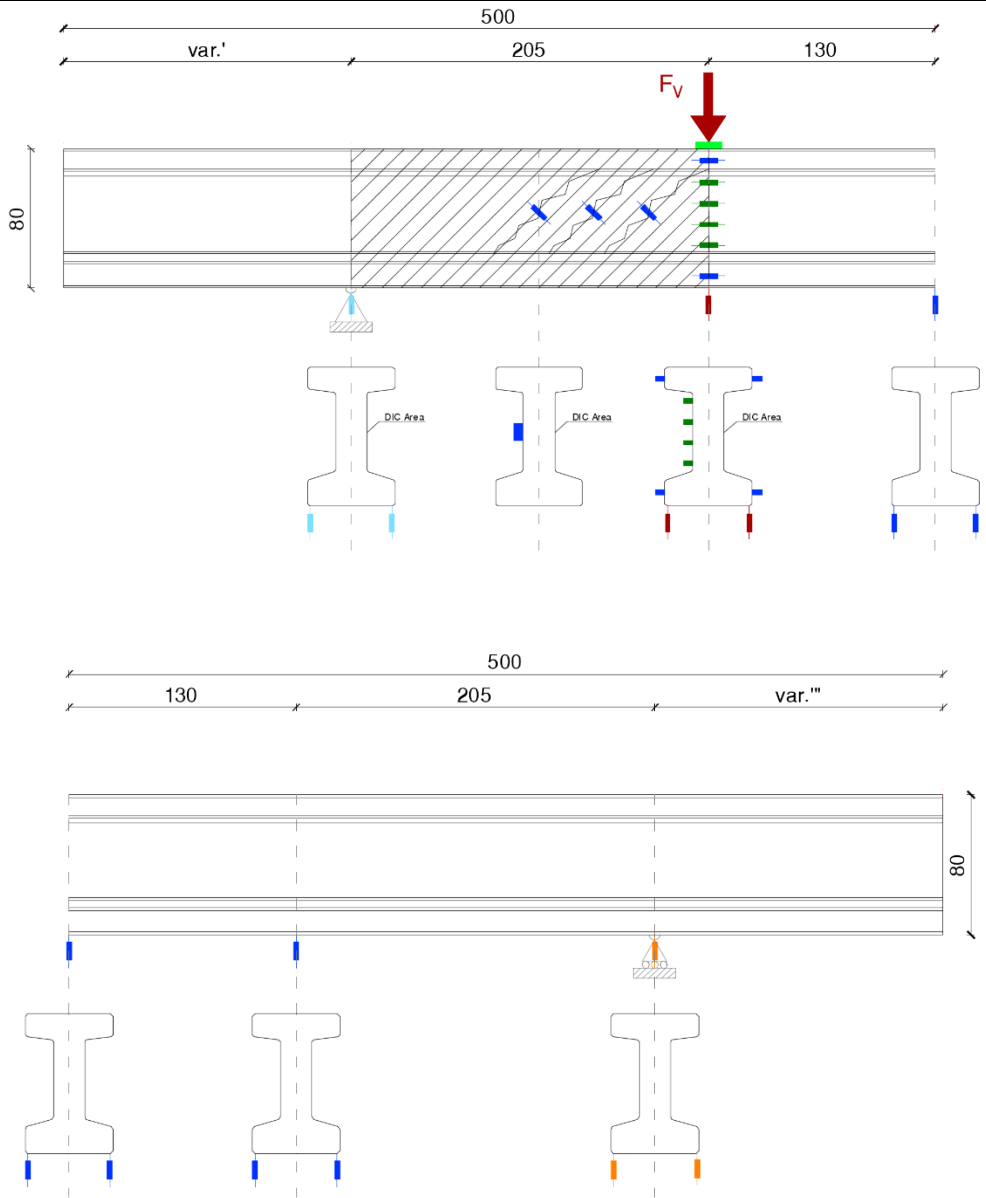


Figure 3-37: Summary diagram of the instrumentation installed on all beams.

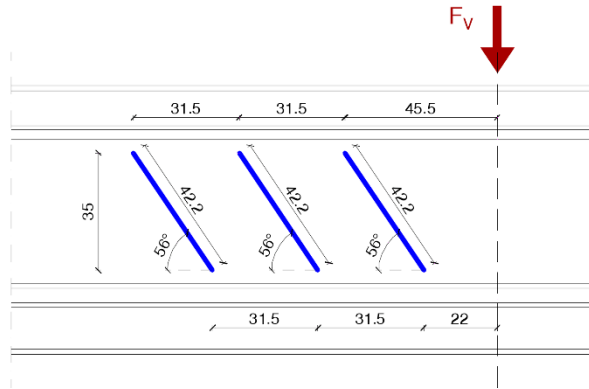


Figure 3-38: Detail of potentiometers arranged diagonally to intercept the inclined cracks.

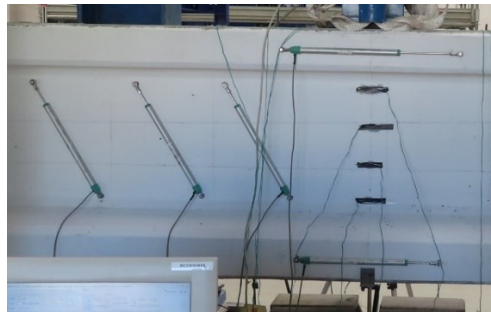


Figure 3-39: Arrangement of the instruments in the pre-stressed Beams A and B on the face side flanges and web.



Figure 3-40: Arrangement of instruments in post-tensioned Beams C on face side flanges and web.

As regards the reading of the vertical displacements, Linear Variable Differential Transformers LVDTs and potentiometers have been set up in some significant points, positioned both on the back side and on the front side, so as to be able to detect any rotation in the transverse plane or torsion of the beam. LVDTs were placed on the supports with a maximum excursion of 20 mm at the hinge and 10 mm at the roller; LVDTs with a maximum excursion of 100 mm were positioned below the load point; instead, potentiometers with a maximum excursion of 250 mm were used in the middle and symmetrically at the loading point.



Figure 3-41: LVDT near the simple support (roller)



Figure 3-42: Potentiometer in the symmetrical position of the load point.

3.3.6.3 Digital Image Correlation

On the opposite side of where the 3 inclined potentiometers were installed on the web, a pattern was set up to monitor the evolution of the crack pattern using Digital Image Correlation (DIC). For the photo acquisition setup (Figure 3-43) the following were used: two LED spotlights oriented so as to obtain a clear and shadow-free surface, and a Canon EOS D5 Reflex with a fixed 35 mm lens to acquire high-quality images. The camera was connected to a PC which adjusted the shutter timing (every 10 seconds) and archived the images for all the beams during the load tests. The photographs were post-processed with the GOM Correlate 2019 software.



Figure 3-43: Setup DIC.

3.3.6.4 **Dynamic**

For Beam A and Beam C2, dynamic identifications were performed using the following instrumentation:

- accelerometers mems PCB -Piezotronics Model: 3741B122G/-0001 adopted for tests relating to Beam C2. They have been installed on stable metal bases. The acquisition frequency was 400 Hz. The main characteristics of the device are listed below:

Performance	SI
Sensitivity(± 5 %)	101.9 mV/(m/s ²)
Measurement Range	± 19.6 m/s ² pk
Frequency Range(± 5 %)	0 to 250 Hz
Frequency Range(± 10 %)	0 to 350 Hz
Resonant Frequency	≥ 1.3 kHz
Phase Response(10 Hz)	<2.5 °
Broadband Resolution(0.5 to 100 Hz)	.0025 m/s ² rms
Non-Linearity	≤ 1 % FS
Transverse Sensitivity	≤ 3 %



- Wilcoxon Model 731 with P31 power unit/amplifier piezoelectric accelerometers used for tests on Beam A. They have been installed on stable metal bases. The acquisition frequency was 600 Hz. The main characteristics of the device are listed below:

SPECIFICATIONS

Sensitivity, ±10%, 25°C		10 V/g
Acceleration range		0.5 g peak
Amplitude nonlinearity		1%
Frequency response:		
	±10%	0.10 - 300 Hz
	±3 dB	0.05 - 450 Hz
Resonance frequency		750 Hz
Transverse sensitivity, max		1% of axial
Temperature response:		
	-10°C	-12%
	+65°C	+5%
Power requirement:		
Voltage source		18 - 30 VDC
Current regulating diode		2 - 10 mA
Electrical noise, equiv. g:		
Broadband 2.5 Hz to 25 kHz		0.5 µg
Spectral 2 Hz		0.03 µg/√Hz
10 Hz		0.01 µg/√Hz
100 Hz		0.004 µg/√Hz
Output impedance, max		100 Ω
Bias output voltage		9 VDC



3.3.7 Materials

During the casting of the concrete, both cubic and cylindrical specimens were taken, and during the preparation of the reinforcement, sections of the bars and strands used were set aside, so as to be able to subsequently proceed with the characterization of the materials (Figure 3-44).



Figure 3-44: Specimens from the casting of the 4 beams and sections of the reinforcing bars.

3.3.7.1 Concrete

As for the concrete, the following were taken:

- 12 cubic specimens (150 mm side) for each beam;
- 6 cylindrical specimens ($\varnothing=100$ mm; $h=200$ mm) for each beam.

According to the design indications provided, the concrete used should have had a resistance class (after 28 days) equal to C50/60 and a maximum diameter of the aggregates of 16 mm. The mix design used by the Camuna Prefabbricati company instead envisaged a maximum aggregate with a diameter of 22 mm and the fabricator immediately specified that the concrete would exhibit resistance to 28 days higher than those foreseen in the design phase. The concrete used had self-levelling and self-compacting characteristics, therefore there was no vibration during casting. The compression tests on the cubes (Figure 3-45) were carried out after 7, 14, 28 days and on the same day of the test according to the UNI standard [UNI EN 12390-3, 2003]. Tests conducted after 28 days returned the results shown in Table 3-1. In Table 3-2 with relative graph Figure 3-46, it is possible to see the evolution of the cubic resistance over time. Table 3-3 shows the data of the cubes relating to the mass.



Table 3-1: Compression test results on concrete

Beam	$R_{c,m,28}$ [MPa]	$f_{c,m,28}$ $= 0.83 \cdot R_{c,m,28}$ [MPa]
A	73.74	61.2
B	75.33	62.5
C1	77.23	64.1
C2	76.12	63.2

Figure 3-45: Compression test on a cube.

Table 3-2: Evolution of cubic strength during maturation.

Beam	7 days			14 days			28 days			Day of test			
	#	R_c [MPa]	$R_{c,m}$ [MPa]	#	R_c [MPa]	$R_{c,m}$ [MPa]	#	R_c [MPa]	$R_{c,m}$ [MPa]	#	Age [days]	R_c [MPa]	$R_{c,m}$ [MPa]
A	1	66.28	65.61	4	74.09	71.45	10	76.19	73.74	7	25	66.99	69.24
	2	61.49		5	71.75		11	68.27		8		64.66	
	3	69.07		6	68.52		12	76.75		9		76.08	
B	1	67.85	65.49	4	68.51	71.96	7	76.16	75.33	10	33	78.25	76.81
	2	69.35		5	72.44		8	77.12		11		80.21	
	3	59.26		6	74.93		9	72.70		12		71.98	
C1	1	63.47	63.01	4	74.69	74.72	7	86.12	77.23	10	60	75.30	72.97
	2	62.77		5	57.57		8	70.14		11		80.77	
	3	62.78		6	74.74		9	75.42		12		62.83	
C2	1	74.81	69.62	4	77.09	73.63	7	83.27	76.12	10	208	88.90	90.94
	2	57.13		5	80.90		8	57.66		11		94.80	
	3	76.93		6	62.91		9	87.42		12		89.12	

3-EXPERIMENTAL PROGRAM

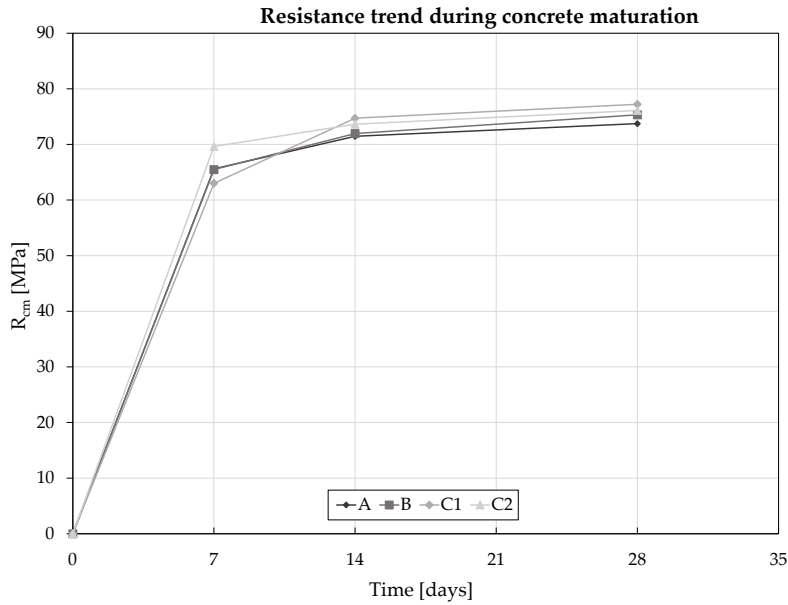


Figure 3-46: Evolution of concrete strength as a function of time (28 Days)

Table 3-3: Data relating to the mass [M] of the cubes (15 cm x 15 cm x 15 cm) and specific mass [γ]

Beam	7 days				14 days				28 days				Day of test			Mean Beam γ_m kg/m ³
	#	M kg	γ kg/m ³	#	M kg	γ kg/m ³	#	M kg	γ kg/m ³	#	M kg	γ kg/m ³	#	M kg	γ kg/m ³	
A	1	8.0	2360.6	4	8.2	2424.3	10	8.1	2398.8	7	7.9	2346.7	2399.8			
	2	8.2	2442.4	5	8.2	2437.0	11	8.2	2416.3	8	8.0	2366.2				
	3	8.1	2413.0	6	8.0	2382.5	12	8.1	2392.9	9	8.2	2416.9				
B	1	8.2	2441.3	4	8.3	2457.8	7	8.3	2458.4	10	8.4	2496.0	2470.7			
	2	8.4	2492.3	5	8.4	2476.7	8	8.3	2445.0	11	8.4	2479.1				
	3	8.3	2463.1	6	8.3	2445.0	9	8.4	2502.5	12	8.4	2490.7				
C1	1	8.2	2424.3	4	8.2	2424.7	7	8.4	2484.7	10	8.2	2436.9	2453.2			
	2	8.3	2472.1	5	8.2	2436.0	8	8.3	2473.2	11	8.3	2457.5				
	3	8.2	2442.1	6	8.4	2484.7	9	8.3	2457.5	12	8.2	2444.1				
C2	1	8.2	2418.4	4	8.3	2461.2	7	8.3	2465.2	10	8.3	2455.4	2449.3			
	2	8.2	2440.7	5	8.2	2441.5	8	8.3	2456.3	11	8.2	2437.9				
	3	8.4	2476.9	6	8.3	2454.8	9	8.3	2452.4	12	8.2	2431.4				

The cylindrical specimens were also tested to obtain information on the elastic modulus of the 4 beams, following the procedure defined in the UNI standard [UNI EN 12390-13, 2013].

Tests conducted after 28 days returned the results shown in Table 3-4.

Table 3-4: Concrete elastic modulus results.

Beam	$E_{c,m}$ [MPa]
A	36'240
B	35'070
C1	35'390
C2	35'760

3.3.7.2 Longitudinal mild and Transverse Reinforcement

The reinforcements used were supplied by Feralpi Siderurgia S.p.A., for the characterization of the materials the following were available:

- 9 pieces of reinforcement in B450C $\varnothing 8$ steel, present in all the beams as a stirrup holder;
- 6 pieces of reinforcement in B450C $\varnothing 12$ steel, present in the Beams C;
- 3 pieces of reinforcement in B450C $\varnothing 26$ steel, present in Beam B;
- 3 pieces of reinforcement in B450A $\varnothing 8$ steel, used as stirrups in all beams;
- 3 pieces of steel reinforcement B450C $\varnothing 12$, used as stirrups in the D-region in all beams.

The stirrups ($\varnothing 8$ and $\varnothing 12$ mm) were supplied in rolls and for this, they underwent a heat treatment before the characterization test, in particular, they were heated for 1 hour at 100°C .

During the design phase only reinforcements in B450C steel were prescribed [NTC, 2018]. The prefabrication company, instead, prepared stirrups $\varnothing 8$ steel B450A. Although the stirrups, therefore, had a lower ductility, this did not generate problems during the tests, where there was no rupture of the transverse reinforcement. In the VT2 finite element models (§5.2.3), however, the mechanical characteristics of the B450C material have been maintained as they are more coherent with the results of the experimental tests.

As far as the tests on the mild reinforcement are concerned, all the values provided by the manufacturer have been verified in the laboratory according to the standard ISO 15630-1 (2010). Below, in Table 3-5 the results obtained from laboratory tests are reported by averaging different samples for each type of diameter.

where:

- $f_{y,m}$ and $f_{u,m}$ are the mean stress at yield and the mean ultimate stress, respectively;
- $\varepsilon_{Agt,m}$ is the ultimate strain;
- $E_{s,m}$ is the elastic modulus.

Table 3-5: Results of tensile tests on reinforcements.

Rebar	Diam.	Spec.	L	f_y	$f_{y,m}$	f_u	$f_{u,m}$	$\epsilon_{A_{gt}}$	$\epsilon_{A_{gt,m}}$	E_s	$E_{s,m}$
	\emptyset	#	mm	MPa	MPa	MPa	MPa	%	%	MPa	MPa
Mild Reinforcement	8	1	500	543.5	532.8	636.4	635.3	13.0	12.2	-	196956
		2	500	534.9		636.0		13.1		186345	
		3	500	523.0		631.4		12.2		217148	
		4	500	509.0		619.9		12.5		194149	
		5	500	520.3		625.2		12.2		202722	
		6	500	540.1		643.0		12.2		186802	
		7	500	543.9		643.1		11.8		194545	
		8	500	551.9		651.0		10.6		207290	
		9	500	529.0		631.8		12.1		186649	
	12	1	500	516.9	525.8	635.5	641.3	14.8	13.9	197974	192245
		2	500	537.2		647.3		12.6		193775	
		3	500	525.5		640.6		14.1		198027	
		4	500	528.4		644.2		13.5		172513	
		5	500	525.2		639.5		13.2		195590	
		6	500	521.5		640.5		15.0		195590	
	26	1	635	508.7	513.7	615.1	618.6	14.5	14.6	185540	184777
		2	630	523.1		624.9		14.6		193800	
		3	635	509.3		615.9		14.7		174993	
Stirrups	8	1	500	578.9	579.7	622.1	624.0	2.7	2.7(*)	200140	203908
		2	500	582.2		622.2		2.1		207677	
		3	500	578.0		627.8		3.2		-	
	12	1	500	518.9	525.0	595.6	602.8	4.7	5.8	180068	182431
		2	500	533.0		609.4		6.8		176698	
		3	500	523.2		603.5		5.8		190526	

(*) the value provided by the manufacturer is $\epsilon_{A_{gt,m}} = 5.2\%$

3-EXPERIMENTAL PROGRAM

3.3.7.3 Prestress Reinforcement

The mechanical characteristics of the strands shown in Table 3-6 are those provided by the data sheet of the manufacturer WBO Italcables, as it was only possible to carry out tensile tests in the elastic stage in the laboratory (§3.3.6.1).

Table 3-6: Characteristics of 7-wire steel strands.

Diameter	Area	$f_{p(1\%)}$	f_{pt}	$\epsilon_{A_{gt}}$	E_p
\emptyset	mm²	MPa	MPa	%	MPa
15.2 [mm] 6/10 [in.]	139	1783	1947	6.3	200'000

3.4 Setup description

The shear strength of the four beams was determined by tests until failure. The tests of the shear strength and stress release were conducted in the Pietro Pisa laboratory of the University of Brescia.

The setup was similar in all beams. The tests were performed in displacement-control mode. A vertical load was applied using an electromechanical jack. This jack, being in displacement control, made it possible to obtain a suitable behaviour of the specimens, especially after cracking and after adding the maximum load.

Below, the procedure for one beam is described. The minimal set-up differences between one beam and another are then highlighted.

All beams have a very similar setup geometry. The difference in the setup is the positioning of the beam on the restraints with respect to the ends to position the section with the first stirrup at 30 cm spacing on the S-Side (Hinge) restraint, as shown in Table 3-7 with reference to Figure 3-47. The distances between the load point and the ground constraints always remain unchanged.

Table 3-7: Dimensions of the constraints with respect to the beam's headers.

[cm]	Constrain S - Hinge		Constrain P - Roller	
Beam A:	var.'	165	var.'''	165
	var. ''	150	var.'''''	150
Beams B, C1 and C2	var.'	155	var.'''	175
	var. ''	140	var.'''''	160

Front view

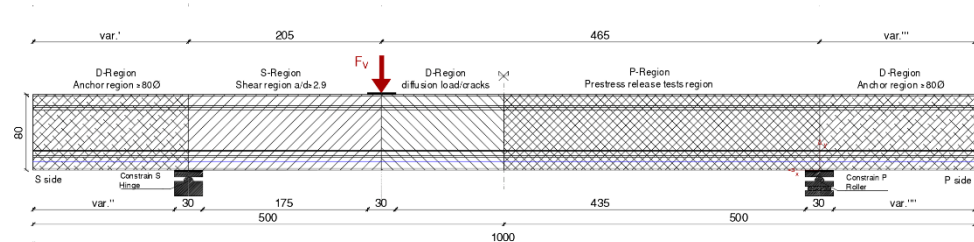


Figure 3-47: Beam setup on constraints with respect to the load point.

The position of the supports and the load point has been identified to have:

- the left support (Constrain S – Hinge) at a distance from the end of the beam such as to be beyond the prestress diffusion zone (D-region). This area can be estimated with a length of about 80ϕ , i.e., 80 times the diameter of the prestressing reinforcement, which with the strands used corresponds to about 120 cm;
- a/d close to 2.9: where "a" represents the distance between the support and the load point while "d" is the effective height of the section;
- the right support (Constrain P – Roller) at a distance such that the portion of the beam between the load point and the support appears to be a little stressed, and consequently does not suffer excessive damage. This is intending to have an area available that is not very disturbed by the propagation of crack patterns, used to perform various types of diagnostic tests for the evaluation of prestress.

The vertical loading system consists of an electromechanical jack fixed to the steel frame, capable of generating a maximum load of 1500 kN (Figure 3-48 and Figure 3-49). The steel loading frame was made up of four pillars (HEB 400) and two transverse beams (HEB 450) at the top. Two additional lateral cross beams stiffened the structure. Each pillar was connected to the laboratory floor through Dywidag bars: the floor is a slab, about one meter high, specially designed to resist a concentrated load of 1000 kN, every 50cm x 50cm. This plate acted as a contrast to the load transmitted by the jack and was brought to the ground by the pillars of the steel loading frame. Between the hydraulic jack and the beam, in addition to a 2000 kN load cell in contact with the piston, a series of steel elements were positioned to compensate for the space between the two elements. For safety reasons, the system has been equipped with bands and plates capable of making all the elements that compose it integral to each other (Figure 3-50).

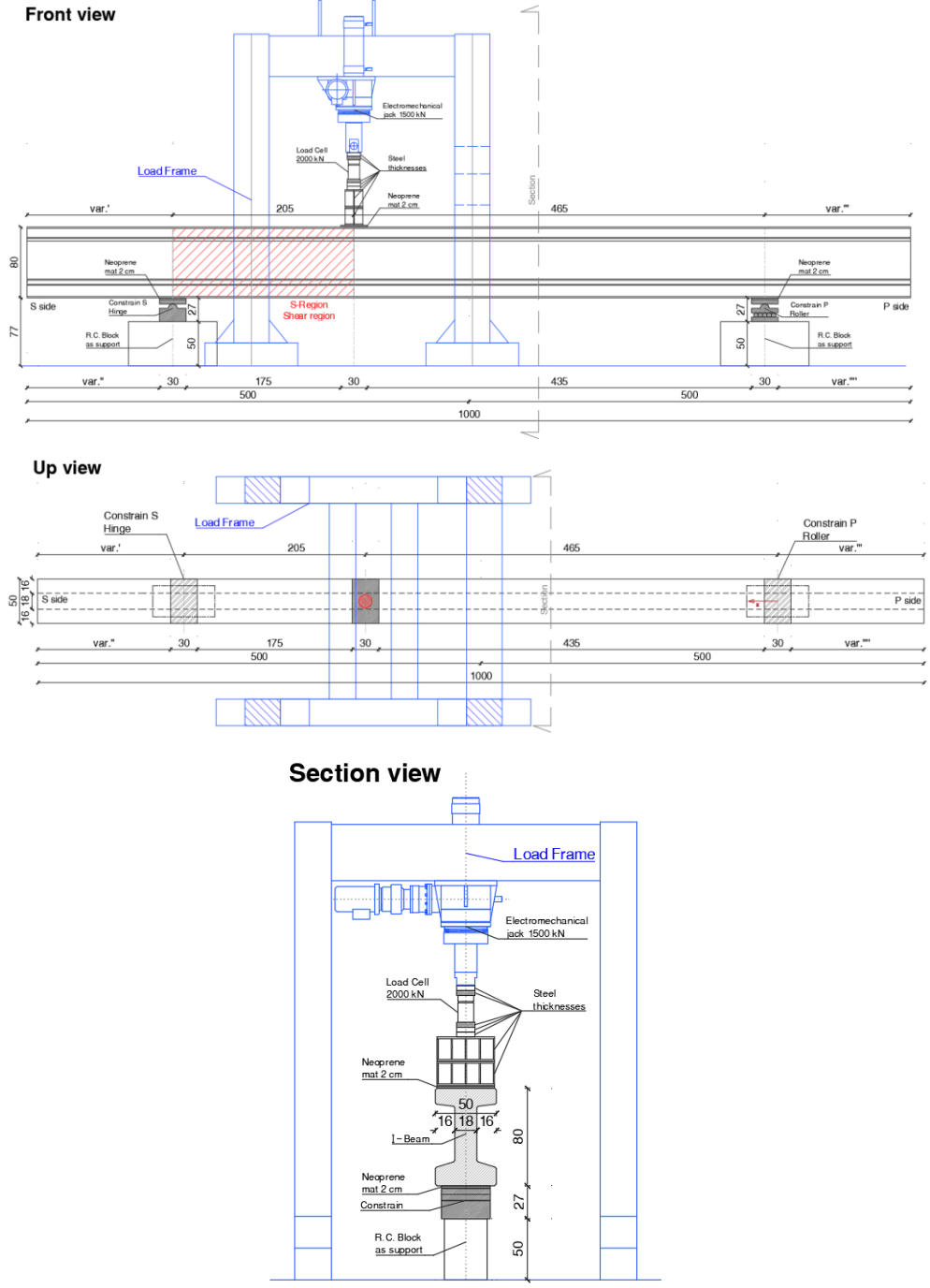


Figure 3-48: Test frame setup.



Figure 3-49: Setup (Picture relative to Beam A).



Figure 3-50: Loading system composed of an electromechanical jack load cell and steel thicknesses.

The supports were placed at the distances from the beam heads as indicated in Table 3-7, so as to be located outside the prestress diffusion zone. The beams were positioned under the test load frame so that the load point was 205 cm from the hinged support and 465 cm from the roller support. The setup was designed to guarantee a shear ratio as constant as possible between the beams and close to the value of 2.9, as shown in Table 3-8.

Table 3-8: a/d in the experimental setup.

a/d	Experimental test setup	
Beam A	$\frac{205}{80 - 9.00}$	2.89
Beam B	$\frac{205}{80 - 7.67}$	2.83
Beams C	$\frac{205}{80 - 9.00}$	2.89

The supports were made with R.C. blocks. 50 cm high on which steel supports were mounted, respectively a hinge (Figure 3-51) and a roller (Figure 3-52), both 25 cm high, a layer of 2 cm thick neoprene was placed between the steel plate and the girder intrados. The hinge was positioned at the support closest to the critical shear area.



Figure 3-51: Hinged support – S side.



Figure 3-52: Roller support – P side.

3-EXPERIMENTAL PROGRAM

Only for the two Beams C, a system necessary to generate the post-tension of the strands was applied to the heads.

To create a system that would allow the prestress to be varied from 0% to 100%, with the technical support of Tensacciai S.r.l.⁸ the system shown in Figure 3-53 and Figure 3-54 was developed.

It consists of: 2 steel counter plates each 50 mm thick, 1600 kN load cell and clamping plate on the passive head (Figure 3-53 and Figure 3-55); 2 steel counter plates each 50 mm thick, ring hydraulic jack (thrust force 1495 kN at 700 bar, maximum extension 100 mm, area 213.6 cm²) with safety ring nut and clamping plate on the active head (Figure 3-54 and Figure 3-56). Once the 7 strands have been inserted in the sheath, clamped in the plates, and the jack under pressure to apply 100% prestress, it is possible to reduce the prestress level by unscrewing the safety ring nut from the jack by a distance calculated based on it wants to apply. The calculation depends on the elastic modulus of the strands. Through a pump and a manual valve (Figure 3-57) it is possible to regulate the inflow and outflow of the oil under pressure to control the prestress level.

More in detail: the system was powered by an oil pumping system, equipped with a pressure gauge. Once the desired pressure was reached, the hydraulic jack was blocked by a ring nut. During the prestress reduction phases, the oil was put under pressure again via the pump, until it reached a level sufficient to unlock the ring nut previously in contact; at this point, the ring nut was moved manually (in the order of 7÷10 mm for a reduction of about 10% of prestress) and the oil was gradually recalled, so as to release the jack until it came back into contact with the ring nut and obtained the desired stress drop (Figure 3-58). With this methodology, there are no losses during the strand tensioning phases because all the slips due to the tightening of the wedges and elastic deformations are compensated with an additional elongation of the jack piston.

⁸ *TENSA – Gruppo DE ECCHER*

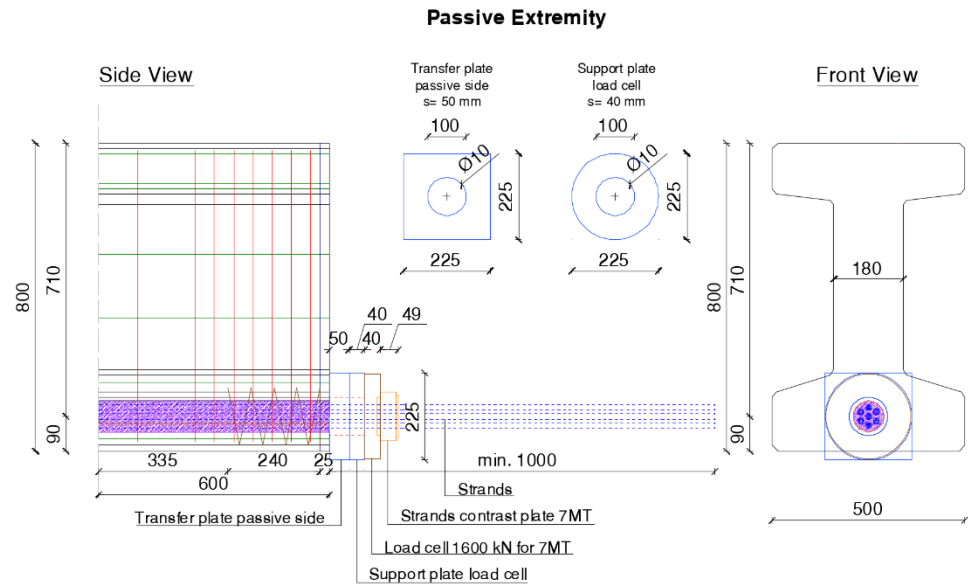


Figure 3-53: System: plates, load cell and clamping plate in the passive head.
 Dimensions in mm.

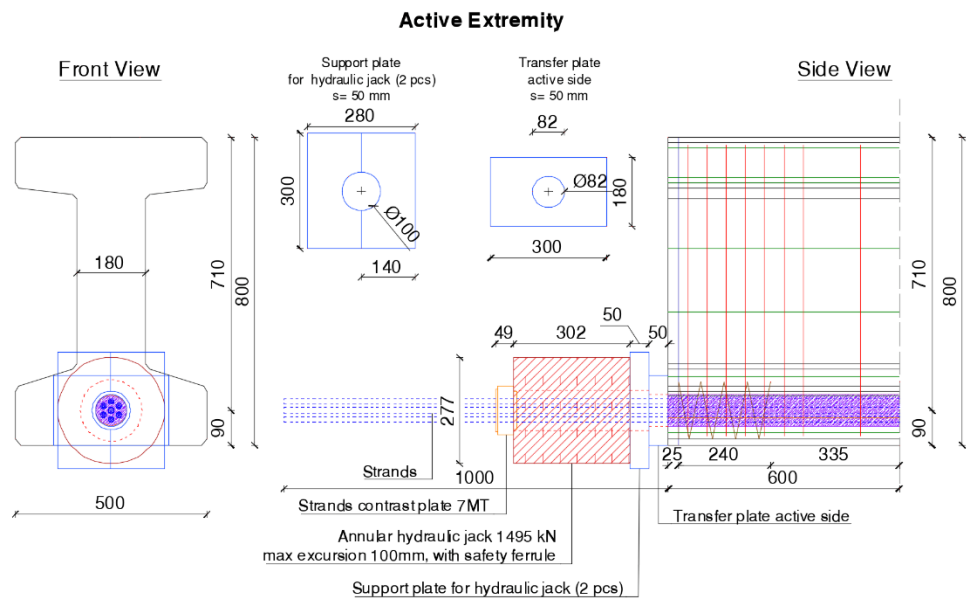


Figure 3-54: System: plates, ring jack and clamping plate in the active head.
 Dimensions in mm.



Figure 3-55: Passive beam head.



Figure 3-56: Active beam head.



Figure 3-57: Oil pump of the ring hydraulic jack.



Figure 3-58: Adjustment of the ring nut during a de-tensioning step.

3.5 Loading Modalities

The load tests on the prestressed beams were conducted in displacement control, increasing the load monotonically, stopping at pre-set load steps in correspondence with which to carry out prestress evaluation tests, using concrete stress release methods. The load tests on the post-tensioned beams were carried out, always in displacement control by increasing the load monotonically: a constant vertical load was maintained for the Beam C1 and going to reduce the prestress, thus evaluating how losses of different entities affect the structural response and the crack pattern. For Beam C2, on the other hand, a fixed prestress level was applied, and the vertical load increased monotonically. Also in these cases, stress release tests were carried out at pre-set load and pre-stress steps. Table 3-9 lists the configurations of vertical load and prestress relating to each beam adopted for the stress release tests and for the load test. Before carrying out the load test which brings the element into irreversible conditions, the beams were subjected to load cycles in the elastic range, using predictions of the ideal load with the numerical model (see §5.2.3), to allow settling of the beam, of the neoprene supports and the verification of the measuring instruments installed. As already mentioned, for all the beams, the DIC was set up in such a way as to be able to monitor the evolution of the crack pattern during the test and, for the post-tensioned beams, also evaluate whether this technology is able to capture a variation of the stress state due to the prestress. All the beams were loaded to the limit of collapse, so as to guarantee sufficient integrity of the element for handling and a possible future structural rehabilitation intervention.

Table 3-9: Vertical load and prestress configurations related to each beam.

Beam	Technology (-)tensioned	Prestress		Vertical Load kN	Semi-destructive method to assess prestress release				Shear Test
		kN	(ref. to 1130 kN)		C	SCi	R	SCw	
A	Pre	955	85%	0	x	x	x		
				700	x	x	x		x
				800					x*
B	Pre	641	57%	0	x	x	x		
				585	x	x	x		x
				790					x*
C1	Post	983	87%	0	x	x			
		825	73%	0	x	x			
		678	60%	0			x		
		1130- 735	100%- 65%	500					x

3-EXPERIMENTAL PROGRAM

		1130-768	100%-68%	550					x
		1130-802	100%-71%	600					x*
C2	Post	1074	95%	400	x	x			x
		735	65%	400	x	x			x
		1130	100	0			x		
		678	60	0			x		
		1130	100	400			x		x
		678	60	400			x		x
		1130	100	0				x	
		993	88%	916					x*
<i>C= Core Trepanning method</i> <i>SCi= Saw-Cut method – Intrados</i>					<i>R= Blunt Pyramidal specimen</i> <i>SCw= Saw-Cut method – Web</i> <i>*=End Shear test, close to beam collapse</i>				

3.5.1 Beam A

At the moment of the load test, Beam A has an overall tension in the 6 6/10" 7-wire strands of 955 kN ($\sigma_{p\infty} = 1145$ MPa), considering 17.8% of overall losses (§3.3.5).

With the beam unloaded and in correspondence with a vertical load of 700 kN (formation of a well-defined shear crack pattern), stress release tests were carried out such as:

- Core Trepanning method (depth 15 cm)
- Saw-Cut method – Intrados
- Blunt Pyramidal specimen

After starting the vertical loading phase, several interruptions were made.

First, it stopped at 350 kN, in the elastic range, the value at which the formation of the first flexural cracks in beam B is expected (Beam pre-tensioned at 70% of Beam A), based on the prediction provided by the numerical model (see §5.2.3).

Subsequently, the load increment was stopped at the first flexural crack openings, which appeared around a vertical load of 500 kN.

The first shear cracks were observed around 550 kN of vertical load, while the release tests were carried out only after the formation of a more organized shear pattern (700 kN).

Finally, the load was increased until a condition close to the ultimate limit state was reached.

The unloading was carried out after having reached a load of approximately 800 kN and a net deflection (purged from the failure of the supports) under the load point of 23.6 mm. A residual deformation of 2.2 mm was found.

A dynamic identification was performed before and after damaging the beam with a vertical load of 800 kN (§4.2.8).

3.5.2 Beam B

At the moment of the load test, Beam B has an overall tension in the 4 6/10" 7-wire strands of 641 kN ($\sigma_{p\infty} = 1153$ MPa), considering 17.2% of overall losses (§3.3.5), equal to 67% of the tension in the strands of Beam A.

With the beam unloaded and in correspondence with a vertical load of 585 kN (formation of a well-defined shear crack pattern), stress release tests were carried out such as:

- Core Trepanning Method (depth 3 and 10 cm)
- Saw-Cut method – Intrados

Several interruptions were made after starting the vertical loading phase.

First, it stopped at 250 kN, in the elastic range, to compare the experimental curve with that obtained from the numerical model (see §5.2.3).

Subsequently, the load increment was stopped at the first flexural crack openings, which appeared around a vertical load of 350 kN.

The first shear cracks were observed around 435 kN of vertical load, while the release tests were carried out only after the formation of a more organized shear pattern (585 kN).

Finally, analogously to what was done in the test on beam A, the load was increased until a condition close to the ultimate limit state was reached.

The unloading was carried out after having reached a load of approximately 790 kN and a net deflection (purged from the failure of the supports) under the load point of 23.4 mm. A residual deformation of 3.4 mm was found.

3.5.3 Beam C1

With the prestressing load control method (horizontal load) the design tension of the 7-wire 6/10" strands of 1130 kN ($\sigma_{p\infty} = 1160$ MPa) was progressively reached. This prestress level was chosen as the initial reference tension because it coincides with the tension assigned to the 6 6/10" 7-wire strands of Beam A, 1161 kN ($\sigma_{pi} = 1392$

3-EXPERIMENTAL PROGRAM

MPa) (§3.3.4) after losses due to wedge-cable sliding during the tensioning phase equal to about 2.5% (§3.3.5).

In the first phase, loading and unloading cycles of the prestress from 0 to 100% (1130 kN) were carried out to tighten the wedges on the strands in the clamping plates, thus dispersing the losses along the excursion of the jack.

The beam, once prestressed to the design value (1130 kN=100%), was subjected to vertical load cycles in the elastic range to allow the settling of the beam, the neoprene supports and verification of the measuring instruments installed.

At this point, the prestress was decreased until it reached about 87% (of the design tension), so as to be close to the estimated tension in Beam A.

In this step, always with the beam unloaded vertically, stress release tests were carried out on the concrete such as:

- Core Trepanning method (depth 10 cm)
- Saw-Cut method – Intrados

Similarly, the same procedures and the same tests were carried out at a prestress level of 73%, representative of a tension in the strands downstream of the long-term losses.

Subsequently, the strands were relaxed until they reached a prestress equal to 60%, to bring back the tension estimated in Beam B.

Also at this step, again with the unloaded beam, stress release tests were carried out on the concrete, in particular:

- Blunt Pyramidal specimen

At this point, the beam was brought back to its initial condition, with a tension in the strands equal to the design one (1130 kN=100%).

The vertical jack was activated until a load of 500 kN was reached. By keeping the load constant, the prestress was then progressively reduced, proceeding in steps of 10%. The first flexural cracks appeared at a prestress level of 80%, the predominantly flexural cracking pattern developed further once the strands were relieved up to 65% of the design tension.

The same procedure was repeated with a constant vertical load of 550 kN, also reducing the prestress level up to 68% under vertical load. In the same way, a last test was performed with a constant vertical load of 600 kN, reaching in this case a prestress level of 71% under vertical load.

The test was interrupted once a condition close to the ultimate limit state was reached, in correspondence with which the beam exhibited a clear deflection (purged from the yielding of the supports) under the load point equal to about 44 mm.

3.5.4 Beam C2

Also, for this beam, with the prestressing load control method (horizontal load) the design tension of the 7 6/10" 7-wire strands of 1130 kN ($\sigma_{p\infty} = 1160$ MPa) was progressively reached.

In the first phase, loading and unloading cycles of the prestress from 0 to 100% (1130 kN) were carried out to tighten the wedges on the strands in the clamping plates, thus dispersing the losses along the excursion of the jack.

The beam, once prestressed to the design value (1130 kN=100%) was subjected to load cycles in the elastic range, to allow the settling of the beam, the neoprene supports and verification of the measuring instruments installed.

Having applied a vertical load of 400 kN, the prestress was reduced in two steps: 95% and 65% of the design tension (1130 kN). For each step, stress release tests were performed on the concrete such as:

- Core Trepanning method (depth 10 cm)
- Saw-Cut method – Intrados

Subsequently, both with zero vertical load and with 400 kN, with prestressing steps of 100% and 60% of the design tension (1130 kN), the following stress release tests were performed:

- Blunt Pyramidal specimen

In the cycles with 60% and 65% prestress and a vertical load of 400 kN, cracks of a flexural origin occurred at the point of load.

Based on the results obtained with the three stress release methods tested, it was decided to experiment with a variant of the Saw-Cut method – Intrados, by making the pair of vertical cuts on the web of the beam and trying to reduce the distance between the notches:

- Saw-Cut method – Web

For greater control over the results, it was decided to carry out tests on Beam C2 with a configuration with zero vertical load and 100% prestress (1130 kN).

Dynamic identification of Beam C2 at different prestressing levels was performed by positioning it with the supports at the ends (effective distance between them equal to 9.70 m) without any vertical load applied (§4.1.2.2).

3-EXPERIMENTAL PROGRAM

At this point, the beam from an initial condition, with a tension in the strands equal to that of the design (1130 kN=100%), was released to reach a tension in the strands similar to that of Beam A (993 kN=88%).

The vertical jack was activated until a condition close to the ultimate limit state was reached with a load of 916 kN, in correspondence with which the beam exhibited a clear deflection (purged from the failure of the supports) under the load point of 60 mm.

The test was mainly interrupted because the force reached in the strands measured by the cell at the beam passive head (1397 kN), increased following the applied vertical load, had almost reached the bearing capacity of the ring jack (1450 kN) positioned at the beam active head.

At a load of 400 kN, the first flexural cracks appeared at the load point. The final crack pattern proved to be mainly governed by flexure even though some inclined cracks were noticed.

4 EXPERIMENTAL RESULTS AND DISCUSSION

The next chapters will show and discuss all the tests performed on the 4 beams related to:

- Assessment of residual stresses with semi-destructive methods;
- Shear tests: assessment of the influence of long-term prestress losses on residual shear strength.

To avoid interference between the results of the two types of tests, regions were identified along the beam, as shown in Figure 4-1.

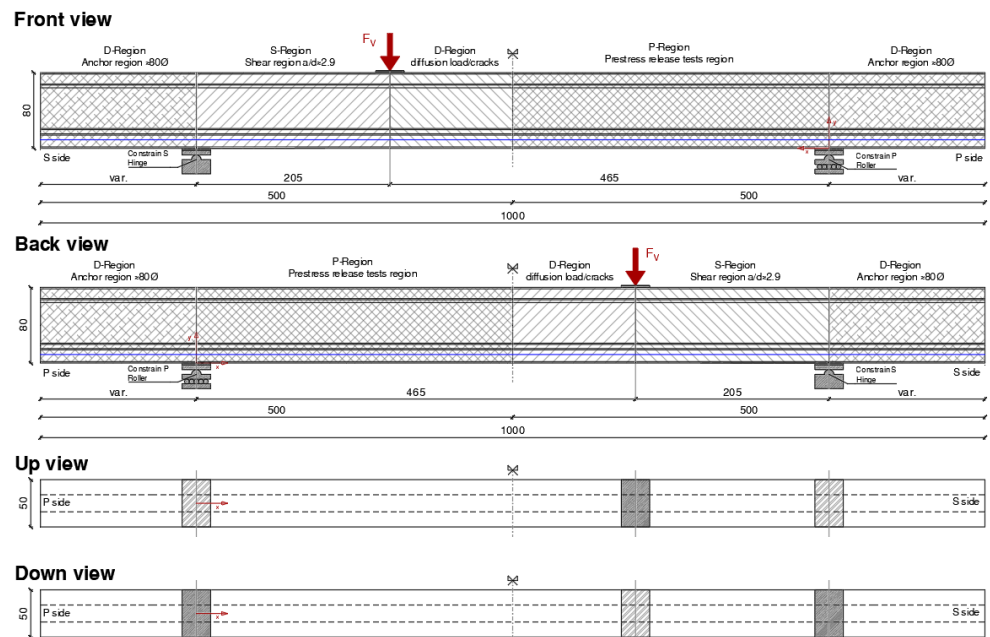


Figure 4-1: Zoning beams.

4.1 Assessment of residual stresses

4.1.1 Introduction

On both pre-tensioned and post-tensioned beams, three semi-destructive methods proposed in the literature for the assessment of residual prestress in situ were applied (§2.2.42.2.4). These techniques involve stress release and thus concrete isolating. A total of 49 tests were carried out:

- N° 11 Core Trepanning method (2 on flanges, 9 on web);
- N° 24 Saw-Cut method (9 on intrados, 15 on web);
- N° 14 Blunt Pyramidal specimen (8 on flanges, 6 on web).

These techniques are based on the idea of isolating, through saw-cuts or core trepanning, a portion of the structural element previously instrumented with strain gauges to obtain the strains ε_c in the concrete due to the cuts. Using Hooke's law and knowing the elastic modulus of concrete, the prestress present in concrete σ_c is obtained:

$$\sigma_c = E_c \cdot \varepsilon_c \quad (4-1)$$

where:

- ε_c = concrete strain, values recorded by strain gauges;
- E_c = elastic modulus of concrete (Table 3-4);
- σ_c = concrete stress.

this is because the deformation undergone by the isolated portion as a result of cutting is equal and of the opposite sign to the deformation induced by prestress and permanent loads.

The tests were carried out at different prestress levels, and for most of them were carried out both with the beam unloaded and with the beam loaded (vertical load). In detail see Table 4-1.

In the post-tensioned beams, a tension equal to the one applied at the factory on the pre-tensioned beams, i.e., 1160 kN, was applied; adjusted for the 2.5% loss associated with the return of the anchorage wedges. Thus, the tension of Beams C, considered as 100% prestressing, turns out to be about 1130 kN while for Beam A a tension (on the day of the test) of 955 kN was estimated (§3.3.5), i.e., 85% prestressing compared to the maximum tension of Beams C. Similarly, the tension of Beam B turns out to be 57% compared to that of the post-tensioned beams, corresponding to 641 kN.

Table 4-1: List of tests divided by type, by prestress level, and by vertical load applied.

Method	Prestress		Beam	Vertical Load
	kN	% (Respect to 1130 kN)		kN
Core Trepanning	1074	95	C2	400
	983	87	C1	0
	955	85	A	0
			A	700
	825	73	C1	0
	735	65	C2	400
	641	57	B	0
B			585	
Saw-Cut - Intrados	1074	95	C2	0
	983	87	C1	0
	955	85	A	0
			A	700
	825	73	C1	0
	735	65	C2	400
	641	57	B	0
B			585	
Blunt Pyramidal specimen	1130	100	C2	0
			C2	400
	955	85	A	0
	678	60	C1	0
			C2	0
C2	400			
Saw-Cut - Web	1130	100	C2	0

The prestressing steps of Beam C, as well as the fixed prestressing level of Beam A and Beam B, were also chosen to assess whether the different release tests were able to capture the concrete stress at different prestressing levels. Tests were carried out with different levels of vertical load to assess whether the applied methods recorded tension changes comparable to the analytical and numerical predictions. The chosen vertical loads corresponded to an in-service load (400 kN) and the load at advanced shear cracking (700 kN and 585 kN).

Considering the load scheme, which provides that 70% of the applied vertical load ends up in the support closest to the load point, i.e. the hinged support, the release tests were carried out in the area highlighted in Figure 4-2 considered a relatively

4-EXPERIMENTAL RESULTS AND DISCUSSION

undisturbed area even with load beam. The tests were carried out at a distance of 50 cm to 325 cm from the farthest support (Constrain S -Roller) from the loading point. It is emphasized that before any cutting or coring was performed, it was checked for each test that there were no cracks in the adjacent area.

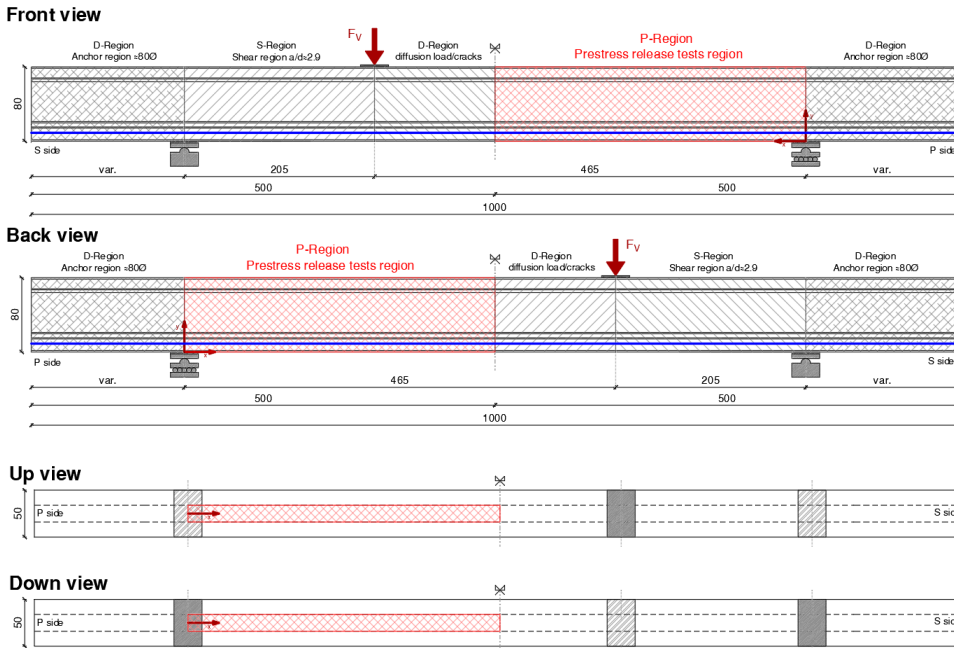


Figure 4-2: Definition of the area where release tests were carried out.

4.1.1.1 Tests Positions

Figure 4-4, Figure 4-5, Figure 4-6 and Figure 4-7 show the locations of the tests performed on each beam. For tests with the Saw-Cut method -Web see also Figure 4-45 and Figure 4-46.

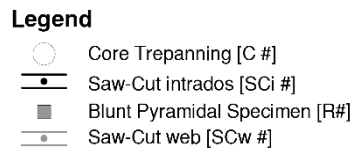


Figure 4-3: Legend related to the following pictures.

Beam A

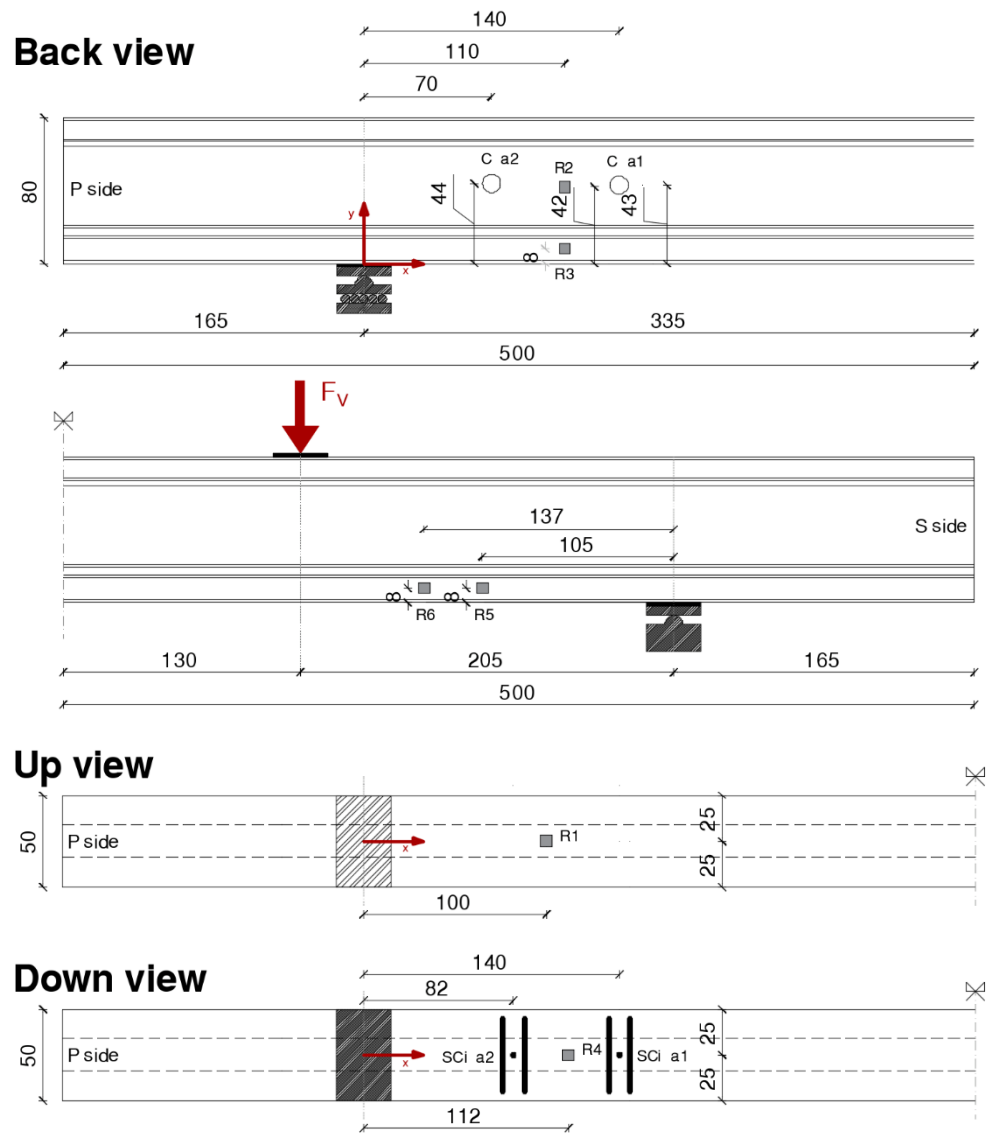


Figure 4-4: Release test position on Beam A.

Beam B

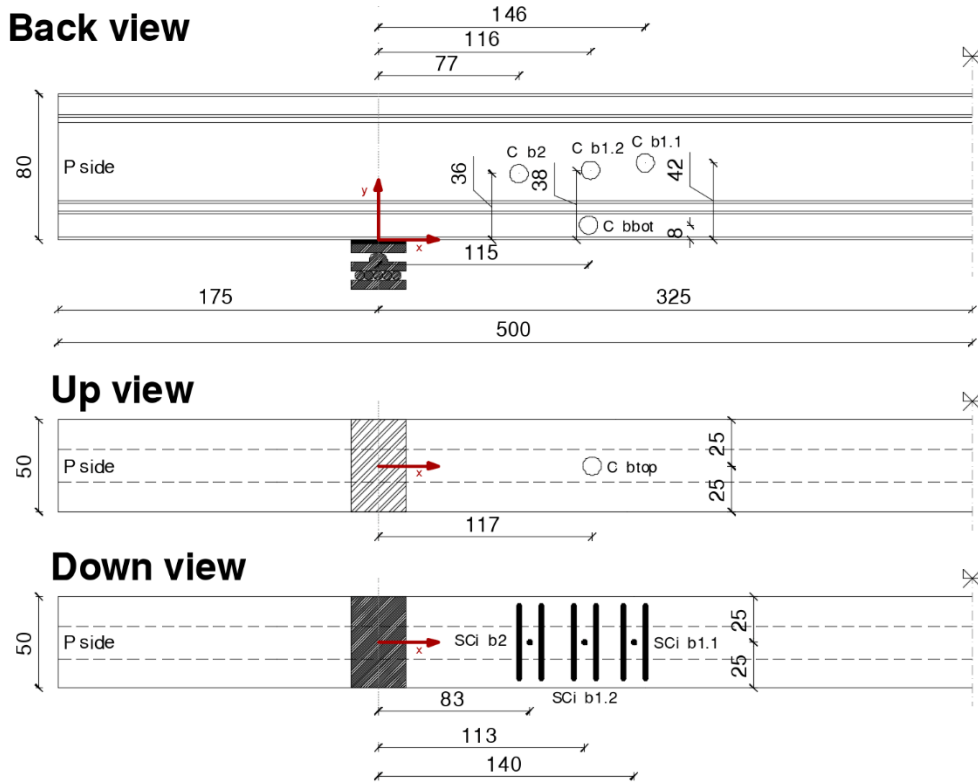


Figure 4-5: Release test position on Beam B.

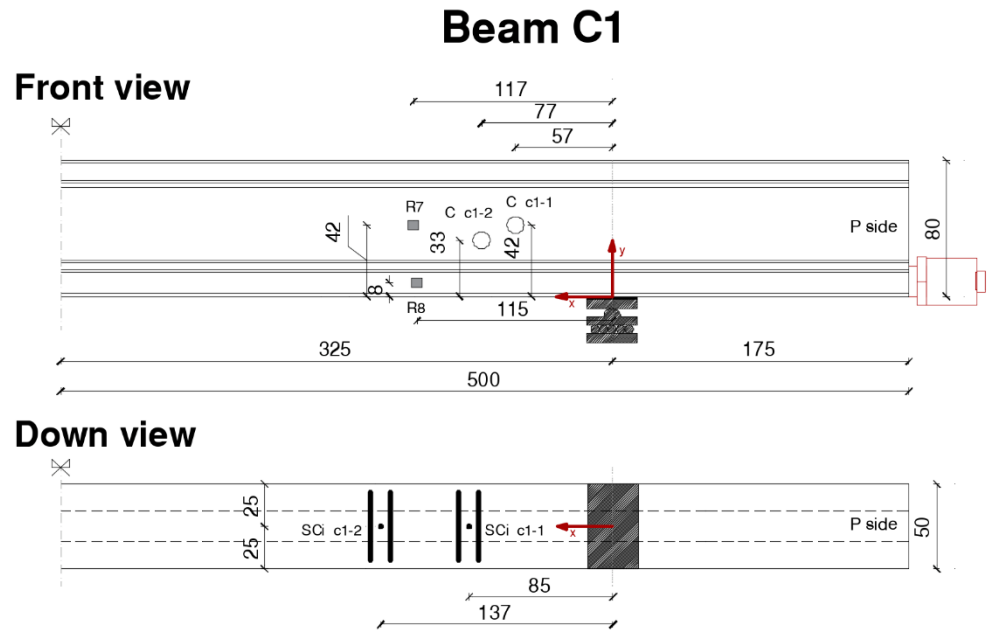


Figure 4-6: Release test position on Beam C1.

Beam C2

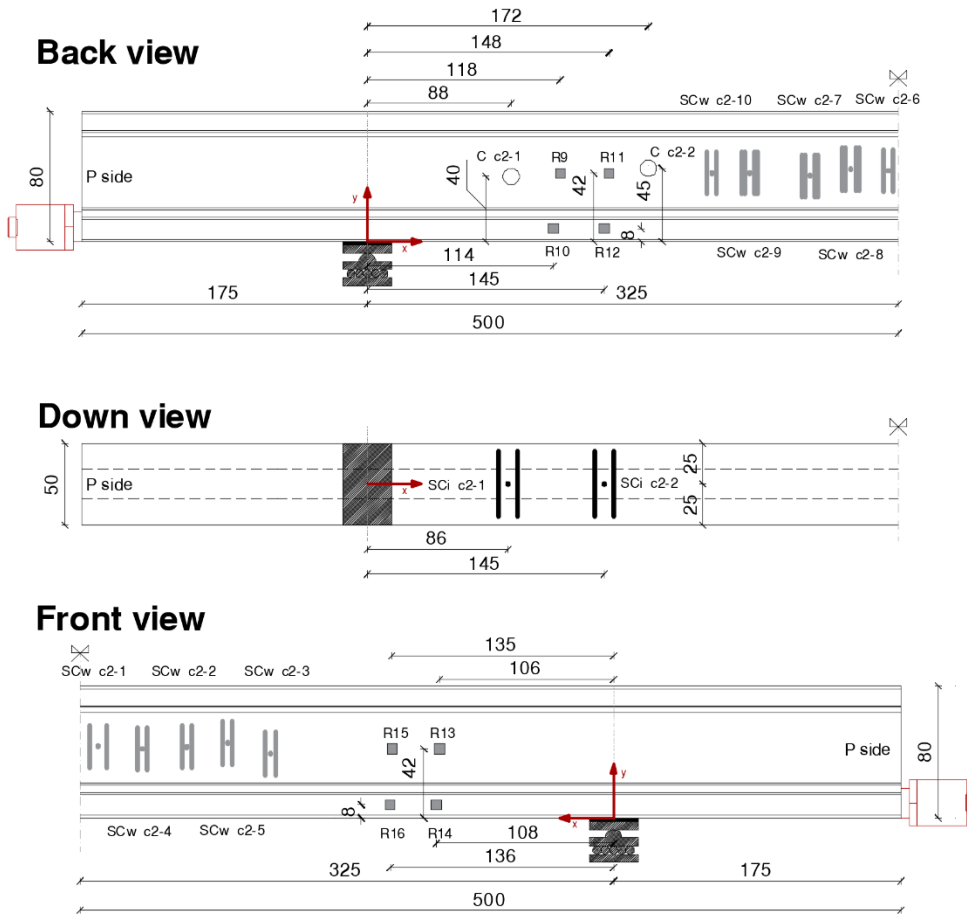


Figure 4-7: Release test position on Beam C2.

4.1.1.2 Procedure for gluing strain gauges

For all types of tests, except for Blunt Pyramidal specimen tests which were carried out by 4 EMME Service S.p.A. using its own procedure, 30-mm-long strain gauges from SHOWA Measuring Instruments Co., Ltd, were glued to the concrete to monitor the concrete release. The characteristics of the strain gauges are shown in Figure 4-8.

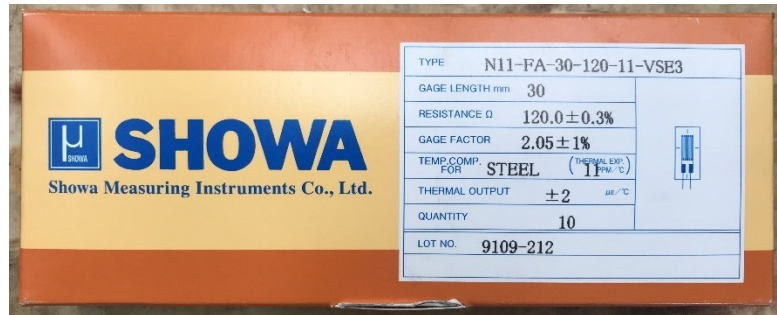







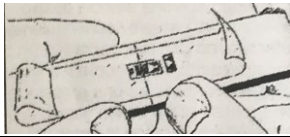


Figure 4-8: Packaging of strain gauges glued to concrete.




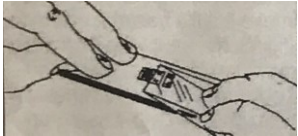
For application, the gluing procedure recommended by Luchsinger Ltd. in the M-Bond 200 User's Manual was followed step by step, as described in Table 4-2.


Table 4-2: Strain gauges gluing procedure.

Step.	Description	Picture
1	Use CSM-3 to clean the surface where strain gauges are glued.	
2	Use fine glass paper (220-320 grit) on the surface where strain gauges are glued.	
3	Wrap a piece of gauze around the tweezers and moisten it with M-Prep Conditioner A (Red tip bottle). Then pass the wet gauze over the surface a couple of times to remove dirt. Repeat a second time with a new gauze.	
4	Wrap a piece of gauze around the tweezers and moisten it with M-Prep Neutralizer 5A (Blue tip bottle). Then pass the damp gauze over the surface a couple of times to remove dirt. Repeat a second time with a new gauze. The surface will look dull.	

4-EXPERIMENTAL RESULTS AND DISCUSSION

5	Open the strain gauge leaving only the bottom side (gluing) on the slide. The upper side is the one with the welds.	
6	Apply scotch tape on the strain gauge leaving 2 flaps on both sides, and peel it off the slide.	
7	Place the strain gauge in position by manoeuvring with the tape flaps and glue it to the surface. Lift one flap of the scotch tape until the bottom of the strain gauge is facing upward	
8	Take Catalyst (blue liquid) , drip it 10 times on the edge of the bottle. Apply by passing only 1 time on the back of the strain gauge and 1 time on the surface. Leave to dry for at least 1 minute.	

NB	The next steps (9-10-11) must be completed quickly (3-5 seconds)	
9	With M-Bond 200 adhesive, apply 1 drop on the strain gauge and 1 drop on the surface.	
10	With one hand hold the tape flap and rotate it so that the strain gauge glues in position. With the second hand hold a gauze (or Teflon) and swipe in the direction of gluing to force air out while holding down.	
11	Apply pressure with your finger on the gauze for 1 minute to allow heat to contribute to the reaction.	
12	Wait 4-5 minutes before removing the tape slowly over itself in a sloping direction.	

13	Test with a tester if the strain gauge reads the correct resistance (120 Ω).	
----	--	---

For all tests, two strain gauges were glued in parallel at the same point to have a repeatability of results. In some cases, unfortunately, there is only one result related to one strain gauge because the other was damaged during the cutting operations.

4.1.1.3 Prediction models

ϵ_c obtained with strain gauges acquisitions were then processed to obtain the σ_c using equation (4-1). For each test this result was compared with a numerical and an analytical model as a function of prestressing, vertical load applied and position on the beam.

VecTor 2 model (§5.2.3) was used for comparison. The stress $\sigma_{c,num}$ returned by VecTor 2 can be visualized using Augustus software, which can post-process the VT2 analysis data. Augustus software allows observing the stress in each finite element of the mesh at different load levels (Figure 4-9).

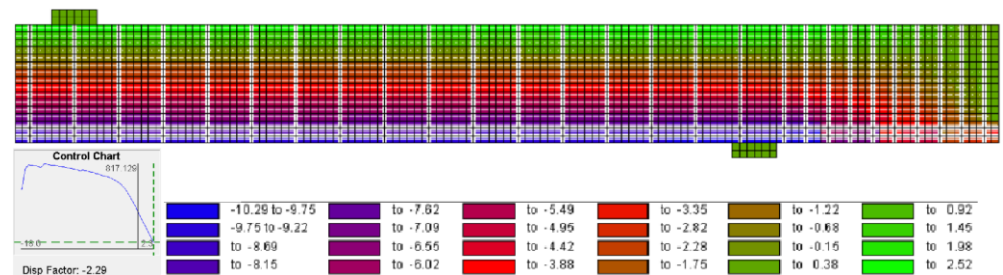


Figure 4-9: Example of Augustus output for concrete stress.

In addition to the numerical model, an analytical model was developed through the implementation of a spreadsheet to calculate the stress $\sigma_{c,ana}$ as a function of the distance from the load point and the position in the section. This model is based on the formulas:

$$\sigma_{sup} = \frac{P_M}{A_{id}} - \frac{P_M \cdot e \cdot (y - y_G)}{I_G} + \frac{M_1 \cdot (y - y_G)}{I_G} \tag{4-2}$$

$$\sigma_{inf} = \frac{P_M}{A_{id}} + \frac{P_M \cdot e \cdot (y_G - y)}{I_G} - \frac{M_1 \cdot (y_G - y)}{I_G} \tag{4-3}$$

4-EXPERIMENTAL RESULTS AND DISCUSSION

where:

- $P_M = \sigma_{strand} \cdot n_{strand} \cdot A_{strand}$
- A_{id} =ideal section area:
 - $A_{id} = A + (n - 1) \cdot (A_{stand} + A_{mild\ reinf.})$
 - $n = 5$ homogenization coefficient
- y_G = centroid of the beam cross-section;
- y = generic position in which stress is evaluated;
- $e = y_G - y_{strand}$ eccentricity of the strands with respect to the centroid;
- I_G = moment of inertia of the section;

$$M_1 = \left[\frac{g_{sw} \cdot l}{2} + F_V \cdot \frac{a}{a + b} \right] \cdot x - \frac{g_{sw} \cdot (x + c)^2}{2}$$

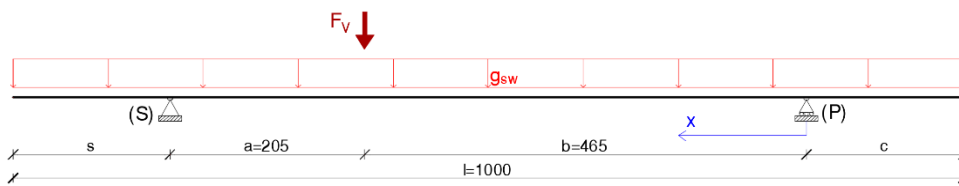


Figure 4-10: Loading scheme for moment calculation.

Equation (4-2) is used to calculate the stress at the points of the section that are above the centroid, while Equation (4-3) is used to calculate the stress at the points of the section that are below the centroid.

These formulas can be used only in the elastic stage, a phase during which I_G and y_G depend only on the geometric characteristics of the section. These formulas were used, for comparisons with experimental values, both at unloaded and loaded beam. In the unloaded beam condition, the whole beam is definitely in the elastic stage, on the other hand, in the loaded beam condition, the sections near the loading point are cracked, while those further away are still in the elastic stage. For this reason, it was decided to perform the release tests near the roller constrain, on which only 30% of the applied load ends up, and it is therefore an area that has never been cracked. For this reason, it was possible to use Equation (4-2) and Equation (4-3) as a comparison for the experimental values.

To evaluate the goodness of the release methods, it was decided to calculate the ratio between mean experimental stress (derived from the pair of strain gauges) [$\sigma_{c,exp}$] and stress returned by VecTor2 [$\sigma_{c,num}$]: the closer this ratio gets to 1, the more the release test returns a value in agreement with the value estimated by finite element analysis. However, if the ratio were evaluated against the analytical calculation [$\sigma_{c,ana}$], the results would be almost identical, since analytical calculation and numerical calculation are very similar to each other (maximum error of 10%) for all tests.

The procedures adopted and results obtained for the different methods used to evaluate residual prestress are described below.

4.1.2 Non-destructive methods applied

In addition to the semi-destructive methods described in the following chapters, two non-destructive methods for evaluating the residual prestress of a prestressed element were used during the experimental program presented in this research.

4.1.2.1 Digital Image Correlation (DIC)

The first technique is to apply Digital Image Correlation (DIC) technology. The aim was to determine whether through the photos, taken at constant time intervals, of the pattern created specifically on the surface of the beam and by varying the prestress inside the beam for the two Beams C, it was possible to trace the variation of the stress state using the GOM software used for image processing. As a result, the software fails to perceive the slightest variations in the beam surface as a result of the prestress variation.

4.1.2.2 Dynamics acquisitions

The second technique employed consists of assessing residual prestress by dynamic acquisitions.

Dynamic identification of Beam C2 at different prestress levels was performed by positioning it with the supports at the ends (Figure 4-11 and Figure 4-12, effective spacing between supports equal to 9.70 m) without any vertical load applied.

Identification of the frequency of the first mode was done by processing the accelerometer recordings of the free vibrations induced by "hammer tests" performed at different prestress levels. The "acceleration time-histories" are processed to obtain the corresponding Fourier spectrum for identification of the peak associated with the fundamental frequency.

The prestress load applied by the jack at the active beam header was decreased gradually from $\approx 1130\text{kN}$ (100% design prestress) to 565kN (i.e., -50%). This decrease may represent long-term losses that a prestressed element can reach under extreme conditions. Five accelerometer mems (model PCB 3741B122G/-0001) were installed along the top flange of the beam, arranged symmetrically with respect to the mid-span according to the layout shown in Figure 4-13. The frequency of signal acquisition was 400 Hz.

An example of accelerometer recordings is shown in Figure 4-14.

Table 4-3 shows the Fourier spectra obtained from the "hammer tests" carried out at the different prestress levels indicated.



Figure 4-11: Passive header restraint – S-side.



Figure 4-12: Passive header restraint – P-side.

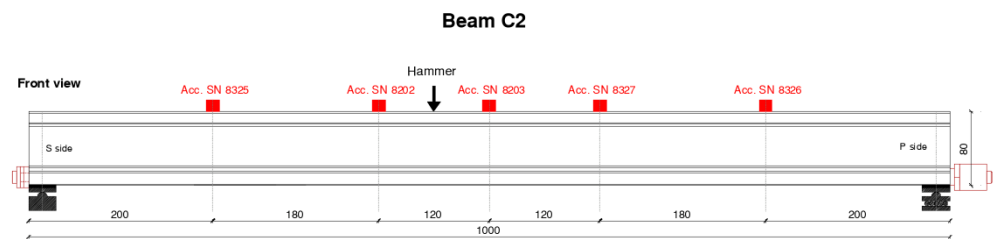


Figure 4-13: Experimental set-up adopted for five mems on Beam C2 for the execution of the "hammer tests" at different levels of prestress.

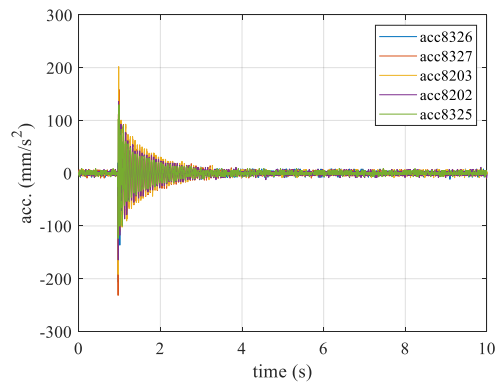
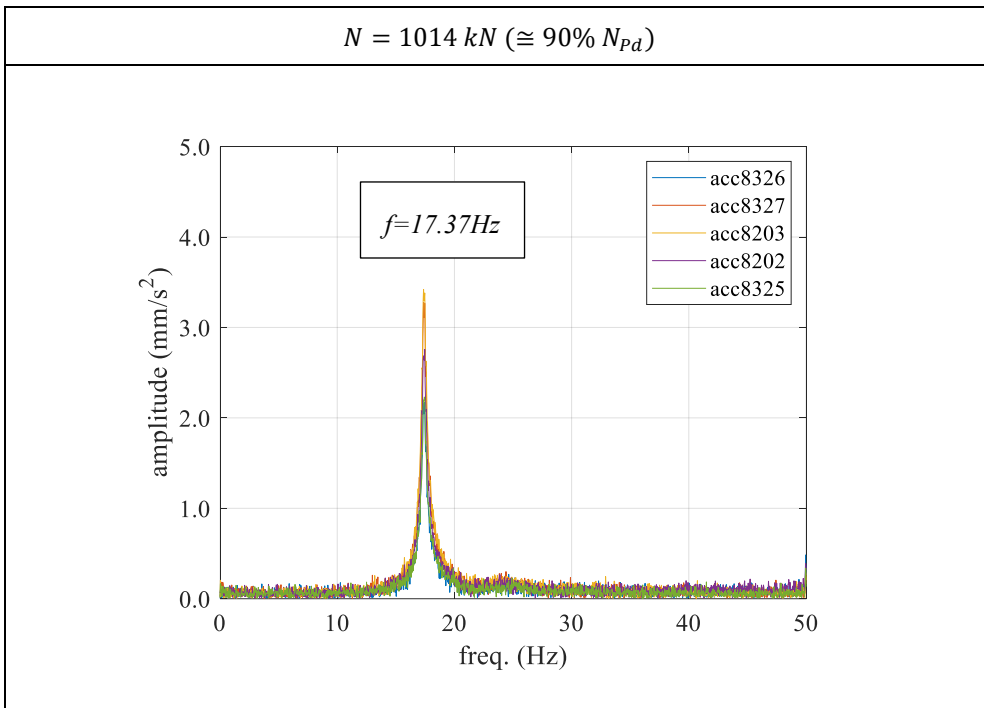
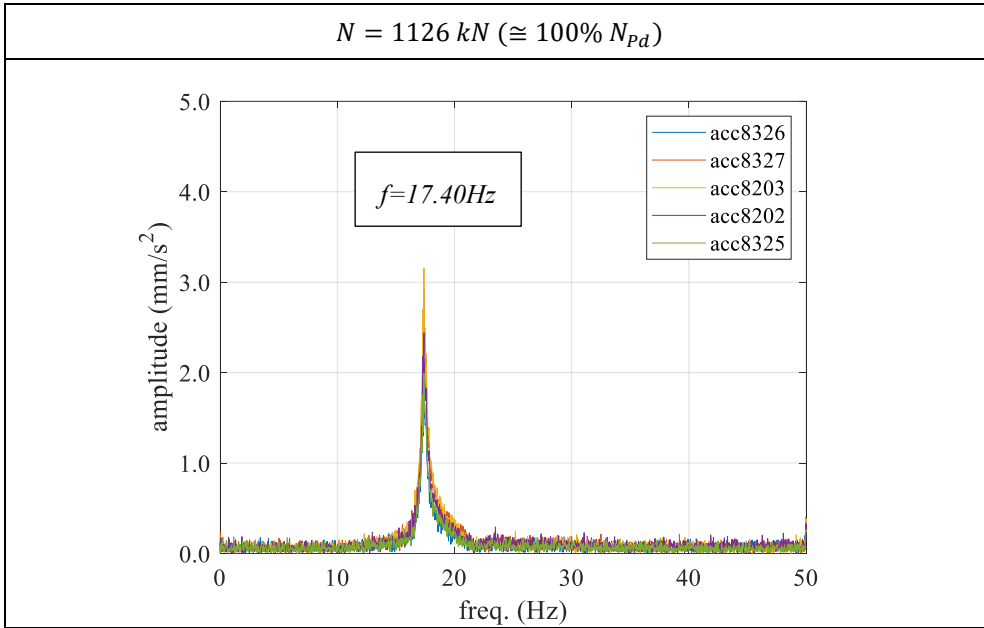
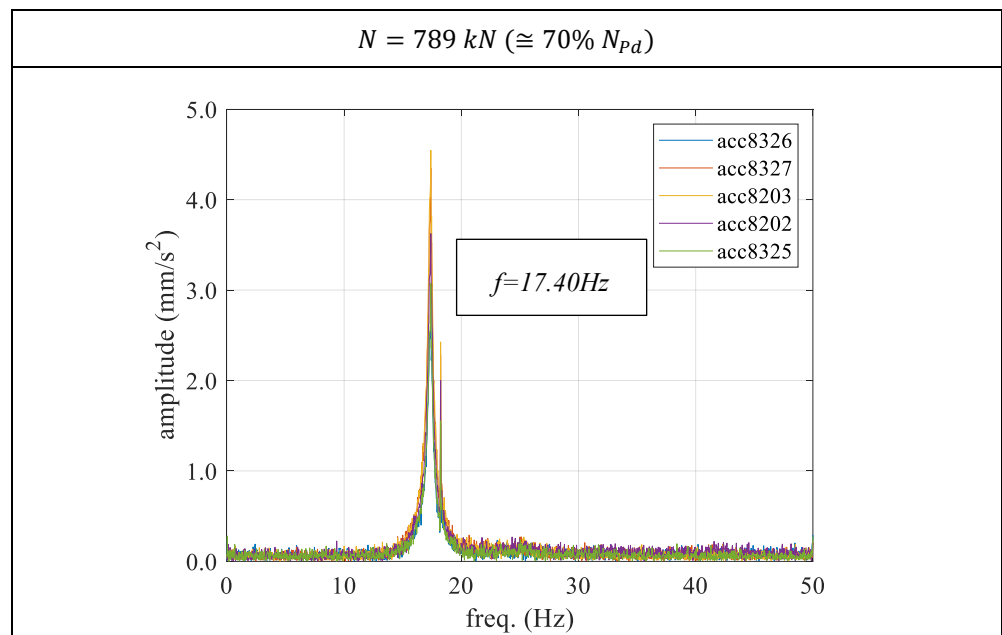
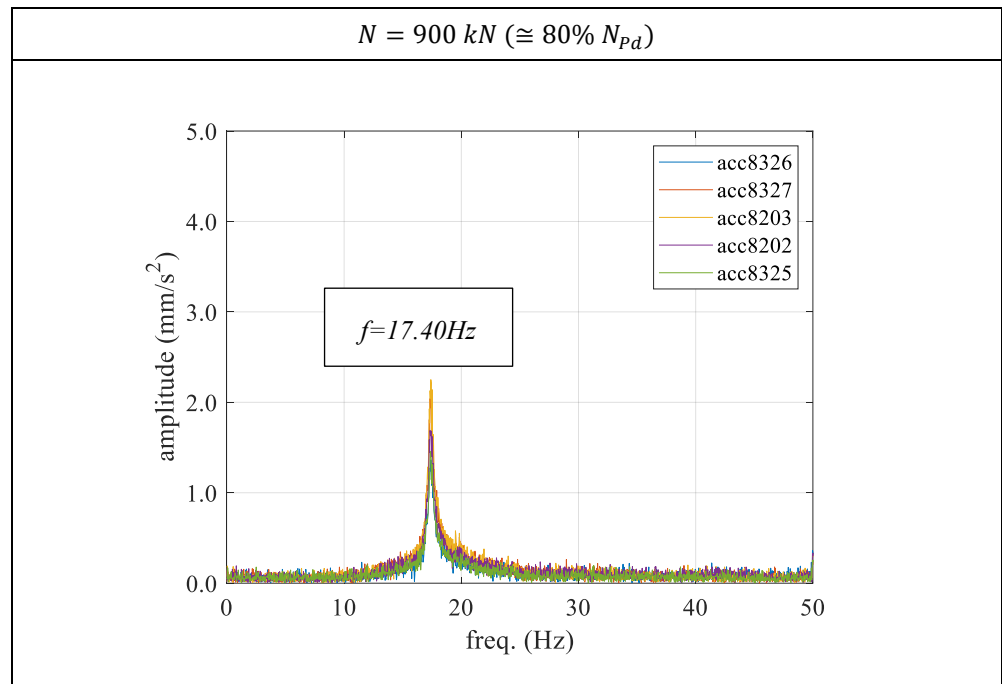


Figure 4-14: Acceleration time-histories recorded for the "hammer test" executed at 100% of the design prestress (1126kN).

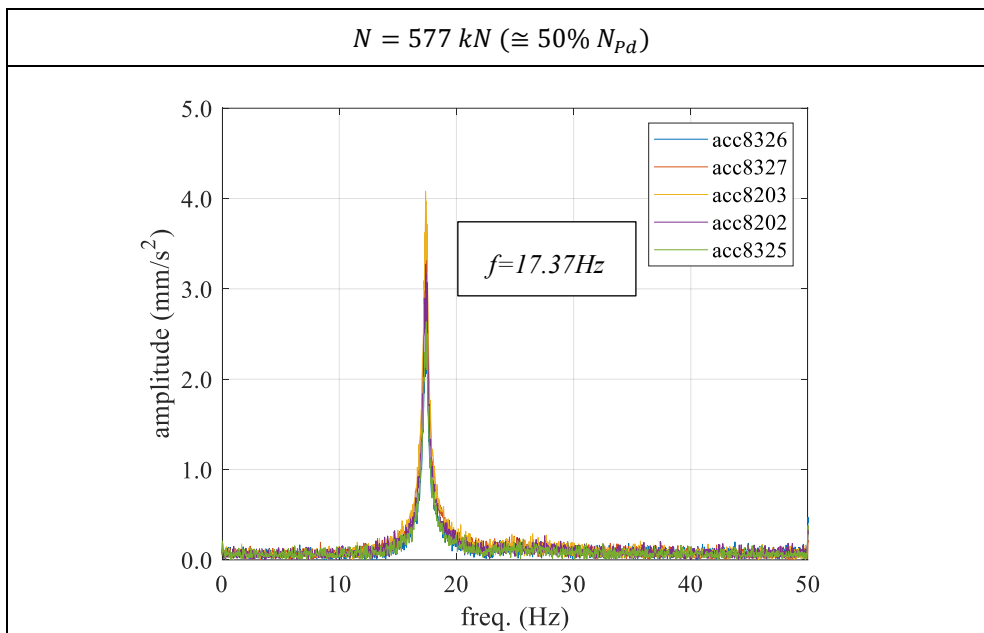
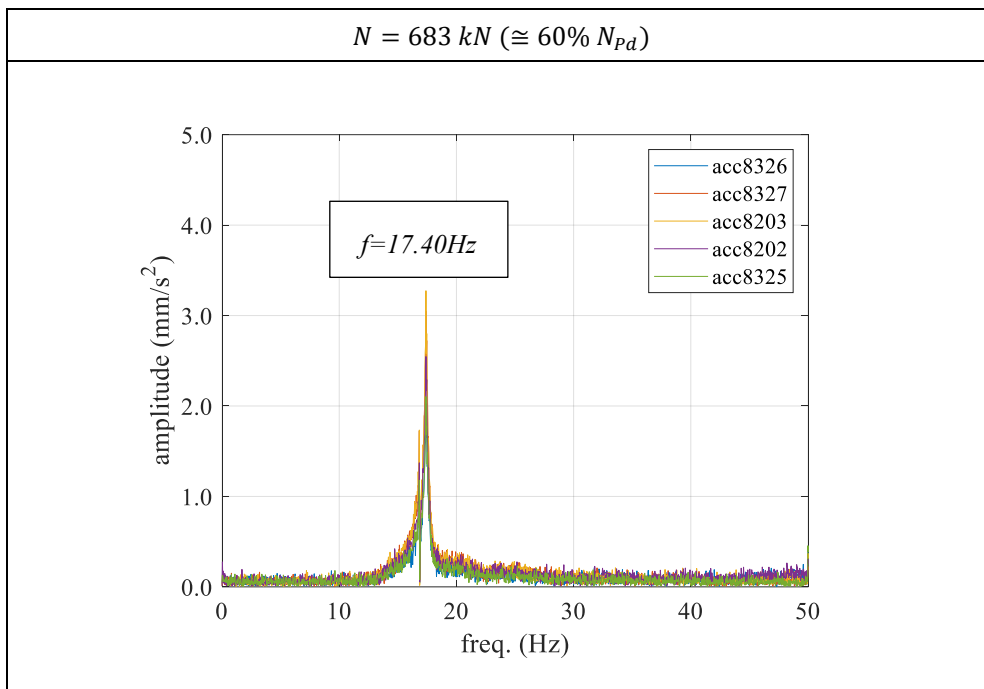
4-EXPERIMENTAL RESULTS AND DISCUSSION

Table 4-3: Single-side Fourier spectra calculated from acceleration time histories of "hammer tests" executed at different levels of prestress.





4-EXPERIMENTAL RESULTS AND DISCUSSION



It is observed that there is no significant change in the fundamental frequency throughout the range of prestress load variation. In fact, the frequency of the beam at different prestress levels is the same as that calculated analytically in non-prestressed beams [Chopra, 2017]:

$$f = \frac{\omega}{2 \cdot \pi} = \frac{1}{2 \cdot \pi} \cdot \left(\frac{\pi^2}{L^2} \cdot \sqrt{\frac{E \cdot J}{m}} \right) \quad (4-4)$$

Where:

- $J_{C2} = 17'643'785'370.1518 \text{ mm}^4$
- $E_{c,C2_exp} = 35760 \text{ MPa}$
- $L = 9700 \text{ mm}$
- $m = 5638 \text{ kg} \left(5.530 \frac{\text{kN}}{\text{m}} \right) \text{ (w/o strands)}$

The frequency resulting from the analytical formula is 17.39 Hz.

To evaluate the accuracy of the dynamic identification system, a mass of 32.6 kg/m was added to the beam (corresponding to an increase of 5.6% of its own weight $\approx +3.2 \text{ kN}$) by placing uniformly distributed concrete cubes on the upper flange (40 8.15kg cubes). The natural frequency calculated with the analytical formula (4-4) is equal to 16.91 Hz and is almost identical to the frequency of 16.87 Hz identified by the "hammer test". It results that the system adopted for the dynamic identification of the beam's frequency is sufficiently accurate to capture even minor variations of the structural system.



Figure 4-15: Beam C2 with part of additional distributed mass: experimental set-up for the "hammer tests" at $N=1126 \text{ kN}$.

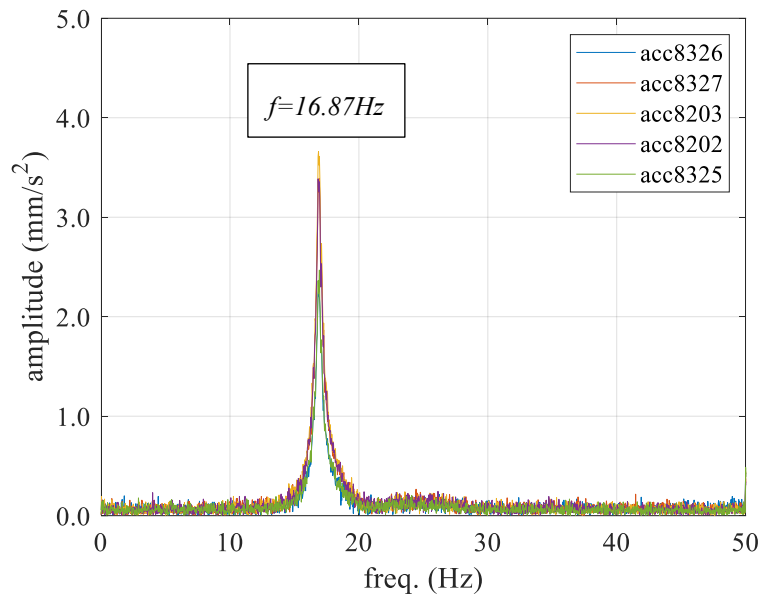


Figure 4-16: Relevant single-side Fourier spectrum of Beam C2 with 32.6kg/m of additional distributed mass with “hammer tests” at $N=1126kN$.

As also observed in other experimental studies [Bonopera et al., 2019; Frizzarin et al., 2019; Kerr, 1976], it can be deduced that fundamental frequencies do not allow determining prestress level of the beam object of these experimental tests.

An alternative proposal would be to proceed with an assessment of the second-order effects on the element at different prestress levels, as reported in literature [Dlupal, 2017].

4.1.3 Core Trepanning method

4.1.3.1 Description

Core drilling was performed with the assistance of Laboratorio Tecnologico Lombardo S.r.l. (LTL). Tests on beams A, B, and C were performed in sequence. The cores on beams A and B were carried out with different coring depths and, for the cores with greater depth, a single continuous coring was not applied, but the coring was performed in steps of a predetermined depth. The aim was to evaluate in this way the sufficient depth to guarantee total isolation of the concrete block, and therefore complete stress release.

Eleven cores were carried out, specifically:

- Two cores 3 cm deep;
- Seven cores 10 cm deep; of which some (five) were carried out continuously, others (two) were carried out in steps of 1,2,3,5,10 cm
- Two cores 15 cm deep.

Table 4-4 lists the tests performed with the Core Trepanning method and their characteristics.

For all cores, 2 strain gauges were glued, which are not acquired simultaneously, but one at a time: before coring, the first strain gauge (hereinafter called SG_A) is connected and waits for the time necessary to stabilize the signal. Then SG_A is removed and the second strain gauge (hereinafter called SG_B) is connected and acquired continuously until the end of the core trepanning. Once the desired core depth is reached, one waits for the SG_B strain gauge signal to stabilize, then connects the strain gauges SG_A (Figure 4-17).

4-EXPERIMENTAL RESULTS AND DISCUSSION

Table 4-4: List of tests performed with the Core Trepanning method with related characteristics.

Beam	Prestress	Vertical Load	Core Trepanning specimen	Strain Gauges (SG)	Recording	Depth (*)	Coordinates from the support (side P) (**)	
							x	y
	%	kN				cm	cm	cm
A	85	0	C_a1	A	Pre-Post	0, 15	140	43
				B	Continuous	0-15		
	700	C_a2	A	Pre-Post	0, 15	70	44	
			B	Continuous	0-15			
B	57	0	C_b1.1	A	Pre-Post	0, 10	146	42
				B	Continuous	0-10 (1,2,3,5,10)		
			C_b1.2	A	Continuous	0-10	116	38
			C_btop	A	Pre-Post	0, 1, 2, 3	116	80
			C_bbot	A	Pre-Post	0, 1, 2, 3	115	8
	585	C_b2	A	Pre-Post	0, 10	77	36	
			B	Continuous	0-10 (1,2,3,5,10)			
C1	87	0	C_c1-1	A	Pre-Post	0, 10	57	42
				B	Continuous	0-10		
	73		C_c1-2	A	Pre-Post	0, 10	77	33
				B	Continuous	0-10		
C2	95	400	C_c2-1	A	Pre-Post	0, 10	88	40
				B	Continuous	0-10		
	65		C_c2-2	A	Pre-Post	0, 10	172	45
				B	Continuous	0-10		

(*) Depths are to be interpreted as follows:

- 0, # and 0-#: the test was performed from 0 to # cm without interruption with one strain gauge acquiring continuously (0-#) and the second acquiring only at the beginning and end of the test (0, #)
- 0, 1, 2, 3: The test was performed from 0 to 3 cm by interrupting the cut at each centimetre depth to reconnect the strain gauges to the acquisition

system. In these tests, it was not possible to keep the SG wires connected to the controller;

- 0-10 (1,2,3,5,10): the test was performed from 0 to 10 cm by interrupting the coring at each depth level indicated to assess the depth required to obtain complete stress release.

(**) For the exact location of the tests, refer to Figure 4-4, Figure 4-5, Figure 4-6, Figure 4-7.

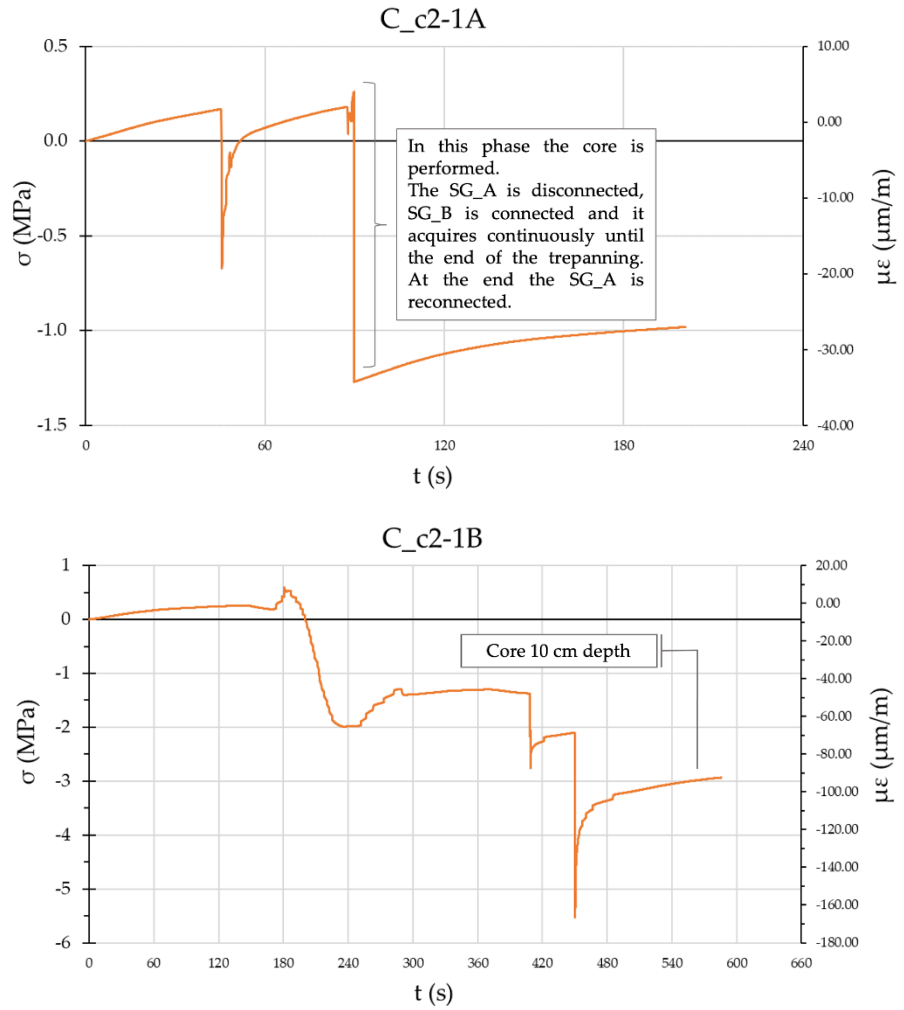


Figure 4-17: Example of strain gauge ϵ strain trends as a function of time while coring (Test C_c2-1: SG_A SG_B Beam C2).

4-EXPERIMENTAL RESULTS AND DISCUSSION

The execution procedure involves the following steps, as illustrated from Figure 4-18 to Figure 4-22

- 1) identification of reinforcement by magnetic survey (covermeter) to locate an area without reinforcement and where the surface is as least porous as possible (Figure 4-18)
- 2) drilling of the web within the planned cut for the strain gauges cables to acquire data continuously during coring (Figure 4-18, Figure 4-20);
- 3) preparation of the strain gauge gluing surface using a grinder, subsequent degreasing with concrete solvent;
- 4) gluing of two 120-Ohm strain gauges of length 30 mm, with horizontal direction (parallel to the longitudinal development of the beam), using the procedure described in Table 4-2.
- 5) protection of the strain gauges by applying silicone; coring is carried out with a wet core drill, so the wiring harnesses were made waterproof (Figure 4-19);
- 6) installation of the instrumentation⁹ to carry out the wet core trepanning (Figure 4-21, Figure 4-22);
- 7) connection of the strain gauges to a single-channel control unit (Figure 4-23), setting an acquisition frequency of 10 Hz. The SG_A is connected and waits for the time required for the signal to stabilize; it is disconnected from the control unit and the SG_B is connected, waiting for the signal of this one to stabilize as well;
- 8) execution of a 102 mm diameter core at variable depth, taking care to penetrate to the predetermined depth with a constant velocity (Figure 4-24, Figure 4-25);
- 9) once the desired penetration depth is reached, wait for the SG_B signal to stabilize, then reconnect the SG_A strain gauge and wait for the signal to stabilize.
- 10) the data export file *.csv provides results in $\mu\epsilon$, the $\Delta\mu\epsilon$ of each strain gauge is calculated by deducting the initial value from the final value;
- 11) $\Delta\mu\epsilon$ are converted to $\Delta\sigma$ through the elastic modulus of the corresponding beam, and the two values are averaged;
- 12) $\Delta\sigma$ obtained, which represents the $\sigma_{c,exp}$ of the concrete before coring with an inverted sign¹⁰, is compared with the numerical prediction $\sigma_{c,num}$.

⁹ Hilti DD 150-U core drill with support frame.

¹⁰ The acquisition equipment used in this test, automatically performs sign conversion, so the results already represent the stress state of the concrete.



Figure 4-18: Identification of cutting area and cable passage hole.



Figure 4-19: Gluing and protecting SGs from water using silicone



Figure 4-20: The opposite side of the core with cable routing through the web and acquisition hardware.



Figure 4-21: Performing the test with a wet core drill (Beam A).



Figure 4-22: Instrumentation used to carry out concrete cores.



Figure 4-23: Single-channel control unit for the acquisition of strain gauges.

4-EXPERIMENTAL RESULTS AND DISCUSSION



Figure 4-24: Detail of the end of test execution.

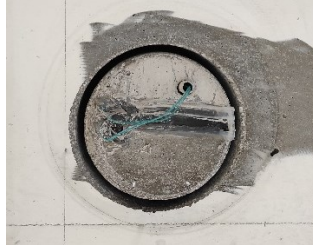


Figure 4-25: Test completed.

4.1.3.2 Results

The results obtained from the tests are shown in Table 4-5. The $\sigma_{c,ana}$ are calculated by the analytical method described in §4.1.1.3, also taking into account the location of each test shown in Table 4-4. The last column shows the ratio between experimentally measured stress [$\sigma_{c,exp}$] and the stress obtained from the numeric model [$\sigma_{c,num}$].

Table 4-5: Test results of Core Trepanning method.

Core Trepanning specimen	Strain Gauges (SG)	Recording	Depth (*)	$\Delta\sigma_c$	$\sigma_{c,exp}$	$\sigma_{c,num}$	$\sigma_{c,ana}$	$\frac{\sigma_{c,exp}}{\sigma_{c,num}}$
			cm	MPa	MPa	MPa	MPa	
C_a1	A	Pre-Post	0, 15	-0.41	-0.09	-3.28	-3.30	0.0
	B	Continuous	0-15	0.23				
C_a2	A	Pre-Post	0, 15	0.12	0.34	-3.71	-3.50	-0.1
	B	Continuous	0-15	0.56				
C_b1.1	A	Pre-Post	0, 10	4.36	3.11	-2.11	-2.20	-1.5
	B	Continuous	0-10 (1,2,3,5,10)	1.87				
C_b1.2	A	Continuous	0-10	2.32	2.32	-3.07	-2.60	-0.8
C_btop	A	Pre-Post	0, 1, 2, 3	4.68	4.68	1.27	1.50	3.7
C_bbot	A	Pre-Post	0, 1, 2, 3	-2.44	-2.44	-5.48	-5.52	0.4
C_b2	A	Pre-Post	0, 10	2.56	2.44	-2.67	-2.58	-0.9
	B	Continuous	0-10 (1,2,3,5,10)	2.32				
C_c1-1	A	Pre-Post	0, 10	1.69	1.93	-3.49	-3.43	-0.6
	B	Continuous	0-10	2.16				
C_c1-2	A	Pre-Post	0, 10	-1.55	-0.41	-4.11	-4.01	0.1
	B	Continuous	0-10	0.73				
C_c2-1	A	Pre-Post	0, 10	-1.14	-2.18	-4.30	-4.17	0.5
	B	Continuous	0-10	-3.23				
C_c2-2	A	Pre-Post	0, 10	-	0.46	-3.10	-2.97	-0.1
	B	Continuous	0-10	0.46				

4-EXPERIMENTAL RESULTS AND DISCUSSION

4.1.3.3 Discussion

Table 4-5 shows both experimental [$\sigma_{c,exp}$] and analytical [$\sigma_{c,ana}$] / numerical [$\sigma_{c,num}$] results, indicating a compressive stress state if <0 , and a tensile stress state if >0 . The stress obtained with SG is considered compressive if the SG undergo extension after coring.

Thus, in some of the experimental tests, the strain gauges cannot even sense the true concrete stress. In particular, in the following cases, a tension, instead of compression, is recorded in the concrete and thus $\sigma_{c,exp}/\sigma_{c,num} < 0$:

- Beam A, prestress 85%, vertical load 700 KN for both SGs on C_a2;
- Beam B, prestress 57%, vertical load 0 KN for both SGs on C_b1.1 and single SG on C_b1.2;
- Beam B, prestress 57%, vertical load 585 KN for both SGs on C_b2;
- Beam C1, prestress 87%, vertical load 0 KN for both SGs on C_c1-1;
- Beam C2, prestress 65%, vertical load 400 KN for single SG on C_c2-2.

This issue related to SG can also be seen in Figure 4-26, where the dispersion of the results of the ratio $\sigma_{c,exp}/\sigma_{c,num}$ with respect to the bisector is shown. Only the difference between tests performed under vertical load versus those performed with the beam unloaded is shown. In cases in which the experimental stress obtained by use of strain gauges has the opposite sign to that assumed by VecTor 2, the data are in the second or fourth quadrant. On the other hand, when the experimental and numerical values agree in sign, i.e., are both tensile or compressive, the data are in the first or third quadrant.

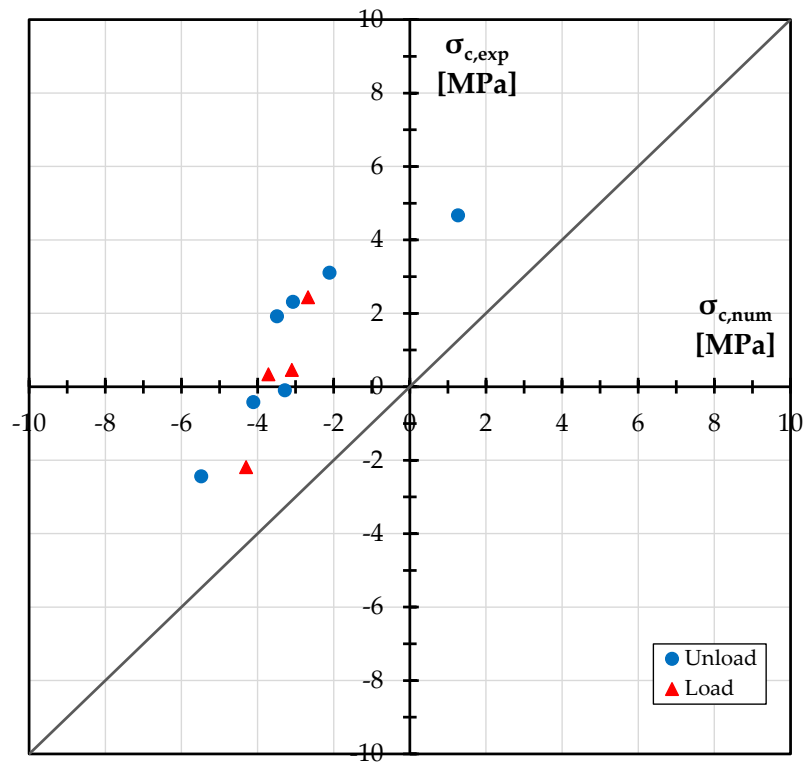


Figure 4-26: Dispersion of results obtained from Core Trepanning method tests with a division between tests performed in the absence and presence of vertical load.

Due to the way the Core Trepanning method tests were performed in this experimental program, good results were not obtained.

As shown in Figure 4-27, the depth of the drilled cores does not seem to have influenced the result: in fact, it can be seen that the cores, regardless of the depth of drilling, are ineffective, so much so that in most cases they fail to capture whether the section is in a tensile or compressive state.

In addition to the depth of penetration, other factors affect the success of the tests:

- Porosity: if the concrete is very porous (see the comparison of porosity between Figure 4-28 and Figure 4-29) it is difficult to identify an area where SGs can be glued so that they are not affected by surface porosity. Consequently, when the concrete surface is very porous, the results provided by strain gauges are not very reliable.

4-EXPERIMENTAL RESULTS AND DISCUSSION

- These are highly sensitive and operator-dependent tests: coring must be performed at as constant a speed as possible, preventing the core drill from getting stuck. To ensure continuous coring, the cutter blade must be sharp. If the core trepanning is disturbed lesions or micro-cracks can form intercepting the strain gauges, and thus making the results unreliable.
- As shown in Figure 4-28 and Figure 4-29, silicone was applied to protect the strain gauges from the water used for wet core trepanning. This factor may have adversely affected the output of the strain gauges. The silicone, while having some elasticity, may have constrained the expansion of the SGs glued to the concrete. Even the silicone may have induced a shortening of the SG during cutting due to its solidification with the SGs, which then recorded values opposite to those predicted.

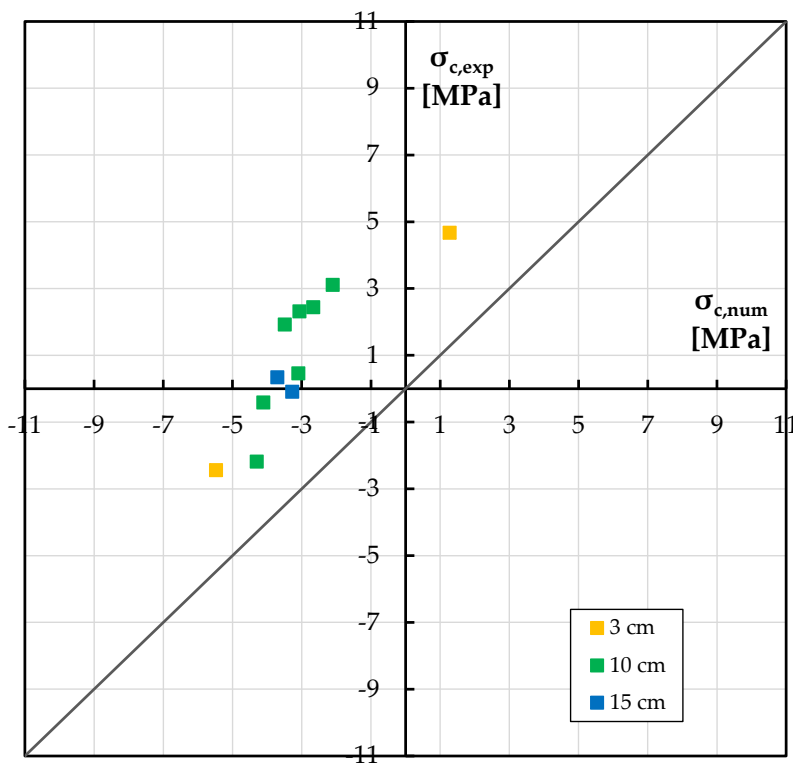


Figure 4-27: Dispersion of the results obtained from the Core Trepanning method tests with subdivision based on the drilling depth.



Figure 4-28: Example of SGs gluing on a low-porous surface.



Figure 4-29: Example of SGs gluing on a very porous surface.

4.1.4 Saw-Cut method - Intrados

4.1.4.1 Description

The intrados saw-cuts were performed with the assistance of Laboratorio Tecnologico Lombardo S.r.l. (LTL). Tests on beams A, B, and C were performed in sequence.

Nine tests were performed at different prestressing levels and different vertical load levels. Table 4-6 lists the tests performed with the Saw-Cut method - intrados and their characteristics.

Each test requires making two cuts in the beam intrados for almost the entire width of the section (≈ 50 cm), using an angle grinder¹¹ $\varnothing 115$ mm and a diamond blade¹². Based on what was published by Kral'ovanec et al. (2021), it was decided to make the cuts 3 cm deep and with a distance between them of 12 cm. This choice, as well as repeating what Kral'ovanec et al. (2021), was also dictated by practical limitations noted during the execution of the laboratory test:

- on the one hand, it is not possible to make cuts deeper than 3 cm because the longitudinal reinforcement would be cut; moreover, the blade of a $\varnothing 115$ mm grinder cut to a maximum depth of 30 mm;
- on the other hand, it is difficult to make cuts at a relative distance of less than 12 cm because a space of about 6 to 8 cm is required for gluing the 30-mm strain gauges, to which about 2 cm on each side is added by the presence of the strain gauge wires.

As well as for the cores, two strain gauges were glued for each test, one (SG_A) acquired before and after the test and the other (SG_B) acquired continuously during cutting (Figure 4-30).

¹¹ Max rpm 13300 80m m/s (Figure 4-34)

¹² Makita GA4530R 720W $\varnothing 115$ mm (Figure 4-33)

Table 4-6: List of tests performed with the Saw-Cut method – intrados with related characteristics.

Beam	Prestress	Vertical Load	Saw-Cut Intrados specimen	Strain Gauges (SG)	Recording	Depth (*)	Coordinates from the support (side P) (**)	
							x	y
	%	kN				cm	cm	cm
A	85	0	SCi_a1	A	Pre-Post	0, 3	140	0
				B	Continuous	0-3 (1, 2, 3)		
	700	SCi_a2	A	Pre-Post	0, 3	82	0	
			B	Continuous	0-3 (1, 2, 3)			
B	57	0	SCi_b1.1	A	Pre-Post	0, 3	140	0
				B	Continuous	0-3 (1, 2, 3)		
		585	SCi_b1.2	A	Pre-Post	0, 3	113	0
				B	Continuous	0-3 (1, 2, 3)		
	87	0	SCi_c1-1	A	Pre-Post	0, 3	85	0
				B	Continuous	0-3 (1, 2, 3)		
73	SCi_c1-2	A	Pre-Post	0, 3	137	0		
		B	Continuous	0-3 (1, 2, 3)				
C2	95	400	SCi_c2-1	A	Pre-Post	0, 3	86	0
				B	Continuous	0-3		
	65	SCi_c2-2	A	Pre-Post	0, 3	145	0	
			B	Continuous	0-3			

(*) Depths are to be interpreted as follows:

- 0, 3 and 0-3: the test was performed from 0 to 3 cm without interruption with one strain gauge acquiring continuously (0-3) and the second acquiring only at the beginning and end of the test (0, 3)
- 0-3 (1,2,3): the test was performed from 0 to 3 cm by interrupting the cut at each depth level indicated to assess the depth required to obtain complete tension release.

(**) For the exact location of the tests, refer to Figure 4-4, Figure 4-5, Figure 4-6, Figure 4-7.

4-EXPERIMENTAL RESULTS AND DISCUSSION

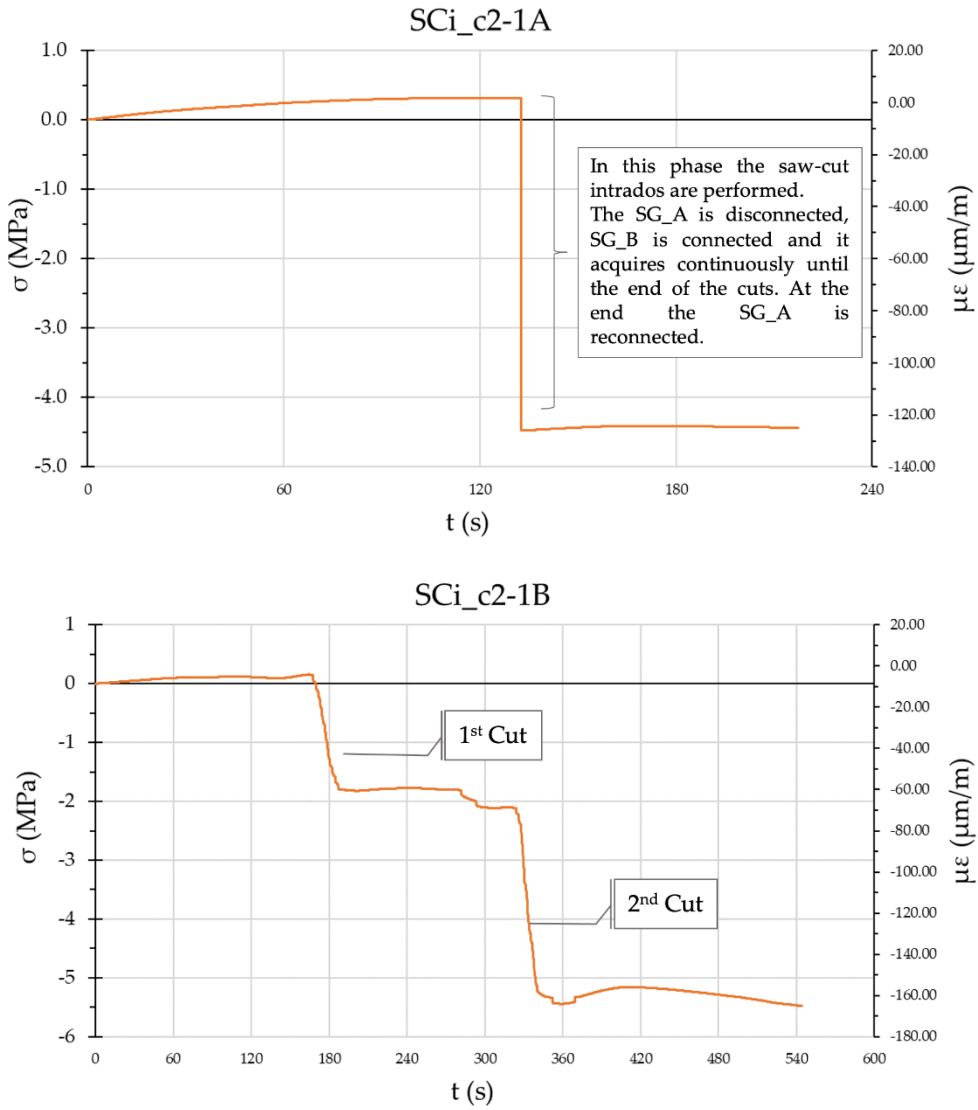


Figure 4-30: Example of strain gauge ϵ strain trends as a function of time during Saw-Cut Intrados (Test SCi_c2-1: SG_A SG_B Beam C2).

The execution procedure involves the following steps, as illustrated in Figure 4-18:

- 1) identification of reinforcement by magnetic survey (covermeter) to locate an area without reinforcement and where the surface is as least porous as possible and without cracks;
- 2) preparation of the strain gauge gluing surface using a grinder, subsequent degreasing with concrete solvent;
- 3) gluing of two 120-Ohm strain gauges of length 30 mm, with horizontal direction (parallel to the longitudinal development of the beam and orthogonal to the cuts), using the procedure described in Table 4-2;
- 4) connection of the strain gauges to a single-channel control unit (Figure 4-31), setting an acquisition frequency of 10 Hz. The SG_A is connected and waits for the time required for the signal to stabilize; it is disconnected from the control unit and the SG_B is connected, waiting for the signal of this one to stabilize as well;
- 5) performing intrados cuts with an angle grinder $\varnothing 115$ mm (Figure 4-33) and diamond blade (Figure 4-34). This is done by making one cut at a time proceeding in 1 cm step until a depth of 3 cm is obtained while keeping a constant cutting speed;
- 6) during the test it is necessary to make sure that the casing of the grinder does not touch the cables of the strain gauges;
- 7) wait for the signal of the connected strain gauges to stabilize ($\approx 1\div 2$ minutes) before proceeding with the next pair of cuts at a depth increased by 1 cm;
- 8) once the desired penetration depth is reached (Figure 4-35), wait for the SG_B signal to stabilize, then reconnect the SG_A strain gauge and wait for the signal to stabilize.
- 9) the data export file *.csv provides results in $\mu\epsilon$, the $\Delta\mu\epsilon$ of each strain gauge is calculated by deducting the initial value from the final value;
- 10) $\Delta\mu\epsilon$ are converted to $\Delta\sigma$ through the elastic modulus of the corresponding beam, and the two values are averaged;
- 11) $\Delta\sigma$ obtained, which represents the $\sigma_{c,exp}$ of the concrete before insulation, by means of the parallel cuts of the surface portion, with an inverted sign¹³, is compared with the numerical prediction $\sigma_{c,num}$.

¹³ The acquisition equipment used in this test, automatically performs sign conversion, so the results already represent the stress state of the concrete.

4-EXPERIMENTAL RESULTS AND DISCUSSION

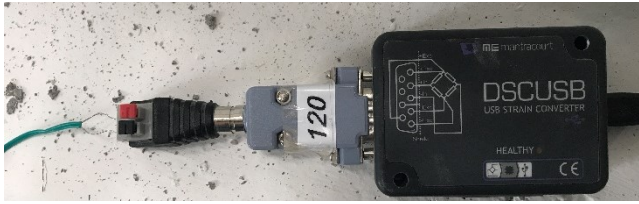


Figure 4-31: Single-channel control unit for the acquisition of strain gauges.



Figure 4-32: Identification of reinforcement and mark of cuts to be carried out at a distance of 12 cm.



Figure 4-33: Model of the angle grinder used.



Figure 4-34: Diamond blade for cutting concrete.



Figure 4-35: Cuts performed.

4.1.4.2 **Results**

The results obtained from the tests are shown in Table 4-7. The $\sigma_{c,ana}$ are calculated by the analytical method described in §4.1.1.3, also taking into account the location of each test shown in Table 4-6. The last column shows the ratio between experimentally measured stress [$\sigma_{c,exp}$] and the stress obtained from the numeric model [$\sigma_{c,num}$].

Table 4-7: Test results of Saw-Cut method – Intrados.

Saw-Cut Intrados specimen	Strain Gauges (SG)	Recording	Depth (*)	$\Delta\sigma_c$	$\sigma_{c,exp}$	$\sigma_{c,num}$	$\sigma_{c,ana}$	$\frac{\sigma_{c,exp}}{\sigma_{c,num}}$
			cm	MPa	MPa	MPa	MPa	
SCi_a1	A	Pre-Post	0, 3	-5.92	-5.23	-9.57	-9.78	0.5
	B	Continuous	0-3 (1, 2, 3)	-4.54				
SCi_a2	A	Pre-Post	0, 3	-2.10	-1.53	-6.11	-6.18	0.3
	B	Continuous	0-3 (1, 2, 3)	-0.97				
SCi_b1.1	A	Pre-Post	0, 3	0.80	-0.03	-5.90	-6.23	0.0
	B	Continuous	0-3 (1, 2, 3)	-0.86				
SCi_b1.2	A	Pre-Post	0, 3	-0.57	-0.41	-5.97	-6.30	0.1
	B	Continuous	0-3 (1, 2, 3)	-0.25				
SCi_b2	A	Pre-Post	0, 3	0.66	1.07	-3.16	-3.21	-0.3
	B	Continuous	0-3 (1, 2, 3)	1.48				
SCi_c1-1	A	Pre-Post	0, 3	-0.65	-2.80	-9.57	-10.00	0.3
	B	Continuous	0-3 (1, 2, 3)	-4.94				
SCi_c1-2	A	Pre-Post	0, 3	-5.28	-5.21	-7.67	-8.29	0.7
	B	Continuous	0-3 (1, 2, 3)	-5.13				
SCi_c2-1	A	Pre-Post	0, 3	-4.71	-5.11	-8.24	-8.77	0.6
	B	Continuous	0-3	-5.50				
SCi_c2-2	A	Pre-Post	0, 3	1.55	0.42	-3.57	-3.50	-0.1
	B	Continuous	0-3	-0.71				

4.1.4.3 Discussion

Table 4-7 shows both experimental [$\sigma_{c,exp}$] and analytical [$\sigma_{c,ana}$] / numerical [$\sigma_{c,num}$] results, indicating a compressive stress state if <0 , and a tensile stress state if >0 . The stress obtained with SG is considered compressive if the SG undergo extension after cutting.

Thus, in some of the experimental tests, the strain gauges cannot even sense the true concrete stress. In particular, in the following cases, a tension, instead of compression, is recorded in the concrete and thus $\sigma_{c,exp}/\sigma_{c,num} < 0$:

- Beam B, prestress 57%, vertical load 585 KN for both SGs on SCi_b2;
- Beam C2, prestress 65%, vertical load 400 KN for both SGs on SCi_c2-2.

This issue related to SG can also be seen in Figure 4-36, where the dispersion of the results of the ratio $\sigma_{c,exp}/\sigma_{c,num}$ with respect to the bisector is shown. Only the difference between tests performed under vertical load versus those performed with the beam unloaded is shown. In cases in which the experimental stress obtained by use of strain gauges has the opposite sign to that assumed by VecTor 2, the data are in the second or fourth quadrant. On the other hand, when the experimental and numerical values agree in sign, i.e., are both tensile or compressive, the data are in the first or third quadrant.

The study by Bagge, Nilimaa, and Elfgren (2017) also concludes that strain gauges sometimes give misleading results, probably due to damage or inadequate gluing of the sensor. The authors do not detect a clear strain plateau in any of the investigated sections. This indicates that the area between the two cuts is only partially isolated and thus is still affected by forces acting on the concrete that increase the strains as a result of deeper cuts.

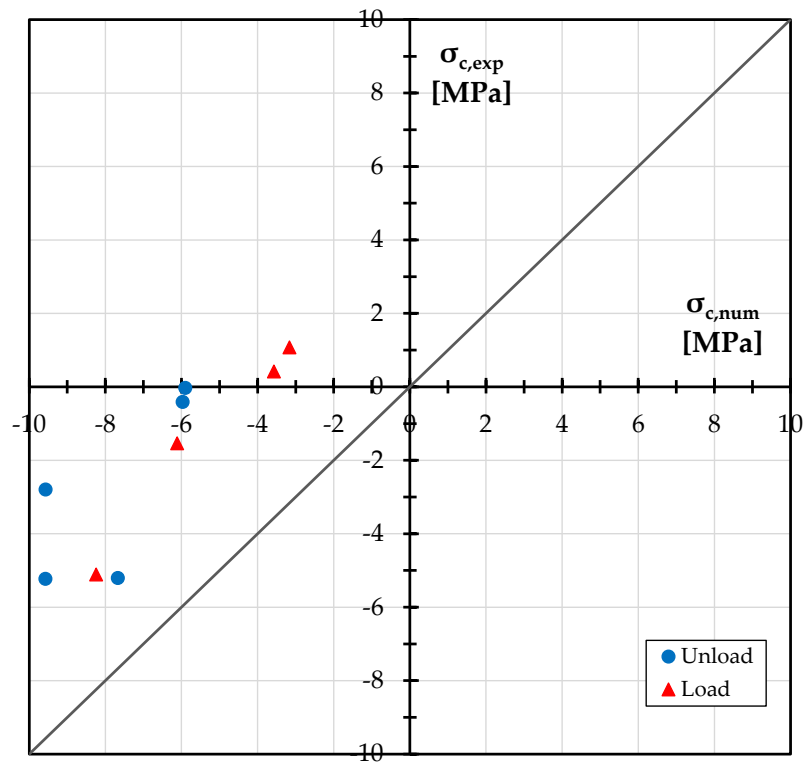


Figure 4-36: Dispersion of results obtained from Saw-Cut method – Intrados with a division between tests performed with or without vertical load.

As with the tests performed with the Core Trepanning method, due to the way the Saw-Cut method – Intrados tests were performed in this experimental program, good results were not obtained.

The results of the release tests performed by intrados saw-cuts were performed some in one step up to the maximum depth of 3 cm, and others by waiting for strain gauge stabilization at each cm depth. The intrados saw-cuts were performed at the same prestress values and vertical load applied for the cores.

For both loaded and unloaded beam tests (excluding the two tests that showed results with opposite signs compare to the prediction), it can be seen that this method provides results far from the numerical and analytical predictions. Cuts were carried out at a depth of 3 cm and a relative distance of 12 cm. The mean of all $\sigma_{c,exp}/\sigma_{c,num}$ is 0.22: probably this geometric cutting configuration does not allow a perfect stress release of the point where the SGs are applied.

4.1.5 Blunt Pyramidal specimen

4.1.5.1 Description

Blunt pyramid specimen tests were performed by technicians of 4 EMME Service S.p.A.. Tests on Beams A and C were performed in sequence, while no tests were performed on Beam B.

Table 4-8 lists the tests performed with the Blunt Pyramidal specimen method and their characteristics. A total of 16 tests were performed at different prestress levels and different vertical loads, however, two tests (R1 and R6) provided values that could not be processed, so they were not discussed in the results.

Each test involves gluing two strain gauges to the concrete surface in parallel and properly protected (according to the specific procedure of 4 EMME Service S.p.A.). Then 4 cuts are carried out orthogonal to each other and inclined 45° toward the centre of the square that is formed, in-depth. The cuts reach a depth of about 25 mm (cover) and are made with a diamond blade installed on an angle grinder Ø125 mm. The grinder is installed on a plate fixed to the beam called "Discovery", which ensures accuracy and regularity for the 4 cutting angles. Unlike in the previous two techniques (core trepanning method e intrados saw-cut method), the two strain gauges (SG_A and SG_B) are acquired simultaneously during the entire test (Figure 4-37); in fact, they are connected by cable to a datalogger that acquires continuously at 0.2 Hz. The datalogger transfers the data wireless to a smartphone.

Table 4-8: List of tests performed with the Blunt Pyramidal specimen with related characteristics.

Beam	Prestress	Vertical Load	Saw-Cut Intrados specimen	Strain Gauges (SG)	Recording	Depth and position	Coordinates from the support (side P) (**)	
							x	y
	%	kN				cm	cm	cm
A	85	0	R2	A	Continuous	2.5 Web	110	42
				B	Continuous			
			R3	A	Continuous	2.5 Flange inf.	110	8
				B	Continuous			
			R4	A	Continuous	2.5 Flange inf. Intra.	112	0
				B	Continuous			

4-EXPERIMENTAL RESULTS AND DISCUSSION

			R5	A	Continuous	2.5 Flange inf.	565	8
				B	Continuous			
C1	60	0	R7	A	Continuous	2.5 Web	117	42
				B	Continuous			
			R8	A	Continuous	2.5 Flange inf.	115	8
				B	Continuous			
C2	100	0	R9	A	Continuous	2.5 Web	118	42
				B	Continuous			
			R10	A	Continuous	2.5 Flange inf.	114	8
				B	Continuous			
		400	R11	A	Continuous	2.5 Web	148	42
				B	Continuous			
			R12	A	Continuous	2.5 Flange inf.	145	8
				B	Continuous			
	60	0	R13	A	Continuous	2.5 Web	106	42
				B	Continuous			
			R14	A	Continuous	2.5 Flange inf.	108	8
				B	Continuous			
		400	R15	A	Continuous	2.5 Web	135	42
				B	Continuous			
			R16	A	Continuous	2.5 Flange inf.	136	8
				B	Continuous			

(**) For the exact location of the tests, refer to Figure 4-4, Figure 4-5, Figure 4-6, Figure 4-7.

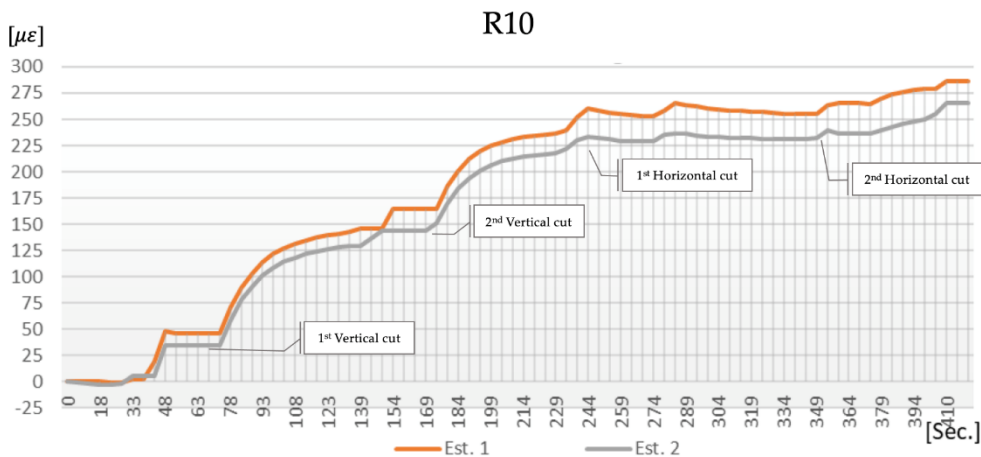


Figure 4-37: Evolution of strain gauge ϵ strains as a function of time per Blunt Pyramid specimen test (Test R10).

The execution procedure involves the following steps, as illustrated from Figure 4-38 to Figure 4-43 :

- 1) identification of the test locations on the surface of the beam;
- 2) identification of reinforcement by magnetic survey (covermeter) adjacent to the theoretical test points and identification of the nearest test point with a minimum distance of 100 mm from the reinforcement. Reinforcement is allowed in the test area if it is at least 30 mm deep from the external surface;
- 3) tracing the anchorage points for the grinder support plate using a level;
- 4) preparation of the strain gauge gluing surface using a grinder, application of putty/filler to close pores and create a smooth surface, scrubbing with abrasive paper, subsequent degreasing with concrete solvent and special adhesion-enhancing gel;
- 5) gluing of two 120-Ohm strain gauges of length 30 mm, with horizontal direction (parallel to the longitudinal development of the beam), using cyanoacrylate glue;
- 6) protection of the strain gauges by aluminium film coated with adhesive mouldable putty;
- 7) installation on the beam of the angle grinder ("Discovery", see Figure 4-38 and Figure 4-39);
- 8) connecting the strain gauges to the Datalogger (Figure 4-40) (fixed on the grinder) in a quarter-bridge configuration by setting a data acquisition of 0.2 Hz, so the unit can acquire data from both strains gauges continuously throughout the test;

- 9) performing two parallel cuts 65 mm apart, first in the vertical direction and then the pair of cuts in the horizontal direction, with a diamond blade \varnothing 125 mm; the cut should be performed with a 45° direction toward the centre in depth, so as to form a truncated-pyramidal element while maintaining a constant penetration speed (Figure 4-41);
- 10) cuts are performed in succession: right side, left side, top cut, bottom cut. The first cut starts after 60 seconds from the activation of data acquisition; the subsequent interval between one cut and the next is 90 seconds (Figure 4-42, Figure 4-42, Figure 4-43);
- 11) beam temperature measurement at the test point;
- 12) the Datalogger transfers wireless the data to an app on the smartphone, which is processed by different technicians than those who performed the test, to have more control over the results;
- 13) from the data provided by 4 EMME Service S.p.A. in terms of $\mu\epsilon$, the $\Delta\mu\epsilon$ of each strain gauge is calculated by deducting the initial value from the final value;
- 14) $\Delta\mu\epsilon$ are converted to $\Delta\sigma$ through the elastic modulus of the corresponding beam, and the two values are averaged;
- 15) $\Delta\sigma$ obtained, which represents the $\sigma_{c,exp}$ of the concrete before coring with an inverted sign, is compared with the numerical prediction $\sigma_{c,num}$.



Figure 4-38: Discovery
4 EMME Service S.p.A.



Figure 4-39: Equipment installation before
vertical cutting.



Figure 4-40: Datalogger
4 EMME Service S.p.A.

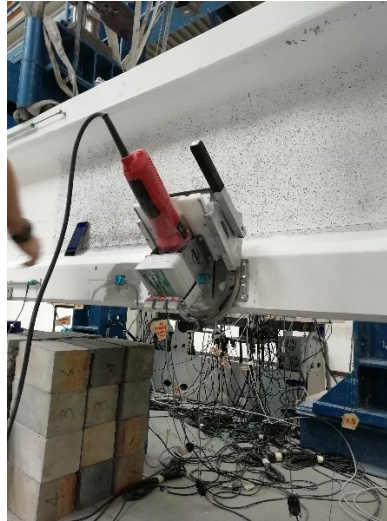


Figure 4-41: Equipment installation before
top horizontal cutting.



Figure 4-42: Test completed.



Figure 4-43: Blunt Pyramidal specimen.

4.1.5.2 Results

The results obtained from the tests are shown in Table 4-9. The $\sigma_{c,ana}$ are calculated by the analytical method described in §4.1.1.3, also taking into account the location of each test shown in Table 4-8. The last column shows the ratio between experimentally measured stress [$\sigma_{c,exp}$] and the stress obtained from the numeric model [$\sigma_{c,num}$].

Table 4-9: Test results of Blunt Pyramidal specimen method.

Blunt Pyramidal specimen	Strain Gauges (SG)	Depth and position	$\Delta\sigma_c$	$\sigma_{c,exp}$	$\sigma_{c,num}$	$\sigma_{c,ana}$	$\frac{\sigma_{c,exp}}{\sigma_{c,num}}$
		cm	MPa	MPa	MPa	MPa	
R2	A	2.5 Web	5.15	-5.58	-3.27	-3.40	1.7
	B		6.02				
R3	A	2.5 Flange inf.	5.58	-5.29	-8.83	-8.64	0.6
	B		5.00				
R4	A	2.5 Flange inf. Intra.	5.76	-5.33	-9.62	-9.86	0.6
	B		4.89				
R5	A	2.5 Flange inf.	8.19	-7.50	-9.64	-8.64	0.8
	B		6.81				
R7	A	2.5 Web	5.38	-5.59	-2.37	-2.39	2.4
	B		5.80				
R8	A	2.5 Flange inf.	7.43	-7.68	-5.86	-5.98	1.3
	B		7.93				
R9	A	2.5 Web	7.58	-7.37	-3.92	-3.96	1.9
	B		7.15				
R10	A	2.5 Flange inf.	10.23	-9.87	-9.82	-10.10	1.0
	B		9.51				
R11	A	2.5 Web	6.37	-6.44	-4.34	-4.28	1.5
	B		6.51				
R12	A	2.5 Flange inf.	7.72	-7.08	-7.00	-7.00	1.0
	B		6.44				
R13	A	2.5 Web	5.01	-5.54	-2.37	-2.38	2.3
	B		6.08				
R14	A		5.94	-5.94	-5.86	-5.99	1.0

4-EXPERIMENTAL RESULTS AND DISCUSSION

	B	2.5 Flange inf.	-				
R15	A	2.5 Web	6.22	-5.65	-2.77	-2.67	2.0
	B		5.08				
R16	A	2.5 Flange inf.	5.01	-4.61	-3.14	-3.10	1.5
	B		4.22				
						Mean	1.40
						St. Dev.	0.58
						CoV	42%

4.1.5.3 Discussion

Table 4-9 shows both experimental [$\sigma_{c,exp}$] and analytical [$\sigma_{c,ana}$] / numerical [$\sigma_{c,num}$] results, indicating a compressive stress state if <0 , and a tensile stress state if >0 . The stress obtained with SG is considered compressive if the SG undergo extension after cutting.

Figure 4-44 shows the dispersion of the results of the ratio $\sigma_{c,exp}/\sigma_{c,num}$ with respect to the bisect. Only the difference between tests performed under vertical load versus those performed with the beam unloaded is shown. In cases in which the experimental stress obtained by use of strain gauges has the opposite sign to that assumed by VecTor2, the data are in the second or fourth quadrant. On the other hand, when the experimental and numerical values agree in sign, i.e., are both tensile or compressive, the data are in the first or third quadrant.

These tests, compared to coring and intrados cuts, have the advantage of being less operator dependent; thus, the risk of obtaining an excessively disturbed specimen is reduced.

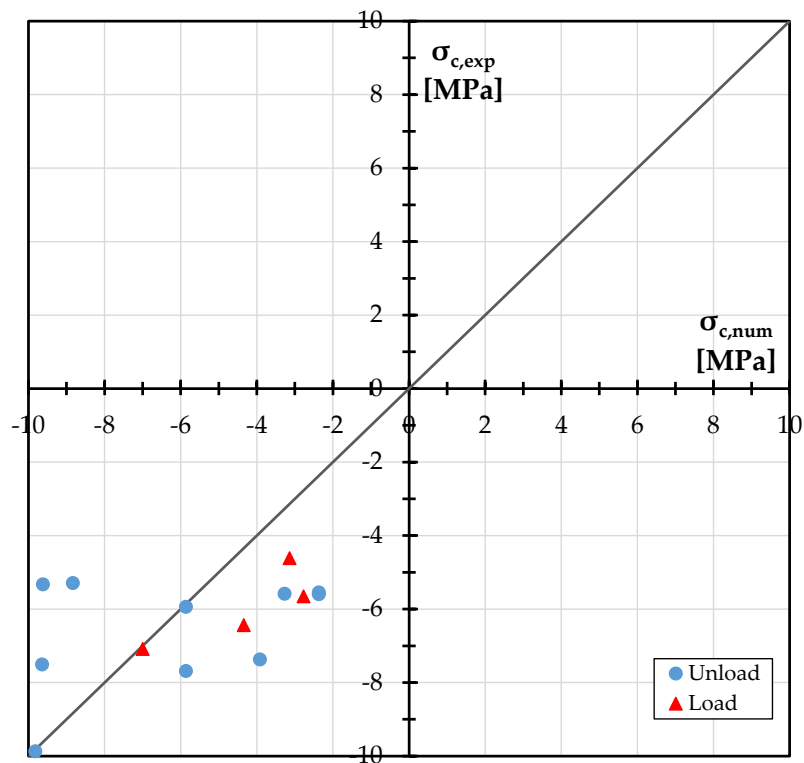


Figure 4-44: Dispersion of results obtained from Blunt Pyramidal specimen method with a division between tests performed with or without vertical load.

The results show that, unlike previous methods, in this case it is possible to correctly capture whether the beam is under tension or compression at the measurement point. With the cuts inclined at 45° towards the centre of the monitored point, characteristic of this method, a complete tension release of the element would be attained, as a complete detachment of the Blunt Pyramidal specimen from the beam occurs. However, most tests show a higher experimental value than the prediction one, and thus, the mean value of $\sigma_{c,exp}/\sigma_{c,num}$ on 14 tests shows an overestimation of the residual prestress of the beam of about 40%, with a standard deviation of 0.58 MPa and a CoV of 42% (Table 4-9).

For the Blunt Pyramidal specimens, performed by 4 EMME Service S.p.A., there is no dependence of the results on porosity because an appropriate filler was used before gluing the SGs to close any pores and thus improve adhesion. In addition, there is greater control and stability in the speed of cut execution due to the use of the so-called device "Discovery."

4.1.6 Saw-Cut method - Web

4.1.6.1 Description

The method applied is the same as that described in the Saw-Cut method - Intrados (§4.1.4.1), except that the cuts were performed in the vertical direction along the beam web. This method was applied without the support of external companies. Based on the results of the methods already performed, considerations were made for the proposal of a simple but effective alternative methodology that could provide information on the stress state of a prestressed beam. The execution difficulties of the previously described methodologies were examined, and uncontrollable variables were eliminated. For example:

- dry cuts were chosen rather than wet cuts, to avoid protecting the SGs so as not to interfere with their deformation;
- it was decided to perform them on a beam (C2) with known prestress, thanks to the controlled post-tensioning system, and in areas where prestressing was distributed uniformly;
- a single known prestress load with zero external vertical load was adopted, thus that there was no stress disturbance;
- the order of test execution was not progressive along the beam; rather, tests were performed at alternating positions to avoid interference;
- the SGs were glued in the less porous locations as possible (as much as possible in the limited space for the execution of all tests), however, away from the longitudinal and transverse reinforcement of the web.

Sixteen tests in ten point-monitored, seven tests on the front side (five point-monitored) and nine on the back side (five point-monitored), were performed only on the C2 post-tensioned beam with a known prestress level of 1130 kN, measured at the post-tensioning system cell. No external vertical load was applied for all tests. However, only 15 tests (9 point-monitored) are represented because in test 5 (SCw 5) during the cut the SGs both were damaged. Table 4-10 shows the list of tests performed with the Saw-Cut method, done on the beam web, and their characteristics.

Each test involves two cuts on the beam web for a portion height of about 25 cm out of 43 cm available, using an angle grinder¹⁴ Ø115 mm and a diamond blade¹⁵. The

¹⁴ Makita GA4530R 720W Ø115 mm

¹⁵ Max rpm 13300 80 m/s

4-EXPERIMENTAL RESULTS AND DISCUSSION

blade of an Ø115 mm grinder can cut to a maximum depth of 30 mm, coincident almost with the cover. The single cut is 4 mm thick. The cuts must be long enough to make the central part almost isolated, but at the same time avoid longitudinal reinforcement. The cuts must absolutely not intercept the transverse reinforcement. See Figure 4-45, Figure 4-46 and Figure 4-47 for geometric and execution details.

Therefore, the choice of test location should be identified with the following requirements:

- away from the longitudinal and transverse reinforcement of the web;
- surface as least porous as possible;
- away from supports, where shear is maximum;
- away from areas of disturbance, such as concentrated loads;
- possibly in the midspan.

Two parallel strain gauges were glued for each test, SG_A and SG_B, both acquired continuously for the entire duration of the test.

Table 4-10: List of tests performed with the Saw-Cut method – Web with related characteristics.

Beam	Prestress	Vertical Load	Saw-Cut Web specimen	Strain Gauges (SG)	Recording	Cut Distance	Depth	Coordinates from the support (side P) (*)	
								x	y
	%	kN				cm	cm	cm	cm
C2	100	0	SCw_1	A	Continuous	10	2	314	43.5
				B	Continuous				
			SCw_2	A	Continuous	10	3	314	43.5
				B	Continuous				
			SCw_3	A	Continuous	6	3	260	43
				B	Continuous				
			SCw_4	A	Continuous	6	3	209	39
				B	Continuous				
			SCw_6	A	Continuous	6	3	287	42
				B	Continuous				
			SCw_6	A	Continuous	6	3	319	43.5
				B	Continuous				

4-EXPERIMENTAL RESULTS AND DISCUSSION

			SCw_7	A	Continuous	10	3	271	40.5
				B	Continuous				
				A	Continuous	6	3	271	40.5
				B	Continuous				
			SCw_8	A	Continuous	10	2	296	44.5
				B	Continuous				
				A	Continuous	10	3	296	44.5
				B	Continuous				
				A	Continuous	6	2	296	44.5
				B	Continuous				
				A	Continuous	6	3	296	44.5
				B	Continuous				
			SCw_9	A	Continuous	10	3	234	42
				B	Continuous				
				A	Continuous	6	3	234	42
				B	Continuous				
			SCw_10	A	Continuous	6	3	211	42
				B	Continuous				

(*) For the exact location of the tests, refer to Figure 4-45 and Figure 4-46.

Front view

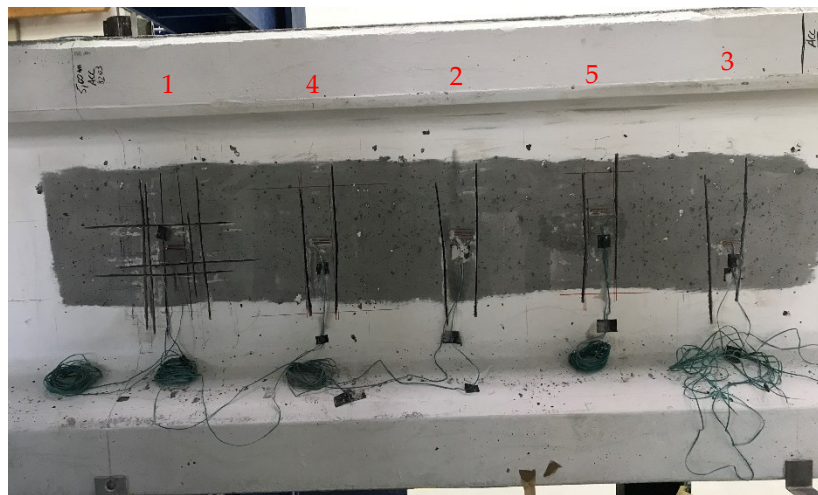
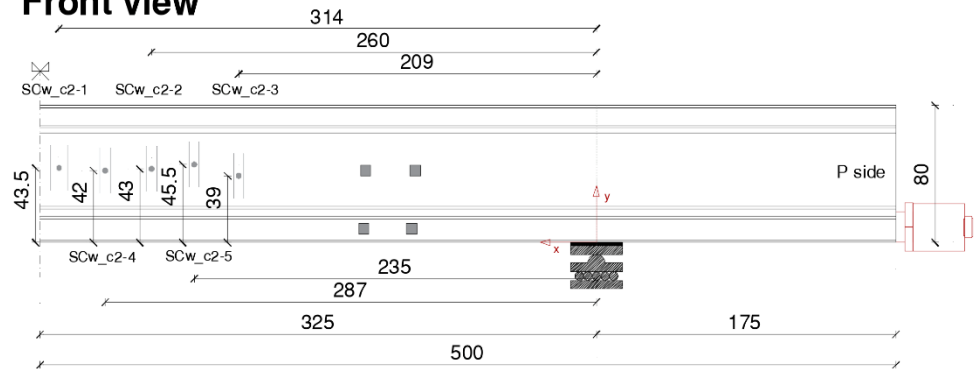


Figure 4-45: Position and picture of stress release tests with Saw-Cut method - Web on Beam C2, front view.

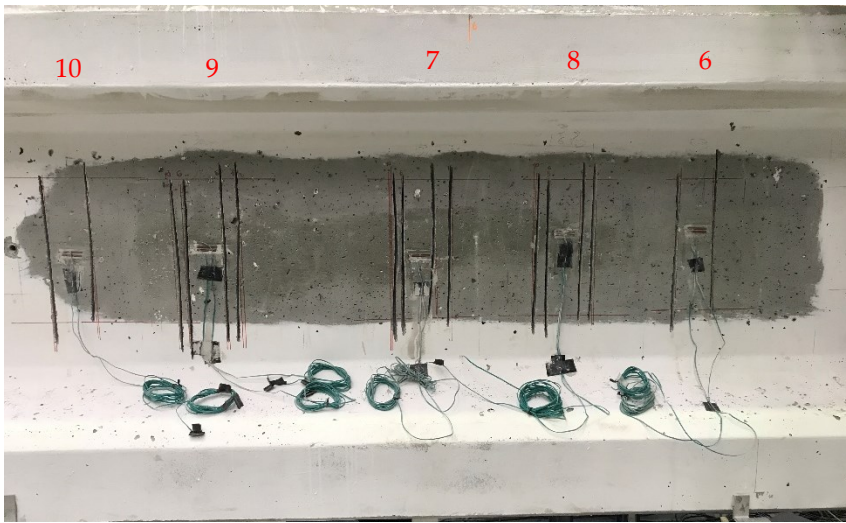
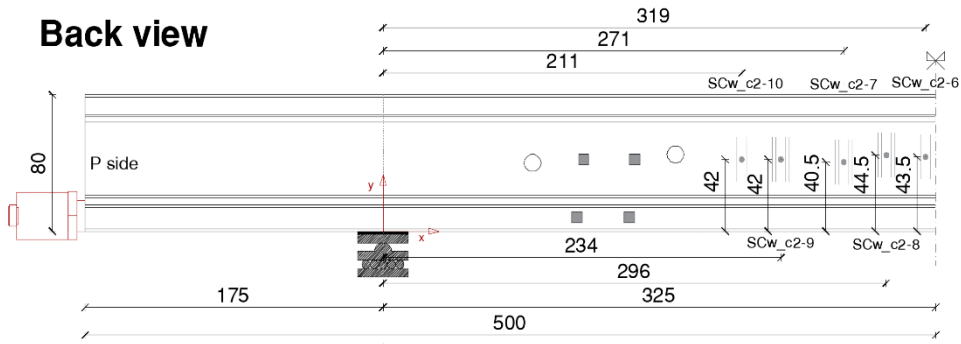


Figure 4-46: Position and picture of stress release tests with Saw-Cut method - Web on Beam C2, back view.

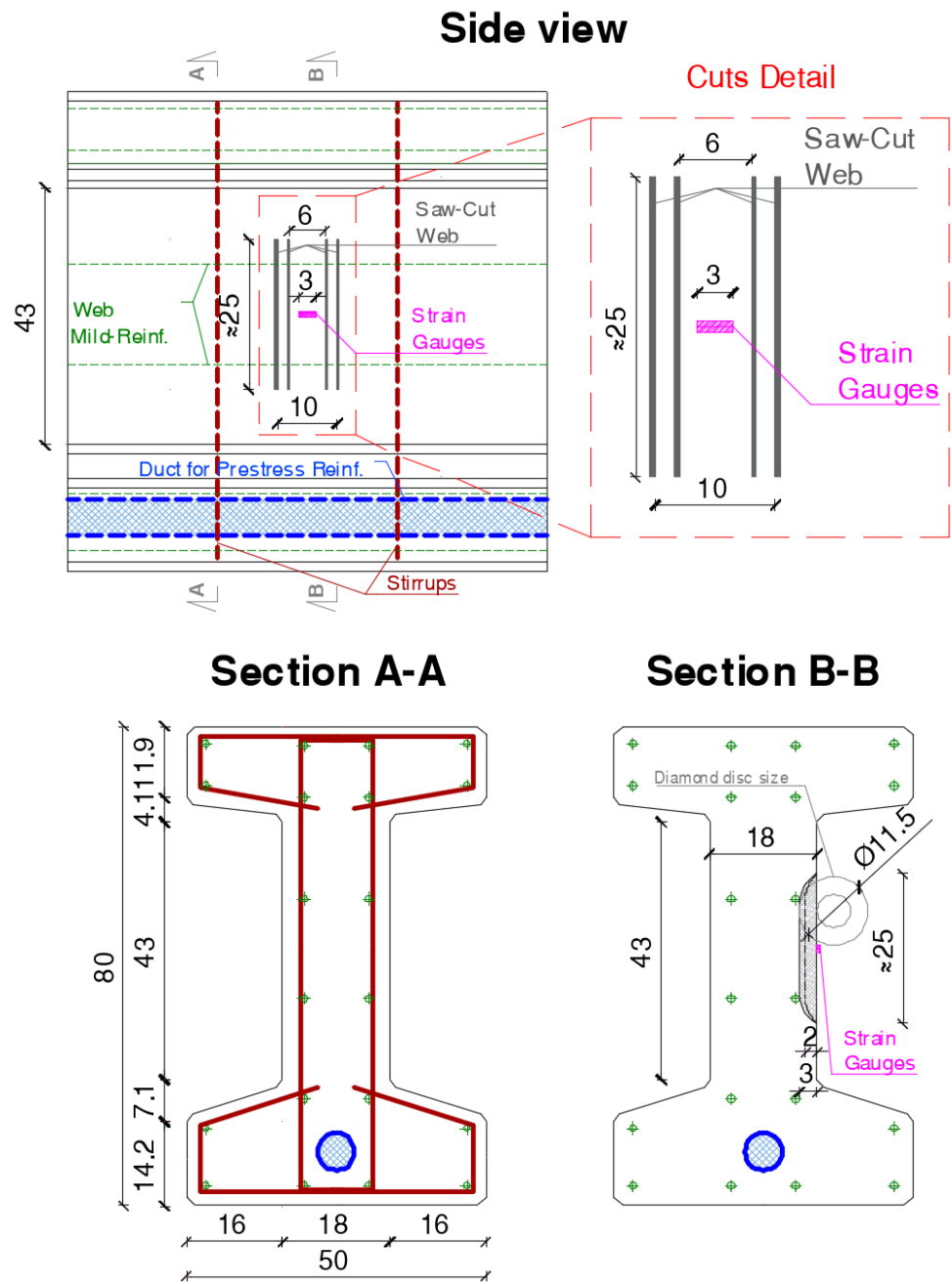


Figure 4-47: Details of Saw-Cut method -Web, dimensions in cm.

4-EXPERIMENTAL RESULTS AND DISCUSSION

Two relative distances between cuts, 6 and 10 cm, and two depths of cuts, 2 and 3 cm, were tested. These four geometric combinations [GC] (Figure 4-48) were carried out for the following reasons:

- Distance 6 cm: this is the minimum distance that can be used with 30 mm long strain gauges because at least 15 mm must be left on each side to prevent the locking nut of the diamond blade on the grinder from intercepting parts of the strain gauge.
- Distance 10 cm: this is a convenient distance to use for strain gauges of length 30 mm, so that it is possible to do not have to pay too much attention to the contact between the grinder and strain gauges during cutting.
- Depth 2 cm: this is a depth that is comparable to the cover, especially for older PRC elements; it avoids the cutting of the longitudinal reinforcement in the web, albeit partially.
- Depth 3 cm: this is the maximum depth that an angle grinder $\varnothing 115$ mm can reach, it is a small and practical device suitable for working at height; in addition, this depth provides greater isolation of the surface area of concrete on which the strain gauges are glued.

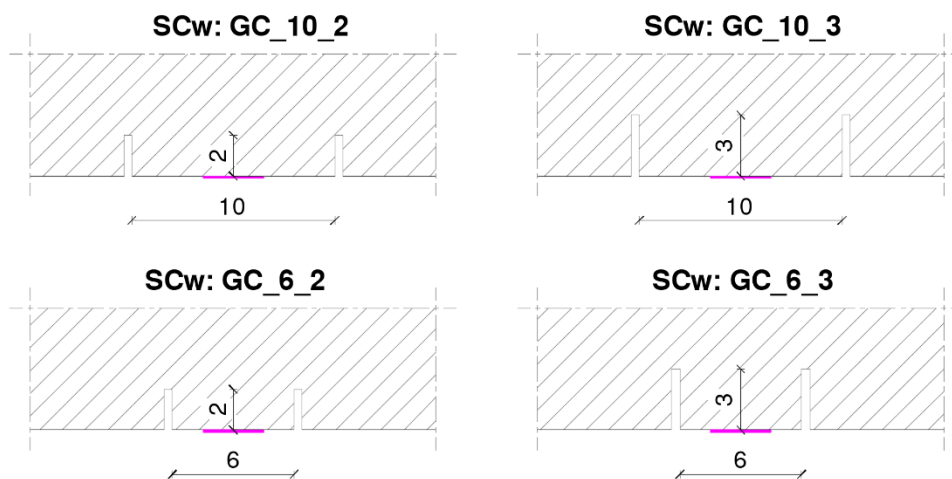


Figure 4-48: View in the horizontal plane of the 4 geometric configurations:
SCw: GC_*distance*_*depth*. Dimensions are in cm.
The dimensions of the 30 mm strain gauges are indicated in magenta.

The execution procedure involves the following steps, as illustrated from Figure 4-49 to Figure 4-57:

- 1) identification of reinforcement by magnetic survey (covermeter) to locate an area without reinforcement and where the surface is as least porous as possible and without cracks;
- 2) preparation of the strain gauge gluing surface using a grinder, subsequent degreasing with concrete solvent (Figure 4-49);
- 3) gluing of two 120-Ohm strain gauges of length 30 mm, with horizontal direction (parallel to the longitudinal development of the beam, orthogonal to the direction of the cuts), using the procedure described in Table 4-2 (Figure 4-50);
- 4) connecting the strain gauges in parallel to a multichannel control unit¹⁶ (Figure 4-51), in a quarter-bridge configuration, setting a data acquisition of 1 Hz from the dedicated HBM Catman software. The control unit can acquire data from both strain gauges continuously throughout the test;
- 5) mark the position of the cuts on the surface (Figure 4-52);
- 6) wait for the signals of both strains gauges to stabilize (Figure 4-53);
- 7) performing web cuts with an angle grinder Ø115 mm (Figure 4-54) and diamond blade (Figure 4-55). This is done by performing one cut at a time proceeding in 1 cm step until a depth of 2 or 3 cm is obtained, while keeping a constant cutting speed;
- 8) during the test, it is necessary to ensure that the grinder does not touch the strain gauge cables;
- 9) the cut should be as long as possible to get as far away as possible from the monitored point; the blade, being circular, does not allow a depth of 3 cm at either end of the cut (see detail in Figure 4-47 on Section B-B);
- 10) once the desired penetration depth is reached (2 or 3 cm) (Figure 4-56, Figure 4-57), wait ≈15 minutes from the last cut performed for the strain gauge signal to stabilize.
- 11) if a second pair of cuts with reduced relative distance is planned for the test, proceed by starting again from step 5);
- 12) stop data acquisition;
- 13) the data export file *.csv provides results in $\mu\epsilon$, the $\Delta\mu\epsilon$ of each strain gauge is calculated by deducting the initial value from the final value;
- 14) $\Delta\mu\epsilon$ are converted to $\Delta\sigma$ through the elastic modulus of the corresponding beam, and the two values are averaged;
- 15) $\Delta\sigma$ obtained, which represents the $\sigma_{c,exp}$ of the concrete before cutting with an inverted sign, is compared with the numerical prediction $\sigma_{c,num}$.

¹⁶ QuantumX HBM- MX1615B Strain Gauge Amplifier - 16 channels, Connection with strain gauge in full, half or quarter-bridge configuration with 120 or 350 Ohm

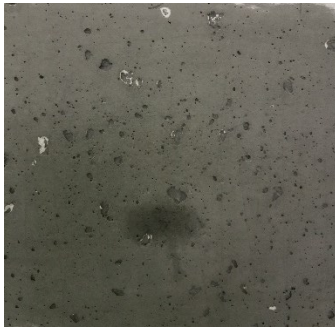


Figure 4-49: Surface preparation for SGs gluing.

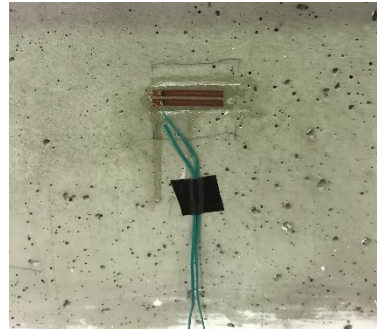


Figure 4-50: Gluing of a pair of SGs.



Figure 4-51: QuantumX HBM control unit- MX1615B strain gauge amplifier - 16 channels.

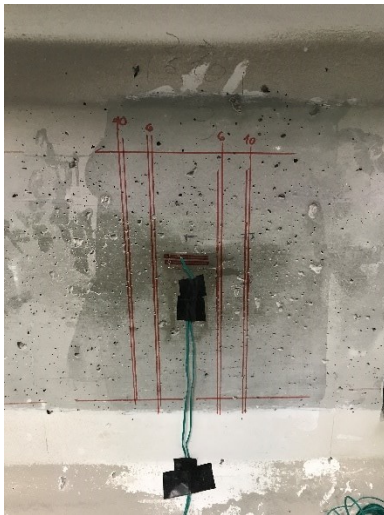


Figure 4-52: Mark the cuts position of the cuts.



Figure 4-53: Cutting equipment.



Figure 4-54: Model of the angle grinder used.

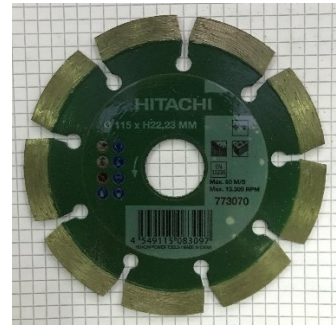


Figure 4-55: Diamond blade for cutting concrete.

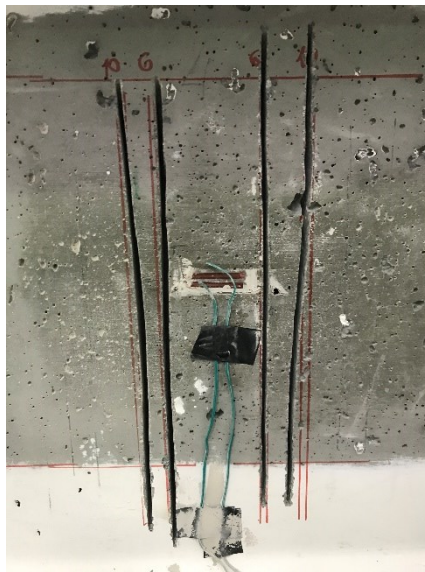


Figure 4-56: Cuts performed.



Figure 4-57: Cut detail.

4-EXPERIMENTAL RESULTS AND DISCUSSION

4.1.6.2 Results

The results obtained from the tests are shown in Table 4-11. The $\sigma_{c,ana}$ are calculated by the analytical method described in §4.1.1.3, also taking into account the location of each test shown in Table 4-10. The last column shows the ratio between experimentally measured stress [$\sigma_{c,exp}$] and the stress obtained from the numeric model [$\sigma_{c,num}$].

Table 4-11: Test results of Saw-Cut method – Web.

Saw-Cut Web specimen	Strain Gauges (SG)	Cut Distance	Depth	$\Delta\sigma_c$	$\sigma_{c,exp}$	$\sigma_{c,num}$	$\sigma_{c,ana}$	$\frac{\sigma_{c,exp}}{\sigma_{c,num}}$
		cm	cm	MPa	MPa	MPa	MPa	
SCw_1	A	10	2	-0.89	-1.16	-3.90	-3.80	0.3
	B			-1.43				
	A	10	3	-1.68	-2.00	-3.90	-3.80	
	B			-2.32				
SCw_2	A	6	3	-3.97	-3.84	-3.90	-3.80	1.0
	B			-3.72				
SCw_3	A	6	3	-4.11	-4.40	-4.60	-4.50	1.0
	B			-4.40				
SCw_4	A	6	3	-5.04	-5.01	-3.90	-3.99	1.3
	B			-4.97				
SCw_6	A	6	3	-	-3.15	-3.90	-3.64	0.8
	B			-3.15				
SCw_7	A	10	3	-4.15	-4.15	-4.30	-4.30	1.0
	B			-				
	A	6	3	-4.93	-4.93	-4.30	-4.30	
	B			-				
SCw_8	A	10	2	-	-1.32	-3.55	-3.60	0.4
	B			-1.32				
	A	10	3	-	-1.90	-3.55	-3.60	
	B			-1.90				
	A	6	2	-	-2.25	-3.55	-3.60	
	B			-2.25				

4-EXPERIMENTAL RESULTS AND DISCUSSION

	A	6	3	-	-2.57	-3.55	-3.60	0.7
	B			-2.57				
SCw_9	A	10	3	-1.90	-1.90	-3.93	-4.00	0.5
	B			-1.90				
	A	6	3	-3.18	-3.16	-3.93	-4.00	0.8
	B			-3.15				
SCw_10	A	6	3	-2.43	-2.29	-3.93	-3.98	0.6
	B			-2.15				

Figure 4-59, Figure 4-60, Figure 4-61, Figure 4-62, Figure 4-63, Figure 4-64, Figure 4-65, Figure 4-66, Figure 4-67 show the continuous acquisitions of all strain gauges.

The geometric cut configurations are defined as follows: GC_*[distance]*_*[depth]* (GC_10_2, GC_10_3, GC_6_2, GC_6_3). As 1st and 2nd are indicated the order of the cuts in the graphs. The graphs represent on the minor y-axis the strain $\mu\epsilon$ that the strain gauges experience as a function of time. Instead on the major y-axis are shown the concrete stresses obtained by equation (4-1). The graphs, then, show the change in $\mu\epsilon$, and thus also in σ , as measured by the strain gauges. Figure 4-58 shows how to interpret the following graphs.

Therefore, to know the stress state of the concrete, the sign of the obtained results must be inverted.

In all the graphs shown, it is possible to appreciate the disturbance of the strain gauges signal when the single cut is performed (≈ 1 minute) and the subsequent stabilization of the signal. In fact, during the execution of the cut, the instrumentation exerts a disturbance that induces a compression of the nearby concrete, which is recorded by the strain gauges (reduction of $\mu\epsilon$, and thus also of σ in the graphs).

As also shown in Table 4-11, some SGs did not record because the strain gauge wires were damaged during cutting.

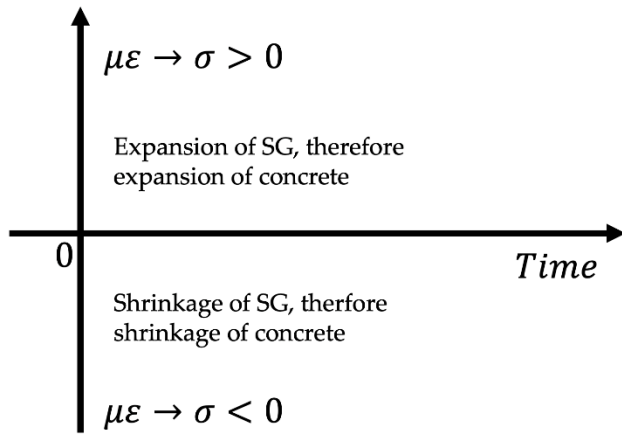


Figure 4-58: Convention for graphs interpretation. Graphs refer to strain gauge measurements.

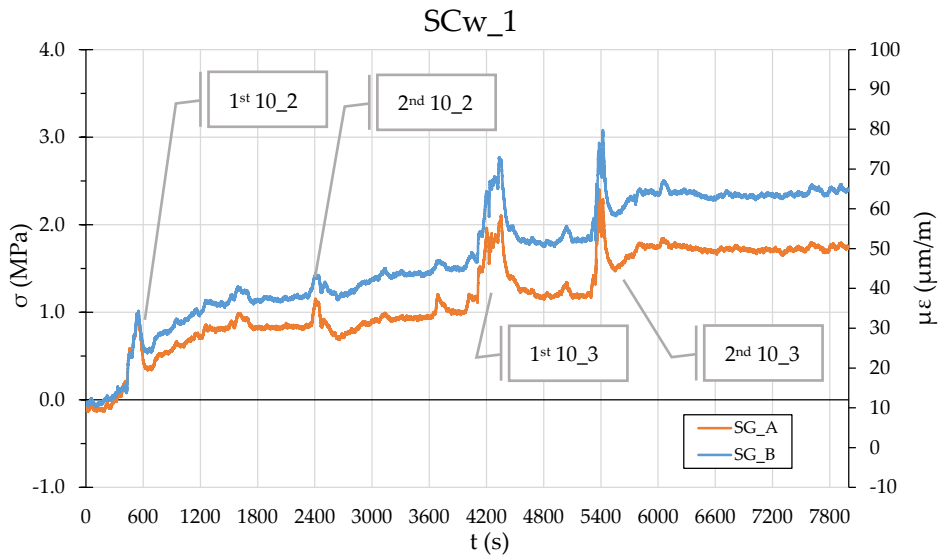


Figure 4-59: SGs recordings – SCw_1.
GC_10_2 and GC_10_3.

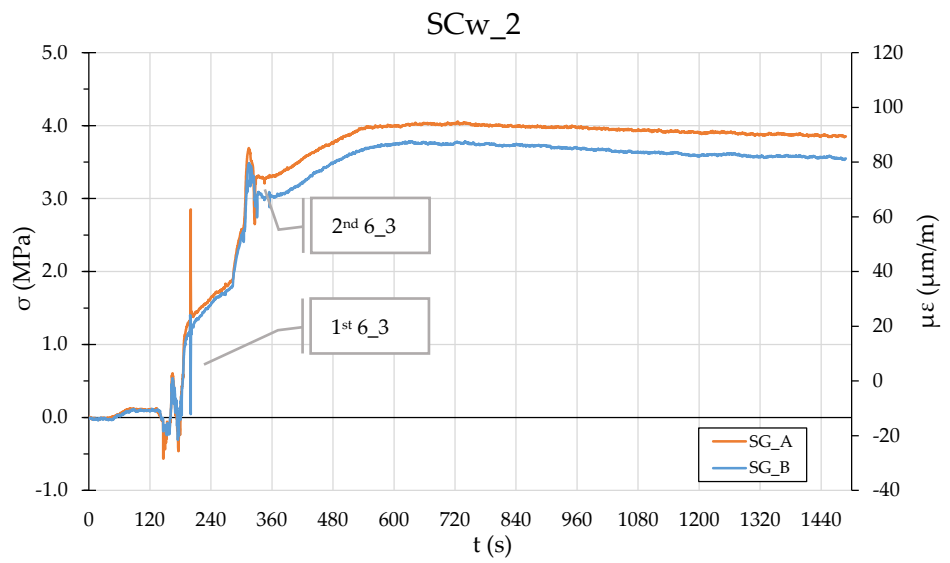


Figure 4-60: SGs recordings – SCw_2.
GC_6_3.

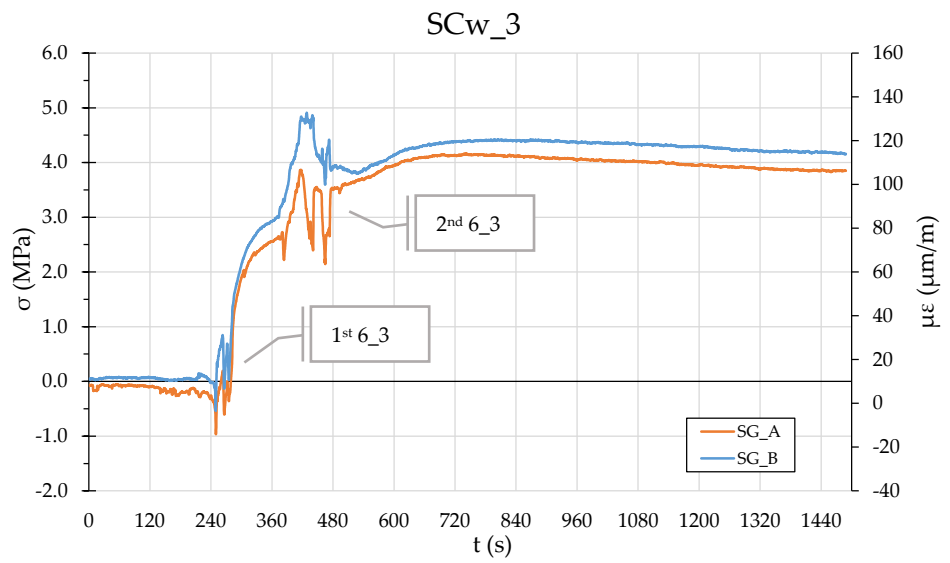


Figure 4-61: SGs recordings – SCw_3.
GC_6_3.

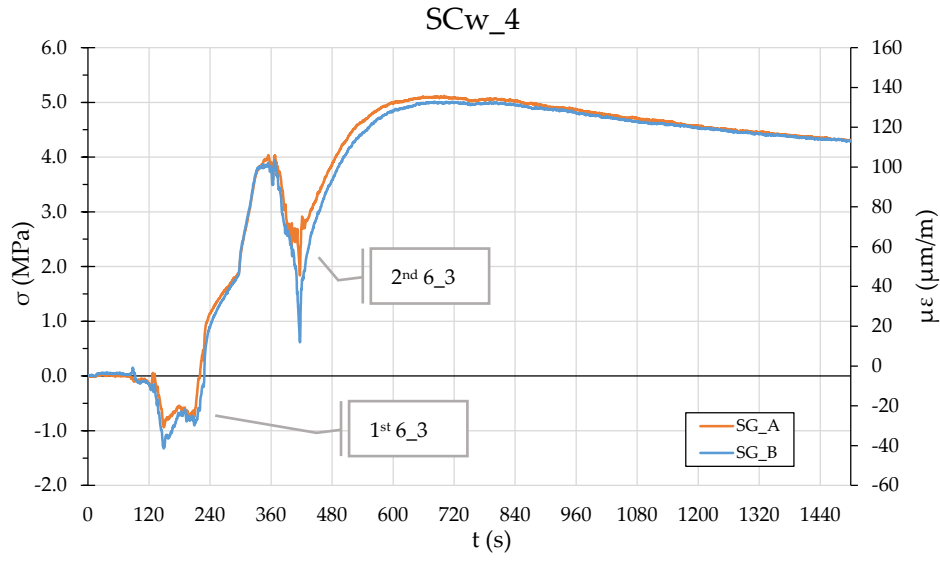


Figure 4-62: SGs recordings – SCw_4.
GC_6_3.

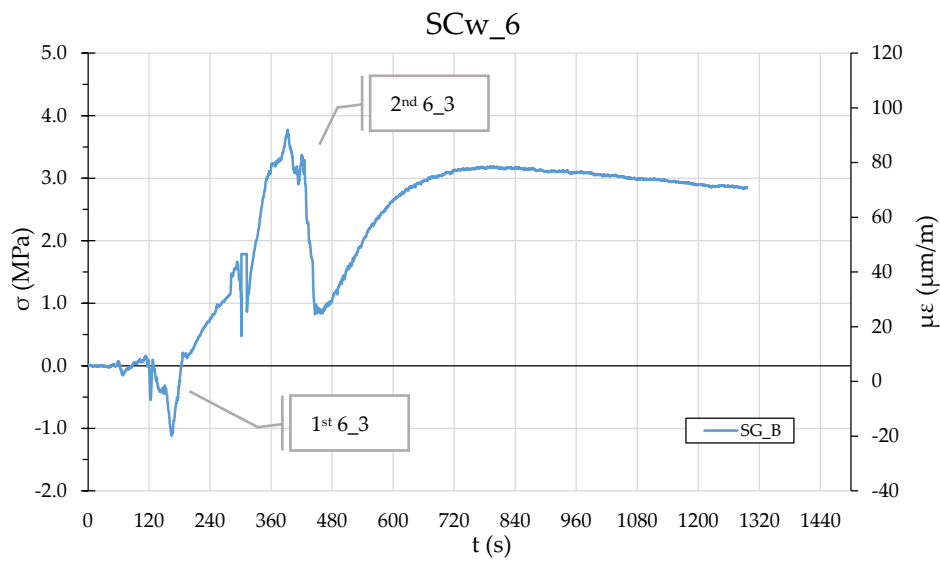


Figure 4-63: SG recordings – SCw_6.
GC_6_3.

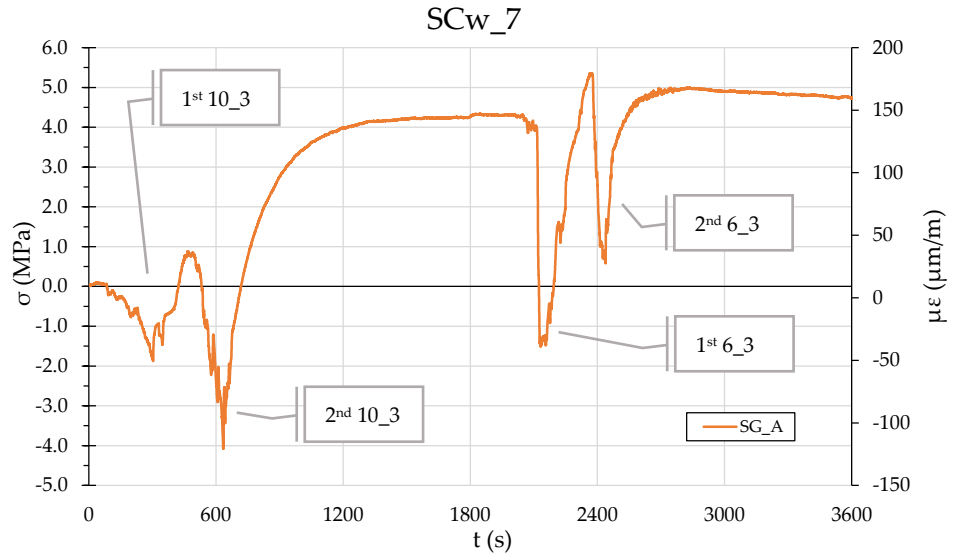


Figure 4-64: SG recordings – SCw_7.
GC_10_3 and GC_6_3.

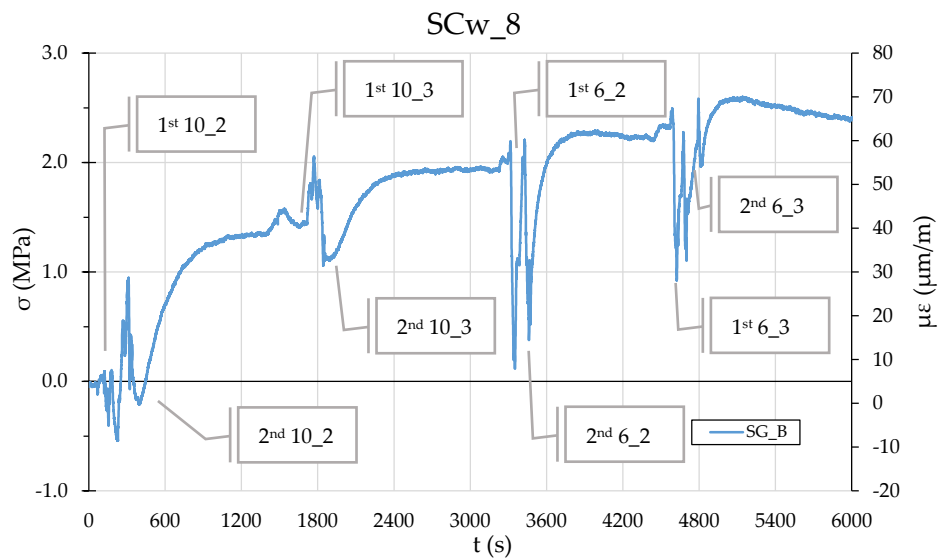


Figure 4-65: SG recordings – SCw_8.
GC_10_2, GC_10_3, GC_6_2, GC_6_3.

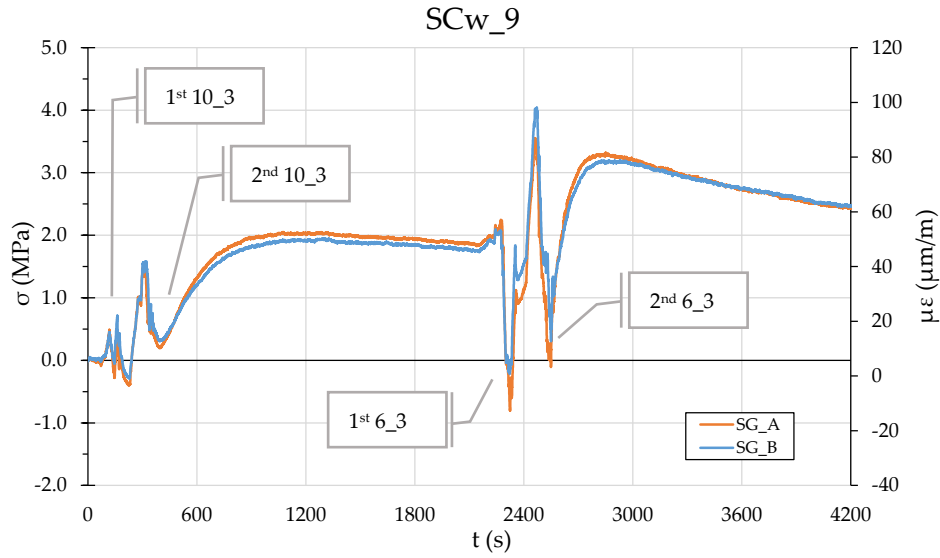


Figure 4-66: SGs recordings – SCw_9.
GC_10_3 and GC_6_3.

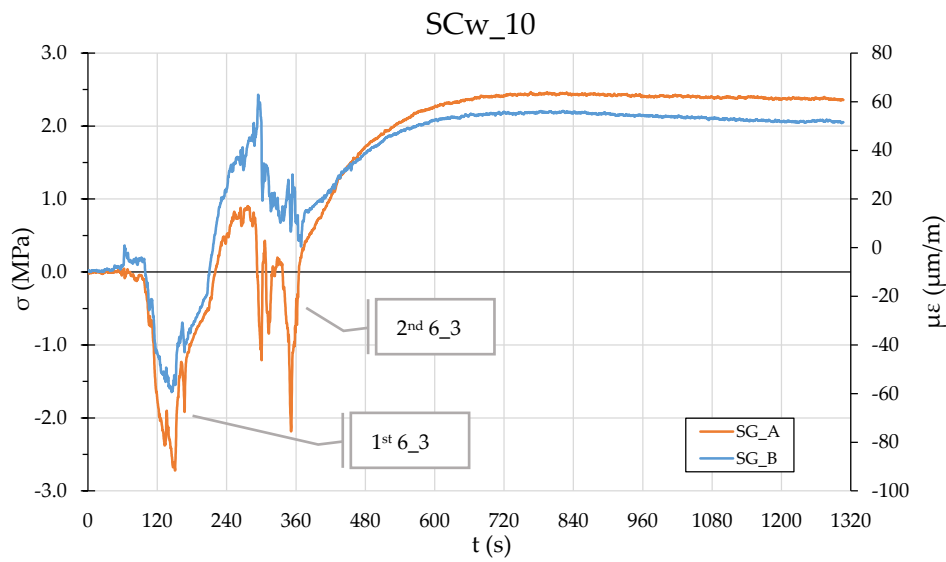


Figure 4-67: SGs recordings – SCw_10.
GC_6_3.

The results shown should be interpreted and divided according to the geometric configuration of the cut and in the order in which the 2 types of inter-cut spacing related to the same test were performed. Therefore, a categorization of $\sigma_{c,exp}/\sigma_{c,num}$ results shown in Table 4-12 are made.

Table 4-12: Results $\sigma_{c,exp}/\sigma_{c,num}$ Saw-Cut method Web are subdivided by geometric categories

$\frac{\sigma_{c,exp}}{\sigma_{c,num}}$	Geometric Configuration [GC]			
	10_2	10_3	6_2	6_3
SCw_1	0.3			
		0.5		
SCw_2				1.0
SCw_3				1.0
SCw_4				1.3
SCw_6				0.8
SCw_7		1.0		
				1.1
SCw_8	0.4			
		0.5		
			0.6	
				0.7
SCw_9		0.5		
				0.8
SCw_10				0.6
n° specimen	2	4	1	8
Mean	0.34	0.62	0.63	0.91
St. Dev.				0.19
CoV				21%

4-EXPERIMENTAL RESULTS AND DISCUSSION

4.1.6.3 Discussion

Table 4-11 shows both experimental [$\sigma_{c,exp}$] and analytical [$\sigma_{c,ana}$] / numerical [$\sigma_{c,num}$] results, indicating a compressive stress state if <0 , and a tensile stress state if >0 . The stress obtained with SG is considered compressive if the SGs undergo extension after cutting.

Figure 4-68 shows the dispersion of the results of the ratio $\sigma_{c,exp}/\sigma_{c,num}$ with respect to the bisector., while in Figure 4-69 one can see the detail of the dispersion of the results divided by geometric cutting category.

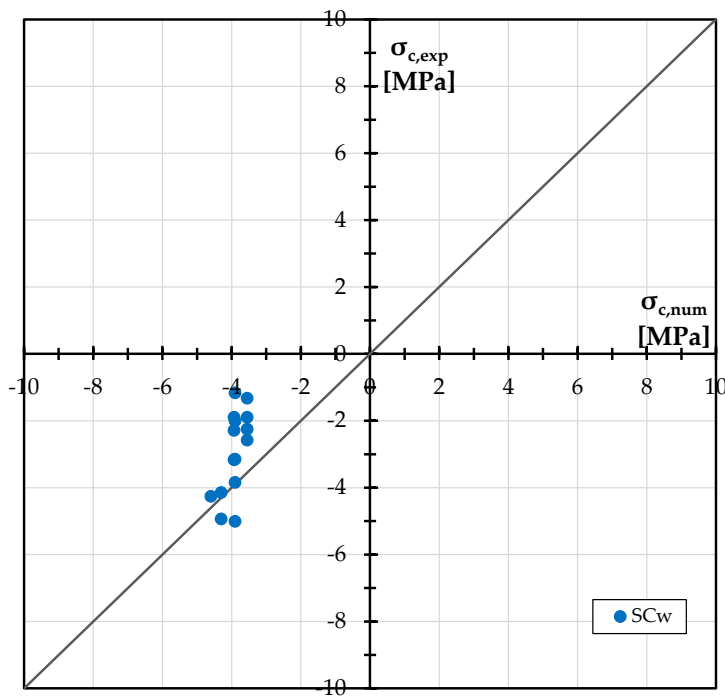


Figure 4-68: Dispersion of results obtained from di Saw-Cut method – Web.

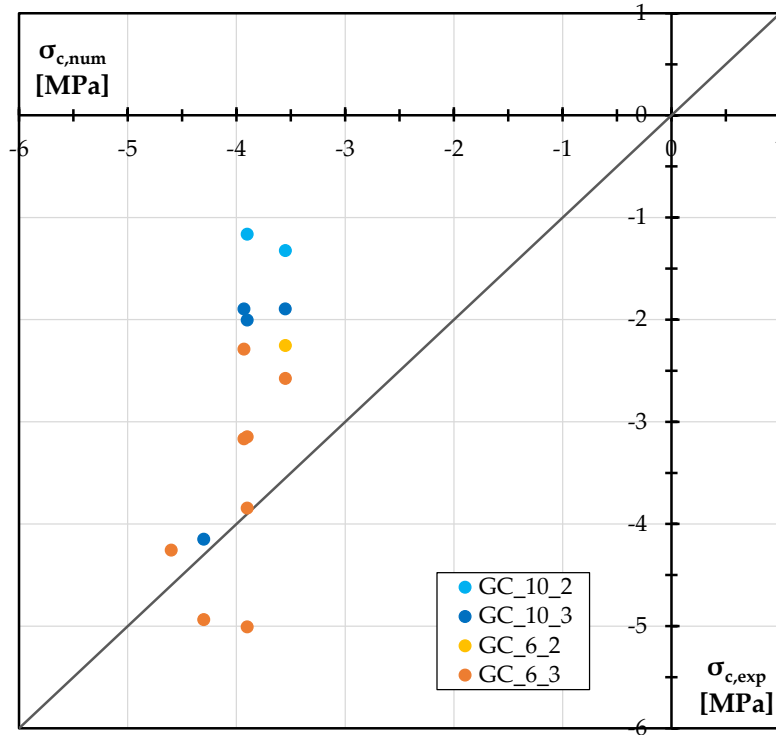


Figure 4-69: Detail of the dispersion of the results obtained from the Saw-Cut method – Web tests divided by geometric configurations.

Compared with the previously described and illustrated methods, the Saw-Cut method – Web seems to get closer to the prediction values, moreover overall it underestimates the real stress value. As shown in Table 4-12, the geometric configuration (GC) GC_10_2 seems to be able to detect only 1/3 of the residual prestress. Tests with this GC are limited, only 2, as well as GC_6_2, only 1 that records a mean value of 60% compared to the real prestress. All three GCs however are comparable with the GCs performed in the SCw_8 test. In fact, for the SCw_8 test, all GCs are performed progressively in the following order: 10_2, 10_3, 6_2 and 6_3. The order was chosen to affect as little as possible subsequent tests performed with greater depth and closer distance. However, looking at the result SCw_8_GC_6_3, it deviates from the mean of all GC_6_3, but is in accordance with SCw_9_GC_6_3, which was also performed after a saw-cut with GC_10_3. It follows that these tests might have been influenced by releasing of the monitored point due to the previous saw-cuts. GC_10_3 are also aligned with each other, recording a value of about 50% of the actual prestresses, except for SCw_7_10_3. The SCw_1_GC_10_3 and SCw_8_GC_10_3 are unaffected by the previous 1 cm less deep cut (SCw_1_GC_10_2 and SCw_8_GC_10_2).

4-EXPERIMENTAL RESULTS AND DISCUSSION

The SCw_10_GC_6_3 test was performed on a relatively porous surface compared to all other tests and close (≈ 10 cm) to a 50 mm deep dowel required for fixing the Core Trepanning method instrumentation (Figure 4-70), so probably the strain gauges did not capture a complete stress release of the concrete.



Figure 4-70: Identification of the surface of test SCw_10_GC_6_3 for gluing.

Overall, GC_6_3 are the ones closer to the true prestress value; in fact, the mean $\sigma_{c,exp}/\sigma_{c,num}$ of the eight tests is 0.91, with a standard deviation of 0.19 MPa and a CoV of 21% (Figure 4-71 and Table 4-12).

The following observations are derived:

- GC_10_2 and GC_6_2 are performed with insufficient depth to isolate the monitored point on the surface.
- GC_10_3 turns out to be a more "convenient" test to perform than GC_10_3, as there is enough space beyond the size of the SGs to perform the cuts without risking damage to the SGs. However, it does not allow complete isolation of the monitored area, and thus the measurement is not complete.
- The most representative GC for a complete stress release is GC_6_3, which provides experimental results closer to prediction. This also turns out to be the most delicate configuration to perform, because using 30 mm SG, the cuts were performed very close to the measuring instrument.

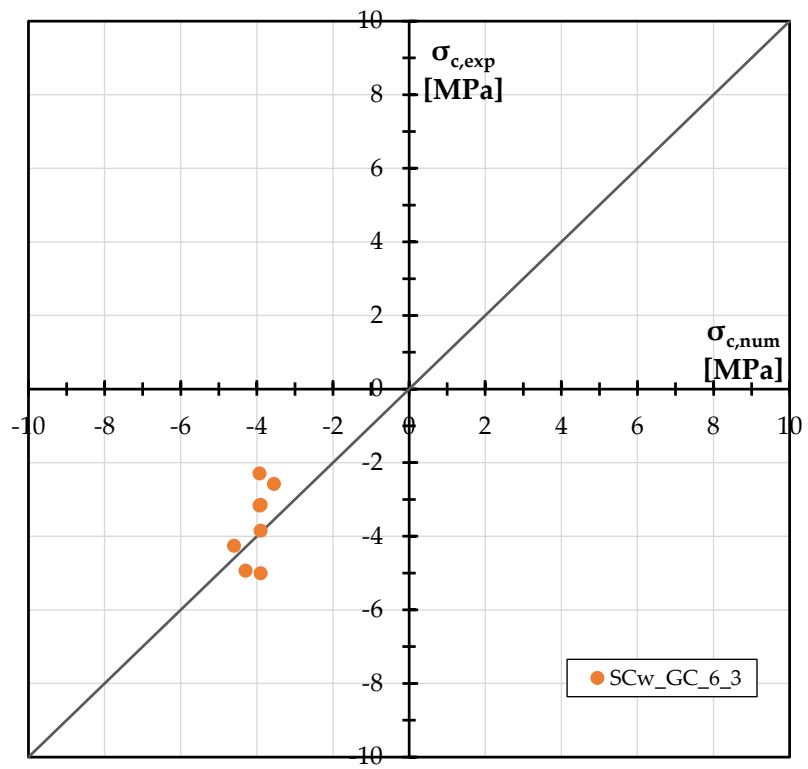


Figure 4-71: Dispersion of results obtained from Saw-Cut method tests - Web with geometric configuration GC_6_3.

4.1.7 Comparison and Discussion

Comparison all methods adopted for this experimental program, the statistical values of the ratio $\sigma_{c,exp}/\sigma_{c,num}$ have been summarized in Table 4-13. For the tests performed with the Core Trepanning method and Saw-Cut method - Intrados the results obtained are very unreliable, so there is no point in reporting the statistical parameters. The same consideration applies to the Saw-Cut method - Web GC tests performed on a low number of specimens. An indication of how close the experimental value is to the numerical value can also be observed in Figure 4-72. In this scatter plot, the closer the points are to the bisector of the first and third quadrants, the more the experimental stresses and the stresses returned by VecTor2 agree with each other.

Table 4-13: Comparison of results between different tension release methods.

Method	Core Trepanning	Saw-Cut Intrados	Blunt Pyramidal specimen	Saw-Cut Web			
	C	SCi	R	SCw GC_10_2	SCw GC_10_3	SCw GC_6_2	SCw GC_6_3
n° Specimen	11	9	16	2	4	1	8
$\frac{\sigma_{c,exp}}{\sigma_{c,num}}$	Mean		1.40	0.34	0.62	0.63	0.91
	St. Dev.		0.58				0.19
	CoV		42%				21%

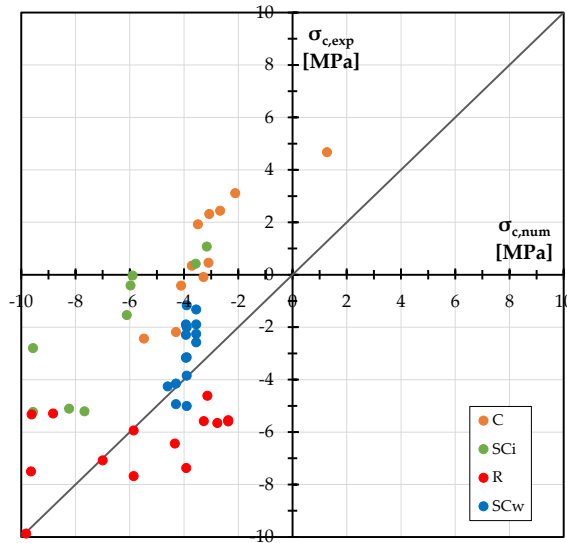


Figure 4-72: Dispersion of results of all tensional release tests performed. C: Core Trepanning, SCi: Saw-Cut Intrados, R: Blunt Pyramidal specimen, SCw: Saw-Cut Web.

Figure 4-73 shows the same ratio $\sigma_{c,exp}/\sigma_{c,num}$ as a function of each individual test. This graph shows that the Core Trepanning, Saw-Cut Intrados and Blunt Pyramidal specimen tests performed by external private laboratories provide less accurate and precise results than the method proposed in this study. Tests using the Blunt Pyramidal specimen method performed by 4 EMME Service S.p.A. overestimate the true concrete stress value by 40%, consequently, it does not appear to be a conservative method. The Saw-Cut method - Web, proposed in this study, underestimates the real prestress by only 10%.

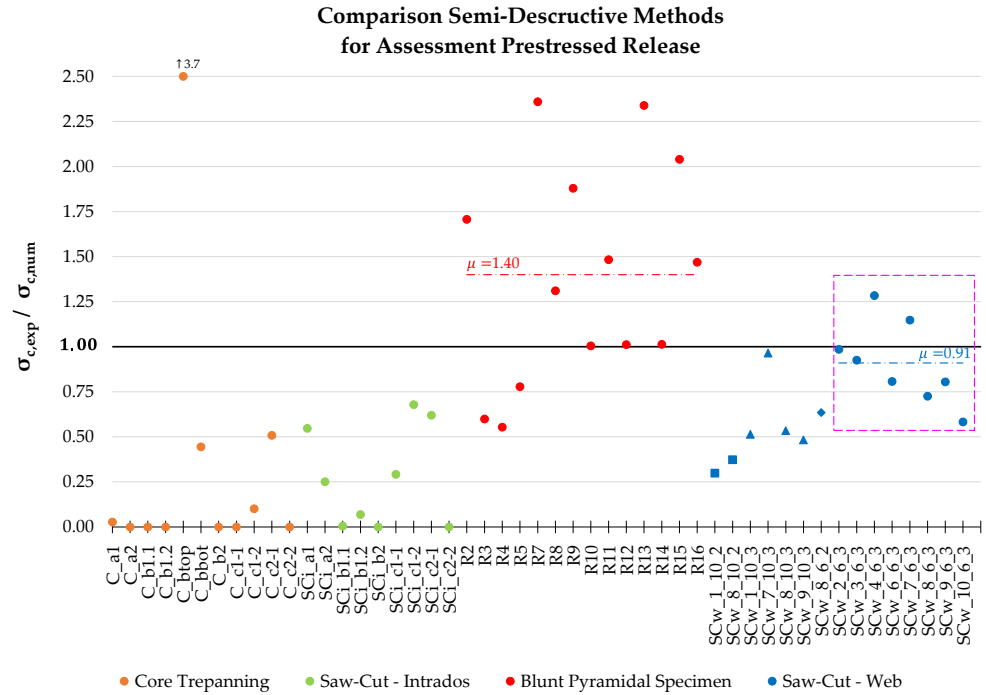


Figure 4-73: $\sigma_{c,exp}/\sigma_{c,num}$ of all tests. Results <0 are represented on the x-axis.

The stress release methods by cutting to isolate a portion of concrete are all based on the same theory; however, the application is delicate and requires precautions. In Table 4-14, the pros and cons of each applied method are analysed according to the experience gained while performing laboratory tests.

4-EXPERIMENTAL RESULTS AND DISCUSSION

Table 4-14: Pros and cons of semi-destructive methods for prestress evaluation applied in this experimental campaign.

Method	Pros	Cons
Core Trepanning	<ul style="list-style-type: none"> - The core provides almost complete isolation of the element because it allows penetration for almost the entire depth of the web. - If the core is pass-through, it can also be used for concrete characterization to determinate ultimate strength and elastic modulus with compressive testing. 	<ul style="list-style-type: none"> - Instrumentation to perform core trepanning is cumbersome, especially if to be applied for work on a high platform; - Operator-dependent testing regarding core drill penetration speed. - During cutting, the element is greatly disturbed by core instrumentation vibration. - Necessity of SG isolation and protection from water. - Performed only on the web since a through hole is needed to connect the SGs to the control unit, except if a wireless system is used.
Saw-Cut Intrados	<ul style="list-style-type: none"> - Instrumentation to perform the test is not cumbersome. - No need to protect strain gauges while performing cuts since it is performed dry. 	<ul style="list-style-type: none"> - Operator-dependent test for speed of diamond blade penetration. Solvable by standardizing cut performing. - Cuts performed transversely to the direction of the prestressing reinforcement risk intercepting the reinforcement as they may exceed the depth of the concrete cover, in fact in older elements the concrete cover may frequently be less than 25 mm.
Blunt Pyramidal specimen	<ul style="list-style-type: none"> - Precise instrumentation that allows for less operator-dependent testing. - No need to protect strain gauges while performing cuts since it is performed dry. - Performed on both the web and the flanges of the element, remaining within a depth of 25 mm comparable to the concrete cover. - Structurally minimally invasive test and easy to repair. 	<ul style="list-style-type: none"> - Needs specific instrumentation not yet commercially available. - Apparently, the test overestimates residual prestress and is therefore an unconservative method.

<p>Saw-Cut Web</p>	<ul style="list-style-type: none"> - Instrumentation to perform the test is not cumbersome. - No need to protect strain gauges while performing cuts since it is performed dry. - If performed in the web in the mid-span does not adversely affect the bearing capacity of the element, subject to magnetic survey (covermeter) to verify that there is no prestressed reinforcement in the web. - Cuts within the stirrups and parallel to them, without the risk of intercepting them. - Structurally minimally invasive test and easy to repair. 	<ul style="list-style-type: none"> - Operator-dependent test for speed of diamond blade penetration, solvable by standardizing cuts. - Risk of cutting the longitudinal reinforcement present in the web, however a structurally minimally invasive damage.
---------------------------	---	---

4.1.8 Concluding Remarks

Comparing and analysing the results obtained, the following conclusions can be drawn:

- a) For non-destructive methods:
 - It was not possible to appreciate a prestressing variation of the beam using DIC technology.
 - Even using dynamic identifications comparing the natural frequencies related to different prestress levels, no differences in the frequencies of the first vibration mode were observed.
 - It must be kept in mind that both these methods are not easily applicable in situ. For the DIC method, being a technique based on the processing of high-resolution photos, it would be necessary to ensure a stable in-situ condition, both in terms of light and instrumentation vibration. In particular, if with in situ dynamic acquisitions one wants to analyse the second-order effects, he/she would need to instrument the entire bridge deck, and consequently, it would become difficult to determine the prestress loss related to a single beam.

b) For semi-destructive methods:

- It emerges that these are, in general, very risky tests and for the greater part, operator dependent. For this reason, it is recommended that they be performed by specialized and adequately trained personnel. It should also be considered that the tests presented were carried out at the P. Pisa laboratory of the University of Brescia, thus under favourable logistical and ambient conditions. It is assumed that performing these tests in situ will present additional uncertainties and execution problems.
- A successful test requires the almost total absence of porosity and the execution of an undisturbed cut, which is difficult to achieve in presence of high-strength concretes.
- In addition, to sufficiently isolate the portion of concrete whose stress release is to be determined, it appeared necessary to achieve a penetration depth of at least 3 cm, and thus, in some cases, greater than the cover, with the risk of damaging the longitudinal reinforcement.
- If all types of stress release tests are evaluated together, it can be concluded that:
 - Core Trepanning method: the isolation of the strain gauges must be improved, and the cuts must be performed very accurately; to date, the results are not reliable.
 - Saw-Cut method – Intrados could hardly be used in situ because the risk of damaging the longitudinal reinforcement is too high if the longitudinal reinforcement is not at a depth greater than 30 mm. However, this test is less reliable than the following two.
 - Blunt Pyramidal specimen is a good methodology for evaluating residual prestress. However, the results show an overestimation of residual prestresses. This condition is not conservative in the assessment of the bearing capacity of the structure.
 - Saw-Cut method – Web proves to be a reliable method, the most precise and accurate among the semi-destructive methods applied in this experimental program. In fact, in addition to being easy to perform and using cheap and commercial instrumentation, it provides results that are closest to the analytical and numerical predictions, remaining overall conservative, as the actual prestress in the element is underestimated by 10%, with a CoV of 21%.
- Following the analysis of the results, it is recommended to couple the in-situ tests with a preliminary numerical/analytical estimation of the expected

value. That's because considering the factors described above, there is a serious risk that the tests may provide unreliable values. In other words, having an analytical prediction to compare with the experimental measurements would allow a possible repetition of the test, instead of waiting for post-processing of the data.

- Since these are generally tests with fairly random results, it is still necessary to perform a sufficient number of tests such that the value obtained is satisfactorily confirmed and considered reliable. As a preliminary proposal, the minimum number of reliable tests should satisfy a maximum value of CoV equal to 25%. Any single test determining a higher CoV should be excluded.

An execution protocol is proposed for conducting a stress release test using the Saw-Cut method – Web:

Saw-Cut method – Web EXECUTION PROTOCOL
<p><u>Test description</u></p> <p>The test consists of performing two parallel cuts on the beam web spaced 60 mm apart, 30 mm deep and at least 250 mm long in which the central point is monitored using a pair of strain gauges positioned along the same direction as the prestress diffusion in the element. At the end of the cuts, the central portion of concrete will be isolated and will have undergone a strain of the opposite sign compared to the stress state occurring before the two cuts. Using the relationship $\sigma = E \cdot \varepsilon$, knowing the elastic modulus of the material, it is possible to derive the stress state of the element starting from the strain recorded by the strain gauges.</p> <p><u>Instrumentation</u></p> <ul style="list-style-type: none"> - Personal safety equipment: safety shoes, safety goggles, dust mask, hearing protectors, gloves. - Angle grinder Ø115-125 mm. - Diamond disc Ø115 Max rpm 13300 80 m/s. - Abrasive disc Ø115 Max rpm 13300 80 m/s. - N° 2 strain gauges 30 mm for each test. - Strain gauges gluing kit. - Acquisition control unit and laptop for on-site data processing. - Generator set or batteries to power the instrumentation.

4-EXPERIMENTAL RESULTS AND DISCUSSION

Location selection

The test location should be identified with the following requirements:

- in the mid-span, where shear is lowest, and thus away from the supports, where shear is highest;
- away from areas of disturbance, such as concentrated loads;
- away from cracks;
- at the half-height of the beam/box girder, which must have a height of at least 35 cm;
- after magnetic survey (covermeter), away from the transverse reinforcement (mid spacing between the stirrups) and if possible, away from the stirrup supports in the web.

In the case of girders with longitudinal prestressing reinforcement placed in the web, check the cover with a limited break-in (distance of about 100 cm from the point where the test is carried out). If the cover is ≥ 35 mm, the test can be performed; if it is < 35 mm, identify a new point that does not involve the prestressing reinforcement.

- In the identified surface portion, choose an area of 60 mm horizontally and 30 mm vertically that is as least porous as possible for gluing the strain gauges.

Executive procedure

The execution procedure involves the following steps:

- 1) identification of reinforcement by magnetic survey (covermeter), as prescribed in § Location selection;
- 2) preparation of the strain gauge gluing surface using a grinder, subsequent degreasing with concrete solvent;
- 3) gluing of 2 120-Ohm strain gauges of length 30 mm, parallel to the longitudinal development of the beam and, then, orthogonal to the cuts to be performed (for application, the gluing procedure recommended by Luchsinger Ltd. In M-Bond 200 User's Manual can be follow);
- 4) connecting the strain gauges in parallel to a multichannel control unit, in a quarter-bridge configuration, setting a data acquisition of $0.5 \div 1.0$ Hz;
- 5) mark the position of the cuts on the surface in relation to the strain gauges position (Figure 4-74);
- 6) wait for the signals of both strains gauges to stabilize;
- 7) before the test, it should be made sure that the diamond blade of the grinder does not touch the cables of the strain gauges;

- 8) the cuts are performed in the direction of blade rotation, so the right cut has a top-down direction, while the left cut has a down-top direction;
- 9) performing web cuts with an angle grinder $\varnothing 115$ mm and diamond blade. This is done by performing one cut at a time until a depth of 3 cm is reached (Figure 4-75) while keeping a constant cutting speed;
- 10) the duration of the execution of a cut should be no less than 60 seconds and no more than 180 seconds;
- 11) the cut should be as long as possible to get as far away as possible from the monitored point; at least 12 cm above and 12 cm below the point monitored with strain gauges (Figure 4-75);
- 12) once the desired penetration depth is reached wait ≈ 15 minutes from the last cut performed for the strain gauge signal to stabilize;
- 13) stop data acquisition;
- 14) temperature detection of the test location;
- 15) the data export file *.csv provides results in $\mu\varepsilon$, the $\Delta\mu\varepsilon$ of each strain gauge is calculated by deducting the initial value from the final value;
- 16) $\mu\varepsilon$ are converted to $\Delta\sigma$ through the elastic modulus [$E_{c,m}$] of the corresponding beam, and the two values are averaged;

$$\Delta\sigma_c [MPa] = E_{c,m} [MPa] \cdot \Delta\varepsilon_c [-]$$

where:

- $\Delta\varepsilon_c$ = strain variation undergone by strain gauges \Rightarrow strain variation undergone by concrete;
- E_c = elastic modulus of concrete determined by one of two following methods:
 - by core removal and laboratory compression test according to [UNI EN 12390-13, 2013]
 - by NTC, 2018 - Chapter 11.2.10.3-Equation 11.2.5 where $f_{c,site}$ can be determined by sclerometer, pull-out, Windsor probe tests:

$$E_c = 22000 \cdot \left(\frac{f_{c,site}}{10} \right)^{0.3}$$

- $\Delta\sigma_c$ = variation of stress in concrete undergone due to cutting \Rightarrow prestress stress in concrete before cutting with sign inverted;
- 17) $\Delta\sigma$ obtained, which represents the $\sigma_{c,exp}$ of the concrete before saw-cuts with an inverted sign, is compared with the analytical prediction $\sigma_{c,ana}$, when available. The result should be $\sigma_{c,exp}/\sigma_{c,ana} \approx 1$;

4-EXPERIMENTAL RESULTS AND DISCUSSION

- 18) perform enough tests such that the value obtained is satisfactorily confirmed, minimum a total of 4 tests performed in the same section: two on each face of the web, shifted at least 40 cm to the right or left of the previous ones. The minimum number of reliable tests should satisfy a maximum value of CoV equal to 25%. Any single test determining a higher CoV should be excluded. If the results do not satisfy this requirement, further tests are carried out, moving from the centre of the beam towards the supports, with a spacing of 40 cm.

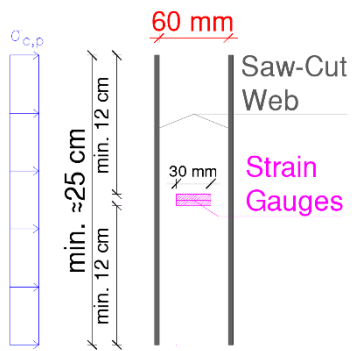


Figure 4-74: Scheme of the execution of parallel cuts – Front view.

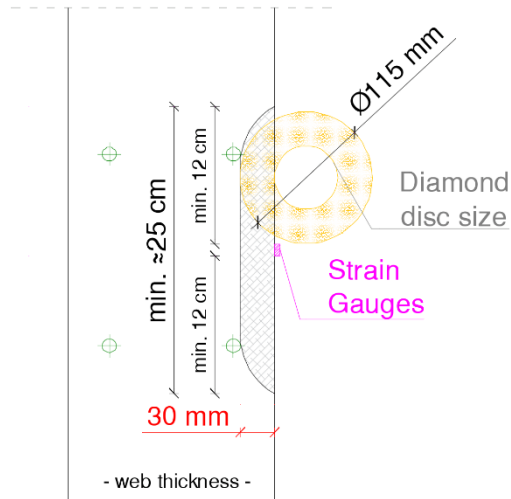


Figure 4-75: Scheme of the execution of parallel cuts – Section view.

4.1.8.1 Recommendation for future research

Based on the proposed model, it might be interesting to evaluate the following variations:

- On a beam with a post-tensioning system install 3 pairs of strain gauges 50 cm apart on the web, with 0% prestressing start data acquisition. Then apply 100% prestress and perform the Saw-Cut method – Web on the centre strain gauge pair. At the end of the test, wait for the stabilization of the SGs, and after a few hours remove the prestress to 0%. In this way, it is possible to know the entire history of prestress and stress release undergone by the monitored surface. The pairs of lateral strain gauges have the function of monitoring whether the neighbouring zones are disturbed by the cutting effect.
- For the Saw-Cut method – Web tests performed relatively close to the support of the beam (not exactly in mid-span) subjected only to its own weight, add one or more strain gauges in the vertical direction to assess how much the vertical component may affect it.
- Based on what Abdunur (1982) also proposed, with the same logic of instrumentation and geometric configuration adopted for SCw_GC_6_3, after performing the cuts, insert two flat jacks into the notch. By actuating them, prestressing of the isolated portion between the two cuts could be re-established and the prestressing level could be double-checked. The flat jacks, usually used for in-situ compression tests on masonry, need to be modified and adapted to be inserted in a thickness comparable to that of a diamond disk.

4.2 Shear Tests

4.2.1 Introduction

In §3.4 and §3.5 setup and methods of load tests are described respectively; this chapter shows the data recorded during the load tests. Tests were carried out to assess how different levels of prestressing affect the shear strength in prestressed elements. The instrumented area is highlighted in Figure 4-76 as “S-Region”.

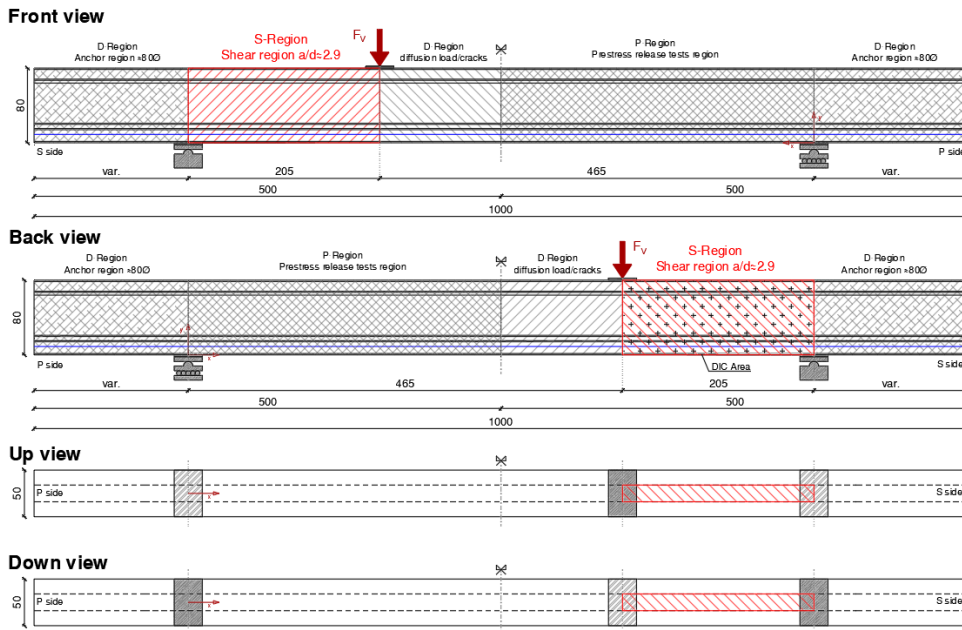


Figure 4-76: Definition of the area designated for shear testing.

Figure 4-77 shows the names of the instruments on the beam portion affected by the shear damage (“S-Region”). It should be noted that values related to both the horizontal potentiometers, placed on the flanges, and those related to the LVDTs at the load point are the average of two instruments installed one on the front side and one on the back side of the beam. The displacement values shown, related to the LVDTs recordings below the load point, are depurated proportionally from the displacement values recorded by the 4 LVDTs (two on the front side and two on the back side) placed at the respective supports (not shown in the figure). It should be noted that in the pre-tensioned beams, strain gauges were installed on the web

4-EXPERIMENTAL RESULTS AND DISCUSSION

instead of potentiometers, as in the post-tensioned beams. These strain gauges, placed below the load point, were only able to return significant values before they were intercepted by flexural cracks. For conversion from strains to concrete stresses recorded by the strain gauges installed on the beams A and B webs, the elastic modulus relative to each beam was used (Table 3-4).

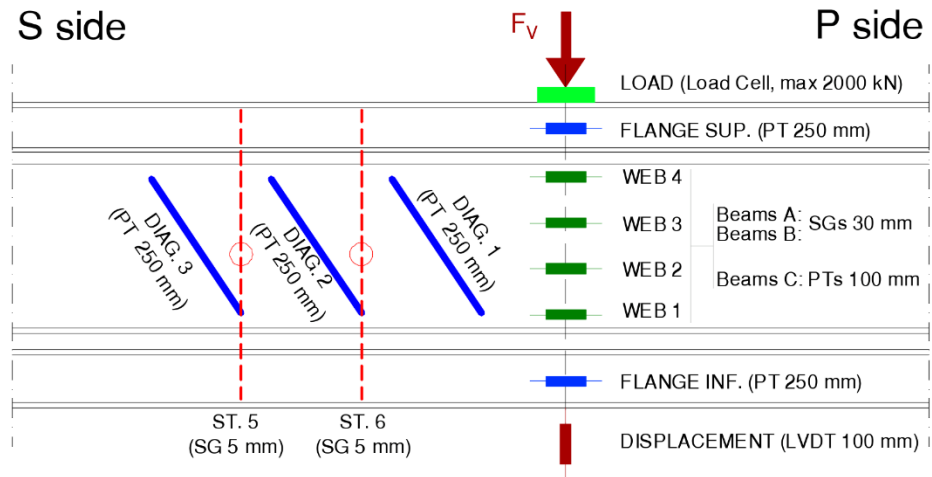


Figure 4-77: Names of instruments installed on beams in Front view:
 PT=Potentiometers, SG=Strain Gauges, LVDT= Linear Variable Displacement Transducer.

As described in §4.1.1.2, strain gauges were installed on stirrups and strands to monitor the stress of the longitudinal pre-stressed, post-stressed and transverse reinforcing members. An elastic modulus for prestressing steel and transverse reinforcement steel, of 200'000 MPa and 195'000 MPa respectively, was used to convert the strains recorded by instruments into stresses. Stress values recorded above 1670 MPa ($f_{p(1\%),k}$) cannot be considered reliable because Hooke's law used to convert strains into stress is no longer valid outside the elastic range.

4-EXPERIMENTAL RESULTS AND DISCUSSION

Since the applied vertical load $[F_V]$ is non-symmetrical to the constraints, reactions at the supports result as follows ($[g_{sw}]$ is the self-weight of the beam) (Figure 4-78, Equation (4-5), Equation (4-6)).

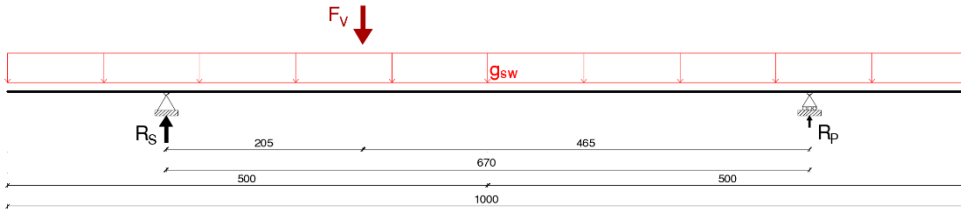


Figure 4-78: Layout of the beam and constraints.

Vertical reaction Support S $[R_S]$

$$\begin{aligned}
 R_S &= F_V [kN] \cdot \frac{465 \text{ cm}}{670 \text{ cm}} + g_{sw} \left[\frac{kN}{cm} \right] \cdot 1000 \text{ cm} \cdot \frac{500 \text{ cm}}{1000 \text{ cm}} \\
 &= F_V [kN] \cdot 0.694 + g_{sw} \left[\frac{kN}{cm} \right] \cdot 1000 \text{ cm} \cdot \frac{1}{2}
 \end{aligned} \tag{4-5}$$

Vertical reaction Support P $[R_P]$

$$\begin{aligned}
 R_P &= F_V [kN] \cdot \frac{205 \text{ cm}}{670 \text{ cm}} + g_{sw} \left[\frac{kN}{cm} \right] \cdot 1000 \text{ cm} \cdot \frac{500 \text{ cm}}{1000 \text{ cm}} \\
 &= F_V [kN] \cdot 0.306 + g_{sw} \left[\frac{kN}{cm} \right] \cdot 1000 \text{ cm} \cdot \frac{1}{2}
 \end{aligned} \tag{4-6}$$

where:

$$g_{sw} \approx 0.06 \text{ kN/cm} = 6 \text{ kN/m} = 25 \text{ kN/m}^3 \cdot 0.24 \text{ m}^2 = \gamma_{R.C.} \cdot A_c \tag{4-7}$$

The value of the vertical reaction at Support S $[R_S]$ will correspond to the maximum shear action affecting the beam.

The prediction of the collapse load of the beams was performed both with the numerical method by creating finite element models with software VecTor 2 (VT2) based on Modified Compression Field Theory – MCFT (§5.2) and with the analytical method, applying the models from Eurocode 2 and *fib* - Model Code (see §6.3) for prestressed members with shear reinforcement:

- Draft EC2 - FprEN_1992-1-1 (2021) - §8.2 - [dEC2-2020];
- Draft MC2020 (2023) - §30.1.3 LoA IIb - [dMC2020] based on SMCFT [Bentz et al., 2006].

Table 4-15 shows the results, both in terms of vertical load applied by the jack [F_v], and of resistance towards the S-Side support [V_R]. The calculation of [V_R] also includes the portion intended for the self-weight of the beam (≈ 60 kN). The results of the two beams with post-tensioning of the strands, Beams C1 and C2, refer to a prestress of 100% (1130 kN) and being with sliding cables it was not possible to apply the model envisaged by dMC2020 - LoA IIb.

Table 4-15: Prediction of shear resistance of beams.

Beam	Numerical (VT2)		Analytical			
			dEC2 - 2020		dMC2020 - LoA IIb	
	F_v [kN]	V_R [kN]	F_v [kN]	V_R [kN]	F_v [kN]	V_R [kN]
A	750	551	487	359	506	372
B	750	551	505	371	491	361
C1 and C2	850	620	492	362	-	-

4.2.2 Beam A

The load-displacement curve in Figure 4-79 shows an initial linear elastic trend up to a value between 450÷480 kN. At this vertical load value, the potentiometer located in the lower flange, under the loading point, begins to record flexural crack openings about 0.2 mm wide, as seen in Figure 4-80.

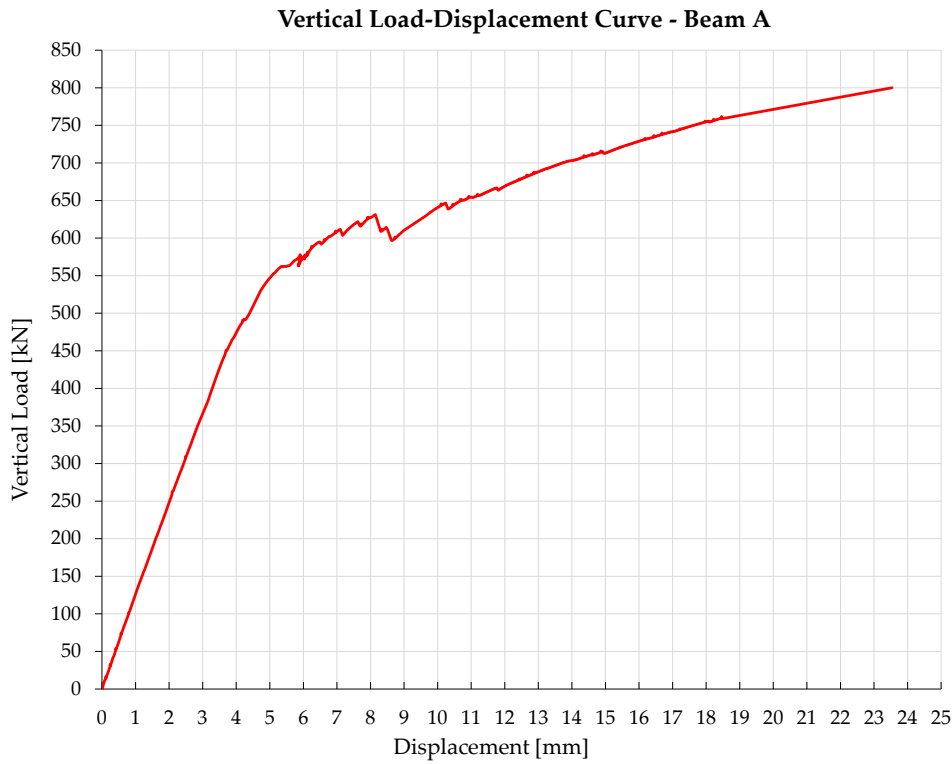


Figure 4-79: Vertical Load-Displacement curve – Beam A.

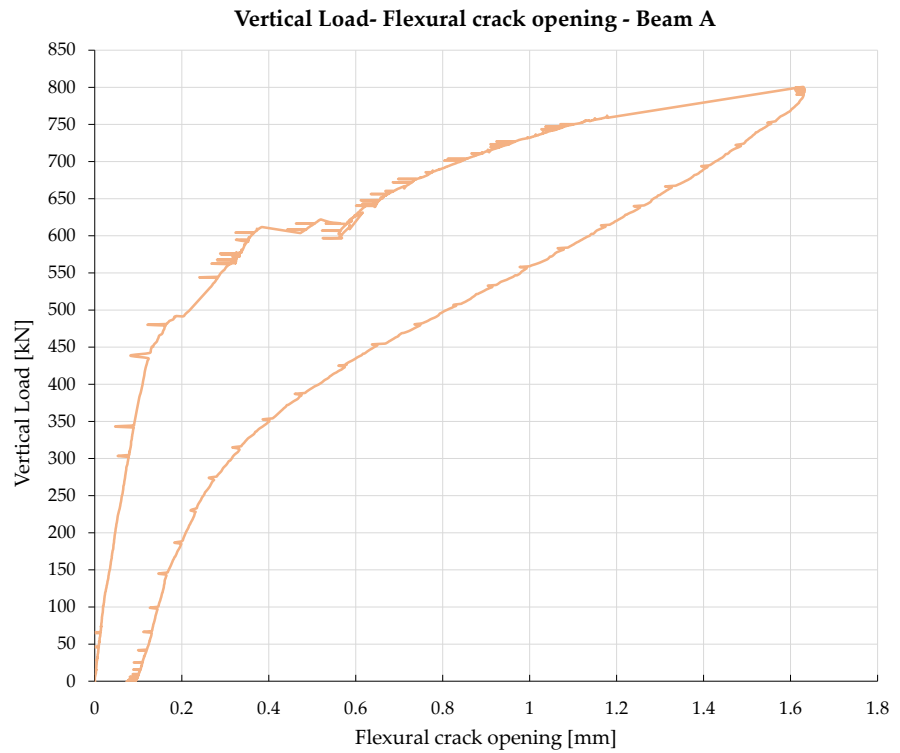


Figure 4-80: Trend of flexural crack opening recorded by the potentiometer
FLANGE INF. – Beam A.

Strands are instrumented and identified according to the scheme shown in Figure 4-81. The section refers to Figure 3-27 with the strain gauges installed below the load point.

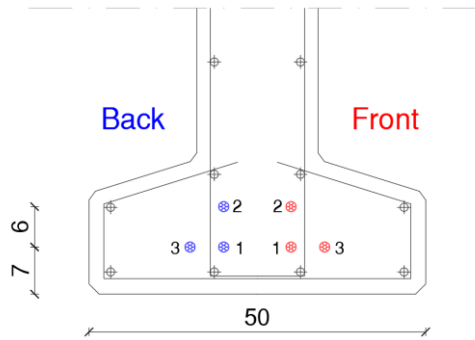


Figure 4-81: Names and colour scales adopted in the representation strands instrumented below the load point – Beam A.

4-EXPERIMENTAL RESULTS AND DISCUSSION

Observing the graph in Figure 4-82 relating to the work rate in the strands at the point of load, it is possible to notice how, at a load between 450÷480 kN, there is a change in slope indicating the moment in which the reinforcement prestress starts to work. Still, in Figure 4-82, it can be observed how the strands work in an almost uniform way; a small difference is observable for the four strands placed at the lower layer (#1 and #3) compared to the two placed higher (#2). It can be seen how the strands placed in the upper layer reach an ultimate deformation, and consequently an ultimate, lower stress, due to the different effective depth to main tension reinforcement [*d*].

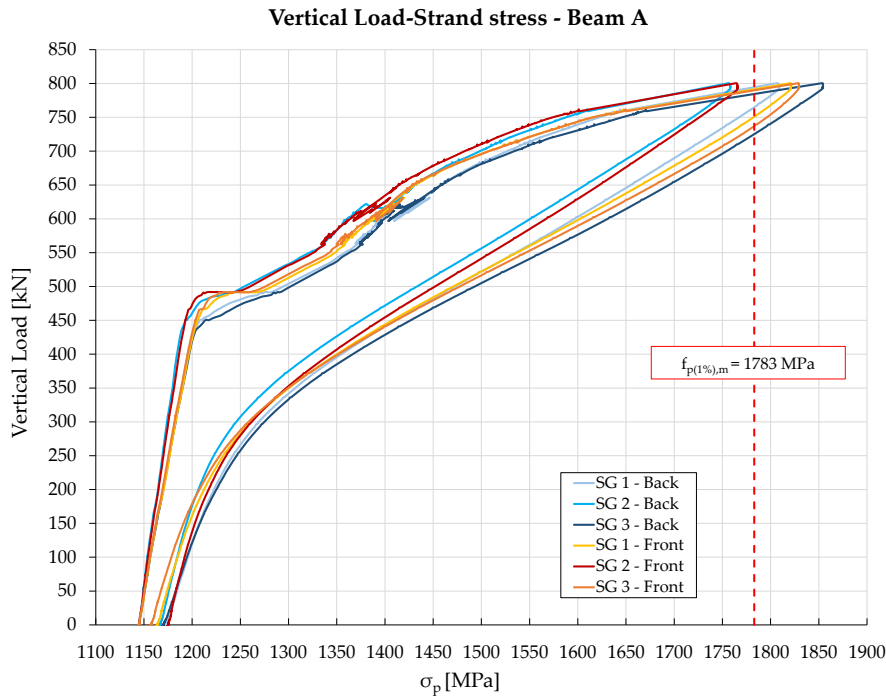


Figure 4-82: Stress trend in the strands as the vertical load increases. – Beam A.

It is important to point out that there is uncertainty about the starting value of the stress in the strands, this is because the tension of the pre-stressed beams has been estimated through an analytical calculation (§3.3.5), which has some approximations.

From the recordings of the SGs it appears that the 4 strands positioned at the lower layer are yielded as they have exceeded the value $f_{p(1%),m} = 1783$ MPa supplied by the manufacturer.

The finite element model created with VecTor 2 (§5.2) interrupts the analysis at an applied external load $F_v = 750$ kN, where the strands under the load point are not yielded but read a $\Delta\varepsilon_{s,p}^{750\text{ kN}} = 0.2\%$. If it considers the initial pre-stress suffered by the strands in the factory of 1145 MPa, and the elastic modulus $E_{p,m} = 200'000$ MPa, it obtains a $\varepsilon_{s,p}^{pre} = 0.57\%$, thus obtaining, at the end of the simulated test, a deformation of $\varepsilon_p^{750\text{ kN}} = \varepsilon_p^{pre} + \Delta\varepsilon_{s,p}^{750\text{ kN}} = 0.57\% + 0.2\% = 0.77\%$, lower than the yield strain of $\varepsilon_{py} = f_{p(1\%),m}/E_{p,m} = 1783\text{ MPa}/200'000\text{ MPa} = 0.89\%$.

Carrying out a rapid calculation for the calculation of the moment leading to the yielding of the strands, it obtains:

$$\begin{aligned} M_y &= [n_{strand} \cdot A_{p,1\emptyset strand} \cdot f_{p(1\%),m} \cdot 0.9 \cdot d_p] + \\ &\quad + [A_{s,1\emptyset 8} \cdot f_{sy,08,m} \cdot 0.9 \cdot (4 \cdot d_{s,1} + 2 \cdot d_{s,2} + 2 \cdot d_{s,3} + 2 \cdot d_{s,4} + 2 \cdot d_{s,5})] \\ &= [6 \cdot 139\text{ mm}^2 \cdot 1783\text{ MPa} \cdot 0.9 \cdot 0.71\text{ m}] + \\ &\quad + [50\text{ mm}^2 \cdot 533\text{ MPa} \cdot 0.9 \\ &\quad \cdot (4 \cdot 0.77\text{ m} + 2 \cdot 0.67\text{ m} + 2 \cdot 0.62\text{ m} + 2 \cdot 0.45\text{ m} + 2 \cdot 0.28\text{ m})] \end{aligned}$$

$$M_y = 950.21 + 170.77 = 1120.98\text{ kNm}$$

equating to:

$$M_y = R_S \cdot a + Q_{sw} \cdot l^2 \cdot \frac{1}{2} = F_v \cdot 0.694 \cdot a + Q_{sw} \cdot l^2 \cdot \frac{1}{2}$$

The vertical load leading to the yield strength of the longitudinal reinforcement is therefore:

$$F_v = \frac{M_y - Q_{sw} \cdot l^2 \cdot \frac{1}{2}}{0.694 \cdot a} = \frac{1120.98\text{ kNm} - 6 \frac{\text{kN}}{\text{m}} \cdot (2.05\text{ m} + 1.65\text{ m})^2 \cdot \frac{1}{2}}{0.694 \cdot 2.05\text{ m}} = 759\text{ kN}$$

It, therefore, appears that the strands yield a vertical load F_v of approx 750-760 kN.

In reality, the potentiometers installed on the lower flange with a vertical load of 800 kN, which brought the beam almost to collapse, recorded a $\Delta\varepsilon_{s,p}^{800\text{ kN}} = 0.34\%$. By adding the pre-stress of the strands of $\varepsilon_{s,p}^{pre} = 0.57\%$, it obtains an overall deformation $\varepsilon_p^{800\text{ kN}} = \varepsilon_p^{pre} + \Delta\varepsilon_{s,p}^{800\text{ kN}} = 0.57\% + 0.34\% = 0.91\%$ greater than the yield strain of the strands by $\varepsilon_{py} = 0.89\%$. The result is consistent with what was recorded by the strain gauges.

Stress values over 1783 MPa ($f_{p(1\%),m}$) are not to be considered reliable since, outside the elastic range, Hooke's law is no longer valid, with which the strains recorded by the strain gauges are been converted into stresses.

4-EXPERIMENTAL RESULTS AND DISCUSSION

Once the vertical load values of 450÷480 kN have been exceeded, the load-displacement curve (Figure 4-79) begins to bend and, in addition to a propagation of the flexural crack pattern which can be appreciated from the graph shown in Figure 4-80, the first shear cracks appear, detected by the diagonal potentiometers installed on the web. During the second phase, around a load value of approximately 610 kN, the load-displacement curve (Figure 4-79) begins to show progressive drops in strength and then resumes a more regular trend. This behaviour is because, at this value of the applied vertical load, the stresses move from the concrete to the transverse reinforcement and the latter begins to work. In this case, as shown in Figure 4-83, the strain gauges on the stirrups (ST.5 and ST.6 in Figure 4-77) record a zero value up to a vertical load value of approximately 610 kN, after which the measurement provided by the strain gauges loses its meaning. It is reasonable to assume that the crack intercepted the stirrups at the area where the strain gauges were installed, damaging them.

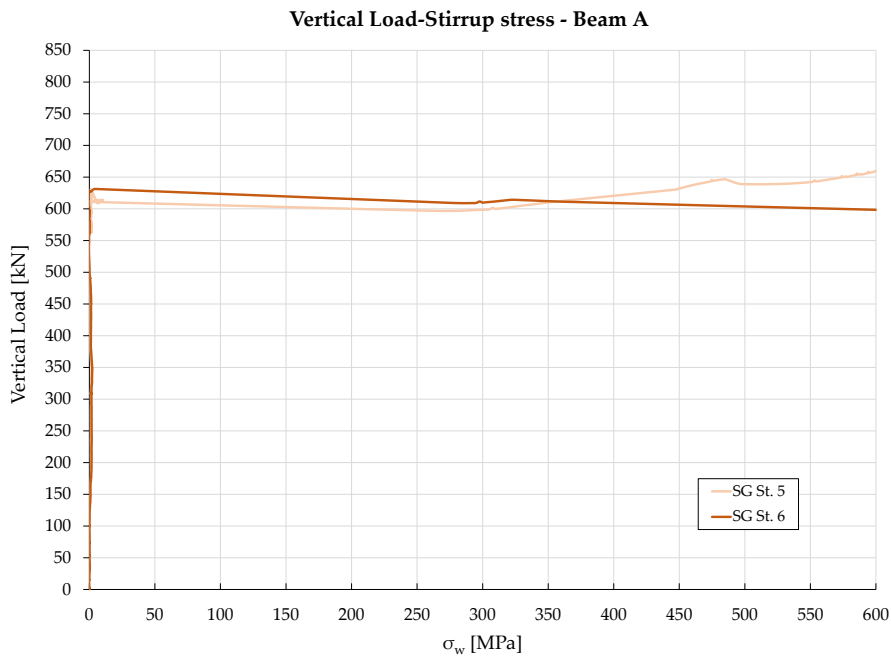


Figure 4-83: Stress trend in ST.5 and ST. 6 as the vertical load increases – Trave A.

The recordings of the diagonal potentiometers installed on the web (DIAG 1, DIAG. 2 and DIAG. 3 in Figure 4-77) make it possible to appreciate the evolution of the shear crack pattern. The transfer of stresses from the concrete to the transverse reinforcement, and therefore the activation of the latter, can be seen in Figure 4-84 with the presence of a horizontal line in the load-crack opening diagram at a vertical load of 610 kN, which represents the increase in the crack opening without the load increasing. In Figure 4-84, it can be seen that DIAG. 1 records a horizontal trend even before the stirrups monitored start working, at around 560 kN. This can be justified by the fact that, as this is the closest potentiometer to the loading point, the instrument recorded an early formation of the cracks and it was also partially affected by flexural cracks propagating into the web. For DIAG. 2 and DIAG. 3, the horizontal trend appears around a vertical load of 610 kN and is representative of the moment in which the stirrups started working; this is consistent with Figure 4-83 (relating to the work rate in the stirrups) where the curve for DIAG 1 changes slope.

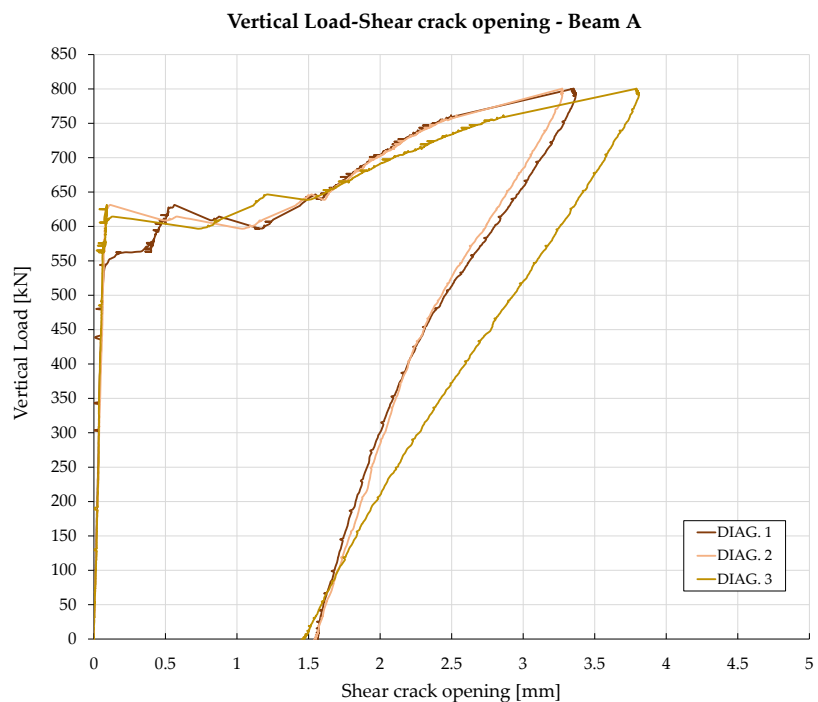


Figure 4-84: Trend of the shear crack opening recorded by the diagonal potentiometers DIAG. 1, DIAG. 2, DIAG. 3. – Beam A

4-EXPERIMENTAL RESULTS AND DISCUSSION

Referring to Figure 4-79, it is observed that the ultimate vertical load achieved is 800 kN with a deflection at the load point of 23.6 mm. It is worth noting that, the shear crack pattern, in Figure 4-85, has multiple cracks passing through a single diagonal potentiometer. For this reason, the crack opening values, recorded by the diagonal potentiometers, should be compared with the data acquired by DIC (Figure 4-86) to trace the width of the individual cracks. Further discussion on the evolution of the crack pattern is in §4.2.7.1.

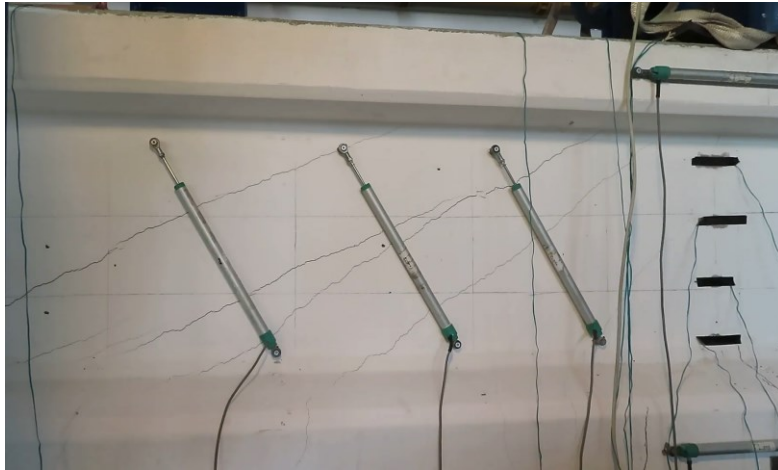


Figure 4-85: Crack pattern at the load of 800 kN – Beam A.

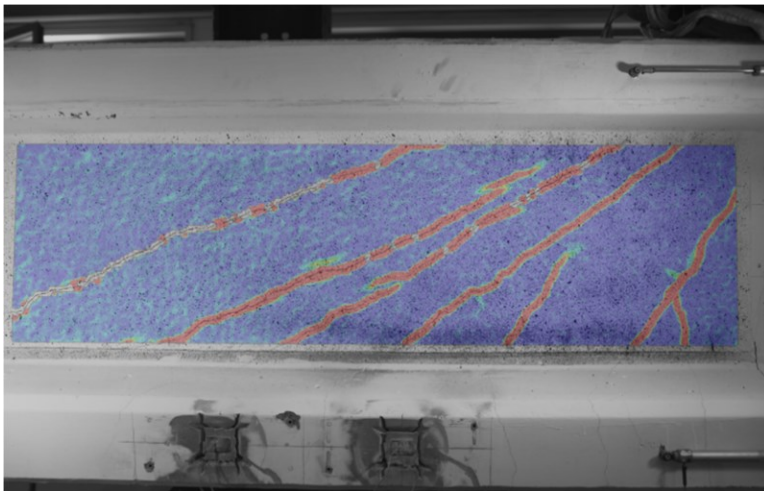


Figure 4-86: Processed data acquired by Digital Image Correlation (DIC) (Beam A) – (the image has been mirrored so that it can be directly compared with the crack picture in Figure 4-85).

Figure 4-87 shows the crack pattern exhibited by the beam at the end of the test. A mainly shear-related crack pattern is observed. The average inclination of the cracks in the S-Region, is 30° from the horizontal.

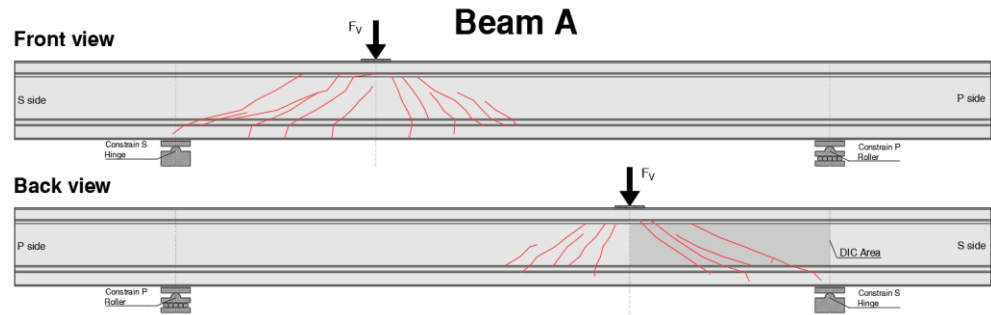


Figure 4-87: Detection of the crack pattern at the end of the load test: $F_v=800$ kN – Beam A.

4.2.3 Beam B

The load-displacement curve in Figure 4-88 shows an initial linear elastic trend up to a value between 380÷400 kN. At this vertical load value, the potentiometer located in the lower flange, under the loading point, begins to record flexural crack openings about 0.1 mm wide, as seen in Figure 4-89.

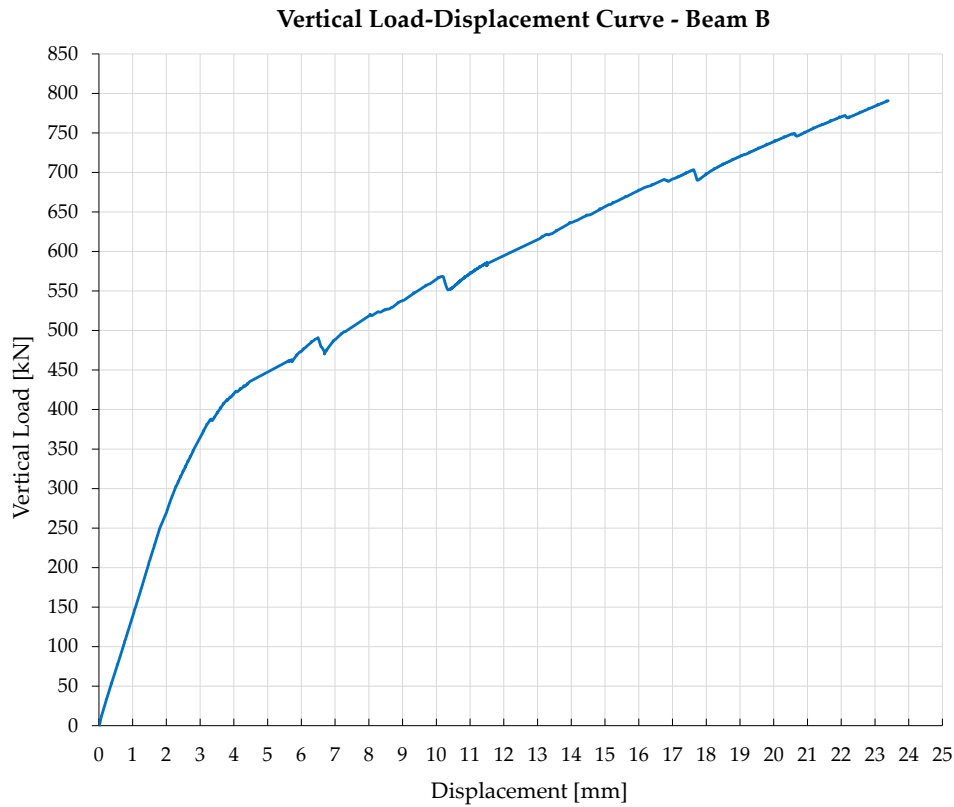


Figure 4-88: Vertical Load-Deflection curve – Beam B.

Vertical Load- Flexural crack opening - Beam B

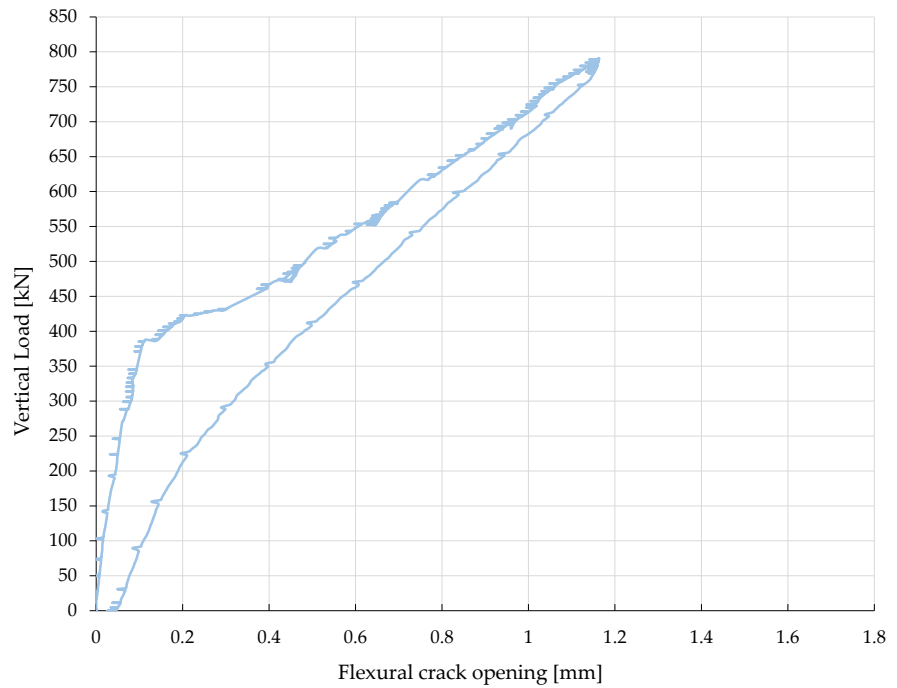


Figure 4-89: Trend of flexural crack opening recorded by the potentiometer FLANGE INF. – Beam B.

Strands are instrumented and identified according to the scheme shown in Figure 4-90. The section refers to Figure 3-30 with the strain gauges installed below the load point.

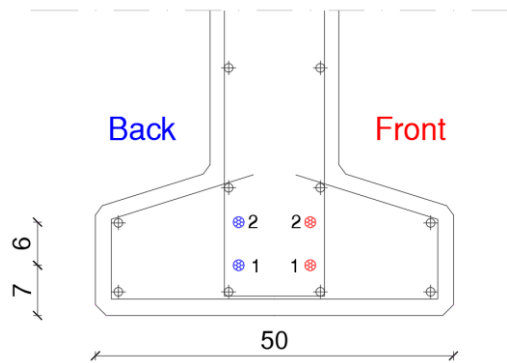


Figure 4-90: Names and colour scales adopted in the representation strands instrumented below the load point – Beam B.

4-EXPERIMENTAL RESULTS AND DISCUSSION

Observing the graph in Figure 4-91 relating to the work rate in the strands at the point of load, it is possible to notice how, at a load between 340÷400 kN, there is a change in slope indicating the moment in which they begin to work. Still, in Figure 4-91, it can be seen how the strands work in an almost uniform way; a small difference is observable for the two strands placed at the lower layer (#1) compared to the two placed higher (#2). It can be seen how the strands placed in the upper layer reach an ultimate deformation, and consequently an ultimate, lower stress, due to the different effective depth to main tension reinforcement [d]. In this case, compared to the results of Beam A, the strain gauge installed on the back side strand 1 seems to have had some problems. This can be seen from the fact that, while the other 3 strands change slope around about 380 kN (the threshold at which the first flexural cracks arise), this detaches from the elastic stage too early.

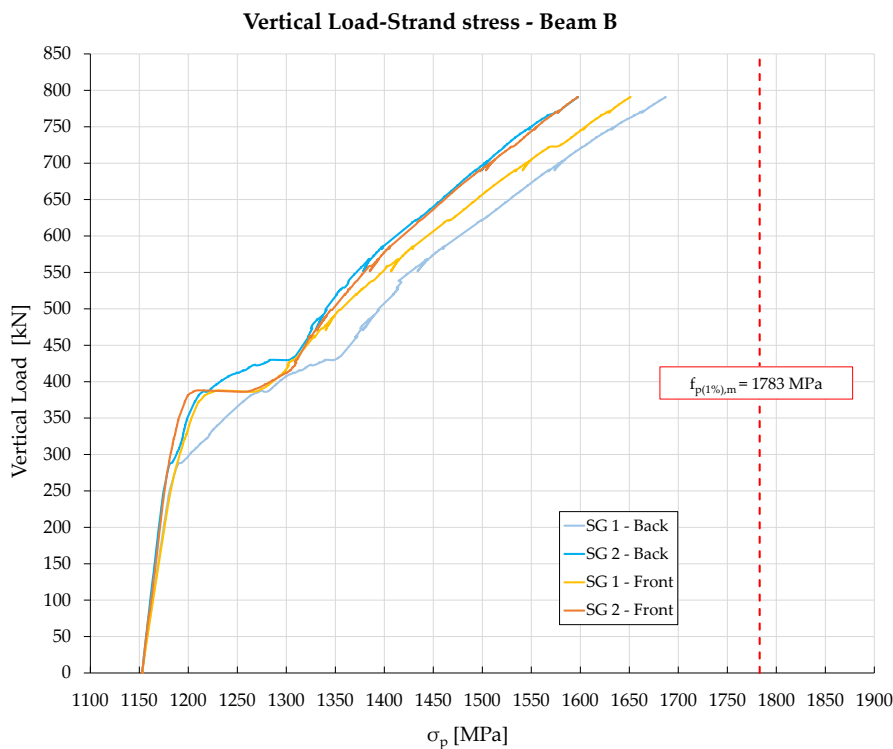


Figure 4-91: Stress trend in the strands as the vertical load increases – Beam B.

It is important to point out that there is uncertainty about the starting value of the stress in the strands, this is because the tension of the pre-stressed beams has been estimated through an analytical calculation (§3.3.5), which has some approximations.

From the recordings of the SGs it appears that all the strands are not yielded as they have not exceeded the value $f_{p(1\%),m} = 1783 \text{ MPa}$ supplied by the manufacturer.

The finite element model created with VecTor 2 (§5.2) interrupts the analysis at an applied external load $F_v = 750 \text{ kN}$, where the strands under the load point are not yielded but read a $\Delta\varepsilon_{s,p}^{750 \text{ kN}} = 0.2\%$. If it considers the initial pre-stress suffered by the strands in the factory of 1153 MPa , and the elastic modulus $E_{p,m} = 200'000 \text{ MPa}$, it obtains a $\varepsilon_{s,p}^{pre} = 0.57\%$, thus obtaining, at the end of the simulated test, a deformation of $\varepsilon_p^{750 \text{ kN}} = \varepsilon_p^{pre} + \Delta\varepsilon_{s,p}^{750 \text{ kN}} = 0.57\% + 0.2\% = 0.77\%$, lower than the yield strain of $\varepsilon_{py} = f_{p(1\%),m}/E_{p,m} = 1783 \text{ MPa}/200'000 \text{ MPa} = 0.89\%$.

Carrying out a rapid calculation for the calculation of the moment leading to the yielding of the strands, it obtains:

$$\begin{aligned} M_y &= [n^\circ_{strand} \cdot A_{p,1\emptyset strand} \cdot f_{p(1\%),m} \cdot 0.9 \cdot d_p] + [A_{s,1\emptyset 26} \cdot f_{sy,\emptyset 26,m} \cdot 0.9 \cdot d_{s,\emptyset 26}] \\ &\quad + [A_{s,1\emptyset 8} \cdot f_{sy,\emptyset 8,m} \cdot 0.9 \cdot (4 \cdot d_{s,1} + 2 \cdot d_{s,2} + 2 \cdot d_{s,3} + 2 \cdot d_{s,4} + 2 \cdot d_{s,5})] \\ &= [4 \cdot 139 \text{ mm}^2 \cdot 1783 \text{ MPa} \cdot 0.9 \cdot 0.70 \text{ m}] + \\ &\quad + [2 \cdot 531 \text{ mm}^2 \cdot 514 \text{ MPa} \cdot 0.9 \cdot 0.70 \text{ m}] + \\ &\quad + [50 \text{ mm}^2 \cdot 533 \text{ MPa} \cdot 0.9 \\ &\quad \quad \cdot (4 \cdot 0.77 \text{ m} + 2 \cdot 0.67 \text{ m} + 2 \cdot 0.62 \text{ m} + 2 \cdot 0.45 \text{ m} + 2 \cdot 0.28 \text{ m})] \end{aligned}$$

$$M_y = 624.55 + 343.90 + 170.77 = 1139.22 \text{ kNm}$$

equating to:

$$M_y = R_s \cdot a + Q_{sw} \cdot l^2 \cdot \frac{1}{2} = F_v \cdot 0.694 \cdot a + Q_{sw} \cdot l^2 \cdot \frac{1}{2}$$

The vertical load leading to the yield strength of the longitudinal reinforcement is therefore:

$$F_v = \frac{M_y - Q_{sw} \cdot l^2 \cdot \frac{1}{2}}{0.694 \cdot a} = \frac{1139.22 \text{ kNm} - 6 \frac{\text{kN}}{\text{m}} \cdot (2.05 \text{ m} + 1.65 \text{ m})^2 \cdot \frac{1}{2}}{0.694 \cdot 2.05 \text{ m}} = 772 \text{ kN}$$

It, therefore, appears that the strands yield a vertical load F_v of approx 770-780 kN.

In reality, the potentiometers installed on the lower flange with a vertical load of 790 kN, which brought the beam almost to collapse, recorded a $\Delta\varepsilon_{s,p}^{800 \text{ kN}} = 0.26\%$. By adding the pre-stress of the strands of $\varepsilon_{s,p}^{pre} = 0.57\%$, it obtains an overall deformation $\varepsilon_p^{800 \text{ kN}} = \varepsilon_p^{pre} + \Delta\varepsilon_{s,p}^{800 \text{ kN}} = 0.57\% + 0.26\% = 0.83\%$ less than the yield strain of the strands by $\varepsilon_{py} = 0.89\%$. The result is consistent with what was recorded by the strain gauges. Considering the various uncertainties due to the estimate of the initial stress of the strands, the tolerance of the load cell and the rounding in the calculations, the strands in this test appear to have approached very close to the yield strength, probably without exceeding it. For this behaviour, compared with Beam A, the

4-EXPERIMENTAL RESULTS AND DISCUSSION

presence of the 2Ø26 of mild reinforcement positioned in the same position as the missing strands could have influenced it.

Once the vertical load values of 340=400 kN have been exceeded, the load-displacement curve (Figure 4-88) begins to bend and, in addition to a propagation of the flexural crack pattern which can be appreciated from the graph shown in Figure 4-89, the first shear cracks appear, detected by the diagonal potentiometers installed on the web. During the second phase, around a load value of approximately 480 kN, the load-displacement curve (Figure 4-88), begins to show progressive drops in strength and then resumes a more regular trend; the most significant drops in strength appear around 570 kN and 700 kN. This behaviour is because, at this value of the applied vertical load, the stresses move from the concrete to the transverse reinforcement and the latter begins to work. In this case, as shown in Figure 4-92, the strain gauges on the stirrups (ST.5 and ST.6 in Figure 4-77) record a zero value up to a vertical load value of approximately 480 kN, after which the measurement provided by the strain gauges loses its meaning. It is reasonable to assume that the crack intercepted the stirrups at the area where the strain gauges were installed, damaging them.

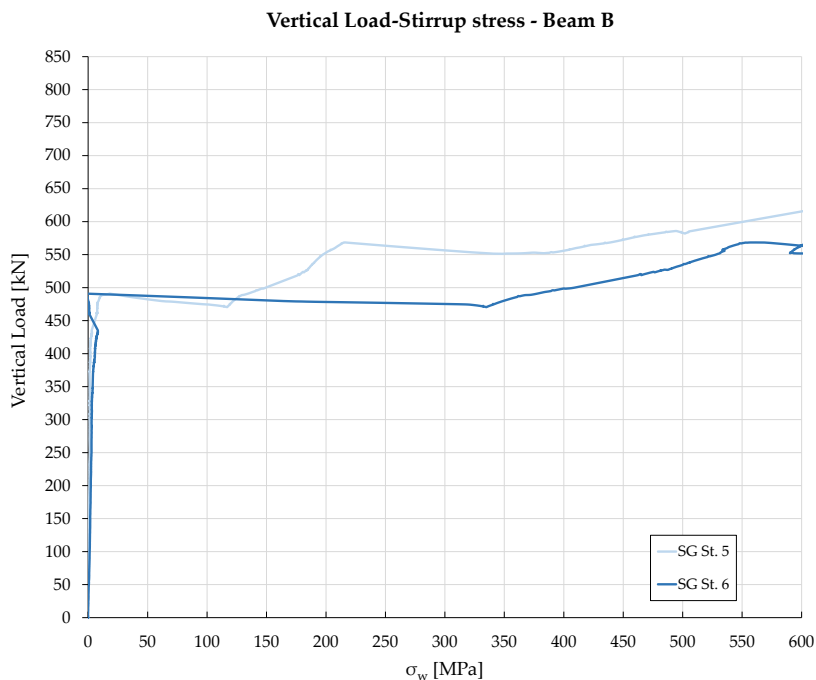


Figure 4-92: Stress trend in ST.5 and ST. 6 as the vertical load increases – Trave B.

The recordings of the diagonal potentiometers installed on the web (DIAG 1, DIAG. 2 and DIAG. 3 in Figure 4-77) make it possible to appreciate the evolution of the shear crack pattern. The transfer of stresses from the concrete to the transverse reinforcement, and therefore the activation of the latter, can be seen in Figure 4-93 with the presence of a horizontal line in the load-crack opening diagram at a vertical load of 480 kN, which represents the increase in the crack opening without the load increasing. In Figure 4-93, it can be seen that DIAG. 1 records a growing trend even before the stirrups monitored start working, at around 440 kN. This can be justified by the fact that, as this is the closest potentiometer to the loading point, the instrument recorded an early formation of the cracks and it was also partially affected by flexural cracks propagating into the web. For DIAG. 2 and DIAG. 3, the horizontal trend appears around a vertical load of 480 kN and is representative of the moment in which the stirrups started working; this is consistent with Figure 4-92 (relating to the work rate in the stirrups) where the curve for DIAG 1 changes slope.

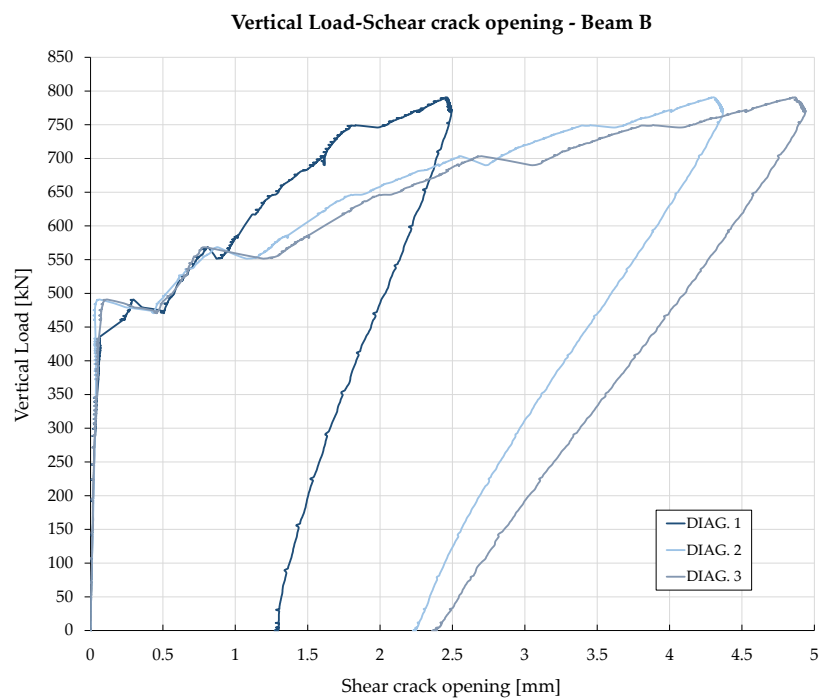


Figure 4-93: Trend of the shear crack opening recorded by the diagonal potentiometers DIAG. 1, DIAG. 2, DIAG. 3. – Beam B.

Referring to Figure 4-88 it is observed that the ultimate vertical load achieved is 790 kN with a deflection at the load point of 23.4 mm. It is worth noting that, the shear crack pattern, in Figure 4-94, has multiple cracks passing through a single diagonal

4-EXPERIMENTAL RESULTS AND DISCUSSION

potentiometer. For this reason, the crack opening values, recorded by the diagonal potentiometers, should be compared with the data acquired by DIC (Figure 4-95) to identify the width of the individual cracks. It can be seen from Figure 4-94 that most of the cracks cross the two potentiometers furthest from the load point (DIAG. 2 and DIAG. 3). This is also consistent with the results represented in the load-shear crack opening curves which, compared with the results of the Beam A test, show a clear difference between the maximum crack opening measured by DIAG. 1 and those measured by the other two potentiometers. Further details on the evolution of the crack pattern are given in §4.2.7.1.

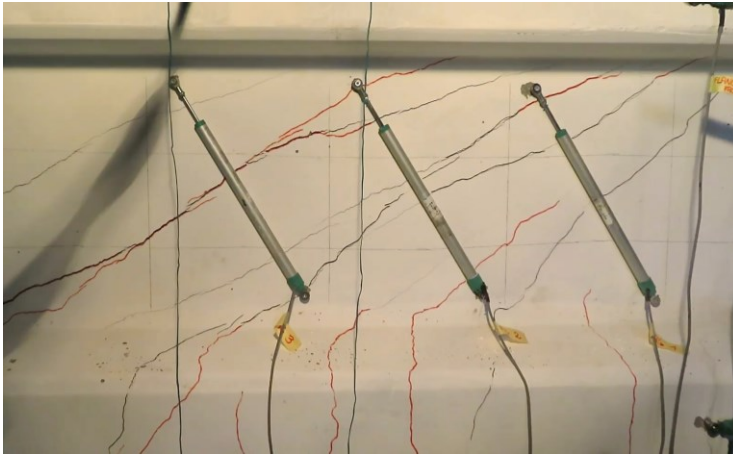


Figure 4-94: Crack pattern at the load of 790 kN – Beam B.

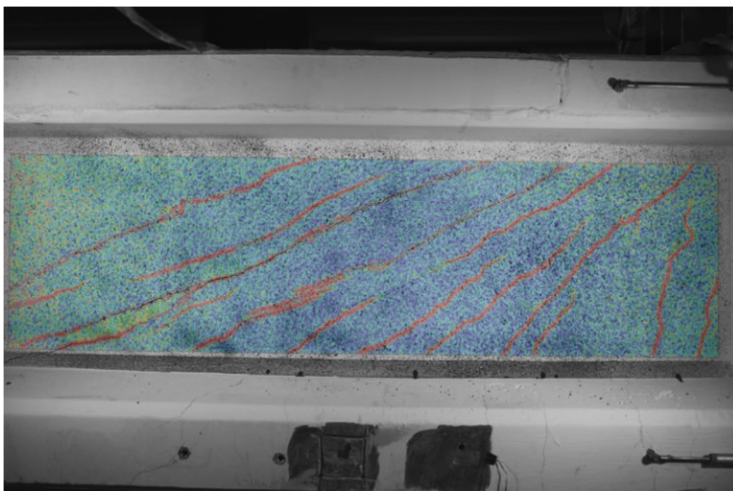


Figure 4-95: Processed data acquired by Digital Image Correlation (DIC) (Beam B) – (the image has been mirrored so that it can be directly compared with the crack picture in Figure 4-94)

Figure 4-96 shows the crack pattern exhibited by the beam at the end of the test. A mainly shear-related crack pattern is observed. The average inclination of the cracks in the S-Region, is 30° from the horizontal.

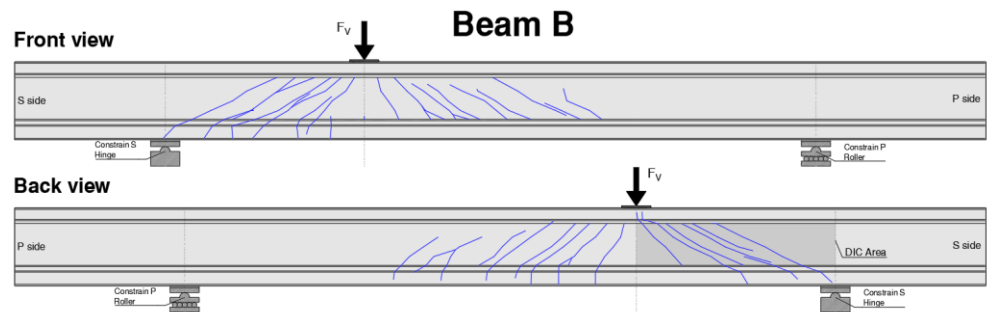


Figure 4-96: Detection of the crack pattern at the end of the load test: $F_v=790$ kN – Beam B.

4.2.4 Beam C1

As shown in Figure 4-97, for Beam C1, the design strand tensioned approximately 1130 kN (100% of prestress) was progressively reached by the post-tensioning system applied to the ends of the beam. The vertical jack was activated (Figure 4-98), until a load of 500 kN was reached; maintaining the vertical load constant, the prestress was progressively reduced, until approximately 60% of the initial tension. Two more cycles were performed using the same procedure, respectively with a constant vertical load of 550 kN and 600 kN. The comparison in Figure 4-98 shows how, both the curves relating to the tests carried out with a constant vertical load of 550 kN and, in particular, with a constant vertical load of 600 kN, despite exhibiting the same initial stiffness, leave the elastic stage much earlier than the curve of the first test (500 kN). This is due to progressive damage of the beam, following the reduction of prestressing, which appeared already from the first test performed with a vertical load of 500 kN. As can be seen in Figure 4-99, the instruments placed on the lower flange of the beam record a progressive crack opening for each vertical load-unload cycle performed.

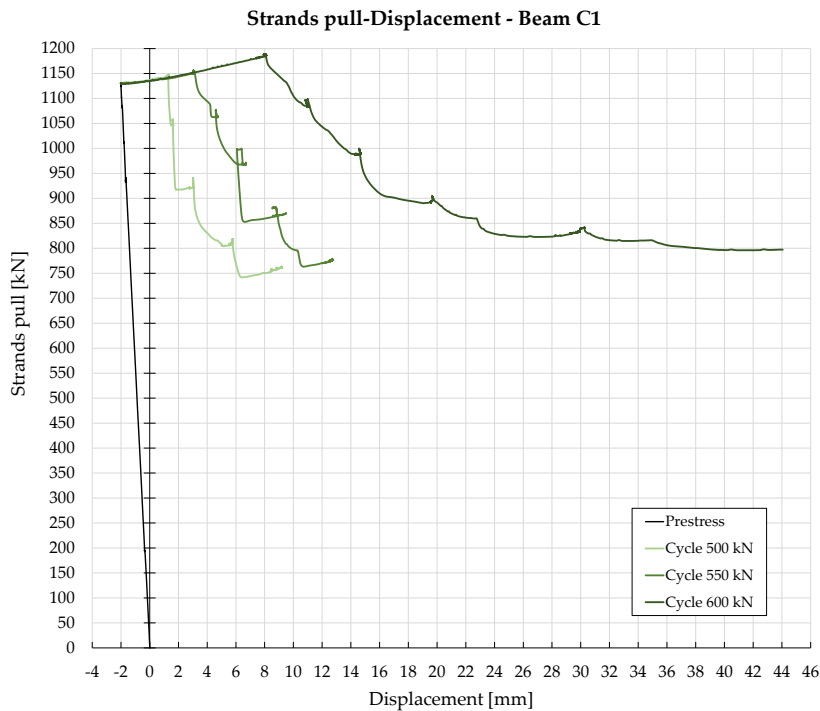


Figure 4-97: Comparison of Strand pull-Displacement curves for tests with different vertical loads applied – Beam C1.

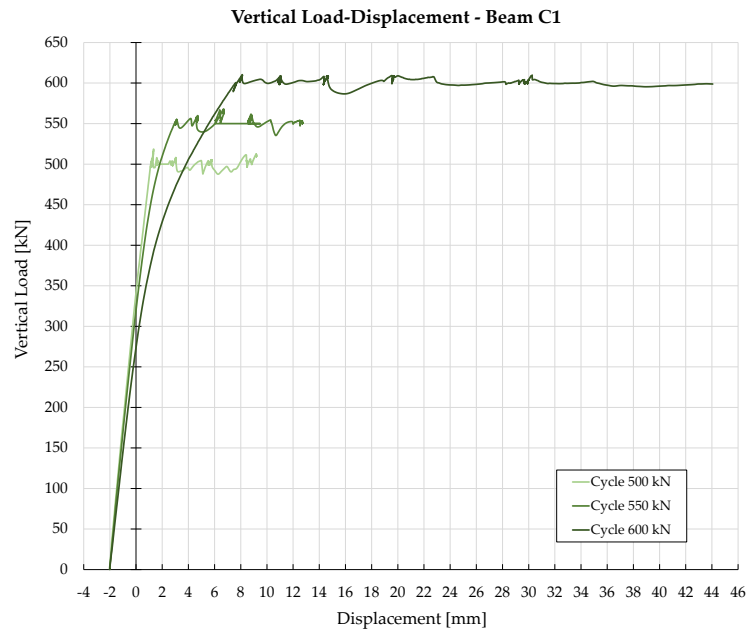


Figure 4-98: Comparison Vertical Load-Displacement – Beam C1.

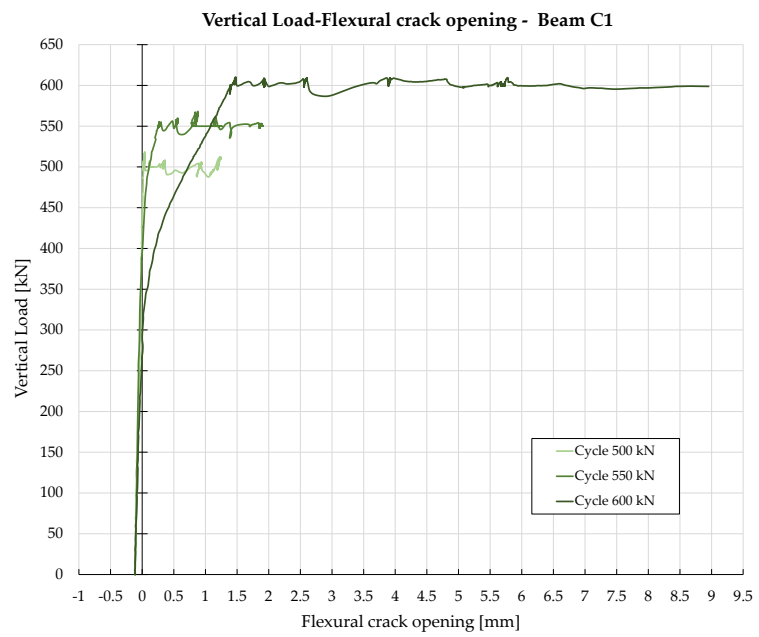


Figure 4-99: Comparison Vertical Load-Flexural crack opening – Beam C1.

4-EXPERIMENTAL RESULTS AND DISCUSSION

In the first load cycle with an applied vertical load of 500 kN, see Figure 4-100 and Figure 4-101, the first flexural cracks appeared at a prestress level of 81%. The crack pattern, which was predominantly flexural, developed further once the strands were relieved to 65% of the design tension. The same procedure was carried out with a constant vertical load of 550 kN, once again reducing the prestress level up to 68% (see Figure 4-102 and Figure 4-103). A final test, with the same procedure, was carried out with a constant vertical load of 600 kN, reaching a prestress level of approximately 71% in this case (see Figure 4-104 and Figure 4-105).

The test was stopped once a condition close to ULS was reached; at this point, the beam exhibited a deflection of approximately 44 mm.

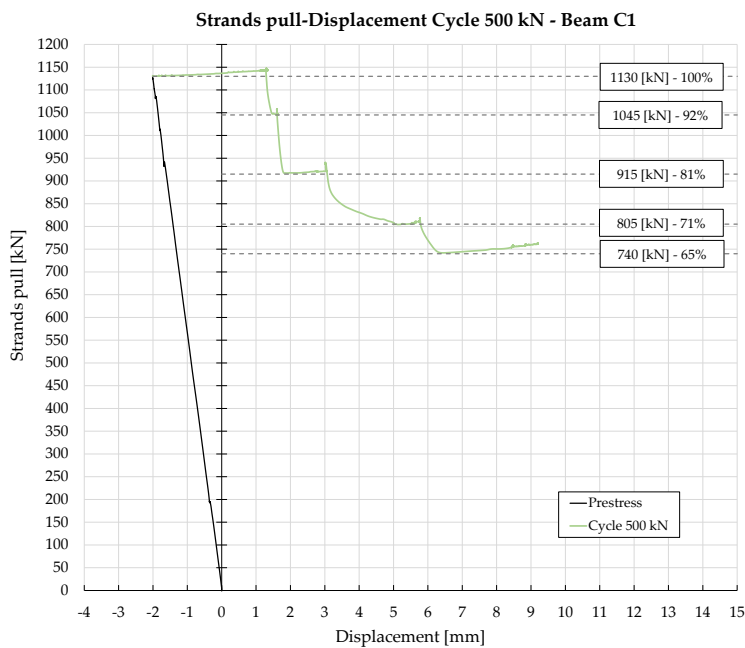


Figure 4-100: Strands pull-Displacement Cycle 500 kN – Beam C1.

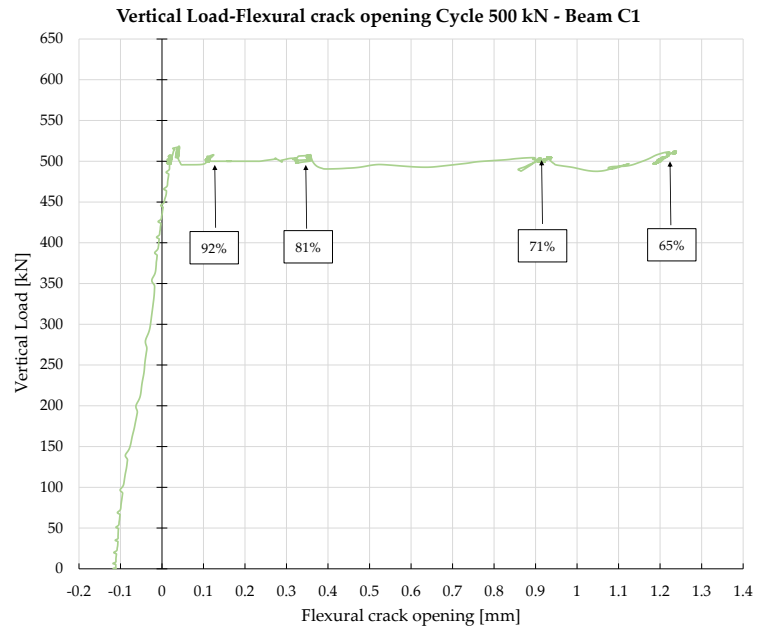


Figure 4-101: Vertical Load-Flexural crack opening Cycle 500 kN – Beam C1.

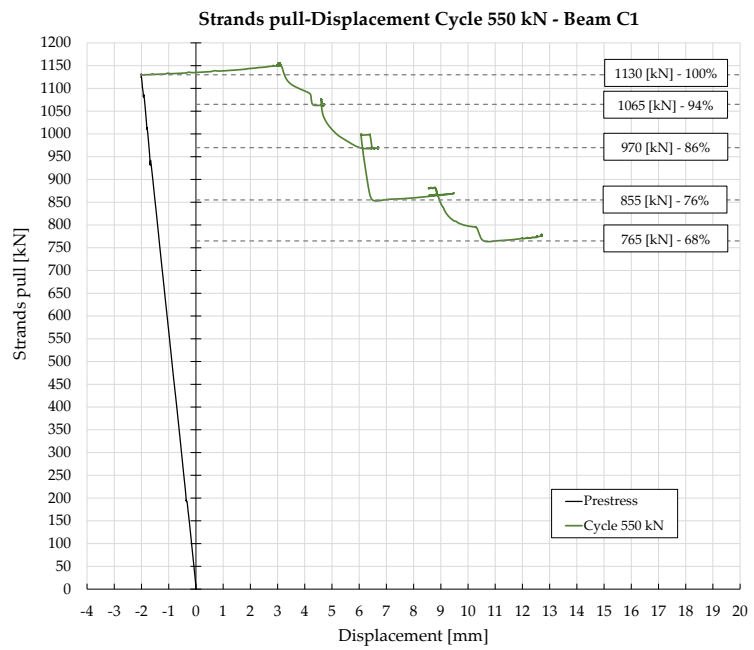


Figure 4-102: Strands pull-Displacement Cycle 550 kN – Beam C1.

4-EXPERIMENTAL RESULTS AND DISCUSSION

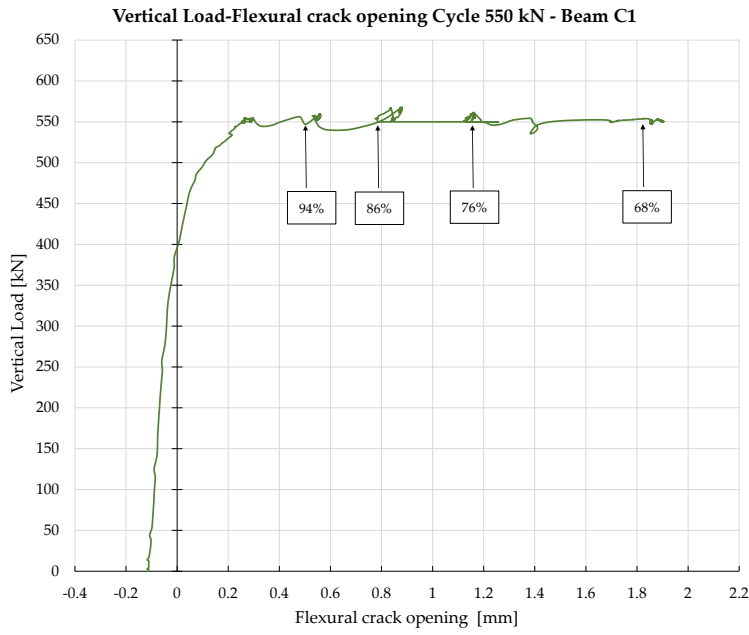


Figure 4-103: Vertical Load-Flexural crack opening Cycle 550 kN - Beam C1.

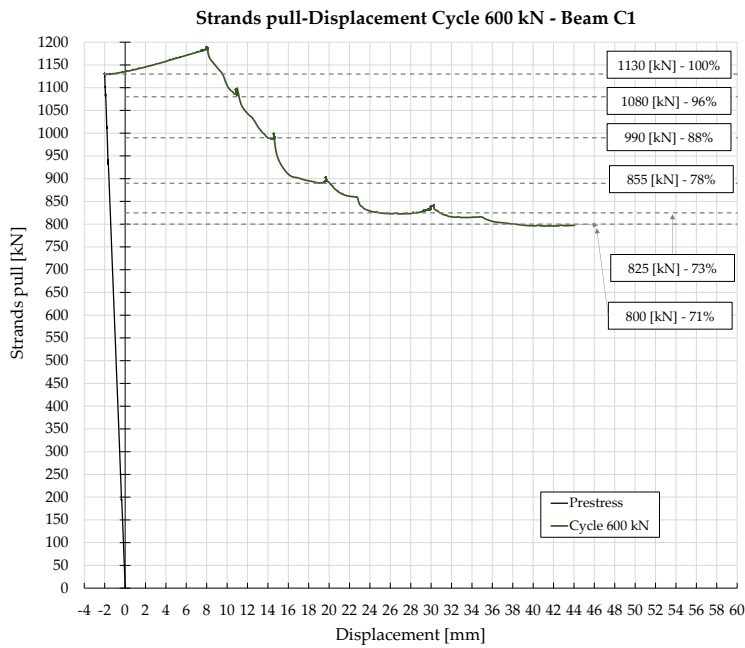


Figure 4-104: Strands pull-Displacement Cycle 600 kN - Beam C1.

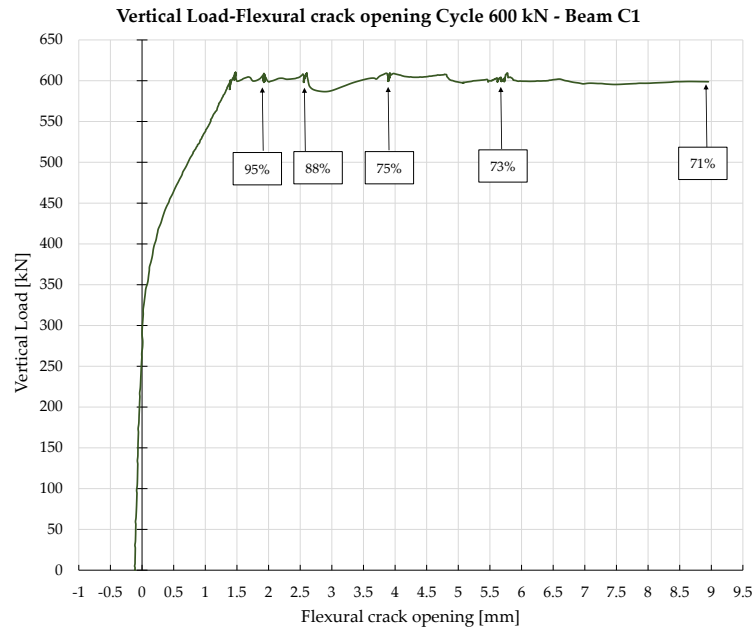


Figure 4-105: Vertical Load-Flexural crack opening Cycle 600 kN - Beam C1.

The reduction of tension in the strands was obtained by using a hydraulic jack in displacement control (as described in §3.4), applying displacements of approximately 7 mm which in the unloaded beam condition corresponded to a reduction in prestress of 10%. However, the same procedure carried out with a vertical load applied to the beam did not allow, with the same displacement imposed on the hydraulic jack, to reach the same percentage of reduction of the tension in the strands due to an increase in the work rate in the latter; this is particularly evident in the third cycle, carried out with a vertical load of 600 kN.

About the prestressing value considered, it can be appreciated from Figure 4-106 how there is a good correspondence between the readings of the strain gauges (installed on each strand, as described in §4.1.1.2) and the load cell placed on the beam header opposite from the hydraulic jack (§3.4).

During the test, the value provided by the load cell placed at the passive header of the beam was used as a reference.

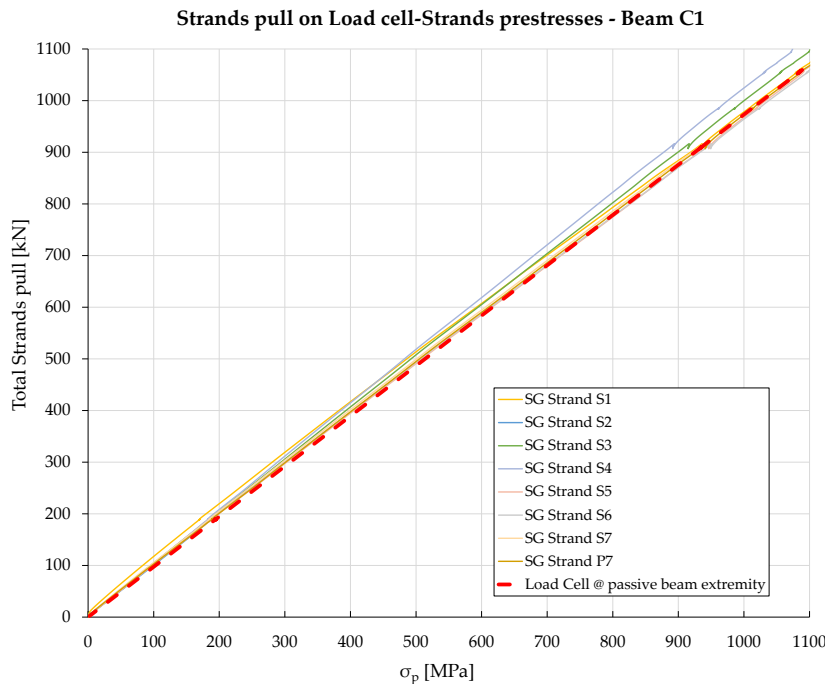


Figure 4-106: Comparison of the strain in the strands measured by strain gauges and the load cell (placed on the beam end opposite from the hydraulic jack) values – Beam C1.

In the final load cycle with a vertical load of 600 kN applied, it was not possible to reduce the tension in the strands to constant values of 10% of the initial pull during the last prestress reduction step. This happened because the deformation imposed by the hydraulic jack caused high deformations in the beam increasing the deflection from 28 mm to 44 mm (Figure 4-104). As a result, the working rate and the strand stress increased. So, the total reduction in strand tension read by the load cell, affected by this additional strand work rate, cannot be 10%.

This can be seen in Figure 4-107, where, in addition to the prestress reduction phase at constant load (600 KN), the unloading of the vertical jack was also plotted, until a vertical load of 0 was reached. The application of the vertical load with low prestressing levels in the beam (70%) caused an increase in the strand tension of 265 KN; in fact, at the end of the unloading phase of the vertical jack, with constant prestressing, the total tension in the strands decreased from 800 KN to 535 KN.

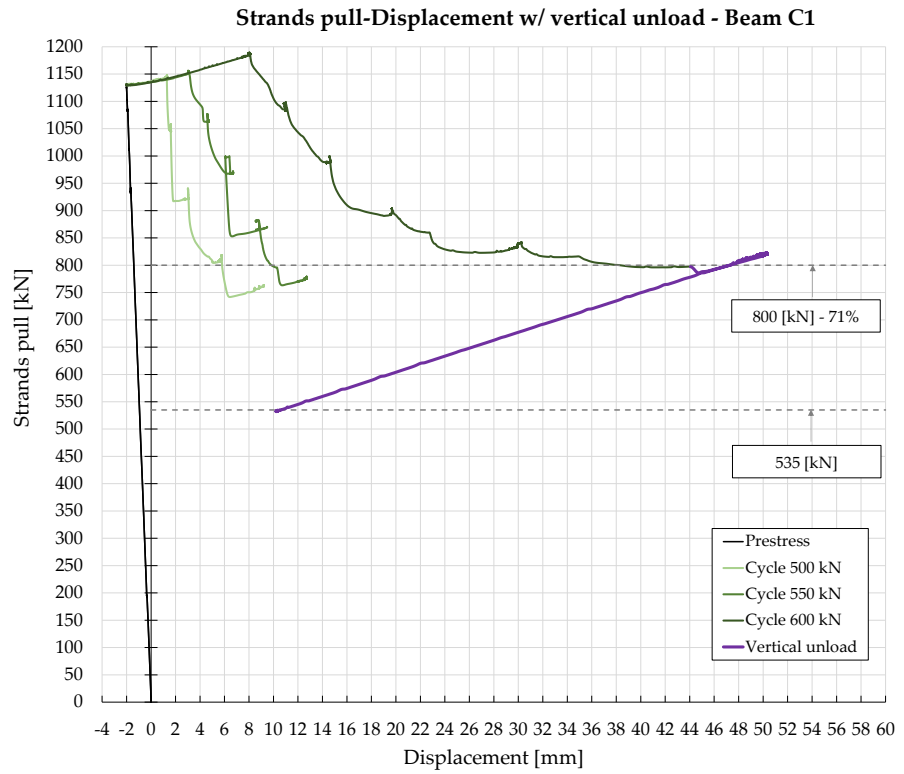


Figure 4-107: Comparison of Strand Tension-Displacement curves for different load cycles with vertical unloading – Beam C1.

Figure 4-108 shows the crack pattern at the end of the test. It can be seen that cracks are mostly flexural cracks, concentrated in the area near the load point.

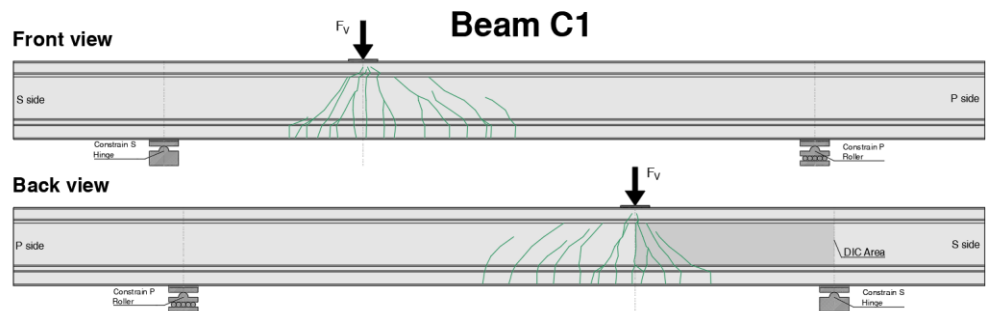


Figure 4-108: Detection of the crack pattern at the end of the load test: $P=70\%$ $F_v=600$ kN – Beam C1.

4.2.5 Beam C2

Beam C2 was prestressed by applying a total tension of 993 kN (88%) to the seven strands (7-wire 6/10") with the controlled post-tensioning system, achieving a similar level of prestressing as that of Beam A. As shown in Figure 4-109, the beam was monotonically loaded until a vertical load of 916 kN was reached, and a displacement of 60 mm in the section below the load point was recorded.

Figure 4-110 shows what is recorded by the potentiometers installed on the lower flange below the load point. It can be seen that flexural cracks begin to develop above 400 kN of vertical load, then increase to a maximum of 9.3 mm. It should be noted that during the stress release tests on the concrete (§4.1), in the configuration of 60%-65% precompression and 400 kN of applied vertical load, flexural cracks developed below the load point (Figure 4-112). Although the prestress was restored to 88% when the vertical load was applied, the beam appeared to be affected by the pre-cracking condition caused by the previous cycle. In fact, from the comparison between the curve of the numerical model and the experimental curve, the latter exhibits a less rigid initial stage (§5.2.5.2).

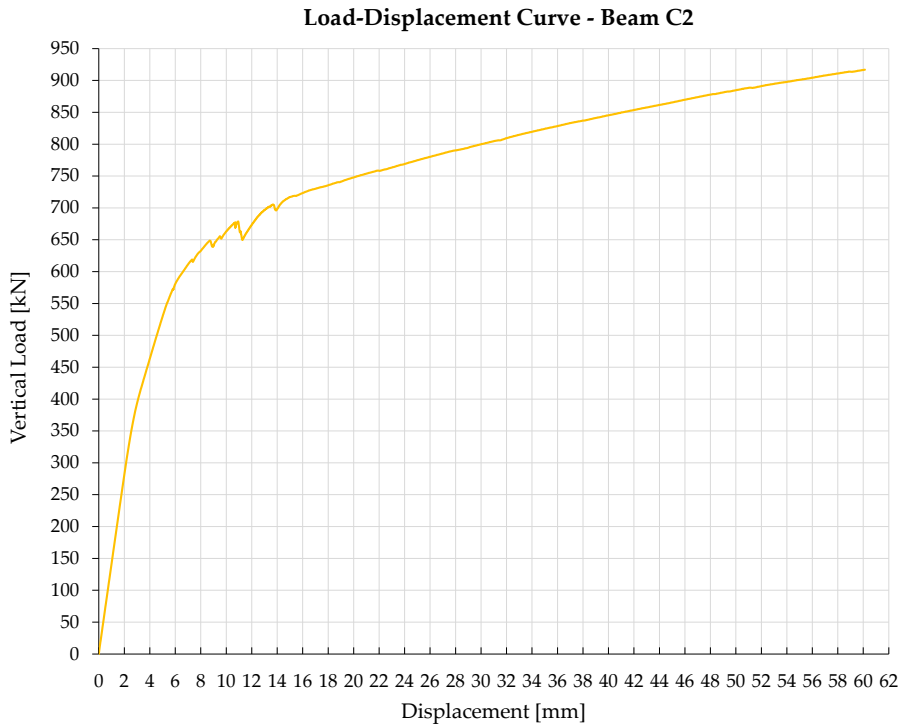
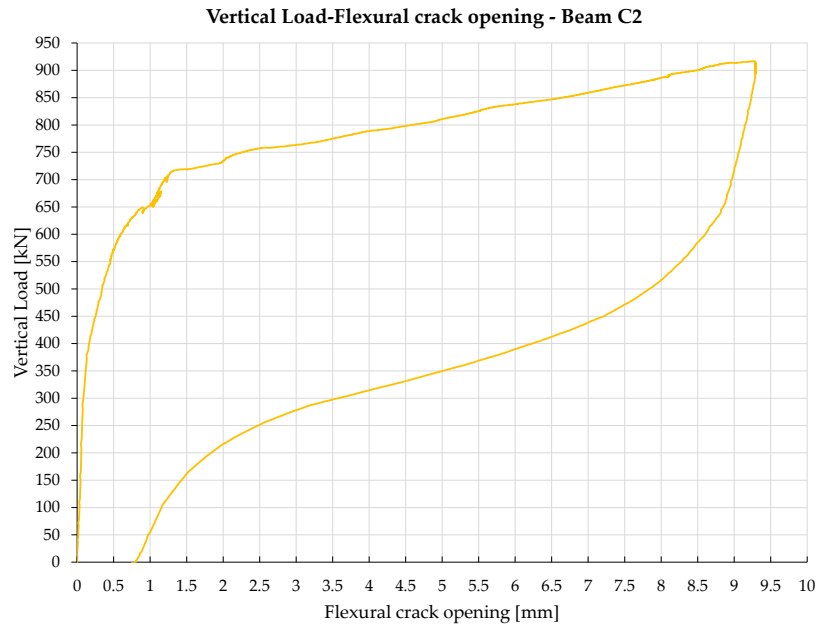


Figure 4-109: Load-Deflection curve – Beam C2.



*Figure 4-110: Trend of flexural crack opening recorded by the potentiometer
FLANGE INF. – Beam C2.*

The test was interrupted mainly because the tension in the strands measured by the load cell at the end of the beam (1397 kN), which increased as a consequence of the vertical load applied, had almost reached the load-bearing capacity of the hydraulic jack (1450 kN) used to tension the strands.

In Figure 4-111, it can be seen that the stress of each strand increases by approximately 435 MPa (an mean of 423 kN across all strands) with an applied vertical load of 916 kN. This means that in this load configuration, the increase in vertical load is approximate twice as much the increase in prestress force.

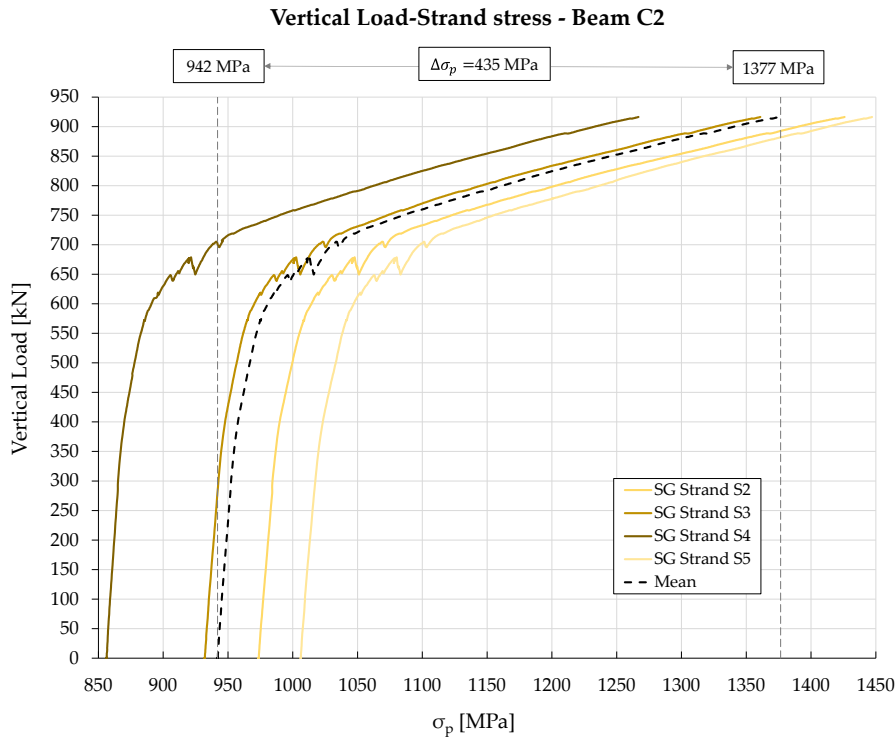


Figure 4-111: Strand stress trend as vertical load increases – Beam C2.

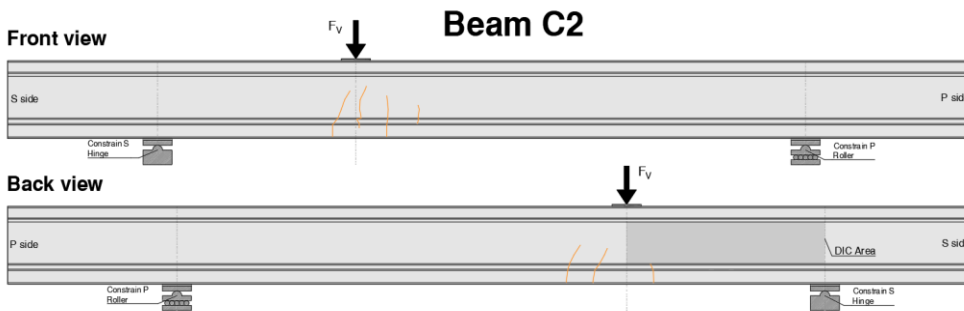


Figure 4-112: Detection of the crack pattern: $P=60\%-65\%$ $F_v=400 \text{ kN}$ – Beam C2.

Figure 4-113 shows the crack pattern at the end of the test. It can be seen that cracks are mostly flexural cracks, concentrated in the area near the load point.

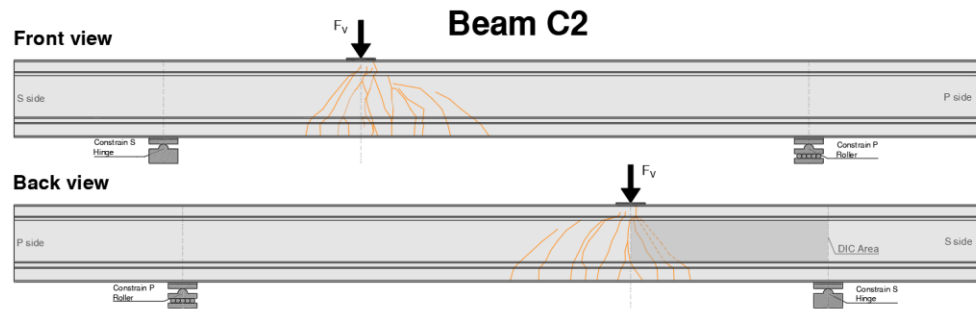


Figure 4-113: Detection of the crack pattern at the end of the load test:
 $P=88\%$ $F_v=916$ kN – Beam C2.

4.2.6 Comparisons and Discussion

4.2.6.1 Results comparison Beam A - Beam B

In the comparison in Figure 4-114 of the Beam A and Beam B experimental curves, it can be seen that both have very similar stiffness in the linear elastic stage. Consistent with the knowledge from PRC theory, the load-displacement curve of the beam with a lower prestress level leaves the elastic stage first while close to an ultimate limit state condition the two curves tend to join.

In the graph represented in Figure 4-114, and in those that follow, the results relative to the test on Beam A and Beam B are shown in red and blue, respectively.

It should be remembered how Beam B, having only four strands inside it compared to the six of Beam A (tensioned at the same value of $\sigma_{p\infty} \approx 1150$ MPa), wants to represent a beam that has manifested prestressing losses of approximately 33% of the initial tension.

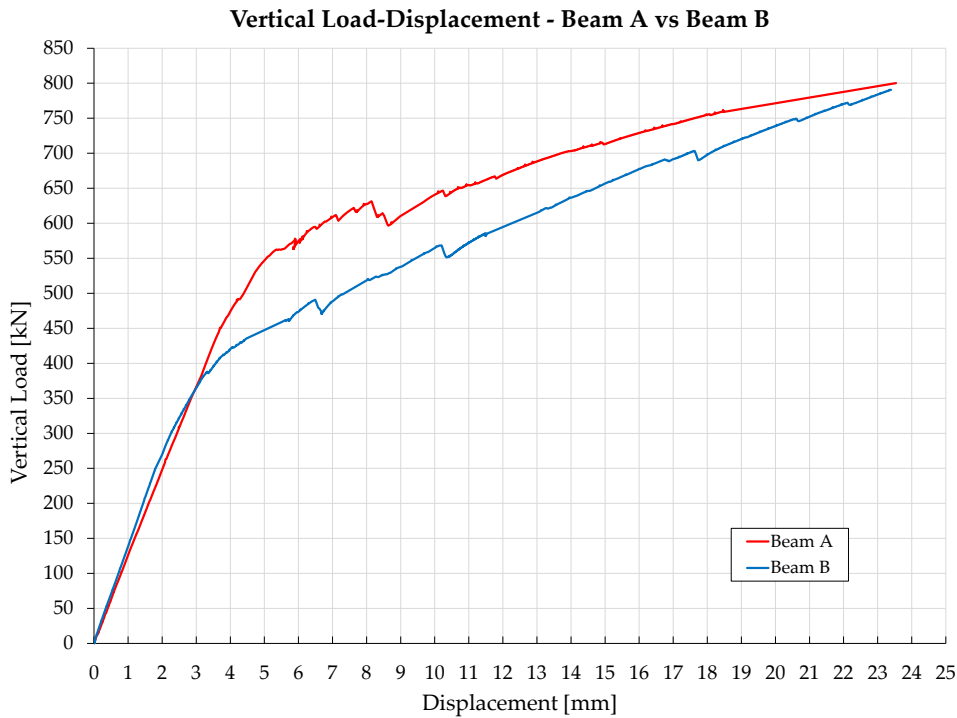


Figure 4-114: Comparison of vertical load-displacement curves of the two pre-tensioned beams – Beams A and B.

About the different flexural behaviour exhibited by the two beams, it can be seen from Figure 4-115 that the first cracks appear in Beam B at a vertical load value of 385 kN, which is approximately 21% lower than the one relative to the first flexural crack recorded in the test on Beam A (490 kN). This can also be appreciated by comparing the recordings provided by the potentiometers installed on the lower flange below the load point, where the first flexural cracks formed, shown in Figure 4-116.

Figure 4-116 shows how near collapse (with a very similar applied vertical load) in Beam A larger bending crack openings were reached than in Beam B by approximately 0.5 mm, in the area of maximum bending moment. This is because the potentiometers installed on Beam A intercept more cracks than those on Beam B, as shown in Figure 4-117 and Figure 4-118 (the screw marks on the surface of the beam indicate where the potentiometers were placed during the tests).

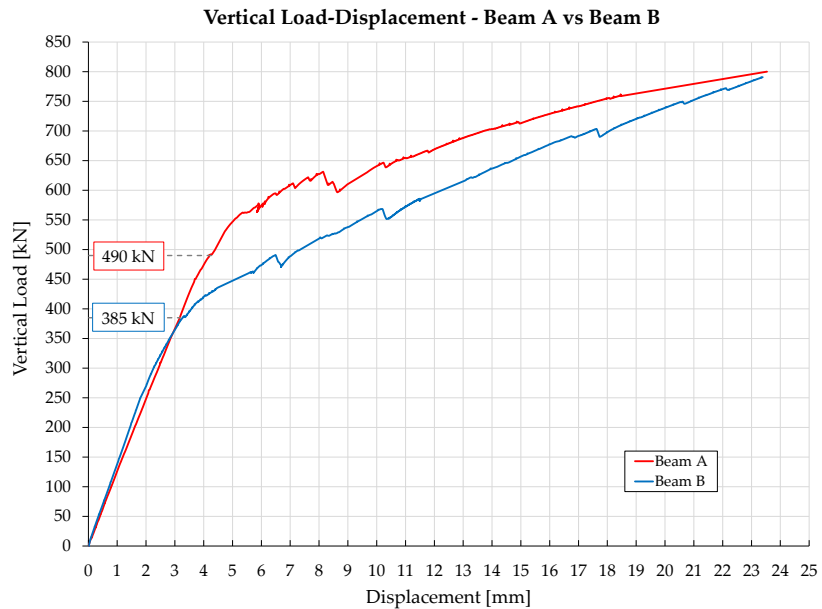


Figure 4-115: Comparison of the first flexural cracking load of pre-tensioned beams – Beams A and B.

4-EXPERIMENTAL RESULTS AND DISCUSSION

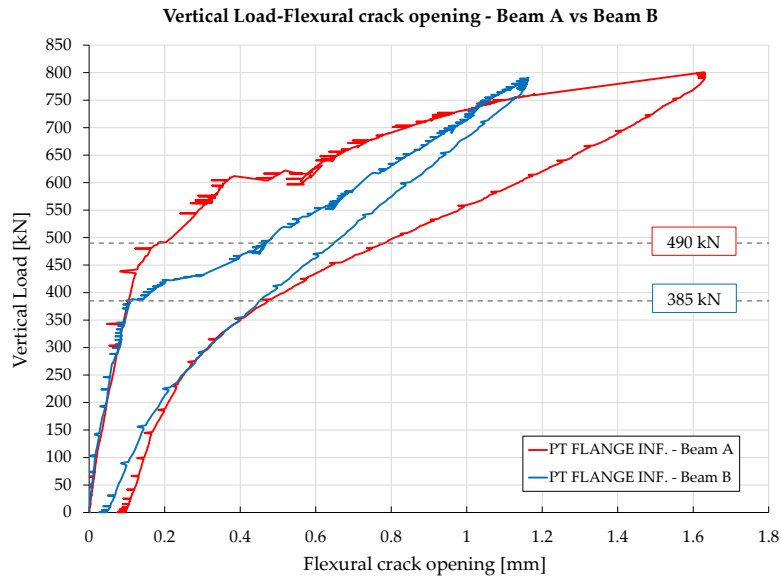


Figure 4-116: Comparison of flexural crack openings in pre-tensioned beams – Beams A and B.

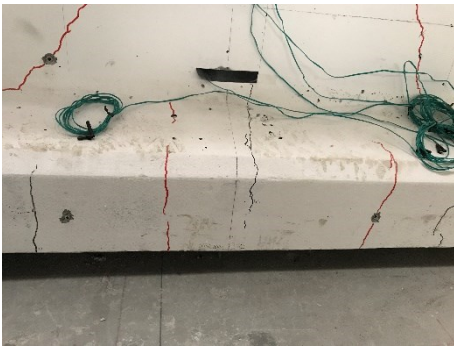


Figure 4-117: Lower flange detail
(Front view) – Beam A.



Figure 4-118: Lower flange detail
(Front view) – Beam B.

From the graph shown in Figure 4-119, it can be seen the vertical load at which the first flexural cracks are formed, coincides with the point at which the strands begin to work.

Referring to Figure 4-119, it's important to point out that there is an uncertainty in the starting value of the stress in the strands. The reason is that the tension of the pre-tensioned beams was estimated using an analytical calculation (§3.3.5), which has approximations.

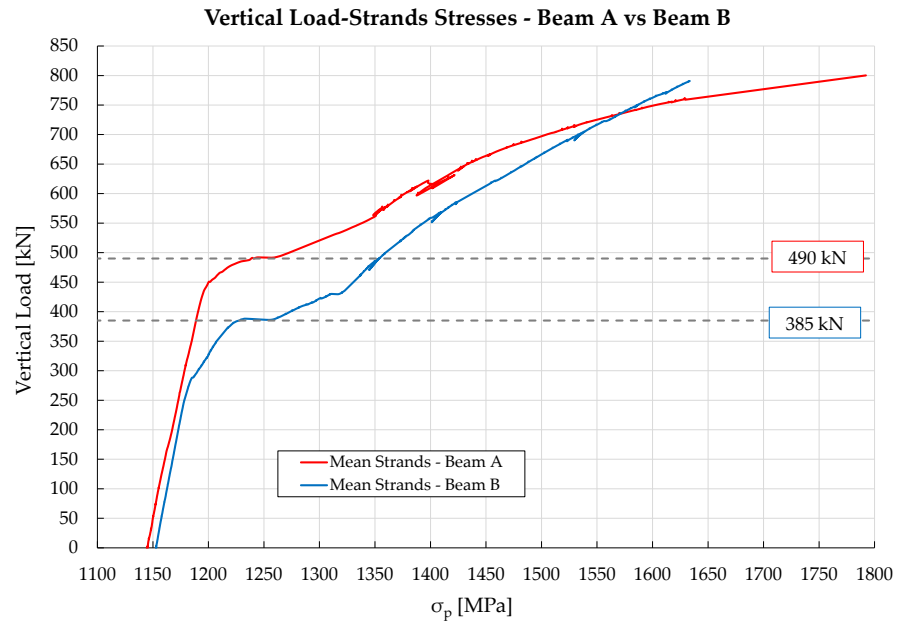


Figure 4-119: Comparison of mean stresses in strands in pre-tensioned beams – Beams A and B.

About the different shear behaviour exhibited by the two beams, it can be seen from Figure 4-120 that, similarly to what happened in flexural behaviour, the first shear cracks appear in Beam B at a vertical load value of 490 kN, which is approximately 22% lower than the one relative to the first shear crack recorded in the test on Beam A (630 kN). This can also be observed by looking at the graph in Figure 4-121 showing the stress trend of the instrumented stirrups n° 6. A shift in the σ can be observed for the same load values at which the first strength drops are seen in the load-displacement curves in Figure 4-120. This behaviour is because, at this value of the applied vertical load, the stresses move from the concrete to the transverse reinforcement and the latter begins to work.

4-EXPERIMENTAL RESULTS AND DISCUSSION

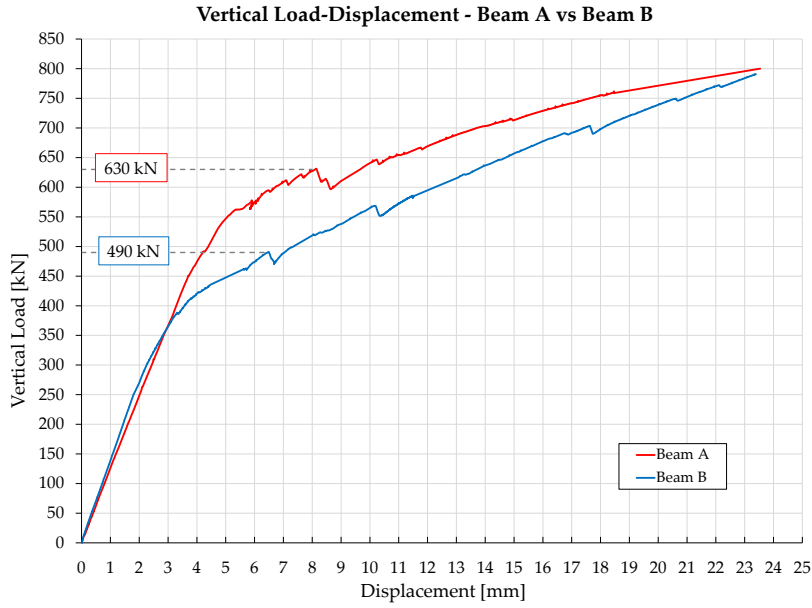


Figure 4-120: Comparison of the first shear cracking load of pre-tensioned beams – Beams A and B.

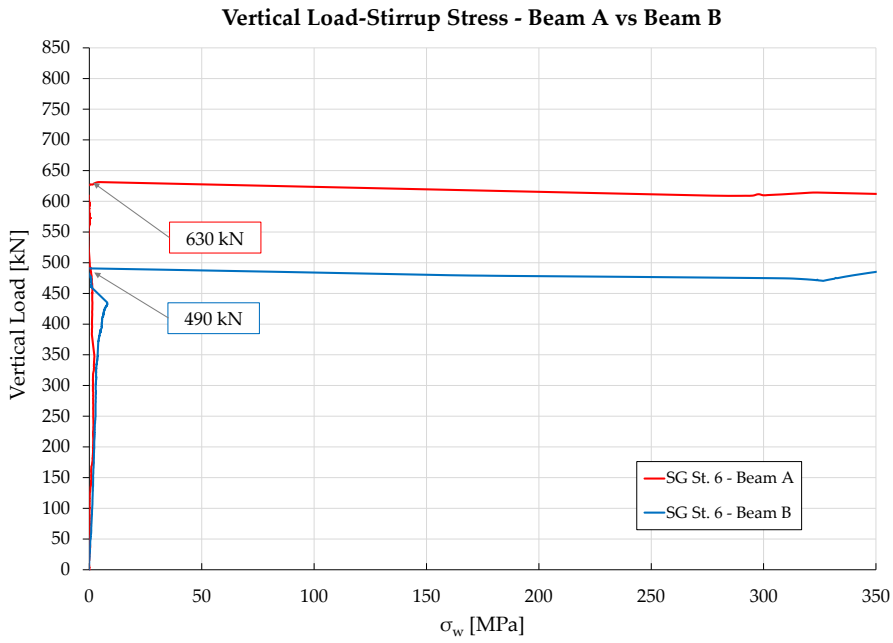


Figure 4-121: Comparison of stresses in stirrups ST. 6 as the vertical load increases – Beams A and B.

From the diagrams shown in Figure 4-122, Figure 4-123 and Figure 4-124, it is possible to have an additional check regarding the first shear crack load. These graphs show the vertical load at which the diagonal potentiometers, installed on the web, begin to register the opening of the cracks. DIAG. 1, in both beams, records crack openings earlier than DIAG 2 and DIAG 3; this can be justified by the fact that, as this is the closest potentiometer to the load point, it was also partially affected by flexural cracks propagating into the web.

DIAG. 2 e DIAG. 3 are not affected by flexural cracks and from the analysis of their graphs (Figure 4-123 and Figure 4-124) it can be seen that the lower prestress present in Beam B caused a crack pattern with greater shear crack openings than those measured in Beam A.

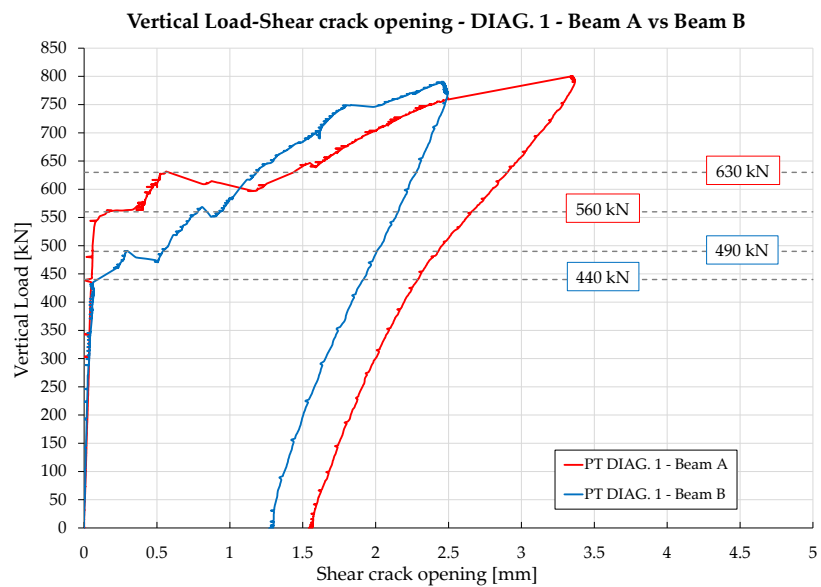


Figure 4-122: Comparison of shear cracks recorded by potentiometers DIAG. 1 in the pre-tensioned beams – Beams A and B.

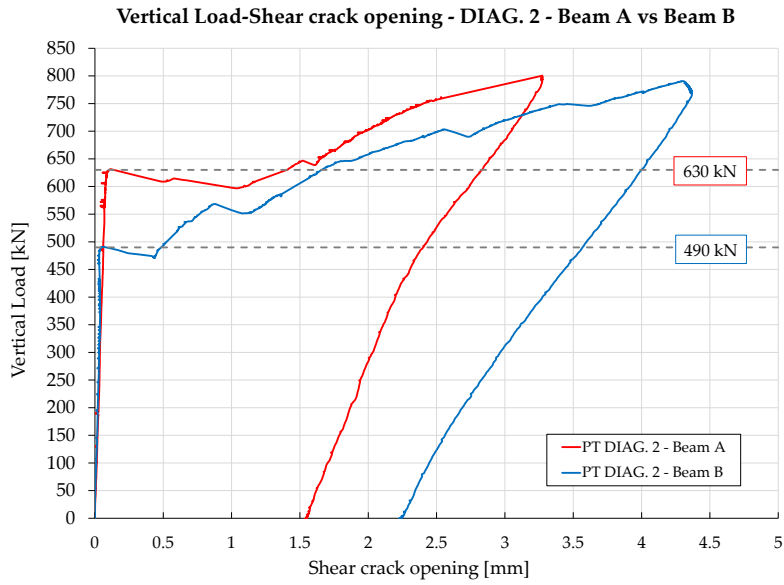


Figure 4-123: Comparison of shear cracks recorded by potentiometers DIAG. 2 in the pre-tensioned beams – Beams A and B.

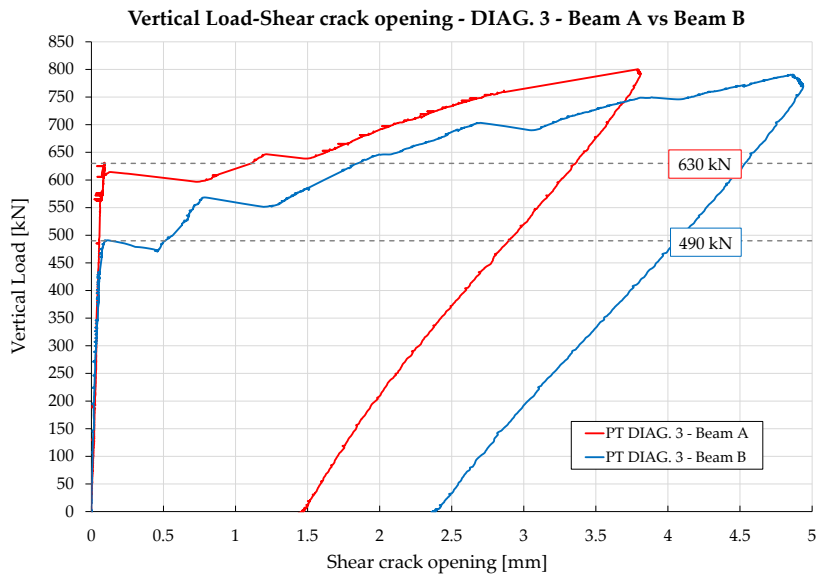


Figure 4-124: Comparison of shear cracks recorded by potentiometers DIAG. 3 in the pre-tensioned beams – Beams A and B.

Figure 4-125 shows a comparison of flexural and shear crack patterns evolution during the two tests (the graph for the shear cracks is relative to DIAG. 2, which is very similar to the DIAG. 3 graph). It should be noted that the graphs represent the sum of several cracks intercepted by the potentiometers. Table 4-16 shows the flexural and shear crack opening values as a function of the vertical load applied.

It can be seen that at 450 kN of vertical load, Beam A did not register any flexural cracks, as it should be with a load comparable to the service one, while in Beam B cracks with an overall opening of 0.4 mm have already been shown. As regards the diagonal cracking on the web of the beams, at 500 kN of vertical load, comparable to the service load, Beam B shows cracks with an overall opening of 0.45 mm, while Beam A exhibits its first shear crack with a load between 600 and 650 kN, when in Beam B the overall crack opening is between 1.57 mm and 1.95 mm.

Figure 4-126 shows a comparison of front and back views of the crack patterns once the tests are completed. It is evident that the crack diffusion on Beam B is more intense. Thanks to the prestress the cracks closed almost completely during the vertical unloading phase.

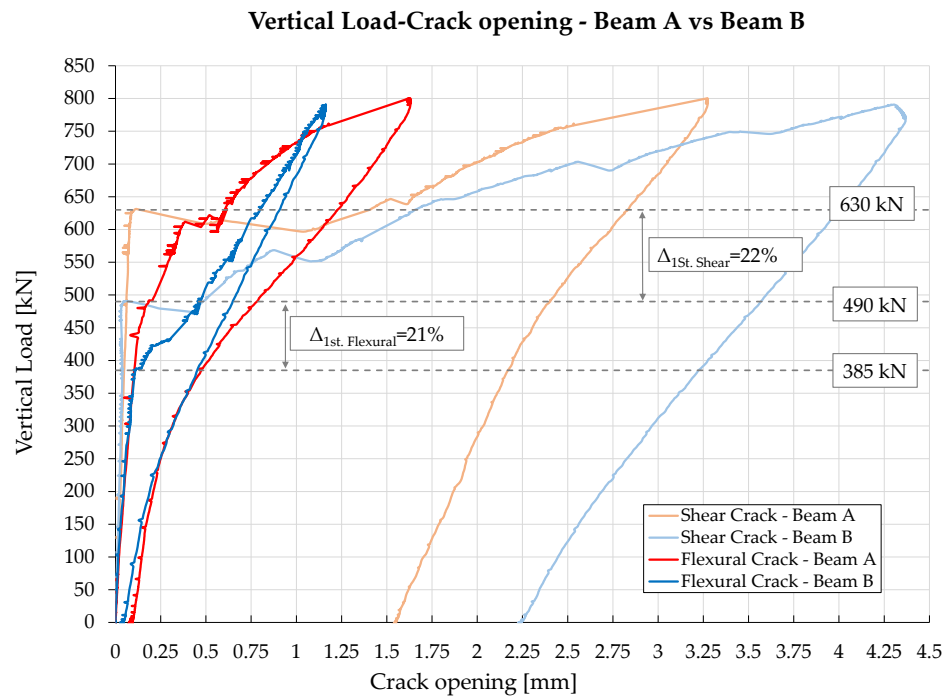


Figure 4-125: Comparison of the evolution of flexural and shear crack patterns during the two tests of the pre-tensioned beams – Beams A and B.

4-EXPERIMENTAL RESULTS AND DISCUSSION

Table 4-16: Comparison of crack openings as a function of the vertical load applied – Beams A and B.

Progression of the FLEXURAL crack pattern			Progression of the SHEAR crack pattern		
Load [kN]	Beam A	Beam B	Load [kN]	Beam A	Beam B
400	-	0.15 mm	400	-	-
450	-	0.40 mm	450	-	-
500	0.20 mm	0.48 mm	500	-	0.45 mm
550	0.30 mm	0.60 mm	550	-	0.75 mm
600	0.35 mm	0.75 mm	600	-	1.57 mm
650	0.67 mm	0.84 mm	650	1.64 mm	1.95 mm
700	0.87 mm	0.97 mm	700	1.95 mm	2.83 mm
750	1.10 mm	1.05 mm	750	2.42 mm	3.71 mm
800	1.63 mm	1.16 mm	800	3.27 mm	4.36 mm

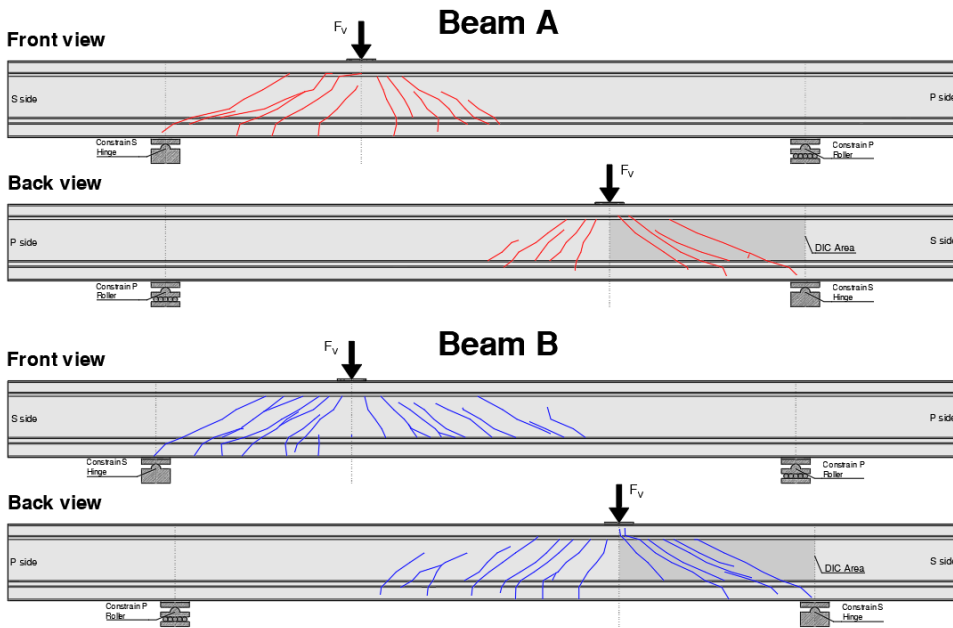


Figure 4-126: Detection of the crack pattern at the end of the load test:
Beam A $F_v=800$ kN, Beam B $F_v=790$ kN.

After the experimental tests were carried out, it emerged that Beam B showed the first flexural and shear cracks for load values approximately 20% lower than what occurred in Beam A in both cases (see Figure 4-25 and Table 4-17).

Table 4-17: Comparison between Beam A and Beam B concerning the first flexural crack load and the first shear crack load. () the percentage referred to 1130 kN.*

	Beam A	Beam B	Difference
Level of prestress	955 kN (85%*)	641 kN (57%*)	28%
1st Flexural crack	490 kN	385 kN	21%
1st Shear crack	630 kN	490 kN	22%

The crack pattern evolution is detailed in §4.2.7.1.

In conclusion, it can be seen that the percentage reduction in the prestressing loss between the two beams (28%) is directly comparable to the percentage of load reduction (20%), which anticipates the exit from the elastic stage and the development of flexural crack patterns. This expected load reduction is a further proof that a long-term reduction of prestressing can generate significant cracking, both in flexure and in shear, even at service loads.

4-EXPERIMENTAL RESULTS AND DISCUSSION

4.2.6.2 Results comparison Beam A - Beam C2

From the comparison of the experimental curves in Figure 4-127 relatives to Beam A and Beam C2, it can be seen that both maintain the same response in terms of resistance up to a load of 600 kN. It should be noted that Beam A has six pre-stressed strands (7-wire 6/10" strands) with an effective tension, net of losses, of 955 kN ($\sigma_{p\infty} = 1145$ MPa), while Beam C2 has seven post-stressed strands (7-wire 6/10" strands) with an effective tension, net of losses, of 993 kN ($\sigma_{p\infty} = 1021$ MPa). A post-tension force was applied to Beam C2 to reproduce the same tension present in Beam A net of prestressing losses. By looking at the two experimental curves, it can be seen that Beam C2 exhibits more ductile behaviour than Beam A.

This may be related to two main factors:

- The lack of bond between the strands and the concrete in Beam C2 causes the prestressing reinforcement to work as a tension tie and create an arching effect.
- Presence of an extra strand in Beam C2 compared to Beam A.

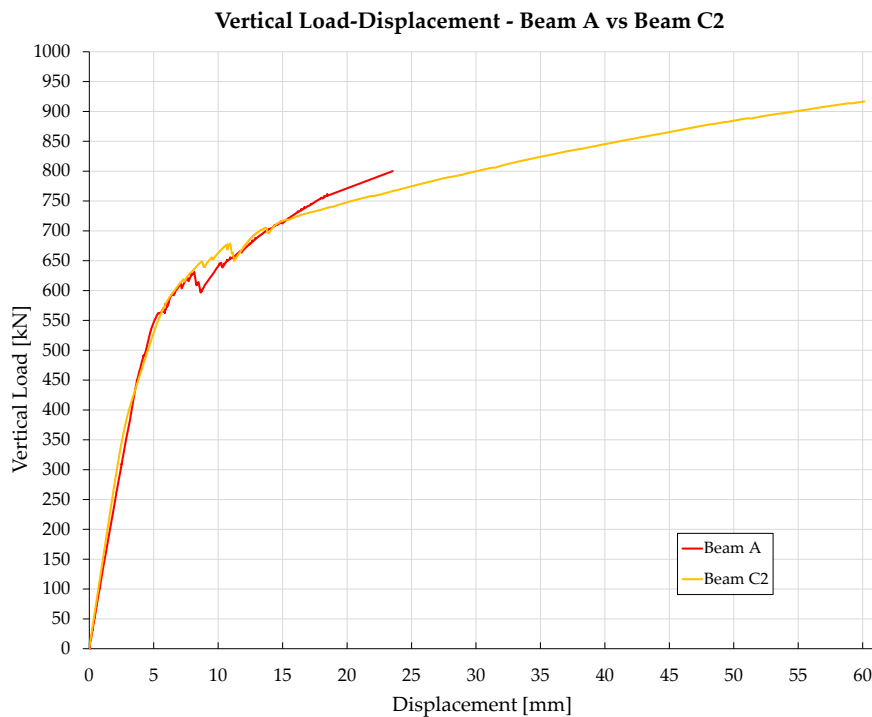


Figure 4-127: Comparison of the two vertical load-displacement curves
– Beams A and C2.

Figure 4-128 shows the comparison of the crack openings recorded by the potentiometers installed on the lower flange under the load point. In a condition close to collapse, the crack opening is six times greater in Beam C2 than in Beam A, whereas up to a service load (400-450 kN), the two curves exhibit the same behaviour.

The exit point from the elastic stage cannot be compared, as Beam C2 shows a loss of stiffness already with an applied vertical load of 400 kN (due to the pre-cracking of the load-unload cycle at 60-65% prestressing).

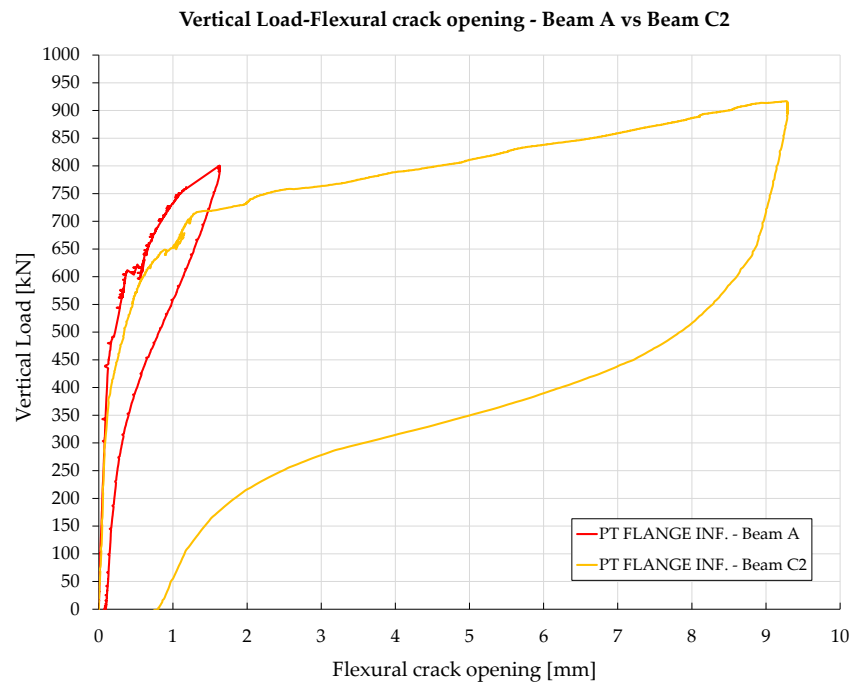


Figure 4-128: Comparison of flexural crack opening – Beams A and C2.

Regarding the diagonal cracks, in Beam C2 they cross only the potentiometer PT_DIAG. 1, while on Beam A they intercept all three inclined instruments.

Figure 4-129 shows the comparison of data recorded by the DIAG. 1 installed on the two beams. It can be seen that the formation of the first inclined crack in the web occurs at a load of 630 kN and 690 kN for Beam A and Beam C2, respectively. Furthermore, it is observed that in Beam C2 the crack formation was more instantaneous than in Beam A. This difference may be related to the fact that Beam C2 has unbonded tendon.

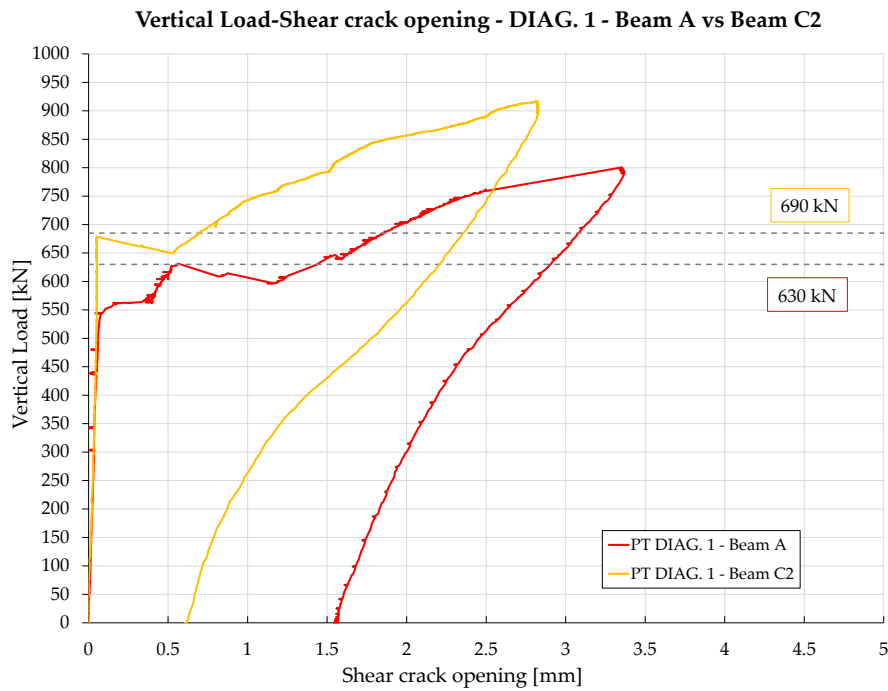
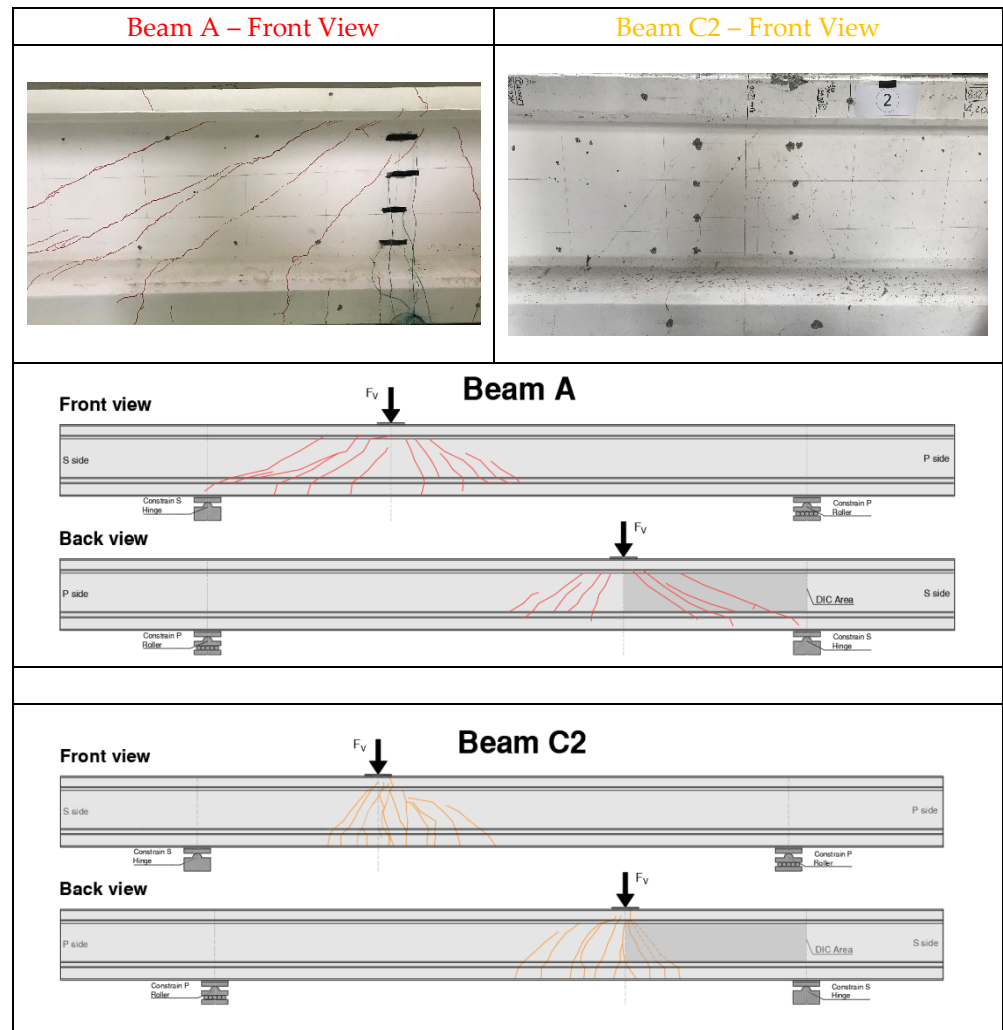


Figure 4-129: Comparison of shear crack opening recorded by potentiometers DIAG. 1 in the prestressed beams – Beams A and C2.

Comparing the crack pattern in Table 4-18, it is evident that the collapse conditions of Beam A and Beam C2 are predominantly shear and flexure, respectively. Moreover, one should note that the cracking in Beam C2 is rather concentrated around the point load, whereas, in Beam A, a more diffused cracking pattern toward the support developed. This is certainly due to the different bond conditions of the strands.

Table 4-18: Comparison of cracking pattern under the load point – Beams A and C2.



Further investigation of the crack pattern evolution is detailed in §4.2.7.2.

4-EXPERIMENTAL RESULTS AND DISCUSSION

4.2.6.3 Results Comparison Beam C1 and Beam C2

The post-tensioning system allowed to control of the level of prestress; three constant vertical loads (typical service loads) were applied for Beam C1, and for each one (500 kN, 550 kN and 600 kN) the prestress was gradually reduced from 100% to $\approx 50\%$. It was observed that the configuration with an applied vertical load of 600 kN and a prestressing level of 71% of the design tension, led Beam C1 to ultimate conditions, almost like the near-collapse conditions reached in the test on Beam C2, although a 34% lower vertical load was applied to Beam C1. Table 4-19 shows the main differences that resulted from the tests carried out on these two beams. Figure 4-130 shows the comparison between the experimental vertical load-displacement curves of the two beams.

Table 4-19: Comparison of prestress level, vertical load and deformation under near-collapse conditions. (*) percentage referred to 1130 kN.

		Beam C1	Beam C2	Δ
Initial Tendon Prestress	[kN]	535 (47%*)	993 (88%*)	193 (41%*)
Vertical Load	[kN]	600	916	316 (34%)
Tendon tension under vertical load	[kN]	800 (71%*)	1395 (123%*)	595 (52%*)
Deflection	[mm]	52	60	8

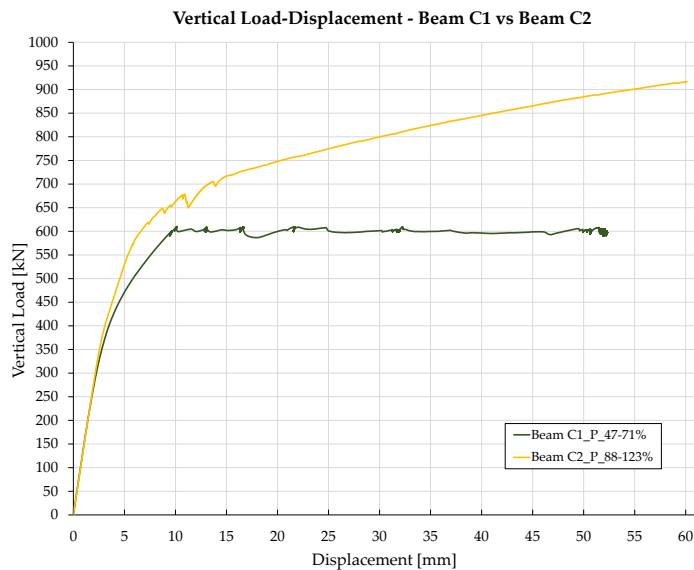
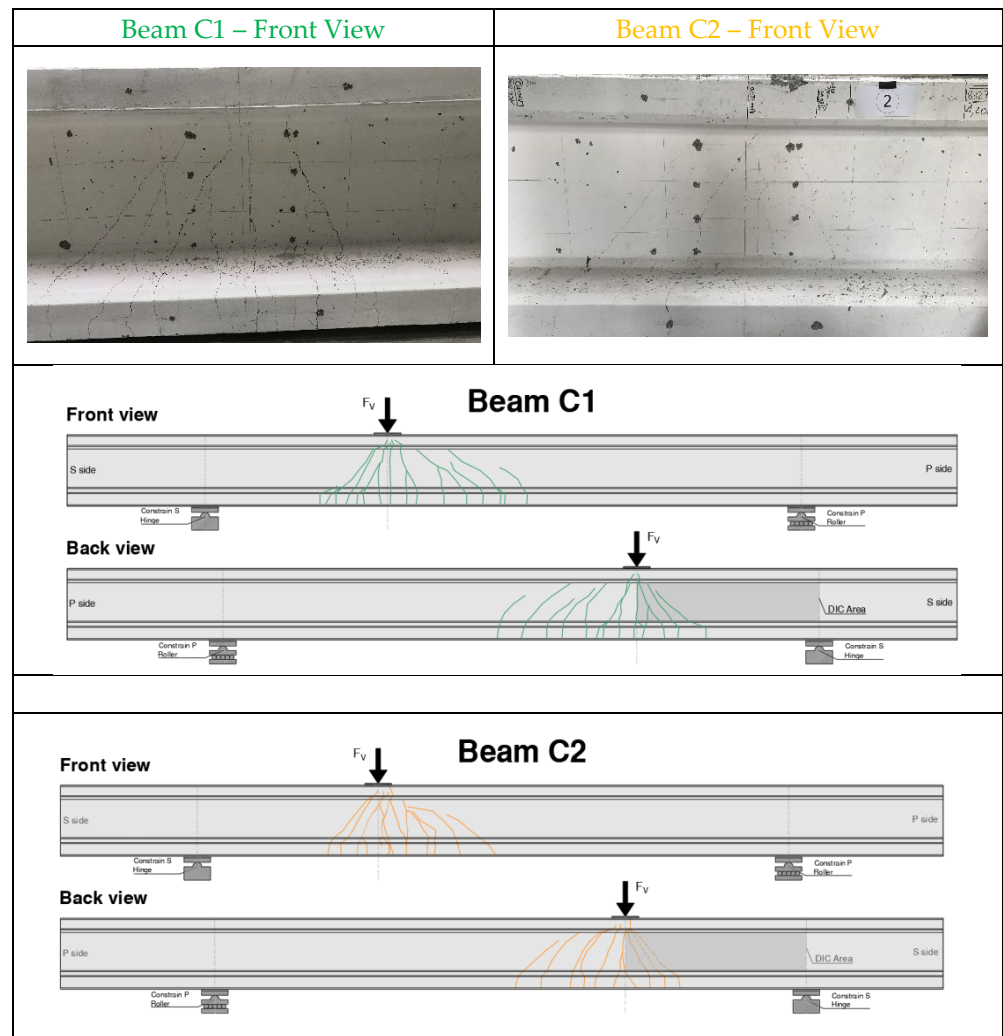


Figure 4-130: Comparison of the two vertical load-displacement curves – Beams C1 and C2.

Table 4-20 shows how the crack pattern below the load point, is very similar for the two post-tensioned beams with unbonded cables, despite the different prestressing and applied load conditions.

It is interesting to note that the prestress difference related to the simulated long-term losses in the beam contributes, in an almost directly proportional way, to the vertical load difference that led to the collapse of the element.

Table 4-20: Comparison of cracking pattern under the load point – Beams C1 and C2.



4.2.7 Comparison of DIC crack pattern maps

4.2.7.1 Comparison: Beam A – Beam B

The diagonal potentiometers installed on the front side of the beam intercept multiple cracks, providing limited information about the crack pattern formation. Thanks to the photographs made using the DIC technique, it was possible to know the crack pattern formation evolution, so it was possible to compare the crack openings under typical service load between the two Beams tested (with different prestressing levels).

From Table 4-21, Table 4-22 and Table 4-23 is possible to appreciate the three different ways used to measure diagonal crack openings:

- PT_DIAG_# = Real Potentiometer intercepting several cracks on the front side of the beam;
- DIG_DIAG_# = GOM software instrument simulating a digital strain gauge, positioned in the same position as PT_DIAG_#, but on the DIC pattern side (back side of the beam), also intercepts multiple cracks;
- $\Sigma_CRACKs_{\#1+\#2+\dots}$ = sum of small instruments of the GOM software simulating digital strain gauges, positioned on all cracks intercepted by the digital strain gauge DIG_DIAG_# (back of beam).

Graphs in Figure 4-131 show the comparison between the two methods used in the calculation of crack openings using the DIC technique. The result obtained by considering the sum of several cracks appears to be more consistent with the measurement made by the physical potentiometer installed on the beam, compared with the results provided by the single digital instrument set up in the GOM software to intercept all the cracks by simulating what happens with the physical potentiometer placed on the opposite face of the beam. The consistency between PT_DIAG_# e $\Sigma_CRACKs_{\#1+\#2+\dots}$ is most visible in the detection of cracks in the elastic stage, whereas the DIG_DIAG_# shows a shift along the x-axis. The differences found between PT_DIAG_# e $\Sigma_CRACKs_{\#1+\#2}$ at high vertical load levels may be caused by the fact that the potentiometer intercepts cracks that are not through the thickness of the web and therefore cannot be identified with the DIC.

Furthermore, the difference between the DIC and instrumentation is between 0.2 mm and 0.1 mm depending on the resolution of the camera and the lens. Considering that the crack pattern and the displacement were not completely equal for both sides of the specimen, the difference was acceptable [Zhang et al., 2020]. In general, the accuracy of DIC is dependent on the quality of the pattern, the subset size, the resolution of the camera and the lens [Amiot et al., 2013; Barranger et al., 2010].

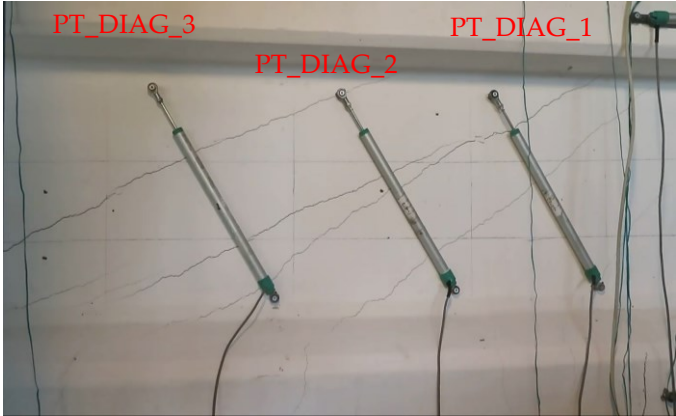
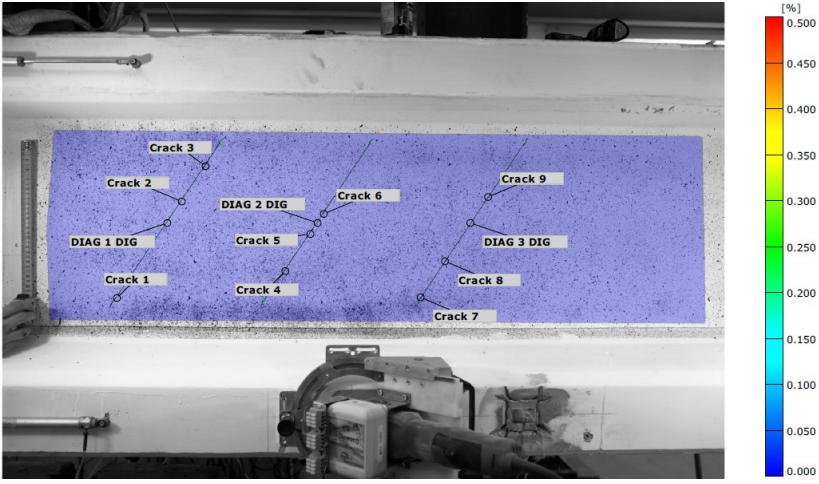
Following these considerations, the results presented below will be the data for $\Sigma_CRACKS_{\#1+\#2+\dots}$

Table 4-21: Comparison of the number of cracks intercepted by real and virtual instruments.

Beam	N° of cracks intercepted by the instrument					
	Real: PT_DIAG_#			Digital: DIG_DIAG_#		
	1	2	3	1	2	3
A	3	3	3	3	3	3
B	3	6	4	4	6	6

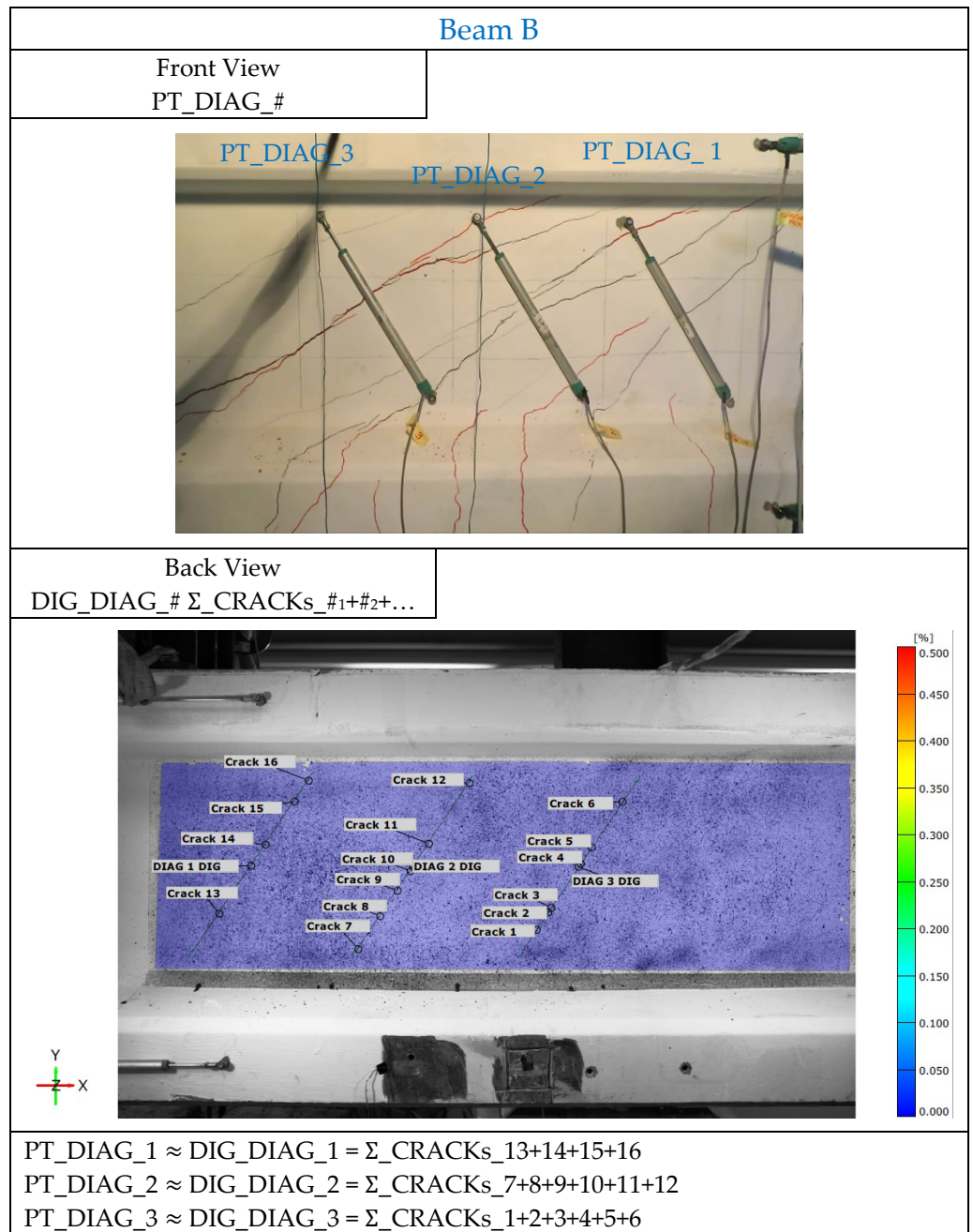
4-EXPERIMENTAL RESULTS AND DISCUSSION

Table 4-22: Comparison of diagonal crack openings (front and back side) – Beam A.

Beam A	
Front View PT_DIAG_#	
Back View DIG_DIAG_# $\Sigma_CRACKs_{\#1+\#2+\dots}$	
<p>PT_DIAG_1 \approx DIG_DIAG_1 = Σ_CRACKs_{1+2+3} PT_DIAG_2 \approx DIG_DIAG_2 = Σ_CRACKs_{4+5+6} PT_DIAG_3 \approx DIG_DIAG_3 = Σ_CRACKs_{7+8+9}</p>	

4-EXPERIMENTAL RESULTS AND DISCUSSION

Table 4-23: Comparison of diagonal crack openings (front and back side) – Beam B.



4-EXPERIMENTAL RESULTS AND DISCUSSION

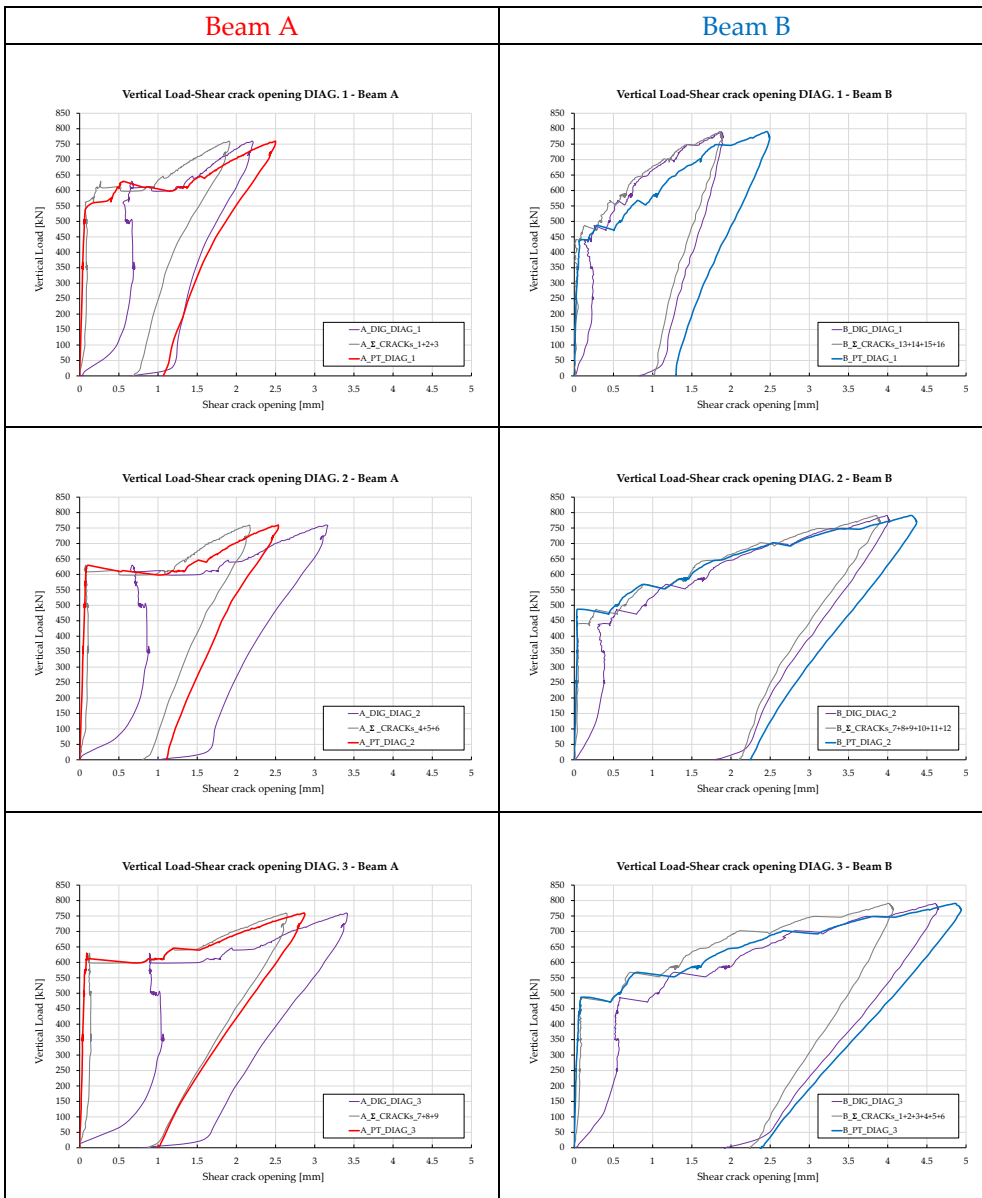


Figure 4-131: Comparison of results obtained from the three different ways used to measure diagonal crack openings.

4-EXPERIMENTAL RESULTS AND DISCUSSION

Table 4-24 shows the crack opening values at different levels of applied vertical load, while Table 4-25 shows an overview of the comparison between the two beams of the crack pattern identified with the DIC technique, at different levels of vertical load.

The comparison of the crack patterns was made at different vertical load levels by identifying the evolution of the individual cracks intercepted by the instruments:

- 440 kN - Table 4-26: First shear crack formation in Beam B identified by GOM;
- 490 kN - Table 4-27: First shear crack formation in Beam B;
- 630 kN - Table 4-28: First shear crack formation in Beam A;
- 690 kN - Table 4-29: First shear crack formation in Beam C2;
- Ultimate condition - Table 4-30.

In the ranges between 440 and 490 kN (Table 4-26 and Table 4-27), at loads still belonging to the elastic stage for Beam A, it is observed that the diagonal cracks in Beam B evolve more than those in Beam A.

This condition continues up to the 630 kN load; above this load, diagonal cracks formed in Beam A. With an applied vertical load of 690 kN, the cracks in Beam A are still the same in number but larger, remaining smaller than those developed in Beam B overall.

The first diagonal crack load in Beam B is heavily influenced by the difference in prestress level compared to Beam A.

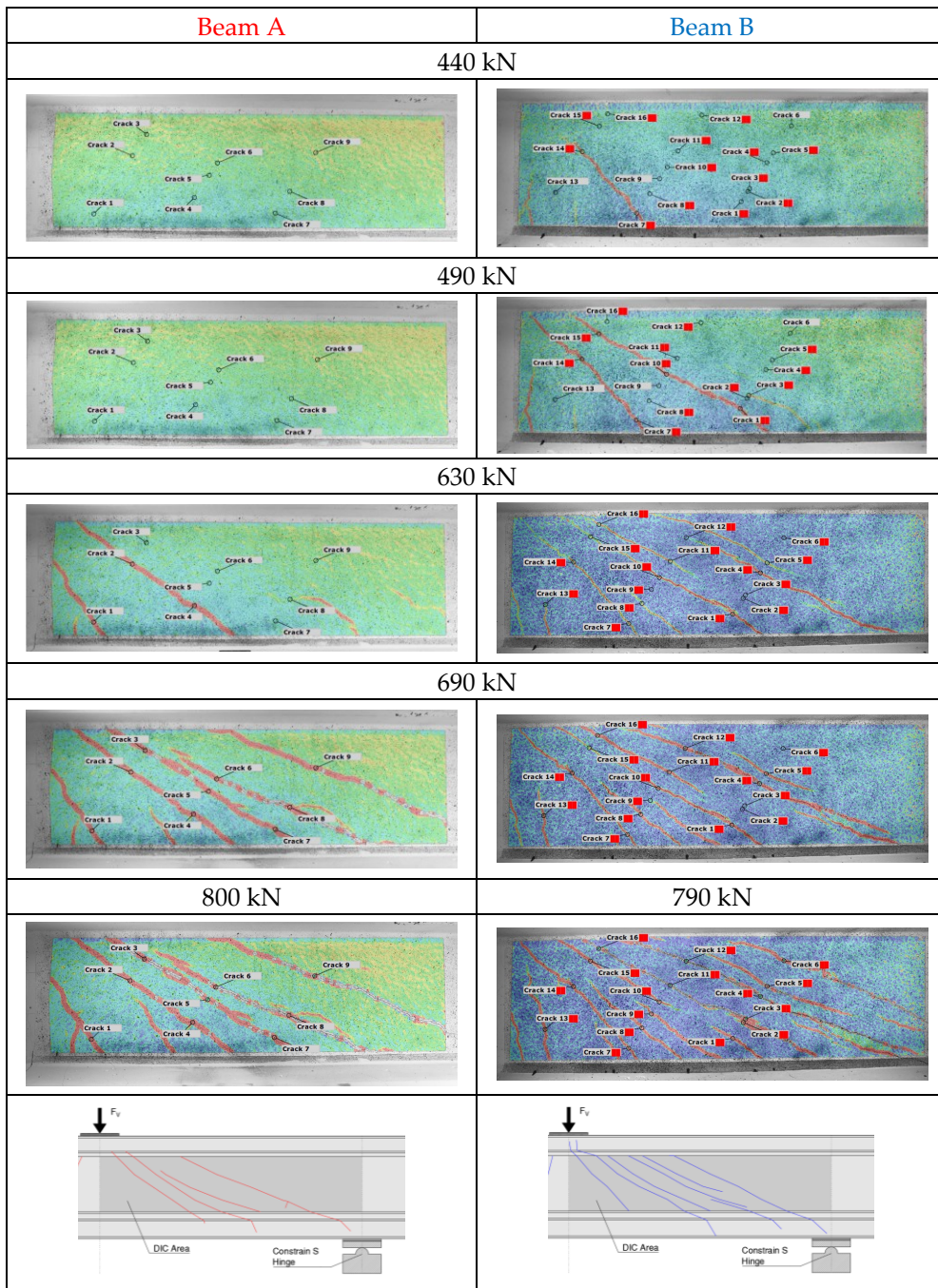
The difference in prestressing of the two beams also influenced the crack map formed as a result of the load tests: the cracks appear more intense and more widely spaced in Beam A, while they are thinner and more diffused in Beam B.

Table 4-24: Comparison of crack openings detected by the three diagonal devices installed.

Step Vertical Load	Σ _CRACKs					
	A	B	A	B	A	B
	1+2+3	13+14+ 15+16	4+5+6	7+8+9 +10+11+12	7+8+9	1+2+3 +4+5+6
[kN]	[mm]	[mm]	[mm]	[mm]	[mm]	[mm]
440	0.09	0.06	0.11	0.18	0.14	0.07
490	0.09	0.31	0.10	0.59	0.14	0.52
630	0.27	0.74	0.08	1.55	0.12	1.50
690	1.39	1.08	1.59	2.27	1.88	2.01
790 (B) 800 (A)	1.90	1.85	2.16	3.85	2.63	4.00

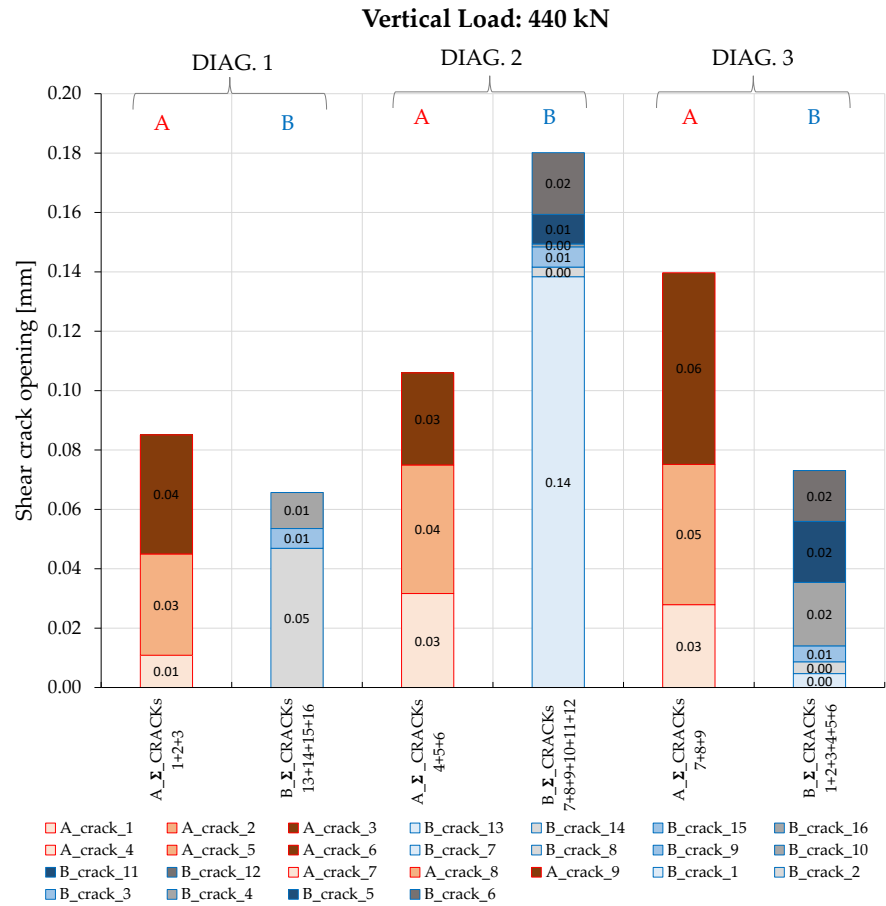
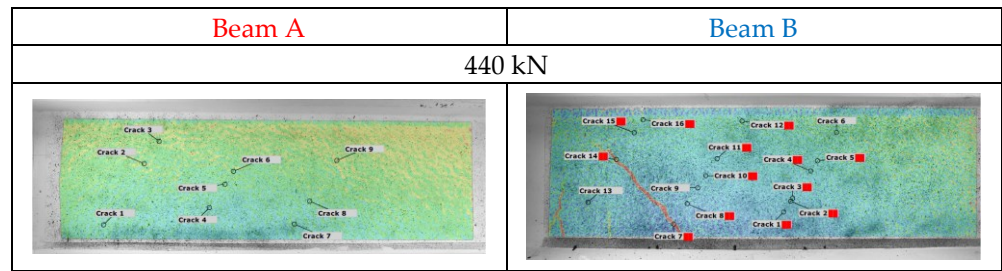
4-EXPERIMENTAL RESULTS AND DISCUSSION

Table 4-25: Comparison of the crack pattern using the DIC technique at different vertical load levels.



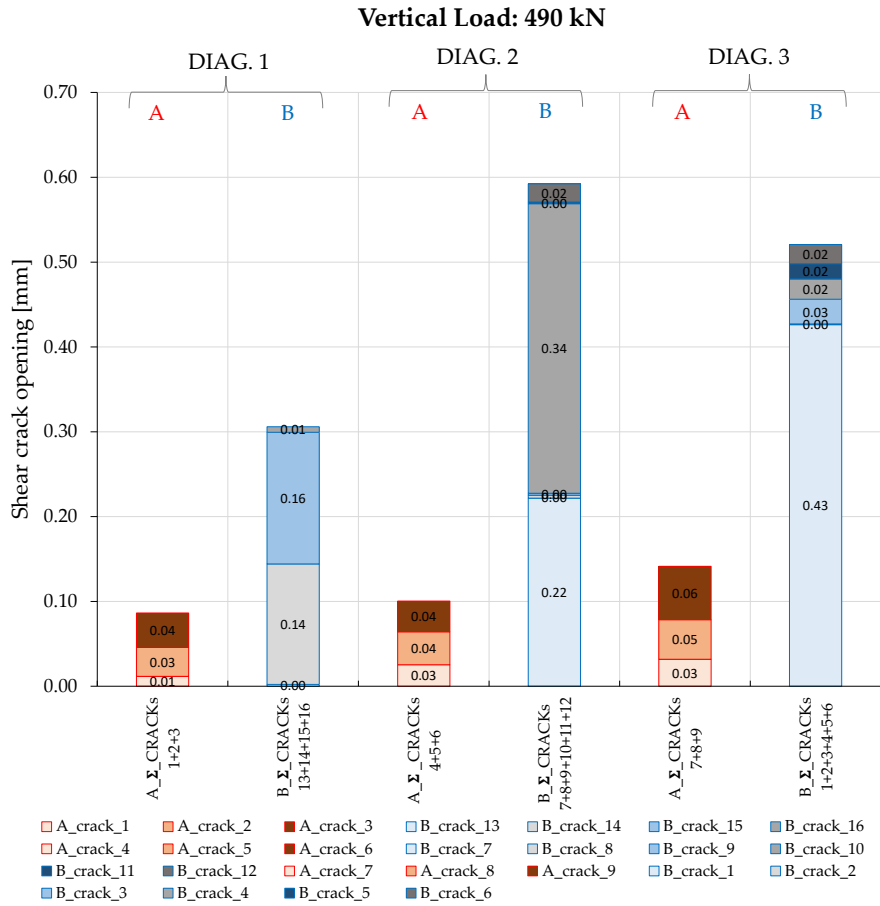
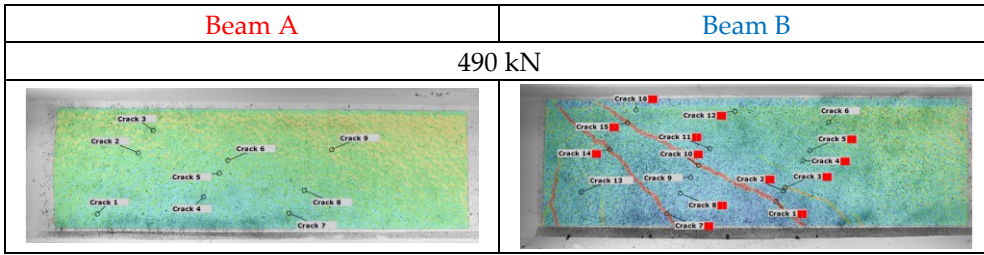
4-EXPERIMENTAL RESULTS AND DISCUSSION

Table 4-26: Comparison of crack pattern between Beam A and Beam B with vertical load: 440 kN.



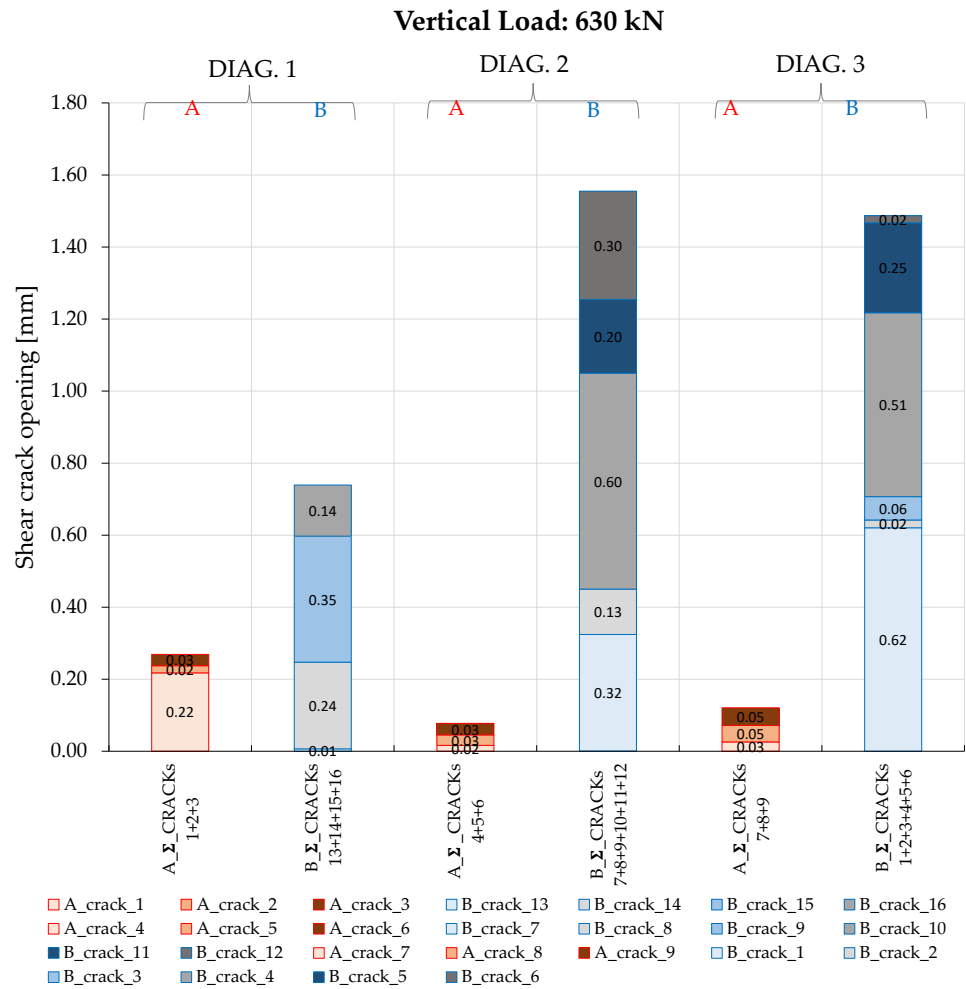
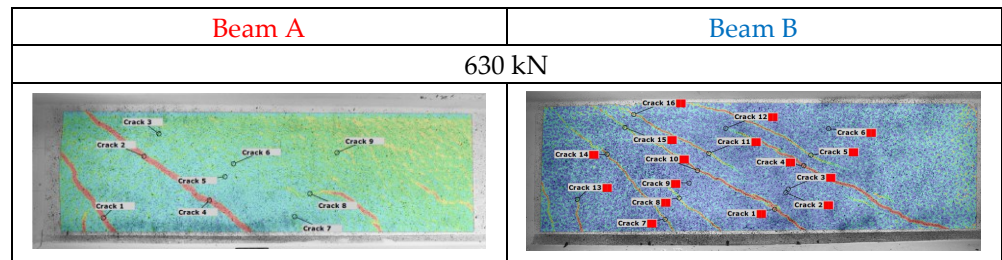
4-EXPERIMENTAL RESULTS AND DISCUSSION

Table 4-27: Comparison of crack pattern between Beam A and Beam B with vertical load: 490 kN.



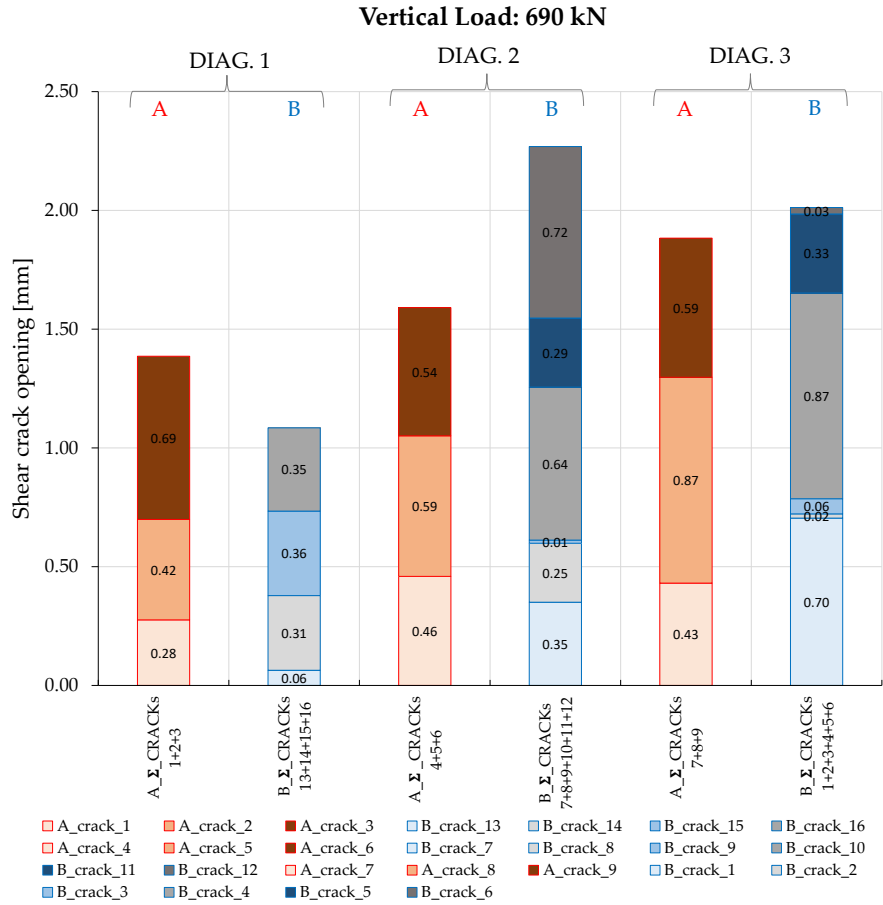
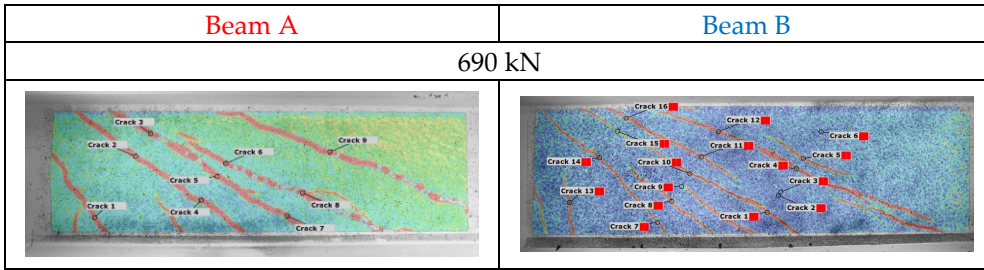
4-EXPERIMENTAL RESULTS AND DISCUSSION

Table 4-28: Comparison of crack pattern between Beam A and Beam B with vertical load: 630 kN.



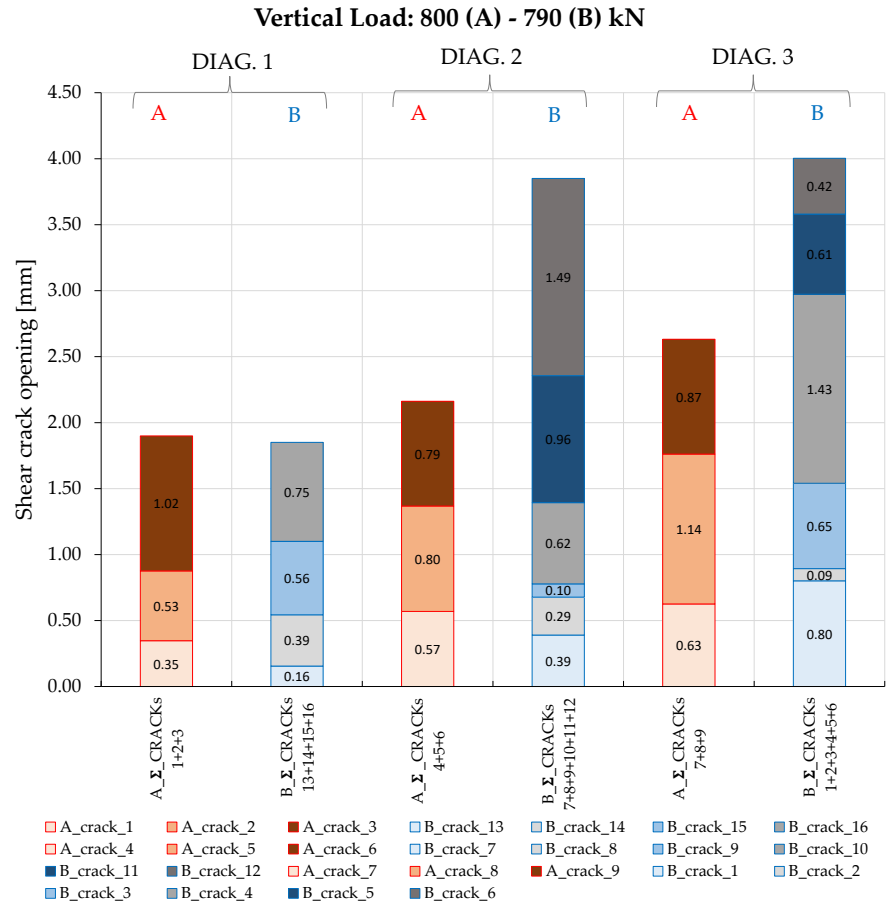
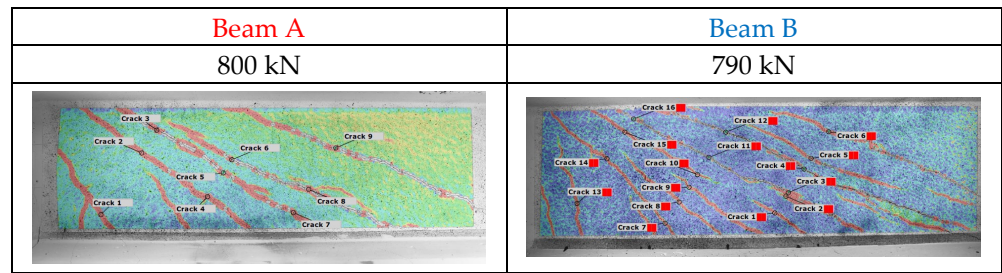
4-EXPERIMENTAL RESULTS AND DISCUSSION

Table 4-29: Comparison of crack pattern between Beam A and Beam B with vertical load: 690 kN.



4-EXPERIMENTAL RESULTS AND DISCUSSION

Table 4-30: Comparison of crack pattern between Beam A and Beam B with vertical load: 800-790 kN.



4-EXPERIMENTAL RESULTS AND DISCUSSION

4.2.7.2 **Comparison: Beam A – Beam C2**

From Table 4-31, Table 4-32 and Table 4-33 is possible to appreciate the three different ways used to measure diagonal crack openings:

- PT_DIAG_# = Real Potentiometer intercepting several cracks on the front side of the beam;
- DIG_DIAG_# = GOM software instrument simulating a digital strain gauge, positioned in the same position as PT_DIAG_#, but on the DIC pattern side (back side of the beam), also intercepts multiple cracks;
- $\Sigma_CRACKS_{\#1+\#2+\dots}$ = sum of small instruments of the GOM software simulating digital strain gauges, positioned on all cracks intercepted by the digital strain gauge DIG_DIAG_# (back of beam).

For the same reasons defined in the previous chapter (§4.2.7.1), the results presented below will be the data for $\Sigma_CRACKS_{\#1+\#2+\dots}$.

Table 4-31: Comparison of the number of cracks intercepted by real and virtual instruments.

Beam	N° of cracks intercepted by the instrument					
	Real: PT_DIAG_#			Digital: DIG_DIAG_#		
	1	2	3	1	2	3
A	3	3	3	3	3	3
C2	2	0	0	3	0	0

Table 4-34 shows an overview of the comparison between the two beams of the crack pattern identified with the DIC technique, at different levels of vertical load, while Table 4-35 shows the crack opening values at different levels of applied vertical load.

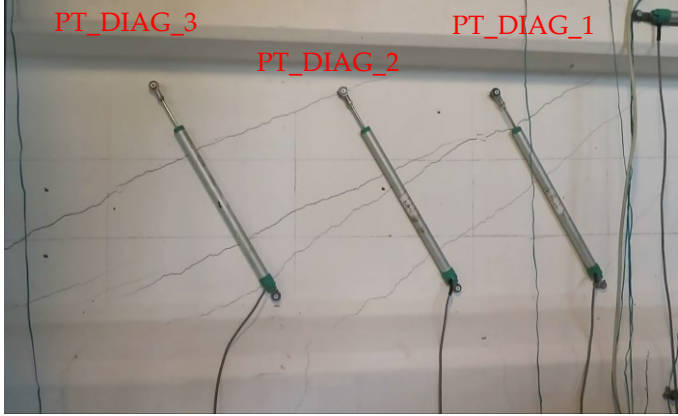
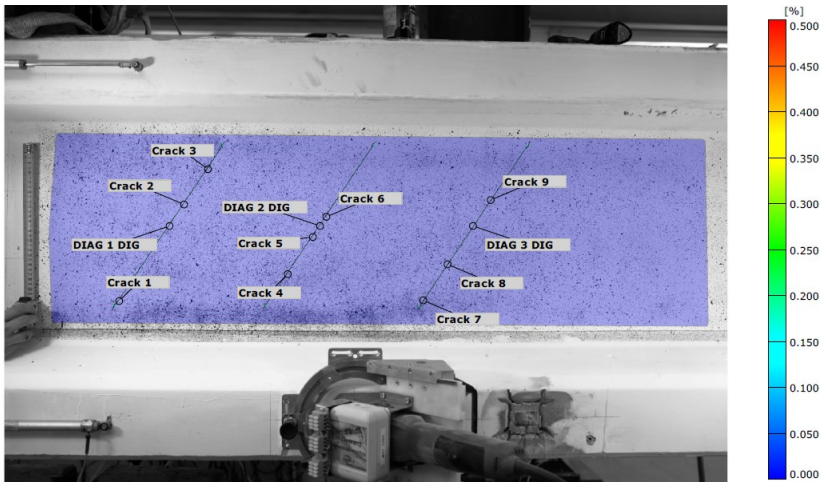
Since the diagonal potentiometers at positions 2 and 3 for Beam C2 did not intercept any cracks (Table 4-33), the comparison will be made only with the results provided by the potentiometer at position 1.

The comparison of the crack patterns was made at different vertical load levels by identifying the evolution of the individual cracks intercepted by the instruments:

- 440 kN - Figure 4-132: First shear crack formation in Beam B identified by GOM;
- 490 kN - Figure 4-132: First shear crack formation in Beam B;
- 630 kN - Figure 4-132: First shear crack formation in Beam A;
- 690 kN - Figure 4-133: First shear crack formation in Beam C2;
- Ultimate condition - Figure 4-133.

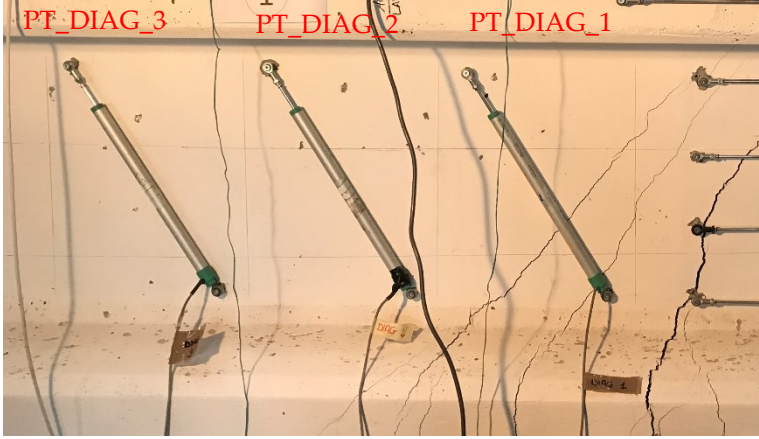
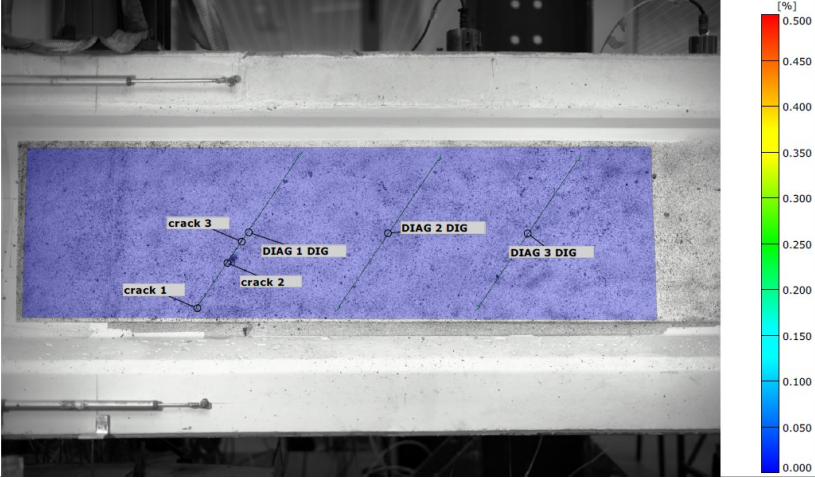
Figure 4-132 shows how the crack in Beam C2 always remains with a smaller opening than those that occurred in Beam A. The large difference between the crack patterns in these two beams is also evident from the images in Table 4-34.

Table 4-32: Comparison of diagonal crack openings (front and back side) – Beam A.

Beam A	
Front View PT_DIAG_#	
Back View DIG_DIAG_# $\Sigma_CRACKs_{\#1+\#2+\dots}$	
$PT_DIAG_1 \approx DIG_DIAG_1 = \Sigma_CRACKs_{1+2+3}$ $PT_DIAG_2 \approx DIG_DIAG_2 = \Sigma_CRACKs_{4+5+6}$ $PT_DIAG_3 \approx DIG_DIAG_3 = \Sigma_CRACKs_{7+8+9}$	

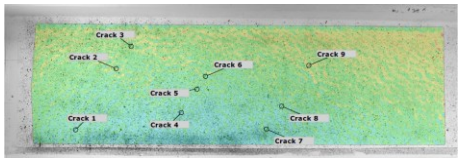
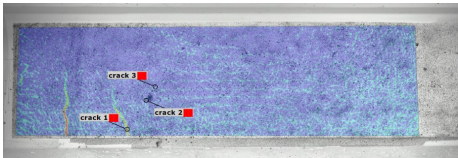
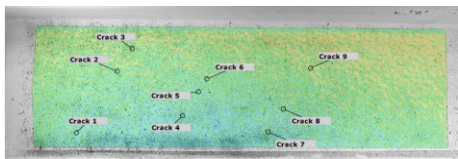
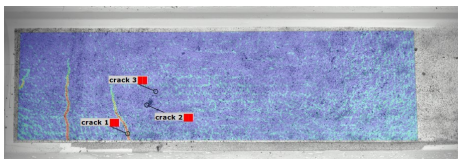
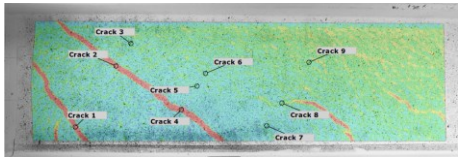
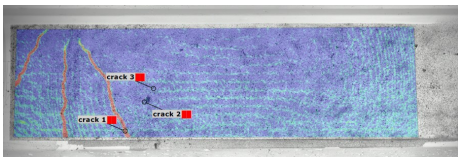
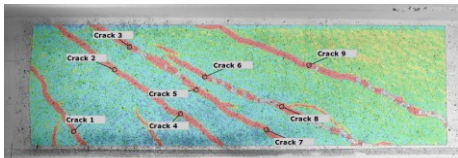
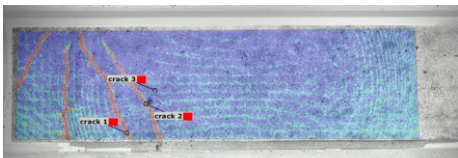
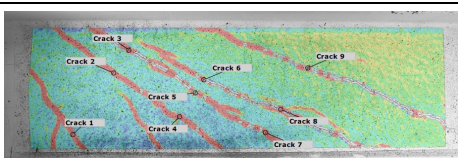
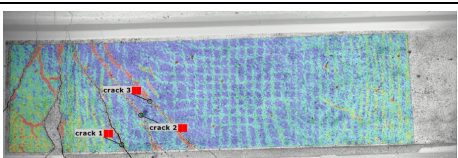
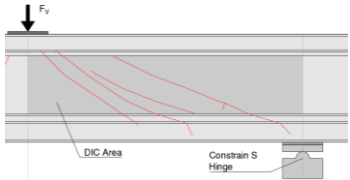
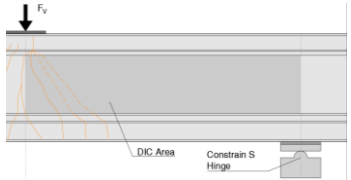
4-EXPERIMENTAL RESULTS AND DISCUSSION

Table 4-33: Comparison of diagonal crack openings (front and back side) – Beam C2.

Beam C2	
Front View PT_DIAG_#	
Back View DIG_DIAG_# $\Sigma_CRACKs_{\#1+\#2+\dots}$	
<p>PT_DIAG_1 \approx DIG_DIAG_1 = Σ_CRACKs_{1+2+3} PT_DIAG_2 \approx DIG_DIAG_2 PT_DIAG_3 \approx DIG_DIAG_3</p>	

4-EXPERIMENTAL RESULTS AND DISCUSSION

Table 4-34: Comparison of the crack pattern using the DIC technique at different vertical load levels.

Beam A	Beam C2
440 kN	
	
490 kN	
	
630 kN	
	
690 kN	
	
800 kN	
	
916 kN	
	

4-EXPERIMENTAL RESULTS AND DISCUSSION

Table 4-35: Comparison of crack openings detected by the three diagonal devices installed.

Step Vertical Load	Σ _CRACKs					
	A	C2	A	C2	A	C2
	1+2+3	1+2+3	4+5+6	-	7+8+9	-
[kN]	[mm]	[mm]	[mm]	[mm]	[mm]	[mm]
440	0.09	0.01	0.11	-	0.14	-
490	0.09	0.03	0.10	-	0.14	-
630	0.27	0.2	0.08	-	0.12	-
690	1.39	0.82	1.59	-	1.88	-
800 (A) 916 (C2)	1.90	4.76	2.16	-	2.63	-

DIAG. 1

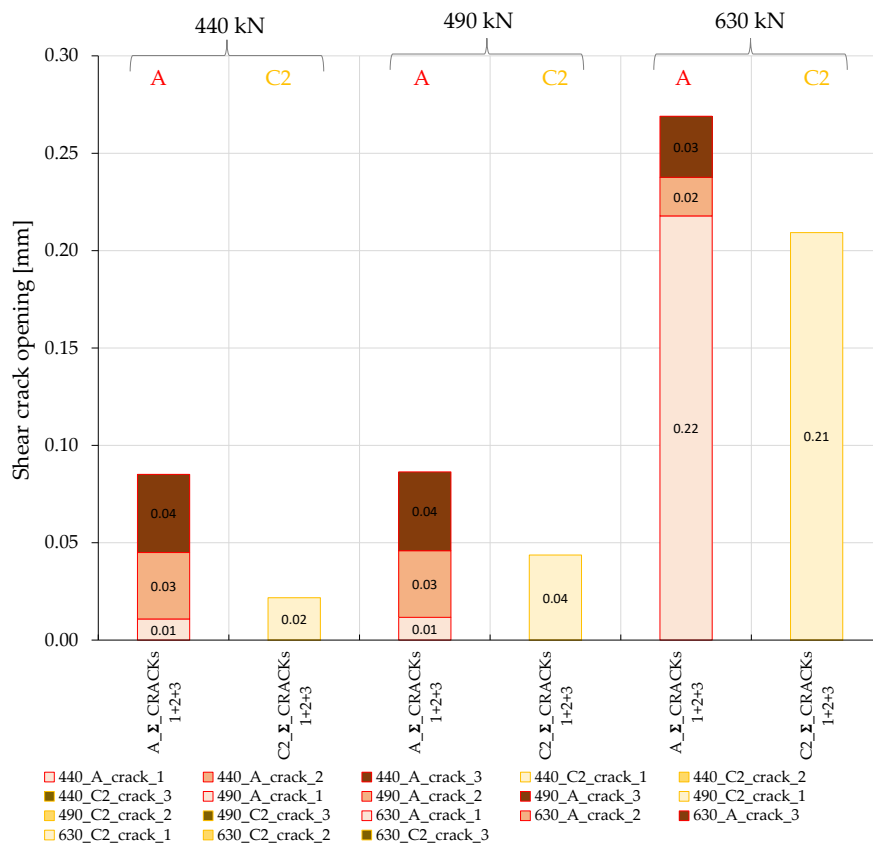


Figure 4-132: Comparison of crack pattern about DIAG. 1 between Beam A and Beam C2 with vertical load: 440-490-630 kN.

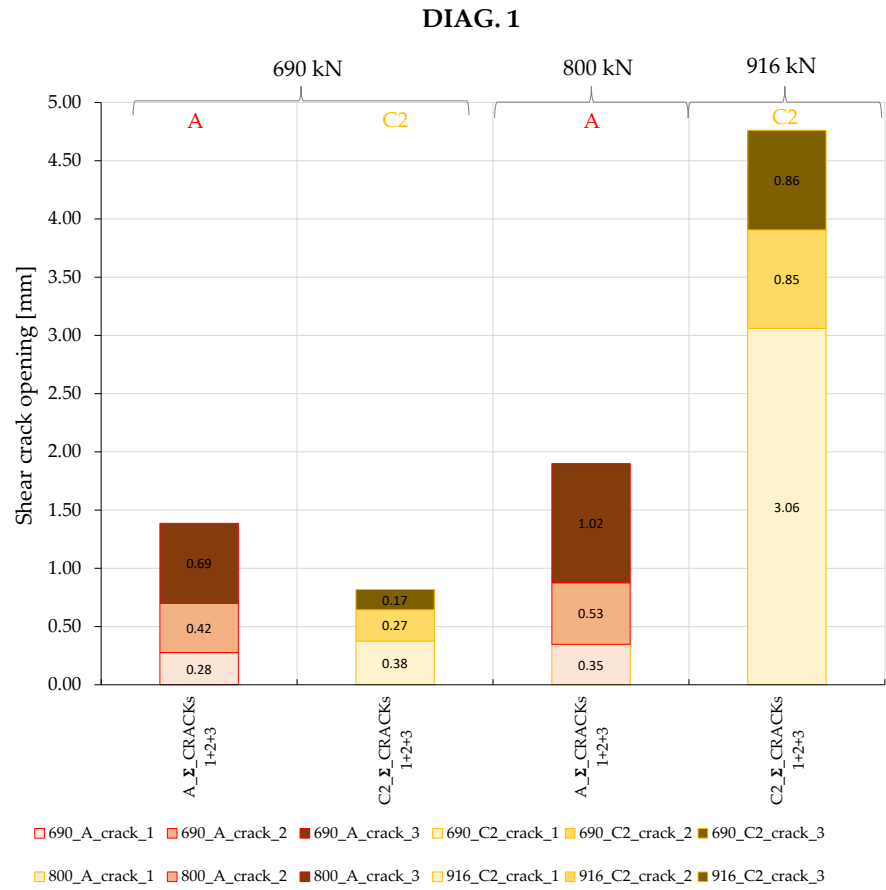


Figure 4-133: Comparison of crack pattern about DIAG. 1 between Beam A and Beam C2 with vertical load: 690-800-916 kN.

4.2.8 Dynamic identification before and after shear damage

A dynamic assessment was carried out on Beam A before and after damage by applying a vertical load of 800 kN. It should be mentioned that Beam A has a prestress of 955 kN (85% of design stress of 1130 kN).

The dynamic identification is done either by recording the free oscillations induced through the "hammer test" or the "ambient vibrations" (i.e., "white noise"). In the first case the acceleration time histories are processed to obtain the relative Fourier spectrum (hence the peak associated with the fundamental frequency) while in the second case, they are processed with the "PP technique" / "FDD technique" to obtain both the fundamental frequency and the relative modal form.

Since it was not possible to correlate a reduction in prestress with a change in the element's own frequency, as explained in §4.1.2.2, the aim became to understand if a change in the modal form could be associated with damage and its location, and consequently to identify a crack pattern attributable to shear damage.

The setup of the positions of constraint remained the same as defined in §3.4 (Figure 4-134). All dynamic acquisitions were carried out with the beam unloaded (also removing the steel thicknesses); therefore, the only load during the dynamic acquisitions was the self-weight. Before and after applying the vertical load (Figure 4-135), five piezoelectric accelerometers (model Wilcoxon 731A) were installed along the upper flange of the beam. The signal acquisition frequency was 600 Hz. The cantilever zones over the supports were not instrumented because they were considered uninteresting for the purposes of this study.

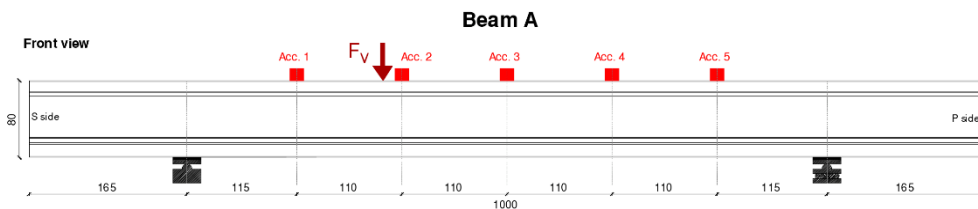


Figure 4-134: Dynamic characterization of Beam A through OMA technique: Layout of sensors adopted for both "hammer tests" and "ambient vibration tests".



Figure 4-135: Dynamic characterization of beam-A through OMA technique:
Picture of the experimental set-up.

Using the Telaio2D¹⁷ Software, the first theoretical modal form was determined. Considering only the beam mass, the modal analysis frequency obtained is 31.45 Hz.

As shown in Figure 4-136, the fundamental frequency measured by the "ambient vibration test" is 31.25 Hz. Figure 4-137 shows that the modal shape obtained with the FDD technique follows that obtained from the modal analysis.

After applying a vertical load of 800 kN, damaging the beam to obtain the crack pattern shown in Figure 4-138, the dynamic identification tests ("hammer test" and "ambient vibration test") were carried out again.

From Figure 4-139 it can be seen that the fundamental frequency of the beam decreased significantly from 31.25 Hz for the uncracked beam to 29.15 Hz for the damaged beam. The comparison between the modal form obtained by modal analysis and the one obtained experimentally is shown in Figure 4-140; in this comparison, two differences can be recognised at the position of accelerometer 1 and accelerometer 2. This difference is caused by their position in the critical shear zone (S-Region) near the S-Side Constrain.

¹⁷ F.E. program for the linear and non-linear seismic analysis of plane frames - by Prof. Pietro Gelfi - University of Brescia.

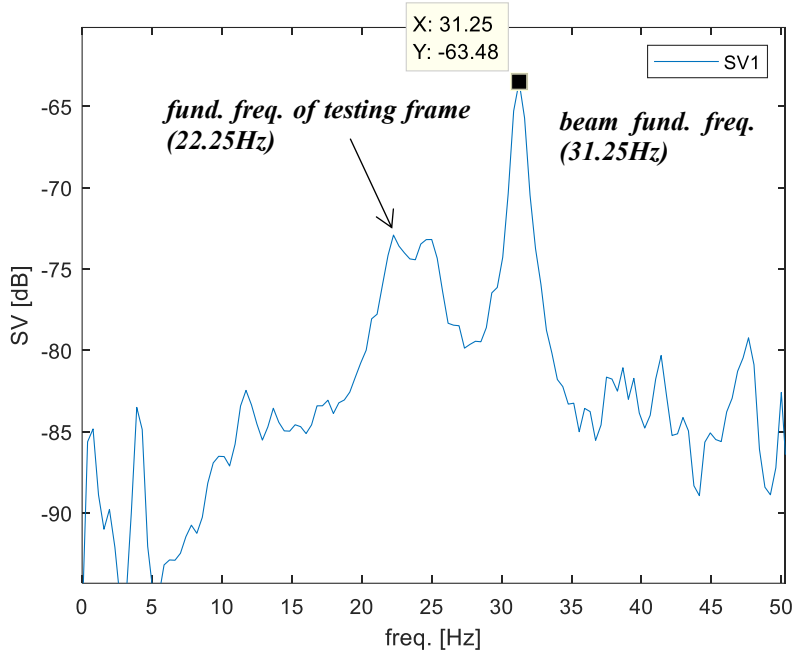


Figure 4-136: Ambient vibration records on virgin Beam A processed through FDD technique: first singular value line.

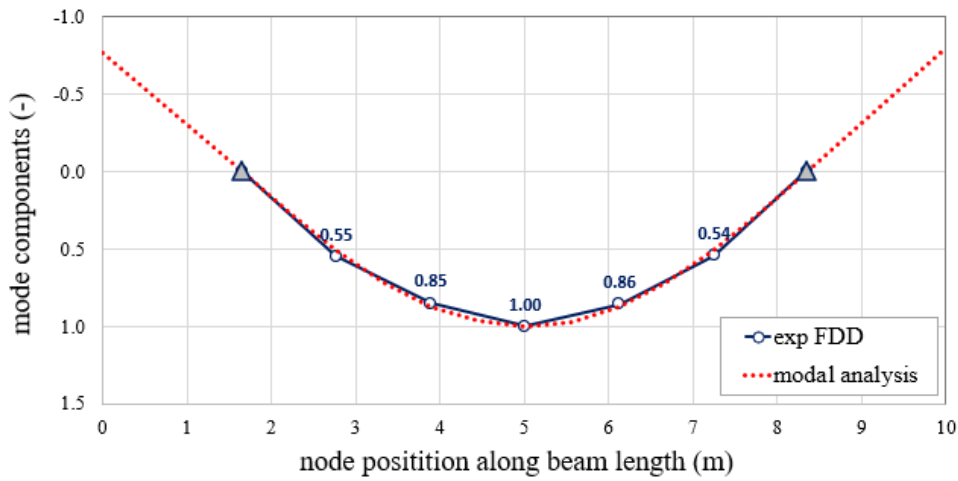


Figure 4-137: Ambient vibration records on virgin Beam A processed through FDD technique: detected mode shape at 31.25Hz. – Front view

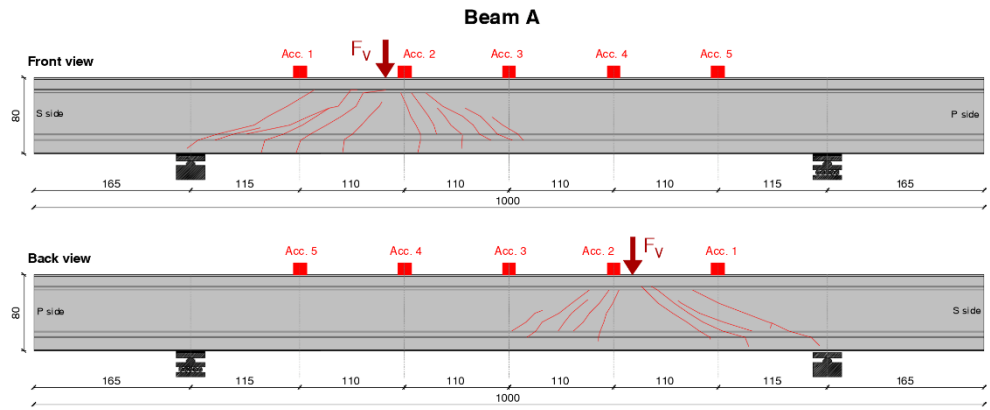


Figure 4-138: Detection of the crack pattern at the end of the load test: $F_v=800\text{ kN}$ – Beam A.

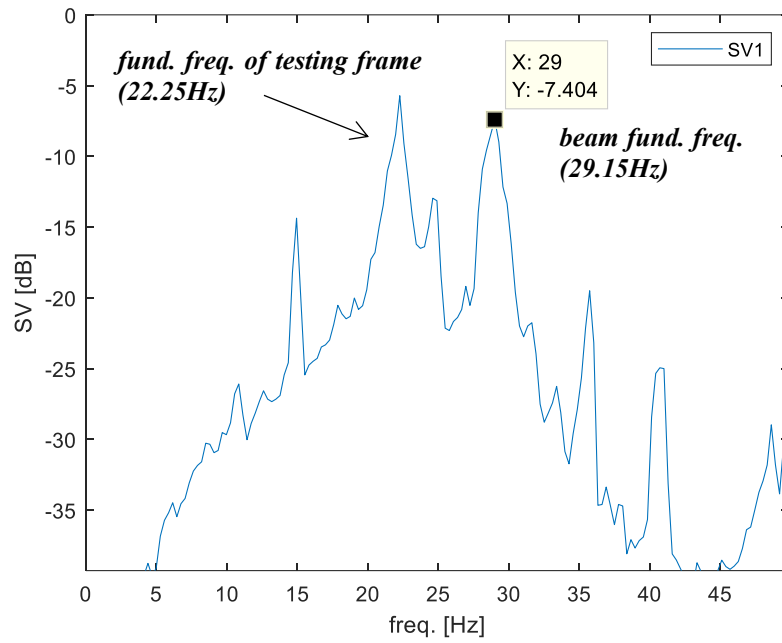


Figure 4-139: Ambient vibration records on damaged Beam A processed through FDD technique: first singular value line.

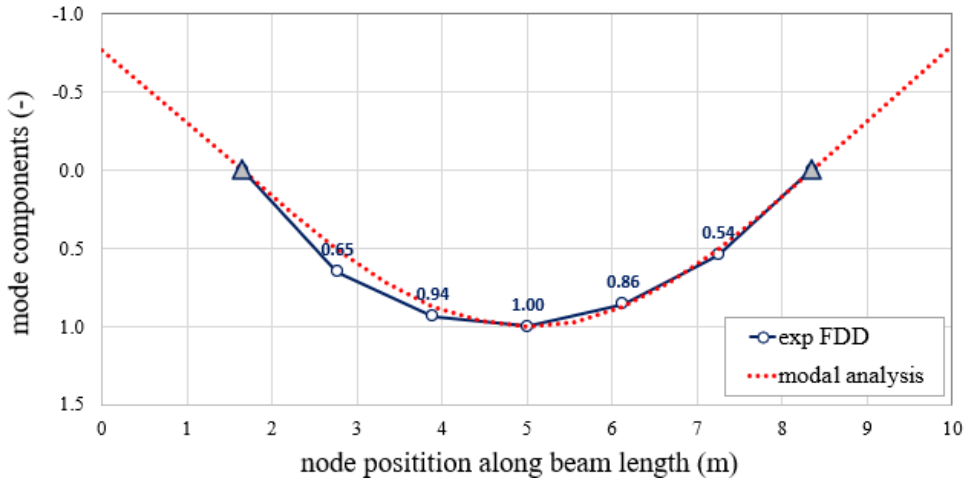


Figure 4-140: Ambient vibration records on damaged Beam A processed through FDD technique: detected mode shape at 29.15Hz – Front view.

It is well-known, as also concluded by Jain and Goel in [Dall’Asta and Dezi, 1996] that a loss of stiffness due to a geometric discontinuity related to cracks formation is correlated with a reduction in the frequency relative to the element's first mode of vibration.

The applied method allows identifying, along the development of the beam, the position of this geometric discontinuity. In this way, the type of cracks formed could be identified depending on their position, the static scheme and the load along the girder.

This technique, applied on a multi-span bridge deck (where access to the intrados may be difficult), could be suitable to identify the location of possible damage.

4.2.9 Concluding Remarks

Experimental tests on the study of the correlation between residual shear strength and prestressing losses have shown that:

- Beam B which, having only 4 strands against the 6 of Beam A (pre-tensioned to the same stress), intends to represent a beam with long-term losses equal to about 28%, has shown the first bending and shear cracks for load values approximately 20% lower than those recorded in Beam A (Table 4-36).

Table 4-36 Comparison between Beam A and Beam B concerning the first flexural crack load and the first shear crack load. (*) the percentage referred to 1130 kN

	Beam A	Beam B	Difference
Level of prestress	955 kN (85%*)	641 kN (57%*)	28%
1st Flexural crack	490 kN	385 kN	21%
1st Shear crack	630 kN	490 kN	22%

- The load of the first diagonal crack formation in Beam B is strongly influenced by the prestress difference to Beam A. The first shear crack formation in Beam B occurs when the load is still close to the service load for Beam A.
- The percentage reduction in the prestressing loss between the two beams (28%) is directly comparable to the percentage reduction in load (20%) which anticipates the exit from the elastic stage and the development of flexural and shear crack patterns. This expected load reduction is a further proof that a long-term reduction of prestressing can generate significant cracking, both in flexure and in shear, even at service loads.
- The crack map that formed at loads close to collapse is notably different on the two pre-tensioned beams: the cracks appear more intense and more widely spaced in Beam A, while they are thinner and more diffused in Beam B
- Comparing two beams that differ only in the prestressing system (Beam A- pre-tensioned bonded strands and Beam C2 post-tensioned unbonded strands) it notes how the difference in bound of the strands which causes the prestressing reinforcement to work as a tension tie and create an arching effect. Consequentially, all the crack map can no longer be directly comparable.
- Comparing the two post-tensioned beams (Beam C1 and Beam C2) it is interesting to note how the difference in prestress, generated by the simulated long-term losses in the beam, contributes almost directly proportionally to the difference in vertical load leading to the failure of the element.

4-EXPERIMENTAL RESULTS AND DISCUSSION

- The dynamic identification method with the FDD technique, which provides information both on the fundamental frequency and on the relative mode shape, allows for identifying the position of a geometric discontinuity along the development of the beam. In this way, it would be possible to trace the nature of the formation of the cracks as a function of their position, the static scheme and the load along the beam. This technique, applied on a multi-span bridge deck (where access to the intrados may be difficult), could be suitable to identify the location of possible damage.

5 NUMERICAL ANALYSIS

In the next chapters will be presented and discussed the results obtained from the finite element models created to simulate:

- Assessment of residual stresses: only the Saw-Cut method – Web proposed in this document was modelled with Midas Gen software;
- Shear tests: the beams tested with load test were modelled with VecTor 2 software.

5.1 Assessment of residual prestress FEM Model

The release test done with the Saw-Cut method – Web, described in §4.1.6 was simulated using a FE model. The non-destructive test was simulated using the software Midas Gen 2022 (version 9.2.5). A 3D model and two 2D plane stress simplified model of the girder beam was created.

Bagge, Nilimaa, and Elfgren (2017) and Kraľovanec et al. (2021) proposed a FE model to simulate the saw-cuts execution, but only 2D models were used.

Bagge, Nilimaa, and Elfgren (2017) applied the Saw-Cut method - Intrados on-site to the beams belonging to a bridge with three spans and subsequently created a 2D model relating to a single span to simulate the effect of the cuts. The real cuts (Figure 5-1) are 30-40 mm deep in 9 steps of 4 mm depth. The cuts are 3 equidistant about 12 cm, having applied 60 mm strain gauges (maximum size of 74 mm).

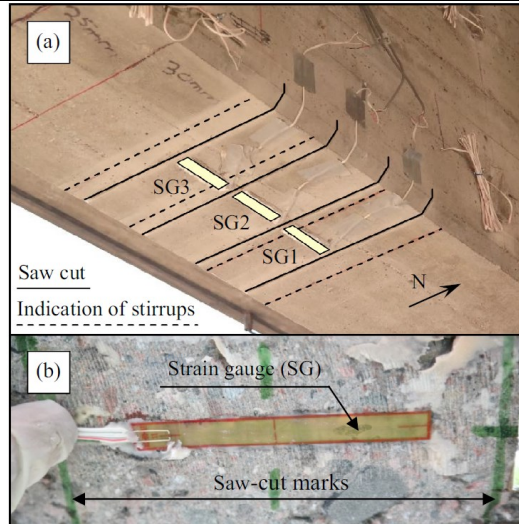


Figure 5-1: Instrumentation for non-destructive residual prestress force determination:
 (a) strain gauges (SG1-3) installed between alignments of saw-cuts with consideration of stirrups' locations (b) close-up of a strain gauge glued on the concrete [Bagge, Nilimaa, and Elfgren, 2017].

For the FEM model created with the ATENA software, the authors considered all materials to have linearly elastic behaviour, modelled using mean values from the diagnostics tests in situ. Quadratic elements with maximal lengths of 300 mm were generally used in the model. However, the top flange was divided into two elements in the vertical direction. In the regions where prestress force was determined in situ by the Saw-Cut method – Intrados, the elements were refined to investigate local effects when isolating a concrete block (Figure 5-2). Each refined region was 1000 mm wide and 250 mm high, and the element size was 5 mm. The analysis was divided into two phases, first dead loads and prestress forces were applied to the structure, and then concrete blocks were gradually isolated. Each saw-cut in every loading stage was simulated by deleting single $5 \times 5 \text{ mm}^2$ finite elements. There were 10 loading sequences in total, corresponding to a total saw-cut depth of 50 mm. Simultaneously with the two phases, concrete strains were recorded longitudinally between the saw-cuts and averaged over a distance of 60 mm for each step. The geometry of each tendon was modelled with a spline, according to the detailed geometry in the construction drawings. Due to lack of knowledge about the true variation of prestress forces along the tendons, a constant force was adopted in the model by introducing the corresponding strain in the elements. This is expected to have a relatively small influence on the results, because very local effects were studied.

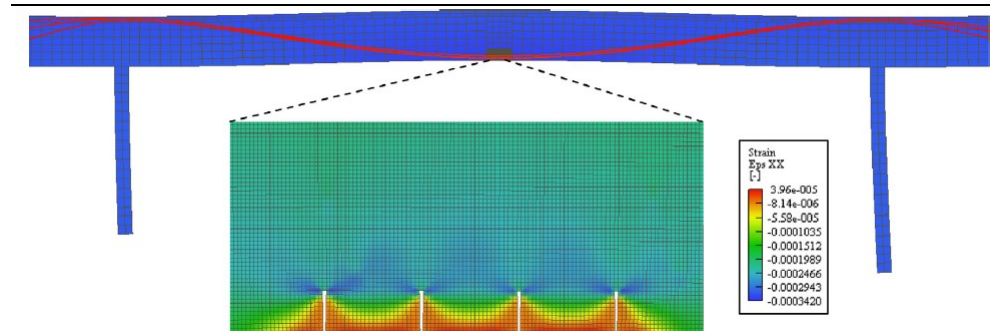


Figure 5-2: FE model for non-destructive evaluation of the residual prestress force in midspan 3: geometrical model (span 3) and strain distribution after saw cut in the region for investigation [Bagge, Nilimaa, and Elfgren, 2017].

Real saw-cut monitoring does not detect the full estimated stress release. The FE 2D model records traction of a few MPa in the points monitored in reality by the SGs.

Kraľovanec et al. (2021) carry out in situ the Saw-Cut method – Intrados on a bridge beam. They make two pairs of equidistant cuts 12 cm and 23 mm deep one pair and 31 mm in the second pair (Figure 5-3).

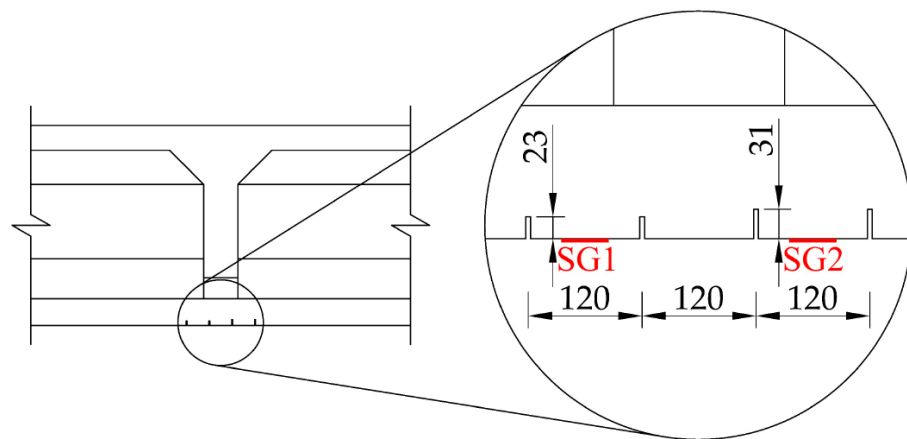


Figure 5-3: Geometric details Saw-Cut method – Intrados [Kraľovanec et al., 2021].

The authors evaluate 2D and 3D models made with the ATENA software, concluding that the 2D model is sufficient because the beam has a length significantly larger than the dimensions of the cross-section. In the middle area of the beam, at a width of 765 mm (the area adjacent to the saw-cuts), the mesh was smoothed into quadrilateral CCQ10SBeta elements with a size of 10 mm. The rest of the modelled beam was composed of quadrilateral CCQ10SBeta elements with a uniform size of 100 mm. The application of the saw-cuts was modelled in the 2D numerical analysis using

5-NUMERICAL ANALYSIS

“construction stages”. First, all macro-elements had the properties of the beam’s concrete. In the next phase, the modulus of elasticity of the macro-elements that represented the saw-cuts was rapidly reduced, thus taking into account the sawing. The stress before and after the application of saw-cuts is shown in Figure 5-4.

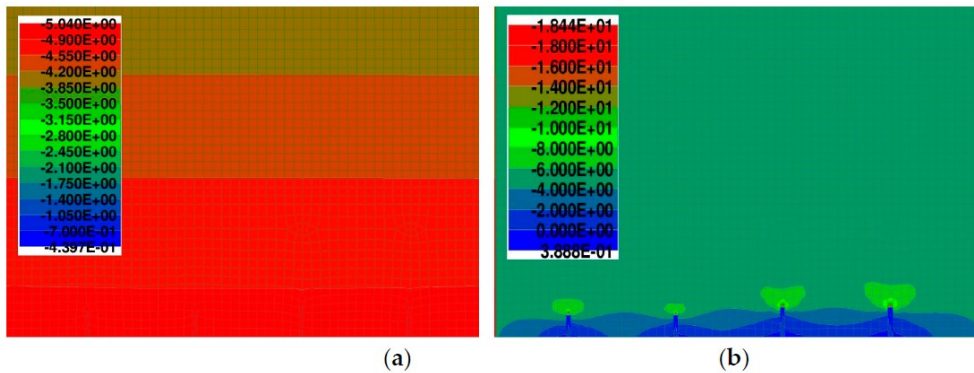


Figure 5-4: Stress before (a) and after (b) application of saw-cuts [Krařovanec et al., 2021].

In this case, it is not specified by the authors, but it seems that for the points corresponding to those monitored with SGs, they provide results close to zero.

5.1.1 Saw-Cut method – Web 3D FEM Model

To study the 360° effect of cuts on the web in 3D, a 3D model of an I-beam with flanges 50 cm wide, 20 cm thickness and web 18 cm wide (y-direction), 80 cm high (z-direction) and 5 m long (x-direction) was developed (Figure 5-5 and Figure 5-6). The model wants to get as close as possible to the real beam tested in the laboratory with a length of 10 m. However, it was considered that 5 m is sufficient to dissipate the disturbance zones at the extremities. The following concrete parameters were considered in the numerical analysis:

- $f_c = 60 \text{ MPa}$
- $E_c = 22000 \cdot \left(\frac{f_c}{10}\right)^{0.3} = 37277 \text{ MPa}$
- $\nu = 0.2$

8-node brick elements were used in this model. The mesh is not uniform (Figure 5-5, Figure 5-6 and Figure 5-7): it is a graded mesh (40x40 mm at extremities) that is fine in the region where the saw-cuts were applied, but not as fine elsewhere. In particular, in the region close to the saw-cuts, brick elements of size 0.5 cm, 1 cm, 1 cm (x,y,z) were used to represent the cuts made by the angle grinder, whose blade generates a cut in the concrete of width 0.4 cm and length 26 cm. To simulate the effect of prestress on the beam, nodal forces were applied in the longitudinal direction of the beam to generate a 5 MPa uniform stress of compression in the section (Figure 5-8). It was decided to adopt a mean prestress level in the concrete of 5 MPa as it is considered a realistic value. The boundary conditions for the fixed end were modelled as rollers in the x-direction, only one node in this end section is fixed in x,y,z directions located at a middle height and middle width.

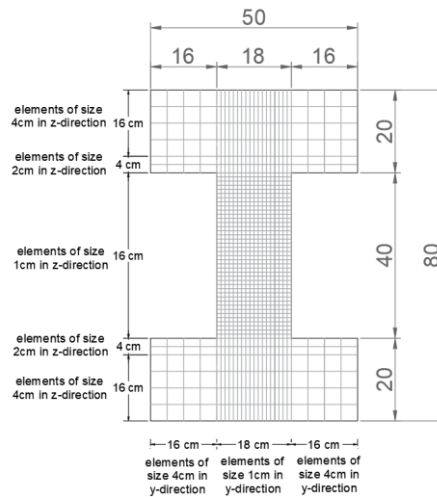


Figure 5-5: 3D model geometries - transverse view.

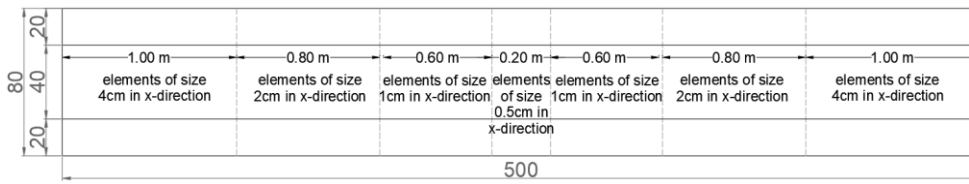


Figure 5-6: 3D model geometries - longitudinal view.

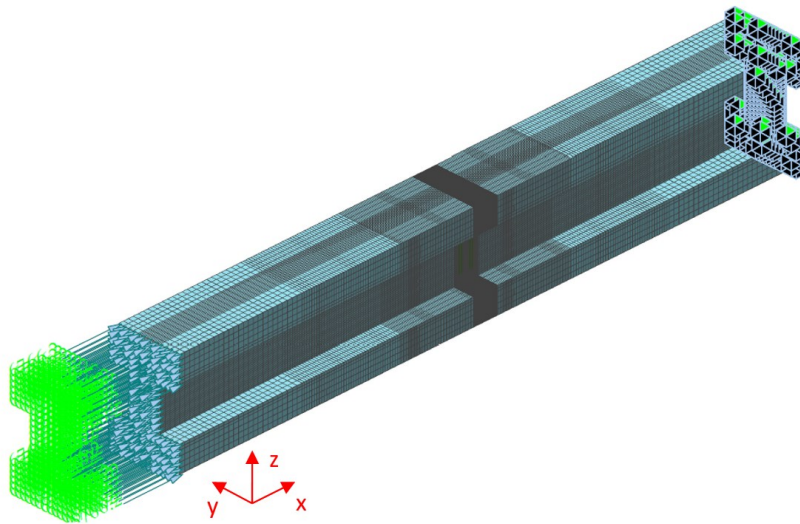


Figure 5-7: 3D model using Midas Gen 2022 software.

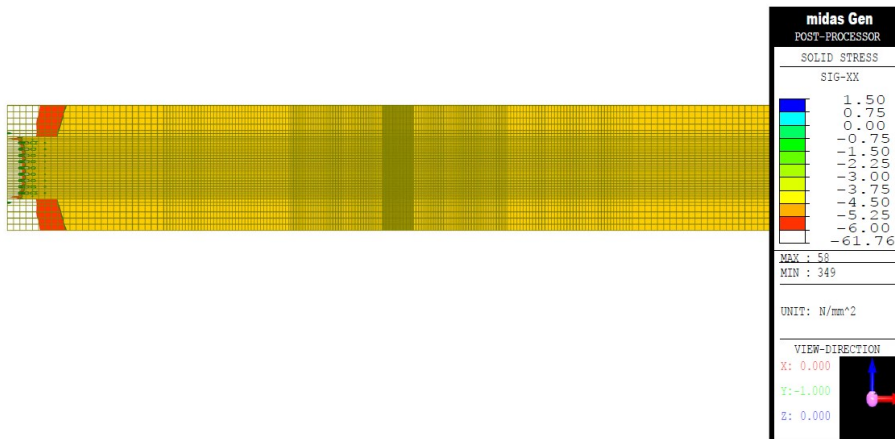


Figure 5-8: 3D model σ_{xx} in xz-plane without saw-cuts application.

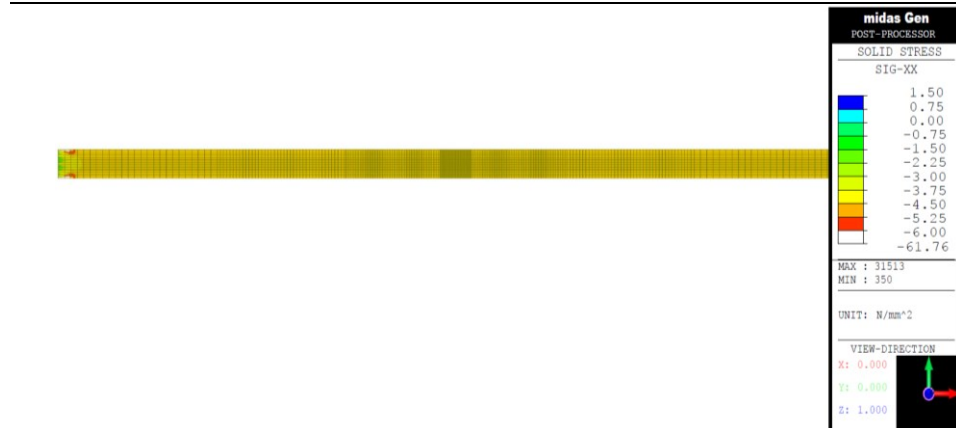


Figure 5-9: 3D model σ_{xx} in xy -plane section without saw-cuts application.

Two models were developed to simulate the release test: in the first, the intact section was modelled, while in the second, elements in the I-beam core were removed to simulate the execution of the 0.5 cm wide (x -direction) and 26-cm-high (z -direction) cuts. In the model with applied cuts, four different geometric configurations (GC) of cuts were taken into account:

- Pair of cuts with a distance of 10 cm and 2 cm deep: SCw_GC_10_2;
- Pair of cuts with a distance of 10 cm and 3 cm deep: SCw_GC_10_3;
- Pair of cuts with a distance of 6 cm and 2 cm deep: SCw_GC_6_2;
- Pair of cuts with a distance of 6 cm and 3 cm deep: SCw_GC_6_3.

In these models, the residual longitudinal stress (σ_{xx}) value after testing was evaluated in the zone where the strain gauges were applied, i.e., the zone between the two saw-cuts. Furthermore, thanks to the 3D model, the influence of the geometric discontinuity generated by the cuts on the stress diffusion within the concrete section in the xz -plane (longitudinal view) and xy -plane (section of plan view ad middle high), was compared and evaluated between the four GCs.

The following images represent the contours of the longitudinal stress (σ_{xx}) to the beam in the two planes just indicated.

5.1.1.1 **SCw_GC_10_2: Saw-cuts with a distance of 10 cm and 2 cm deep**

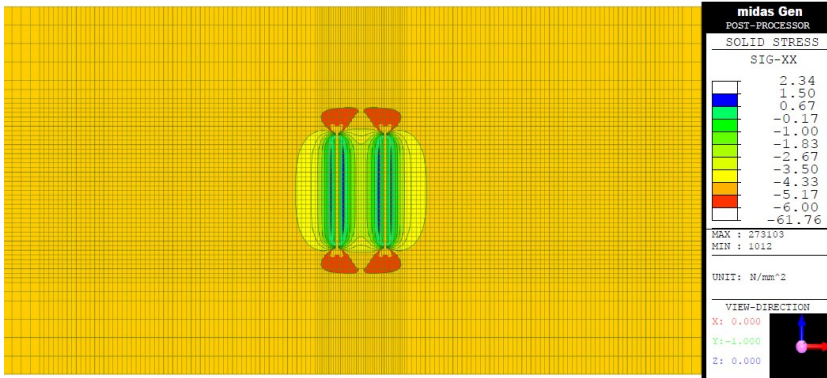


Figure 5-10: SCw_GC_10_2 σ_{xx} of the 3D model in the xz-plane after saw cuts.

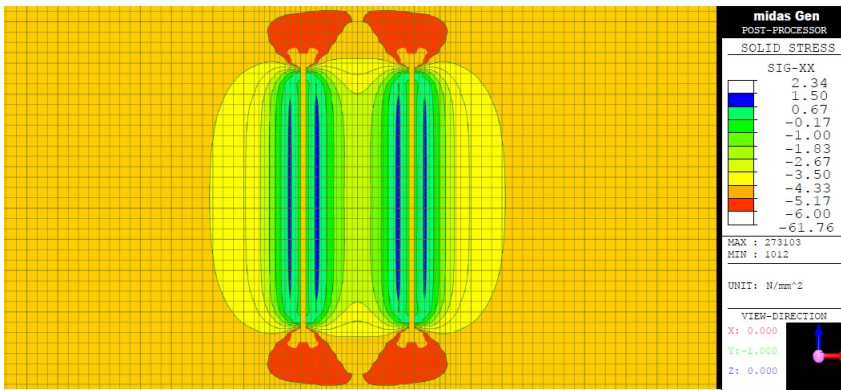


Figure 5-11: Zoom SCw_GC_10_2 σ_{xx} of the 3D model in the xz-plane after saw cuts.

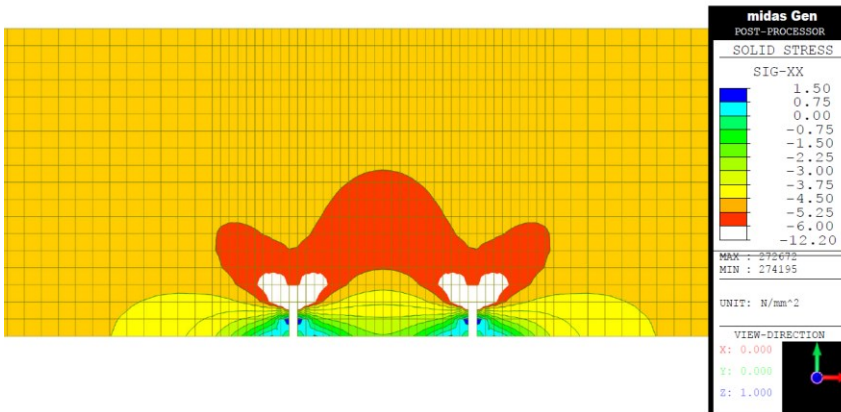


Figure 5-12: SCw_GC_10_2 σ_{xx} of the 3D model in the xy-plane section after saw cuts.

5.1.1.2 SCw_GC 10 3: Saw-cuts with a distance of 10 cm and 3 cm deep

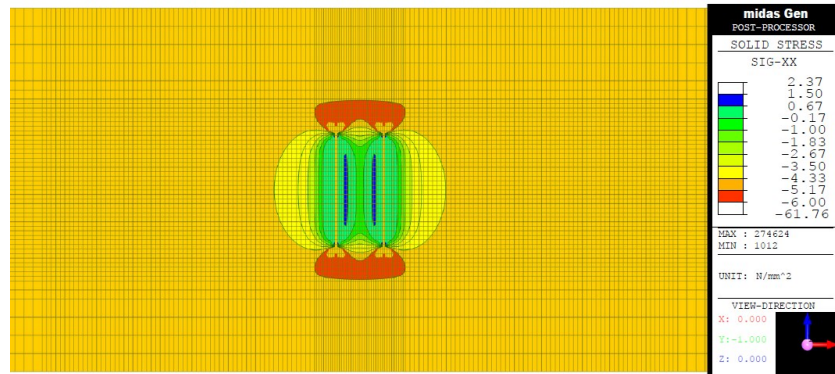


Figure 5-13: SCw_GC_10_3 σ_{xx} of the 3D model in the xz-plane after saw cuts.

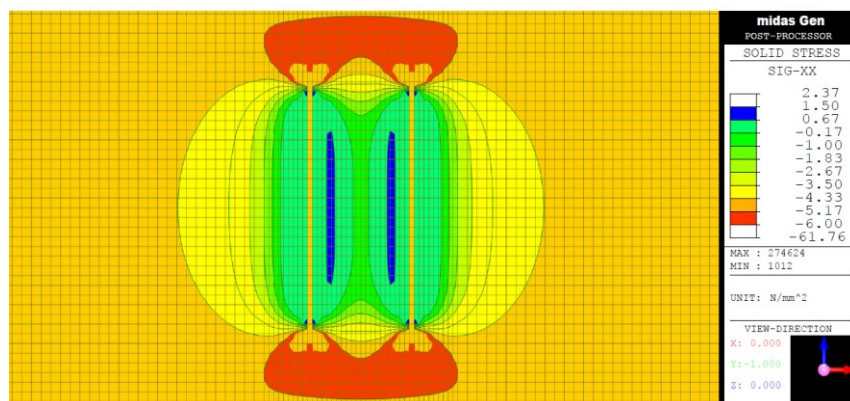


Figure 5-14: Zoom SCw_GC_10_3 σ_{xx} of the 3D model in the xz-plane after saw cuts.

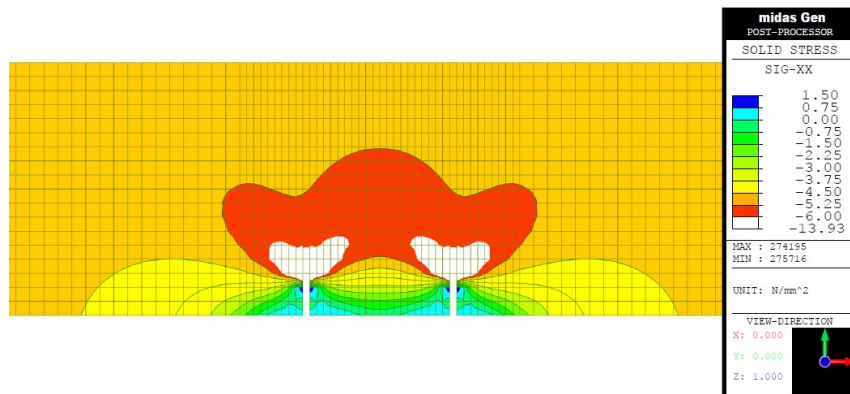


Figure 5-15: SCw_GC_10_3 σ_{xx} of the 3D model in the xy-plane section after saw cuts.

5.1.1.3 SCw_GC_6_2: Saw-cuts with a distance of 6 cm and 2 cm deep

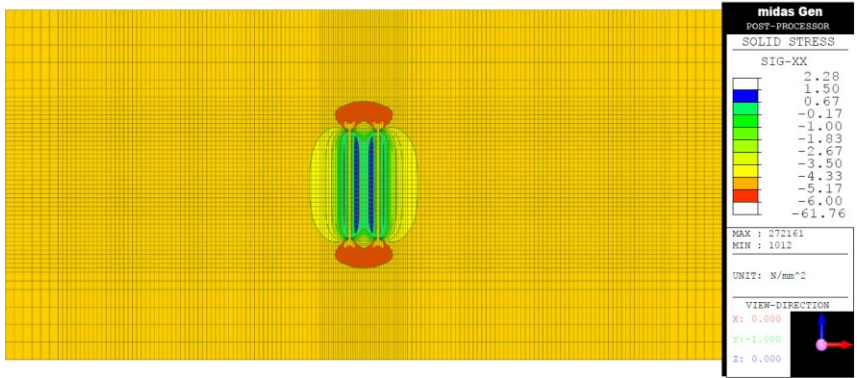


Figure 5-16: SCw_GC_6_2 σ_{xx} of the 3D model in the xz-plane after saw cuts.

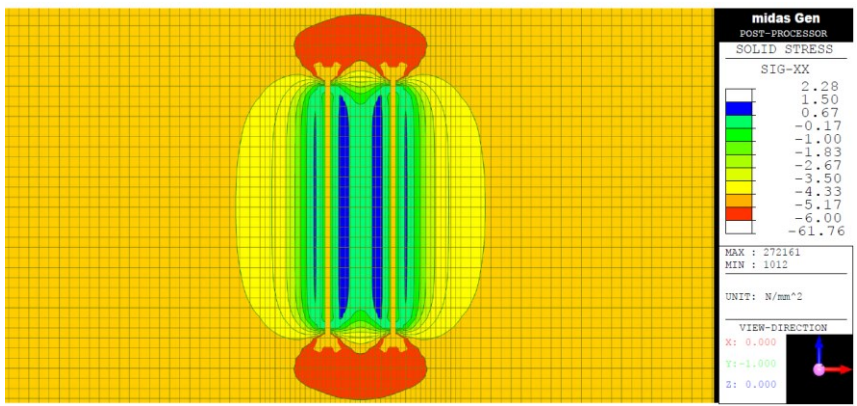


Figure 5-17: Zoom SCw_GC_6_2 σ_{xx} of the 3D model in the xz-plane after saw cuts.

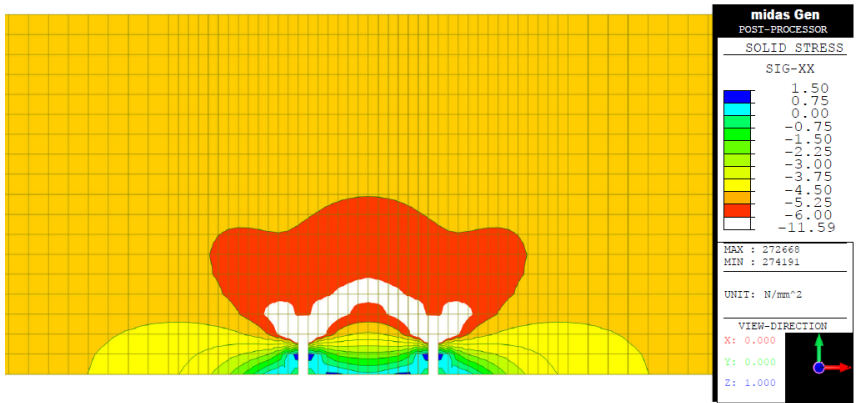


Figure 5-18: SCw_GC_6_2 σ_{xx} of the 3D model in the xy-plane section after saw cuts.

5.1.1.4 SCw_GC_6_3: Saw-cuts with a distance of 6 cm and 3 cm deep

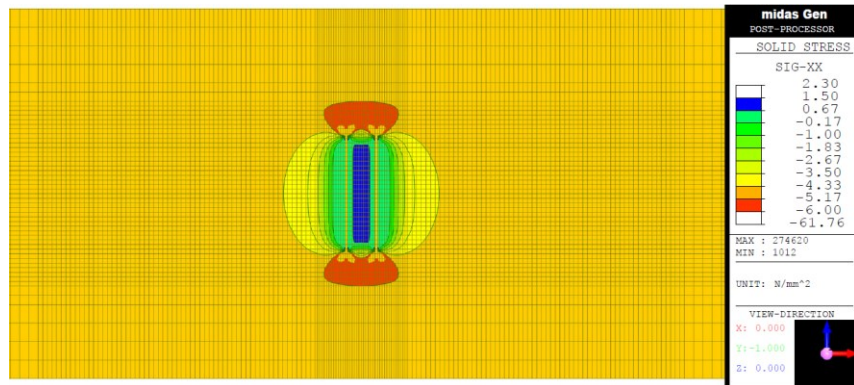


Figure 5-19: SCw_GC_6_3 σ_{xx} of the 3D model in the xz-plane after saw cuts.

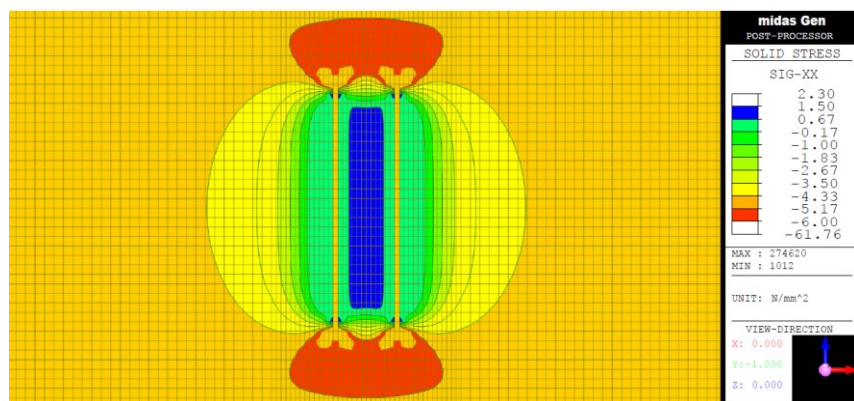


Figure 5-20: Zoom SCw_GC_6_3 σ_{xx} of the 3D model in the xz-plane after saw cuts.

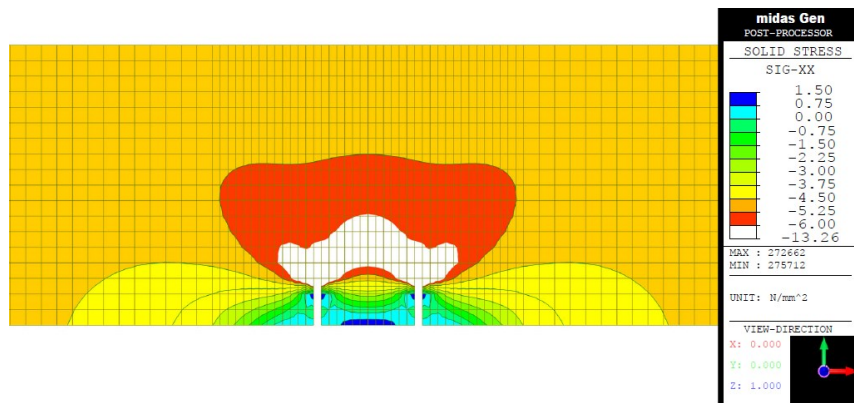


Figure 5-21: SCw_GC_6_3 σ_{xx} of the 3D model in the xy-plane section after saw cuts.

5.1.1.5 Discussion

As observed experimentally, the models of the two configurations with pairs of cuts with a distance of 10 cm (GC_10_2 and GC_10_3) do not allow a complete tension release, in fact, the region between the two saw-cuts is still compressed after the release test, both in xz -plane and in xy -plane section.

In contrast, the models of the two configurations with pairs of cuts with a distance of 6 cm (GC_6_2 and GC_10_3), which experimentally have been the most reliable (§4.1.6), show minor residual tensile stresses in the area between the two cuts. Specifically, in the model with cuts 6 cm apart and 2 cm deep a tensile stress of 0.5 MPa is detected, while in the model with cuts 6 cm apart and 3 cm deep a tensile stress of 1.5 MPa is computed. This tensile stress in the longitudinal direction is due to the formation of arch-shape stress distribution and it was not appreciated experimentally as schematically represented in Figure 5-22.

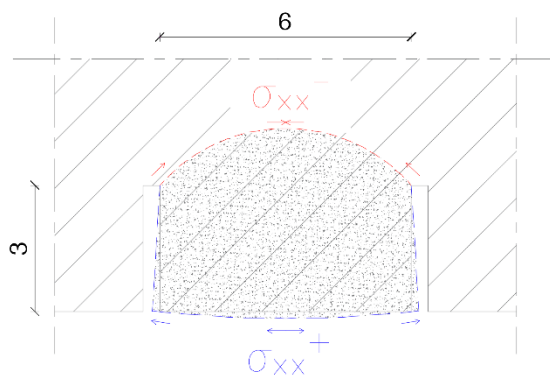


Figure 5-22: Simplified scheme of the arch distribution of the internal σ_{xx} of the beam in xy -plane section (dimensions in cm).

As already indicated above Bagge, Nilimaa, and Elfgren (2017) and Kralovanec et al. (2021), who simulated saw-cuts 12 cm apart and 5 cm and 3 cm deep, respectively in a 2D FE model, also obtained tensile stress in the region between the saw-cuts. A 2D model is shown below.

5.1.2 Saw-Cut method – Web 2D FEM Model

In 2D, two simplified models were developed: one represents the xz -plane, while the second represents the xy -plane section of the 3D model. In 2D models, only the configuration with pairs of saw-cuts with a distance of 6 cm and 3 cm deep was considered. The material properties, geometry, mesh on xz -plane, axial load, constraints and characteristics of the model are the same as those of the 3D model, instead in 2D models 4-node plane stress elements were used. The contours of the longitudinal stress (σ_{xx}) to the beam are shown below.

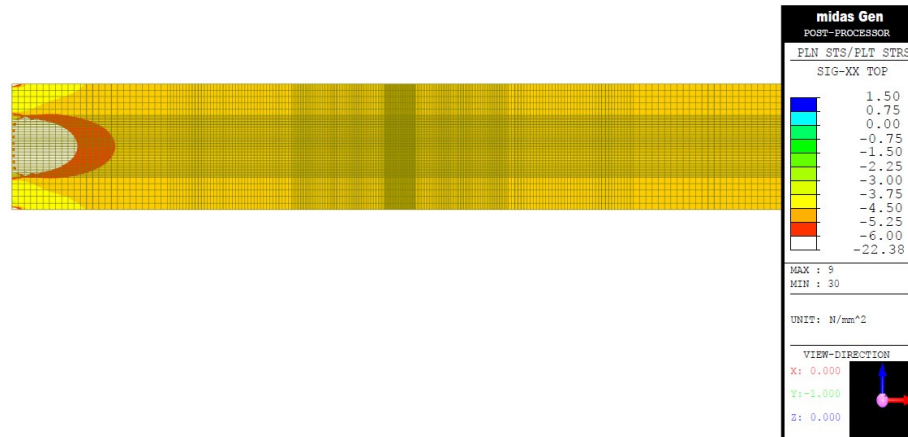


Figure 5-23: 2D model σ_{xx} in xz -plane without saw-cuts application.

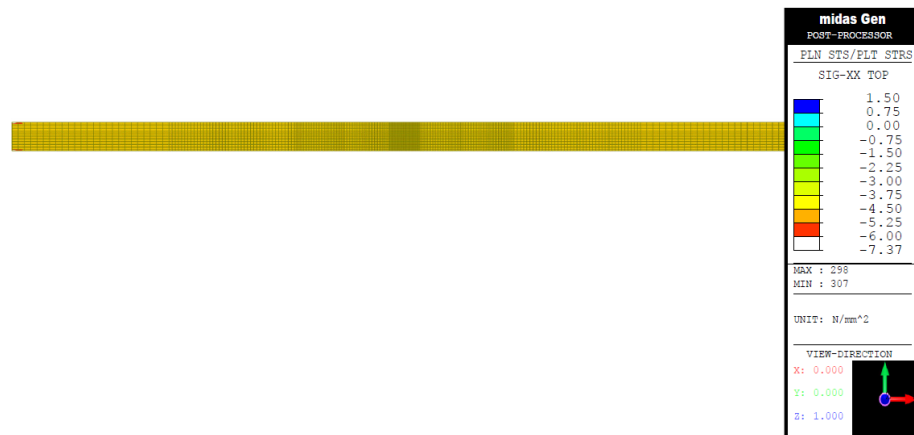


Figure 5-24: 2D model σ_{xx} in xy -plane section without saw-cuts application.

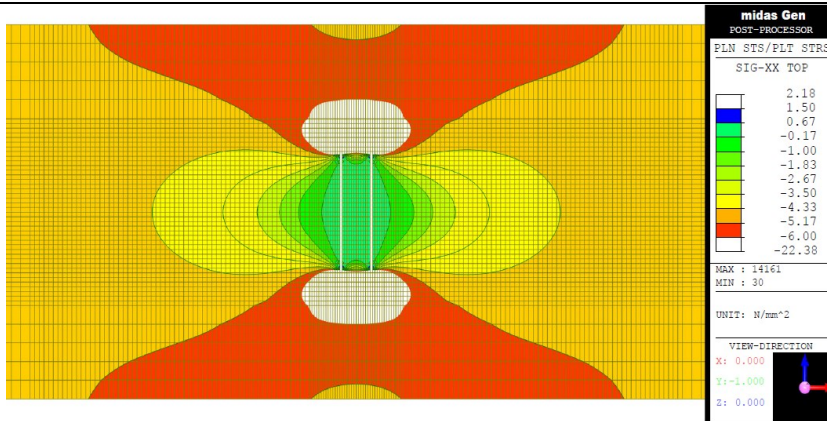


Figure 5-25: SCw_GC_6_3 σ_{xx} of the 2D model in the xz-plane after saw-cuts.

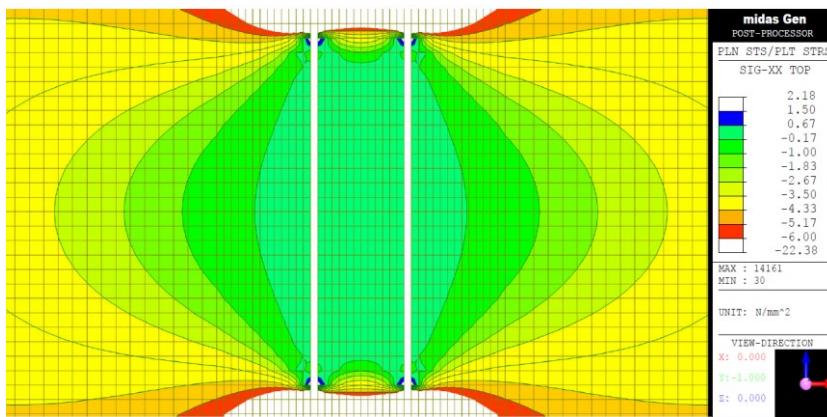


Figure 5-26: Zoom SCw_GC_6_3 σ_{xx} of the 2D model in the xz-plane after saw-cuts.

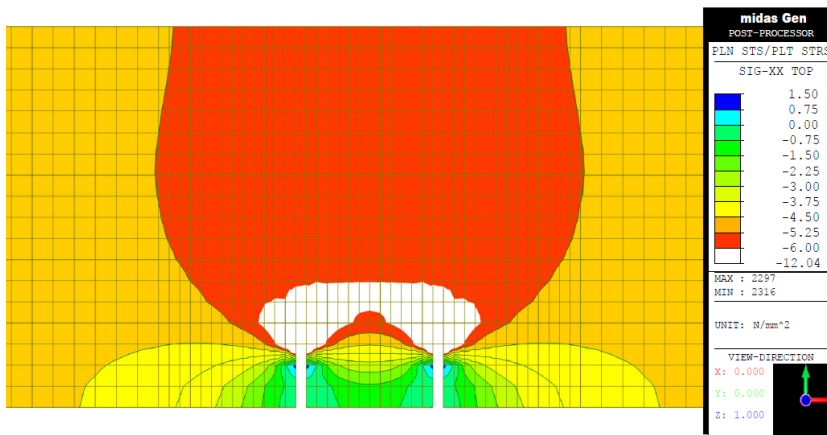


Figure 5-27: SCw_GC_6_3 σ_{xx} of the 2D model in the xy-plane section after saw-cuts.

5.1.2.1 Discussion

Comparing the 3D model and the simplified 2D models, it can be seen that for modelling pairs of cuts made on the web, the 2D models are not reliable, as they fail in capturing the correct stress state in the region between the two saw-cuts. In particular, in the xz-plane model a stress of 0 MPa is obtained, while in the xy-plane section model a compressive stress of -1 MPa is obtained.

5.1.3 Concluding Remarks

From finite element models that simulate the Saw-Cut method – Web the following conclusions can be drawn:

- The model with GC_6_2, as also in the real tests, proves to be the one with a more reliable geometry for a complete stress release, however, it turns out that the area monitored with strain gauges does not reach $\sigma_{xx} = 0$ but goes into traction. This may be due to an arch-effect diffusion of the compression stresses, which by self-balancing bring the surface points between the two cuts, which are no longer constrained, into traction.
- Comparing the two models, it emerges that the 2D, compared to the 3D, has no consistency in the results σ_{xx} between the two view planes to simulate a complete stress release, therefore it is not very reliable for the representation of reality.

5.2 Shear Test FEM Model

5.2.1 Introduction

During the design phases of the beams, to determine the correct geometry of the section, the number of strands and the maximum prestress to be applied, the position of the load point with respect to the supports, the distance of the stirrups and the longitudinal mild reinforcement, few numerical finite element models have been developed. The goal was to identify that configuration allowed to obtain a collapse of the brittle beam, naturally with the geometric limits available from the catalogues of the various fabricators. Once the beams were made, the finite element model was updated as executive drawings and by inserting the mechanical characteristics of the materials obtained from the tests on the samples and from the certificates of the materials. In this way it was possible to obtain the prediction curves of the experimental tests.

The software used both in the design phase and in the prediction phase of the experimental tests is VecTor 2, a nonlinear finite element analysis (NLFEA) program for the analysis of two-dimensional reinforced continuum structures subjected to quasi-static or dynamic load conditions (developed by Professor Frank J. Vecchio at University of Toronto). As subsequently detailed in §5.2.2, VecTor 2 is based on Modified Compression Field Theory (MCFT) and Disturbed Stress Field Model (DSFM).

5.2.2 VecTor 2

VecTor 2 (VT2) is a finite element program developed by Professor F. Vecchio at the University of Toronto which, through a non-linear analysis, allows to study of two-dimensional reinforced concrete structures.

The post-processing graphical capabilities of the analysis results are provided by the Augustus software; instead, the insertion of the input data of VecTor 2 is allowed by the FormWorks software. The latter has a user interface for generating, viewing and checking the finite element model.

By combining a realistic model of the non-linear behaviour of reinforced concrete structures with the computational power of finite element analyses, VecTor2 provides a much more accurate estimation of element behaviour (strength, post-peak behaviour, collapse mode, deformation and cracking) than that obtained with the linear-elastic method.

This software models cracked concrete as an orthotropic material, the cracks are spread on the surface and rotated according to the forces. The theories behind this software are:

- Modified Compression Field Theory (MCFT) [Vecchio and Collins, 1986]
- Disturbed Stress Field Model (DSFM) [Vecchio, 2000, 2001; Vecchio et al., 2001]

Starting from these theories, the analytical model was developed, with the aim of predicting the behaviour of reinforced concrete elements subjected to normal and shear actions in the plane. The choice of constitutive models determines the accuracy of the analysis results.

VecTor2 is a two-dimensional program which considers a plane stress state in the longitudinal and vertical direction of the beam, neglecting the stress distribution in the transverse direction.

Despite this, its use is justified by the fact that the transverse dimension of the beams, in relation to the longitudinal and vertical dimensions, is not such as to determine a distribution of forces substantially different from the flat one. For this reason, for this type of element, it makes sense to use a two-dimensional software, since it can be considered the same as a 3D modelling.

5.2.2.1 Modified Compression Field Theory (MCFT)

The Modified Compression Field Theory (MCFT) [Vecchio and Collins, 1986] is an analytical model for predicting strain as a function of applied load for reinforced concrete structures.

The MCFT represents an evolution of Compression Field Theory (CFT) [Collins, 1978; Collins and Mitchell, 1980; Mitchell and Collins, 1974]. The latter neglects the resistant contribution of the concrete after it has cracked, in this way, on the one hand, it overestimates the deformation, on the other, it underestimates the resistant capacity. The MCFT instead takes into account the fact that the concrete, once cracked, is still able to resist traction between one crack and another.

In the MCFT, reinforced concrete is considered as a series of rectangles subjected to shear and normal stresses, as shown in Figure 5-28, i.e. characterized by a membrane behaviour.

The MCFT determines the local stresses and strains to which the concrete elements and reinforcements are subjected, establishing the opening and orientation of the cracks during the load-displacement curve. The process appears to be of an iterative type, with the verification of the convergence of the results obtained. Failure to comply with the latter leads to having to discard the results.

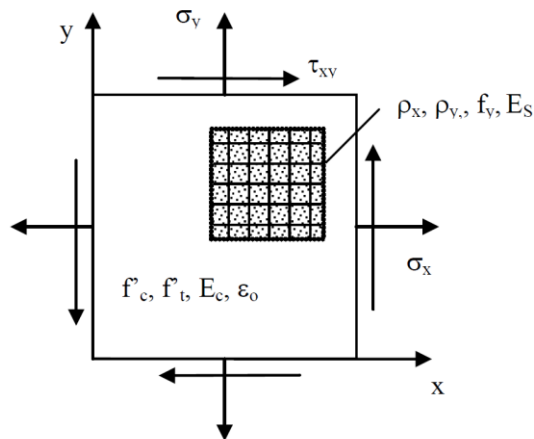


Figure 5-28: Element subjected to local normal and shear stresses [Wong et al., 2013].

MCFT considers concrete as an orthotropic material, using a diffuse rotating crack model, that is each finite element formed by concrete is treated as a continuous solid with distributed cracks. These are freely oriented, remaining coaxial with the main compressive stress direction of the concrete.

In addition to being computationally convenient, the crack-rotation approach is consistent with literature models observed in many real structures.

The theory is composed of three sets of relations:

- equilibrium relationships involving the mean stresses in concrete and reinforcement;
- congruence relationships existing between the concrete elements and those of reinforcement;
- stress-strain bond relationships inherent in the materials that make up the structure.

These constitutive bonds derive from tests of reinforced concrete panels, tested with the use of the "Panel Element Tester" purposely built at the University of Toronto.

The MCFT formulation includes realistic stress-strain bond models based on experimentally observed phenomena, instead, the formation of cracks follows relationships expressed in terms of mean stresses and strains.

The MCFT uses the following assumptions:

- the reinforcing bars, both longitudinal and transverse, are uniformly distributed;
- uniformly distributed and inclined cracks;
- uniformly applied shear and uniform normal stresses;
- each strain state corresponds to a single stress state, i.e. there is a one-to-one correspondence between stress and strain and therefore the load history is not considered;
- stresses and deformations are given by the mean between the values of σ and ε obtained considering several cracks;
- the main stress direction ($\theta\sigma$) coincides with the main strain direction ($\theta\varepsilon$);
- perfect bond between steel and concrete;
- the stress-strain relationships of concrete and reinforcement are independent of each other;
- the shear stresses in the reinforcement are negligible.

In this model, reinforced concrete is considered a new material with its own stress and strain characteristics. In this model the equilibrium, compatibility and constitutive relationship are formulated in terms of mean stresses and strains; this is because these relationships are obtained by integrating stresses and strains on the section.

5.2.2.1.1 *Equilibrium Relationships*

Consider the diagram of the membrane element as shown in Figure 5-29.

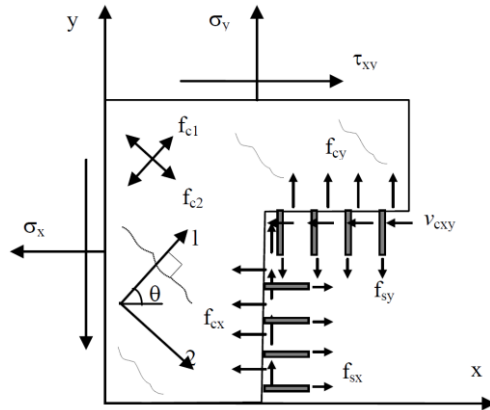


Figure 5-29: Schematization of the forces acting on the body for writing the equilibrium equations [Wong et al., 2013].

The equilibrium of forces in the x and y directions requires that the results of the applied normal stresses, σ_x and σ_y , are balanced by the results of the mean stresses in concrete (f_{cx} and f_{cy}) and steel (f_{sx} and f_{sy}). The moment equilibrium requires that the applied shear stresses, τ_{xy} , be entirely entrusted to the concrete (v_{cxy}), thus assuming that there is no dowel effect due to the reinforcement. These equilibrium relationships, in terms of mean stresses, can be summarized as follows:

$$\sigma_x = f_{cx} + \rho_{sx} \cdot f_{sx} \tag{5-1}$$

$$\sigma_y = f_{cy} + \rho_{sy} \cdot f_{sy} \tag{5-2}$$

$$\tau_{xy} = v_{cxy}. \tag{5-3}$$

where ρ_{sx} and ρ_{sy} are the percentages of reinforcement present in the x and y directions, respectively.

Concrete is an orthotropic material with respect to the main directions of stress: using the Mohr circle it is possible to obtain the mean stresses in the x and y direction (f_{cx} and f_{cy}) knowing the mean tensile stress in the principal direction (f_{c1}):

$$f_{cx} = f_{c1} - v_{cxy} \cdot \cot(90 - \theta_\sigma) \tag{5-4}$$

$$f_{cy} = f_{c1} - v_{cxy} \cdot \tan(90 - \theta_\sigma) \tag{5-5}$$

5.2.2.1.2 Compatibility Relationships

The compatibility relationships concern the mean strains of the concrete and the reinforcing bars, as shown in Figure 5-30.

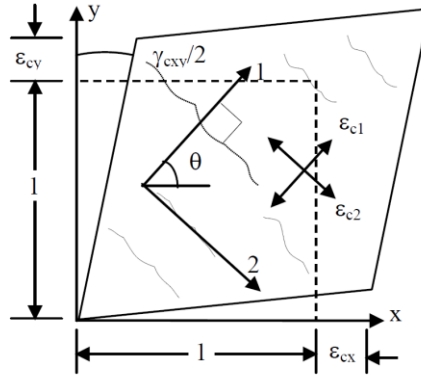


Figure 5-30: Mean strains of concrete [Wong et al., 2013].

From the hypothesis of perfect bond, it follows that the concrete and the reinforcing bars deform in the same way. Therefore, the mean strains in concrete (ϵ_c) and the strains of non-prestressed steel elements (ϵ_s) are the same.

Although the MCFT can handle any number of rebar directions, here consider the rebar arranged orthogonally, as shown in Figure 5-30. The strains of the reinforcing bars, arranged parallel to the x and y directions, are called ϵ_{sx} , ϵ_{sy} , respectively.

The compatibility relationships are expressed by the following equations:

$$\epsilon_x = \epsilon_{cx} = \epsilon_{sx} \quad (5-6)$$

$$\epsilon_y = \epsilon_{cy} = \epsilon_{sy} \quad (5-7)$$

If the value of the angular slide γ_{xy} is known, the relationships for determining the mean principal strain of tension, ϵ_{c1} , and compressive, ϵ_{c2} , of concrete can be extrapolated via Mohr's circle, as follows:

$$\epsilon_{c1}, \epsilon_{c2} = \frac{1}{2}(\epsilon_x + \epsilon_y) \pm \frac{1}{2} \left[(\epsilon_x - \epsilon_y)^2 + \gamma_{xy}^2 \right]^{1/2} \quad (5-8)$$

$$\theta = \theta_\epsilon = \theta_\sigma = \frac{1}{2} \cdot \tan^{-1} \left(\frac{\gamma_{xy}}{\epsilon_x - \epsilon_y} \right) \quad (5-9)$$

These relations also determine the directions of the main axis of traction, θ_ϵ , and that of compression, θ_σ , with respect to the x -axis.

5.2.2.1.3 *Constitutive Relationships*

The stress-strain relationships are used to correlate the stresses, present in the equilibrium equations, with the deformations, present in the compatibility equations. These relationships, expressed in terms of mean stresses and strains, can be significantly different from the well-known relationships linking local stresses and strains determined by tests on standard materials. Vecchio and Collins (1986) carried out tests on 30 panels of dimensions 890 x 890 x 70 mm subjected to a state of plain-stress thanks to the aid of the Panel Element Tester. The test results were used to develop constitutive models regarding both compression and tension-cracked concrete. It should be noted that, in addition to these constitutive models, new relationships were implemented in VecTor 2 in the following years. Concerning compressed concrete, the constitutive relationship relates to the principal compressive stress (f_{c2}) not only with the principal compressive strain (ε_{c2}), but also with the principal tensile strain (ε_{c1}). In fact, the results of the tests show that the compressive strength and stiffness decrease as the principal tensile strains ε_{c1} increase. This phenomenon, known as "compression softening", implies that the compressive strength in the presence of transverse traction will be lower than that obtained in the standard uniaxial compression tests on cylindrical specimens. The proposed equation is the following:

$$f_{c2} = \frac{f'_c \cdot \left[2 \left(\frac{\varepsilon_{c2}}{\varepsilon_0} \right) - \left(\frac{\varepsilon_{c2}}{\varepsilon_0} \right)^2 \right]}{0.8 - 0.34 \cdot \left(\frac{\varepsilon_{c1}}{\varepsilon_0} \right)} \quad (5-10)$$

The numerator term is the parabolic Hognestad relation valid for simply compressed concrete with uniaxial compression. The value ε_0 is the cylindrical strain of concrete (negative value) corresponding to the peak compressive stress, f'_c , determined by uniaxial compression tests performed on cylindrical specimens. The term in the denominator instead takes into account the "compression softening".

For concrete tension, the constitutive relationship relates to the principal tensile stress, f_{c1} , to the principal tensile strain, ε_{c1} . First, it is necessary to determine the uniaxial cracking stress, f'_t , and the corresponding cracking strain, ε_{cr} . In the absence of information, they can be estimated as follows:

$$f_t = 0.33 \cdot \sqrt{f_c} \quad (\text{in MPa}) \quad (5-11)$$

$$\varepsilon_{cr} = \frac{f_t}{E_c} \quad (5-12)$$

where E_c is the initial elastic modulus of the concrete, estimated as:

$$E_c = 5000 \cdot \sqrt{f_c} \quad (\text{in MPa}) \quad (5-13)$$

Before cracking, the concrete has a linear elastic behaviour, described by the relationship:

$$f_{c1} = E_c \cdot \varepsilon_{cr} \quad \text{per } 0 < \varepsilon_{c1} < \varepsilon_{cr} \quad (5-14)$$

After cracking, between cracks the concrete still resists traction and therefore tensile stresses still exist in the concrete due to the tight fit between the concrete and the steel. This phenomenon, known as "tension stiffening", predicts that the tensile stress of the concrete collapses as the principal tensile strain of the concrete increases. The equation proposed by the MCFT is the following:

$$f_{c1} = \frac{f_t'}{1 + \sqrt{200 \cdot \varepsilon_{c1}}} \quad (5-15)$$

For compressive and tensile reinforcement, the MCFT uses a bilinear relationship between mean stress, f_s , and mean strain, ε_s . Initially, there is a linear elastic stage followed then, after yielding, by a plateau, as described by the following equations:

$$f_{sx} = E_s \cdot \varepsilon_{sx} \leq f_{sx,yield} \quad (5-16)$$

$$f_{sx} = E_s \cdot \varepsilon_{sx} \leq f_{sx,yield} \quad (5-17)$$

where E_s is the elastic modulus of the reinforcing steel, $f_{sx,yield}$ and $f_{sy,yield}$ are the yield strengths of the steel in the x and y direction, respectively.

5.2.2.1.4 Consideration on Local Crack Conditions

Given a condition of congruent mean deformation, through the previous relations, it is possible to determine the mean stresses in the concrete and in the reinforcement, but also the value of the applied shear and axial force which guarantee the equilibrium. However, these relationships do not provide indications regarding the local stress values: in particular in correspondence with the crack the tensile stress in the bars will be greater than the mean value, instead between one crack and another, where the concrete is intact, the stress in the bars will be less than the mean value. On the contrary, the tensile stresses in the concrete will be zero in correspondence with the crack and maximum where it is still intact. These local stress variations cannot be ignored because the ultimate bearing capacity of a member can be governed by the ability of the reinforcement to transmit stress through cracks; i.e. the response of the element could be governed by a local failure of the reinforcement where the crack occurs or by a shear failure along the crack itself. To account for these possible local failures, the MCFT limits the local stresses in the proximity of the crack and the mean tensile stress of the concrete.

5-NUMERICAL ANALYSIS

The stress state is very different if it is evaluated where the concrete is intact or if it is evaluated in correspondence with the crack. Figure 5-31 compares the mean stresses, calculated in a section in the area where the concrete is intact (a), with the local stresses in correspondence with the crack (b), assumed orthogonal to the main direction of traction.

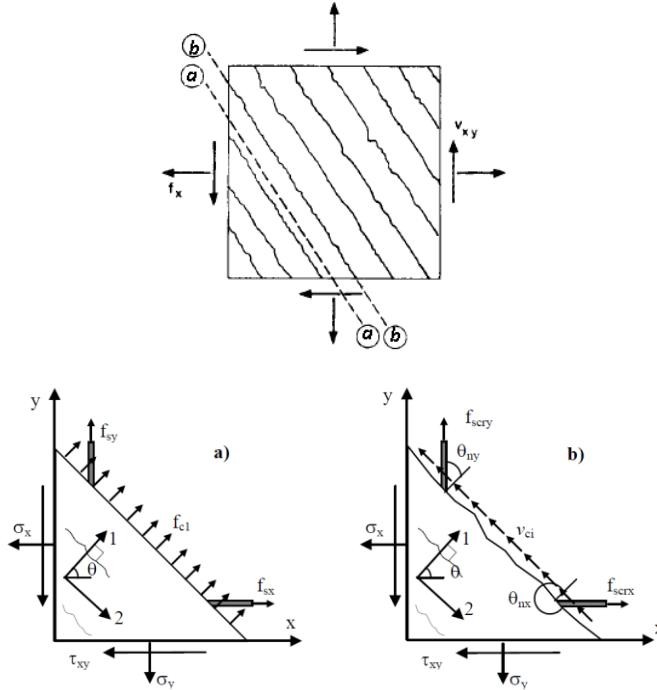


Figure 5-31: Comparison of mean and local stresses at a crack: a) mean stresses between cracks b) local stresses at the free surface of the crack [Wong et al., 2013].

At the crack, the tensile strength of the concrete is zero; therefore, to transmit the stress, it is necessary that the stress and strain of the reinforcement increase locally. The static equivalence of the mean and local tensile stresses in the direction normal to the crack results in the following equation:

$$f_{c1} = \rho_x \cdot (f_{s,cr,x} - f_{s,x}) \cdot \cos^2 \theta_{nx} + \rho_y \cdot (f_{s,cr,y} - f_{s,y}) \cdot \cos^2 \theta_{ny} \quad (5-18)$$

where:

- $f_{s,cr,x}$ and $f_{s,cr,y}$ represent the stress of the reinforcement at the crack;
- θ_{nx} e θ_{ny} represent the angle between the crack normal and the reinforcing bar.

Considering the previous equation, it is evident that the mean tensile stress of the concrete is limited by the yield point of the reinforcement. If in Equation (5-18) the local stress at the crack is replaced with the yield stress, then the terms in stirrups define an increase in the resistant capacity of the reinforcement, which allows a reduction of the tensile stress of the concrete in the phase post-cracking:

$$f_{c1} \leq \rho_x \cdot (f_{s,x,yield} - f_{s,x}) \cdot \cos^2 \theta_{nx} + \rho_y \cdot (f_{s,y,yield} - f_{s,y}) \cdot \cos^2 \theta_{ny} \quad (5-19)$$

If a principal reference system is considered between the cracks, as in Figure 5-31a, there are no shear stresses. However, since the reinforcing bar usually passes through the crack with a certain angle of inclination, local shear stresses, v_{ci} , are present on the crack surface. The static equivalence of the mean and local stresses in the direction tangential to the crack determines the local shear stresses as follows:

$$v_{ci} = \rho_x \cdot (f_{s,cr,x} - f_{s,x}) \cdot \cos \theta_{nx} \cdot \text{sen} \theta_{nx} + \rho_y \cdot (f_{s,cr,y} - f_{s,y}) \cdot \cos \theta_{ny} \cdot \text{sen} \theta_{ny} \quad (5-20)$$

Regardless of the above equation, since shear is a brittle behaviour, local shear stresses can only become large before shear-slide failure occurs.

The shear stress is limited by the meshing mechanism of the aggregates, the effectiveness of which decreases as the crack opening increases, w , and as the maximum size of the aggregates increases, a . The MCFT, therefore, limits the shear stress on the crack as follows:

$$v_{ci} \leq \frac{\sqrt{f'_c}}{0,31 + 24 \cdot \frac{w}{a + 26}} \quad (5-21)$$

The average crack opening, w , is given by the product of the tensile strain of the concrete and the average crack spacing, s_θ :

$$w = \varepsilon_{ci} \cdot s_\theta \quad (5-22)$$

$$s_\theta = \frac{1}{\frac{\cos \theta}{s_{mx}} + \frac{\text{sen} \theta}{s_{my}}} \quad (5-23)$$

The mean crack spacing in the x direction, s_{mx} , and in the y direction, s_{my} , can be estimated by knowing the bond stress and the arrangement of the reinforcements.

If the maximum concrete tensile stress or the local shear stress in a crack is exceeded, the strain state of the member is changed in such a way that a lower concrete tensile stress is caused.

5-NUMERICAL ANALYSIS

5.2.2.1.5 Summary

The following figures summarize the main aspects of MCFT. Figure 5-32 is taken from Bentz et al. (2006), while Figure 5-33 sum up the contents of VecTor 2 user's manual [Wong et al., 2013]. The slight difference between the two figures is in the form, not in the content.

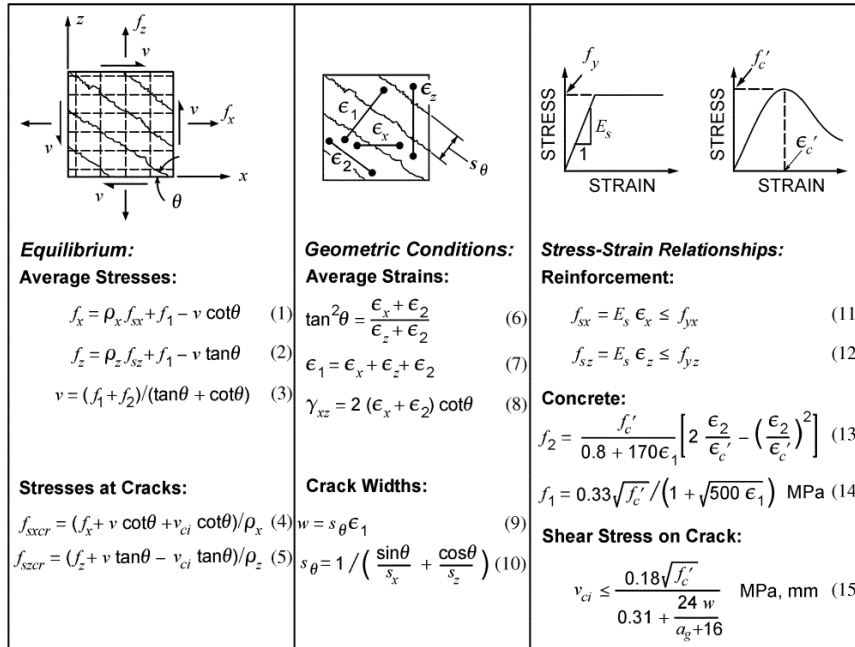


Figure 5-32: Summary of MCFT [Bentz et al., 2006].

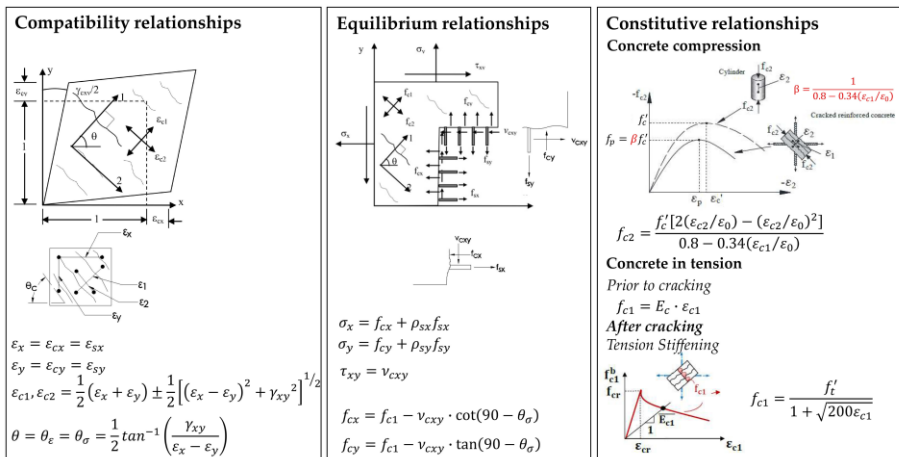


Figure 5-33: Aspects of the Modified Compression Field Theory [Wong et al., 2013].

5.2.3 Numerical Modelling of Test Specimens

Several models of the whole beam were made, one for each prestress level and prestress technology was investigated. A model for Beam A and one for Beam B were made, where they differed only in the prestress value assigned to the prestressed reinforcement. These were made for "regions", while the Beam C models were made for "points". As visible in Figure 5-34, the cross-section, which is the same for all beams, has been optimized and simplified through 4 rectangles.

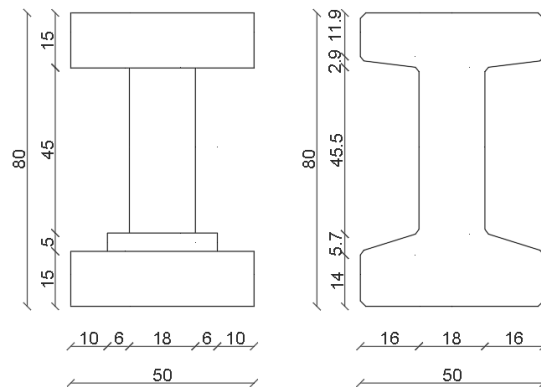


Figure 5-34: Approximation(left) of the real section (right) used in numerical analyses.

The mesh used is made up of square elements having dimensions of 50 mm x 50 mm, which correspond to 16 elements in height and 200 in length. In the "Job" section, 2 load conditions were used: in the first, only the own weight was applied, represented by a distributed load consisting of point forces applied on the 201 nodes of the upper limb, while the second load condition consists of a displacement imposed at the point of application, which grows monotonously until the ultimate strength of the beam is reached. The numerical test was therefore carried out in displacement control. The support areas and load points have been modelled using a steel plate and a layer of elastic material, in such a way as to have a distribution of the forces and to prevent their concentration in these points from causing local problems. The characteristics assigned to these materials are fictitious, their purpose within the model is only to avoid a critical point. The elastic material, which in reality would correspond to neoprene, has been defined as Bearing (Unidirectional) (Material 5 in Figure 5-44). It has a thickness equal to the base of the beam section and a high elastic modulus of 10000 MPa.

5-NUMERICAL ANALYSIS

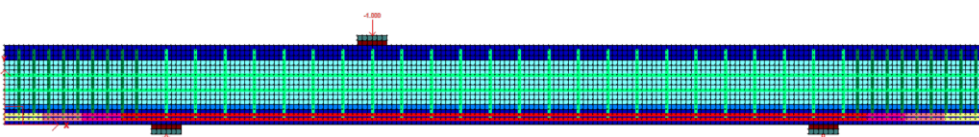
The steel plates were modelled with the Structural Steel material (Material 6 in Figure 5-44) which was assigned the same thickness T , equal to the thickness of the lower flange, and a value f_y , equal to 1000 MPa. It should be noted that, having the models of pre-tensioned and post-tensioned beams with a different useful height "d" (for reasons related to the constraints imposed by the mesh), the load point has been moved by ± 5 cm with respect to the setup actually used in the laboratory (§3.4), so that the a/d ratio was as close as possible between the experimental setup and the numerical model, as shown in Table 5-1.

Table 5-1: Comparison a/d on the numerical model and experimental setup.

a/d	Numerical Model		Experimental test setup	
Beam A	$\frac{210}{80 - 6.67}$	2.86	$\frac{205}{80 - 9.00}$	2.89
Beam B	$\frac{210}{80 - 7.50}$	2.89	$\frac{205}{80 - 7.67}$	2.83
Beams C	$\frac{200}{80 - 10.00}$	2.86	$\frac{205}{80 - 9.00}$	2.89

The transverse reinforcement was inserted as truss elements, as was the longitudinal prestressed reinforcement. Longitudinal mild reinforcement has been inserted as a "smeared" within each reinforcing property of the material. To create more detailed and refined models, it has been tried to apply the following variations (Figure 5-35):

- the stirrup supports in the web have been introduced as truss, instead of as smeared;
- the stirrups were interrupted 5 cm from the upper and lower edge to simulate the concrete cover;
- a 5 cm concrete cover was introduced, using a smeared material without reinforcement.



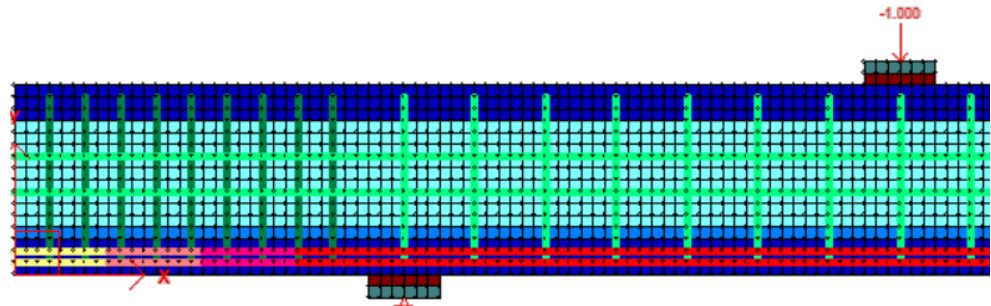


Figure 5-35: Refined model.

However, the results of the analyses carried out with the refined model did not bring appreciable differences, neither from the point of view of the load-displacement curve nor as regards the crack pattern. Instead, what has been noticed is a worsening of the convergence, probably due to a richer and more complex model. It was therefore decided to keep the one without these additional details as the reference model.

5.2.3.1 Pre - Tensioned Beams A and B

For the pre-tensioned beams, A and B (Figure 5-36), 6 and 4 strands each with an area of 139 mm^2 were respectively inserted, modelled as truss elements. The prestress amount is defined by entering the "prestrain" value, i.e. the strain assigned to the strands, which, dimensionless, multiplied by the elastic modulus returns the stress in the strands. In the models of the beams with pre-tensioned cables, the first 120 cm of the strands were modelled with 3 different types of "Prestressing Steel", each 40 cm long, in which 25%, 50% and 75% of the studied prestress level: this is to simulate the diffusion of prestress in the D-region even if, since this is in the area outside the supports, this choice should not influence the result of the analysis.

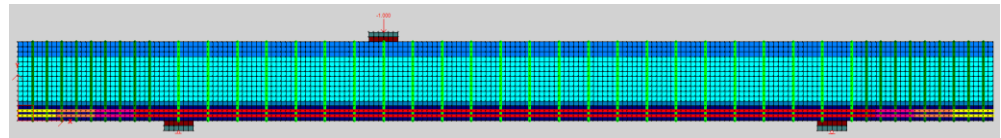


Figure 5-36: FEM Model, Beams A and B.

As regards the beam with pre-tensioned cables at 70% (Beam B), for a question of ease of execution, the prefabrication company proposed to tense only 4 of the 6 strands envisaged to obtain a prestress level of 67%, compared to string 6 strands to 70%.

5-NUMERICAL ANALYSIS

This choice was approved, however, prescribing additional reinforcement, equal to $2\phi 26$, necessary to compensate for the absence of the 2 sheathed and subsequently removed strands, so as to be able to more correctly simulate the behaviour of a prestressed beam subject to a loss of the initial prestress by 30%. It was verified, through the VT2 program, that the trend of the forecast curves was not affected too markedly by the solution adopted: as can be seen from Figure 5-37. The finite element software foresees, for the beam with 4 strands having 100% prestress and 2 supplementary $\phi 26$ bars, an anticipated collapse with respect to the beam with 6 strands at 70% of prestress. This was not considered a critical issue as, in the tests on the prestressed beams with pre-tensioned cables, the objective was to focus on the behaviour in service and on the evolution of the crack patterns, rather than evaluating the ultimate limit state.

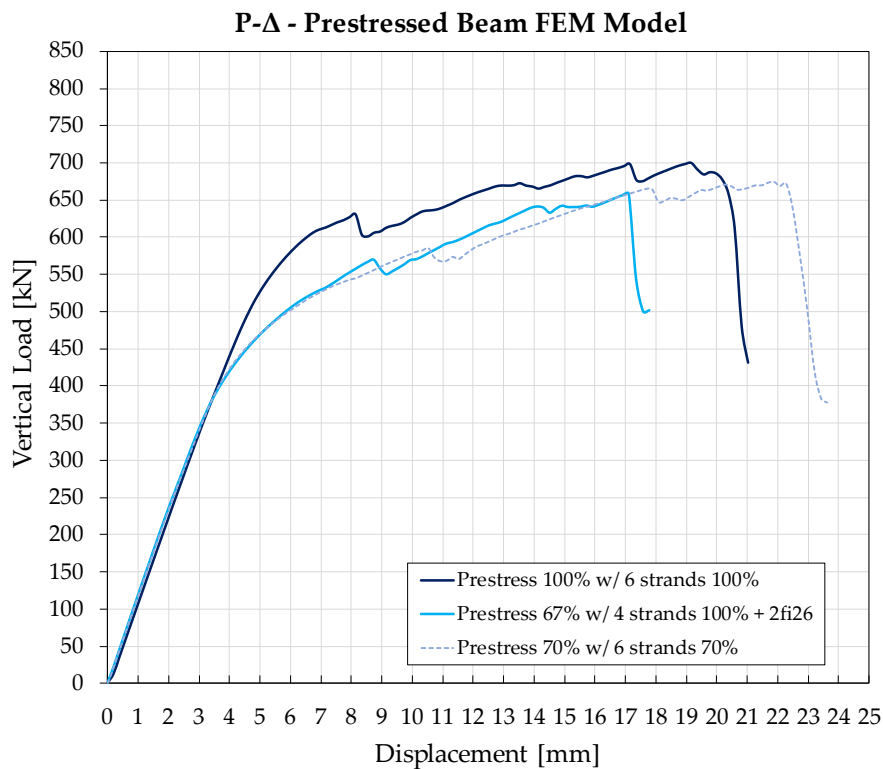


Figure 5-37: Comparison between the numerical prediction of the beam with 7 strands pre-tensioned at 70% and the same beam with 4 strands pre-tensioned at 100%.

Also in this phase, the evolution of the shear crack pattern in the two pre-tensioned beams was evaluated to understand, downstream of the design carried out, how

appreciable the differences between the behaviour of the two beams would have been during the tests.

From Figure 5-38 it is possible to observe how the evolution of the crack opening from the first crack to 1 mm is proportional to the prestress reduction. Once the 1 mm opening of the shear cracks is exceeded, the curve of Beam B tends to converge towards the curve of Beam A, until it collapses.

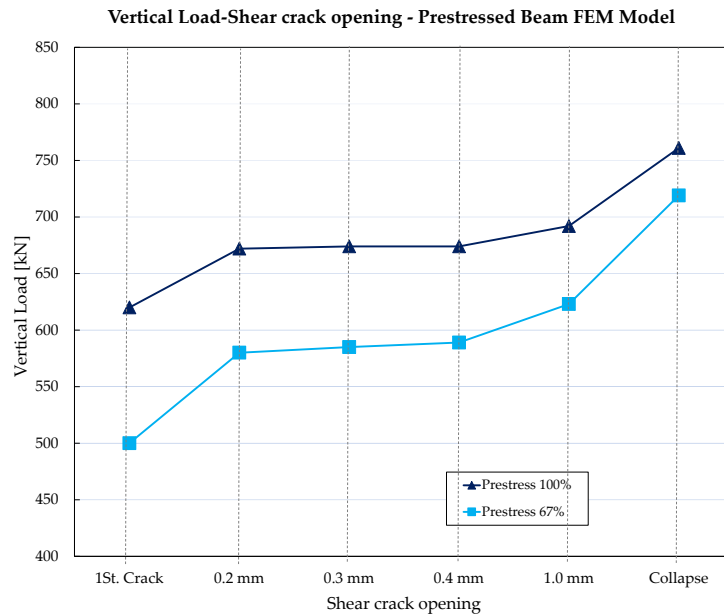


Figure 5-38: Comparison of the beam with pre-tensioned cables regarding the evolution of the shear crack pattern in numerical models.

This was possible thanks to the Augustus software, capable of post-processing the VT2 analysis data, placing itself at different steps and observing the development of the different crack widths (Figure 5-39).

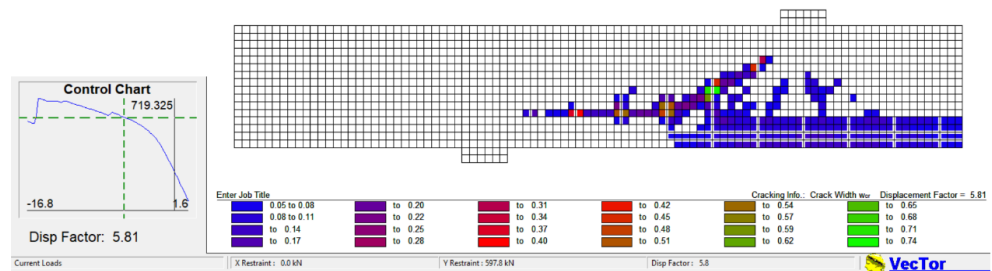


Figure 5-39: Augustus output that allows the evaluation of the width of the cracks.

5.2.3.2 Post - Tensioned Beams C1 and C2

As far as the post-tensioned beams are concerned, a “point” model has been created in which the point of the mesh below the load point has been doubled at the height of the strands. The prestressing reinforcement has been inserted as a truss constrained in five points: on the heads, in correspondence with the supports and under the load point, so as to behave like a tension tie that can follow the deformation of the beam (Figure 5-40). The points of the truss mesh at the supports and the one under the load point are connected to the rest of the model via a “Link-Element” (Figure 5-41), assigning to this the property “Unbonded Bars or Tendons”. By doing so it was possible to model the condition of the post-tensioned strands which, unlike the models of beams A and B in which there is perfect bond between the strands and the concrete, transmit the prestress to the beam via anchor plates placed in the ends. The anchoring steel plates of the strands were modelled with the Structural Steel material (Material 7 in Figure 5-44) which was assigned an f_y value of 1000 MPa.

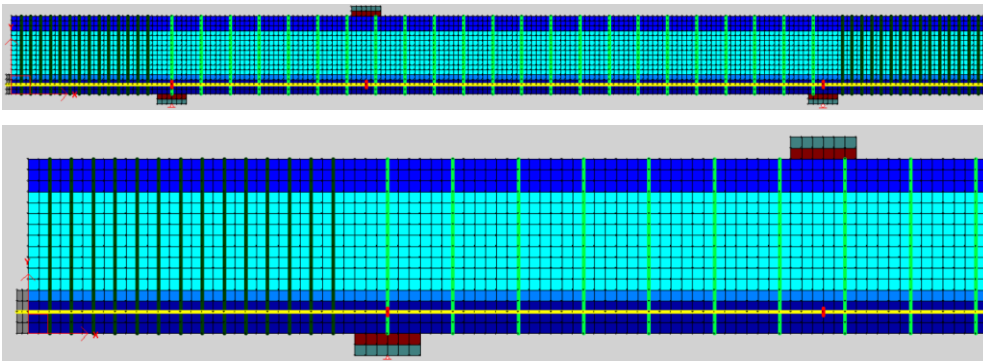


Figure 5-40: FEM Model, Beams C with detail of area most subjected to shear.

Different models were performed, each with a different assigned prestress level (Figure 5-42). Based on the simulations it was possible to evaluate the level of prestress and vertical load to be applied to obtain a collapse with shear cracks.

As previously mentioned, the post-tensioned beams have not been modelled with the aim of obtaining behaviour with collapse due to shear, but with the idea of creating beams with the same characteristics, both in geometric terms and in terms of percentage reinforcement, identical to the pre-stressed beams, with the difference, however, that the strands are made of unbonded cables, which implies a different behaviour at the ultimate limit state.

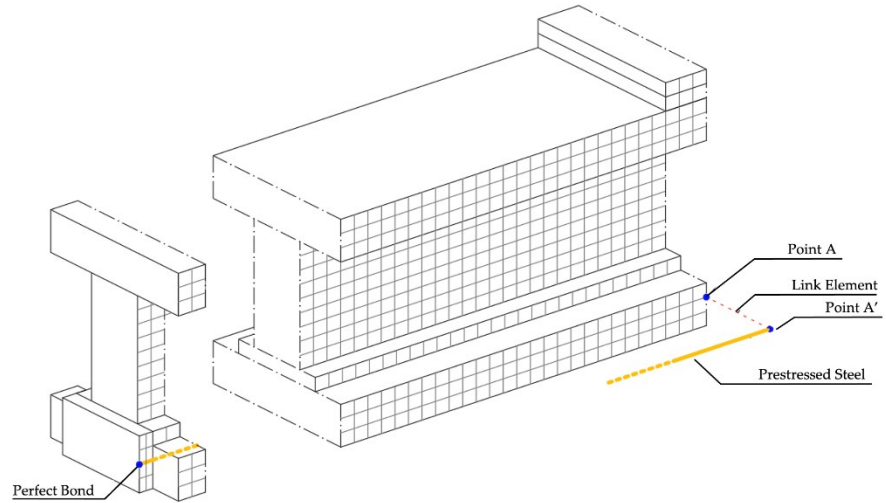


Figure 5-41: Schematic of the modelling of unbonded prestressing reinforcement in post-tensioned beams.

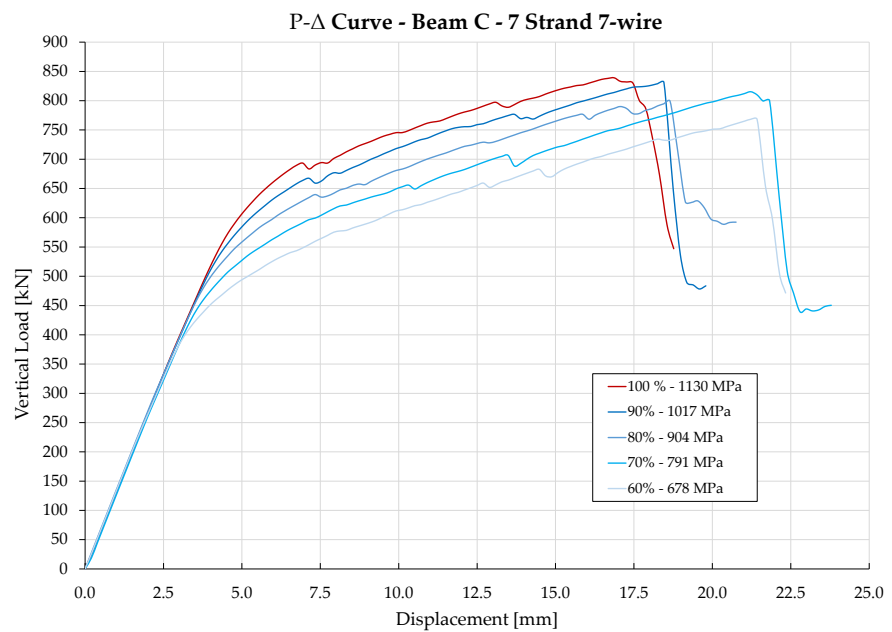


Figure 5-42: Vertical Load-Displacement curve of Beams C models with different prestress levels.

5.2.4 Modelling of Materials

During the design phase, characteristic values of the mechanical properties of the materials were entered into VT2. Once the beams were built, the values were updated with those provided by the fabricator and with the results obtained from the characterization tests of the materials carried out in the laboratory.

5.2.4.1 Concrete

For all beams, the section was divided into 4 reinforced concrete materials (Figure 5-43). The 4 materials differ from each other only in thickness "T". The other data can be observed in Figure 5-44. The cylindrical compressive strength f'_c was changed for each model. Consequently, VT2 calculates the following values:

$$f'_t = 0.33 \cdot \sqrt{f'_c} \quad (5-24)$$

$$E_c = 5500 \cdot \sqrt{f'_c} \quad (5-25)$$

$$\varepsilon_{cr} = \frac{f'_t}{E_c} \quad (5-26)$$

The value of the elastic modulus E_c used by VT2 calculated with the formula (5-25) is in line with the value determined in the laboratory and provided by the fabricator's tests.

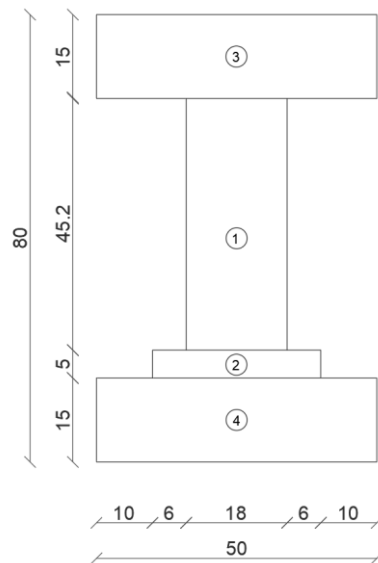


Figure 5-43: Division of the material section according to the thickness "T".

Define Material Properties

Material Types

Type:

- Material 1
- Material 2
- Material 3
- Material 4
- Material 5
- Material 6
- Material 7

Buttons: Add, Update, Delete

Reinforcement Components

Component:

- Reinforcement 1

Buttons: Add, Update, Delete

Material Properties

Reference Type: Reinforced Concrete

Thickness, T: 500 mm

Cylinder Compressive Strength, f_c : 63 MPa

Tensile Strength, f_t : * 0 MPa

Initial Tangent Elastic Modulus, E_c : * 36000 MPa

Cylinder Strain at f_c , ϵ_{oc} : * 0 me

Poisson's Ratio, μ_u : * 0

Thermal Expansion Coefficient, C_c : * 0 /°C

Maximum Aggregate Size, α : * 22 mm

Density: * 0 kg/m³

Thermal Diffusivity, K_c : * 0 mm²/s

Maximum Crack Spacing...

perpendicular to x-reinforcement, S_x : * 1000 mm

perpendicular to y-reinforcement, S_y : * 1000 mm

Color: [Blue]

Smeared Reinforcement Properties

Reference Type: Ductile Steel Reinforcement

Fibre Type:

Out of Plane Reinforcement:

Reinforcement Direction from X-Axis: 0 °

Reinforcement Ratio, ρ_o : 0.54 %

Reinforcement Diameter, D_b : 8 mm

Yield Strength, F_y : 540 MPa

Ultimate Strength, F_u : 600 MPa

Elastic Modulus, E_s : 200000 MPa

Strain Hardening Strain, ϵ_{sh} : 10 me

Ultimate Strain, ϵ_u : 150 me

Thermal Expansion Coefficient, C_s : * 0 /°C

Prestrain, Dep : 0 me

Unsupported Length Ratio, b/t : 0

Material types to be used for rectangular, quadrilateral and triangular elements only. * Enter '0' for VT2 default value.

Buttons: OK, Cancel

Figure 5-44: Interface for defining material properties.

Instead of using the models (related to the materials) provided by default by the program, following the characterization tests the "Concrete Models" in Figure 5-45 were modified.

In particular, being in the presence of high-strength concrete, it was deemed appropriate to switch from the pre and post-peak default models (highlighted in red in Figure 5-45) to more suitable models, in this case the one proposed by Popovics (HSC) and use the Base Curve instead of the Modified Park-Kent model (Figure 5-46).

Define Job

The screenshot shows a software interface for defining job models. The 'Concrete Models' section is highlighted with a red box. It contains the following settings:

- Compression Pre-Peak: Hognestad (Parabola)
- Compression Post-Peak: Modified Park-Kent
- Compression Softening: Vecchio 1992-A (e1/e2-Form)

Other settings in the interface include:

- Confined Strength: Kupfer / Richart
- Dilation: Variable - Isotropic
- Cracking Criterion: Mohr-Coulomb (Stress)
- Crack Stress Calc: Basic (DSFM/MCFT)
- Crack Width Check: Agg/2.5 Max Crack Width
- Crack Slip Calc: Walraven
- Tension Stiffening: Modified Bentz 2003
- Tension Softening: Linear
- FRC Tension: SDEM - Monotonic
- Creep and Relaxation: (empty)
- Hysteretic Response: Nonlinear w/ Plastic Offsets
- Reinforcement Models:
 - Hysteretic Response: Bauschinger Effect (Seckin)
 - Dowel Action: Tassios (Crack Slip)
 - Buckling: Akkaya 2012 (Modified Dhakal-Me)
- Bond Models:
 - Concrete Bond: Elgehausen
- Analysis Models:
 - Strain History: Previous Loading Considered
 - Strain Rate Effects: C: n/c S: n/c
 - Structural Damping: Not Considered
 - Geometric Nonlinearity: Considered
 - Cracking Spacing: CEB-FIP 1978 - Deformed

Buttons for 'Reset Options', 'Basic', and 'Advanced' are also visible.

Figure 5-45: Interface for choosing the models to apply.

This close-up screenshot shows the 'Concrete Models' section with the following settings:

- Compression Pre-Peak: Popovics (HSC)
- Compression Post-Peak: Base Curve

Figure 5-46: Concrete models used in the numerical model calibrated following material tests.

For the Compression Pre-Peak model, the Hognestad model, set by default by VT2 and used in the preliminary models, is recommended for concretes with strengths up to about 40 MPa. The trend of the stress-strain curve is described by means of a parabola (Figure 5-47). Collins and Porasz modified the stress-strain curve proposed by Thorenfeldt, Tomaszewicz, Jensen (1987) and Popovics (1973) to describe the compressive behaviour of high-strength concretes.

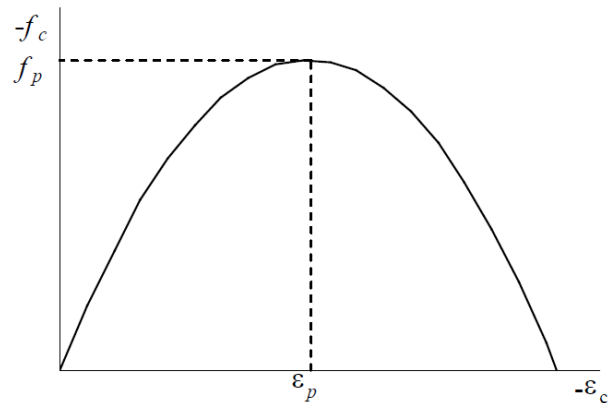


Figure 5-47: Parabola through which Hognestad models the pre- and post-peak behaviour of concrete [Wong et al., 2013].

The VT2 software manual [Wong et al., 2013] reports how, through experimental studies, it has been demonstrated that as the compressive strength of concrete increases, the stress-strain curve remains linear up to higher stress and strain percentages. Furthermore, as the strength class of the concrete increases, so does the slope with which the stage of the post-peak curve descends (Figure 5-48).

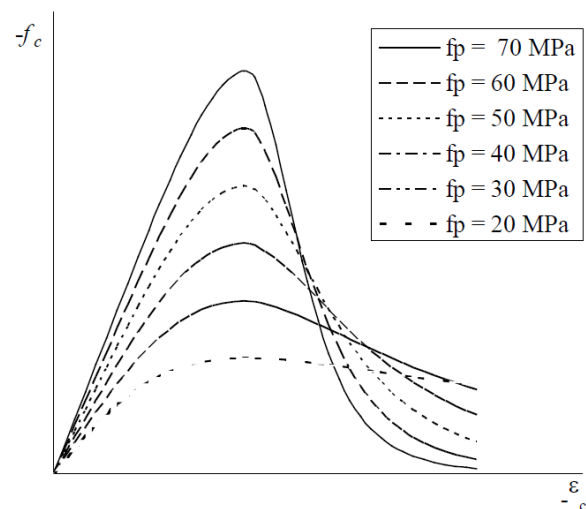
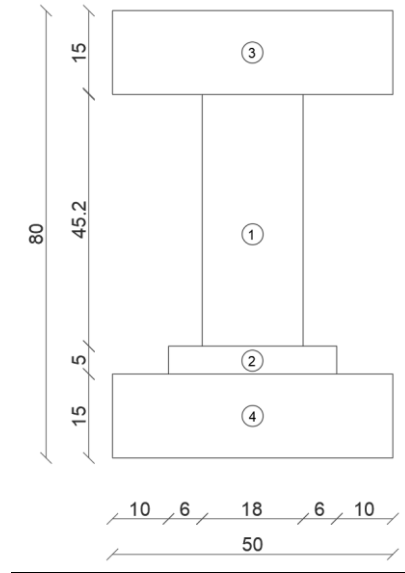


Figure 5-48: Curve proposed by the Popovics High Strength model [Wong et al., 2013].

For the Compression Post-Peak model, the Base curve is set, that is, the same model indicated in the Compression Pre-Peak, i.e. Popovics (HSC), is considered in the Compression Post-Peak.

5.2.4.2 Reinforcement

The longitudinal mild reinforcement, both for the pre-tensioned beams and for the post-tensioned beams, has been entered as "smeared" by defining the relative percentage of reinforcement in each of the 4 materials. (Figure 5-44 right side):



Material	Beam	Mild Reinforcement	ρ [%]
1	all	4 \emptyset 8	0.248
2	all	2 \emptyset 8	0.67
3	all	8 \emptyset 8	0.804
4	A	6 \emptyset 8	0.603
	B	6 \emptyset 8 + 2 \emptyset 26	0.603+2.124
	C1, C2	2 \emptyset 8 + 4 \emptyset 12	1.106

Figure 5-49: Longitudinal mild reinforcement inserted into VecTor 2 model.

Table 5-2 shows the input values for the mild longitudinal reinforcement.

Table 5-2: Mild longitudinal reinforcement values.

f_y [MPa]	f_u [MPa]	E_s [MPa]	ϵ_{sh} [m ϵ]	ϵ_u [m ϵ]
540	600	200'000	10 (1%)	150 (15%)

The transverse reinforcement was inserted as truss elements (Figure 5-50).

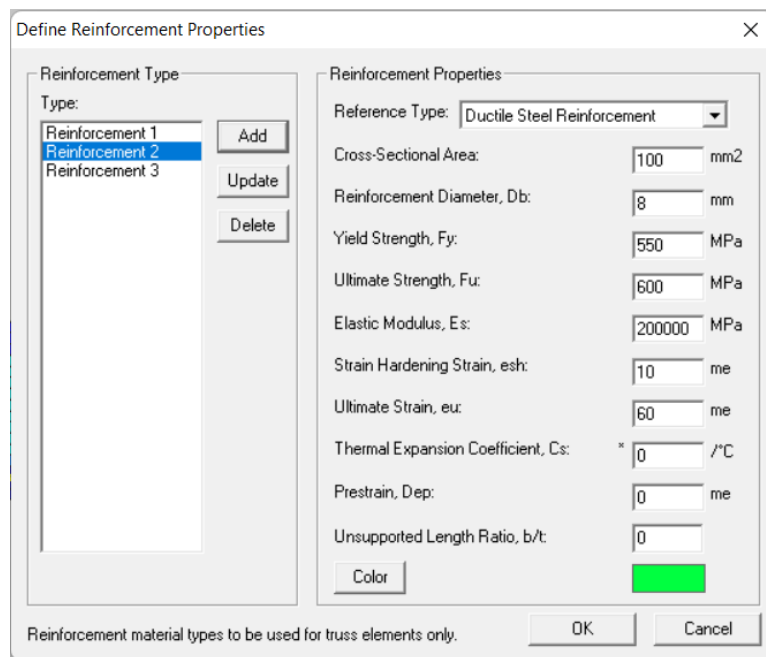


Figure 5-50: Interface for defining reinforcement properties.

Table 5-3 shows the input values for transverse reinforcement. They derive from the characterization tests carried out by the supplier (verified again in the laboratory). Except for the ϵ_u value of $\emptyset 8$, for which the value relating to steel B450C was used instead of B450A, as the results obtained are more relevant to those of the experimental tests. For all the beams, only 2 types of diameters have been entered: $\emptyset 8$ used in the internal area of the supports, and $\emptyset 12$ for confinement for the prestressing D-Regions in the external parts of the supports. The latter have been modelled for completeness, but should not affect the shear resistance capacity of the beam.

Table 5-3: Transverse reinforcement values.

\emptyset	f_y [MPa]	f_u [MPa]	E_s [MPa]	ϵ_{sh} [mε]	ϵ_u [mε]
8	550	600	200'000	10 (1%)	60 (6%)
12	550	600	200'000	10 (1%)	150 (15%)

Figure 5-51 shows the stress-strain graph (default) considered by VT2 for "ductile steel reinforcement".

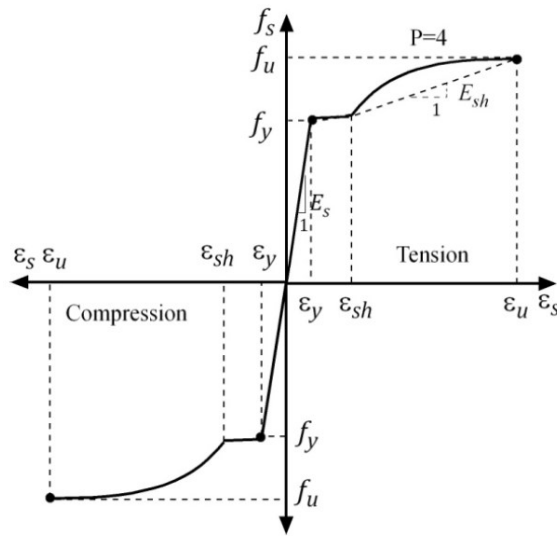


Figure 5-51: Stress-strain graph (default) considered by VT2 for "ductile steel reinforcement" [Wong et al., 2013].

As for the strands, they too were modelled through truss elements, both in the pre-stressed and in the post-tensioned beams with the properties indicated in Table 5-4. The equivalent diameter of a 6/10" strand is 13.3 mm; for Beam A 6 were inserted and for Beam B 4 both were divided over 2 levels as per the executive design, while for Beams C the 7 strands were all positioned at the same height.

Table 5-4: Prestressed reinforcement values.

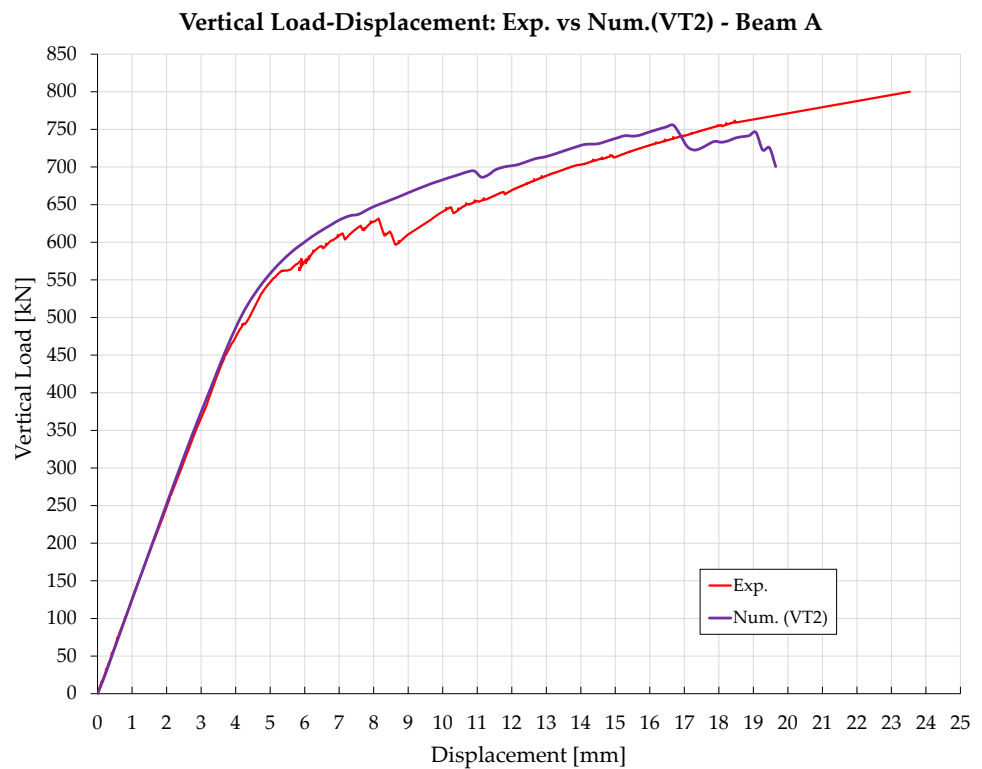
f_y [MPa]	f_u [MPa]	E_s [MPa]	ϵ_{sh} [mε]	ϵ_u [mε]
1670	1860	195'000	10 (1%)	40 (4%)

5.2.5 Comparison of Numerical and Experimental Results

5.2.5.1 Pre-Tensioned Beams

5.2.5.1.1 *Beam A*

The comparison between the numerical prediction, obtained through VT2, and the experimental curve of Beam A is shown below. Figure 5-52 shows a good agreement in the results, especially as regards the stiffness and the exit point from the elastic stage which, in this experimental test, appears to be more disturbed by progressive collapses of strength, compared to what was observed on the Beam B (see Figure 5-58).



*Figure 5-52: Load-Displacement Curve – Beam A.
Comparison between experimental result and numerical prediction.*

The main difference between the two curves is the behaviour near the ultimate limit state: in fact, the numerical model predicts a failure correctly correlated to a shear failure, for load and displacement values lower than what has been observed experimentally.

This was not considered a problem, since the research work carried out has, as the main objective, that of investigating, rather than collapse, the behaviour in operation and the influence of prestress losses on the formation of crack patterns (in particular, for the two pretension beams). Therefore, referring to the estimate provided by the numerical model, regarding the shear crack opening exhibited by Beam A, and represented in Figure 5-53, it can be seen how the software was able to accurately capture the load relating to the formation of the first shear crack. The numerical prediction also seems to be able to estimate, albeit only qualitatively, the evolution of the crack opening as the load increases. In Figure 5-53 a comparison is made between the results relating to the opening of the crack released by VT2 and those acquired by the DIAG. 2 potentiometer, positioned on the web in the area of formation of the crack pattern inclined by about 56° with respect to the horizontal, thus to intercept the series of shear cracks. DIAG. 2 is located between DIAG. 3, closest to the S-Side support, and DIAG. 1 closest to the loading point (see Figure 4-77).

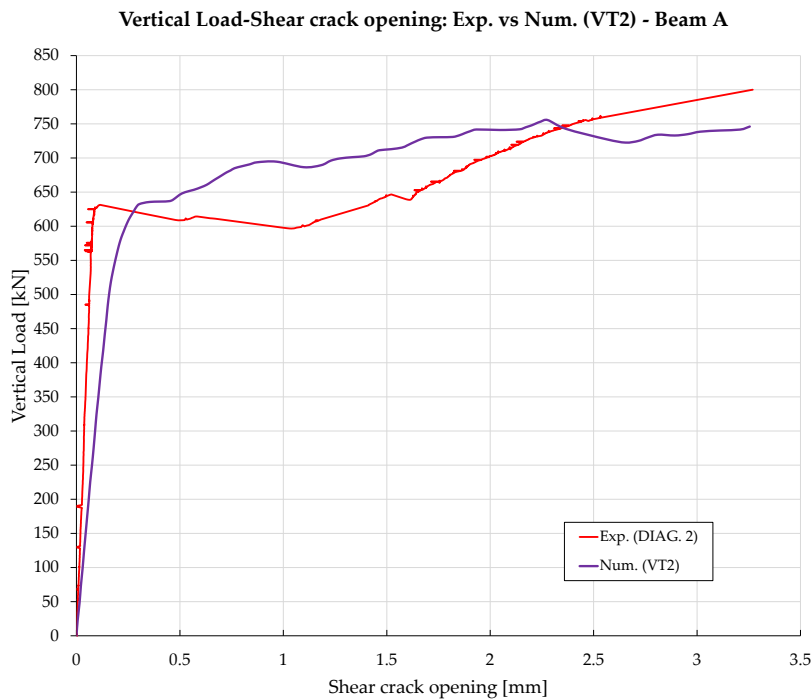


Figure 5-53: Trend of the shear crack opening recorded by the potentiometer DIAG. 2 – Beam A.
Comparison between experimental result and numerical prediction.

In Figure 5-54 the prediction of the evolution of the crack pattern was evaluated and compared with the experimental results. This was done using the Augustus software, capable of post-processing the data from the VT2 analyses, placing itself at different steps and thus observing the development of the different crack widths (Figure 5-55). This is correlated both to a subjective component, during the reading and interpretation of the output data, and to the fact that Augustus seems to simulate the crack pattern as a single crack, while multiple cracks are observed experimentally. Nonetheless, the overall crack opening appears similar; this is also noticeable from the data recorded by the diagonal potentiometers (see Figure 4-84). It is therefore only a qualitative assessment which, in any case, seems to highlight how the numerical model, also in this case, is able to adequately catch the evolution of the crack pattern. On the abscissa axis, 4 significant points were chosen to compare the load at which this crack opening was reached, namely: 0.1 mm, 0.2 mm, 1 mm and 3 mm (condition close to ULS). It is important to point out that the crack opening values acquired by Augustus, shown in Figure 5-54, are to be considered affected by a certain degree of imprecision.

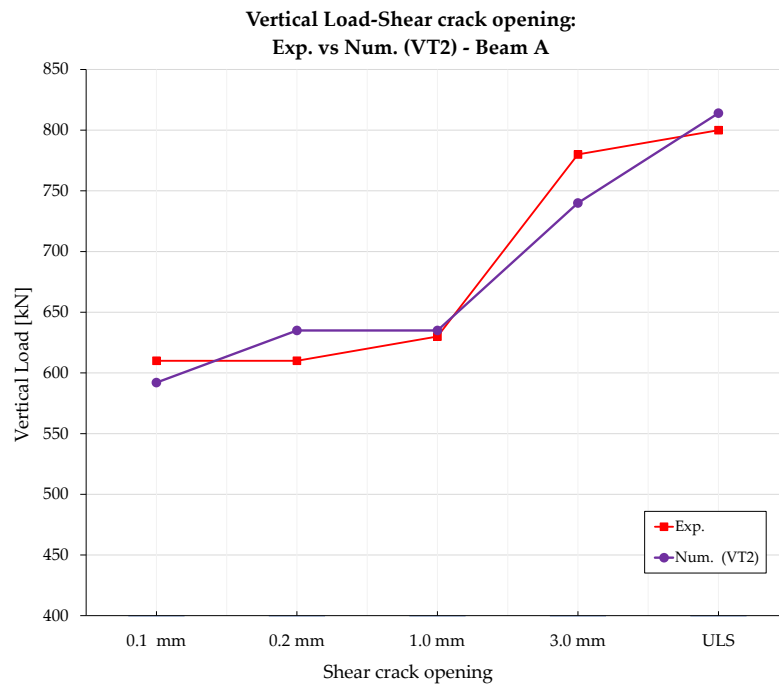


Figure 5-54: Comparison between numerically predicted and experimentally recorded shear crack opening evolution – Beam A.

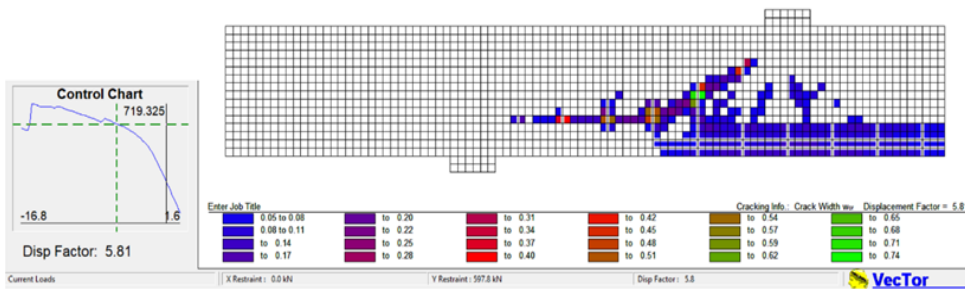
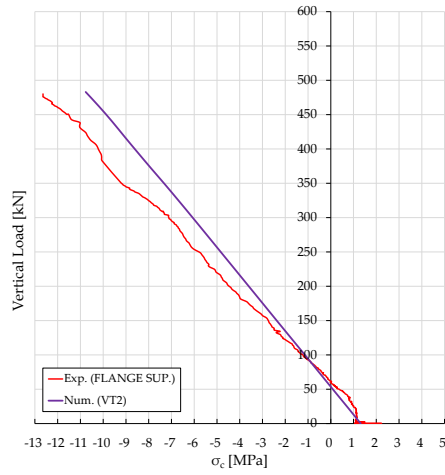


Figure 5-55: Augustus output that allows the evaluation of the width of the cracks.

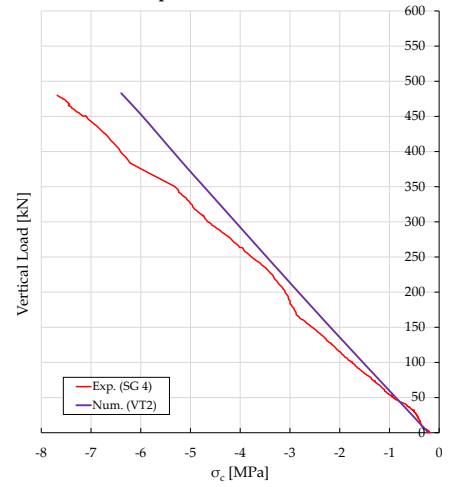
Moving on to the estimation of the stress trends in the section, comparing what was predicted by the numerical model and what was recorded by the strain gauges and potentiometers installed on the beam (whose position is indicated in Figure 4-77), a good agreement between experimental result and numerical prediction, as can be appreciated from the diagrams represented in Figure 5-56. Figure 5-56 shows the comparison between the numerical prediction and the experimental result of the stress trend of the concrete at the load point. While for the numerical prediction the stress in the beam caused by the prestressing is known, therefore corresponding to the stress value in unloaded beam condition, it is not so for the experimental results.

To be able to compare the trend predicted by VT2 and the experimental trend, it was, therefore, necessary to hypothesize this value using analytical formulas (§4.1.1.3). From the graphs of Figure 5-56 it can be seen that there is a good correspondence between previsions and experimental results for all levels of the monitored section.

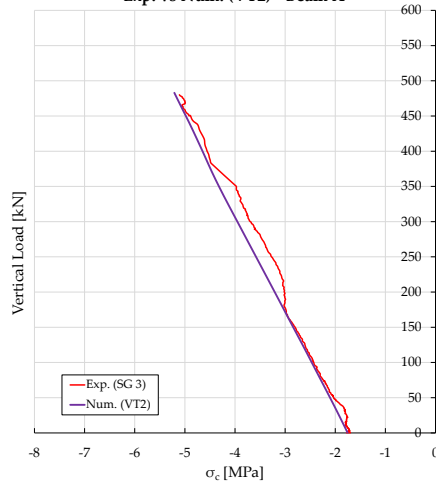
Vertical Load-Flange Sup. Stress (PT FLANGE SUP):
Exp. vs Num. (VT2) - Beam A



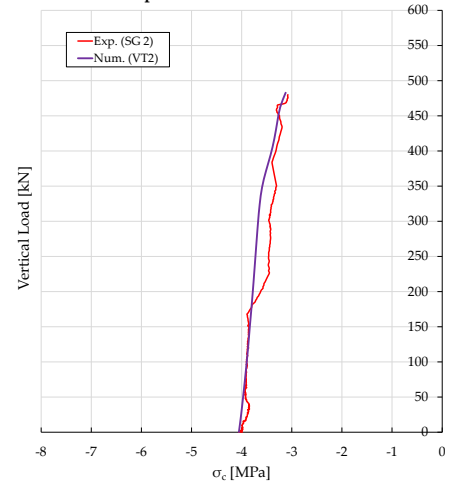
Vertical Load-Web Stress (SG 4):
Exp. vs Num. (VT2) - Beam A



Vertical Load-Web Stress (SG 3):
Exp. vs Num. (VT2) - Beam A



Vertical Load-Web Stress (SG 2):
Exp. vs Num. (VT2) - Beam A



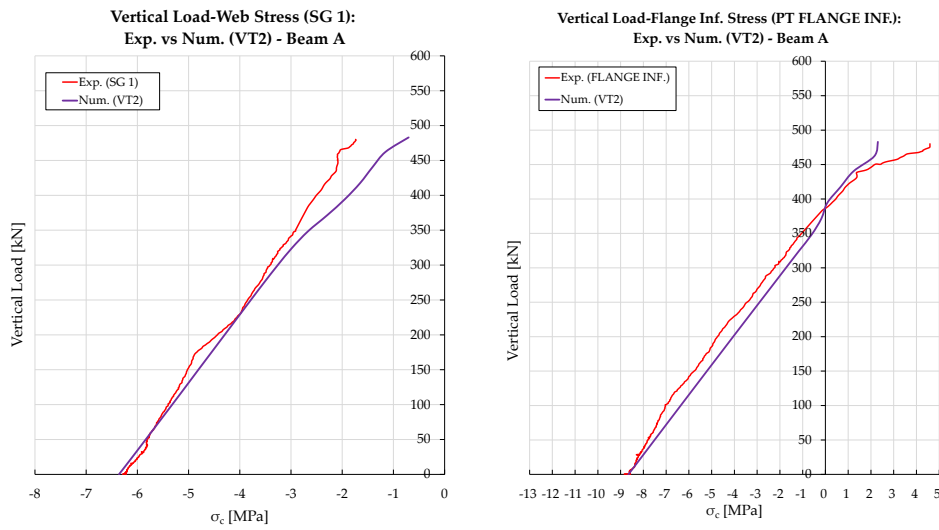


Figure 5-56: Stress trend of concrete at the load point: comparison between experimental result and numerical prediction – Beam A.

Figure 5-57 shows the “butterfly” trend of the stresses predicted numerically by VT2 and recorded by the strain gauges and potentiometers installed below the load point. To make this comparison, a load of 400 kN was set to remain in the elastic range: it can be seen that there is a good correspondence between the prediction and the experimental result, even if a lower precision can be found as regards the values recorded by the potentiometers, less accurate than strain gauges.

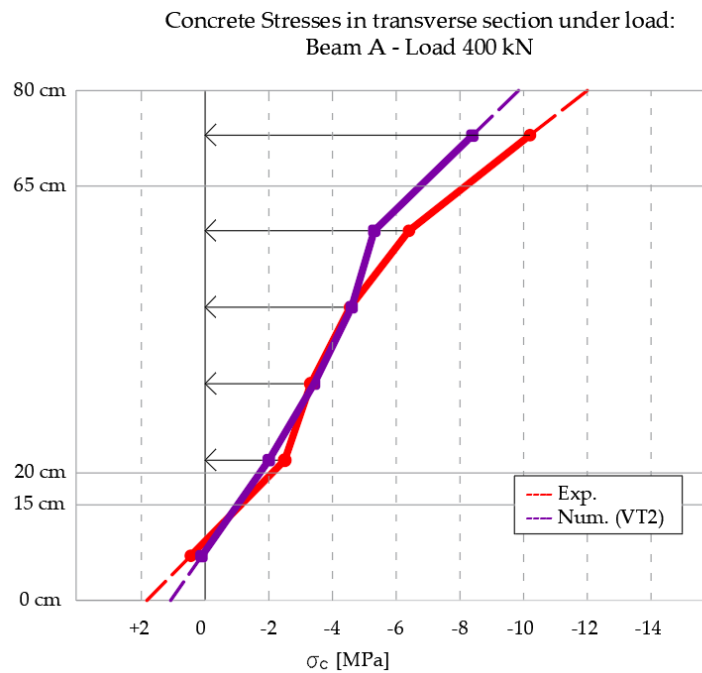


Figure 5-57: Stress trend in Beam A at the load point in the elastic stage.
 $F_V=400$ kN – Beam A.

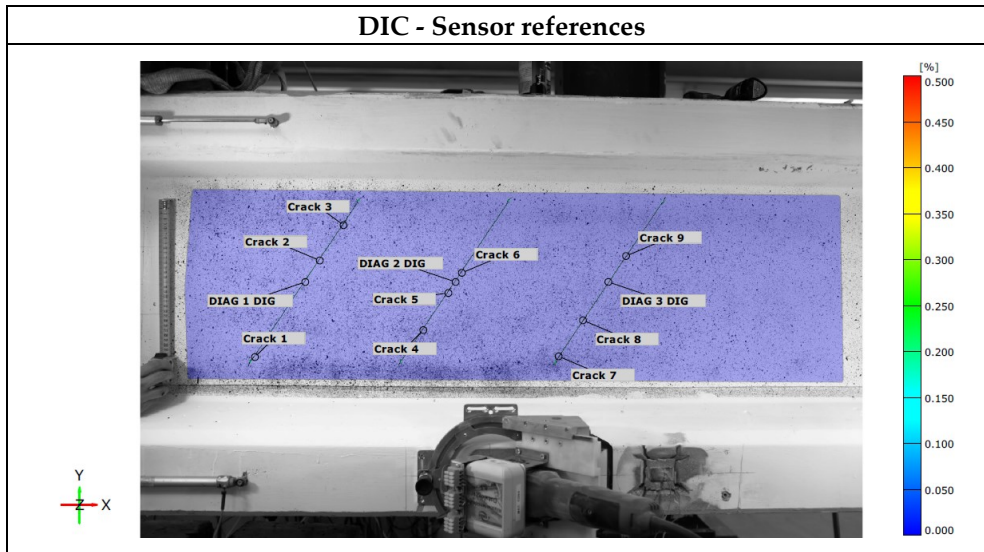
In Table 5-5 the crack patterns of Beam A are compared at different load levels. The comparison is made between the numerical model (VecTor 2) and the experimental model (DIC image processing), i.e. the images post-processed by the GOM software. At the end of the test, a survey of the crack pattern was also carried out. However, the latter is not as precise as the DIC images as once the vertical load was removed, due to the prestressing the cracks closed again. The five load levels are:

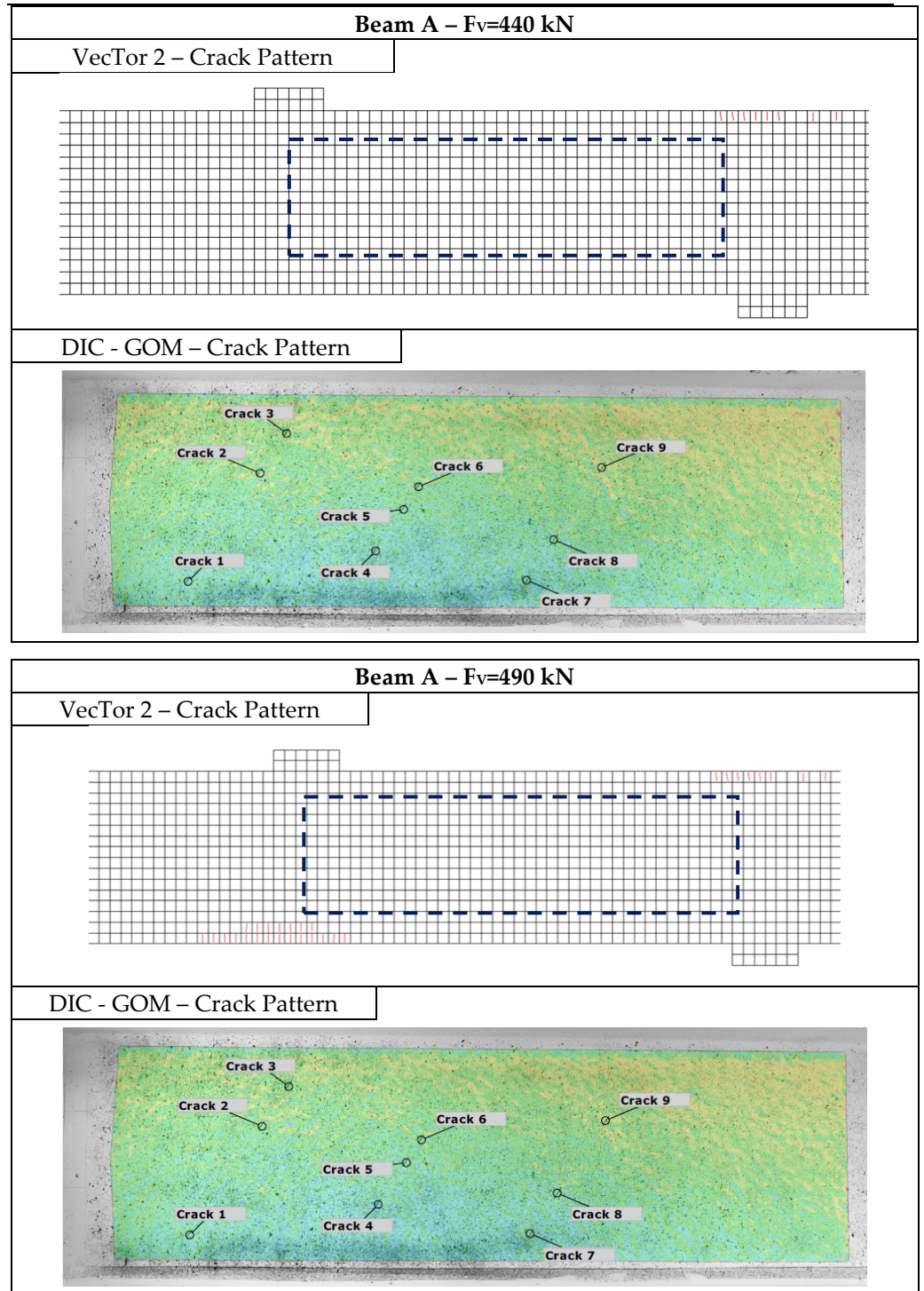
- 440 kN: First shear crack formation Beam B identified by GOM;
- 490 kN: First shear crack formation Beam B;
- 630 kN: First shear crack formation Beam A;
- 690 kN First shear crack formation Beam C2;
- 800 kN Ultimate condition Beam A (750 kN for VT2).

The first image of Table 5-5 indicates the reference of the potentiometers on the opposite side of the beam (DIAG # DIG) and the cracks intercepted by them (Crack #). It can be observed that there is a good correspondence between the crack pattern of the numerical model and that detected by DIC.

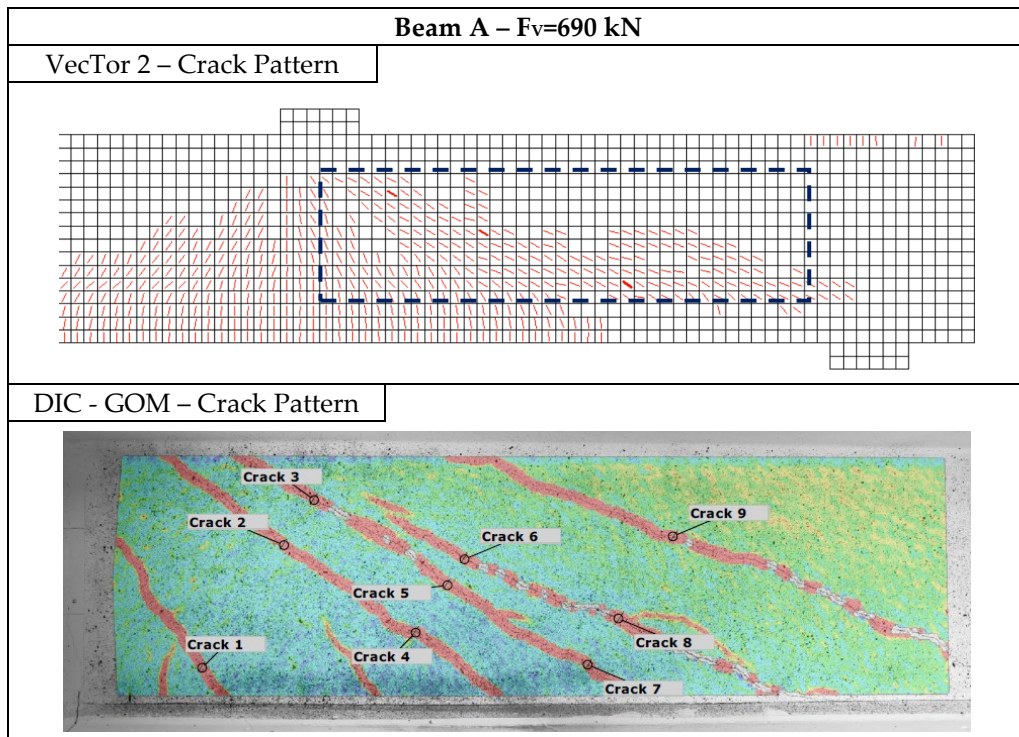
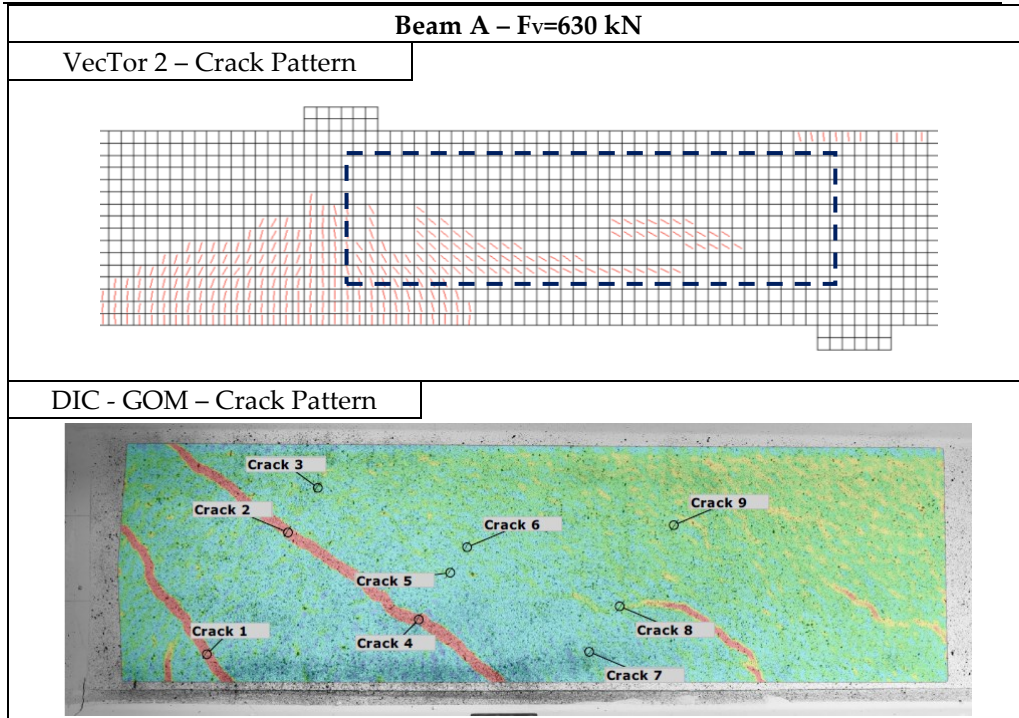
5-NUMERICAL ANALYSIS

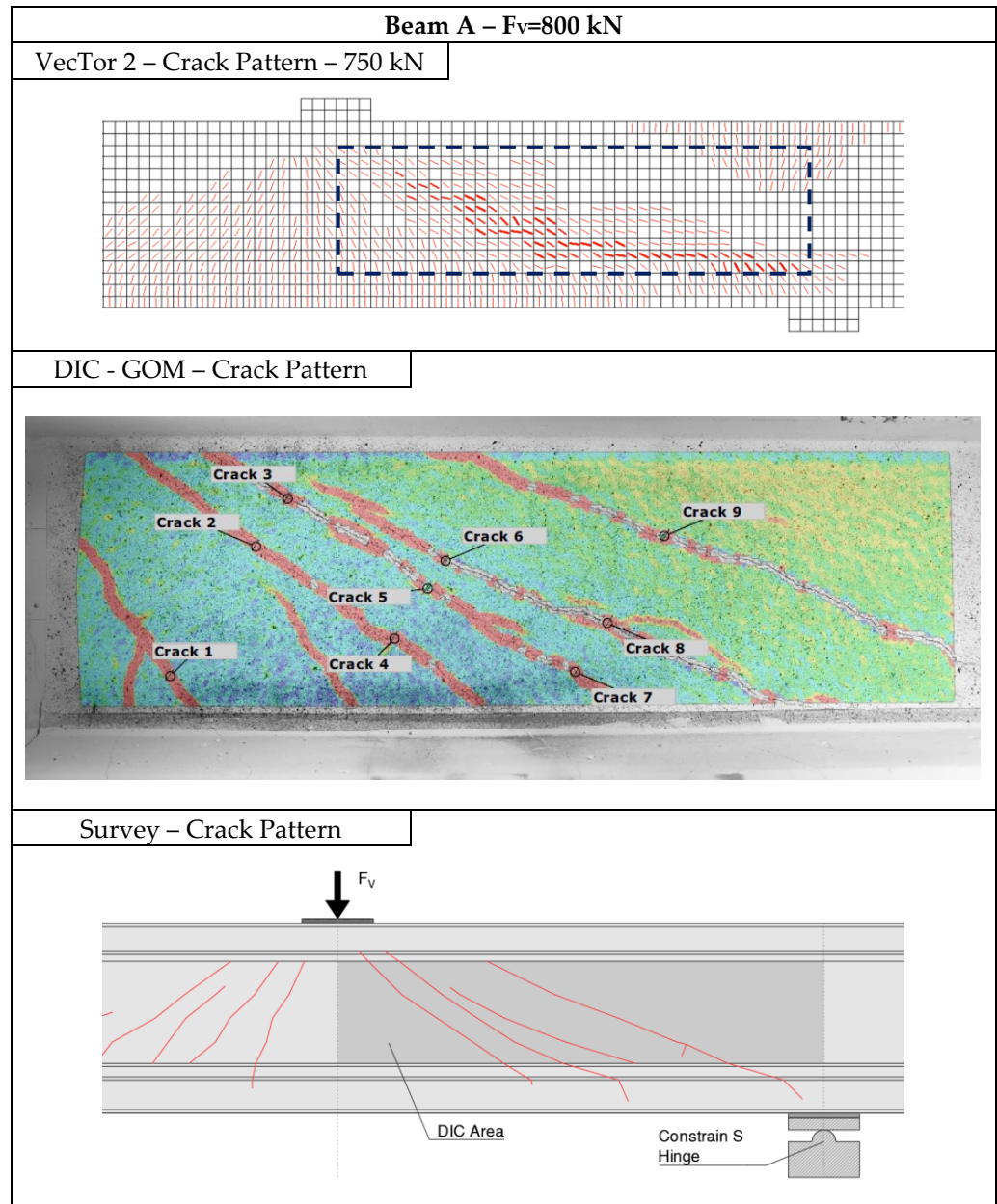
Table 5-5: Comparison of the crack pattern between numerical and experimental models at different vertical load levels – Beam A.





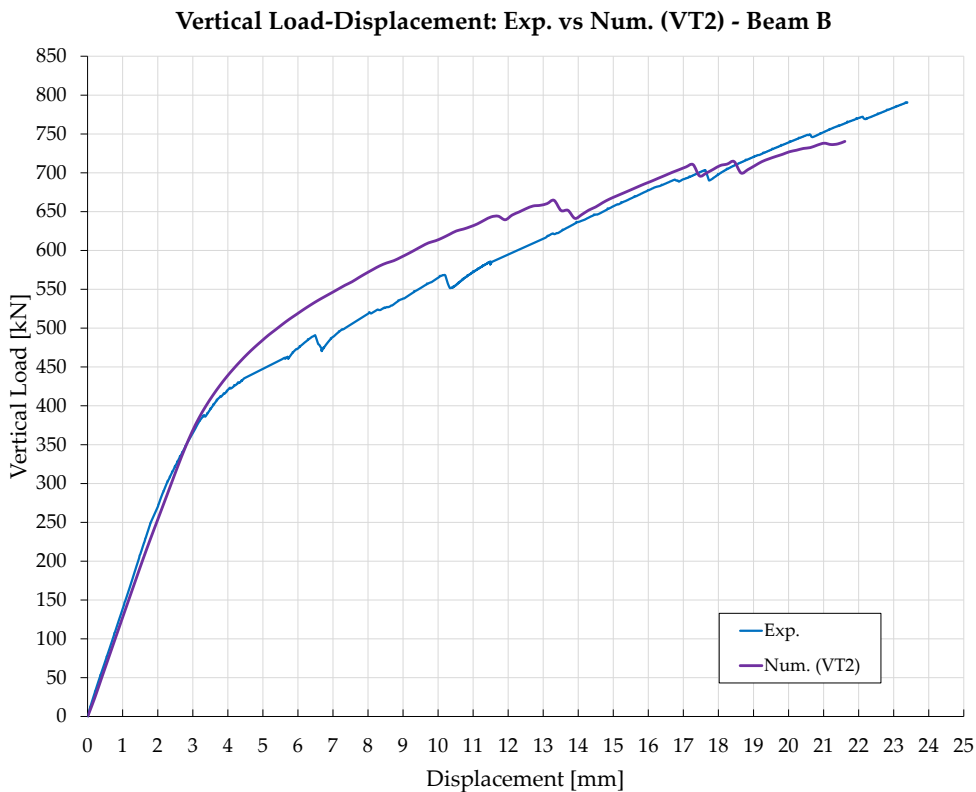
5-NUMERICAL ANALYSIS





5.2.5.1.2 *Beam B*

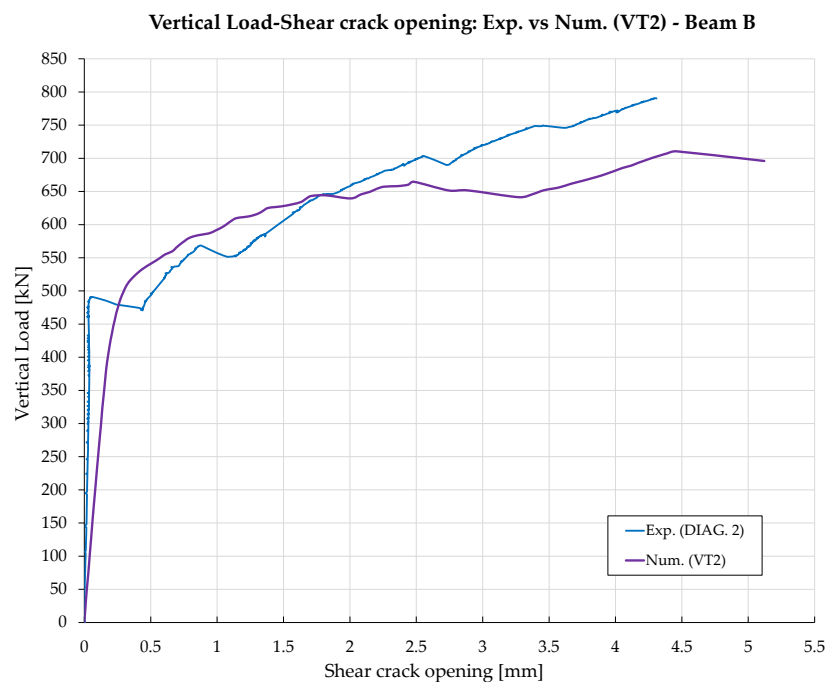
The comparison between the numerical prediction, obtained through VT2, and the experimental curve of Beam B is shown below. Figure 5-58 shows a good agreement in the results, especially as regards the slope of the elastic stage. The numerical prediction seems, in this case, to be a little less accurate regarding the exit point from the elastic stage, compared to the comparison between the numerical prediction and the experimental result of Beam A. (see Figure 5-52).



*Figure 5-58: Load-Displacement Curve – Beam B.
Comparison between experimental result and numerical prediction.*

Also, in this case, the main difference between the two curves is the behaviour near the ultimate limit state. In fact, the numerical model predicts a collapse, correctly correlated to a shear failure, for lower load and deflection values than those achieved experimentally. As mentioned for Beam A, this was not considered a problem and the numerical model was exploited, mainly, to compare predictions and experimental results regarding the beams' behaviour in-service conditions.

Therefore, referring to the estimate provided by the numerical model, regarding the shear crack opening exhibited by Beam B, and represented in Figure 5-59 it can be seen that, also in this case, the software was able to capture, quite accurately, the formation load of the first shear crack. The numerical prediction also seems to be able to estimate, qualitatively, also the evolution of the crack opening as the load increases, albeit in a less precise way than what was seen in the comparison between VT2 and the experimental results of Beam A. In Figure 5-59 the comparison is made between the results relating to the opening of the crack released by VT2 and those acquired by the DIAG. 2 potentiometer, positioned on the web in the area where the crack pattern is formed, inclined by about 56° with respect to the horizontal, so as to intercept the series of shear cracks. DIAG. 2 is located between DIAG. 3, closest to the S-Side support, and DIAG. 1 closest to the loading point (see Figure 4-77).



*Figure 5-59: Trend of the shear crack opening recorded by the potentiometer
DIAG. 2 – Beam B.*

Comparison between experimental result and numerical prediction.

In the numerical-experimental comparison, the prediction of the evolution of the crack pattern was evaluated, using the Augustus software, and comparing it with the experimental results.

As shown in Figure 5-60, since it is a purely qualitative evaluation, this seems to highlight how the numerical model, also in this case, is able to adequately catch the evolution of the crack pattern; albeit in a less precise way than seen in the comparison between VT2 and the experimental results of Beam A. Also in this case, on the abscissa axis, 4 significant points were chosen to compare the load at which this crack opening was reached, namely: 0.1 mm, 0.2 mm, 1 mm and 4 mm (a condition close to ULS).

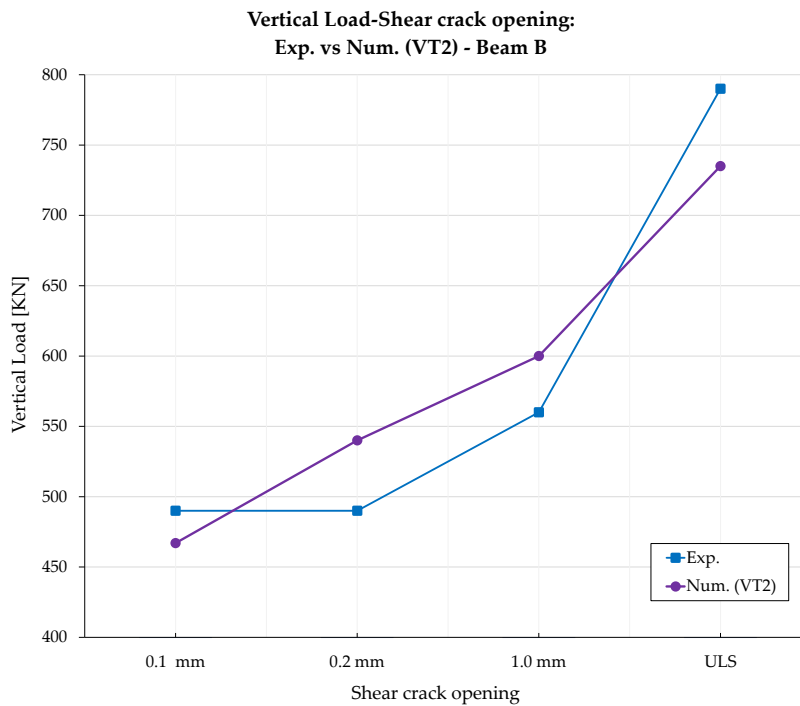
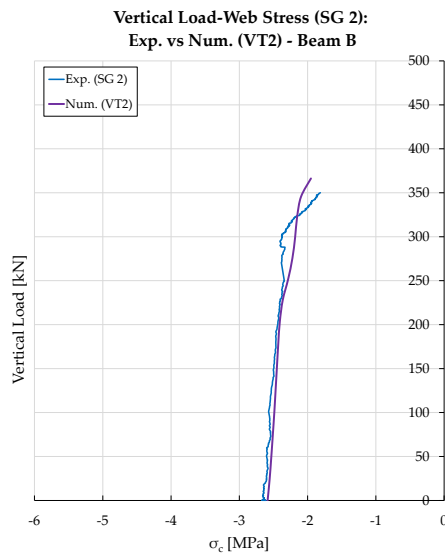
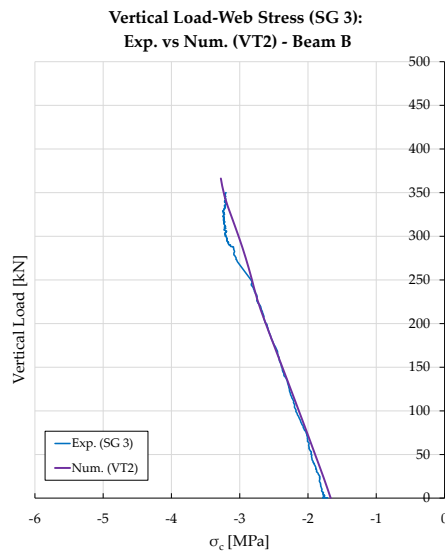
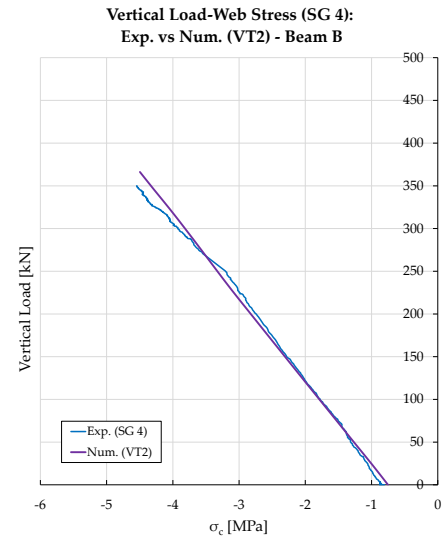
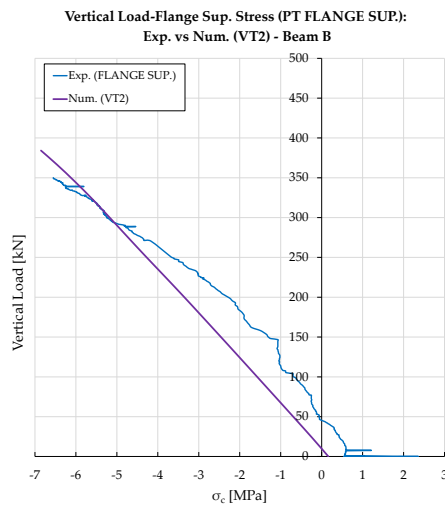


Figure 5-60: Comparison between numerically predicted and experimentally recorded shear crack opening evolution – Beam B.

Moving on to the estimation of the stress trends in the section, comparing what was predicted by the numerical model and what was recorded by the strain gauges and potentiometers installed on the beam (whose position is indicated in Figure 4-77), a good agreement between experimental result and numerical prevision it has been reached, as can be appreciated from the diagrams represented in Figure 5-61.

Figure 5-61 shows the comparison between the numerical prediction and the experimental result of the stress trend of the concrete at the load point. While for the numerical prediction the stress in the beam caused by the prestressing is known, corresponding therefore to the stress value in unloaded beam condition, it is not so for the experimental results. In order to be able to compare the trend predicted by VT2 and the experimental trend, it was, therefore, necessary to hypothesize this value using analytical formulas (§4.1.1.3). From the graphs of Figure 5-61 it can be seen that there is a good correspondence between prevision and experimental result for all levels of the monitored section.



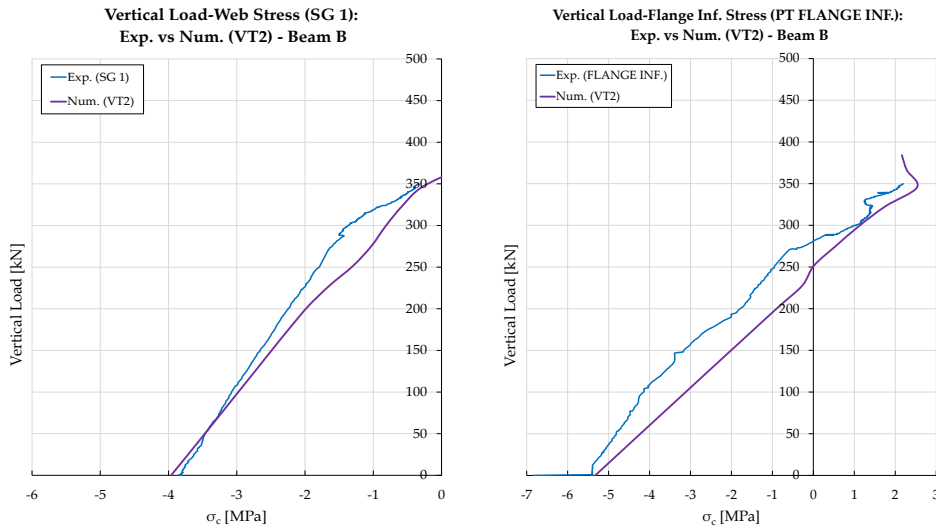


Figure 5-61: Stress trend of concrete at the load point: comparison between experimental result and numerical prediction – Beam B.

Figure 5-62 shows the “butterfly” trend of the stresses predicted numerically by VT2 and recorded by the strain gauges installed under the load point. To make this comparison, a load of 400 kN was set to remain in the elastic range: it can be seen that there is a good correspondence between prediction and experimental result.

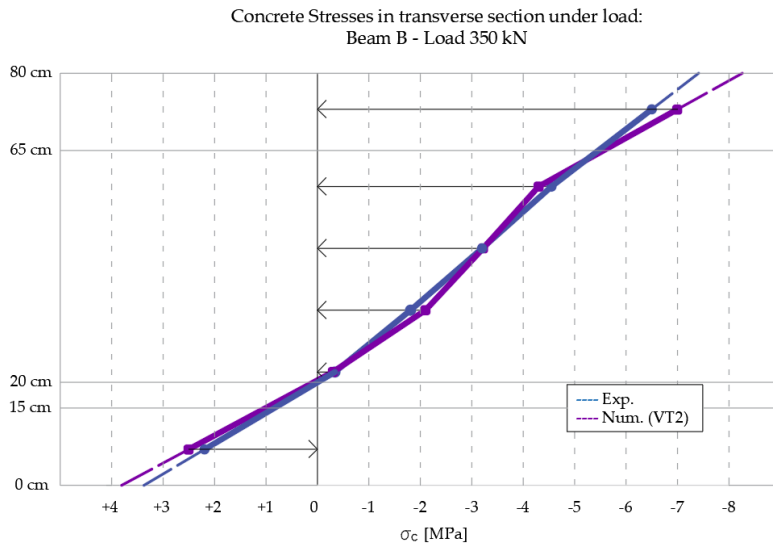


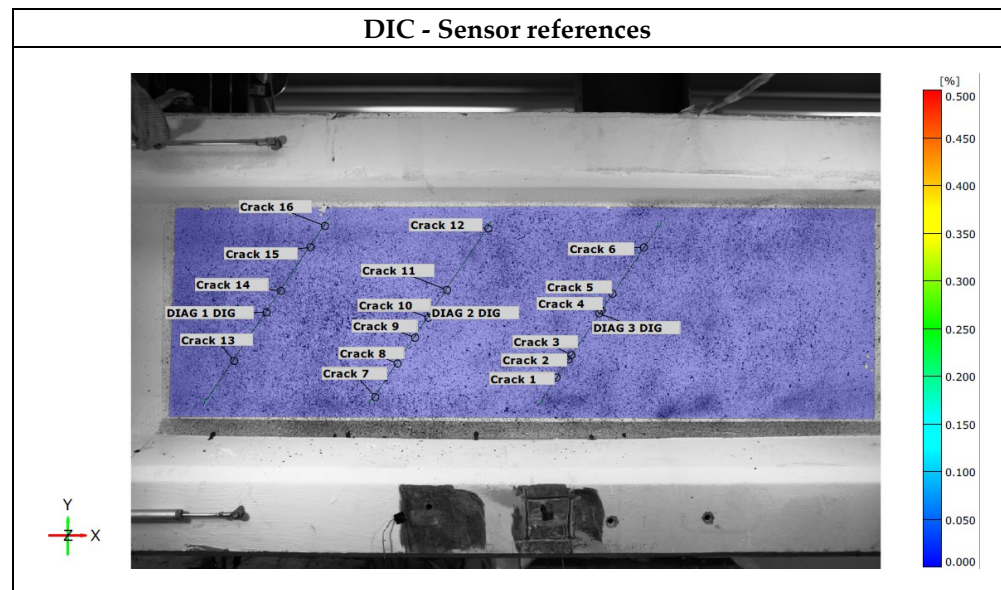
Figure 5-62: Stress trend in Beam B at the load point in the elastic stage. $F_v=350\text{ kN}$ – Beam B.

In Table 5-6 the crack patterns of Beam B are compared at different load levels. The comparison is made between the numerical model (VecTor 2) and the experimental model (DIC image processing), i.e. the images post-processed by the GOM software. At the end of the test, a survey of the crack pattern was also carried out. However, the latter is not as precise as the DIC images as once the vertical load was removed, due to the prestressing the cracks closed again. The five load levels are:

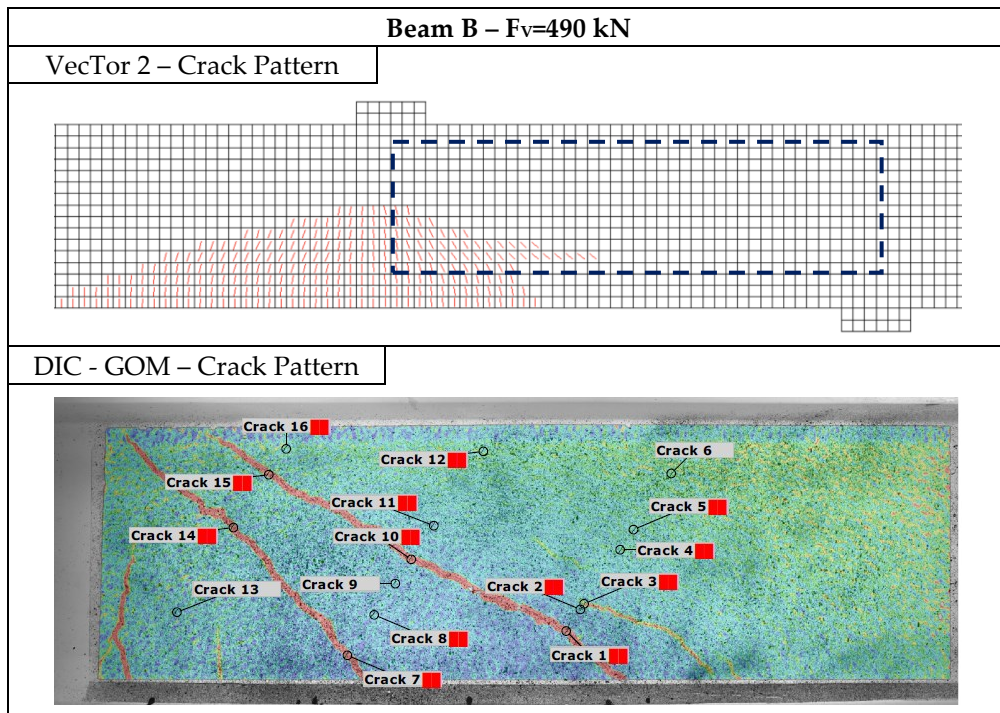
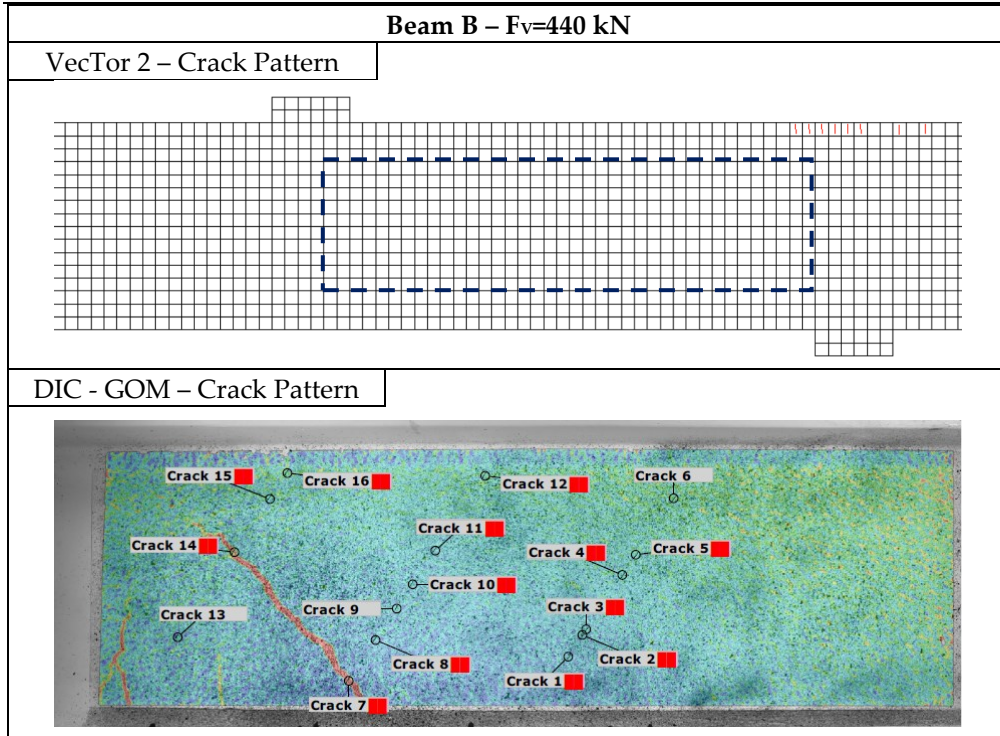
- 440 kN: First shear crack formation Beam B identified by GOM;
- 490 kN: First shear crack formation Beam B;
- 630 kN: First shear crack formation Beam A;
- 690 kN First shear crack formation Beam C2;
- 790 kN Ultimate condition Beam B (740 kN for VT2).

The first image of Table 5-6 indicates the reference of the potentiometers on the opposite side of the beam (DIAG # DIG) and the cracks intercepted by them (Crack #). It can be observed that there is a good correspondence between the crack pattern of the numerical model and that detected by DIC. Looking at the comparison with the ultimate condition, it can be seen that the finite element simulation identifies the cracks located along one direction, while in reality the pattern is more ramified.

Table 5-6: Comparison of the crack pattern between numerical and experimental model at different vertical load levels – Beam B.

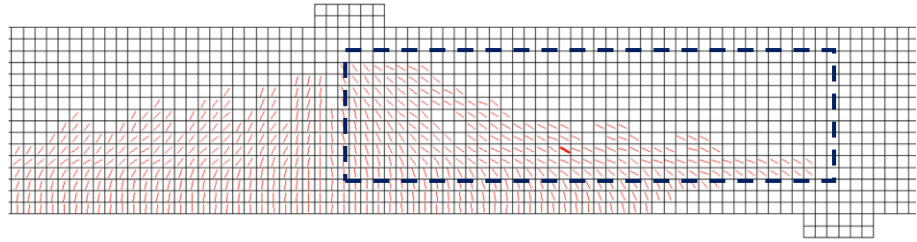


5-NUMERICAL ANALYSIS

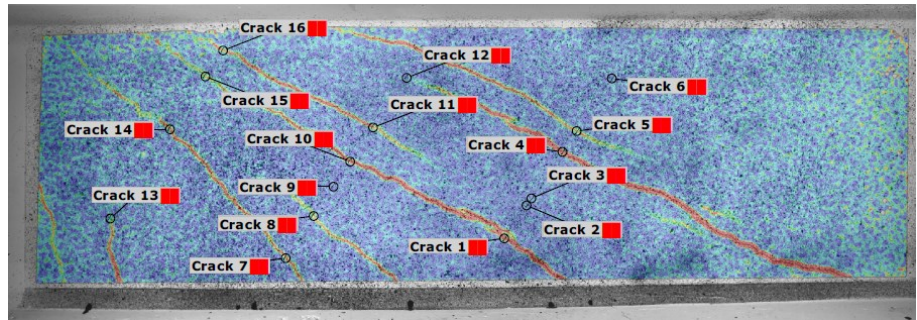


Beam B – $F_v=630$ kN

VecTor 2 – Crack Pattern

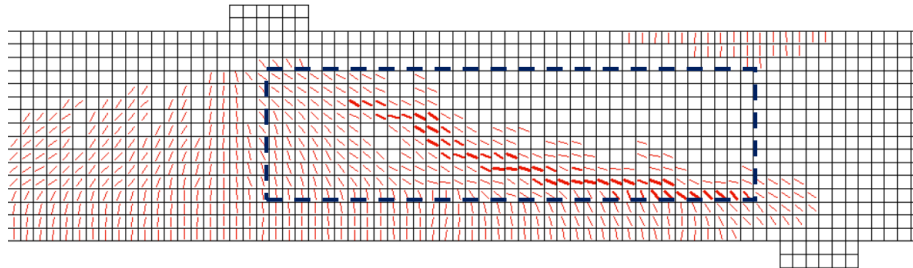


DIC - GOM – Crack Pattern

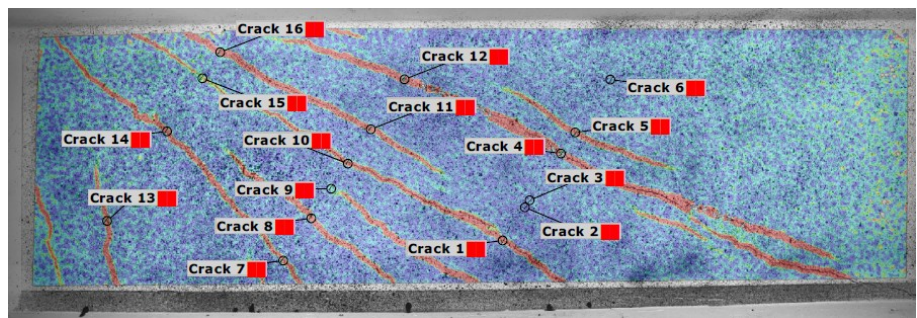


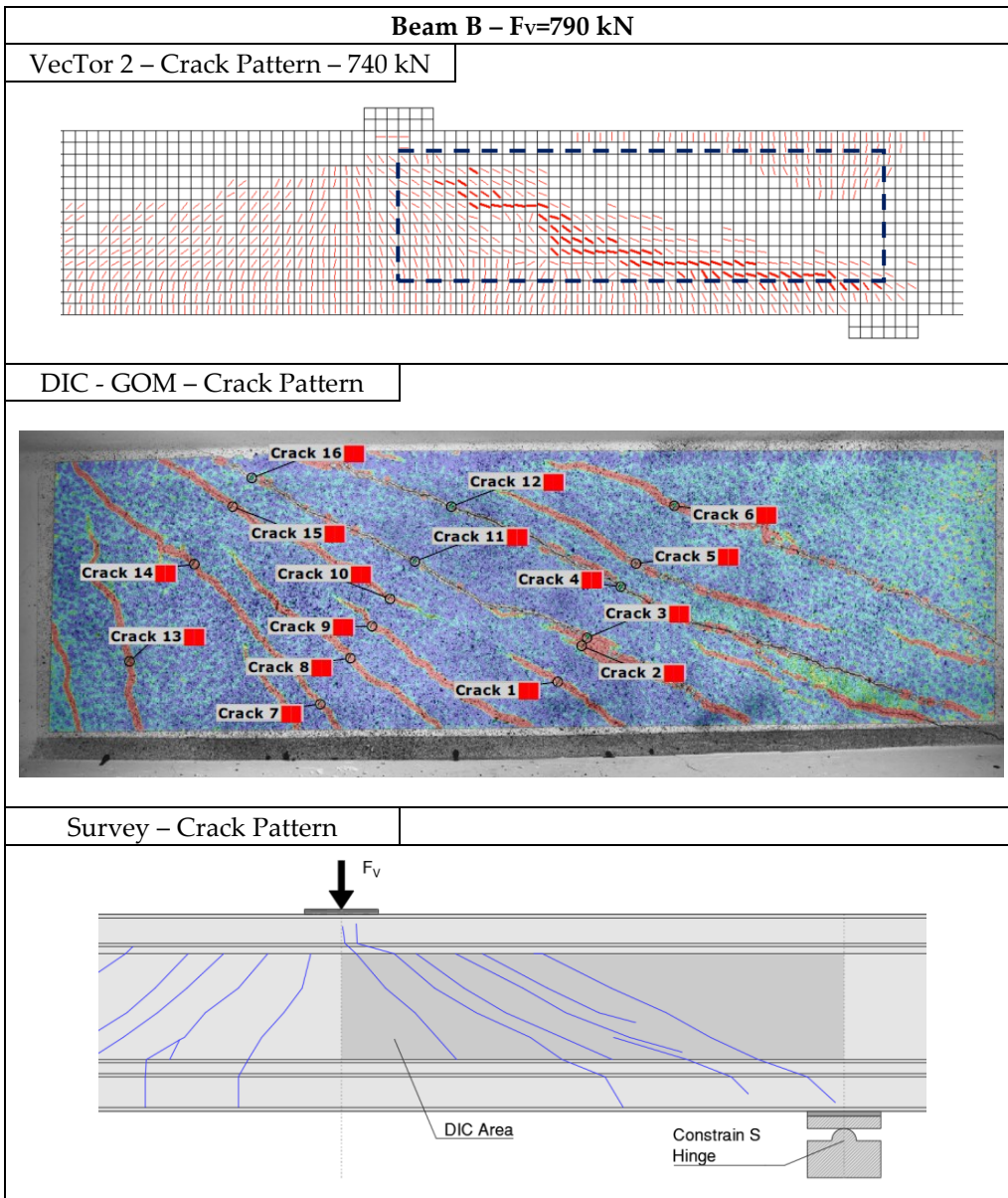
Beam B – $F_v=690$ kN

VecTor 2 – Crack Pattern



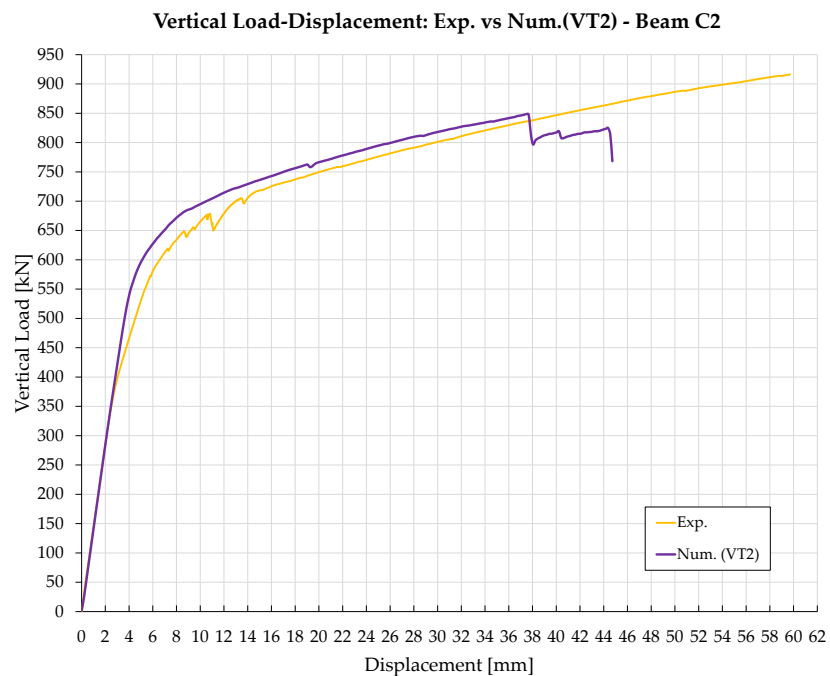
DIC - GOM – Crack Pattern





5.2.5.2 Post Tensioned Beams

The comparison between the numerical prediction, obtained through VT2, and the experimental curve of Beam C2 is shown below. For Beam C1 there is no load-displacement curve that can be compared with the numerical prediction; this is because the test procedure did not foresee a monotonic growth of the vertical load up to the ultimate limit state, but, as detailed above, a reduction of the prestress keeping the vertical load constant. From Figure 5-63 it is possible to note a good agreement in the results, especially as regards the initial stiffness. It can be observed that at 400 kN of vertical load the experimental curve begins to deviate from the numerical prediction. This is because, as already mentioned, Beam C2 had already cracked during a previous load-unload cycle during the stress release tests (§4) with configuration: constant vertical load of 400 kN and prestress reduction from 100% up to 60%. At loads higher than 400 kN, the curve maintains good parallelism with the numerical prediction.

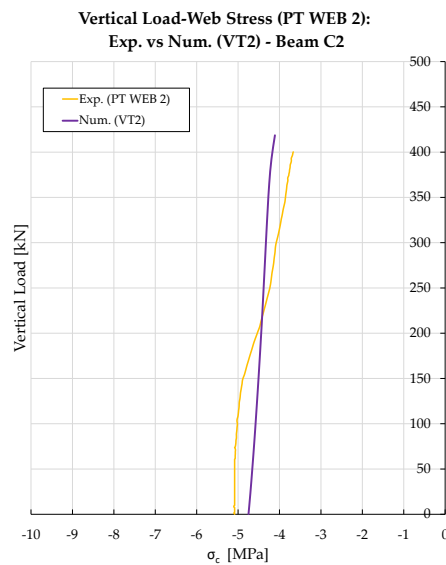
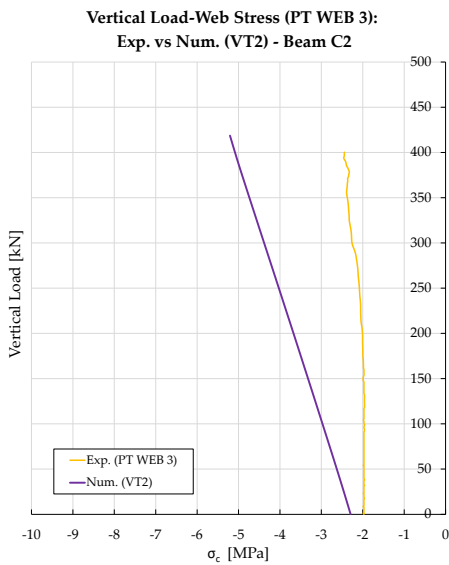
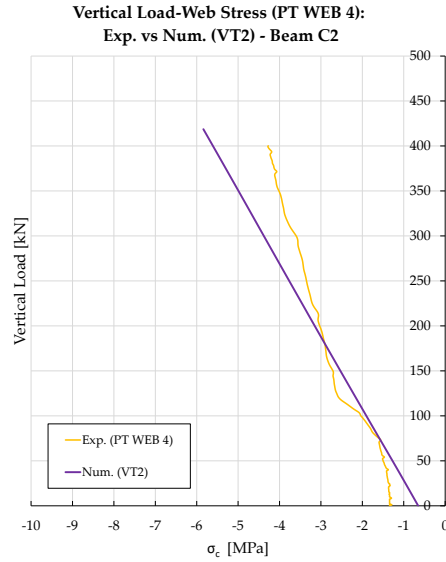
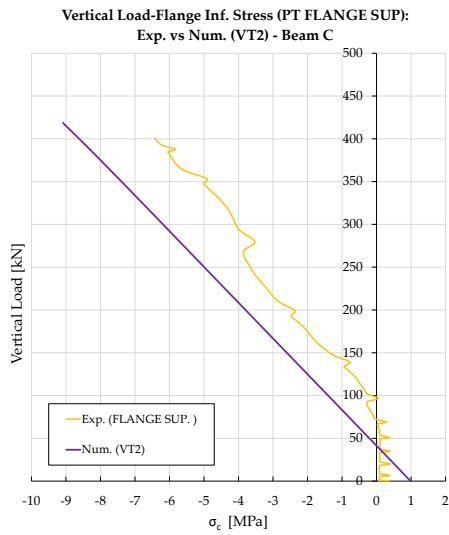


*Figure 5-63: Load-Displacement Curve – Beam C2.
Comparison between experimental result and numerical prediction.*

Moving on to the estimate of the stress trends in the section, comparing what was predicted by the numerical model and what was recorded by the potentiometers installed on the beam (whose position is indicated in Figure 4-77), in this case, a lower agreement emerged between the result and the prevision than as seen for the pre-

5-NUMERICAL ANALYSIS

stressed beams, as can be appreciated from the diagrams represented in Figure 5-64. This trend could be correlated to the instruments used, in fact only potentiometers were used for the post-tensioned beam, certainly less accurate than the strain gauges installed on Beams A and B. In Figure 5-64, differently from what was done for the pre-stressed beams, the stress in the unloaded beam condition was not hypothesized through analytical formulas, but it is a value obtained experimentally during the tension of the strands from 0% up to the design value (100%).



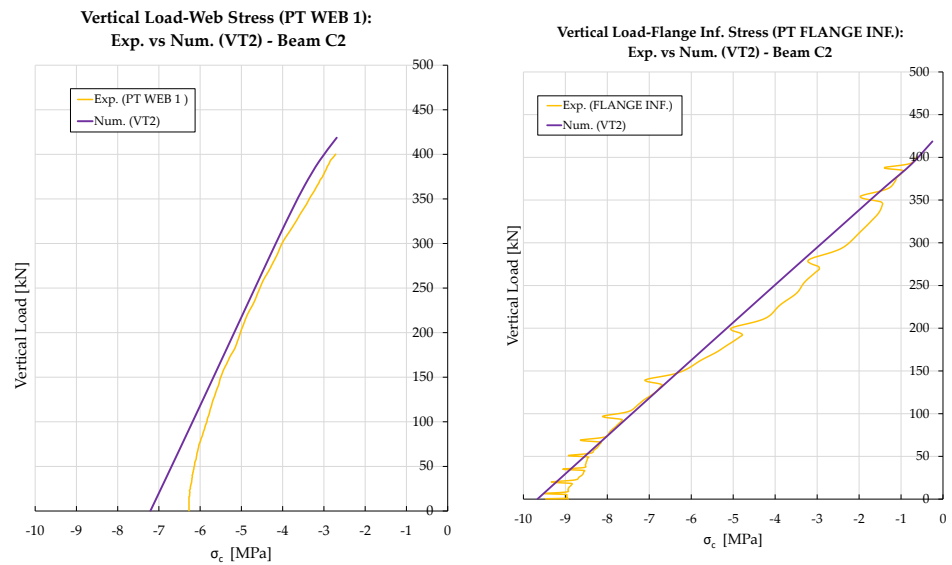


Figure 5-64: Stress trend of concrete at the load point:
comparison between experimental result and numerical prediction – Beam C2.

Figure 5-65 shows the “butterfly” trend of the stresses predicted numerically by VT2 and recorded by the potentiometers installed at the load point. To make this comparison, a load of 400 kN was set to remain in the elastic range: it can be noted that, as observed in the trends in Figure 5-64, there is not a good correspondence between prevision and experimental results. Considering the trend of the effort in the section, it is presumable to assume that there were some problems in recording the values of the PT WEB 3 and PT WEB 4 instruments; in fact, it is possible to observe a stress trend which is not monotonous in the section, but presents peaks.

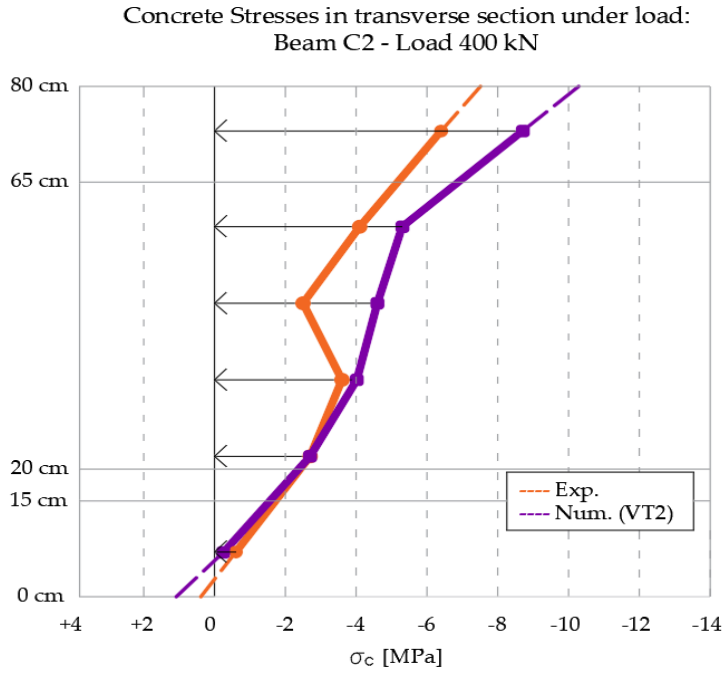


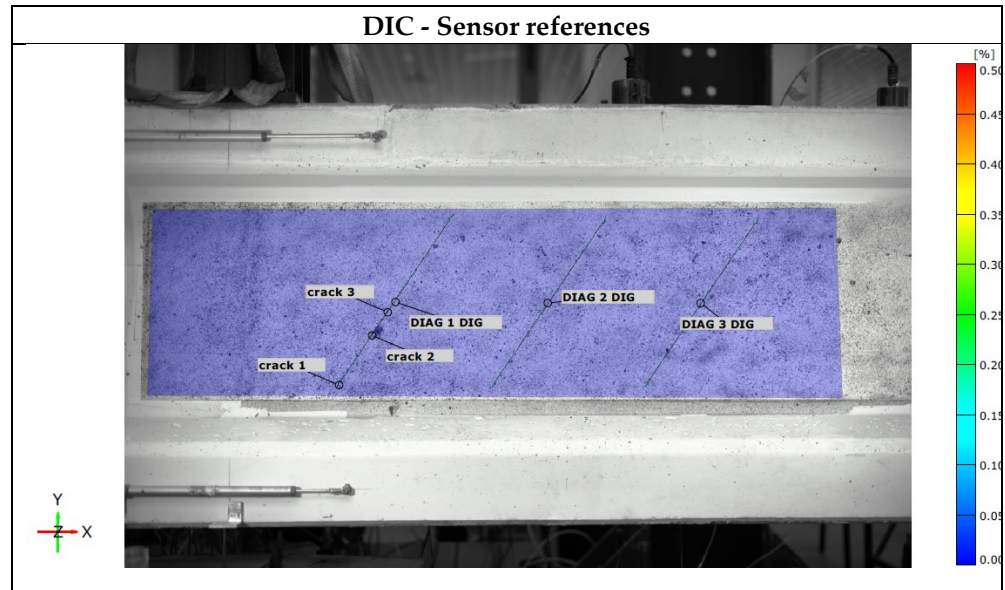
Figure 5-65: Stress trend in Beam C2 at the load point in the elastic stage.
 $F_v=400\text{ kN}$ – Beam C2.

In Table 5-7Table 5-5 the crack patterns of Beam C2 are compared at different load levels. The comparison is made between the numerical model (VecTor 2) and the experimental model (DIC image processing), i.e. the images post-processed by the GOM software. At the end of the test, a survey of the crack pattern was also carried out. However, the latter is not as precise as the DI images as once the vertical load was removed, due to the prestressing the cracks closed again. The five load levels are:

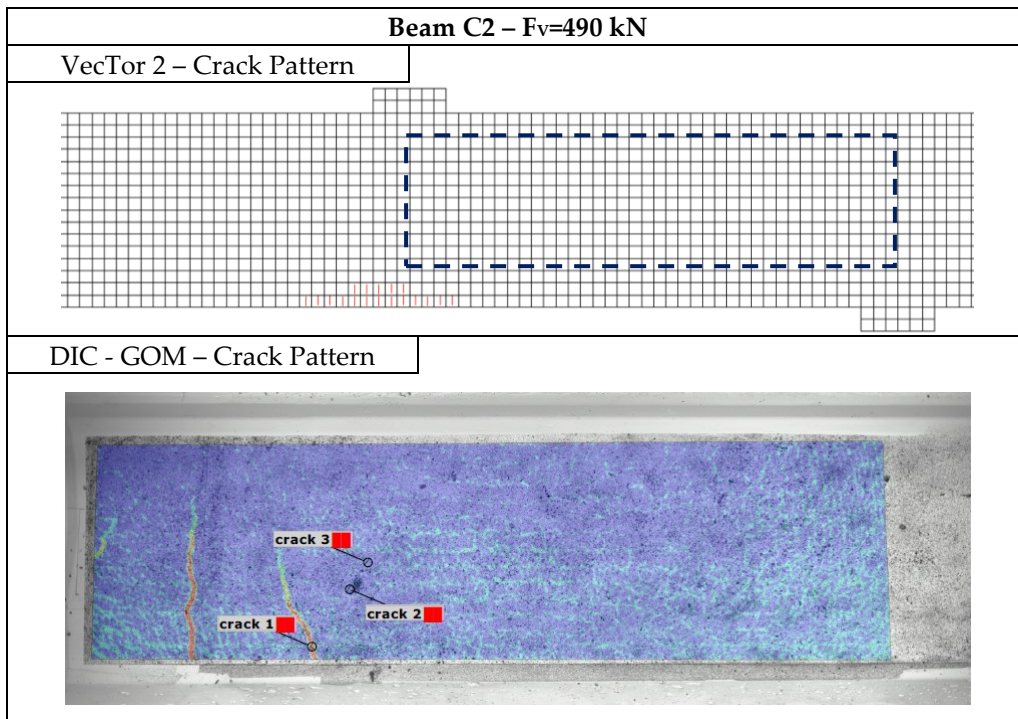
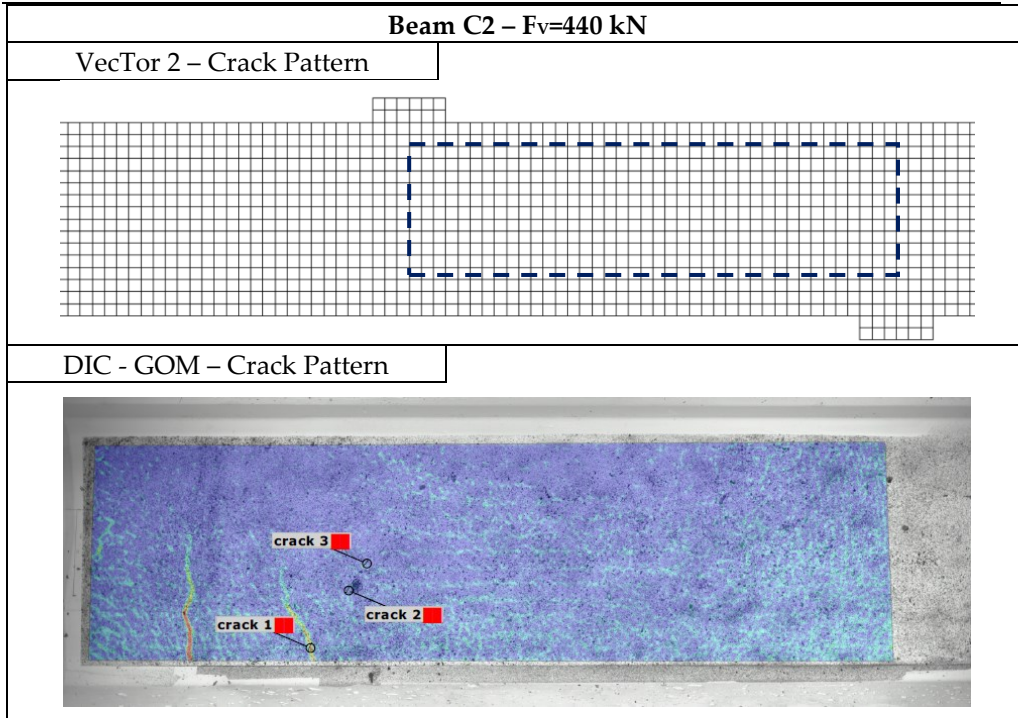
- 440 kN: First shear crack formation Beam B identified by GOM;
- 490 kN: First shear crack formation Beam B;
- 630 kN: First shear crack formation Beam A;
- 690 kN First shear crack formation Beam C2;
- 916 kN Ultimate condition Beam C2 (850 kN for VT2).

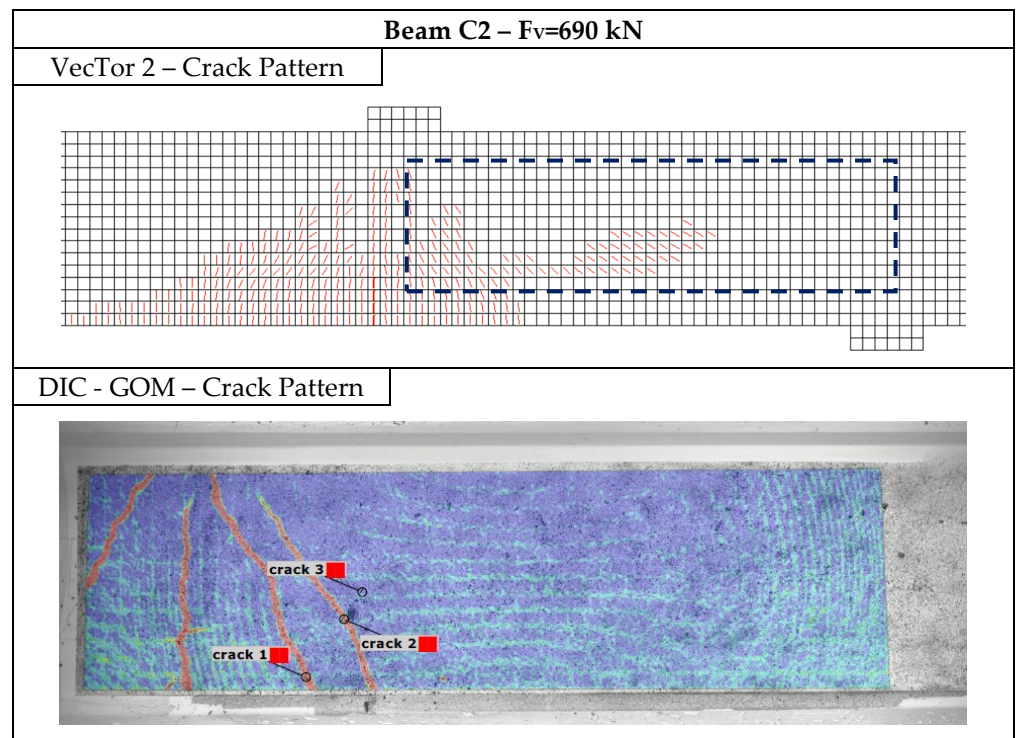
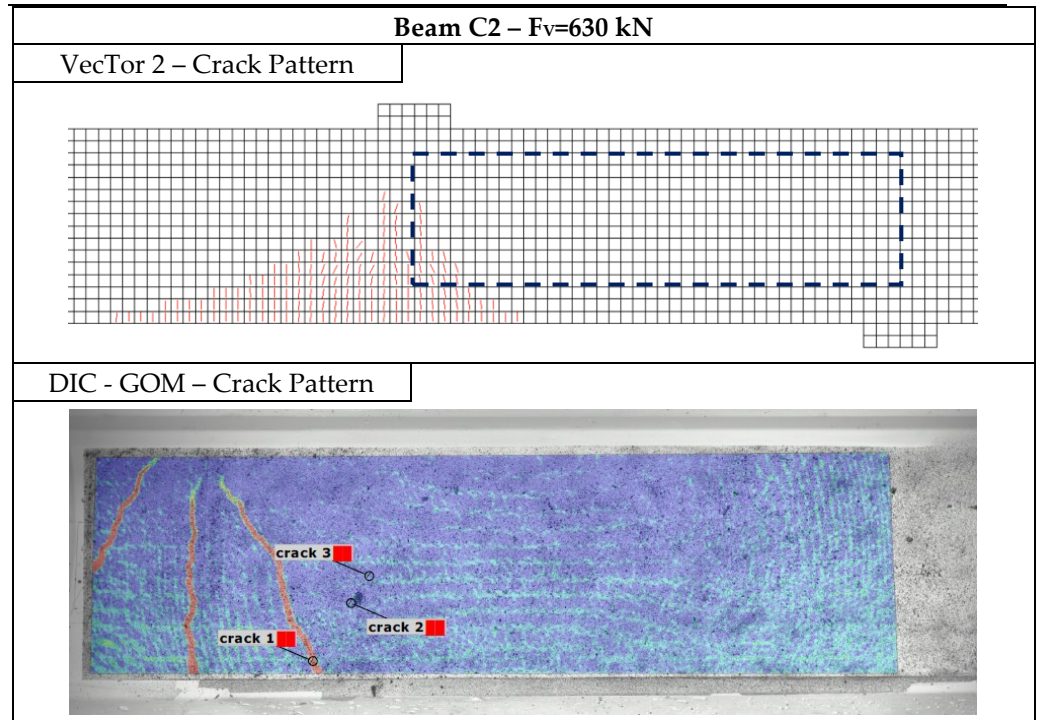
The first image of Table 5-7 indicates the reference of the potentiometers on the opposite side of the beam (DIAG # DIG) and the cracks intercepted by them (Crack #). It can be observed that there is a good correspondence between the crack pattern of the numerical model and that detected by DIC.

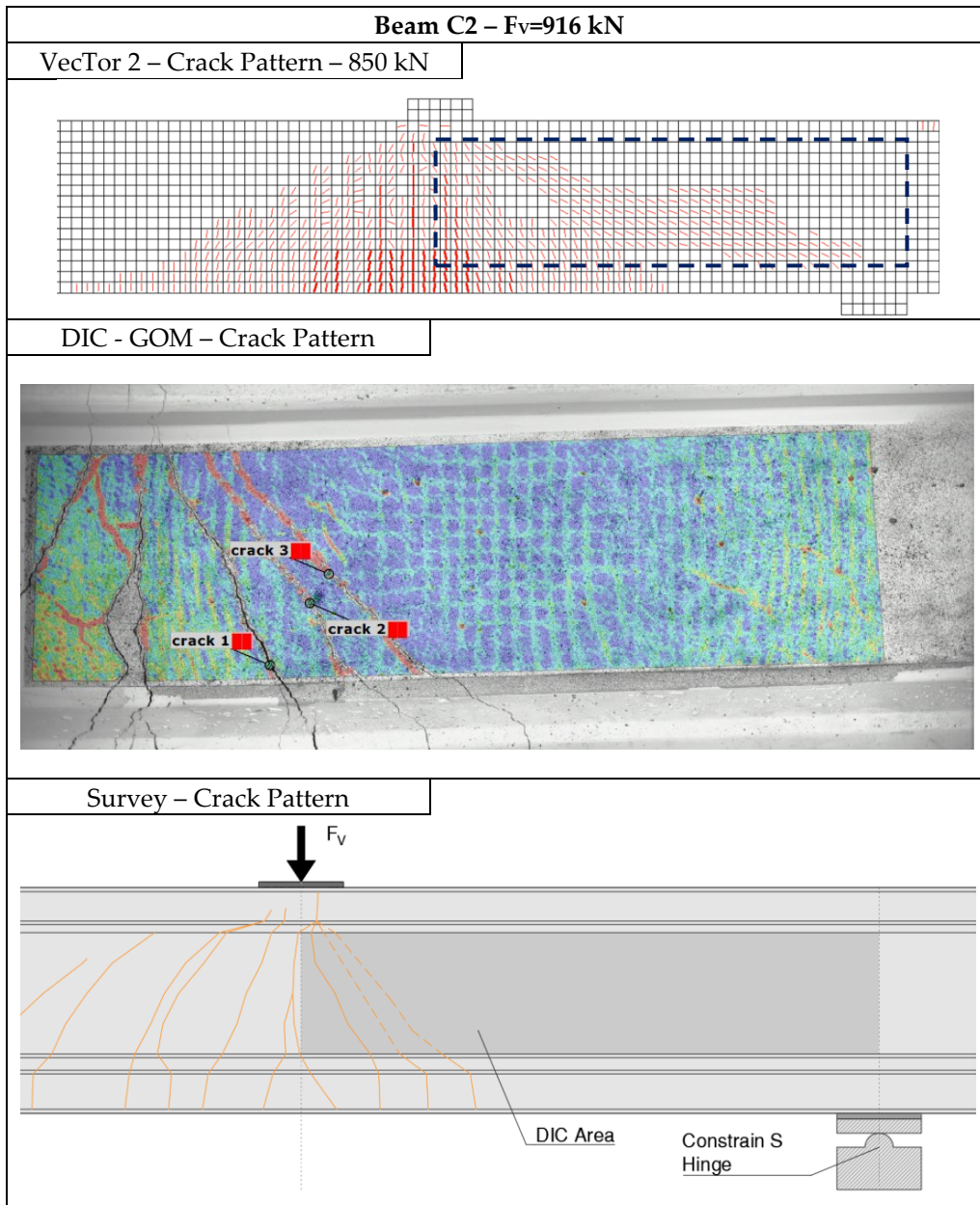
Table 5-7: Comparison of the crack pattern between numerical and experimental model at different vertical load levels – Beam C2.



5-NUMERICAL ANALYSIS







5.2.6 Concluding Remarks

From finite element models that simulate the Shear Tests, the following conclusions can be drawn:

- 1) Comparing the experimental curves with those obtained numerically with VecTor 2, it is possible to note a rather good agreement, especially in terms of elastic and cracked stiffness, cracking formation and evolution.
- 2) The main difference between the vertical load-displacement curves is the behaviour near the ultimate limit state: the numerical model predicts a collapse correctly correlated to a shear failure, for values of load and displacement lower than what has been observed experimentally.
- 3) Moving on to the estimation of the stress trends in the section, comparing what was predicted by the numerical model and what was recorded by the strain gauges and potentiometers installed on the beams, a good agreement between the result and predictions emerged overall, also in this case.
- 4) Regarding the prediction of the shear crack pattern, the VT2 software was able to accurately capture the formation load of the first shear crack. The numerical prediction also seems to be able to estimate, albeit only qualitatively, the evolution of the crack opening as the load increases.

6 NEW MODEL FOR PREDICTING THE SHEAR STRENGTH OF EXISTING PRC BEAMS WITH STIRRUPS

6.1 Introduction

Among other phenomena, the bond between concrete and reinforcement, the multi-axial state of stress, the anisotropy caused by diagonal concrete cracking and the brittle failure all have an impact on the strength of structural concrete parts subjected to shear. In addition, compared to reinforced concrete members, prestressing significantly alters the stresses and strains fields, the cracking load, and the fracture patterns, altering not only the structural response under typical service loads but also the mode of failure and the ultimate capacity. Refined analytical and numerical models have been then created in an attempt to forecast such complex behaviour [Bairan and Mari, 2006, 2007; Bentz, 2000; Ferreira et al., 2013; Mohr et al., 2010; Navarro Gregori et al., 2007; Vecchio, 2000; Vecchio and Collins, 1986]. In particular, it is possible to take into consideration, among other things, crack-induced anisotropy, which causes shear loads to migrate through the cross-section as the fractures deepen and widen. For reinforced concrete beams with shear reinforcement, several well-established theories have been developed, such as the truss analogy-based simple model [Morsch, 1909], and more advanced concepts like the Compression Field Theory [Bentz and Collins, 2006; Collins, 1978; Vecchio and Collins, 1986] and strut-and-tie models for short members and loads near to supports, like Walraven and Lehwalter (1989). These models have helped to clarify how resistant mechanisms have changed in response to experimentally observed behaviour [Marí et al., 2016]. Due to their complexity, time requirements, and dependence on the multiple input parameters needed, the aforementioned models' application in daily engineering practice is still limited. Contrarily, the majority of simple equations in use today are semi-empirical, lack a clear mechanical meaning, exhibit significant dispersion and bias when compared to databases of experimental results, and are difficult to adapt to new technologies (new materials, external strengthening, etc.). Furthermore, performance-based design implementation is made difficult by empirical methodologies. Simplified models for the shear strength of RC and PRC members have also been developed, based on sound theories, with the aim of offering helpful formulations for everyday engineering practice. The most relevant among them, are those carried out by Choi et al. (2007), Collins et al. (2015),

6-NEW MODEL FOR PREDICTING THE SHEAR STRENGTH OF EXISTING PRC BEAMS WITH STIRRUPS

Muttoni and Ruiz (2008), Recupero et al. (2003); Reineck (1991), Tureyen and Frosch (2003), Wolf and Frosch (2007), Zararis and Papadakis (2001) some of which have been included in structural design codes, such as the CSA A23.3-14 (2014) or the *fib* - Model Code 2010 (2013). On the contrary, other codes have incorporated empirical formulations, such as the ACI 318-11 (2011) and the Eurocode 2 (2002) for concrete structures. However, there is still much to be learned about the shear strength of structural concrete members. In fact, there isn't yet a widely accepted simplified and accurate design formulation that can be applied to a wide range of circumstances without the need for modifications to previous or new experimental findings and that consistently achieves high levels of accuracy. Despite the substantial research conducted over more than six decades that aimed to establish the governing parameters, their influence on the shear strength, and the failure modes, the discussion remains even more unresolved for prestressed concrete components.

In this Chapter, an analytical model that allows the definition of the shear strength of new and existing prestressed reinforced concrete beams with stirrups is proposed. In particular, the model derives from the equations of the latest draft of *fib* - Model Code 2020 (2023). These equations are specially modified to take into account the prestress. The formulation is applied and validated against some experimental tests, resulting in a good agreement.

6.2 State of the art of code analytical models

An assessment of the shear strength of a prestressed beam that has been in service for many years can be difficult, as a loss of prestress in the long term could have also led to a reduction in its bearing capacity, in addition to the general degradation it may have suffered. Therefore, it is possible to speak of residual shear strength. In situations where, following a visual inspection, the structural element belonging to a bridge shows diagonal cracks near the supports, the infrastructure manager must carry out a check and, based on the result, proceed with a reinforcement intervention structural, or in cases of advanced damage, to the replacement of the element or deck. Of course, the outcome of the structural assessment affects the intervention choices in an impactful way, especially in terms of economics, safety, viability, etc. During a verification assessment, following a field inspection, the following should be considered: (§6.3.5.2 [MIMS - Bridges Guidelines, 2022]):

- any deficiencies due to durability problems, in particular, any reduction in the section due to deterioration or leaching of the surface concrete which can lead to a reduction in the useful section;
- any decrease in the steel area due to corrosion;

- the possible absence or lack of stirrups caused by corrosion of the same which generally has reduced concrete cover or the possible ineffectiveness of the stirrups due to corrosion of the reinforcement edges.

Therefore, the relation $V_{Rd} \geq V_{Ed}$ could not be verified for the combination of the following aspects:

- the soliciting actions imposed by the current regulations are greater than those envisaged by the regulation at the time of the design of the work; this condition is a consequence of the increase in traffic with a heavy load;
- the formulas of the various standards used to evaluate the shear resistance of transversely reinforced elements are too conservative for prestressed elements.

Recently issued standards, such as the Italian one relating to the inspection, monitoring, classification and verification of all national bridges with a span > 6 m [MIMS - Bridges Guidelines, 2022] propose a reduction in the amplification coefficients of the stressing actions, compared to those envisaged for new constructions, valid for limited periods of time necessary for an intervention by the manager. However, strength evaluation formulas still remain very conservative, such as the one proposed for the aforementioned bridge guidelines (Eq: 4.1.24 [NTC, 2018]). In particular, equation (6-1) is indicated in §4.1.2.3.5.1. "Elements without shear resistant transverse reinforcement (or with minimal shear reinforcement)" [NTC, 2018] is proposed to be used in cases of PRC elements in simple support, in areas not cracked by bending moment (with stresses not exceeding f_{ctd}). The same expression, in a slightly less simplified form, is also present in §7.3.3.4 "Hollow core slabs" – LoA I – Eq. 7.3-44 of *fib* - Model Code 2010 (2013).

$$V_{Rd} = 0.7 \cdot b_w \cdot d \cdot (f_{ctd}^2 + \sigma_{cp} \cdot f_{ctd})^{\frac{1}{2}} \quad (6-1)$$

The analytical formulas for shear strength verification proposed by international standards are conservative for PRC elements as it is a technology that can show critical issues in the long term, if no maintenance is carried out.

In the paper by Osborn et al. (2012) three methods are used: the first is a simplified method provided by the AASHTO LRFD [AASHTO - American Association of State Highway and Transportation Officials - Load and Resistance Factor Design, 2010], the second is instead the nominal method required by the same regulations while the third and last formulation used consists of a strut-and-tie model, described in the appendix of the American Concrete Institute ACI 318 - Building Code of 2008.

6-NEW MODEL FOR PREDICTING THE SHEAR STRENGTH OF EXISTING PRC BEAMS WITH STIRRUPS

In general, the shear-bearing capacity is determined as a combination of three contributions:

$$V_n = V_s + V_c + V_p$$

where:

- V_s = contribution of the transverse reinforcement;
- V_c = contribution of the shear strength of concrete;
- V_p = contribution of the vertical component of the prestressing force.

Both the simplified method and the nominal one foresaw by the AASHTO LRFD allow to calculate the shear resistance, with reference to bridge beams in PRC, through a sectional analysis. In the simplified method, the calculation of V_c (concrete shear strength contribution) is very similar to that envisaged by the ACI and is associated with two different formulations based on what type of shear crack pattern develops, i.e. "flexure-shear cracking" or "web-shear cracking". The second method envisaged by the American legislation (nominal method of the AASHTO LRFD) is instead based on the Modified Compression Field Theory (§5.2.2.1). In a publication by Osborn et al. (2012), to predict the shear-bearing capacity of CAP beams, a very simple strut-and-tie (STM) model was developed following the indications of the AASHTO LRFD and the ACI. The authors underline how, although STM schemes are rarely used in the design of this type of beam, these models can prove to be very useful both in the design and analysis phases. The authors state that the simplified and nominal shear design procedures in the AASHTO LRFD specifications were very conservative and predicted between 28 and 55% of the measured shear capacity of the prestressed AASHTO Type II girders. They also claim that Strut-and-tie models predicted shear capacities to be within 2 and 22% of the respective measured shear values. While less frequently used, the strut-and-tie methodology is more applicable for D-region shear calculations and produced more accurate results, for this loading, in comparison with the AASHTO simplified and nominal procedures.

Following tests carried out in situ, Gehrlein and Fischer (2019) compared the experimental results with different calculation models, including the EC2, the DIN standards and the Canadian standard (CSA). The latter, based on the Modified Compression Field Theory, is the one that comes closest to the bearing capacity actually exhibited by the tested beams, as can be appreciated from the graph in Figure 6-1. The comparison highlights how the ratio between calculated shear strength and the experimental result is on average between 5.72 times, following the EC2 and 1.19 times, following the Canadian CSA standard.

The authors, as well as Park et al. (2013) and Huber, Vill, et al. (2018), highlight, in particular, the great difference between the result provided by Eurocode 2 and the

6-NEW MODEL FOR PREDICTING THE SHEAR STRENGTH OF EXISTING PRC BEAMS WITH STIRRUPS

experimentally determined shear bearing capacity and how, consequently, it is necessary to conduct research to validate more realistic approaches leading to more sustainability of existing bridges.

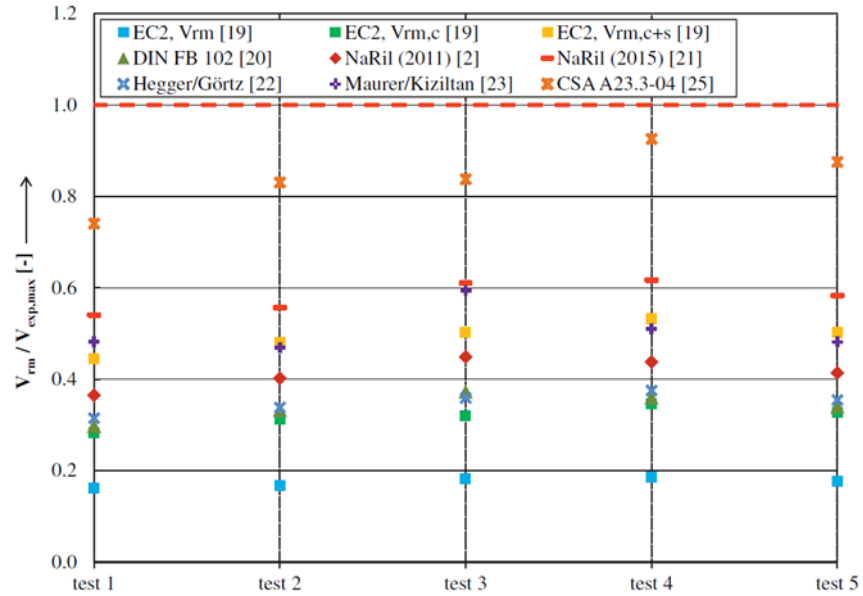


Figure 6-1: Relationship between predicted shear strength and actual bearing capacity according to different approaches [Gehrlein and Fischer, 2019].

Nagrodzka-Godycka and Wiśniowska (2017), apply to 42 experimental tests relative to PRC beams, three codes: PN-EN 1992-1-1:2008 EC2 (2008), ACI 318-14 (2014) and *fib* - Model Code 2010 (2013). Table 6-1 presents the statistical data of the results. Although the second level of approximation was the only method that never estimated shear strength to be greater than it appeared during tests, it had a much higher variety of results than the third level of approximation. It can be also seen in Table 6-1 that the statistics for the second level of approximation are worse than for the third level of approximation. Both PN-EN 1992-1-1:2008 and ACI 318-14 provided acceptable results, with a low number of underestimations, however, it was the third level of approximation of Model Code 2010 that had the most accurate results.

Marí et al. (2016) apply the codes ACI 318-11 (2011), CSA A23.3-14 (2014) and Eurocode 2 (2002) to some complete databases developed by ACI-DafStb for reinforced and prestressed concrete beams ([Reineck et al., 2014; Reineck and Dunkelberg, 2015]) concluding that for prestressed elements the formulas are too conservative.

6-NEW MODEL FOR PREDICTING THE SHEAR STRENGTH OF EXISTING PRC BEAMS WITH STIRRUPS

Table 6-1: Statistic data for prestressed beams [Nagrodzka-Godycka and Wiśniowska, 2017].

	$\frac{V_{test}}{V_{PN-EN}}$	$\frac{V_{test}}{V_{ACI}}$	$\frac{V_{test}}{V_{MC,II}}$	$\frac{V_{test}}{V_{MC,III}}$
Number of beams	42	42	42	42
Average	1.66	1.56	1.98	1.55
Standard deviation	0.61	0.56	0.69	0.51
Variation coefficient	36.7 %	35.6 %	35.0 %	33.1 %

Overall, it follows that the models proposed for national and international standards are very conservative and in the evaluation phase of existing prestressed elements, this can lead to several critical issues. It is therefore noted the need to refine the models to adapt them, as much as possible, to the real load-bearing capacity of the prestressed elements.

6.3 Comparison between codes to predict the shear strength

Taking into consideration the main standards, a comparison is made of the analytical formulas used to evaluate the shear strength of elements: prestressed, with transverse reinforcement, isostatic:

- EC2 - EN 1992-1-1 (2005) - §6.2 – [EC2-2005]
- Draft EC2 - FprEN_1992-1-1 (2021) - §8.2 - [dEC2-2020]
- MC2010 (2013) – §7.3.3. LoA I, LoA II, LoA III - [MC2010]
- Draft MC2020 (2023) - §30.1.3 LoA I, LoA IIa, LoA IIb - [dMC2020]
- SIA 262:2013 (2013) – Swiss-based on MC2010 (2013) – LoA I and LoA II
- NTC2018 – Italy – based on EC2 - EN 1992-1-1 (2005)

The *fib* - Model Code 2010 proposes three analytical methods for calculating the design shear resistance of a structure: correspond at three levels of approximations, with complexity and accuracy increasing as the level rises. The level of approximation IV, which is the next category of complexity, includes nonlinear finite element analysis (NLFEA). About the Model Code 2010 (MC2010) and Draft Model Code 2020 (dMC2020), it is decided to focus only on analytical models with an advanced level of approximation, excluding finite element evaluation. Therefore, the comparison will be performed between the following models:

- EC2-2005 → Table 6-2
- dEC2-2020 → Table 6-2
- MC2010 – LoA II → Table 6-3 and Table 6-4
- dMC2020 – LoA IIa → Table 6-3 and Table 6-4
- MC2010 – LoA III → Table 6-3 and Table 6-5
- dMC2020 – LoA IIb → Table 6-3 and Table 6-5

For the definition of the nomenclature used, please refer to the respective standard.

Comparing EC2-2005 and dEC2-2020 in Table 6-2 it is observed that both consider only the contribution of the stirrups for the shear resistance of the beam. As well as MC2010 – LoA II and dMC2020 – LoA IIa in Table 6-4. However, the MCs define an angle of inclination of the strut θ_{min} which varies according to the deformed shape ε_x (Table 6-3) identified in the section at $z/2$, while the EC2 impose a fixed angle θ for the PRC elements, lower than that for the RC. The same reasoning of θ_{min} applies to the ν and k_ε (strength reduction factor of concrete carrying the compression field) in $V_{Rd,max}$. The decision to fix such important parameters leads to an overestimation of the true resistance that the element can generate before shear failure. Both MC2010 – LoA III and dMC2020 – LoA IIb in Table 6-3 and Table 6-5, are instead based on the Simplified Modified Compression Field Theory [SMCFT] [Bentz et al., 2006]

6-NEW MODEL FOR PREDICTING THE SHEAR STRENGTH OF EXISTING PRC BEAMS WITH STIRRUPS

[deriving precisely from [MCFT] (§5.2.2.1) [Vecchio and Collins, 1986]. These models also consider the contribution that the concrete is able to provide when the cracks are not yet too open and the aggregates interlock in the cracks still play an important role.

Table 6-2: Comparison of formulas for calculating shear strength for prestressed shear reinforced beams: EC2-2005 and dEC2-2020.

EC2-2005		dEC2-2020
$V_{Rd} = \min(V_{Rd,s}; V_{Rd,max})$		$\tau_{Ed} = \frac{V_{Ed}}{b_w \cdot z}$
$1 \leq \cot \theta \leq 2.5$		$1 \leq \cot \theta \leq \cot \theta_{min}$ $\cot \theta_{min} = 3.0$ (PRC)
$V_{Rd,s} = \frac{A_{sw}}{s} \cdot z \cdot f_{ywd} \cdot \cot \theta$		$\begin{cases} \tau_{Rd,sy} = \rho_w \cdot f_{ywd} \cdot \cot \theta \\ \rho_w = \frac{A_{sw}}{b_w \cdot s} \end{cases}$ $V_{Rd,sy} = \frac{A_{sw}}{s} \cdot z \cdot f_{ywd} \cdot \cot \theta$
$V_{Rd,max} = \alpha_{cw} \cdot \frac{b_w \cdot z \cdot v_1 \cdot f_{cd}}{(\cot \theta + \tan \theta)}$		$\sigma_{cd} \leq v \cdot f_{cd}$
α_{cw}	When	$\sigma_{cd} = \tau_{Ed} \cdot (\cot \theta + \tan \theta) \leq v \cdot f_{cd}$ $\sigma_{cd} = \frac{V_{Ed}}{b_w \cdot z} \cdot (\cot \theta + \tan \theta) \leq v \cdot f_{cd}$ $V_{Ed} \leq \frac{b_w \cdot z \cdot v \cdot f_{cd}}{(\cot \theta + \tan \theta)}$
1.0	No PRC	
$\left(1 + \frac{\sigma_{cp}}{f_{cd}}\right)$	$0 \leq \sigma_{cp} \leq 0.25 \cdot f_{cd}$	
1.25	$0.25 \cdot f_{cd} \leq \sigma_{cp} \leq 0.5 \cdot f_{cd}$	
$2.25 \cdot \left(1 + \frac{\sigma_{cp}}{f_{cd}}\right)$	$0.5 \cdot f_{cd} \leq \sigma_{cp} \leq 1.0 \cdot f_{cd}$	
$v_1 = 0.6$ if $f_{ck} \leq 60$ MPa $v_1 = 0.9 - \frac{f_{ck}}{200} > 0.5$ if $f_{ck} \geq 60$ MPa		$v = 0.5$

6-NEW MODEL FOR PREDICTING THE SHEAR STRENGTH OF EXISTING PRC
BEAMS WITH STIRRUPS

Table 6-3: Comparison of formulas for calculating shear strength for prestressed shear reinforced beams: MC2010 and dMC2020.

MC2010	dMC2020
$V_{Rd} \geq V_{Ed}$	
$\varepsilon_x = \frac{\left(\frac{M_{Ed}}{z_v} + V_{Ed} + N_{Ed} \cdot \frac{(z_p - e_p)}{z_{(v^*)}} \right)}{2 \cdot \left(\frac{z_s}{z_{(v^*)}} \cdot E_s \cdot A_s + \frac{z_p}{z_{(v^*)}} \cdot E_p \cdot A_p \right)} \geq 0$ <p style="text-align: right; font-size: small;">(*) The subscript v is present only in dMC2020</p>	
$\begin{aligned} M_{Ed} &= M_{Ed0} - F_p \cdot e_p \cdot \cos \delta_p \\ V_{Ed} &= V_{Ed0} - F_p \cdot \sin \delta_p \\ N_{Ed} &= N_{Ed0} - F_p \cdot \cos \delta_p \end{aligned}$	
$V_{Rd} = V_{Rd,c} + V_{Rd,s} \leq V_{Rd,max}$	

6-NEW MODEL FOR PREDICTING THE SHEAR STRENGTH OF EXISTING PRC BEAMS WITH STIRRUPS

Table 6-4: Comparison of formulas for calculating shear strength for prestressed shear reinforced beams: LoA II MC2010 and LoA IIIa dMC2020.

MC2010 - LoA II	dMC2020 - LoA IIIa
$V_{Rd} = V_{Rd,s} \leq V_{Rd,max}$	
$\theta_{min} \leq \theta \leq 45^\circ$ $\theta_{min} = 20^\circ + 10000 \cdot \varepsilon_x$	$1 \leq \cot \theta \leq \cot \theta_{min}$ $\cot \theta_{min} = \cot(20^\circ + 4000 \cdot \varepsilon_x)$
$V_{Rd,s} = \frac{A_{sw}}{s_w} \cdot z_{(v)} \cdot f_{ywd} \cdot \cot \theta$ <small>(*) The subscript <i>v</i> is present only in dMC2020</small>	
$V_{Rd,max} = k_c \cdot \frac{f_{ck}}{\gamma_c} \cdot b_w \cdot z_v \cdot \sin \theta \cdot \cos \theta$ $k_c = k_\varepsilon \cdot \eta_{fc}$ $\eta_{fc} = \left(\frac{30}{f_{ck}}\right)^{1/3} \leq 1.0$ (f_{ck} in MPa)	$V_{Rd,max} = \frac{k_\varepsilon \cdot f_{cd} \cdot b_w \cdot z_v}{\cot \theta + \tan \theta}$
$k_\varepsilon = \frac{1}{1.2 + 55 \cdot \varepsilon_1} \leq 0.65$	$k_\varepsilon = \frac{1}{1 + 110 \cdot \varepsilon_1} \leq 1.0$
$\varepsilon_1 = \varepsilon_x + (\varepsilon_x + 0.002) \cdot \cot^2 \theta$	$\varepsilon_1 = \varepsilon_x + (\varepsilon_x + 0.001) \cdot \cot^2 \theta$

6-NEW MODEL FOR PREDICTING THE SHEAR STRENGTH OF EXISTING PRC
BEAMS WITH STIRRUPS

Table 6-5: Comparison of formulas for calculating shear strength for prestressed shear reinforced beams: LoA III MC2010 and LoA IIB dMC2020.

MC2010 - LoA III	dMC2020 - LoA IIB
$V_{Rd} = V_{Rd,c} + V_{Rd,s} \leq V_{Rd,max}(\theta_{min})$	$V_{Rd} = V_{Rd,c} + V_{Rd,s} \leq V_{Rd,max}$
$\theta_{min} \leq \theta \leq 45^\circ$ $\theta_{min} = 20^\circ + 10000 \cdot \varepsilon_x$	$\cot \theta = \cot(29^\circ + 7000 \cdot \varepsilon_x)$
$V_{Rd,s} = \frac{A_{sw}}{s_w} \cdot z_{(v*)} \cdot f_{ywd} \cdot \cot \theta$ <small>(*) The subscript v is present only in dMC2020</small>	
$V_{Rd,c} = k_v \cdot \frac{\sqrt{f_{ck}}}{\gamma_c} \cdot b_w \cdot z_v$	
$k_v = \frac{0.4}{1 + 1500 \cdot \varepsilon_x} \cdot \left(1 - \frac{V_{Ed}}{V_{Rd,max}(\theta_{min})}\right)$ ≥ 0	$k_v = \frac{0.4}{1 + 1500 \cdot \varepsilon_x}$
$V_{Rd,max} = k_c \cdot \frac{f_{ck}}{\gamma_c} \cdot b_w \cdot z_v \cdot \sin \theta \cdot \cos \theta$ $k_c = k_\varepsilon \cdot \eta_{fc}$ $\eta_{fc} = \left(\frac{30}{f_{ck}}\right)^{1/3} \leq 1.0$ (f_{ck} in MPa)	$V_{Rd,max} = \frac{k_\varepsilon \cdot f_{cd} \cdot b_w \cdot z_v}{\cot \theta + \tan \theta}$
$k_\varepsilon = \frac{1}{1.2 + 55 \cdot \varepsilon_1} \leq 0.65$	$k_\varepsilon = \frac{1}{1 + 110 \cdot \varepsilon_1} \leq 1.0$
$\varepsilon_1 = \varepsilon_x + (\varepsilon_x + 0.002) \cdot \cot^2 \theta$	$\varepsilon_1 = \varepsilon_x + (\varepsilon_x + 0.001) \cdot \cot^2 \theta$

Recalling that these models are optimized for RCs, to remain somewhat conservative in dMC2020 – LoA IIB, also considering the contribution of concrete, it was decided to keep the value of θ as defined in SMCFT [Bentz et al., 2006]. However, this leads to penalising the correct estimation of the shear strength of prestressed members with transverse reinforcement.

6.4 Analytical Model Proposed

Since the assessment of the shear resistance of prestressed elements with transverse reinforcement is a delicate subject, it was decided to adopt an advanced level of approximation. For this reason, the formulation proposed here starts from dMC2020 – LoA IIb (*fib* - Draft MC2020, 2023), which is one of the most refined models on shear strength, among those currently present in international standards. For the definition of the new model for the prediction of the shear resistance of prestressed beams with bonded tendons and with stirrups, called UniBS_Proposal, what has already been illustrated in Table 6-3 and Table 6-5, is detailed below.

First, verification of members in shear requires the state of strain to be taken into account. Consider the beam with a generic cross-section shown in Figure 6-2. The average state of strain (ϵ_x) is conventionally calculated by the Draft Model Code 2020 at the mid-depth of the effective shear depth or core layer being considered, as in Equation (6-2) and Figure 6-2. The actions are reported by Draft Model Code 2020 with the subscripts “Ed”. However, in the cases examined below, the actions derive from experimental tests, not including any load amplification coefficient. In the same way, materials used are not those of design and, therefore, mean values for strengths are utilized.

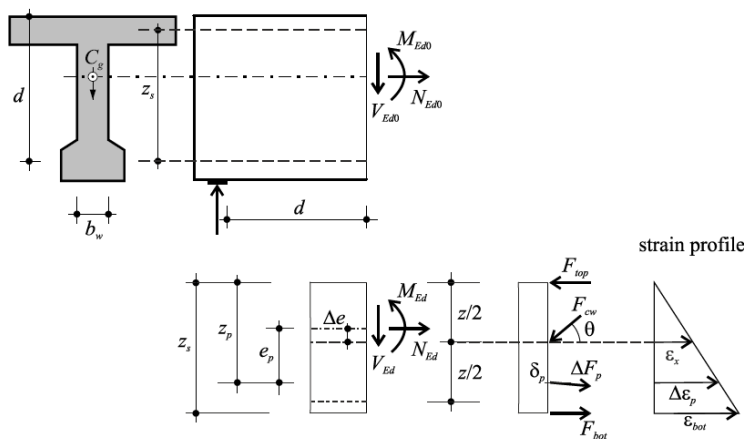


Figure 6-2: Definitions in dMC2020

$$\epsilon_x = \frac{\left(\frac{M_E}{z_v} + V_E + N_E \cdot \frac{(z_p - e_p)}{z_v} \right)}{2 \cdot \left(\frac{z_s}{z_v} \cdot E_s \cdot A_s + \frac{z_p}{z_v} \cdot E_p \cdot A_p \right)} \tag{6-2}$$

where:

- E_s and E_p is the Young modulus of mild steel and prestress steel;
- A_s and A_p are the cross-section of the tensile mild reinforcements and prestressed reinforcement;
- z_s and z_p are the effective shear depth of the tensile mild reinforcements and prestressed reinforcement;
- $z_v = \frac{z_s^2 \cdot A_s + z_p^2 \cdot A_p}{z_s \cdot A_s + z_p \cdot A_p} \geq 0.72 \cdot h$ (h is the depth)
- $z_v = 0.9 \cdot d$, where d is the effective depth.
- M_E is the acting bending moment:
 - $M_E = M_{E0} - F_p \cdot e_p \cdot \cos \delta_p$ (for isostatic beam)
 - $M_{E0} = V_E \cdot (a - z_v)$ is calculated in the most critical shear section, which by convention is taken at a distance from the load point (in the direction of the support) equal to $z_v = 0.9 \cdot d$, for a beam in simple support with a highly concentrated point load. It is, therefore, necessary to iterate until V_E does correspond to the resistance shear (hereinafter referred to as V_R).
 - F_p = prestressed force
- V_E is the shear actions;
 - $V_E = V_{E0} - F_p \cdot \sin \delta_p$
to facilitate the application of the formulas, the horizontal component of the shear force (which would be equal to $V_{Eh} = V_{E0} \cdot \cot \theta$, where θ is angle of inclination of the strut) is taken conventionally to be equal to the shear by the Draft Model Code 2020. It is therefore assumed, only in this case, that $\cot(\theta) = 1$.
- N_E is axial action as positive for tension and negative for compression:
 - $N_E = N_{E0} - F_p \cdot \cos \delta_p$

In Equation (6-2) with respect to dMC2020 – LoA IIB $\varepsilon_x < 0$ are also accepted.

The shear strength of members with shear reinforcement is so calculated according to the approximation dMC2020 – LoA IIB.

It is worth noting that approximation dMC2020 – LoA IIB is applicable only in elements where the percentage of stirrups (ρ_w) is greater than the minimum, defined as:

$$\rho_w \geq 0.08 \cdot \frac{\sqrt{f_c}}{f_{yw}} \quad (6-3)$$

where f_c and f_{yw} are the concrete cylinder compressive strength and the yield strength of the stirrup, both in MPa.

6-NEW MODEL FOR PREDICTING THE SHEAR STRENGTH OF EXISTING PRC BEAMS WITH STIRRUPS

The shear strength (V_R) is obtained through the following equation:

$$V_R = V_{R,s} + V_{R,c} + V_{R,pf} \leq V_{R,max} \quad (6-4)$$

In which:

- $V_{R,s}$ is stirrups on the shear resistance;
- $V_{R,c}$ is the contribution of the concrete to the shear resistance;
- $V_{R,pf}$ is the contribution of the compressed flange due to the shear friction;
- $V_{R,max}$ is the maximum shear resistance related to the crushing of concrete carrying the compression field.

In general, to estimate the experimental results with a good approximation, it is necessary to use formulas that consider distinctly the contribution of both concrete and steel. This is why as already mentioned in §6.2, some shear strength formulations, such as the one used by the Eurocode 2 (European standard, 2003), are badly suited for this purpose.

The inclination of the compressive stress stage θ with respect to the longitudinal axis of the beam is the same as the SMCFT [Bentz et al., 2006]:

$$\theta = 29^\circ + 7000 \cdot \varepsilon_x \quad (6-5)$$

The contribution of stirrups $V_{R,s}$ is calculated as:

$$V_{R,s} = \frac{A_{sw}}{s_w} \cdot z_v \cdot f_{yw} \cdot \cot \theta \quad (6-6)$$

where A_{sw} is the stirrups cross-section (area of the single vertical arm multiplied by the number of arms), f_{yw} is the yield strength of steel stirrups and s_w the distance between stirrups. The formulations proposed here can be easily modified even if the stirrups are inclined by an α angle with respect to the vertical. For more information, refer to the dMC2020.

The contribution of the concrete $V_{R,c}$ is calculated as:

$$V_{R,c} = k_v \cdot \sqrt{f_{ck}} \cdot b_w \cdot z_v \quad (6-7)$$

where b_w is the beam web width and k_v is a coefficient that depends on ε_x and is calculated as:

$$k_v = \frac{0.4}{1 + 1500 \cdot \varepsilon_x} \quad (6-8)$$

The contribution of the prestress in compressed flange due to the shear friction $V_{R,pf}$ is calculated as this proposal:

$$V_{R,pf} = \lambda \cdot \mu_f \cdot A_{cc} \cdot \sigma_{cp} \quad (6-9)$$

Where:

- λ in the calibration coefficient, assumed 0.45. This coefficient is used to consider the non-superposition principle of the shear strength effects and best fitting;
- μ_f is the friction coefficient, assumed 1.4, equal to $\tan \varphi$ (see MC2010(2013) §6.3.3 – *Shear friction* and Park and Paulay (1975) §7.8.2 used for concrete cast monolithically);
- A_{cc} is the compressed concrete area, calculated with neutral axis in ULS conditions;
- σ_{cp} is the mean stress in the concrete cross section due to prestressing.

The additional contribution that the presence of prestress can provide in the shear resistance has been considered as the confinement it exerts in the non-cracked area of the beam. Prestressed elements usually have significant enlargements at the ends of the section, such as "I" or "T" sections. Just before a shear failure, where cross-sectional cracking affects the web, the top flange again transfers compressive and shear stresses, thus contributing to shear strength [Ayensa et al., 2019; Fernández Ruiz and Muttoni, 2008; Frosch and Wolf, 2003; Huber et al., 2020; Park et al., 2013; Ramadan et al., 2022; Rupf et al., 2013; Sarsam et al., 2018; Sato et al., 1996; Zhou et al., 2021]. Diffuse prestressing in the concrete increases the compressive stress state in that area.

Another contribution of these elements is that being prestressed elements, they are usually made with concretes with high compressive strength, a reasoning that is also valid for the past. Theoretically, the exact position of the neutral axis should be calculated, thus identifying the area of still-reacting concrete. To do this it has assumed initial values of ε_{top} and ε_{bottom} relative to the control section in PRC positioned at $(a - 0.9 \cdot d)$ from the support closest to the load point. The curvature was then calculated and subsequently the ε values were obtained in the positions of the reinforcement, both prestressed and mild. The compressive and tensile forces acting on the control section have been calculated, passing from the stresses σ through the relations that bind $\sigma - \varepsilon$ for the respective materials (prestressed reinforcement: Ramberg–Osgood relationship; concrete: EC2 (2005) §3.1.5; mild reinforcement: elasto-plastic relationship).

6-NEW MODEL FOR PREDICTING THE SHEAR STRENGTH OF EXISTING PRC BEAMS WITH STIRRUPS

The portion of compressed concrete was discretized into 6 fibres so as to more accurately determine the stress, and therefore the action, following the non-linear trend.

The horizontal force equilibrium is then carried out by varying ε_{bottom} until the sum of the compression forces is equal to the sum of the tensile forces acting in the control section. Finally, the moment with respect to the position of the neutral axis in the control section is calculated and ε_{top} is varied until this moment coincides with the experimentally calculated one ($M_{exp} = V_{exp} \cdot (a - 0.9 \cdot d)$). To determine the correct position of the neutral axis in ULS condition, and then calculate the value of the compressed concrete area [A_{cc}], two iterations are needed.

The λ value is the coefficient necessary to algebraically add the contribution of shear friction to the shear resistance provided by the stirrups and to the contribution of the concrete for the determination of the overall shear resistance. In fact, the shear strength is defined by the contribution of several resistant mechanisms (concrete compression, aggregate interlock, dowel action) which do not activate simultaneously, but evolve into variable resistance contributions during the collapse phases of the element and therefore it is not possible to apply the superimposition principle of effects. The proposed value of λ also considers the best fitting of this analytical model applied to the available database. A fundamental hypothesis for the application of this model is having neglected in $V_{R,pf}$ the compression due to the moment contribution generated by external forces.

Finally, the maximum shear resistance related to the crushing of concrete carrying the compression field, $V_{R,max}$, is defined as:

$$V_{R,max} = \frac{k_{\varepsilon} \cdot f_c \cdot b_w \cdot z_v}{\cot \theta + \tan \theta} \quad (6-10)$$

where k_{ε} is the strength reduction factor of concrete carrying the compression field:

$$k_{\varepsilon} = \frac{1}{1 + 110 \cdot \varepsilon_1} \leq 1.0 \quad (6-11)$$

$$\varepsilon_1 = \varepsilon_x + (\varepsilon_x + 0.001) \cdot \cot^2 \theta \geq 0 \quad (6-12)$$

In Equation (6-12) it can be seen that with respect to dMC2020 – LoA IIb only $\varepsilon_1 \geq 0$ is accepted having also adopted $\varepsilon_x < 0$.

6.5 Database and Validation of the Model

The proposed model has been applied to some experimental tests on prestressed reinforced concrete beams with stirrups, simple supported as well as to the experimental tests described in §3.

Multiple literature papers were analysed to create a good database. Perumalla and Laskar (2020) constituted a starting point, thanks to its extensive bibliography: [Alshegeir and Ramirez, 1992; Avendaño and Bayrak, 2008; Bennett and Balasooriya, 1971; Choulli et al., 2008; Durrani and Robertson, 1987; Elzanaty et al., 1986; Garber et al., 2016; Hanson and Hulsbos, 1964, 1965; Huber and Kollegger, 2015; Kaufman and Ramirez, 1988; Labib et al., 2014; Laskar et al., 2010; Lee et al., 2010; Llanos et al., 2009; Ma et al., 2000; Oh and Kim, 2004; Rangan, 1991; Ross et al., 2015; Sudhira De Silva, 2006, 2007; Villamizar et al., 2017; de Wilder et al., 2015; Xuan et al., 1988].

From these, all information on more than 200 beams tests were extracted. However, it was necessary to apply filters to focus only on compatible elements for the model being studied:

- $a/d \geq 2.5$: the proposed formulation derives from the Draft Model Code 2020 and is better suited to shear-resistant contributions correlated to the "beam mechanism". The beam mechanism is difficult to occur in beams with a/d lower than 2.5 [Kani, 1966, 1967]. For these cases, it is better to use specific formulations, such as the strut and tie theory.
- $\rho_x \leq 3\%$: percentage of longitudinal reinforcement not too high for a beam.
- $\rho_z > 0\%$: presence of stirrups.
- Bonded Prestressed Reinforce Concrete Beams: "I", "T" or rectangular cross-section prestressed hollow members, not box or π sections.
- $\sigma_{cp} < 11 \text{ MPa}$: limit to the tension of the concrete exerted by the prestressing.
- Failure Mode= Shear, Shear/Flexure etc... (No Flexure)

Considering these observations, it was finally decided to apply the method only to 66 experimental tests of [Bennett and Balasooriya, 1971; Choulli et al., 2008; Durrani and Robertson, 1987; Hanson and Hulsbos, 1964, 1965; Huber and Kollegger, 2015; Oh and Kim, 2004; Rangan, 1991; de Wilder et al., 2015; Xuan et al., 1988] and Brescia beams.

Some papers from which the analysed samples were selected are briefly described below. For more details, see the papers.

6-NEW MODEL FOR PREDICTING THE SHEAR STRENGTH OF EXISTING PRC BEAMS WITH STIRRUPS

The tests carried out by Hanson and Hulsbos (1964) concern ten prestressed beams, with a height of 46 cm and a web thickness of 7.6 cm. The a/d ratio of the beams varies from 2.12 to a value of 7.75. The beams are all prestressed and have been divided into three regions, A B C, which each contain a different transverse reinforcement. This choice is justified by the fact that a subdivision into different regions allows the execution of a greater number of shear tests. The tests take place in two parts: the first failure is reached within zone A or B, then the supports are moved and the remaining zones are tested. For the purposes of the analytical calculation, only the first test was considered, with the collapse in region B, for which the relative ultimate shear value and the configuration of the stirrups of that region were reported.

Durrani and Robertson (1987) perform 13 tests on prestressed T-section beams. They are 4.57 m long beams supported over a 3.35 span. The thickness of the web is 7.6 cm. The flange is 61 cm wide and the section is 50.8 cm high. The stirrups are placed about 15 cm apart. Of these beams, nine fall within the filters applied to define the database of this thesis.

Xuan et al. (1988) tested six post-tensioned beams with bonded cables with a "T" section. The only parameter that varies between these beams is the transverse reinforcement configuration. All the specimens tested had the same dimensions: the cross-section of the beams was 650 mm flange width, 490 mm overall depth, 60 mm flange thickness, and a tapered web with 85 mm bottom to 140 mm top width. The beam length was 4500 mm. To make the beams critical in shear, the total span was chosen as 3000 mm and the shear span-to-depth ratio a/d was 2.91. Of the six, only 1 remains excluded from the filters applied for the database analysed in this thesis.

Bennett and Balasooriya (1971) make and test 26 beams to investigate the following aspects: shear span/depth ratio, average prestress in concrete and strength of concrete, percentage of web reinforcement, breadth of web and depth of the web and average prestress in concrete. All are I-beams with a flange thickness of 25.4 mm and total height ranging from 45.7 cm to 25.4 cm. Among these 26, only four beams meet the criteria for the database analysed in this thesis.

In the experimental program of Rangan (1991) a total of 16 prestressed beams with I-section, symmetrical, with flanges 40 cm wide and 10 cm thick, web with a thickness of 62÷72 mm and overall height of 61.5 cm were tested. The author declares that all the beams broke due to the collapse of the concrete strut compressed in the core. In fact, the shear reinforcement consisted of two stirrups $\emptyset 6\div 8$ every 5 cm.

Oh and Kim (2004) test two prestressed beams at three inclined tendons, each composed of 6 strands. The section is I-shaped with a wide lower flange, of 60 cm and an upper flange of 80 cm wide, both 15 cm high. The 80 cm high web is 18 cm thick. The beam is 120 cm high overall and 10.60 m long (10 m span between support). Stirrups $\varnothing 13$ were used with a spacing of 20 cm in the shorter area between the load point and the support and 40 cm in the remaining part of the beam. In fact, the test was performed on three points, with a non-symmetrical load and an a/d ratio of 3.3. The geometry of the reinforcement designed for these beams distinguishes them in the database for their high shear strength (1150÷1160 kN) compared to the rest of the tests analysed.

Choulli et al. (2008) realize six prestressed beams with an "I" cross-section of length 10 m and are shear tested in two points at different times. The cross-section has an upper flange 70 cm wide and 8 cm high, a lower flange 50 cm wide and 14 cm high, where the strands are placed, and a 10 cm thick web; the total height is 70 cm. Only four of the six beams have transverse reinforcement. The a/d value is approximately 3.1. Only the first test on each beam was considered in the database.

In the study of De Wilder et al. (2015) nine prestressed beams with two load points were tested in shear. The beams all have a height of 80 cm and a web thickness of 18 cm, the w/d ratio varies between 3.13 and 3.91. Of the nine beams, only six were shear reinforced while three only had longitudinal reinforcement. The prestress was applied with a prestressed reinforcement made up of strands, the number of which is different in the different beams, thus defining a different level of prestress. The test led to the failure of six of the nine beams tested due to effects attributable to shear. For the analytical study using the database, only the beams made with transverse reinforcement and shear collapse were entered.

Huber and Kollegger (2015) tested four post-tensioned beams with bonded cables (the steel ducts were grouted after post-tensioning), with a "T" cross-section 75 cm high, 22.5 cm web thickness and an internal length at the supports of 4.90 m. All beams have two tendons each made up of four strands. In two beams the tendons are straight, while in the other two beams one cable is straight while the second is inclined. The transverse reinforcement in the testing zone consisted of stirrups 2 legs with a diameter of 4 mm resulting in a low geometrical shear reinforcement ratio ρ_w of 0.056 (stirrups spacing $s_w = 200$ mm), respectively, 0.089 ($s_w = 125$ mm). The longitudinal reinforcement consisted of 4 bars with a diameter of 16 mm and was kept constant over the whole length of the beam.

The two prestressed beams Beam A and Beam B described in this research work have also been included in the database.

6-NEW MODEL FOR PREDICTING THE SHEAR STRENGTH OF EXISTING PRC BEAMS WITH STIRRUPS

In Table 6-6 and Table 6-7 the main information of the samples used for the validation of the proposed model is represented. The order of the tests depends on the failure mode. The nomenclature used is the same as described in §6.4. The characteristics of the materials are intended as mean values

In Table 6-8 some ranges of values belonging to the database (DB) are graphically represented:

- percentage of longitudinal reinforcement $[\rho_{s+p}]$,
- percentage of transverse reinforcement $[\rho_w]$,
- effective height $[d]$,
- web thickness $[b_w]$.

It can be observed that the percentage of mild longitudinal and prestressing reinforcement ρ_{s+p} is lower than 1.0% for 77% of the DB, while the percentage of transverse reinforcement ρ_w is lower than 0.25 for 55% of the DB. As regards the geometry of the beams, it can be seen that 82% of the DB has an effective height d of less than 60 cm and 74% of the DB has a web thickness b_w of less than 8 cm. These last two percentages demonstrate how the number of prestressed samples made for the evaluation of shear strength is not very representative of the real dimensions of the beams used on site, above all for the construction of bridges.

6-NEW MODEL FOR PREDICTING THE SHEAR STRENGTH OF EXISTING PRC
BEAMS WITH STIRRUPS

Table 6-6: Principal's information about specimens that make up the database – Pt.1/2

N° Samples Pt. 1 of 2	Authors		Year		Specimen		Section		b _w mm	h mm	d mm	a/d	Z _{wp,calc} mm	Q _{wp} %	A _s mm ²	f _{ym} MPa	Q _w %	S _w mm	A _{sw} mm ²	f _{ysw} MPa	Q _p %	A _p mm ²	c _p mm	f _{pt0,3mm} MPa	σ _{ep} MPa	F _p kN	f _{cm} MPa	Failure Mode	V _{u,exp} kN
	ID	Type	ID	Type	Q _s %	Q _{wp,calc} mm	Q _s %	A _s mm ²																					
1	Hanson and Hulsbos	1965	E14	I	76	457	360	2.5	329	0.98	0.00	0	0	0.37	222	64	410	0.98	426	96	1648	6.4	430	46.8	S	239.4			
2	Hanson and Hulsbos	1965	E17	I	76	457	360	3.4	329	0.98	0.00	0	0	0.20	203	32	410	0.98	426	96	1648	6.1	411	45.4	S	169.1			
3	Hanson and Hulsbos	1965	E18	I	76	457	360	3.4	329	0.98	0.00	0	0	0.16	254	32	410	0.98	426	96	1648	6.1	412	45.8	S	172.2			
4	Durrani and Robertson	1987	3	T	76	508	318	2.8	366	0.42	0.00	0	0	0.14	152	16	637	0.42	297	142	1014	3.7	310	46.1	S	154.3			
5	Durrani and Robertson	1987	4	T	76	508	318	2.8	366	0.42	0.00	0	0	0.14	152	16	637	0.42	297	142	1014	3.7	310	44.1	S	165.2			
6	Durrani and Robertson	1987	5	T	76	508	318	2.8	366	0.42	0.00	0	0	0.18	152	21	458	0.42	297	142	1014	3.7	310	44.6	S	167.0			
7	Durrani and Robertson	1987	6	T	76	508	318	2.8	366	0.42	0.00	0	0	0.03	305	8	637	0.42	297	142	1014	3.7	310	41.9	S	155.7			
8	Durrani and Robertson	1987	8	T	76	508	318	2.8	366	0.42	0.00	0	0	0.17	152	19	402	0.42	297	142	1014	3.7	310	39.4	S	170.4			
9	Durrani and Robertson	1987	10	T	76	508	318	2.8	366	0.42	0.00	0	0	0.17	152	19	402	0.42	297	142	1014	3.7	310	42.0	S	172.4			
10	Durrani and Robertson	1987	11	T	76	508	318	2.8	366	0.42	0.00	0	0	0.22	152	26	535	0.42	297	142	1014	3.7	310	41.8	S	179.0			
11	Durrani and Robertson	1987	12	T	76	508	318	2.8	366	0.42	0.00	0	0	0.06	152	6	683	0.42	297	142	1014	3.7	310	41.5	S	159.0			
12	Durrani and Robertson	1987	13	T	76	508	318	2.8	366	0.42	0.00	0	0	0.06	152	6	683	0.42	297	142	1014	3.7	310	41.3	S	144.6			
13	Xuan	1988	PSN2-WD	T	85	490	406	2.9	365	3.00	1.53	1298	434	0.22	152	28	587	0.24	198	180	1560	4.0	366	38.1	S	217.7			
14	Xuan	1988	PSN3-D2	T	85	490	406	2.9	365	3.00	1.53	1298	434	0.48	150	61	344	0.24	198	180	1560	3.6	332	33.3	S	258.1			
15	Xuan	1988	PSN4-WDH	T	85	490	406	2.9	365	3.00	1.53	1298	434	0.22	152	28	593	0.24	198	180	1560	3.4	310	31.5	S	247.1			
16	Xuan	1988	PSN5-S6M	T	85	490	406	2.9	365	3.00	1.53	1298	434	0.24	150	31	483	0.24	198	180	1560	3.3	301	32.5	S	253.9			
17	Xuan	1988	PSN6-WS	T	85	490	406	2.9	365	3.00	1.53	1298	434	0.24	152	31	579	0.24	198	180	1560	3.1	282	34.3	S	253.8			
18	Choulli et al.	2007	C2TE	I	100	750	671	3.1	604	0.60	0.00	0	0	0.50	200	101	525	0.60	930	257	1670	7.1	1383	90.0	S	721.0			
19	Choulli et al.	2007	S2TE	I	100	750	671	3.1	604	0.60	0.00	0	0	0.50	200	101	525	0.60	930	257	1670	7.1	1383	90.0	S	683.0			
20	Choulli et al.	2007	S2TW	I	100	750	671	3.1	604	0.60	0.00	0	0	0.50	200	101	525	0.60	930	257	1670	7.1	1383	96.0	S	625.0			
21	Choulli et al.	2007	S2TW	I	100	750	671	3.1	604	0.60	0.00	0	0	0.50	200	101	525	0.60	930	257	1670	7.1	1383	96.0	S	605.0			
22	Huber and Kolleger	2015	PC056st	T	225	750	683	3.6	615	0.88	0.34	804	580	0.09	125	25	653	0.54	1120	280	1670	3.9	904	50.6	S	453.0			
23	Huber and Kolleger	2015	PC089st	T	225	750	683	3.6	615	0.88	0.34	804	580	0.09	125	25	653	0.56	1120	253	1670	3.8	896	49.4	S	549.0			
24	Huber and Kolleger	2015	PC056in	T	225	750	668	3.7	602	0.89	0.34	804	581	0.06	200	25	653	0.56	1120	253	1670	3.8	896	50.5	S	537.0			
25	Huber and Kolleger	2015	PC089in	T	225	750	668	3.7	602	0.89	0.34	804	582	0.09	125	25	653	0.56	1120	253	1670	3.8	896	49.4	S	537.0			
26	De Wilder et al.	2015	B101	I	70	630	511	3.1	460	1.33	0.00	0	0	0.27	150	28	608	1.33	797	146	1737	10.7	949	77.5	S	377.2			
27	De Wilder et al.	2015	B102	I	70	630	511	3.9	460	1.33	0.00	0	0	0.27	150	28	608	1.33	797	146	1737	10.7	949	77.5	S	321.6			
28	De Wilder et al.	2015	B104	I	70	630	511	3.1	460	1.34	0.00	0	0	0.27	150	28	608	1.34	799	146	1737	5.4	479	88.9	S	281.8			
29	De Wilder et al.	2015	B105	I	70	630	511	3.9	460	1.34	0.00	0	0	0.27	150	28	608	1.34	800	146	1737	5.4	480	88.9	S	251.2			

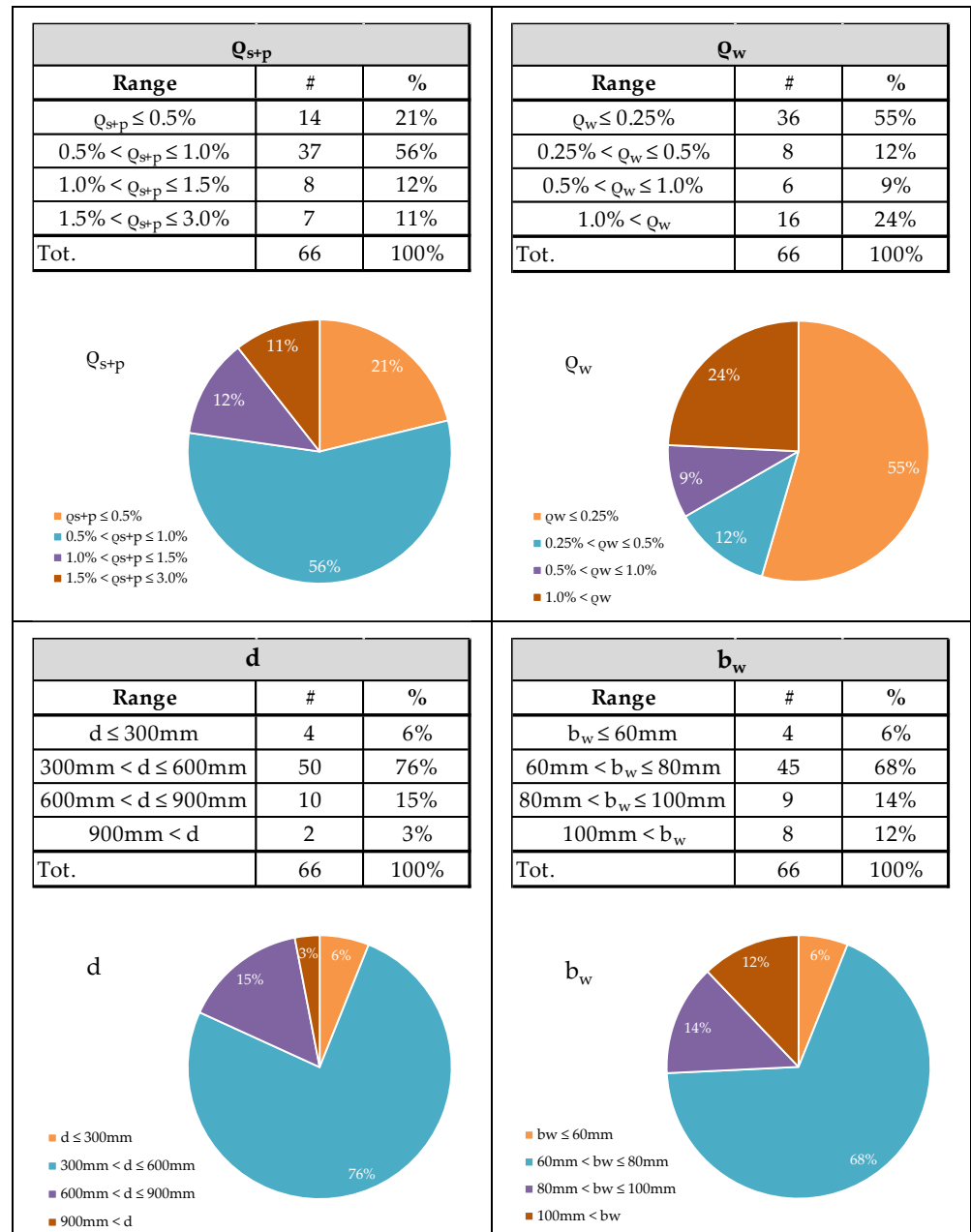
6-NEW MODEL FOR PREDICTING THE SHEAR STRENGTH OF EXISTING PRC BEAMS WITH STIRRUPS

Table 6-7: Principal's information about specimens that make up the database – Pt.2/2

N° Samples Pt. 2 of 2	Authors	Year	Specimen		b _w mm	h mm	d mm	a/d	Z _{wp} peak mm	Q _{wp} %	Q _s %	A _s mm ²	f _{sym} MPa	Q _w %	s _w mm	A _{sw} mm ²	f _{sym} MPa	Q _p %	A _p mm ²	c _p mm	f _{pt} 0.5m MPa	σ _{cp} MPa	F _p kN	f _{cm} MPa	Failure Mode	V _{uexp} kN
			ID	Type																						
66			Beam A	I	180	800	721	2.9	649	0.43	0.08	201	533	0.19	300	101	550	0.35	834	228	1670	3.9	954	61.2	SF	592.1
30	University of Brescia	2022	Beam B	I	180	800	746	2.9	672	0.75	0.52	1263	533	0.19	300	101	550	0.23	556	219	1670	2.6	641	62.5	SF	578.3
31	University of Brescia	2022	Girder 1	I	180	1200	1093	3.3	984	1.69	1.10	3877	345	0.74	200	265	345	0.62	1782	315	1620	4.5	1796	42.8	SF	1151.5
32	Oh and Kim	2004	Girder 2	I	180	1200	1093	3.3	984	1.69	1.10	3877	345	0.74	200	265	345	0.62	1782	315	1620	4.5	1796	42.8	SF	1151.5
33	Oh and Kim	2004	F-4	I	76	457	394	3.2	354	0.83	0.00	0	0	0.20	212	32	410	0.83	426	126	1874	6.2	408	47.5	SF	169.1
34	Hanson and Hulsbos	1964	F-8	I	76	457	394	3.2	354	0.83	0.00	0	0	0.15	152	18	252	0.83	426	126	1874	6.2	408	47.5	SF	120.2
35	Hanson and Hulsbos	1964	F-9	I	76	457	394	3.2	354	0.83	0.00	0	0	0.28	85	18	252	0.83	426	126	1874	6.2	408	47.5	SF	112.6
36	Hanson and Hulsbos	1964	F-11	I	76	457	394	3.2	354	0.83	0.00	0	0	0.18	127	18	252	0.83	426	126	1874	6.2	408	47.5	SF	115.7
37	Hanson and Hulsbos	1964	F-12	I	76	457	394	3.2	354	0.83	0.00	0	0	0.12	203	18	252	0.83	426	126	1874	6.2	408	47.5	SF	102.4
38	Hanson and Hulsbos	1964	F-13	I	76	457	394	3.2	354	0.83	0.00	0	0	0.16	145	18	252	0.83	426	126	1874	6.2	408	47.5	SF	108.1
39	Hanson and Hulsbos	1964	F-14	I	76	457	394	3.2	354	0.83	0.00	0	0	0.10	229	18	252	0.83	426	126	1874	6.2	408	47.5	SF	98.8
40	Hanson and Hulsbos	1964	F-15	I	76	457	394	3.2	354	0.83	0.00	0	0	0.09	254	18	252	0.83	426	126	1874	6.2	408	47.5	SF	75.7
41	Hanson and Hulsbos	1964	F-16	I	76	457	394	3.2	354	0.83	0.00	0	0	0.13	186	18	252	0.83	426	126	1874	6.2	408	47.5	SF	85.4
42	Hanson and Hulsbos	1964	F-19	I	76	457	394	3.2	354	0.83	0.00	0	0	0.27	159	32	410	0.83	426	126	1874	6.2	408	47.5	SF	176.2
43	Hanson and Hulsbos	1964	F-X1	I	76	457	394	3.1	354	0.83	0.00	0	0	0.21	203	32	410	0.83	426	126	1874	6.2	408	47.5	SC	142.4
44	Hanson and Hulsbos	1964	F-2	I	76	457	394	2.6	354	0.83	0.00	0	0	0.21	203	32	410	0.83	426	126	1874	6.2	408	47.5	SC	178.0
45	Hanson and Hulsbos	1964	F-3	I	76	457	394	2.6	354	0.83	0.00	0	0	0.23	102	18	252	0.83	426	126	1874	6.2	408	47.2	SC	178.0
46	Hanson and Hulsbos	1964	F-5	I	76	457	394	3.2	354	0.83	0.00	0	0	0.22	106	18	252	0.83	426	126	1874	6.2	408	44.2	SC	143.3
47	Hanson and Hulsbos	1964	F-6	I	76	457	394	6.5	354	0.83	0.00	0	0	0.13	182	18	252	0.83	426	126	1874	6.2	408	43.0	SC	85.0
48	Hanson and Hulsbos	1964	F-7	I	76	457	394	3.9	354	0.83	0.00	0	0	0.17	254	32	410	0.83	426	126	1874	6.2	408	48.6	SC	129.5
49	Hanson and Hulsbos	1964	F-10	I	76	457	394	4.5	354	0.83	0.00	0	0	0.13	178	18	252	0.83	426	126	1874	6.2	408	48.6	SC	110.4
50	Hanson and Hulsbos	1964	3C3	I	25	254	229	3.0	206	1.25	0.00	0	0	3.27	38	32	265	1.25	193	79	1670	10.2	198	33.6	SC	78.7
51	Bennet and Balasooriya	1971	3C4	I	25	254	229	3.0	206	1.25	0.00	0	0	3.27	38	32	265	1.25	193	79	1670	10.2	198	33.6	SC	78.7
52	Bennet and Balasooriya	1971	3C5	I	25	254	229	3.0	206	1.25	0.00	0	0	3.27	38	32	265	1.25	193	79	1670	10.2	198	33.6	SC	78.7
53	Bennet and Balasooriya	1971	3E5	I	38	254	229	3.0	206	1.10	0.00	0	0	2.18	38	32	265	1.10	193	79	1670	10.8	230	31.6	SC	48.8
54	Bennet and Balasooriya	1971	3E3	I	38	254	229	3.0	206	1.10	0.00	0	0	2.18	38	32	265	1.10	193	79	1670	10.8	230	31.6	SC	89.9
55	Rangan	1991	II-1	I	64	615	567	2.5	510	0.78	0.68	2000	455	1.89	50	60	485	0.10	279	194	1740	1.0	323	45.0	SC	460.9
56	Rangan	1991	II-2	I	63	615	567	2.5	510	0.78	0.68	2000	455	1.89	50	60	485	0.10	279	194	1740	1.0	323	45.0	SC	378.8
57	Rangan	1991	II-3	I	73	615	567	2.5	510	0.78	0.68	2000	455	1.65	50	60	485	0.10	279	194	1740	1.0	323	44.6	SC	489.2
58	Rangan	1991	II-4	I	74	615	567	2.5	510	0.78	0.68	2000	455	2.72	50	101	485	0.10	279	194	1740	1.0	323	43.0	SC	479.4
59	Rangan	1991	III-1	I	66	615	569	2.5	512	0.69	0.55	1620	455	1.83	50	60	485	0.14	398	183	1740	1.5	462	40.0	SC	368.0
60	Rangan	1991	III-2	I	66	615	569	2.5	512	0.69	0.55	1620	455	3.05	50	101	485	0.14	398	183	1740	1.5	462	37.0	SC	390.5
61	Rangan	1991	III-3	I	77	615	569	2.5	512	0.69	0.55	1620	455	1.57	50	60	485	0.14	398	183	1740	1.5	462	39.0	SC	396.5
62	Rangan	1991	III-4	I	73	615	569	2.5	512	0.69	0.55	1620	455	2.75	50	101	485	0.14	398	183	1740	1.5	462	37.0	SC	453.0
63	Rangan	1991	IV-1	I	62	615	540	2.6	486	0.37	0.11	330	455	3.24	50	101	485	0.26	716	172	1740	2.7	831	37.1	SC	375.0
64	Rangan	1991	IV-2	I	64	615	540	2.6	486	0.37	0.11	330	455	1.89	50	60	485	0.26	716	172	1740	2.7	831	33.0	SC	337.8
65	Rangan	1991	IV-3	I	72	615	540	2.6	486	0.37	0.11	330	455	2.79	50	101	485	0.26	716	172	1740	2.7	831	36.0	SC	464.8
66	Rangan	1991	IV-4	I	72	615	540	2.6	486	0.37	0.11	330	455	1.68	50	60	485	0.26	716	172	1740	2.7	831	28.7	SC	390.6

6-NEW MODEL FOR PREDICTING THE SHEAR STRENGTH OF EXISTING PRC BEAMS WITH STIRRUPS

Table 6-8: Graphic representations of some ranges of values belonging to the database: longitudinal reinforcement percentage $[\rho_{s+p}]$, transverse reinforcement percentage $[\rho_w]$, effective height $[d]$, web thickness $[b_w]$.



6.6 Results and Discussion

The results deriving from the application of the method to the 66 experimental samples [Bennett and Balasooriya, 1971; Choulli et al., 2008; Durrani and Robertson, 1987; Hanson and Hulsbos, 1964, 1965; Huber and Kollegger, 2015; Oh and Kim, 2004; Rangan, 1991; de Wilder et al., 2015; Xuan et al., 1988] and Brescia beams are reported in Table 6-9 and Table 6-10. The order of the tests depends on the failure mode. The nomenclature used is the same as described in §6.4. Please note that the shear strength value determined with the UniBS_Proposal model is calculated as follows:

$$V_{u,ana} = V_{R,s} + V_{R,c} + V_{R,pf} \leq V_{R,max}$$

The last column shows the ratio between the experimental strength value and that analytically calculated with the UniBS_Proposal model [$V_{u,exp}/V_{u,ana}$].

In Table 6-11 and Table 6-12 (where the order of the tests is always a function of the failure mode) the shear strength results of each specimen in the database are shown by applying the formulas of the codes described in §6.3. For each model the ratio $V_{u,exp}/V_{u,ana}$ is also expressed to be compared with each other.

Figure 6-3 shows the scatter plot of the experimental shear strength values, on the ordinate axis, and those calculated analytically for all the models applied to the database, on the abscissa axis. Figure 6-4 shows a focus on the comparison between the model of the dMC2020_LoA IIB and UniBS_Proposal, being very similar to each other. If the points remain above the bisector, it means that the analytical model underestimates the real shear strength of the tested member and is therefore conservative.

The $V_{u,exp}/V_{u,ana}$ ratio was also expressed as a function of the number of specimens in the graphs of Figure 6-5 and Figure 6-6. This last graph is always a focus for the comparison between the dMC2020_LoA IIB and UniBS_Proposal models, being very similar to each other. If the points remain above the threshold of $V_{u,exp}/V_{u,ana} = 1.0$, it means that the analytical model underestimates the real shear strength of the tested element, and therefore it is conservative. In these two graphs, as in the tables, the order of the samples depends on the failure mode; the abscissa axis was divided into 3 zones: Shear (S) up to the specimen 29, Shear-Flexure (SF) for samples between 30 and 43; and Shear Compression (SC) for specimens from 44 to 66.

In Figure 6-3 it can be seen that two samples show resistance results, both experimental and analytical, higher than 1100 kN. These belong to the experimental program of Oh and Kim (2004) where by testing full-scale beams with a length of 10 m and an I-section height of 1.20 m. In these cases, it appears that the models proposed for the EC2 are less conservative than those proposed for the *fib* - Model Code. To better analyse this phenomenon, in Figure 6-7, where the ratio $V_{u,exp}/V_{u,ana}$ is expressed as a function of the effective height [d], it can be observed that as the effective height increases, and therefore of the beam section dimensions, models that consider only the stirrups contribution to the shear resistance of prestressed members tend to predict the real strength more accurately, while the more refined *fib* - Model Code models tend to predict quite accurately regardless of the size of the element. From Figure 6-7, and also in graph "d" of Table 6-8, it is evident that the database is not very representative of real cases relating to prestressed PRC beams where usually the height of a bridge beam, with spans of a certain importance, is hardly less than 60-80 cm.

Overall, in Figure 6-5 it can be seen that the application of the models to this database provides results that underestimate on mean by 2.5 times the real shear strength of the element. The models that consider only the contribution of the stirrups: [$V_{R,s}$] such as EC2-2005, dEC2-2020, MC2010 – LoA II and dMC2020 – LoA IIa, emerge from the more refined models that also consider the contribution of the concrete [$V_{R,c}$] such as MC2010 – LoA III, dMC2020 – LoA IIb and UniBS_Proposal. In most cases, the results of the MC2010 – LoA II and dMC2020 – LoA IIa models coincide, therefore only one of the two values is visible graphically. Some specimens by Durrani and Robertson (1987) (n°:7, 11 and 12 of the database), with the application of models that consider only the contribution of the stirrups, show a very high underestimation of the analytical value, as the reinforcement transverse was deliberately designed with requirements lower than the prescriptions of the ACI Code ($\rho_w = 0.03 \div 0.06$). With this it can be noted how influential the shear resistance contribution provided by concrete can be in conditions of low shear reinforcement. The same reasoning holds for all the tests of Hanson and Hulsbos (1964) with $V_{u,exp}/V_{u,ana} \geq 3$ which have a very low percentage of shear reinforcement: $\rho_w = 0.09 \div 0.18$.

Looking at Figure 6-6 at the focus for the comparison between the dMC2020_LoA I Ib and UniBS_Proposal models, it can be seen how the addition of the contribution provided by the prestress causes the ratios $V_{u,exp}/V_{u,ana}$ to shift sharply of the dMC2020_LoA I Ib, bringing them closer to 1.0 on mean. In the area of the graph where the tests which collapsed due to compression of the strut (Shear Compression) are collected, it is noted that out of 23 tests, 14 values (specimens n° 51, 52, 53, 54, 55, 56, 58, 59, 60, 62, 63, 64, 65, 66) have been correctly predicted by both models which adopt the same formula of $V_{R,max}$.

In Table 6-13 with graphical reference to Figure 6-8, the results of, mean, standard deviation (ST.DEV.), coefficient of variation (CoV) and mean absolute percentage error (MAPE) relating to $V_{u,exp}/V_{u,ana}$ are shown and compared for all models applied to the database. From the comparison, it can be seen that the model proposed for dEC2-2020 is the best performing among the models that only consider the contribution of the stirrups for shear strength, even if it has a slightly higher CoV than the models MC2010 – LoA II and dMC2020 – LoA IIa. Between MC2010 – LoA III and dMC2020 – LoA I Ib, the latter seems to greatly improve the mean of the analytical forecasts compared to the experimental ones. With the UniBS_Proposal model, which is based on the formulations of the dMC2020 – LoA I Ib but also adds a contribution that can be evaluated only for the prestressed elements, it presents a substantial improvement for all parameters, obtaining a mean of the predictions almost equal to the real resistance values.

In Table 6-14 with graphical reference to Figure 6-9, the statistical parameters of the UniBS_Proposal model are analysed according to the type of collapse recorded during the tests. It can be observed how the model captures the real strength values conservatively for pure shear and shear compression failures, while underestimating the strength for shear-flexure failures by a few points.

6-NEW MODEL FOR PREDICTING THE SHEAR STRENGTH OF EXISTING PRC BEAMS WITH STIRRUPS

Table 6-9: Application of the UniBS_Proposal model to the database – Pt.1/2

N° Samples Pt 1 of 2	Authors	Year	Specimen ID	Failure Mode	V _E kN	M _E kNm	N _E kN	ε _x mm/m	θ deg	ε ₁ mm/m	k _c -	k _v MPa	A _{cc} mm ²	X from top mm	V _{R,s} kN	V _{R,c} kN	V _{R,opt} kN	V _{R,max} kN	V _{u,ana} kN	V _{u,exp} / V _{u,ana} -	
																					V _E kN
66																					
1	Hanson and Hulsbos	1965	E14	S	185.2	68.5	-429.9	0.68	33.7	4.437	0.67	0.20	23092	151	58.5	34.0	92.6	364.2	185.2	1.29	
2	Hanson and Hulsbos	1965	E17	S	142.0	88.1	-411.2	0.89	35.2	4.676	0.66	0.17	21553	130	30.3	29.0	82.7	354.3	142.0	1.19	
3	Hanson and Hulsbos	1965	E18	S	138.3	84.6	-412.1	0.78	34.5	4.560	0.67	0.18	21343	128	24.9	31.3	82.1	357.1	138.3	1.25	
4	Durrani and Robertson	1987	3	S	143.9	40.4	-310.2	1.43	39.0	5.132	0.64	0.13	38659	63	30.5	24.1	89.3	401.8	143.9	1.07	
5	Durrani and Robertson	1987	4	S	139.1	37.6	-310.2	1.29	38.1	5.036	0.64	0.14	35633	58	31.5	25.2	82.3	384.2	139.1	1.19	
6	Durrani and Robertson	1987	5	S	137.3	36.5	-310.2	1.24	37.7	4.998	0.65	0.14	35058	58	30.3	26.0	81.0	388.4	137.3	1.22	
7	Durrani and Robertson	1987	6	S	127.5	30.8	-310.2	0.97	35.8	4.758	0.66	0.16	38737	64	8.6	29.4	89.5	363.2	127.5	1.22	
8	Durrani and Robertson	1987	8	S	131.1	32.9	-310.2	1.07	36.5	4.852	0.65	0.15	34138	56	25.3	26.9	78.9	342.6	131.1	1.30	
9	Durrani and Robertson	1987	10	S	130.3	32.4	-310.2	1.05	36.3	4.834	0.65	0.16	33254	55	25.4	28.1	76.9	365.1	130.3	1.32	
10	Durrani and Robertson	1987	11	S	138.3	37.1	-310.2	1.27	37.9	5.019	0.64	0.14	30666	50	42.6	24.8	70.9	363.7	138.3	1.29	
11	Durrani and Robertson	1987	12	S	130.1	32.3	-310.2	1.04	36.3	4.829	0.65	0.16	37957	62	14.4	28.0	87.7	360.8	130.1	1.22	
12	Durrani and Robertson	1987	13	S	137.1	36.4	-310.2	1.24	37.7	4.995	0.65	0.14	42575	70	13.7	25.1	98.4	359.4	137.1	1.05	
13	Xuan	1988	PSN2-WD	S	217.5	111.3	-366.0	0.61	33.2	4.344	0.68	0.21	46135	137	61.1	40.1	116.3	366.7	217.5	1.00	
14	Xuan	1988	PSN3-D2	S	216.1	116.3	-332.1	0.65	33.5	4.402	0.67	0.20	44849	121	77.3	36.3	102.6	320.6	216.1	1.19	
15	Xuan	1988	PSN4-WDH	S	195.7	103.6	-310.2	0.57	33.0	4.302	0.68	0.21	44994	123	62.2	37.4	96.1	303.1	195.7	1.26	
16	Xuan	1988	PSN5-56M	S	188.3	99.3	-301.0	0.55	32.8	4.266	0.68	0.22	44768	120	56.8	38.8	92.8	312.7	188.3	1.35	
17	Xuan	1988	PSN6-WS	S	190.3	104.4	-281.8	0.59	33.1	4.321	0.68	0.21	44605	119	65.2	38.6	86.6	330.1	190.3	1.33	
18	Choulli et al.	2007	C2TE	S	465.0	340.4	-1382.9	0.78	34.5	4.564	0.67	0.18	28465	41	232.1	105.4	127.5	1689.8	465.0	1.55	
19	Choulli et al.	2007	C2TW	S	477.9	359.6	-1382.9	0.93	35.5	4.725	0.66	0.17	35546	51	223.2	95.5	159.2	1692.6	477.9	1.43	
20	Choulli et al.	2007	S2TE	S	466.0	341.9	-1382.9	0.80	34.6	4.577	0.67	0.18	28278	40	231.4	108.0	126.7	1802.7	466.0	1.34	
21	Choulli et al.	2007	S2TW	S	478.7	360.8	-1382.9	0.94	35.6	4.734	0.66	0.17	35259	50	222.7	98.1	157.9	1805.6	478.7	1.26	
22	Huber and Kolleger	2015	PC056st	S	463.8	598.6	-904.0	1.33	38.3	5.061	0.64	0.13	110468	199	63.9	131.5	268.4	2185.8	463.8	0.98	
23	Huber and Kolleger	2015	PC089st	S	485.1	638.2	-902.0	1.44	39.1	5.141	0.64	0.13	107325	185	99.3	125.5	260.2	2226.1	485.1	0.98	
24	Huber and Kolleger	2015	PC056in	S	439.5	587.1	-892.6	1.30	38.1	5.041	0.64	0.14	102808	165	63.0	129.0	247.6	2088.4	439.5	1.25	
25	Huber and Kolleger	2015	PC089in	S	464.8	635.5	-885.6	1.44	39.1	5.142	0.64	0.13	102969	166	97.2	121.6	246.1	2136.7	464.8	1.16	
26	DeWilder et al.	2015	B101	S	361.2	273.3	-947.6	1.05	36.3	4.832	0.65	0.16	36291	268	71.7	44.1	245.4	777.5	361.2	1.05	
27	DeWilder et al.	2015	B102	S	315.2	346.4	-948.7	1.43	39.0	5.132	0.64	0.13	31620	201	65.1	36.1	214.1	779.9	315.2	1.02	
28	DeWilder et al.	2015	B104	S	221.1	182.0	-479.4	0.98	35.9	4.773	0.66	0.16	28997	164	72.9	49.1	99.2	891.2	221.1	1.27	
29	DeWilder et al.	2015	B105	S	219.0	266.9	-480.0	1.60	40.2	5.241	0.63	0.12	35319	147	62.4	35.7	121.0	895.0	219.0	1.15	

6-NEW MODEL FOR PREDICTING THE SHEAR STRENGTH OF EXISTING PRC BEAMS WITH STIRRUPS

Table 6-10: Application of the UniBS_Proposal model to the database – Pt.2/2

N° Samples Pt 2 of 2	Authors	Year	Specimen ID	Failure Mode	V _E kN	M _E kNm	N _E kN	ε _x mm/m	θ deg	ε ₁ mm/m	k _z -	k _v MPa	A _{cc} mm ²	X _{from top} mm	V _{R,s}	V _{R,c}	V _{R,pt}	V _{R,max}	V _{u,ana}	V _{u,exp}
															kN	kN	kN	kN	kN	kN
30	University of Brescia	2022	Beam A	SF	463.8	448.4	-954.3	1.33	38.3	5.063	0.64	0.13	77290	175	151.5	122.1	190.3	2234.5	463.8	1.28
31	University of Brescia	2022	Beam B	SF	442.7	507.3	-640.8	1.11	36.8	4.888	0.65	0.15	80696	194	165.7	143.6	133.4	2357.3	442.7	1.31
32	Oh and Kim	2004	Girder 1	SF	1212.2	2605.0	-1796.1	1.22	37.6	4.983	0.65	0.14	162861	372	585.8	163.4	463.0	2366.4	1212.2	0.95
33	Oh and Kim	2004	Girder 2	SF	1232.2	2657.3	-1796.1	1.26	37.8	5.008	0.64	0.14	160977	362	581.0	193.6	457.7	2434.4	1232.2	0.94
34	Hanson and Hulsbos	1964	F-4	SF	150.4	86.4	-408.1	0.92	35.5	4.714	0.66	0.17	22896	148	31.0	30.0	89.4	367.6	150.4	1.12
35	Hanson and Hulsbos	1964	F-8	SF	136.9	108.8	-408.1	1.27	37.9	5.021	0.64	0.14	25064	177	13.4	25.6	97.9	400.3	136.9	0.88
36	Hanson and Hulsbos	1964	F-9	SF	138.3	180.6	-408.1	2.71	45.0	6.420	0.59	0.08	26870	118	18.8	14.5	105.0	363.6	138.3	0.81
37	Hanson and Hulsbos	1964	F-11	SF	123.3	124.2	-408.1	1.48	39.4	5.167	0.64	0.12	22107	138	15.3	21.6	86.4	351.2	123.3	0.94
38	Hanson and Hulsbos	1964	F-12	SF	113.6	139.3	-408.1	1.71	41.0	5.306	0.63	0.11	21590	131	9.0	20.2	84.3	378.6	113.6	0.90
39	Hanson and Hulsbos	1964	F-13	SF	135.3	175.7	-408.1	2.59	45.0	6.181	0.60	0.08	28051	123	11.0	14.7	109.6	357.7	135.3	0.80
40	Hanson and Hulsbos	1964	F-14	SF	125.4	190.8	-408.1	2.82	45.0	6.643	0.58	0.08	26696	117	7.0	14.1	104.3	363.8	125.4	0.79
41	Hanson and Hulsbos	1964	F-15	SF	107.4	183.4	-408.1	2.55	45.0	6.095	0.60	0.08	21958	136	6.3	15.3	85.8	378.6	107.4	0.70
42	Hanson and Hulsbos	1964	F-16	SF	114.7	228.5	-408.1	3.49	45.0	7.989	0.53	0.06	24154	106	8.6	11.8	94.4	332.2	114.7	0.75
43	Hanson and Hulsbos	1964	F-19	SF	156.3	91.9	-408.1	1.07	36.5	4.856	0.65	0.15	22257	140	39.8	29.6	87.0	430.3	156.3	1.13
44	Hanson and Hulsbos	1964	F-X1	SC	176.6	101.4	-408.1	1.40	38.8	5.116	0.64	0.13	31865	266	28.6	23.5	124.4	387.2	176.6	0.81
45	Hanson and Hulsbos	1964	F-2	SC	192.5	76.1	-408.1	1.01	36.1	4.802	0.65	0.16	33832	292	31.6	28.8	132.2	380.1	192.5	0.92
46	Hanson and Hulsbos	1964	F-3	SC	185.8	71.6	-408.1	0.88	35.1	4.667	0.66	0.17	33654	289	22.3	32.0	131.5	396.3	185.8	0.96
47	Hanson and Hulsbos	1964	F-5	SC	156.7	92.2	-408.1	1.08	36.6	4.864	0.65	0.15	27915	214	20.3	27.4	109.1	372.3	156.7	0.91
48	Hanson and Hulsbos	1964	F-6	SC	127.7	227.9	-408.1	3.57	45.0	8.148	0.53	0.06	27600	121	8.8	11.1	107.8	306.0	127.7	0.67
49	Hanson and Hulsbos	1964	F-7	SC	139.5	111.9	-408.1	1.35	38.5	5.079	0.64	0.13	23614	157	23.2	24.1	92.3	385.4	139.5	0.93
50	Hanson and Hulsbos	1964	F-10	SC	123.1	124.0	-408.1	1.48	39.3	5.164	0.64	0.12	22716	146	10.9	23.4	88.7	410.7	123.1	0.90
51	Bennet and Balasooriya	1971	3C3	SC	55.8	11.2	-197.5	-0.25	27.2	2.575	0.78	0.64	8428	66	88.2	19.4	54.2	55.8	55.8	1.41
52	Bennet and Balasooriya	1971	3C4	SC	49.4	12.2	-145.5	0.41	31.9	4.062	0.69	0.25	8572	72	73.0	7.1	40.6	49.4	49.4	1.14
53	Bennet and Balasooriya	1971	3C5	SC	50.6	19.7	-58.7	2.37	45.0	5.743	0.61	0.09	7595	50	45.4	2.6	14.5	50.6	50.6	0.97
54	Bennet and Balasooriya	1971	3E3	SC	99.3	29.5	-230.1	2.18	44.2	5.527	0.62	0.09	8113	53	46.6	4.7	55.0	99.3	99.3	0.91
55	Rangan	1991	II-1	SC	457.6	344.7	-323.2	1.03	36.2	4.817	0.65	0.16	47876	203	408.1	34.4	31.2	457.6	457.6	1.01
56	Rangan	1991	II-2	SC	314.0	216.8	-323.2	0.60	33.2	4.333	0.68	0.21	48921	221	760.4	38.1	31.9	314.0	314.0	1.21
57	Rangan	1991	II-3	SC	472.9	358.3	-323.2	1.08	36.5	4.859	0.65	0.15	48369	199	403.4	38.1	31.5	517.6	472.9	1.03
58	Rangan	1991	II-4	SC	506.4	388.0	-323.2	1.18	37.2	4.945	0.65	0.14	48558	201	654.1	35.8	31.6	506.4	506.4	0.95
59	Rangan	1991	III-1	SC	420.7	289.0	-461.7	0.88	35.1	4.666	0.66	0.17	52424	269	426.5	36.9	48.8	420.7	420.7	0.87
60	Rangan	1991	III-2	SC	388.7	260.6	-461.7	0.77	34.4	4.547	0.67	0.19	50691	243	730.1	38.2	47.2	388.7	388.7	1.00
61	Rangan	1991	III-3	SC	479.7	341.3	-461.7	1.08	36.5	4.859	0.65	0.15	51730	239	405.2	37.7	48.2	479.7	479.7	0.83
62	Rangan	1991	III-4	SC	430.6	297.7	-461.7	0.91	35.4	4.701	0.66	0.17	50083	223	703.6	38.5	46.6	430.6	430.6	1.05
63	Rangan	1991	IV-1	SC	346.6	173.7	-831.0	0.43	32.0	4.083	0.69	0.24	59755	397	758.9	44.8	100.1	346.6	346.6	1.08
64	Rangan	1991	IV-2	SC	318.7	148.1	-831.0	0.23	30.6	3.751	0.71	0.30	54934	313	480.9	52.9	92.0	318.7	318.7	1.06
65	Rangan	1991	IV-3	SC	391.3	214.5	-831.0	0.73	34.1	4.505	0.67	0.19	56101	308	699.0	40.0	94.0	391.3	391.3	1.19
66	Rangan	1991	IV-4	SC	312.0	142.0	-831.0	0.19	30.3	3.662	0.71	0.31	56613	315	487.1	58.5	94.9	312.0	312.0	1.25

6-NEW MODEL FOR PREDICTING THE SHEAR STRENGTH OF EXISTING PRC BEAMS WITH STIRRUPS

Table 6-11: Shear strength value calculated for each specimen in the database by applying the formulas of the models used by the various codes – Pt.1/2

N° Samples Pt.1 of 2	DATABASE							dEC2-2020		MC2010 LoA_II		MC2010 LoA_III		dMC2020 LoA_IIa		dMC2020 LoA_IIb		UniBS Proposal	
	Authors	Year	Specimen ID	Failure Mode	V _{u,exp} kN	V _{u,calc} kN		V _{u,exp} V _{u,ana}	V _{u,exp} V _{u,ana}	V _{u,exp} V _{u,ana}	V _{u,exp} V _{u,ana}	V _{u,exp} V _{u,ana}	V _{u,exp} V _{u,ana}	V _{u,exp} V _{u,ana}	V _{u,exp} V _{u,ana}	V _{u,exp} V _{u,ana}	V _{u,exp} V _{u,ana}	V _{u,exp} V _{u,ana}	V _{u,exp} V _{u,ana}
						V _{u,calc} kN	V _{u,calc} kN												
1	Hanson and Hulsbos	1965	E14	S	2394	977	2.45	115.5	2.07	107.4	2.23	123.2	1.94	107.4	2.23	139.2	1.72	185.2	1.29
2	Hanson and Hulsbos	1965	E17	S	1691	534	3.16	63.0	2.69	58.7	2.88	88.3	1.91	58.7	2.88	106.2	1.59	142.0	1.19
3	Hanson and Hulsbos	1965	E18	S	1722	427	4.03	50.3	3.42	46.9	3.67	80.3	2.14	46.9	3.67	98.7	1.74	138.3	1.25
4	Durrani and Robertson	1987	3	S	154.3	61.7	2.50	74.0	2.09	67.8	2.28	96.4	1.60	67.8	2.28	100.2	1.54	143.9	1.07
5	Durrani and Robertson	1987	4	S	165.2	61.7	2.68	74.0	2.23	67.8	2.44	95.8	1.72	67.8	2.44	99.8	1.66	139.1	1.19
6	Durrani and Robertson	1987	5	S	167.0	58.6	2.85	70.3	2.38	64.4	2.59	94.9	1.76	64.4	2.59	99.2	1.68	137.3	1.22
7	Durrani and Robertson	1987	6	S	155.7	15.4	10.10	18.5	8.41	16.9	9.19	62.0	2.51	16.9	9.19	83.3	1.87	127.5	1.22
8	Durrani and Robertson	1987	8	S	170.4	46.7	3.65	56.0	3.04	51.3	3.32	84.2	2.02	51.3	3.32	95.7	1.78	131.1	1.30
9	Durrani and Robertson	1987	10	S	172.4	46.7	3.69	56.0	3.08	51.3	3.36	86.1	2.00	51.3	3.36	96.3	1.79	130.3	1.32
10	Durrani and Robertson	1987	11	S	179.0	82.9	2.16	99.5	1.80	91.1	1.96	102.8	1.74	91.1	1.96	104.0	1.72	138.3	1.29
11	Durrani and Robertson	1987	12	S	159.0	26.4	6.02	31.7	5.01	29.1	5.47	70.2	2.26	29.1	5.47	90.9	1.75	130.1	1.22
12	Durrani and Robertson	1987	13	S	144.6	26.4	5.47	31.7	4.56	29.1	4.98	70.1	2.06	29.1	4.98	90.7	1.59	137.1	1.05
13	Xuan	1988	PSN2-WD	S	2177	1001	2.18	1201	1.81	1085	2.01	1249	1.74	1093	1.99	131.8	1.65	217.5	1.00
14	Xuan	1988	PSN3-D2	S	2581	1281	2.01	1337	1.68	1281	2.01	1375	1.88	1345	1.92	1391	1.86	216.1	1.19
15	Xuan	1988	PSN4-WDHH	S	2471	1011	2.44	121.3	2.04	105.7	2.34	1184	2.09	108.5	2.28	123.4	2.00	195.7	1.26
16	Xuan	1988	PSN5-56M	S	2539	916	2.77	109.9	2.31	97.3	2.61	1127	2.25	99.1	2.56	118.7	2.14	188.3	1.35
17	Xuan	1988	PSN6-WS	S	2538	1063	2.39	127.6	1.99	1080	2.35	1221	2.08	112.6	2.25	125.1	2.03	190.3	1.33
18	Choulli et al.	2007	C2TE	S	721.0	398.7	1.81	478.4	1.51	409.0	1.76	428.0	1.68	417.4	1.73	423.3	1.70	465.0	1.55
19	Choulli et al.	2007	C2TW	S	683.0	398.7	1.71	478.4	1.43	409.0	1.67	428.0	1.60	417.4	1.64	423.3	1.61	477.9	1.43
20	Choulli et al.	2007	S2TE	S	625.0	398.7	1.57	478.4	1.31	409.0	1.53	429.7	1.45	417.4	1.50	424.7	1.47	466.0	1.34
21	Choulli et al.	2007	S2TW	S	605.0	398.7	1.52	478.4	1.26	409.0	1.48	429.7	1.41	417.4	1.45	424.7	1.42	478.7	1.26
22	Huber and Kolleger	2015	PC056st	S	453.0	126.1	3.59	151.3	2.99	138.5	3.27	291.5	1.55	138.5	3.27	304.6	1.49	463.8	0.98
23	Huber and Kolleger	2015	PC089st	S	475.0	201.7	2.35	242.1	1.96	216.8	2.19	322.6	1.47	219.1	2.17	328.0	1.45	485.1	0.98
24	Huber and Kolleger	2015	PC056in	S	549.0	123.4	4.45	148.1	3.71	135.6	4.05	280.2	1.96	135.6	4.05	292.4	1.88	439.5	1.25
25	Huber and Kolleger	2015	PC089in	S	537.0	197.4	2.70	238.9	2.27	217.0	2.47	310.5	1.73	217.0	2.47	315.2	1.70	464.8	1.06
26	De Wilder et al.	2015	B101	S	377.7	131.8	2.87	158.5	2.38	144.8	2.61	185.2	2.04	144.8	2.61	208.4	1.81	361.2	1.05
27	De Wilder et al.	2015	B102	S	321.6	131.8	2.44	158.5	2.03	144.8	2.22	185.2	1.74	144.8	2.22	208.4	1.54	315.2	1.02
28	De Wilder et al.	2015	B104	S	281.8	131.8	2.14	158.5	1.78	141.5	1.99	166.8	1.69	142.9	1.97	166.7	1.69	321.1	1.27
29	De Wilder et al.	2015	B105	S	251.2	131.8	1.91	158.5	1.58	127.3	1.97	150.4	1.67	134.4	1.87	148.0	1.70	219.0	1.15

6-NEW MODEL FOR PREDICTING THE SHEAR STRENGTH OF EXISTING PRC BEAMS WITH STIRRUPS

Table 6-12: Shear strength value calculated for each specimen in the database by applying the formulas of the models used by the various codes – Pt.2/2

N° Samples Pt. 2 of 2	DATABASE										MC2010 LoA_II	MC2010 LoA_III	dMC2020 LoA_IIa	dMC2020 LoA_IIb	Units Proposal							
	Authors	Year	Specimen ID	Failure Mode	V _{u,exp} kN	EC2-2005		dEC2-2020		MC2010 LoA_II						MC2010 LoA_III		dMC2020 LoA_IIa		dMC2020 LoA_IIb		
						V _{u,ana} kN	V _{u,exp} /V _{u,ana}	V _{u,ana} kN	V _{u,exp} /V _{u,ana}	V _{u,ana} kN						V _{u,exp} /V _{u,ana}	V _{u,ana} kN	V _{u,exp} /V _{u,ana}	V _{u,ana} kN	V _{u,exp} /V _{u,ana}	V _{u,ana} kN	V _{u,exp} /V _{u,ana}
30	University of Brescia	2022	Beam A	SF	592.1	299.1	1.98	359.0	1.65	308.2	1.92	373.3	1.59	316.1	1.87	372.0	1.59	463.8	1.28			
31	University of Brescia	2022	Beam B	SF	578.3	309.5	1.87	371.4	1.56	279.0	2.07	365.3	1.58	305.8	1.89	361.3	1.60	442.7	1.31			
32	Oh and Kim	2004	Girder 1	SF	1151.5	1126.5	1.02	1351.8	0.85	886.0	1.30	938.6	1.12	1026.8	1.12	893.8	1.29	1212.2	0.95			
33	Oh and Kim	2004	Girder 2	SF	1156.0	1126.5	1.03	1351.8	0.86	886.0	1.30	967.5	1.19	1026.8	1.13	922.7	1.25	1232.2	0.94			
34	Hanson and Hulsbos	1964	F-4	SF	169.1	55.3	3.06	66.3	2.55	60.7	2.78	92.2	1.83	60.7	2.78	111.3	1.52	150.4	1.12			
35	Hanson and Hulsbos	1964	F-8	SF	120.2	26.1	4.60	31.4	3.83	21.8	5.51	21.8	5.51	21.8	5.51	21.8	5.51	21.8	5.51			
36	Hanson and Hulsbos	1964	F-9	SF	112.6	47.1	2.39	56.5	1.99	51.7	2.18	77.5	1.45	51.7	2.18	79.5	1.42	138.3	0.81			
37	Hanson and Hulsbos	1964	F-11	SF	115.7	31.4	3.69	37.6	3.08	34.5	3.36	72.5	1.60	34.5	3.36	83.8	1.38	123.3	0.94			
38	Hanson and Hulsbos	1964	F-12	SF	102.4	19.6	5.22	23.5	4.35	21.5	4.75	65.6	1.56	21.5	4.75	74.3	1.38	113.6	0.90			
39	Hanson and Hulsbos	1964	F-13	SF	108.1	27.4	3.95	32.9	3.29	30.1	3.59	71.2	1.52	30.1	3.59	75.6	1.43	135.3	0.80			
40	Hanson and Hulsbos	1964	F-14	SF	98.8	17.4	5.67	20.9	4.73	19.1	5.16	63.9	1.55	19.1	5.16	67.9	1.46	125.4	0.79			
41	Hanson and Hulsbos	1964	F-15	SF	75.7	15.7	4.83	18.8	4.02	17.2	4.39	59.2	1.28	17.2	4.39	62.5	1.21	107.4	0.70			
42	Hanson and Hulsbos	1964	F-16	SF	85.4	21.4	3.99	25.7	3.33	23.5	3.63	57.0	1.50	23.5	3.63	59.2	1.44	114.7	0.75			
43	Hanson and Hulsbos	1964	F-19	SF	176.2	73.6	2.39	88.4	1.99	80.9	2.18	111.2	1.58	80.9	2.18	118.1	1.49	156.3	1.13			
44	Hanson and Hulsbos	1964	F-XI	SC	142.4	57.5	2.48	69.0	2.06	63.2	2.25	95.4	1.49	63.2	2.25	114.7	1.24	176.6	0.81			
45	Hanson and Hulsbos	1964	F-2	SC	178.0	57.5	3.09	69.0	2.58	63.2	2.82	94.9	1.88	63.2	2.82	114.1	1.56	192.5	0.92			
46	Hanson and Hulsbos	1964	F-3	SC	178.0	39.2	4.54	47.0	3.78	43.1	4.13	82.1	2.17	43.1	4.13	102.5	1.74	185.8	0.96			
47	Hanson and Hulsbos	1964	F-5	SC	143.3	37.7	3.80	45.2	3.17	41.4	3.46	79.1	1.81	41.4	3.46	99.0	1.45	156.7	0.91			
48	Hanson and Hulsbos	1964	F-6	SC	85.0	21.9	3.88	26.3	3.23	24.1	3.53	60.1	1.41	24.1	3.53	63.0	1.35	127.7	0.67			
49	Hanson and Hulsbos	1964	F-7	SC	129.5	46.0	2.81	55.2	2.34	50.6	2.56	86.4	1.50	50.6	2.56	97.5	1.33	139.5	0.93			
50	Hanson and Hulsbos	1964	F-10	SC	110.4	22.4	4.93	26.9	4.11	24.6	4.48	70.1	1.57	24.6	4.48	83.5	1.32	123.1	0.90			
51	Bennet and Balasooriya	1971	3C3	SC	78.7	45.5	1.73	44.0	1.79	26.8	2.94	26.8	2.94	30.9	2.55	54.9	1.43	55.8	1.41			
52	Bennet and Balasooriya	1971	3C4	SC	56.4	41.1	1.37	39.8	1.42	25.1	2.25	25.1	2.25	28.0	2.02	49.4	1.14	49.4	1.14			
53	Bennet and Balasooriya	1971	3C5	SC	48.8	37.4	1.31	41.3	1.18	49.2	0.99	49.2	0.99	27.6	1.77	48.7	1.00	50.6	0.97			
54	Bennet and Balasooriya	1971	3E3	SC	89.9	82.6	1.09	79.9	1.13	45.7	1.97	45.7	1.97	56.1	1.60	78.3	1.15	99.3	0.91			
55	Rangan	1991	II-1	SC	460.9	310.9	1.48	367.2	1.26	254.8	1.81	254.8	1.81	248.1	1.86	446.7	1.03	457.6	1.01			
56	Rangan	1991	II-2	SC	378.8	216.3	1.75	253.0	1.50	175.1	2.16	175.1	2.16	173.9	2.18	314.0	1.21	314.0	1.21			
57	Rangan	1991	II-3	SC	489.2	351.5	1.39	415.1	1.18	311.0	1.57	311.0	1.57	279.3	1.75	450.1	1.09	472.9	1.03			
58	Rangan	1991	II-4	SC	479.4	343.8	1.39	405.7	1.18	305.7	1.57	305.7	1.57	273.1	1.76	506.4	0.95	506.4	0.95			
59	Rangan	1991	III-1	SC	368.0	290.2	1.27	338.2	1.09	217.2	1.69	217.2	1.69	231.1	1.59	420.7	0.87	420.7	0.87			
60	Rangan	1991	III-2	SC	390.5	269.2	1.45	312.8	1.25	199.4	1.96	199.4	1.96	182	2.14	388.7	1.00	388.7	1.00			
61	Rangan	1991	III-3	SC	396.5	330.4	1.20	384.7	1.03	275.6	1.44	275.6	1.44	260.9	1.52	454.0	0.87	479.7	0.83			
62	Rangan	1991	III-4	SC	453.0	297.8	1.52	346.0	1.31	236.0	1.92	236.0	1.92	236.1	1.92	430.6	1.05	430.6	1.05			
63	Rangan	1991	IV-1	SC	375.0	279.5	1.51	279.5	1.34	164.9	2.27	164.9	2.27	196.3	1.91	346.6	1.08	346.6	1.08			
64	Rangan	1991	IV-2	SC	337.8	229.5	1.47	256.7	1.32	157.4	2.15	157.4	2.15	180.3	1.87	318.7	1.06	318.7	1.06			
65	Rangan	1991	IV-3	SC	464.8	280.0	1.66	315.0	1.48	187.7	2.48	187.7	2.48	221.2	2.10	391.3	1.19	391.3	1.19			
66	Rangan	1991	IV-4	SC	390.6	227.1	1.72	251.1	1.56	159.0	2.46	159.0	2.46	176.4	2.21	312.0	1.25	312.0	1.25			

6-NEW MODEL FOR PREDICTING THE SHEAR STRENGTH OF EXISTING PRC BEAMS WITH STIRRUPS

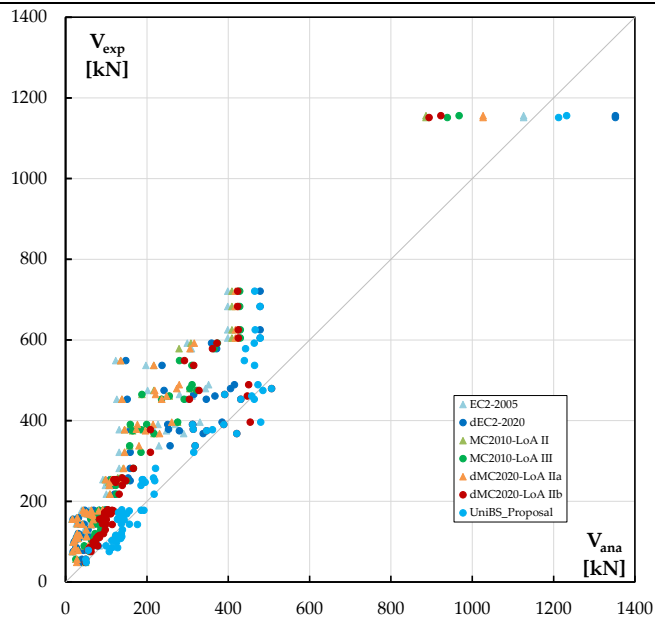


Figure 6-3: Scatterplot of experimental versus analytically calculated shear strength results for all models applied to the database.

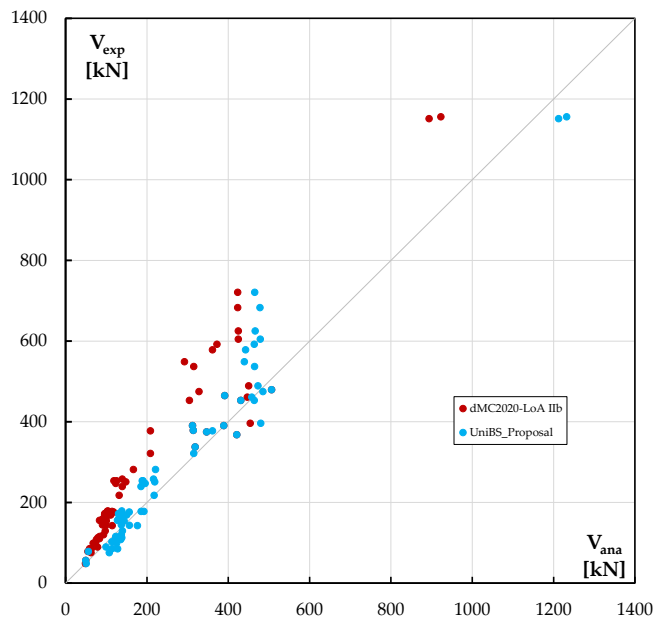


Figure 6-4: Scatterplot comparison of results of experimental versus analytically calculated shear strength, between dMC2020_LoA IIb and UniBS_Proposal.

6-NEW MODEL FOR PREDICTING THE SHEAR STRENGTH OF EXISTING PRC BEAMS WITH STIRRUPS

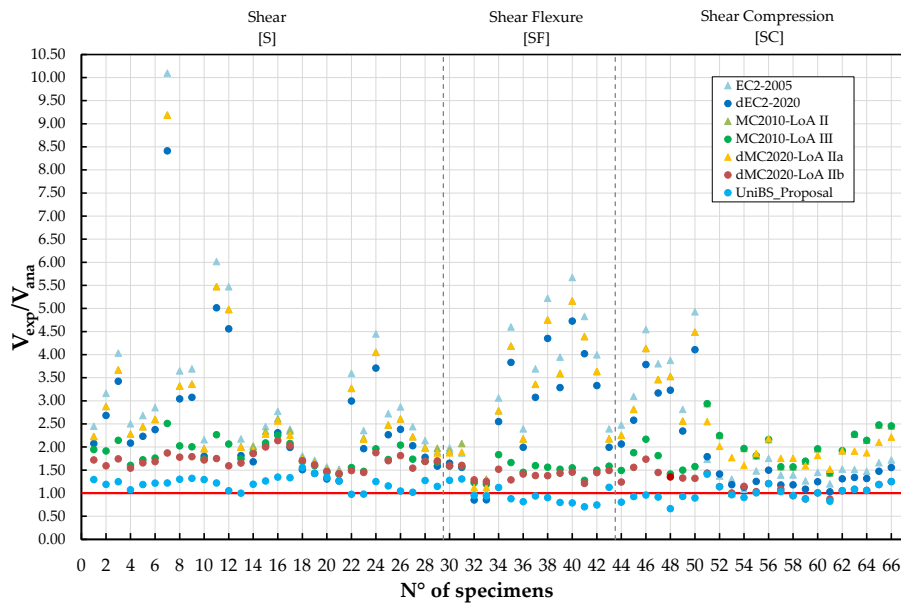


Figure 6-5: Comparison $V_{u,exp}/V_{u,ana}$ of all the models applied according to the number of database samples sorted according to the failure mode.

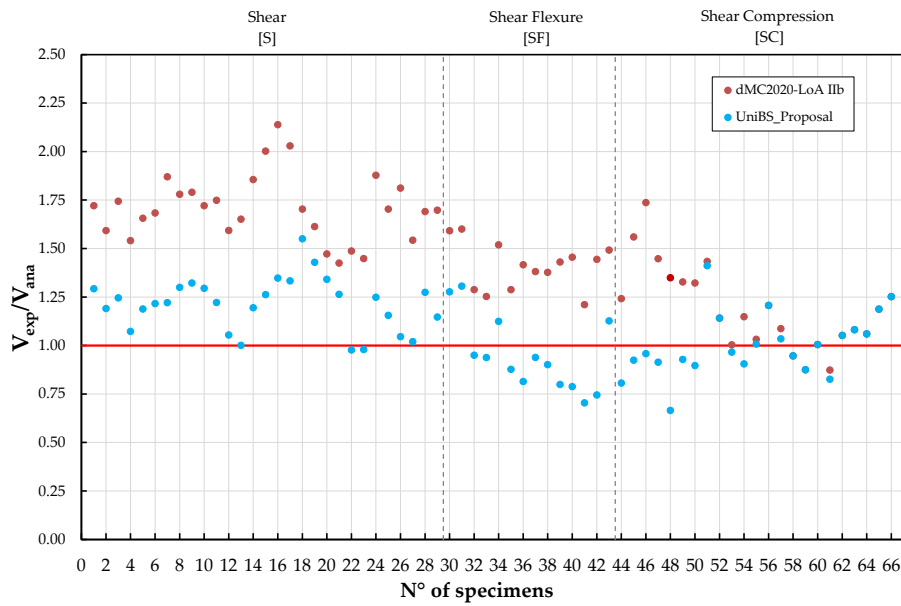


Figure 6-6: Comparison of $V_{u,exp}/V_{u,ana}$ of the dMC2020_LoA IIb and UniBS_Proposal models as a function of the number of database samples sorted according to the failure mode.

6-NEW MODEL FOR PREDICTING THE SHEAR STRENGTH OF EXISTING PRC BEAMS WITH STIRRUPS

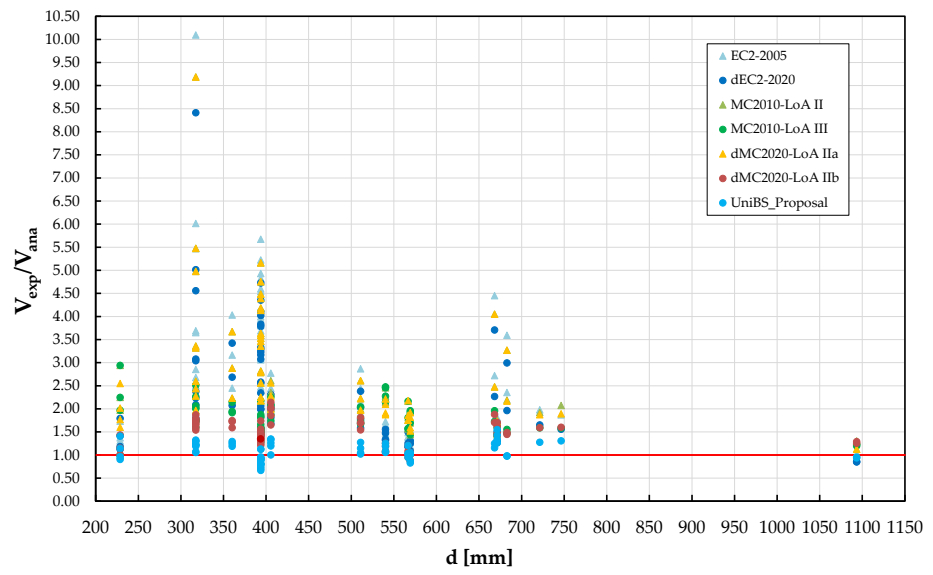


Figure 6-7: $V_{u,exp}/V_{u,ana}$ of all models applied as a function of the effective height [d] of the samples in the database.

6-NEW MODEL FOR PREDICTING THE SHEAR STRENGTH OF EXISTING PRC BEAMS WITH STIRRUPS

Table 6-13: Statistical parameters related to the $V_{u,exp}/V_{u,ana}$ of all the models applied.

N° Samples	EC2 2005	dEC2 2020	MC2010		dMC2020		UniBS Proposal
			LoA_II	LoA_III	LoA_IIa	LoA_IIb	
66							
MEAN [Exp/Ana]	2.79	2.35	2.74	1.79	2.70	1.47	1.08
ST. DEV.	1.550	1.274	1.283	0.348	1.294	0.291	0.194
CoV	55.5	54.2%	46.9%	19.4%	47.9%	19.8%	17.9%
MAPE	54%	48%	57%	42%	57%	30%	16%

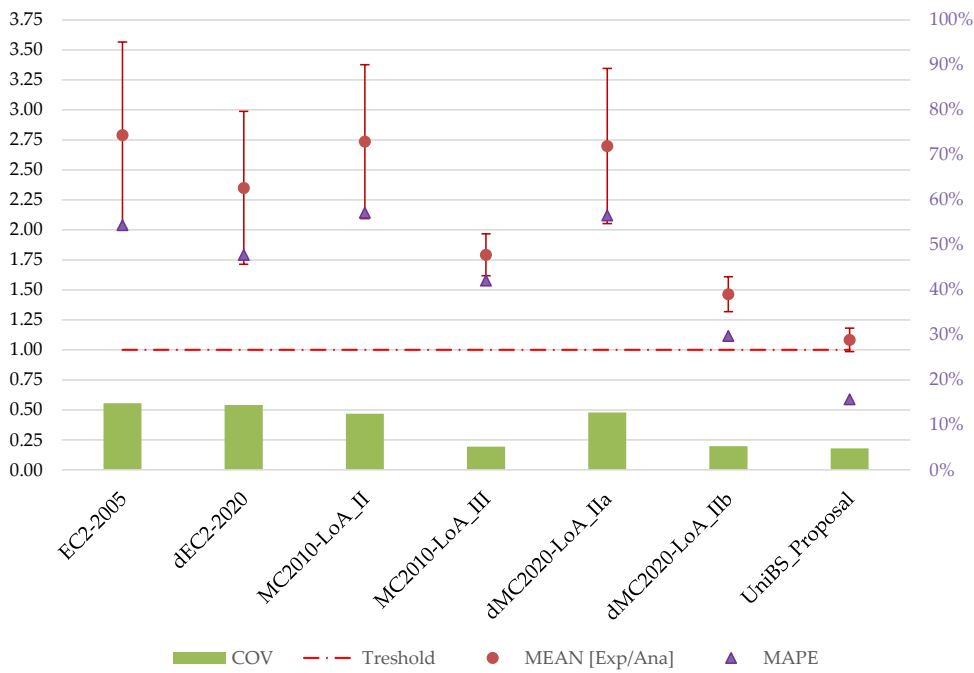


Figure 6-8: Graphical representation of the statistical parameters related to the $V_{u,exp}/V_{u,ana}$ of all the models applied.

6-NEW MODEL FOR PREDICTING THE SHEAR STRENGTH OF EXISTING PRC
BEAMS WITH STIRRUPS

Table 6-14: Statistical parameters related to the $V_{u,exp}/V_{u,ana}$ of the UniBS_Proposal model divided by failure mode.

	UniBS Proposal	Shear [S]	Shear-Flexure [SF]	Shear Compression [SC]
N° Samples	66	29	14	23
MEAN [Exp/Ana]	1.08	1.21	0.95	1.00
ST. DEV.	0.194	0.135	0.184	0.159
CoV	17.9%	11.1%	19.4%	15.9%
MAPE	16%	17%	19%	13%

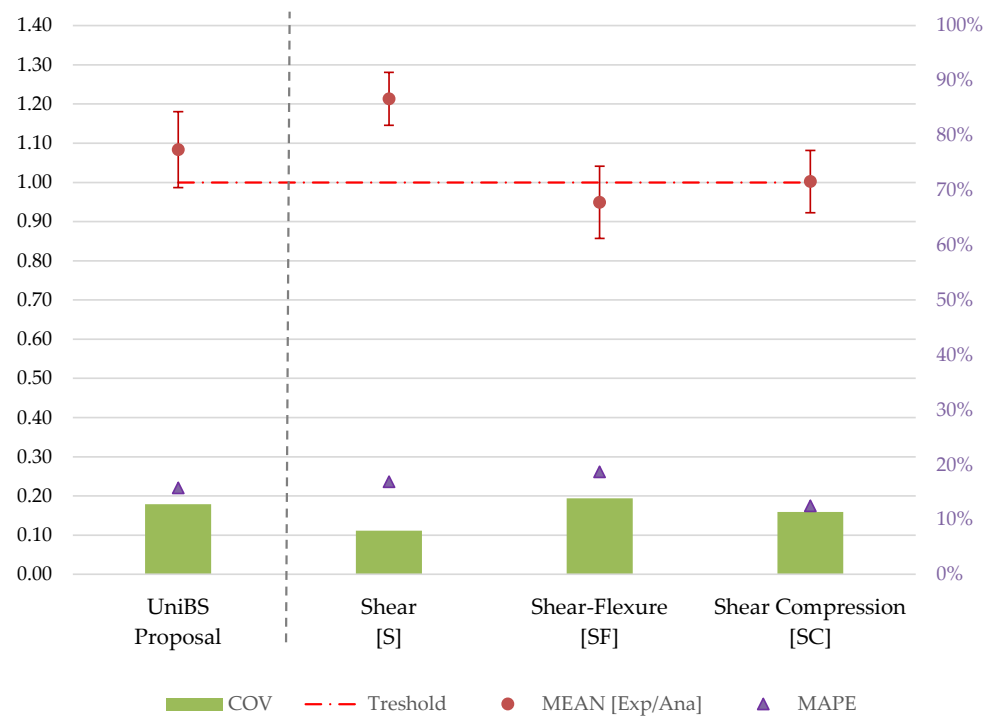


Figure 6-9: Graphic representation of the statistical parameters related to the $V_{u,exp}/V_{u,ana}$ of the UniBS_Proposal model divided by failure mode.

6.7 Concluding Remarks

From an application of the current standards describing the shear resistance of PRC elements with stirrups and the proposal of a new model in this regard the following conclusions can be drawn:

- The models proposed in the current standards (Eurocode 2 and *fib* - Model Code) and current drafts are too conservative as they underestimate the real resistance of the element by 2.5 times on average.
- In the literature, there are few samples relating to prestressed elements with stirrups, tested under shear. Among these, there are even fewer with real dimensions that are not affected by the scale effect. Small specimens with geometric and reinforcement details that are very different from the design reality are often tested in the laboratory. There is therefore a need to increase the database with tests of height greater than 60-80 cm so that they are more representative of actual cases.
- The plasticity base models, which consider only the contribution of the stirrups for the shear resistance of the element, tend to underestimate the response in the prestressed elements because they neglect the resistance contribution of the concrete, especially for those elements with little shear reinforcement. The latter are quite common in existing structures, where the minimum transverse reinforcement is often lower than the current minimum one, if not even missing in some cases (prestressed elements).
- The underestimation of the analytical predictions applied to the database proposed here demonstrates how the contribution of prestress in shear strength is little considered. Thanks to the section geometries usually adopted with important flanges for PRC members, the fact that PRC members are almost always made with High Strength Concrete (HSC) and that prestressing provides additional compression, for PRC members the contribution of the compressed flange is to be considered essential. The UniBS_Proposal model, which considers the contribution of the transfer of tangential stresses in ultimate conditions in the compressed flange, provides rather good reliability with a mean of $V_{u,exp}/V_{u,ana} = 1.08$ and CoV=18%.

7 CONCLUSIONS

With the international race for the census and the evaluation of the conditions of degradation imposed in this historical period for the bridges, due to the poor/absence of maintenance during the last decades, there is the need to investigate more accurately the nature of the main damages. In this way, it is possible to correctly assess the type of structural rehabilitation that directs the available resources avoiding impacting interventions, especially in economic terms, safety, feasibility, etc. The in-situ assessment of the residual prestress and how much the prestress influences the shear resistance in the elements in PRC, are two topics that are still little explored and that require further investigation, as with the knowledge of these two aspects, many questions could be answered on the "health" of a bridge deck. The present research work, therefore, intends to deepen these two aspects, in particular the evaluation of the effectiveness of some diagnostic techniques proposed in the literature for the assessment of in-situ prestressing and the influence of prestress losses on the crack pattern and shear strength of full-scale bridge beams. For these purposes, an experimental program was conducted aimed at the construction of 4 PRC beams with a length of 10 m, an 80 cm high I-section, and minimum web reinforcement. Two beams were constructed with the technology of bonded prestressing strands, which differ from each other by 30% of the assigned level of prestress. The other two identical beams were designed with a system of post-tensioning stands (unbonded) that allows the variation of the level of prestress in a controlled way, covering more long-term loss scenarios. On these elements, three semi-destructive methods for in-situ prestressing evaluation based on tension release were applied: core trepanning, saw-cut at intrados, and blunt pyramidal specimen. In addition, a new method, similar to the parallel saw cuts at intrados, but performed on the web, is proposed and validated. On this method, which proved to be the most reliable among the tested methods, 2D and 3D finite element models were done. Subsequently, a 3-point loading test was performed on each beam, evaluating the evolution of the crack pattern with the Digital Image Correlation (DIC) technique and comparing the results with those obtained from the numerical simulation performed with the VecTor 2 software. During the various phases whether a non-destructive investigation such as dynamic identification could detect damage due to shear injuries and a reduction in prestress loss was evaluated. Finally, since the verification formulas for shear strength proposed by the models of various codes (e.g., Eurocode 2, *fib* - Model Code, CSA, ACI) are very conservative for prestressed elements with stirrups, an analytical formulation based on the draft of the *fib* - Model Code 2020 LoA IIb is proposed. The formulation was validated by applying it to some experimental tests available in the literature.

7.1 Overall conclusions

The main conclusions of this thesis are summarized in the following, divided according to the topic.

- 1) Regarding the concrete stress release tests performed for this work based on stress release, it has shown that:
 - a) For non-destructive methods:
 - With the DIC technique and through dynamic identifications it is not possible to determine a reduction of the prestress level. Furthermore, these two methodologies are difficult to apply on-site.
 - b) For semi-destructive methods:
 - It emerged that, in general, these are very risky tests and for the most part, operator dependent. Accuracy and care in the preparation and execution of the test are essential.
 - The Core Trepanning method and the Saw-Cut method – Intrados provided unreliable results and present some critical issues related to the type of instrumentation and the relative invasiveness of the test.
 - The Blunt Pyramidal specimen provides more reliable results, but with an average overestimation of the residual prestress. This condition is not conservative in the assessment of the bearing capacity of the structure.
 - The Saw-Cut method – Web proves to be a reliability method, more precise and accurate among the semi-destructive methods adopted in this experimental program. In fact, in addition to being easy to perform, with cheap and commercial instruments, applying the configuration of parallel cuts 6 cm apart and 3 cm deep, provides results that come closest to the analytical and numerical forecasts, remaining overall in conservative conditions, as it is underestimated of 10% the actual prestress in the element, with a CoV of 21%.
 - Since in general tests with rather random results, it is in any case necessary to carry out a sufficient number of tests such as to satisfactorily confirm the value obtained. As a preliminary proposal, the minimum number of reliable tests should satisfy a maximum value of CoV equal to 25%. Any single test determining a higher CoV should be excluded. However, it is advisable to compare the results with a numerical/analytical estimate of the expected prestress value, where available.
 - From the finite element models performed for the Saw-Cut method - Web with a configuration of parallel cuts 6 cm apart and 3 cm deep, it emerges that a 2D model, compared to a 3D one, is not reliable enough to identify

the correct force that is formed in the area inside the cuts, as it does not consider the influence of their depth.

- 2) Regarding the experimental tests on the study of the correlation between residual shear strength and prestressing losses, it has shown that:
 - The percentage reduction in the prestressing loss between the two beams (28%) is directly comparable to the percentage reduction in load (20%) which anticipates the exit from the elastic stage and the development of flexural and shear crack patterns. This expected load reduction is a further proof that a long-term reduction of prestressing can generate significant cracking, both in flexure and in shear, even at service loads.
 - Comparing two beams of the same geometry and reinforcement, which differ only in the pre-tensioning bonded strands and post-tensioning unbonded strands system, it is possible to note how the difference in bond of the strands which causes the prestressing reinforcement to work as a tension tie and create an arching effect
 - The dynamic identification method with the FDD technique allows the position of a geometric discontinuity along the development of the beam to be identified, thus tracing the nature of the formation of the cracks as a function of their position, the static scheme and the load along the beam.
 - Comparing the experimental curves with those obtained numerically with VecTor 2, it is possible to note a rather good agreement. Regarding the prediction of the shear crack pattern, the VT2 software was able to accurately capture the formation load of the first shear crack. The numerical prediction also seems to be able to estimate, albeit only qualitatively, the evolution of the crack opening as the load increases.

- 3) Regarding the assessment of the analytical models proposed by the main standards and the proposal of a model that better considers the contribution of the prestressing for the elements in PRC with stirrups, it has shown that:
 - The models proposed in the current standards (Eurocode 2 and *fib* - Model Code) and current drafts are too conservative as they underestimate the real resistance of the element by 2.5 times on average.
 - In the literature, there are few samples relating to prestressed elements with stirrups, tested under shear. Among these, there are even fewer with real dimensions that are not affected by the scale effect. Small specimens with geometric and reinforcement details that are very different from the design reality are often tested in the laboratory.
 - The plasticity base models, which consider only the contribution of the stirrups for the shear resistance of the element, tend to underestimate the response in the prestressed elements because they neglect the resistance contribution of the concrete, especially for those elements with little shear

reinforcement. The UniBS_Proposal model, in addition to the contribution of the aggregate interlock provided by the concrete, also considers the contribution of the transfer of tangential stresses in ultimate conditions in the compressed flange, providing good reliability with a mean of $V_{u,exp}/V_{u,ana} = 1.08$ and $CoV=18\%$ applied to a database of 66 shear tests.

7.2 Recommendation for future research

This work can be a good starting point for future developments and in-depth studies. For this reason, some suggestions and recommendations are given below.

- As far as the stress release tests are concerned, starting from the Saw-Cut method – Web it could be interesting to monitor the evolution of the stress on the concrete surface with strain gauges, starting from the application of the prestress to the element, up to the end of the test execution. In this way, it is possible to know the entire history of prestress and tension release suffered by the monitored surface. Furthermore, following what was also proposed by Abdunur (1982), with the same instrumentation logic and geometric configuration adopted for the SCw_GC_6_3, after having made the cuts, insert two specially made flat jacks into the slots. By activating them, the prestressing of the isolated portion between the two cuts could be restored and have double control of the prestressing level. In addition to this, parallel shear tests could be performed on elements with a simpler geometry, subjected to an axial load to reduce elements of uncertainty as much as possible and have greater control over the results.
- It would be interesting to carry out further experimental tests in order to evaluate how the prestress affects the critical values of the a/d ratio, and how it, therefore, modifies the Kani valley. Furthermore, the finite element models could be further refined to better predict the behaviour of the elements under load.
- For the definition of a more accurate analytical model for prestressed elements with transverse reinforcement, there is the need to increase the database with experimental tests, in the laboratory but also in situ, with dimensions and reinforcement more representative of real cases (e.g., cross-section height above 60-80 cm).

8 ACKNOWLEDGMENTS

First, I would like to thank my supervisor Professor Fausto Minelli who gave me the opportunity to prepare this work. I would like to express to him my deepest gratitude since he followed me for all these years and without his support, I would not have been able to complete this research. The meetings with him, guided by his erudition and patience, were a source of inspiration and motivation to achieve the goals. I am grateful that he provided me with the opportunity to work under his supervision.

I would also like to thank Eng. Luca Facconi for his patience and the help he gave me whenever I asked. In a particular way I would like to thank Eng. Nico Di Stefano and Eng. Enrico Faccin, two colleagues but also friends, who helped me throughout the completion of this work, both physically in the laboratory, technically with the analytical work, but also giving me valuable advice supporting me in difficult choices throughout the whole PhD course. I would also like to thank Professor Nino Spinella and Professor Matteo Colombo for their constructive comments as reviewers.

I would particularly like to thank Giulia Rossini and Matteo Lamberti for support and assistance in all phases of this experimental campaign.

Thanks to ReLUIS for funding this experimental campaign.

Thank Camuna Prefabbricati S.r.l. for the supply of the beams and to Eng. Alessandro Garatti for consultancy during the design phase.

A heartfelt thanks go to Tensacciai S.r.l. - TENSA – DE ECCHER Group, which provided technical support and the necessary material for the post-tensioning operations of the strands, in particular, I want to thank Eng. Giacomo Liberali and Eng. Alessandro Angelo Capaccio. Thanks also to Eng. Andrea Castiglioni di Caronno for the precious advice provided during the design phase of the beams.

Thanks also go to 4 EMME Service S.p.A. and Laboratorio Tecnologico Lombardo S.r.l. (LTL) for the execution of stress release methods on PRC elements.

Thanks to the staff of the Department of Civil Engineering and of the Laboratory for Testing Materials “Pietro Pisa” of the University of Brescia, with emphasis to Mr. Andrea del Barba, Mr. Luca Martinelli and Eng. Ivan Trabucchi.

The help from Eng. Emanuele Gandelli, Dr. Leonard Memko and Dr. Francesco Guarino assistance in carrying out the experiments and data processing is gratefully acknowledged.

8-ACKNOWLEDGMENTS

In addition, I would like to express my deepest appreciation to my friends and colleagues who have helped me both professionally and emotionally: Fabiola Iavarone, Lucia Licciardello, Anthony Paderno, Simone Pelucco, Michele Menghini and Roberto Ventura.

Thanks also go to my parents, Mariarosa and Severino, and my sister Francesca for the continued encouragement.

Finally, I would like to give my heartfelt thanks to my wonderful wife, Michela, for her constant support during these years.

9 REFERENCES

- AASHTO - American Association of State Highway and Transportation Officials. (2010). *AASHTO LRFD Bridge Design Specifications*. 4th Ed. edited by ACI - American Concrete Institute. Washington, DC.
- Abdunur, C. (1982). "DIRECT MEASUREMENT OF STRESSES IN CONCRETE STRUCTURES." Pp. 39–44 in *Reports of the Working Commissions (International Association for Bridge and Structural Engineering)*. Vol. 39.
- ACI-Committee-318. (2011). *Building Code Requirements of Structural Concrete and Commentary*.
- Ahmad, S., S. Badshah, I. Ul Haq, S. A. Malik, M. Amjad, and M. N. Tamin. (2019). "Numerical Investigation of 1 × 7 Steel Wire Strand under Fretting Fatigue Condition." *Materials* 2019, Vol. 12, Page 3463 12(21):3463.
- AICAP. (2016). *Raccomandazioni Aicap "REALIZZAZIONE E GESTIONE DEL CALCESTRUZZO STRUTTURALE PRESOLLECITATO CON ARMATURA POST-TESA."*
- Alshegeir, A. and J. A. Ramirez. (1992). "Strut-Tie Approach in Pretensioned Beams." *Structural Journal* 89(3):296–304.
- Amiot, F., M. Bornert, P. Doumalin, J. C. Dupré, M. Fazzini, J. J. Orteu, C. Poilâne, L. Robert, R. Rotinat, E. Toussaint, B. Wattrisse, and J. S. Wienin. (2013). "Assessment of Digital Image Correlation Measurement Accuracy in the Ultimate Error Regime: Main Results of a Collaborative Benchmark." *Strain* 49(6):483–96.
- ANAS S.p.A. (2020). "Ispezione Approfondita Di Impalcati Da Ponte Con Travi in c.a.p. a Cavi Post-Tesi." *Centro Sperimentale Stradale Di Cesano* (April).
- ASCE. (2017). *Infrastructure Report Card: A Comprehensive Assessment of America's Infrastructure*.
- ASTM E837-13a. (2013). "Standard Test Method for Determining Residual Stresses by the Hole-Drilling Strain-Gage Method." *Standard Test Method E837-13a* 1–16.
- Avendaño, A. R. and O. Bayrak. (2008). *Shear Strength and Behavior of Prestressed Concrete Beams*. Austin.

9-REFERENCES

- Ayensa, A., E. Oller, B. Beltrán, E. Ibarz, A. Marí, and L. Gracia. (2019). "Influence of the Flanges Width and Thickness on the Shear Strength of Reinforced Concrete Beams with T-Shaped Cross Section." *Engineering Structures* 188:506–18.
- Azizinamini, A., B. J. Keeler, J. Rohde, and A. B. Mehrabi. (1996). "Application of a New Nondestructive Evaluation Technique to a 25-Year-Old Prestressed Concrete Girder." *PCI Journal* 41(3):82–95.
- Bagge, N., J. Nilimaa, and L. Elfgren. (2017). "In-Situ Methods to Determine Residual Prestress Forces in Concrete Bridges." *Engineering Structures* 135:41–52.
- Bagge, N., J. Nilimaa, A. Puurula, B. Täljsten, T. Blanksvärd, G. Sas, L. Elfgren, and A. Carolin. (2017). "Full-Scale Tests to Failure Compared to Assessments - Three Concrete Bridges." Pp. 1917–24 in *High Tech Concrete: Where Technology and Engineering Meet - Proceedings of the 2017 fib Symposium*. Springer International Publishing.
- Bairan, J. M. and A. R. Mari. (2006). "Coupled Model for the Non-Linear Analysis of Anisotropic Sections Subjected to General 3D Loading. Part 1: Theoretical Formulation." *Computers & Structures* 84(31–32):2254–63.
- Bairan, J. M. and A. R. Mari. (2007). "Multiaxial-Coupled Analysis of RC Cross-Sections Subjected to Combined Forces." *Engineering Structures* 29(8):1722–38.
- Baran, E., C. K. Shield, and C. E. French. (2005). "A Comparison of Methods for Experimentally Determining Prestress Losses in Pretensioned Prestressed Concrete Girders." *Special Publication* 231:161–80.
- Barranger, Y., P. Doumalin, J. C. Dupré, and A. Germaneau. (2010). "Digital Image Correlation Accuracy: Influence of Kind of Speckle and Recording Setup." *EPJ Web of Conferences* 6:31002.
- Bencivenga, P., G. Buratti, A. Cosentino, G. de Matteis, F. Morelli, W. Salvatore, and M. Zizi. (2022). "Evolution of Design Traffic Loads for Italian Road Bridges." *LECTURE NOTES IN CIVIL ENGINEERING* 200:1351–58.
- Bennett, E. W. and B. M. A. Balasooriya. (1971). "Shear Strength of Prestressed Beams With Thin Webs Failing in Inclined Compression." *Journal Proceedings* 68(3):204–12.
- Bentz, E. (2000). "Sectional Analysis of Reinforced Concrete Members."
- Bentz, E. C. and M. P. Collins. (2006). "Development of the 2004 Canadian Standards Association (CSA) A23.3 Shear Provisions for Reinforced Concrete." *Canadian Journal of Civil Engineering* 33(5):521–34.

- Bentz, E., F. Vecchio, and M. Collins. (2006). "Simplified Modified Compression Field Theory for Calculating Shear Strength of Reinforced Concrete Elements." *ACI Journal* .
- Bonopera, M. and K. C. Chang. (2021). "Novel Method for Identifying Residual Prestress Force in Simply Supported Concrete Girder-Bridges." *Advances in Structural Engineering* 24(14):3238–51.
- Bonopera, M., K. C. Chang, C. C. Chen, Y. C. Sung, and N. Tullini. (2019). "Experimental Study on the Fundamental Frequency of Prestressed Concrete Bridge Beams with Parabolic Unbonded Tendons." *Journal of Sound and Vibration* 455:150–60.
- Bonopera, M., K. C. Chang, and Z. K. Lee. (2020). "State-of-the-Art Review on Determining Prestress Losses in Prestressed Concrete Girders." *Applied Sciences (Switzerland)* 10(20):1–14.
- Breccolotti, M. (2018). "On the Evaluation of Prestress Loss in PRC Beams by Means of Dynamic Techniques." *International Journal of Concrete Structures and Materials* 12(1):1–15.
- Breccolotti, M. and A. L. Materazzi. (2015). "Prestress Losses and Camber Growth in Wing-Shaped Structural Members." *PCI Journal* 60(1):98–117.
- Chang, C. W., P. H. Chen, and H. S. Lien. (2009). "Evaluation of Residual Stress in Pre-Stressed Concrete Material by Digital Image Processing Photoelastic Coating and Hole Drilling Method." *Measurement: Journal of the International Measurement Confederation* 42(4):552–58.
- Choi, K. K., H. G. Park, and J. K. Wight. (2007). "Unified Shear Strength Model for Reinforced Concrete—Part I: Development." *Structural Journal* 104(2):142–52.
- Chopra, A. K. (2017). *Dynamics of Structures. Theory and Applications to Earthquake Engineering*. Vol. 2017. edited by Pearson.
- Choulli, Y., A. R. Mari, and A. Cladera. (2008). "Shear Behaviour of Full-Scale Prestressed i-Beams Made with Self Compacting Concrete." *Materials and Structures/Materiaux et Constructions* 41(1):131–41.
- Civjan, S. A., J. O. Jirsa, R. L. Carrasquillo, and D. W. Fowler. (1998). "Instrument to Evaluate Remaining Prestress in Damaged Prestressed Concrete Bridge Girders." *PCI Journal* 43(2):62–71.
- Collins, M. P. (1978). "Towards a Rational Theory for RC Members in Shear." *Journal of the Structural Division* 104(4):649–66.

9-REFERENCES

- Collins, M. P., E. C. Bentz, and E. G. Sherwood. (2008). "Where Is Shear Reinforcement Required? Review of Research Results and Design Procedures." *Structural Journal* 105(5):590–600.
- Collins, M. P., E. C. Bentz, E. G. Sherwood, and L. Xie. (2015). "An Adequate Theory for the Shear Strength of Reinforced Concrete Structures." <https://doi.org/10.1680/Macr.2008.60.9.635> 60(9):635–50.
- Collins, M. P. and D. Mitchell. (1980). "SHEAR AND TORSION DESIGN OF PRESTRESSED AND NON-PRESTRESSED CONCRETE BEAMS." *Journal - Prestressed Concrete Institute* 25(5):32–100.
- CSA A23.3-14. (2014). *Canadian Standard Association A23.3-14 Design of Concrete Structures*.
- Dall'Asta, A. and L. Dezi. (1996). "Discussion of Prestress Force Effect on Vibration Frequency of Concrete Bridges by M. Saiidi, B. Douglas, and S. Feng." *Journal of Structural Engineering* 122(4):458–458.
- DIN 4227:1953. (1953). *Spannbeton - Richtlinien Für Bemessung Und Ausführung*.
- Dlubal. (2017). "Considering Second-Order Theory in Dynamic Analysis | Dlubal Software." Retrieved March 24, 2023 (<https://www.dlubal.com/en/support-and-learning/support/knowledge-base/001394>).
- Draft EC2 - FprEN_1992-1-1. (2021). *Draft Eurocode-2. Design of Concrete Structures- Part1-1: General Rules and Rules for Buildings*.
- Draft MC2020. (2023). *Fib Model Code for Concrete Structures - Draft 2020 - Ch. 30.1 - Version TS-V3 12-05-2023*.
- Durrani, A. J. and I. N. Robertson. (1987). "SHEAR STRENGTH OF PRESTRESSED CONCRETE T BEAMS WITH WELDED WIRE FABRIC AS SHEAR REINFORCEMENT." *PCI Journal* 32(2):46–61.
- EC2. (2002). *Eurocode-2. Design of Concrete Structures- Part1-1: General Rules and Rules for Buildings*. Brussels.
- EC2. (2004). *Eurocode-2. Design of Concrete Structures- Part1-1: General Rules and Rules for Buildings*. Brussels.
- EC2 - EN 1992-1-1. (2005). *Eurocode-2. Design of Concrete Structures- Part1-1: General Rules and Rules for Buildings*.
- Eder, R. W., R. A. Miller, T. M. Baseheart, and J. A. Swanson. (2005). "Testing of Two 50-Year-Old Precast Post-Tensioned Concrete Bridge Girders." *PCI Journal* 50(3):90–95.

- Elzanaty, A. H., A. H. Nilson, and F. O. Slate. (1986). "Shear Capacity of Prestressed Concrete Beams Using High-Strength Concrete." *Journal Proceedings* 83(3):359–68.
- Fernández Ruiz, M. and A. Muttoni. (2008). "Shear Strength of Thin-Webbed Post-Tensioned Beams." *Structural Journal* 105(3):308–17.
- Ferreira, D., J. Bairán, and A. Marí. (2013). "Numerical Simulation of Shear-Strengthened RC Beams." *Engineering Structures* 46:359–74.
- fib - Fédération Internationale du Béton. (2013). *Fib Model Code for Concrete Structures 2010- Vol. 1*.
- Frizzarin, M., F. Faleschini, M. A. Zanini, P. Franchetti, and C. Pellegrino. (2019). "Experimental Detection of the Residual Prestressing Level in Pre-Tensioned and Post-Tensioned Reinforced Concrete Beams by Means of Nondestructive Tests." *Experimental Detection of the Residual Prestressing Level in Pre-Tensioned and Post-Tensioned Reinforced Concrete Beams by Means of Nondestructive Tests* 130–37.
- Frosch, R. J. and T. S. Wolf. (2003). *Simplified Shear Design of Prestressed Concrete Members*.
- Gabanelli, M. (2019). "Viadotti: 1.425 Sono Senza Un Proprietario e Nessuno Fa La Manutenzione ." *Corriere Della Sera*. Retrieved March 13, 2023 (<https://www.corriere.it/dataroom-milena-gabanelli/viadotti-1425-sono-senza-proprietario-nessuno-fa-la-manutenzione-ponti-crolli-ecco-mappa/ae3102d2-263f-11e9-9b5e-1a58eb1d569a-va.shtml>).
- Garber, D. B., J. M. Gallardo, D. J. Deschenes, and O. Bayrak. (2015). "Experimental Investigation of Prestress Losses in Full-Scale Bridge Girders." *ACI Structural Journal* 112(5):553–64.
- Garber, D. B., J. M. Gallardo, D. J. Deschenes, and O. Bayrak. (2016). "Nontraditional Shear Failures in Bulb-T Prestressed Concrete Bridge Girders." *Journal of Bridge Engineering* 21(7):04016030.
- Gehrlein, S. F. and O. Fischer. (2019). "Full-scale Shear Capacity Testing of an Existing Prestressed Concrete Bridge." *Civil Engineering Design* 1(2):64–73.
- Gehrlein, S. F., J. Landler, T. Oberndorfer, and O. Fischer. (2018). "In-Situ Shear Tests on a 64-Year-Old Road Bridge." in *fib Congress 2018*. Melbourne.
- Guo, E. H., F. Pecht, L. Ricalde, D. Barbagallo, and X. Li. (2008). "Data Analysis on Residual Stresses Measured in Concrete Beams." *Proc. of the 9th International Conference on Concrete Pavements*.

9-REFERENCES

- Halsey, J. T. and R. Miller. (1996). "Destructive Testing of Two Forty-Year-Old Prestressed Concrete Bridge Beams." *PCI Journal* 41(5):84–93.
- Hanson, J. M. and C. L. Hulsbos. (1964). "Ultimate Shear Tests Of Prestressed Concrete I-Beams Under Concentrated And Uniform Loadings." *PCI Journal* 9(3):15–28.
- Hanson, J. M. and C. L. Hulsbos. (1965). "OVERLOAD BEHAVIOR OF PRETENSIONED PRESTRESSED CONCRETE I- BEAMS WITH WEB REINFORCEMENT." *Highway Research Record* (76).
- Ho, D. D., J. T. Kim, N. Stubbs, and W. S. Park. (2016). "Prestress-Force Estimation in PSC Girder Using Modal Parameters and System Identification." [Http://Dx.Doi.Org/10.1260/1369-4332.15.6.997](http://dx.doi.org/10.1260/1369-4332.15.6.997) 15(6):997–1012.
- Hop, T. (1991). "The Effect of Degree of Prestressing and Age of Concrete Beams on Frequency and Damping of Their Free Vibration." *Materials and Structures* 1991 24:3 24(3):210–20.
- Huber, P., T. Huber, and J. Kollegger. (2017). "Assessment of the Shear Strength of Existing Post-Tensioned Bridges." Pp. 2120–25 in *IABSE Conference, Vancouver 2017: Engineering the Future - Report*. International Association for Bridge and Structural Engineering (IABSE).
- Huber, P., T. Huber, and J. Kollegger. (2018). "Influence of Loading Conditions on the Shear Capacity of Post-Tensioned Beams with Low Shear Reinforcement Ratios." *Engineering Structures* 170:91–102.
- Huber, P., T. Huber, and J. Kollegger. (2020). "Experimental and Theoretical Study on the Shear Behavior of Single- and Multi-Span T- and I-Shaped Post-Tensioned Beams." *Structural Concrete* 21(1):393–408.
- Huber, P. and J. Kollegger. (2015). "Shear Strength of Post-Tensioned Concrete Girders with Minimum Shear Reinforcement." in *CCC 2015 - 11th Central European Congress on Concrete Engineering - October 2015*.
- Huber, P., B. Kromoser, and T. Huber. (2016). "Berechnungsansatz Zur Ermittlung Der Schubtragfähigkeit Bestehender Spannbetonbrückenträger Mit Geringem Querkraftbewehrungsgrad - Approach for the Determination of the Shear Strength of Existing Post-Tensioned Bridge Girders with a Minimum Amount of Transverse Reinforcement." *Bauingenieur* 91(6):227–37.
- Huber, P., A. Schweighofer, and J. Kollegger. (2013). "Shear Strength of over 50 Years Old Posttensioned Concrete Bridge Girders." in *May 2013_fib Symposium*. Tel Aviv.

- Huber, P., M. Vill, A. Schweighofer, and J. Kollegger. (2018). "Full-Scale Shear Tests on Post-Tensioned Bridge Girders of Existing Bridges." *Structural Concrete* 19(1):5–15.
- ISO 15630-1. (2010). *Steel for the Reinforcement and Prestressing of Concrete-Test Methods-Part 1: Reinforcing Bars, Wire Rod and Wire*.
- James, M. L., G. M. Smith, and L. D. Lutes. (1964). "Dynamic Properties of Reinforced and Prestressed Concrete Structural Components." *Journal Proceedings* 61(11):1359–82.
- Jang, J. B., H. P. Lee, K. M. Hwang, and Y. C. Song. (2011). "Prediction of Prestress Force on Grouted Tendon by Experimental Modal Analysis." *Conference Proceedings of the Society for Experimental Mechanics Series* 4:33–39.
- Kani, G. N. J. (1966). "Basic Facts Concerning Shear Failure." *Journal Proceedings* 63(6):675–92.
- Kani, G. N. J. (1967). "How Safe Are Our Large Reinforced Beams?" *Journal Proceedings* 64(3):128–41.
- Kaufman, M. K. and J. A. Ramirez. (1988). "Re-Evaluation of the Ultimate Shear Behavior of High-Strength Concrete Prestressed I-Beams." *Structural Journal* 85(3):295–303.
- Kerr, A. D. (1976). "On the Dynamic Response of a Prestressed Beam." *Journal of Sound and Vibration* 49(4):569–73.
- Kesavan, K., K. Ravisankar, S. Parivallal, and P. Sreeshylam. (2005). "Technique to Assess the Residual Prestress in Prestressed Concrete Members." Pp. 33–38 in *Experimental Techniques*. Vol. 29. John Wiley & Sons, Ltd.
- Khaled, T. (1999). *Residual Stress Measurement by the Hole Drilling Method*.
- Kim, J. T., J. H. Park, D. S. Hong, and W. S. Park. (2010). "Hybrid Health Monitoring of Prestressed Concrete Girder Bridges by Sequential Vibration-Impedance Approaches." *Engineering Structures* 32(1):115–28.
- Kim, J.-T., Y.-S. Ryu, and C.-B. Yun. (2003). "Vibration-Based Method to Detect Prestress Loss in Beam-Type Bridges." <https://doi.org/10.1117/12.484638> 5057:559–68.
- Koppel, S. and T. Vogel. (1997). "Feldversuch Steilerbachbrücke." *IBK Bericht* 231:66.
- Koteš, P. and J. Vičan. (2012). "Reliability Levels for Existing Bridges Evaluation According to Eurocodes." *Procedia Engineering* 40:211–16.

9-REFERENCES

- Kraľovanec, J., M. Moravčík, P. Bujňáková, and J. Jošt. (2021). "Indirect Determination of Residual Prestressing Force in Post-Tensioned Concrete Beam." *Materials* 14(6):1338.
- Kralovanec, J. and J. Prokop. (2021). "Indirect Methods for Determining the State of Prestressing." Pp. 1236–43 in *Transportation Research Procedia*. Vol. 55. Elsevier.
- Kukay, B., P. J. Barr, M. W. Halling, and K. Womack. (2010). "Determination of the Residual Prestress Force of In-Service Girders Using Non-Destructive Testing." *Structures Congress 2010* 709–16.
- Labia, Y., M. S. Saiidi, and B. Douglas. (1997). "FULL-SCALE TESTING AND ANALYSIS OF 20-YEAR-OLD PRETENSIONED CONCRETE BOX GIRDERS." *ACI Structural Journal* 94(5).
- Labib, E. L., H. B. Dhonde, T. T. C. Hsu, and Y. L. Mo. (2014). "Shear Design of High Strength Concrete Prestressed Girders." *Frontiers of Structural and Civil Engineering* 8(4):373–87.
- Laskar, A., T. T. C. Hsu, and Y. L. Mo. (2010). "Shear Strengths of Prestressed Concrete Beams Part 1: Experiments and Shear Design Equations." *Structural Journal* 107(3):330–39.
- Latte Bovio, F., F. Chichi, S. Celati, M. Ciano, S. Ferrari, M. Gammino, D. Gaudio, M. Guelpa, M. la Porta, D. Maestrini, G. Marconi, I. Mazzatura, D. Morandi, F. Morelli, M. Mori, I. Panzera, P. Papeschi, A. Piscini, and W. Salvatore. (2022). "Assessment of Inspection Procedures for Pre-Stressed Concrete Bridges with Post-Tensioned Cables." *Lecture Notes in Civil Engineering* 200 LNCE:1090–99.
- Law, S. S. and Z. R. Lu. (2005). "Time Domain Responses of a Prestressed Beam and Prestress Identification." *Journal of Sound and Vibration* 288(4–5):1011–25.
- Law, S. S., S. Q. Wu, and Z. Y. Shi. (2008). "Moving Load and Prestress Identification Using Wavelet-Based Method." *Journal of Applied Mechanics, Transactions ASME* 75(2):0210141–47.
- Lee, S. C., J. Y. Cho, and B. H. Oh. (2010). "Shear Behavior of Large-Scale Post-Tensioned Girders with Small Shear Span-Depth Ratio." *Structural Journal* 107(2):137–45.
- Llanos, G., B. E. Ross, and H. R. Hamilton III. (2009). *Shear Performance of Existing Prestressed Concrete Bridge Girders*.
- Lofrano, E., A. Paolone, S. Perno, P. Zazzo, and A. Santori. (2018). "Comparative Studies on the 'Stress Relaxation' Methods for p.s.c. - Indagini Comparative Sui Metodi Di 'Rilascio Di Tensione' per Il c.a.p." in *Italian Concrete Days - AICAP 2018*. Rome.

- Lu, Z. R. and S. S. Law. (2006). "Identification of Prestress Force from Measured Structural Responses." *Mechanical Systems and Signal Processing* 20(8):2186–99.
- Lupoi, A. and G. de Benedetti. (2021a). "Efficiency and Effectiveness Evaluation of Post-Tensioned Prestressed Girders by Cls Relaxation Tests - Valutazione Sull'efficienza e Sull'efficacia Delle Travi Da Ponte in c.a.p. a Cavi Post-Tesi Mediante l'esecuzione Di Prove Di Rilascio."
- Lupoi, A. and G. de Benedetti. (2021b). *Ispezioni Speciali Di Travi in c.a.p. Con Sistemi Post Tesi: Campagna Sperimentale Ed Analisi Critica Degli Esiti per Valutare l'efficacia e l'applicabilità Delle Principali Tecniche Di Indagine*. Riservato.
- Ma, Z., M. K. Tadros, and M. Baishya. (2000). "Shear Behavior of Pretensioned High-Strength Concrete Bridge I-Girders." *Structural Journal* 97(1):185–92.
- Maas, S., A. Zürbes, D. Waldmann, M. Waltering, V. Bungard, and G. de Roeck. (2012). "Damage Assessment of Concrete Structures through Dynamic Testing Methods. Part 1 - Laboratory Test." *Journal of Engineering Structures* 34:351–62.
- Marí, A., J. M. Bairán, A. Cladera, and E. Oller. (2016). "Shear Design and Assessment of Reinforced and Prestressed Concrete Beams Based on a Mechanical Model." *Journal of Structural Engineering* 142(10):04016064.
- Marks, D. G. and D. A. Lange. (2009). "Development of Residual Stress Measurement for Concrete Pavements through Cantilevered Beam Testing." University of Illinois at Urbana-Champaign.
- Martinello, S. (2021). "Tecniche Di Misura Dello Stato Tensionale." *LeStrade*, April, 92–98.
- MIMS - Ministero delle Infrastrutture e della Mobilità Sostenibili. (2022). *Linee Guida per La Classificazione e Gestione Del Rischio, La Valutazione Della Sicurezza Ed Il Monitoraggio Dei Ponti Esistenti*. Vol. 96/2021.
- Minelli, F. (2005). "Plain and Fiber Reinforced Concrete Beams under Shear Loading: Structural Behavior and Design Aspects." PhD Thesis, University of Brescia.
- Mitchell, D. and M. P. Collins. (1974). "Diagonal Compression Field Theory-A Rational Model For Structural Concrete in Pure Torsion." *Journal Proceedings* 71(8):396–408.
- Miyamoto, A., K. Tei, H. Nakamura, and J. W. Bull. (2000). "Behavior of Prestressed Beam Strengthened with External Tendons." *Journal of Structural Engineering* 126(9):1033–44.

9-REFERENCES

- Mohr, S., J. M. Bairán, and A. R. Marí. (2010). "A Frame Element Model for the Analysis of Reinforced Concrete Structures under Shear and Bending." *Engineering Structures* 32(12):3936–54.
- Morsch, E. (1909). *Concrete-Steel Construction: Der Eisenbetonbau*. edited by Kessinger Publishing.
- Muttoni, A. and M. F. Ruiz. (2008). "Shear Strength of Members without Transverse Reinforcement as Function of Critical Shear Crack Width." *ACI Structural Journal* 105(2):163–72.
- Nagrodzka-Godycka, K. and M. Wiśniowska. (2017). "Verification of Selected Calculation Methods Regarding Shear Strength in Reinforced and Prestressed Concrete Beams." Pp. 136–43 in *Procedia Engineering*. Vol. 193. Elsevier Ltd.
- Navarro Gregori, J., P. Miguel Sosa, M. A. Fernández Prada, and F. C. Filippou. (2007). "A 3D Numerical Model for Reinforced and Prestressed Concrete Elements Subjected to Combined Axial, Bending, Shear and Torsion Loading." *Engineering Structures* 29(12):3404–19.
- Noh, M. H., T. R. Seong, J. Lee, and K. S. Park. (2015). "Experimental Investigation of Dynamic Behavior of Prestressed Girders with Internal Tendons." *International Journal of Steel Structures* 2015 15:2 15(2):401–14.
- NTC. (2018). *Aggiornamento Delle "Norme Tecniche per Le Costruzioni."* Italy.
- Oh, B. H. and K. S. Kim. (2004). "Shear Behavior of Full-Scale Post-Tensioned Prestressed Concrete Bridge Girders." *Structural Journal* 101(2):176–82.
- Osborn, G. P., P. J. Barr, D. A. Petty, M. W. Halling, and T. R. Brackus. (2012). "Residual Prestress Forces and Shear Capacity of Salvaged Prestressed Concrete Bridge Girders." *Journal of Bridge Engineering* 17(2):302–9.
- Owens, A. (1988). "APPLICATION OF RESIDUAL STRESS TECHNIQUES IN THE DETERMINATION OF IN-SITU LOAD IN REINFORCEMENT BARS." *Experimental Techniques* 12(5):23–27.
- Owens, A. (1993). "In-situ Stress Determination Used in Structural Assessment of Concrete Structures." *Strain* 29(4):115–24.
- Parivallal, S., K. Ravisankar, K. Nagamani, and K. Kesavan. (2011). "Core-Drilling Technique for in-Situ Stress Evaluation in Concrete Structures." *Experimental Techniques* 35(4):29–34.
- Park, H. G., S. Kang, and K. K. Choi. (2013). "Analytical Model for Shear Strength of Ordinary and Prestressed Concrete Beams." *Engineering Structures* 46:94–103.
- Park, R. and T. Paulay. (1975). *Reinforced Concrete Structures*. John Wiley & Sons, Inc.

- Pecht, F., E. Guo, and J. Gagnon. (2008). "Core-Ring Strain Gage Procedure for Measuring Residual Stress in a Concrete Beam." *Proc. of the 6th International Conference on Road and Airfield Pavement Technology*.
- Peng, F. and W. Xue. (2021). "Experimental Investigation on Shear Behavior of FRP Post-Tensioned Concrete Beams without Stirrups." *Engineering Structures* 244:112835.
- Perumalla, M. and A. Laskar. (2020). "Evaluation of Design Methods for Prestressed Concrete Members with Stirrups Using a New Traditional Shear Database." *Structures* 23:621–34.
- Pessiki, S., M. Kaczinski, and H. H. Wescott. (1996). "Evaluation of Effective Prestress Force in 28-Year-Old Prestressed Concrete Bridge Beams." *PCI Journal* 41(6):78–89.
- Pietrangeli, M. P. (2011). "Evoluzione Della Progettazione Dei Ponti e Degli Interventi Sull'esistente." in *Giornate AICAP, 26° convegno nazionale*.
- Prisco, M., M. Colombo, P. Martinelli, and D. Coronelli. (2018). "The Technical Causes of the Collapse of Annone Overpass on SS.36." *Presented at the Italian Concrete Days 2018*.
- Proverbio, E., G. Ricciardi, V. Venturi, M. Venturi, G. Laganà, A. Recupero, G. Epasto, and G. Campanella. (2008). "NUOVE TECNOLOGIE PER LA VALUTAZIONE DEL DEGRADO E IL CONTROLLO DI STRUTTURE IN CALCESTRUZZO ARMATO PRECOMPRESSO." *Strade & Autostrade* (3):108–13.
- Qi, J. N., J. Q. Wang, Z. J. Ma, and T. Tong. (2016). "Shear Behavior of Externally Prestressed Concrete Beams with Draped Tendons." *ACI Structural Journal* 113(4):677–88.
- Ramadan, O. M., A. H. Abdel-Kareem, I. A. El-Azab, and H. R. Abousafa. (2022). "Flange Contribution to the Shear Strength of RC T-Beams with Flange in Compression." *Buildings* 2022, Vol. 12, Page 803 12(6):803.
- Rangan, V. B. (1991). "Web Crushing Strength of Reinforced and Prestressed Concrete Beams." *Structural Journal* 88(1):12–16.
- Recupero, A., A. D'Aveni, and A. Gherzi. (2003). "N-M-V Interaction Domains for Box and I-Shaped Reinforced Concrete Members." *Structural Journal* 100(1):113–19.
- Reineck, K. H. (1991). "Ultimate Shear Force of Structural Concrete Members Without Transverse Reinforcement Derived From a Mechanical Model (SP-885)." *Structural Journal* 88(5):592–602.

9-REFERENCES

- Reineck, K.-H., E. Bentz, B. Fitik, D. Kuchma, and O. Bayrak. (2014). "ACI-DAfStb Databases for Shear Tests on Slender Reinforced Concrete Beams with Stirrups." *ACI Structural Journal* 111.
- Reineck, K.-H. and D. Dunkelberg. (2015). "ACI-DAfStb Databases 2015 with Shear Tests for Evaluating Relationships for the Shear Design of Structural Concrete Members without and with Stirrups."
- Robertson, I. N. (2005). "Prediction of Vertical Deflections for a Long-Span Prestressed Concrete Bridge Structure." *Engineering Structures* 27(12):1820–27.
- Romano, F. and C. Mazzotti. (2022). "Prestress Release Tests on Prestressed Reinforced Concrete Elements - Prove Di Rilascio Tensionale Su Elementi in Calcestruzzo Armato." Pp. 541–47 in *IL CALCESTRUZZO NELLA TRANSIZIONE ECOLOGICA - Italian Concrete Conference 2022*. Naples.
- Ross, B. E., H. R. (Trey) Hamilton, and G. R. Consolazio. (2015). "Experimental Study of End Region Detailing and Shear Behavior of Concrete I-Girders." *Journal of Bridge Engineering* 20(6):04014087.
- Ruan, X. and Y. Zhang. (2015). "In-Situ Stress Identification of Bridge Concrete Components Using Core-Drilling Method." *Structure and Infrastructure Engineering* 11(2):210–22.
- Rupf, M., M. Fernández Ruiz, and A. Muttoni. (2013). "Post-Tensioned Girders with Low Amounts of Shear Reinforcement: Shear Strength and Influence of Flanges." *Engineering Structures* 56:357–71.
- Saiidi, M., B. Douglas, and S. Feng. (1994). "Prestress Force Effect on Vibration Frequency of Concrete Bridges." *Journal of Structural Engineering* 120(7):2233–41.
- Sánchez-Beitia, S. and L. Schueremans. (2009). "The Hole Drilling Technique for on Site Deduction of the Stresses States in Stone Masonry by Using Eight Strain Gages." *Construction and Building Materials* 23(5):2041–46.
- Sarsam, K., R. Khaleel, and N. Mohammed. (2018). "Influence of Flange on the Shear Capacity of Reinforced Concrete Beams." *MATEC Web of Conferences* 162:04003.
- Sato, Y., T. Ueda, and Y. Kakuta. (1996). "SHEAR STRENGTH OF REINFORCED AND PRESTRESSED CONCRETE BEAMS WITH SHEAR REINFORCEMENT." *Doboku Gakkai Ronbunshu* 1996(544):43–52.
- Shi, L., H. He, and W. Yan. (2014). "Prestress Force Identification for Externally Prestressed Concrete Beam Based on Frequency Equation and Measured Frequencies." *Mathematical Problems in Engineering* 2014.

- Shin, H.-C., V. Chiarito, and F. Amini. (2011). "Measurements of Strain Relief in Concrete Cubes with Slot Cutting."
- SIA 262:2013. (2013). *Costruzioni Di Calcestruzzo*. Zurich.
- Spinella, N., P. Colajanni, A. Recupero, and F. Tondolo. (2019). "Ultimate Shear of RC Beams with Corroded Stirrups and Strengthened with FRP." *Buildings* 2019, Vol. 9, Page 34 9(2):34.
- Sudhira De Silva, 睦好 宏史, Eakarath Wichukreangkrai. (2006). "Experimental Study on Shear Cracking Behavior in I-Shaped Partially Prestressed Concrete Beams." *コンクリート工学年次論文集 = Proceedings of the Japan Concrete Institute / 日本コンクリート工学協会 編* 28(2):817-22.
- Sudhira De Silva, 睦好 宏史, 浅本 晋吾. (2007). "Shear Cracking Behavior of High-Strength Prestressed Reinforced Concrete Beams." *コンクリート工学年次論文集 = Proceedings of the Japan Concrete Institute / 日本コンクリート工学協会 編* 29(3):679-84.
- Torsion, A.-A. C. 445 on S. and. (1998). "Recent Approaches to Shear Design of Structural Concrete." *Journal of Structural Engineering* 124(12):1375-1417.
- Toyota, Y., T. Hirose, S. Ono, and K. Shidara. (2017). "Experimental Study on Vibration Characteristics of Prestressed Concrete Beam." *Procedia Engineering* 171:1165-72.
- Trautner, C., M. McGinnis, and S. Pessiki. (2010). "Analytical and Numerical Development of the Incremental Core-Drilling Method of Non-Destructive Determination of in-Situ Stresses in Concrete Structures." *Journal of Strain Analysis for Engineering Design* 45(8):647-58.
- Trautner, C., M. McGinnis, and S. Pessiki. (2011). "Application of the Incremental Core-Drilling Method to Determine In-Situ Stresses in Concrete." *Materials Journal* 108(3):290-99.
- Tureyen, A. K. and R. J. Frosch. (2003). "Concrete Shear Strength: Another Perspective." *Structural Journal* 100(5):609-15.
- Unger, J. F., A. Teughels, and G. de Roeck. (2006). "System Identification and Damage Detection of a Prestressed Concrete Beam." *Journal of Structural Engineering* 132(11):1691-98.
- UNI EN 12390-3. (2003). "Prova Sul Calcestruzzo Indurito Resistenza Alla Compressione Dei Provini."
- UNI EN 12390-13. (2013). *Prova Sul Calcestruzzo Indurito Parte 13: Determinazione Del modulo Di Elasticita Secante in Compressione*.

9-REFERENCES

- Vecchio, F. J. (2000). "Disturbed Stress Field Model for Reinforced Concrete: Formulation." *Journal of Structural Engineering* 126(9):1070–77.
- Vecchio, F. J. (2001). "Disturbed Stress Field Model for Reinforced Concrete: Implementation." *Journal of Structural Engineering* 127(1):12–20.
- Vecchio, F. J. and M. P. Collins. (1986). "MODIFIED COMPRESSION-FIELD THEORY FOR REINFORCED CONCRETE ELEMENTS SUBJECTED TO SHEAR." *Journal of the American Concrete Institute* 83(2):219–31.
- Vecchio, F. J., D. Lai, W. Shim, and J. Ng. (2001). "DISTURBED STRESS FIELD MODEL FOR REINFORCED CONCRETE: VALIDATION." *Journal of Structural Engineering* 127(4).
- Villamizar, S., J. A. Ramirez, and G. Aguilar. (2017). "Shear Strength and Behavior of High-Strength Concrete Prestressed Beams." *Structural Journal* 114(1):277–89.
- Walraven, J. C. and N. Lehwalter. (1989). "Bearing Capacity of Concrete Compression Struts in Strut and Tie Models, Considering the Example of Short Compact Beams - Die Tragfähigkeit von Betondruckstreben in Fachwerkmodellen Am Beispiel von Gedrungenen Balken." *Beton- Und Stahlbetonbau* 84(4):81–87.
- Wang, T. H., R. Huang, and T. W. Wang. (2013). "THE VARIATION OF FLEXURAL RIGIDITY FOR POST-TENSIONED PRESTRESSED CONCRETE BEAMS." *Journal of Marine Science and Technology* 21(3):8.
- de Wilder, K., P. Lava, D. Debruyne, Y. Wang, G. de Roeck, and L. Vandewalle. (2015). "Stress Field Based Truss Model for Shear-Critical Prestressed Concrete Beams." *Structures* 3:28–42.
- Wolf, T. S. and R. J. Frosch. (2007). "Shear Design of Prestressed Concrete: A Unified Approach." *Journal of Structural Engineering* 133(11):1512–19.
- Wollman, G. P. and C. L. Roberts-Wollman. (6AD). *PTI - Post-Tensioning Institute Chapter VIII - Anchorage Zone Design*.
- Wong, P. S., H. Trommels, and F. J. Vecchio. (2013). "VecTor2 and FormWorks User's Manual, 2nd Edition." *Department of Civil Engineering, University of Toronto* 311.
- Xie, L., E. C. Bentz, and M. P. Collins. (2011). "Influence of Axial Stress on Shear Response of Reinforced Concrete Elements." *Structural Journal* 108(6):745–54.
- Xiong, H.-X. and Y.-T. Zhang. (2009). "Theoretical Analysis of Natural Frequency of Externally Prestressed Concrete Beam Based on Rigidity Correction." *Academic Journal of Xi'an Jiaotong University* 21(1):31–35.

- Xuan, X., S. Rizkalla, and K. Maruyama. (1988). "Effectiveness of Welded Wire Fabric as Shear Reinforcement in Pretensioned Prestressed Concrete T-Beams." *Structural Journal* 85(4):429–36.
- Yang, J., T. Guo, and A. Li. (2020). "Experimental Investigation on Long-Term Behavior of Prestressed Concrete Beams under Coupled Effect of Sustained Load and Corrosion." <https://doi.org/10.1177/1369433220919067> 23(12):2587–96.
- Zararis, P. D. and G. Ch. Papadakis. (2001). "Diagonal Shear Failure and Size Effect in RC Beams without Web Reinforcement." *Journal of Structural Engineering* 127(7):733–42.
- Zhang, F., G. I. Z. Garnica, Y. Yang, E. Lantsoght, and H. Sliedrecht. (2020). "Monitoring Shear Behavior of Prestressed Concrete Bridge Girders Using Acoustic Emission and Digital Image Correlation." *Sensors* 2020, Vol. 20, Page 5622 20(19):5622.
- Zhou, W., H. Li, and W. Zhang. (2021). "Experimental Behavior of the Shear Strength of Full-Scale Precast Prestressed Double Tees." *Journal of Building Engineering* 42:102455.
- Zwicky, D. and T. 1955- Vogel. (2000). "Bruchversuche an Ausgebauten Brückenträgern Aus Spannbeton." *IBK Bericht* 258.
- Zwoyer, E. M. and C. P. Siess. (1954). "Ultimate Strength in Shear of Simply-Supported Prestressed Concrete Beams Without Web Reinforcement." *Journal Proceedings* 51(10):181–200.

